THE PHYSICS AND CHEMISTRY OF SOLIDS

AN INTERNATIONAL JOURNAL

VOLUME 19 1961

Editor-in-Chief HARVEY BROOKS *Cambridge, Mass.*

Associate Editors H. B. G. CASIMIR *Eindhoven* G. J. DIENES *Brookhaven* JACQUES FRIEDEL *Paris*

E. M. LIFSHITZ *Moscow*

Editorial Advisory Board

U.S.A.

E. N. ADAMS, Yorktown Heights, [N.Y.
D. ALPERT, Illinois
L. APKER, Schenectady
J. BARDEEN, Illinois
D. S. BILLINGTON, Oak Ridge
R. G. BRECKENRIDGE, Cleveland
LEO BREWER, Berkeley, Calif.
E. BURSTEIN, Penn.
J. A. BURTON, New Jersey
N. CABRERA, Virginia
G. C. DANIELSON, Iowa
I. ESTERMANN, Washington, D.C.
J. C. FISHER, Schenectady
F. HERMAN, Princeton
CONYERS HERRING, New Jersey
A. R. VON HIPPEL, Cambridge, Mass
J. H. HOLLOMON, Schenectady
W. V. HOUSTON, Houston
H. B. HUNTINGTON, Troy
H. M. JAMES, Purdue
C. KITTEL, Berkeley, Calif.
W. KOHN, Pittsburgh
J. A. KRUMHANSL, Cleveland
A. W. LAWSON, Chicago
H. W. LEVERENZ, Princeton
O. T. MARZKE, Pittsburgh
B. T. MATTHIAS, New Jersey
L. R. MAXWELL, Silver Spring
JOSEPH E. MAYER, Chicago
E. W. MONTROLL, Maryland
DAVID PINES, Princeton
GEORGE T. RADO, Washington, D.C.
H. REISS, New Jersey
J. R. REITZ, Cleveland
A. ROSE, Princeton
O. C. SIMPSON, Argonne
R. SMOLUCHOWSKI, Pittsburgh
F. H. SPEDDING, Iowa
D. TURNBULL, Schenectady
J. H. VAN VLECK, Harvard
B. E. WARREN, Cambridge, Mass.
EUGENE P. WIGNER, Princeton
B. H. ZIMM, Schenectady

Canada

R. E. BURGESS, Vancouver
D. K. C. MACDONALD, Ottawa
W. B. PEARSON, Ottawa

United Kingdom

A. CHARLESBY, Shrivenham, Berks.
W. J. DUNNING, Bristol
F. C. FRANK, Bristol
H. K. HENISCH, Reading
H. JONES, London
J. W. MITCHELL, Bristol
A. B. PIPPARD, Cambridge
M. H. L. PRYCE, Bristol
R. A. SMITH, Malvern
K. W. H. STEVENS, Nottingham
F. C. TOMPKINS, London

France

E. F. BERTAUT, Grenoble
A. GUINIER, Orsay
LOUIS NÉEL, Grenoble
LOUIS WEIL, Grenoble

Germany

M. BORN, Bad Pyrmont
ULRICH DEHLINGER, Stuttgart
R. HILSCH, Göttingen
G. LEIBFRIED, Aachen
E. MOLLWO, Erlangen
H. PICK, Stuttgart
H. WELKER, Erlangen

Italy

F. G. FUMI, Pavia

Czechoslovakia

J. TAUC, Praha

Japan

TOSHINOSUKE MUTO, Tokyo

The Netherlands

A. MICHELS, Amsterdam
G. W. RATHENAU, Amsterdam

Sweden

J. O. LINDE, Stockholm
PER-OLOV LÖWDIN, Uppsala

Switzerland

G. BUSCH, Zurich
P. SCHERRER, Zurich

U.S.S.R.

G. S. ZHDANOV, Moscow

PERGAMON PRESS NEW YORK · LONDON · PARIS · LOS ANGELES

Vol. 1
1961

THE PHYSICS AND CHEMISTRY OF SOLIDS

AN INTERNATIONAL JOURNAL

VOLUME 19 1961

Editor-in-Chief HARVEY BROOKS *Cambridge, Mass.*

Associate Editors H. B. G. CASIMIR *Eindhoven* G. J. DIENES *Brookhaven* JACQUES FRIEDEL *Paris*

E. M. LIFSHITZ *Moscow*

Editorial Advisory Board

U.S.A.

E. N. ADAMS, Yorktown Heights, [N.Y.
D. ALPERT, Illinois
L. APKER, Schenectady
J. BARDEEN, Illinois
D. S. BILLINGTON, Oak Ridge
R. G. BRECKENRIDGE, Cleveland
LEO BREWER, Berkeley, Calif.
E. BURSTEIN, Penn.
J. A. BURTON, New Jersey
N. CABRERA, Virginia
G. C. DANIELSON, Iowa
I. ESTERMANN, Washington, D.C.
J. C. FISHER, Schenectady
F. HERMAN, Princeton
CONYERS HERRING, New Jersey
A. R. VON HIPPEL, Cambridge, Mass
J. H. HOLLOMON, Schenectady
W. V. HOUSTON, Houston
H. B. HUNTINGTON, Troy
H. M. JAMES, Purdue
C. KITTEL, Berkeley, Calif.
W. KOHN, Pittsburgh
J. A. KRUMHANSL, Cleveland
A. W. LAWSON, Chicago
H. W. LEVERENZ, Princeton
O. T. MARZKE, Pittsburgh
B. T. MATTHIAS, New Jersey
L. R. MAXWELL, Silver Spring
JOSEPH E. MAYER, Chicago
E. W. MONTROLL, Maryland
DAVID PINES, Princeton
GEORGE T. RADO, Washington, D.C.
H. REISS, New Jersey
J. R. REITZ, Cleveland
A. ROSE, Princeton
O. C. SIMPSON, Argonne
R. SMOLUCHOWSKI, Pittsburgh
F. H. SPEDDING, Iowa
D. TURNBULL, Schenectady
J. H. VAN VLECK, Harvard
B. E. WARREN, Cambridge, Mass.
EUGENE P. WIGNER, Princeton
B. H. ZIMM, Schenectady

Canada

R. E. BURGESS, Vancouver
D. K. C. MACDONALD, Ottawa
W. B. PEARSON, Ottawa

United Kingdom

A. CHARLESBY, Shrivenham, Berks.
W. J. DUNNING, Bristol
F. C. FRANK, Bristol
H. K. HENISCH, Reading
H. JONES, London
J. W. MITCHELL, Bristol
A. B. PIPPARD, Cambridge
M. H. L. PRYCE, Bristol
R. A. SMITH, Malvern
K. W. H. STEVENS, Nottingham
F. C. TOMPKINS, London

France

E. F. BERTAUT, Grenoble
A. GUINIER, Orsay
LOUIS NÉEL, Grenoble
LOUIS WEIL, Grenoble

Germany

M. BORN, Bad Pyrmont
ULRICH DEHLINGER, Stuttgart
R. HILSCH, Göttingen
G. LEIBFRIED, Aachen
E. MOLLWO, Erlangen
H. PICK, Stuttgart
H. WELKER, Erlangen

Italy

F. G. FUMI, Pavia

Czechoslovakia

J. TAUC, Praha

Japan

TOSHINOSUKE MUTO, Tokyo

The Netherlands

A. MICHELS, Amsterdam
G. W. RATHENAU, Amsterdam

Sweden

J. O. LINDE, Stockholm
PER-OLOV LÖWDIN, Uppsala

Switzerland

G. BUSCH, Zurich
P. SCHERRER, Zurich

U.S.S.R.

G. S. ZHDANOV, Moscow

PERGAMON PRESS NEW YORK · LONDON · PARIS · LOS ANGELES

Vol. 1
1961

CONTENTS LISTS FOR VOLUME 19, NOS. 1–4

Volume 19 Numbers 1/2

page

H. SHENKER: Low-field breakdown, non-ohmic conductivity, and photoconductivity of CdS at low temperatures . . . 1

R. R. HAERING and E. N. ADAMS: Esaki tunneling in the presence of magnetic fields . . . 8

C. S. FULLER: Kinetics of donor reactions in oxygen-doped germanium . . . 18

J. W. CABLE, M. K. WILKINSON and E. O. WOLLAN: Neutron diffraction investigation of antiferromagnetism in $CrCl_3$ . . . 29

I. M. LIFSHITZ and V. V. SLYOZOV: The kinetics of precipitation from supersaturated solid solutions . . . 35

S. L. STRONG: Crystal structure distortions in MnO_2 and MnF_2 at their antiferromagnetic Curie temperature 51

HIROSHI SATO: Remarks on the magnetic properties of Au–Mn system . . . 54

S. K. GHOSH: Variation of field effect mobility and Hall effect mobility with the thickness of the deposited films of tellurium . . . 61

P. N. ARGYRES: Derivation of the Boltzmann transport equation for inelastic collisions . . . 66

J. R. REITZ, R. N. SEITZ and R. W. GENBERG: Closed-shell ion–ion interactions in calcium fluoride . . . 73

M. MENES and D. I. BOLEF: Nuclear quadrupole coupling in alkali iodide crystals . . . 79

F. G. ALLEN: Field emission from silicon and germanium; field desorption and surface migration . . . 87

V. CELLI: Screw dislocation in crystals with diamond structure . . . 100

A. J. ROSENBERG and A. J. STRAUSS: Solid solutions of In_2Te_3 in Sb_2Te_3 and Bi_2Te_3 . . . 105

T. RISTE and L. TENZER: A neutron diffraction study of the temperature variation of the spontaneous sublattice magnetization of ferrites and the Néel theory of ferrimagnetism . . . 117

IWAO TERAMOTO and SHIGETOSHI TAKAYANAGI: Relations between the electronic properties and the chemical bonding of $Sb_xBi_{2-x}Te_{3-y}Se_y$ system . . . 124

B. T. MATTHIAS, V. B. COMPTON and E. CORENZWIT: Some new superconductivity compounds . . . 130

R. D. BLAUGHER and J. K. HULM: Superconductivity in the σ and α-Mn structures . . . 134

W. BURTON LEWIS and F. E. PRETZEL: Properties of lithium hydride—III. Paramagnetic resonance of color centers . . . 139

J. C. WOOLLEY, B. R. PAMPLIN and J. A. EVANS: Electrical and optical properties of InAs–In_2Te_3 alloys . . . 147

B. W. FAUGHNAN and M. W. P. STRANDBERG: The role of phonons in paramagnetic relaxation . . . 155

D. M. SMYTH: Deviations from stoichiometry in MnO and FeO . . . 167

Letter to the Editor:

K. ŠMIROUS: Preparation of single crystals of $Zn_xCd_{1-x}Sb$ by interruption of free crystallization of the melt 170

Book Review:

P. R. AIGRAIN: "Electronic Processes in Solids" (reviewed by H. Y. FAN) . . . 172

Volume 19 Numbers 3/4

R. SUBRAMANIAN: Neutron scattering from isotropic lattices . . . 173

W. S. BOYLE and R. E. HOWARD: Transition to the high field limit in the Zeeman spectra of germanium donors 181

J. B. GRUN, M. SIESKIND et S. NIKITINE: Etude spectrophotométrique des spectres continus de Cu_2O à diverses températures . . . 189

A. F. GIBSON, J. W. GRANVILLE and E. G. S. PAIGE: A study of energy-loss processes in germanium at high electric fields using microwave techniques . . . 198

M. A. C. S. BROWN: Deviations from Ohm's law in germanium and silicon . . . 218

C. E. OLSEN: The electrical resistivity of $ZrZn_2$ . . . 228

R. C. NEWMAN and J. WAKEFIELD: The diffusivity of carbon in silicon . . . 230

G. BOGNER: Messungen der elektrischen Leitfähigkeit und des Halleffekts an ZnO-Kristallen und ihre Deutung durch Störbänder . . . 235

C. S. FULLER and F. H. DOLEIDEN: The ionization behavior of donors formed from oxygen in germanium . . . 251

A. S. BALCHAN and H. G. DRICKAMER: The effect of pressure and temperature on the absorption edges of three silver halides . . . 261

A. C. DAMASK, Z. A. FUHRMAN and E. GERMAGNOLI: Electrical resistivity changes in annealed Cu_3Au above the critical temperature . . . 265

A. R. ALLNATT and P. W. M. JACOBS: A.C. polarization effects in the ionic conductivity of potassium chloride crystals . . . 281

page

J. S. Clark and N. Brown: A study of a dilute concentration of disorder in the β-Cu–Zn superlattice . . 291
P. Jaszczyn: L'influence d'irradiation aux neutrons rapides sur le luminophore ZnS–Mn 299
A. Aharoni and M. Schieber: Magnetic moments of yttrium–iron garnets containing light rare earth ions . 304
R. W. Damon and J. R. Eshbach: Magnetostatic modes of a ferromagnetic slab 308
J. E. Aubrey: Cyclotron resonance in bismuth—II. 321
A. Glasner, A. Rejoan and R. Reisfeld: Diffusion of thallous ions in potassium bromide, measured by the spectrophotometric method 331
W. C. Hahn, Jr. and A. Muan: Activity measurements in oxide solid solutions: the systems NiO–MgO and NiO–MnO in the temperature interval 1100–1300°C 338

Book Reviews:

D. Curie: "Luminescence Cristalline" (reviewed by F. E. Williams) 349
G. S. Christiansen and P. H. Garrett: "Structure and Charge, an Introduction to the Science of Matter" (reviewed by J. E. Burke) 349
M. J. Buerger: "Crystal-Structure Analysis" (reviewed by R. E. Marsh) 350

Errata:

J. B. Mullin and K. F. Hulme: Orientation-dependent distribution coefficients in melt-grown InSb crystals 352
G. B. Guthrie and J. P. McCullough: Some observations on phase transformations in molecular crystals 352

Tôme 19 Nos 1/2

H. Shenker: Rupture en champ faible, conductivité non-ohmique et photoconductivité de CdS à basse température 1
R. R. Haering et E. N. Adams: Effet tunnel d'Esaki en présence de champ magnétique 8
C. S. Fuller: Cinétique des réactions faisant intervenir les donneurs dans le germanium dopé par l'oxygène 18
J. W. Cable, M. K. Wilkinson et E. O. Wollan: Etude par diffraction de neutrons de l'antiferromagnetisme de $CrCl_3$ 29
I. M. Lifshitz et V. V. Slyozov: La cinétique de la précipitation à partir de solutions solides sursaturées . 35
S. L. Strong: Distorsion de la structure cristalline de MnO_2 et MnF_2 à leur point de Curie antiferromagnétique 51
H. Sato: Remarques sur les propriétés magnétiques du système Au–Mn 54
S. K. Ghosh: Variation de la mobilité d'effet de champ et de la mobilité d'effet Hall en fonction de l'épaisseur des films de tellurium obtenus par dépôts. 61
P. N. Argyres: Dérivation de l'équation de transport de Boltzmann pour les collisions inélastiques . . 66
J. R. Reitz, R. N. Seitz et R. W. Genberg: Interactions ioniques à couches complètes dans le fluorure de calcium. 73
M. Menes et D. I. Bolef: Couplage quadrupolaire des noyaux dans les cristaux d'iodures alcalins . . 79
F. G. Allen: Emission de champ dans le silicium et le germanium. Désorption et migration de surface provoquée par le champ 87
V. Celli: Dislocation vis dans un cristal ayant la structure du diamant 100
A. J. Rosenberg et A. J. Strauss: Solutions solides de In_2Te_3, dans Sb_2Te_3 et Bi_2Te_3 105
T. Riste et L. Tenzer: Etude par diffraction de neutrons de la variation en température de l'aimantation spontanée de sous-réseaux de ferrites en liaison avec la théorie de Néel du ferrimagnétisme . . . 117
Iwao Teramoto et Shigetoshi Takayanagi: Relations entre les propriétés électroniques et les liaisons chimiques dans les systèmes $Sb_xBi_{2-x}Te_{3-y}Se_y$ 124
B. T. Matthias, V. B. Compton et E. Corenzwit: Quelques nouveaux composés supraconducteurs . . 130
R. D. Blaugher et J. K. Hulm: Supraconductivité dans les structures σ et α-Mn 134
W. Burton Lewis et F. E. Pretzel: Propriétés de l'hydrure de lithium—III Résonance paramagnétique des centres colorés 139
J. C. Woolley, B. R. Pamplin et J. A. Evans: Propriétés électriques et optiques des alliages $InAs–In_2Te_3$. 147
B. W. Faughnan et M. W. P. Strandberg: Le rôle des phonons dans la relaxation paramagnétique . . 155
D. M. Smyth: Ecarts par rapport à la stoechiométrie dans MnO et FeO 167

Lettre au Rédacteur:

K. Šmirous: Préparation de monocristaux de $Zn_xCd_{1-x}Sb$ par interruption de la libre cristallisation de l'alliage fondu 170

Revue de Livre:

P. R. Aigrain: "Electronic Processes in Solids" (revu par H. Y. Fan) 172

Vol. 1
1961

Tôme 19 Nos 3/4

page

R. SUBRAMANIAN: Diffusion des neutrons par les réseaux isotropes . . . 173

W. S. BOYLE et R. E. HOWARD: Transition vers la limite de grand champ du spectre Zeeman des donneurs dans le germanium . . . 181

J. B. GRUN, M. SIESKIND et S. NIKITINE: Etude spectrophotométrique des spectres continus de Cu_2O à diverses températures . . . 189

A. F. GIBSON, J. W. GRANVILLE et E. G. S. PAIGE: Etude dans le germanium des processus de pertes d'énergie à champs électriques éléves par des techniques de micro-ondes . . . 198

M. A. C. S. BROWN: Déviations par rapport à la loi d'Ohm dans le germanium et le silicium . . . 218

C. E. OLSEN: Résistivité électrique de $ZrZn_2$ . . . 228

R. C. NEWMAN et J. WAKEFIELD: La diffusion du carbone dans le silicium . . . 230

G. BOGNER: Mesures de résistivité électrique et de l'effet Hall sur des cristaux de ZnO. Leur signification du point de vue des bandes d'impuretés . . . 235

C. S. FULLER et F. H. DOLEIDEN: L'ionisation des états donneurs créés par l'oxygène dans le germanium . 251

A. S. BALCHAN et H. G. DRICKAMER: L'effet de la pression et de la température sur les limites d'absorption de trois halogénures alcalins . . . 261

A. C. DAMASK, Z. A. FUHRMAN et E. GERMAGNOLI: Changements de résistivité électrique dans Cu_3-Au recuit au-dessus de la température critique . . . 265

A. R. ALLNATT et P. W. M. JACOBS: Effets de polarisation en courant alternatif sur la conductibilité ionique des cristaux de chlorure de potassium . . . 281

J. S. CLARK et N. BROWN: Etude d'un faible désordre dans la surstructure β-Cu–Zn . . . 291

P. JASZCZYN: L'influence d'irradiation aux neutrons rapides sur le luminophore ZnS–Mn . . . 299

A. AHARONI et M. SCHIEBER: Moments magnétiques de grenats yttrium–fer contenant des ions de terres rares légers . . . 304

R. W. DAMON et J. R. ESHBACH: Modes magnétostatiques d'une plaque ferromagnétique . . . 308

J. E. AUBREY: Résonance cyclotron dans le bismuth—II . . . 321

A. GLASNER, A. REJOAN et R. REISFELD: Diffusion d'ions thalleux dans le bromure de potassium, mesurée par la méthode spectrophotométrique . . . 331

W. C. HAHN, Jr. et A. MUAN: Mesures d'activités dans des solutions solides d'oxydes: les systèmes NiO–MgO et NiO–MnO dans l'intervalle de température 1100–1300°C . . . 338

Revue des Livres:

D. CURIE: "Luminescence Cristalline" (revu par F. E. Williams) . . . 349

G. S. CHRISTIANSEN et P. H. GARRETT: "Structure and Change, an Introduction to the Science of Matter" (revu par J. E. Burke) . . . 349

M. J. BUERGER: "Crystal-Structure Analysis" (revu par R. E. Marsh) . . . 350

Errata:

J. B. MULLIN et K. F. HULME: Coefficients de distribution dépendants de l'orientation dans les cristaux de InSb obtenus par fusion . . . 352

G. B. GUTHRIE et J. P. MCCULLOUGH: Quelques observations sur les changements de phase des cristaux moléculaires . . . 352

Band 19 Nr. 1/2

H. SHENKER: Durchschläge bei kleinen Feldern, nichtohmsche Leitfähigkeit und die Photoleitfähigkeit von CdS bei tiefen Temperaturen. . . . 1

R. R. HAERING und E. N. ADAMS: Esaki-Tunneleffekt bei Gegenwart magnetischer Felder. . . . 8

C. S. FULLER: Die Kinetik von Donatorreaktionen in mit Sauerstoff dotiertem Germanium . . . 18

J. W. CABLE, M. K. WILKINSON und E. O. WOLLAN: Untersuchung des Antiferromagnetismus von $CrCl_3$ mit der Neutronenbeugung . . . 29

I. M. LIFSHITZ und V. V. SLYOZOV: Die Ausscheidungskinetik bei übersättigten festen Lösungen . . . 35

S. L. STRONG: Verzerrungen der Kristallstruktur in MnO_2 und MnF_2 bei ihrer antiferromagnetischen Curietemperatur . . . 51

H. SATO: Bemerkungen über die magnetischen Eigenschaften des Au–Mn-Systems . . . 54

S. K. GHOSH: Die Abhängigkeit der Feld-und Hallbeweglichkeit von der Dicke aufgedampfter Tellurfilme . 61

P. N. ARGYRES: Eine Ableitung der Boltzmannschen Transportgleichung für inelastische Streuprozesse . . 66

J. R. REITZ, R. N. SEITZ und R. W. GENBERG: Die Ion–Ion-Wechselwirkungen geschlossener Schalen in Calziumfluorid . . . 73

page

M. Menes und D. I. Bolef: Kern-Quadrupol-Kopplung in Alkalijodidkristallen 79
F. G. Allen: Feldemission von Silizium und Germanium; Felddesorption und Oberflächenwanderung . 87
V. Celli: Schraubenversetzungen in Kristallen mit Diamantstruktur 100
A. J. Rosenberg und A. J. Strauss: Feste Lösungen von In_2Te_3 in Sb_2Te_3 und Bi_2Te_3 105
T. Riste und L. Tenzer: Untersuchung der Temperaturabhängigkeit der spontanen Magnetisierung des Untergitters in Ferriten mit Hilfe der Neutronenbeugung und die Néelsche Theorie des Ferrimagnetismus 117
Iwao Teramoto und Shigetoshi Takayanagi: Beziehungen zwischen den Eigenschaften der Elektronen und der chemischen Bindung des $Sb_xBi_{2-x}Te_{3-y}Se_y$-Systems 124
B. T. Matthias, V. B. Compton und E. Corenzwit: Einige neue supraleitende Verbindungen 130
R. D. Blaugher und K. F. Hulm: Supraleitfähigkeit in den σ-und α-Manganstrukturen 134
W. Burton Lewis und F. E. Pretzel: Eigenschaften von Lithiumhydrit—III. Paramagnetische Resonanz von Farbzentren 139
J. C. Woolley, B. R. Pamplin und J. A. Evans: Elektrische und optische Eigenschaften der InAs–In_2Te_3 Legierungen 147
B. W. Faughan und M. W. P. Strandberg: Die Rolle der Phononen bei der paramagnetischen Relaxation . 155
D. M. Smyth: Abweichungen von der Stöchiometrie in MnO und FeO 167

Brief an den Herausgeber:

K. Šmirous: Herstellung von $Zn_xCd_{1-x}Sb$-Einkristallen durch Unterbrechung der freien Kristallisation aus der Schmelze 170

Buchbesprechung:

P. R. Aigrain: "Electronic Processes in Solids" (besprochen von H. Y. Fan) 172

Band 19 Nr. 3/4

R. Subramanian: Neutronenstreuung an bei isotropen Gittern 173
W. S. Boyle und R. E. Howard: Der Übergang zum Grenzfall hoher Felder im Zeemanspektrum der Donatoren in Germanium 181
J. B. Grun, M. Sieskind und S. Nikitine: Spektrophotometrische Untersuchung der kontinuierlichen Spektren des Cu_2O bei verschiedenen Temperaturen 189
A. F. Gibson, J. W. Granville und E. G. S. Paige: Eine Untersuchung der Energieverluste in Germanium bei hohen elektrischen Feldern mit Hilfe der Mikrowellentechnik 198
M. A. C. S. Brown: Abweichungen vom Ohmschen Gesetz in Germanium und Silizium 218
C. E. Olsen: Der elektrische Widerstand von $ZrZn_2$ 228
R. C. Newman und J. Wakefield: Die Diffusion des Kohlenstoffs in Silizium 230
G. Bogner: Messungen der elektrischen Lietfähigkeit und des Halleffects an ZnO-Kristallen und ihre Deutung durch Störbänder 235
C. S. Fuller und F. H. Doleiden: Das Ionisationsverhalten von durch Sauerstoff gebildeten Donatoren in Germanium 251
A. S. Balchan und H. G. Drickamer: Die Druck- und Temperaturabhängigkeit der Absorptionskanten der drei Silberhalogenide 261
A. C. Damask, Z. A. Fuhrman und E. Germagnoli: Änderungen des elektrischen Widerstandes oberhalb der kritischen Temperatur in angelassenem Cu_3Au 265
A. R. Allnatt und P. W. M. Jacobs: Wechselstrom-Polarisationseffekte bei der Ionenleitfähigkeit von Kaliumchloridkristallen 281
J. S. Clark und N. Brown: Eine Untersuchung der in verdünnter Konzentration auftretenden ungeordneten Bereichen in der β-Cu–Zn-Überstruktur 291
P. Jaszczyn: Der Einfluss einer Bestrahlung mit schnellen Neutronen auf den ZnS–Mn-Phosphor . . . 299
A. Aharoni und M. Schieber: Magnetische Momente von Yttrium–Eisen Granaten die Ionen der leichten seltenen Erden enthalten 304
R. W. Damon und J. R. Eshbach: Magnetostatische Wellen einer ferromagnetischen Scheibe 308
J. E. Aubrey: Zyklotronresonanz in Wismut—II 321
A. Glasner, A. Rejoan und R. Reisfeld: Diffusion von Thalliumionen in Kaliumbromid gemessen mit der spektrophotometrischen Methode 331
W. C. Hahn, Jr. und A. Muan: Aktivitätsmessungen in festen Oxydlösungen: Die Systeme NiO–MgO und NiO–MnO im Temperaturbereich 1100–1300°C 338

Buchbesprechungen:

D. Curie: "Luminescence Cristalline" (besprochen von F. E. Williams) 349

Vol. 1
196

page

Р. С. Нейман и И. Уейкфилд: Коэфициент диффузии углерода в кремнии 230
Г. Богнер: Измерения электрической проводимости и эффекта Холла кристаллов ZnO и влияние на них примесей 235
К. С. Фуллер и Ф. Долейден: Ионизационное поведение доноров, образованных кислородом в германии 251
А. С. Балчан, Г. Дрикамер: Влияние давления и температуры на край поглощения в трех галогенидах серебра 261
А. Дамаск, З. А. Фурман и Е. Германьоли: Изменения электрического сопротивления в отоженном Cu_3Au при температурах выше критической 265
А. Р. Аллнатт и П. В. М. Джекобс: Поляризуционные эффекты в ионной проводимости для переменного тока в кристаллах 281
Дж. С. Кларк и Н. Броун: Исследование слабой концентрации беспорядка в сверхструктуре β-Cu–Zn . 291
П. Яшцын: Влияние облучения быстрыми нейтронами на люминофор ZnS–Mn 299
А. Ааарони, М. Шибер: Магнитные моменты иттрий-железных гранатов, содержащих легкие редкоземельные ионы 304
Р. В. Дамон и Дж. Р. Эшбах: Магнетостатические моды ферромагнитного стержня 308
Дж. Обри: Циклотронный резонанс в висмуте—II 321
А. Гласнер, А. Реджоан и Р. Рейсфельд: диффузия таллиевых ионов в бромиде калия, измеренная спектрофотометрическим методом 331
В. Хан, мл. и А. Мюан: Измерения активности в окисных твердых растворах: системы NiO–MgO и NiO–MnO в интервале температур 1100–1300°С 338

Рецензии на книги:

Д. Кури: "Luminescence Cristalline" (рецензент Ф. И. Виллиамс) 349
Дж. С. Кристянсен и П. Х. Гаррет: "Structure and Change, an Introduction to the Science of Matter" (рецензент Д. Ж. И. Бурк) 349
М. Дж. Бургер: "Crystal-Structure Analysis" (рецензент Р. И. Марш) 350

Опечатка:

Ж. Б. Муллин и К. Ф. Хулм: Коэффициенты зависящего от ориентации распределения образованных при расплавлении кристаллов 352
Г. Б. Гугри и Дж. П. МакКуллоу: Некоторые наблюдения фазовых переходов в молекупярных кристаллох 352

ol. 19
1961

AUTHOR INDEX TO VOLUME 19

(B) denotes book review (E) denotes erratum

Adams, E. N. 8
Aharoni, A. 304
Allen, F. G. 87
Allnatt, A. R. 281
Argyres, D. N. 66
Aubrey, J. E. 321
Balchan, A. S. 261
Blaugher, R. D. 134
Bogner, G. 235
Bolef, D. I. 79
Boyle, W. S. 181
Brown, M. A. C. S. 218
Brown, N. 291
Burke, J. E. 349 (B)
Cable, J. W. 29
Celli, V. 100
Clark, J. S. 291
Damask, A. C. 265
Damon, R. W. 308
Doleiden, F. H. 251
Drickamer, H. G. 261
Eshbach, J. R. 308
Evans, J. A. 147
Fan, H. Y. 172 (B)
Faughnan, B. W. 155
Fuhrman, Z. A. 265
Fuller, C. S. 18, 251
Genberg, R. W. 73
Germagnoli, E. 265
Ghosh, S. K. 61
Gibson, A. F. 198
Glasner, A. 331
Granville, J. W. 198
Grun, J. B. 189
Guthrie, G. B. 352 (E)
Haering, R. R. 8
Hahn, W. C. Jr. 338
Howard, R. E. 181
Hulm, J. K. 134
Hulme, K. F. 352 (E)
Jacobs, P. W. M. 281
Jaszczyn, P. 299
Lewis, W. B. 139
Lifshitz, I. M. 35
Marsh, R. E. 350 (B)
McCullough, J. P. 352 (E)
Menes, M. 79
Muan, A. 338
Mullin, J. B. 352 (E)
Newman, R. C. 230
Nikitine, S. 189
Olsen, C. E. 228
Paige, E. G. S. 198
Pamplin, B. R. 147
Pretzel, F. E. 139
Reisfeld, R. 331
Reitz, J. R. 73
Rejoan, A. 331
Riste, T. 117
Rosenberg, A. J. 105
Sato, H. 54
Schieber, M. 304
Seitz, R. N. 73
Shenker, H. 1
Sieskind, M. 189
Slyozov, V. V. 35
Šmirous, K. 170
Smyth, D. M. 167
Strandberg, M. W. P. 155
Strauss, A. J. 105
Strong, S. L. 51
Subramanian, R. 173
Takayanagi, S. 124
Tenzer, L. 117
Teramoto, I. 124
Wakefield, J. 230
Wilkinson, M. K. 29
Williams, F. E. 349 (B)
Wollan, E. O. 29
Woolley, J. C. 147

page

G. S. Christiansen und P. H. Garrett: "Structure and Change, an Introduction to the Science of Matter" (besprochen von J. E. Burke) 349
M. J. Buerger: "Crystal-Structure Analysis" (besprochen von R. E. Marsh) 350

Errata:
J. B. Mullin und K. F. Hulme: Orientierungsabhängige Verteilungskoeffizienten in aus der Schmelze gezüchteten InSb–Kristallen 352
G. B. Guthrie und J. P. McCullough: Einige Beobachtungen über Phasentransformationen in Molekülkristallen 352

Том 19 На. 1/2

Г. Шенкер: Низковольтный пробой, не-омическая проводимость и фотопроводимость CdS при низких температурах 1
Р. Р. Херринг и Е. Н. Адамс: Туннельный эффект Есаки в магнитном поле 8
К. С. Фуллер: Кинетика донорных реакций в германии, загрязненном кислородом 18
Дж. В. Кейбл, М. К. Вилькинсон и Е. О. Воллан: Нейтронографическое исследование антиферромагнетизма $CrCl_3$ 29
И. М. Лифшиц и В. В. Слезов: О кинетике диффузионного распада пер есыщенных твердых растворов 35
С. Л. Стронг: Дефекты кристаллической структуры в MnO_2 и MnF_2 и их антиферромагнитная точка Кюри 51
Х. Сато: Замечания о магнитных свойствах системы Au–Mn 54
С. К. Гош: Изменение подвижности в зависимости от толщины напыленной пленки теллура . . . 61
П. Н. Аргирес: Отклонение от Больтцманновского уравнения переноса при неупругих столкновениях . 66
Дж. Р. Рейтц, Р. Н. Зейтц и Р. В. Генберг: Взаимодействие ионов с замкнутыми оболочками в флюорите кальция 73
М. Менес и Д. И. Болеф: Ядерная квадрупольная связь в кристаллах иодидов щелочных металлов . 79
Ф. Аллен: Холодная эмиссия из кремния и германия 87
В. Челли: Винтовые дислокации в кристаллах типа алмаза 100
А. Ц. Розенберг и А. Страусс: Твердые растворы In_2Te_3 в Sb_2Te_3 и Bi_2Te_3 105
Т. Ристе и Л. Тензер: Исследование зависимости непосредственной подрешеточной магнетизации ферритов от температуры с помощью нейтронной диффракции и теория ферримагнетизма Неела . . 117
И. Терамото и Ш. Такаянаги: Взоимоотношение между электронными свойствами и химической связью в системе $Sb_xBi_{2-x}Te_{3-y}Se_y$ 124
Б. Т. Маттиас, В. Б. Комптон и Е. Коренцвит: Некоторые новые сверхпроводящие соединения . . 130
Р. Д. Блауер и И. К. Хулм: Сверхпроводимость структур σ- и α-Mn 134
В. Б. Льюис и Ф. Е. Претцель: Свойства гидрида лития—Ш. Парамагнитный резонанс центров окраски 139
Дж. Вуллей, Б. Р. Памплин и Дж. А. Эванс: Электрические и оптиче ские свойства сплавов $InAs–In_2Te_3$ 147
Б. В. Фогнан и М. В. Страндберг: Роль фононов в парамагнитной релаксации 155
Д. М. Смит: Отклонения от стехиометрии в MnO и FeO 167

Письмо в редакцию:
К. Шмироус: Изготовление монокристаллов $Zn_xCd_{1-x}Sb$ путем прерывания свободной кристаллизации расплава 170

Рецензия на книга:
П. Р. Егрейн: "Electronic Processes in Solids" (рецензент Х. Фан) 172

Том 19 На. 3/4

Р. Субраманиан: Рассеяние нейтронов изотропными решетками 173
В. М. Бойль и Р. Е. Говард: Переход к пределу сильных полей в зеемановском спектре доноров в германии 181
Дж. Грун, М. Сискинд и С. Никитин: Спектрофотометрическое исследование сплошного спектра Cu_2O при различных температурах 189
А. Ф. Гибсон, Ж. Гранвилль и Е. Пэйдж: Исследование процессов потери энергии в германии в сильных электрических полях с помощью микроволновой техники 198
М. Броун: Отклонения от закона Ома в германии и кремнии 218
К. Е. Олсен: Электрическое сопротивление $ZrZn_2$ 228

Vol. 1
196

J. Phys. Chem. Solids Pergamon Press 1961. Vol. 19, Nos. 1/2, pp. 1–7. Printed in Great Britain.

LOW-FIELD BREAKDOWN, NON-OHMIC CONDUCTIVITY, AND PHOTOCONDUCTIVITY OF CdS AT LOW TEMPERATURES*

H. SHENKER

U.S. Naval Research Laboratory, Washington 25, D.C.

(*Received* 1 *August* 1960)

Abstract—Low temperature electrical conductivity and photoconductivity effects were investigated in highly doped CdS samples having room temperature resistivities in the range 0·08–15 ohm-cm. These samples were found to have a low-field breakdown effect at electric fields which varied from 265 V/cm to as high as 5500 V/cm depending on the sample. At fields below the breakdown field, the conductivity was concluded to be of the impurity band conduction type since the Hall mobility at 4·2°K was found to be less than 0·03 cm²/V-sec. At these fields the conductivity was found to increase markedly as the applied electric field was increased. These crystals were found to exhibit an impurity photoconductivity effect with a maximum response at 28μ and a long-wave cut-off at 32μ.

INTRODUCTION

WITH DUE regard for its larger energy gap and our relatively poor knowledge of and control over its impurity content, there should be a parallel between many of the low temperature properties of CdS and those of germanium and silicon. In the present work, CdS crystals heavily doped with *n*-type impurities were used. It was found, in analogy with effects found in germanium and silicon, that these crystals exhibited impurity band type conduction, low-field breakdown effect, and impurity photoconductivity. In contrast with germanium, it was found that the conductivity at 4·2°K at electric fields below the breakdown field depended strongly upon the applied field; in several cases the conductivity increased by three orders of magnitude before the breakdown field was reached.

DESCRIPTION OF SAMPLES

The samples used in this work were grown by the method described by BISHOP and LIEBSON[1]. While the crystals were not intentionally doped, the source of doping was traced to halogen impurities in the H_2S used. Changing to a more highly purified gas yielded insulating crystals. Therefore, although the nature of the impurities is not known with certainty, it is probably mostly Cl with smaller amounts of the other halogens. BUBE[2] reports the impurity energy level of Cl in CdS as 0·038 eV based on resistance vs. temperature measurements; in the present work a value of 0·034 eV was found based on Hall measurements. The agreement between these values despite the difference in measurement methods and the different degree of doping of the samples is consistent with Cl being the major impurity in our samples. The crystals have the same green-yellow color that is usually associated with high-purity CdS. The room temperature resistivity of the crystals was between 0·08 and 15 ohm-cm. Using reasonable values of mobility, the resistivity values lead to $N_D - N_A$ values between 2×10^{15} and 8×10^{17}/cm³. One of the crystals was intentionally doped with silver after growth. All the electrical measurements were made with the current direction parallel to the "*c*" axis unless otherwise mentioned.

A Hall measurement was made on one sample between 4·2° and 300°K. The mobility at 4·2°K

* A preliminary report on this work was presented at the meeting of the American Physical Society in New York, January, 1960.

was found to be less than 0·03 cm²/volt-sec. The data was analyzed on the assumption that only one type of carrier was effective. For the sake of simplicity and also because the proper value of the multiplying factor is not known, the number of carriers, n, was taken as given by the equation, $n = 1/(R_H ec)$. The values obtained for

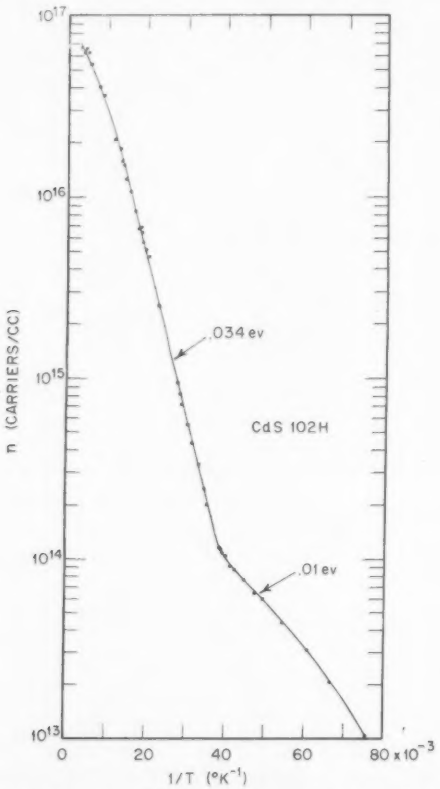

FIG. 1. Density of current carriers in the conduction band as a function of the reciprocal of the absolute temperature for a typical CdS crystal.

n and the mobility are given in Figs. 1 and 2 respectively. The determination of the impurity energy levels from a curve, such as shown in Fig. 1, without having information on the number of acceptor impurities as well as the number of shallow donor impurities, i.e. impurities which are almost completely ionized in the temperature range of interest, is uncertain. This problem has been discussed widely in the standard works on semiconductors, for example in the books by SHOCKLEY[3] and SMITH[4]. In general if the net number of acceptor impurities, N_A', i.e. the number of singly-ionized acceptor impurities less the number of singly-ionized shallow donor impurities, is much smaller than n, then $\ln n \propto E_t/2kT$ while if it is much larger than n, then $\ln n \propto E_t/kT$. In a semiconductor with one donor level and a small amount of compensation, the slope of the

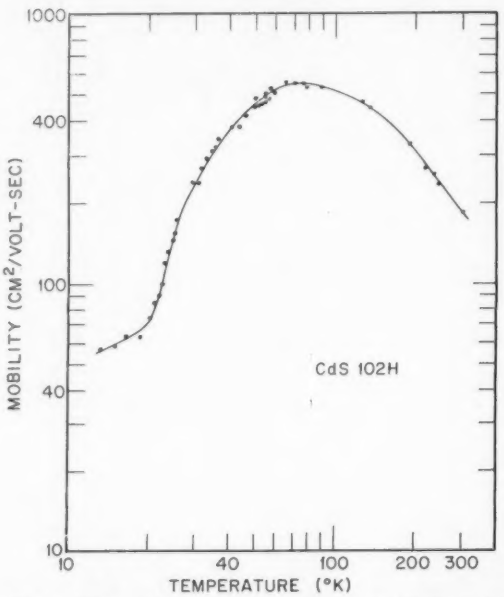

FIG. 2. Hall mobility vs. temperature for the CdS crystal of Fig. 1.

$\ln n$ vs. $1/T$ curve is $E_t/2k$ for high values of T (low values of $1/T$) and changes to twice this slope at low temperatures (high values of $1/T$). This is not the case in the present instance. Instead the slope at high temperatures reduces to a smaller slope in the low temperature region with a transition region at about 25°K. This decrease in slope, which is in a temperature region in which there is still a sizeable Hall mobility, is undoubtedly due to a shallower level of donor impurities. Since in the higher temperature range these impurities will offset the acceptor impurities, N_A' will be small and, therefore, $\ln n \propto E_t/2kT$. Since there does not appear to be any peculiarity about the curve in the vicinity of the transition point, it is reasonable

to assume that N_A' will be small in the 20 to 25°K temperature region so that the relation, $\ln n \propto E_i'/2kT$, will be valid here also, where E_i' is the energy level of the shallower impurity. It is seen that the curve tends to a larger slope at the lowest temperatures plotted; this appears to be due to a transition to the E_i'/k slope, so that N_A' is of the order of 10^{13}/cm^3 in this region.

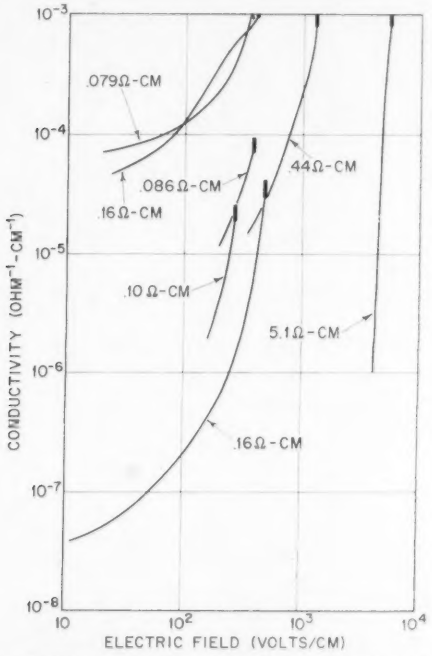

FIG. 3. The electrical conductivity vs. applied electric field for several CdS samples at 4·2°K. The curves are labeled with the room temperature resistivity of the samples.

From the above analysis we conclude that there are more than $6{\cdot}6\times10^{16}$/cm^3 of donor impurities at 0·034 eV below the conduction band and there are somewhat more than 10^{14}/cm^3 donor impurities at 0·01 eV below the conduction band. As shown in Fig. 2, the mobility of the sample has a maximum value of 570 cm^2/volt-sec at 70°K. At the higher temperatures, the mobility is proportional to $T^{-1\cdot3}$ while between 20 and 30°K it is proportional to $T^{3\cdot7}$. This latter variation is much larger than would be expected from ionized impurity scattering. The reason for the low temperature "tail" in the mobility was not determined.

NON-LINEAR CONDUCTIVITY EFFECTS BELOW THE BREAKDOWN FIELD

A large part of the experimental work involved the measurement of the current–voltage relation for the CdS crystals at liquid helium temperatures in the cold dark. At first, a direct-current measurement using the customary four-terminal technique was adopted. It was found that the molten-indium contacts were very close to ohmic so that a two-terminal method yielded the same results as the four-terminal method and had the advantages that shorter samples could be measured and that it was simpler to adapt to pulsed electric-field measurements. For many of the crystals, heating effects were found to be important even though the crystals were immersed in liquid helium; therefore, most of the final measurements were made using triangular voltage pulses having a rise time of about 10 microseconds and a decay time of about 50 microseconds. Measurements of current vs. voltage were made directly on an oscilloscope.

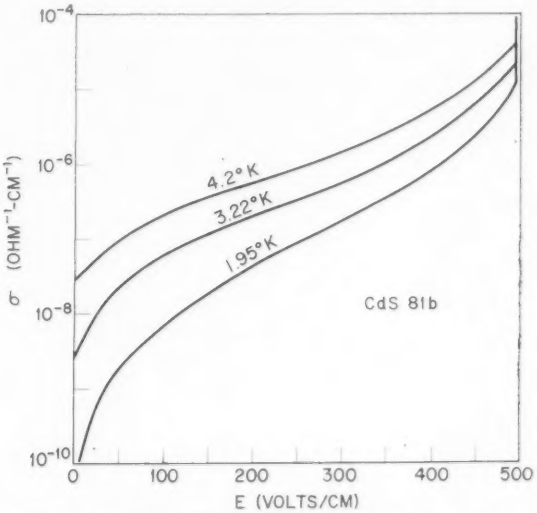

FIG. 4. The electrical conductivity vs. applied electric field obtained by a d.c. measurement for a CdS sample. at several low temperatures.

The curves of conductivity vs. electric field are shown on a log–log plot in Fig. 3. The heavy vertical lines indicate the onset of breakdown. The change of conductivity with applied electric field is very marked. Similar curves shown on a

semi-log plot for a single sample at 4·2°K and lower temperatures are shown in Fig. 4. From these curves it can be seen that the conductivity is exponentially dependent upon the first power of the electric field even for the smallest field used, and has one slope up to about 40 V/cm and changes to a smaller slope from 100 to 240 V/cm. As the temperature is lowered, the zero-field conductivity, σ_0, decreases, but the slope of the curves at low fields increases. If one considers just the portion

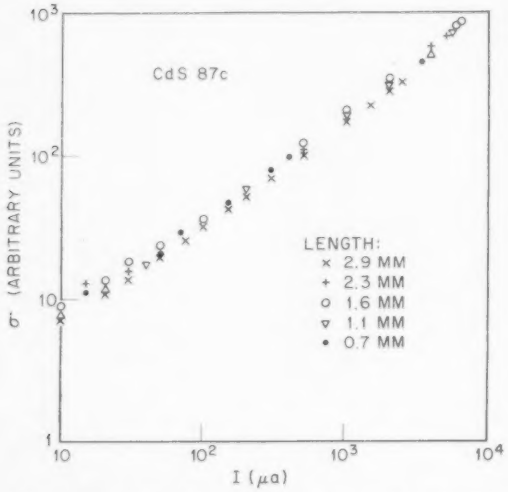

FIG. 5. The electrical conductivity vs. sample current for a CdS crystal at 4·2°K with different distances between contacts.

of the curves below 40 V/cm, then the conductivity may be expressed by the equation:

$$\sigma = \sigma_0(T) \exp(a(T)E).$$

It is found that

$$\sigma_0(T) = \sigma_{00} \exp(-0{\cdot}0020/kT)$$

and

$$a(T) = a_0 \exp(+0{\cdot}0005/kT)$$

where there is some uncertainty in the values of $a(T)$. Most crystals show similar effects although the details of the curves may be different.

In order to determine the effect of crystal length upon the non-ohmic characteristic of the crystals, measurements were made on several crystals of the current–voltage relation as the electrodes were placed closer and closer together on the crystal. The results of the most complete set of measurements is shown in Fig. 5. Here the conductivity is plotted against sample current for different lengths of the same crystal. It is seen that the conductivity vs. crystal current relation does not change with sample length to within the experimental error of determining the effective distance between contacts. This result conclusively rules out contact effects and space-charge-limited currents as possible causes of the non-ohmic effects.

For magnetic fields up to 9000 Oe, there was no observable change in the conductivity.

THE LOW-FIELD BREAKDOWN EFFECT

The current vs. applied voltage curve of CdS exhibits a sharp break when the voltage is increased with the current increasing one or more orders of magnitude without any change in voltage. The exact shape of the curve appears to be determined by thermal heating which may change the breakdown e.m.f. Except for the magnitude of the electric field required, the current vs. voltage curve near the breakdown field is very much like the one obtained for germanium.[5,6] For several crystals the breakdown field was measured as a function of the distance between contacts, and it was determined that within experimental error the breakdown electric field is independent of the length of the sample. This observation rules out as possible causes for the low-field breakdown effects such as contact effects and space-charge-limited current effects. In Fig. 3 the vertical thick lines indicate the onset of low-field breakdown for several samples. One of the samples, 79Ag, was deliberately doped with silver after growth, this sample had an exceptionally high breakdown field of 5500 V/cm.

The field required for breakdown did not depend on whether the measurement was made parallel or perpendicular to the c axis of the crystal. The breakdown field increased only slightly when a magnetic field was applied perpendicular to the current direction; an increase of 2 per cent in the breakdown field with an applied field of 8000 Oe was typical. Similarly the breakdown field changed only a small amount with temperature; a decrease of the breakdown field of 1 per cent for a temperature rise of 2·5°K was typical.

An attempt was made to measure the Hall effect by a pulse method while the sample was in the breakdown condition. Difficulty was experienced with this measurement due to the high impedance of the sample prior to breakdown. It was determined, however, that the Hall mobility was less than 200 cm^2/volt-sec.

INFRARED PHOTOCONDUCTIVITY AND TRANSMISSION

The infrared transmission of several samples of CdS with different room-temperature conductivities was measured and the results are shown in Fig. 6. Since the crystals were very brittle, no

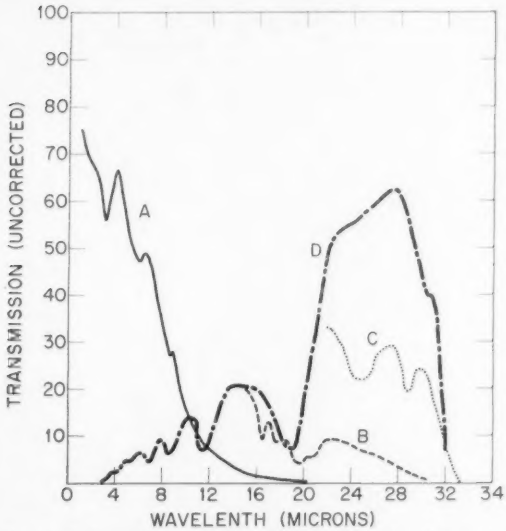

FIG. 6. Infrared transmission and photoconductivity vs. wavelength of CdS crystals at 4·2°K.

Curve A is the transmission of a highly doped CdS sample.
Curve B is the transmission of a less highly doped CdS sample.
Curve C is the transmission of an insulating CdS sample.
Curve D is the photoresponse of a CdS sample on a constant energy basis.

effort was made to polish them, but selected flat platelets were used. It is not known what fraction of the light was reflected or scattered by unevennesses in the surfaces or striations in the interior of the crystal. Sample A was the most heavily doped, and, as expected, it shows the largest absorption, particularly above 15 μ where it becomes almost opaque. Sample B was less highly doped and shows a smaller absorption although it, too, becomes very absorbing at the long wavelengths. Sample C was an insulating crystal and is seen to be much more transparent than the other two. The apparent transmission goes to zero at 33 μ, however, this is probably due to the high reflection due to lattice absorption effects as reported by COLLINS[7]. From the present transmission data it appears impossible to obtain the energy level of the impurity because of interference by absorption due to the lattice.

Curve D shows the relative photoconductivity of a highly doped sample when placed in a helium photoconductivity Dewar with a KRS-5 window. The plot shows the conductivity vs. wavelength computed on a constant energy input basis, and in this case the peak response is at 28 μ. At its peak the detectivity of the CdS detector was approximately equal to that of a thermocouple. On a constant photon flux basis, the sensitivity is approximately constant from 21 to 28 μ. The principal source of noise was $1/f$ noise which is presumed to arise in the contacts. There is a great deal of presently unexplained structure in the photo-response curve. In order to untangle the causes for this structure it will undoubtedly be necessary to obtain transmission and photoconductivity data from the same sample.

DISCUSSION

Data on crystals which are similar to the ones reported on are not available in the literature. BUBE[2] reported resistance vs. temperature measurements on a Cl doped conducting crystal which had a large degree of compensation so that the relation, $\ln n \propto E_t/kT$, held. On this basis, he obtained an energy level of 0·038 eV for Cl in CdS which, considering the difference in degree of compensation and measurement techniques, is in reasonable agreement with the value of 0·034 eV found in the present work. Below 20°K, BUBE found that the slope of the $\ln \rho$ vs. T^{-1} curve corresponded to 0·0015 eV, which on the basis of present evidence is probably due to an impurity band conduction effect.

Extensive Hall effect measurements were made on conducting CdS crystals from 25 to 700°K by KROGER *et al*[8]. Their Cl doped crystals all

had large amounts of compensation so that their results are not directly comparable with the present work. It is interesting to note that for some of their samples they also found a rapid variation of the mobility with temperature in the 25 to 50°K range. They reported that their samples exhibited impurity band conduction. This has been dramatically confirmed in the present work at helium temperatures where the mobility was found to be less than 0·03 cm^2/V-sec.

MIYAZAWA *et al.*[9] have reported mobility measurements on conducting CdS crystals with no intentionally added compensation for temperatures above 80°K. There is close agreement in the shape of the mobility vs. temperature curve between their results and the present work although their samples have a smaller doping level and a slightly higher mobility.

In view of the above comparisons, it may be concluded that the present Hall measurement results are not inconsistent with previously reported results.

LAMPERT *et al.*[10] gave as a criterion for the non-occurrence of low-field breakdown the existence of a condition in which the "hot" carrier can lose a large fraction of its energy through the emission of a single phonon before it reaches the threshold energy for impurity ionization. From the data of COLLINS[7], the energy of the transverse optical phonon of CdS is 0·027 eV. In the present samples there are impurities at 0·034 and 0·01 eV so that if the 0·01 eV donors are responsible for the low-field breakdown, LAMPERT's criterion is obeyed. The addition of Ag in sample 79Ag undoubtedly compensated out most if not all of the 0·01 eV level donors so that it is not surprising that the breakdown field is so large in this instance. In contrast to the situation in germanium where the effect of magnetic field on the breakdown field is large, the effect in the case of CdS is small. This small effect is undoubtedly correlated with the low mobility of free carriers in CdS. According to the data presented in Table 1, the breakdown field is not particularly correlated with the room temperature conductivity of the samples. This is not surprising since the number of 0·01 eV level donors is not necessarily correlated with the conductivity of the samples.

Table 1. *Breakdown field and conductivity at zero field of* CdS *samples.*

Sample	σ ($ohm^{-1}\,cm^{-1}$) (300°K)	Breakdown field (V/cm)	σ_0 ($ohm^{-1}\,cm^{-1}$) (4·2°K)
87c	12·7	1280	$4{\cdot}0\times10^{-6}$
80a	11·6	376	$1{\cdot}6\times10^{-6}$
81c	10·0	265	$9{\cdot}5\times10^{-7}$
81b	6·2	475	$6{\cdot}0\times10^{-8}$
91a	6·2	490	$3{\cdot}5\times10^{-5}$
82d	1·56	695	$<10^{-8}$
82b	1·09	780	$<10^{-8}$
79Ag	0·20	5500	$<10^{-9}$
XIX-2	0·067	590	$<10^{-8}$

While there is little question that the conductivity at low electric fields is due to impurity band conduction, there is a question as to which one of the donor levels is principally responsible for the conduction. From the data in Table 1, it is seen that the zero-field conductivity at 4·2°K is correlated with the room temperature conductivity except for sample 91a which has an anomalously high conductivity. This correlation is to be expected if the zero-field conductivity is due principally to impurity band conduction associated with the 0·034 eV donors since the number of these donors is directly proportional to the room temperature conductivity. On the other hand, since the 0·034 eV band is full as indicated by the presence of 0·01 eV donors, the "compensation"

Vol. 196

type of impurity band conduction discussed by MOTT[11], PRICE[12], and CONWELL[13] should not occur. Nor is it to be expected that the overlap of this band with the conduction band is sufficient to yield appreciable conductivity. Experimentally, it is found that when additional acceptors are added, as in the case of the silver doped sample, the conductivity goes down markedly. This would not occur if the conductivity were due to conduction in a full 0·034 eV donor band. While the situation is not clear-cut, the weight of the evidence is that the impurity band conduction is in the 0·01 eV donor band. The non-ohmic characteristic of the impurity band conduction is not generally found in germanium and silicon although a similar effect has been observed in one sample of silicon at this laboratory. No definite explanation of the non-ohmic conductivity is known at the present time. A possible explanation is as follows: If the impurity band responsible for the conduction is not entirely filled, if its width is greater than kT, and if the electrons in this band are "heated" by the electric field, then the relative occupation of the levels in the band will be changed with the application of the electric field thus giving rise to an increase in the conductivity. This effect could be investigated by looking at samples with controlled numbers and types of impurities and compensations. At present it is not feasible to do this with CdS, but silicon appears to be a suitable material for such research.

Acknowledgements—The author is indebted to M. BISHOP for growing most of the samples used in this work, to B. HENVIS for performing the infrared measurements, to Dr. R. F. WALLIS for many helpful discussions, and to Dr. R. ROBINSON of the Armour Research Foundation for a stimulating discussion which helped initiate this research.

REFERENCES

1. BISHOP M. E. and LIEBSON S. H., *J. Appl. Phys.* **24,** 660, 963 (1953).
2. BUBE R. H., *J. Chem. Phys.* **23,** 18 (1955).
3. SHOCKLEY W., *Electrons and Holes in Semiconductors.* Van Nostrand, New York (1950).
4. SMITH R. A., *Semiconductors.* Cambridge University Press, London (1959).
5. SCLAR N. and BURSTEIN E., *J. Phys. Chem. Solids* **2,** 1 (1957).
6. KOENIG S. H. and GUNTHER-MOHR G. R., *J. Phys. Chem. Solids* **2,** 268 (1957).
7. COLLINS R. J., *J. Appl. Phys.* **30,** 1135 (1959).
8. KROGER F. A., VINK H. J. and VOLGER J., *Philips Res. Rep.* **10,** 39 (1955).
9. MIYAZAWA H., MAEDA H. and TOMISHIMA H., *J. Phys. Soc. Japan* **14,** 41 (1959).
10. LAMPERT M. A., HERMAN F. and STEELE M. C., *Phys. Rev. Letters* **2,** 394 (1959).
11. MOTT N. F., *Canad. J. Phys.* **34,** 1356 (1956).
12. PRICE P. J., *IBM Journal* **2,** 123 (1958).
13. CONWELL E. M., *Phys. Rev.* **103,** 51 (1956).

Vol. 19
1961

J. Phys. Chem. Solids Pergamon Press 1961. Vol. 19, Nos. 1/2, pp. 8–17. Printed in Great Britain.

ESAKI TUNNELING IN THE PRESENCE OF MAGNETIC FIELDS

R. R. HAERING and E. N. ADAMS

IBM Research Center, Yorktown Heights, New York

(*Received* 26 *September* 1960)

Abstract—The theory for Esaki tunneling in the presence of a magnetic field is given for both transverse and longitudinal magnetic fields; it is shown that there are important qualitative differences between the two cases. Expressions are given for the normalized current $I(B)/I(0)$ in both field orientations in the limit of strong magnetic field. It is found that oscillations of the de Haas–Van Alphen type are not to be expected.

1. INTRODUCTION

IT HAS been observed by ESAKI[1] and by CALAWA *et al.*[2] that the tunnel current in an Esaki diode may be markedly reduced by the application of a sufficiently large magnetic field. The effect is observed whether the magnetic field is parallel or perpendicular to the direction of current flow (hereafter referred to as the longitudinal or transverse case, respectively). CALAWA *et al.*[2] have attributed this effect to the "formation of magnetic sub-bands" and have given a theoretical expression for the current reduction caused by a longitudinal field. A similar expression has been deduced by PRICE[3] for the same field orientation.

In this paper we present a simple theory of tunneling in the presence of a magnetic field valid for the transverse as well as for the longitudinal field orientation. Our object is primarily to exhibit the physical origin and the order of magnitude of such magnetic field effects. No attempt is made to represent the complex features of real band structures and the theory is quantitative only to the extent of relating the tunnel current in very strong field to that in zero field. We shall begin with a brief qualitative account of the physical mechanisms of current reduction.

There are several ways in which the magnetic field affects tunneling, each having the effect of altering the rate of decay of the wave function in the junction region. This decay rate depends exponentially on the quantity

$$(1/\hbar)\int\{2m[V(x)-E_x]\}^{1/2}\,dx$$

where the x direction is normal to the junction, $V(x)$ is the junction potential (including a magnetic potential in the transverse case) and E_x is the energy of motion perpendicular to the junction.

One way in which the magnetic field affects the tunneling is to change the effective energy gap and hence the junction potential $V(x)$. This, for example, is the principal result of the spin paramagnetic interaction with the magnetic field. A second way is to reduce the kinetic energy E_x available for tunneling. This is the effect of the orbital quantization in strong fields, i.e. fields for which $\omega\tau>1$ and $\hbar\omega$ is an appreciable fraction of the energy gap (ω = cyclotron frequency, τ = scattering time).

The situations in the longitudinal and transverse orientations are somewhat different. In the longitudinal case the energy $(E-E_x)$ not available for tunneling is the quantized energy of motion $(n+\frac{1}{2})\hbar\omega$ about the field. Since the available energy for tunneling E_x is a maximum for states with $n=0$, it follows that the tunneling current in large longitudinal fields is predominantly due to states of zero point motion about the field. Longitudinal tunneling is therefore a *low* quantum number effect, and the resulting current reduction is very much the same as if the zero point energy

$\hbar\omega/2$ were added to the energy gap. In the transverse case, the quantized energy of motion about the field must provide the kinetic energy for tunneling, hence tunneling proceeds chiefly from states of the *largest* possible magnetic quantum number $n_{\max}$. Because of circling of the carrier motion, however, only a part of the energy $(n_{\max}+\frac{1}{2})\hbar\omega$ is available for tunneling, the exact fraction depending on the spatial location of the orbit center. The critical energy in this case is not the zero point energy $\hbar\omega/2$, but rather the quantity $m\omega^2a^2$, where a is the width of the junction and m is the reduced carrier mass.

Current oscillations of the de Haas–Van Alphen type are not to be expected in the presence of a longitudinal field because the density of E_z states is a smooth function of magnetic field. However, this is not the case in a transverse field and one may well ask whether such oscillations should not be present in such a field. Indeed, if one calculates the tunnel current resulting from states for which the distance between the junction plane and the magnetic orbit center is fixed, one obtains such oscillations. However, the *total* tunneling current, which is obtained by integrating over all possible orbit center positions, does not display these oscillations, because of the dependence of the magnetic quantum $\hbar\omega$ on the position of the orbit center. This effect is discussed more fully in a later section.

2. MODEL FOR TUNNELING

We shall discuss the simple case of two parabolic bands with extrema at $\boldsymbol{k}=0$. Fig. 1 illustrates the p–n junction schematically. In this figure, ϵ denotes the energy gap, qV denotes the applied voltage and Fa denotes the height of the junction potential. Clearly we have

$$Fa = \mu_1+\mu_2-qV+\epsilon$$

where μ_1 and μ_2 are the conduction and valence band Fermi levels respectively (measured relative to the appropriate band edge). In what follows we shall refer to the conduction and valence bands as bands number one and two respectively.

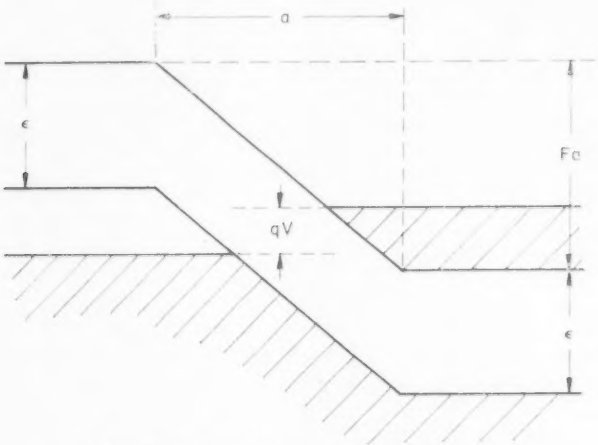

FIG. 1. Schematic diagram of p–n junction.

It will be convenient to assume a linear dependence of the junction potential on distance within the range of the junction.* If the junction is perpendicular to the x-axis, we therefore write for the junction potential (cf. Fig. 1)

$$\begin{aligned} V(x) &= 0 && x \geqslant 0 \\ &= -Fx && -a \leqslant x \leqslant 0 \\ &= Fa && x \leqslant -a \end{aligned}$$

* The more realistic case of quadratic dependence on distance can be handled in a similar fashion, but leads to analytic complexity of the results which somewhat obscures the physical simplicity of the tunneling process.

Vol. 19
1961

The presence of this junction potential affects the motion of electrons and holes in two ways. First of all there is the *intra-band* effect of localizing electrons and holes in the regions $x \gtrsim 0$ and $x \lesssim -a$ respectively. Secondly, there is an *inter-band* effect, resulting from the fact that the potential $V(x)$ has matrix elements coupling different bands. As a result, electron–hole annihilation (tunneling) is possible. Our approach will be to calculate the electron and hole wave functions taking account of the intra-band effects. Once these wave functions have been obtained the tunneling rate may be calculated in the usual way using the inter-band Hamiltonian.

The motion of electrons and holes in the presence of a junction potential V and a magnetic field $\boldsymbol{B}$ is governed by the equations

$$\left[\frac{1}{2m_1}\left(\boldsymbol{p}-\frac{e}{c}\boldsymbol{A}\right)^2+V\right]\psi_1 = E_1\psi_1 \qquad (2.1)$$

and

$$\left[-\frac{1}{2m_2}\left(\boldsymbol{p}-\frac{e}{c}\boldsymbol{A}\right)^2-\epsilon+V\right]\psi_2 = E_2\psi_2 \qquad (2.2)$$

In equations (2.1) and (2.2) m_1 and m_2 are the effective masses for the two bands, V is the junction potential and $\boldsymbol{A}$ is the vector potential describing the magnetic field. In the following discussion, the magnetic field will define the z-direction and the gauge $\boldsymbol{A} = (0, Bx, 0)$ will be chosen. Energies are to be measured relative to the bottom of the conduction band unless otherwise stated.

Equations (2.1) and (2.2) ignore the effect of the magnetic field on the electron spin. It may readily be shown that this effect does not affect the tunneling rate if the g-factors for the conduction and valence bands are equal. If they are not, the net effect is a change in the energy gap which may be accounted for in the manner of PRICE[3]. We shall include such g-factor effects only in our final expressions.

The normalized solutions of equations (2.1) and (2.2) are obtained in the WKB approximation in Appendix A. Using these solutions and the inter-band matrix element of the junction potential, V_{12}, we can calculate the tunneling transition probability per unit time for a state ψ_1 as

$$W_{12} = \frac{2\pi}{\hbar}|V_{12}|^2 \sum_{\substack{\text{final}\\ \text{states}}} |\langle\psi_2|\psi_1\rangle|^2\delta(E_1-E_2) \qquad (2.3)$$

Equation (2.3) deserves some comment. First of all, it should be pointed out that the inter-band interaction used in (2.3) is not the only interaction which can cause transitions, although we believe it to be the most important one. Other processes, involving the emission or absorption of photons or phonons are also possible. These differ from the interaction V_{12} insofar as the latter leads to conservation of electron energy as well as to conservation of electron momentum parallel to the junction plane. On the other hand, a photon assisted tunneling process leads to momentum but not energy conservation, whereas a phonon assisted process results in the conservation of neither energy nor momentum.

Secondly, it should be pointed out that the δ-function in energy in equation (2.3) ignores the existence of scattering processes. These may be taken into account in a crude way by considering each energy level to be broadened by an amount $\hbar/\tau$, where τ is the scattering time. As a result, we may think of the δ-function as having a width $\hbar/\tau$. Exact energy conservation is, therefore, not required and transitions from a given initial state E_1 are possible to final states with energies in the range

$$E_1-\frac{\hbar}{2\tau} \lesssim E_2 \lesssim E_1+\frac{1}{2}\frac{\hbar}{\tau}$$

The matrix element $\langle\psi_2|\psi_1\rangle$ appearing in equation (2.3) is calculated in Appendix B for each of the cases of interest. These matrix elements are used in the following sections to calculate the resulting tunneling current.

3. TUNNELING IN THE ABSENCE OF A MAGNETIC FIELD

We shall here give a brief summary of the results obtained by PRICE and RADCLIFFE[4] and by KANE[5] for zero field tunneling. The tunneling transition probability per unit time for a state $|E_1k_yk_z\rangle$ is obtained by substituting equation (B.2) into (2.3). Since the density of available final states is $T_2/2\pi\hbar$

in the WKB approximation, we obtain

$$W_{12}^0 = \frac{2\pi}{\hbar}|V_{12}|^2\left(\frac{\pi\hbar}{T_1T_2F}\right)\left(\frac{2m}{\epsilon}\right)^{1/2}\left(\frac{T_2}{2\pi\hbar}\right)\exp\left[-\frac{2}{3\hbar mF}p_0^3\right] \tag{3.1}$$

The total number of transitions per second due to states of energy E_1 is thus

$$N_{12}^0 = \frac{L_yL_z}{(2\pi\hbar)^2}\frac{|V_{12}|^2}{F}\left(\frac{2m}{\epsilon}\right)^{1/2}\int dk_y dk_z \exp\left[-\frac{2}{3\hbar mF}p_0^3\right] \tag{3.2}$$

Expanding p , we write

$$p_0^3 \simeq (2m\epsilon)^{3/2}\left[1+\frac{3}{2}\frac{E_\perp}{\epsilon}\right]$$

The limits of integration in (3.2) depend on the energy $E_\perp$. However, in a typical case the quantity

$$\lambda = \frac{2}{3}\frac{(2m\epsilon)^{3/2}}{\hbar mF} \tag{3.3}$$

is large ($\sim$10–20 for InSb) and μ_1, $\mu_2 \lesssim \epsilon$. In such a case we may extend the range of integration to infinity with negligible error.[4] We then obtain

$$N_{12}^0 \simeq L_yL_z|V_{12}|^2\left(\frac{m}{4\pi\hbar^3\epsilon}\right)\exp[-\lambda] \tag{3.4}$$

The net current due to states of energy E is $qN_{12}^0[f(E)-f(E-qV)]$ where

$$f(E) = \frac{1}{1+\exp\left[\dfrac{E-\mu_1}{kT}\right]}$$

and the total current density is:

$$j_0 = q|V_{12}|^2\left(\frac{m}{4\pi\hbar^3\epsilon}\right)\exp[-\lambda]\int_0^{\mathrm{Max}[Fa-\epsilon,0]} dE[f(E)-f(E-qV)] \tag{3.5}$$

4. TUNNELING IN A LONGITUDINAL MAGNETIC FIELD

The calculation of the current density for this case differs from that in the previous section only in a trivial way. That this is the case follows from the fact that the available final states (i.e. the states with $n' = n$, $k_y' = k_y$) form a quasicontinuum, just like in the zero field case. The density of state arguments in Section 3 are therefore still valid so that we may write

$$W_{12}^l = \frac{2\pi}{\hbar}|V_{12}|^2\left(\frac{\pi\hbar}{T_1T_2F}\right)\left(\frac{2m}{\epsilon}\right)^{1/2}\left(\frac{T_2}{2\pi\hbar}\right)\times \exp\left[-\frac{2}{3\hbar mF}p_l^3\right] \tag{4.1}$$

The total number of transitions per second due to states of energy E_1 is now

$$N_{12}^l = 2\left(\frac{T_1}{2\pi\hbar}\right)\left(\frac{L_y}{2\pi}\right)\int dk_y \sum_n W_{12}^l$$

Since k_y determines the center of the oscillators in (A.7), the range of integration is such that $-\frac{1}{2}L_x \leqslant X_0 \leqslant \frac{1}{2}L_x$. Hence we obtain

$$N_{12}^l = \frac{L_xL_y}{(2\pi\hbar)^2}\frac{|V_{12}|^2}{F}\left(\frac{2m}{\epsilon}\right)^{1/2}\left(\frac{2\pi m\omega}{\hbar}\right)\sum_n \times \exp\left[-\frac{2}{3\hbar mF}p_l^3\right] \tag{4.2}$$

An expansion similar to that used to obtain (3.4) now yields

$$N_{12}^l \simeq N_{12}^0\left(\frac{\hbar\omega}{2}\frac{\partial\lambda}{\partial\epsilon}\right)\mathrm{csch}\left(\frac{\hbar\omega}{2}\frac{\partial\lambda}{\partial\epsilon}\right) \tag{4.3}$$

where λ is given by (3.3). Ignoring the shift of Fermi level with field one therefore finds for the

normalized current density:

$$j_t/j_0 \simeq \left(\frac{\hbar\omega}{2}\frac{\partial\lambda}{\partial\epsilon}\right)\mathrm{csch}\left(\frac{\hbar\omega}{2}\frac{\partial\lambda}{\partial\epsilon}\right) \qquad (4.4)$$

This result was first communicated to us by PRICE[3]; a similar result has been given by CALAWA *et al.*[2]

5. TUNNELING IN A TRANSVERSE MAGNETIC FIELD

If we consider a given initial state $|E_1k_yk_z\rangle$ we may write for the energy of this state:

$$E_1 \simeq (n+\tfrac{1}{2})\hbar\omega_1(X_0)+\frac{\hbar^2k_z^2}{2m_1} \qquad (5.1)$$

However, because of the presence of the junction potential, the level spacing $\hbar\omega_1(X_0)$ now depends on X_0, i.e. on k_y and on n. An expression similar to (5.1) is valid for the final states.

$$E_2 \simeq Fa-\epsilon-(n'+\tfrac{1}{2})\hbar\omega_2(X_0')-\frac{\hbar^2k_z'^2}{2m_2} \qquad (5.2)$$

Since k_y and k_z are both conserved, tunneling is possible only for a discrete set of states, namely those for which

$$\frac{\hbar^2k_z^2}{2m} = Fa-\epsilon-(n+\tfrac{1}{2})\hbar\omega_1(X_0)-(n'+\tfrac{1}{2})\hbar\omega_2(X_0) \qquad (5.3)$$

For this reason, we have no *a priori* justification for using $T_1/2\pi\hbar$ and $T_2/2\pi\hbar$ as densities of available states. The use of these expressions can however be justified, as we shall now show.

In order to avoid mathematical complexity it will be convenient to discuss the case of heavy hole tunneling ($m_2 \gg m_1\, m_1 \sim m$), so that $\hbar\omega_2 \ll \hbar\omega_1$. In this case we may use an average density of states $T_2/2\pi\hbar$ for the valence band states and consider density of state fluctuations only for the conduction band states. We then show why the case of light hole tunneling ($m_2 \sim m_1$) is not substantially different.

The tunneling rate for a state $|E_1k_yk_z\rangle$ is now:

$$W_{12}^t = \frac{2\pi}{\hbar}|V_{12}|^2\left(\frac{\pi\hbar}{T_1T_2F}\right)\left(\frac{2m}{\epsilon}\right)^{1/2}\left(\frac{T_2}{2\pi\hbar}\right)\times$$
$$\times\exp\left\{-\frac{3}{2}\lambda\left[\frac{2}{3}+\alpha\left(\frac{\hbar\omega}{2}\frac{\partial\lambda}{\partial\epsilon}\right)^2+\frac{\hbar^2k_z^2}{2m\epsilon}+\frac{\hbar^2}{2m\epsilon}\left(k_y-\frac{2m\epsilon\omega}{6\hbar F}\right)^2\right]\right\} \qquad (5.4)$$

where

$$\alpha \equiv \frac{1}{45}\left[1+\frac{2\gamma}{(1+\gamma)^2}\right], \quad \gamma \equiv m_2/m_1.$$

Using equation (5.1) the number of states of *fixed* k_y and energy E_1 is

$$N(E_1) = \sum_{n=0}^{n_m}\frac{L_z}{2\pi\hbar}\left(\frac{2m}{E_1-(n+\frac{1}{2})\hbar\omega}\right)^{1/2} \qquad (5.5)$$

where n_m is the largest integer for which $E_1-(n+\frac{1}{2})\hbar\omega$ is positive.

The total tunneling rate due to states of energy E_1 and *fixed* k_y is therefore

$$N_{12}^t(k_y) = \frac{2\pi}{\hbar}|V_{12}|^2\left(\frac{\pi\hbar}{T_1T_2F}\right)\left(\frac{2m}{\epsilon}\right)^{1/2}\left(\frac{T_2}{2\pi\hbar}\right)\left(\frac{L_z}{2\pi\hbar}\right)\times$$
$$\times\sum_{n=0}^{n_m}\left(\frac{2m}{E_1-(n+\frac{1}{2})\hbar\omega}\right)^{1/2}\exp\left\{-\frac{3}{2}\lambda\left[\frac{2}{3}+\alpha\left(\frac{\hbar\omega}{2}\frac{\partial\lambda}{\partial\epsilon}\right)^2+\frac{E_1-(n+\frac{1}{2})\hbar\omega}{\epsilon}+\frac{\hbar^2}{2m\epsilon}\left(k_y-\frac{6m\epsilon\omega}{6\hbar F}\right)^2\right]\right\} \qquad (5.6)$$

The sum over n in equation (5.6) may be carried out by means of the Poisson summation formula. In carrying out the sum we will ignore the dependance of ω on n. This approximation will overestimate any effect due to the periodicity of the density of states. The result is (cf.

Vol. 1
1961

Appendix C):

$$N_{12}^{t} \simeq \frac{2\pi}{\hbar}|V_{12}|^2\left(\frac{\pi\hbar}{T_1T_2F}\right)\left(\frac{2m}{\epsilon}\right)^{1/2}\left(\frac{T_2}{2\pi\hbar}\right)\left(\frac{T_1}{2\pi\hbar}\right)\left(\frac{L_z}{2\pi\hbar}\right)\frac{(2\pi\hbar m^2F\epsilon)^{1/2}}{(2m\epsilon)^{3/4}}\times$$

$$\times\exp\left\{-\frac{3}{2}\lambda\left[\frac{2}{3}+\alpha\left(\frac{\hbar\omega}{2}-\frac{\partial\lambda}{\partial\epsilon}\right)^2+\frac{\hbar^2}{2m\epsilon}\left(k_y-\frac{2m\epsilon\omega}{6\hbar F}\right)^2\right]\right\}+N_{\text{osc}}^{t} \tag{5.7}$$

In equation (5.7), N_{osc}^{t} is the contribution of terms proportional to

$$\cos\left[2\pi m\left(\frac{E_1}{\hbar\omega}-\frac{1}{2}\right)-\phi\right] \quad m=1,2,3$$

in (C.3). These terms are analogous to the de Haas–Van Alphen effect in the susceptibility and lead to oscillations periodic in $1/B$. However, it is to be noted that equation (5.7) must still be integrated over k_y if one is to obtain the total tunneling rate due to states of energy E_1. Now it has been pointed out earlier that the quantity $\hbar\omega$ depends on X_0 and hence on k_y. Over the range of k_y of interest in (5.7), namely

$$\Delta k_y \sim \left[\frac{mF}{\hbar(2m\epsilon)^{1/2}}\right]^{1/2}$$

the quantity $1/\hbar\omega$ varies approximately over the range $(0,\ m_1c/\hbar eB)$. As a result, the contribution of N_{osc} to the *total* tunneling rate averages out for all energies unless $E_1/\hbar\omega \ll 1$, in which case the transition rate becomes vanishingly small anyhow. Thus, oscillations which are quantum effects of density of states will not be observed, and such quantum effects will not be of any qualitative importance.

The total transition rate may be obtained by integrating the non-oscillatory part of (5.7) over k_y in the manner of (3.2). It is readily verified that one then obtains

$$N_{12}^{t} = N_{12}^{0}\exp\left[-\alpha\left(\frac{\hbar\omega}{2}-\frac{\partial\lambda}{\partial\epsilon}\right)^2\times\frac{3}{2}\lambda\right] \tag{5.8}$$

If the Fermi level shift is again ignored, the normalized current is,

$$\frac{j_t}{j_0} = \exp\left[-\frac{3}{2}\lambda\alpha\left(\frac{\hbar\omega}{2}-\frac{\partial\lambda}{\partial\epsilon}\right)^2\right] \tag{5.9}$$

This result may be also written:

$$\frac{j_t}{j_0} = \exp\left[-2\alpha\left(\frac{\epsilon}{Fa}\right)^2 m\omega^2a^2\frac{\partial\lambda}{\partial\epsilon}\right] \tag{5.10}$$

It is to be noted that this is precisely the result one would have obtained if $T_1/2\pi\hbar$ had been used as the density of available conduction states.

6. DISCUSSION

When equations (4.4) and (5.10) are modified to include g-factor effects one obtains for the normalized currents:

$$\frac{j_t}{j_0} = \left(\frac{\hbar\omega}{2}-\frac{\partial\lambda}{\partial\epsilon}\right)\operatorname{csch}\left(\frac{\hbar\omega}{2}-\frac{\partial\lambda}{\partial\epsilon}\right)\cosh\left(E_p\frac{\partial\lambda}{\partial\epsilon}\right) \tag{6.1}$$

$$\frac{j_t}{j_0} = \exp\left[-2\alpha\left(\frac{\epsilon}{Fa}\right)^2 m\omega^2a^2\frac{\partial\lambda}{\partial\epsilon}\right]^2\cosh\left(E_p\frac{\partial\lambda}{\partial\epsilon}\right) \tag{6.2}$$

where

$$E_p = \tfrac{1}{2}(g_1-g_2)\mu_BB$$

and μ_B is the Bohr magneton.

Equation (6.1) agrees exactly with a result obtained by PRICE[3], and agrees with the result of CALAWA *et al.*[2] provided that in the latter work the quantity g is replaced by (g_1-g_2), the difference of the g-factors for the two bands.

Because of the different dependences of j_t and j_t on magnetic field, energy gap and junction field, one cannot make a general statement about the relative magnitudes of these currents. For the particular junction described by CALAWA *et al.*[2] our equations suggest (we do not have access to data which would permit a truly quantitative comparison) that j_t is larger than j_l, in agreement with the experimental finding.

It is noteworthy that the ratio j_l/j_t, which is independent of the spin moment, can be used to obtain a reasonably direct experimental measure of the electric field in the junction. Once this field is known, either equation (6.1) or (6.2) could be used to obtain an experimental value of the difference of g-factors for the bands, which could be correlated with results of magneto-optical studies.

APPENDIX A. CALCULATION OF WAVE FUNCTIONS

In the absence of a magnetic field equation (2.1) has a solution of the form

$$\psi_1(xyz) = \frac{1}{\sqrt{(L_y L_z)}} e^{ik_y y} e^{ik_z z} \phi_1(x) \quad \text{(A.1)}$$

where ϕ_1 is the normalized solution of

$$\phi_1'' + \left(\frac{p_1}{\hbar}\right)^2 \phi_1 = 0 \quad \text{(A.2)}$$

with

$$p_1^2 = 2m_1[E_1 - E_{1\perp} - V(x)]$$

and

$$E_{1\perp} = \frac{\hbar^2}{2m_1}[k_y^2 + k_z^2]$$

The normalized solution of (A.2) is easily written down in the WKB approximation. We find:

$$\phi_1(x) = 2\left(\frac{m_1}{T_1}\right)^{1/2} \frac{1}{\sqrt{(p_1)}} \cos\left[\frac{1}{\hbar}\int_{\xi_1}^{x} p_1\, dx - \frac{\hbar}{4}\right] \xi_2 > x > \xi_1 \quad \text{(A.3)}$$

$$= \left(\frac{m_1}{T_1}\right)^{1/2} \frac{1}{\sqrt{(|p_1|)}} \exp\left[-\frac{1}{\hbar}\int_{x}^{\xi_1} |p_1|\, dx\right] \quad x < \xi_1 \quad \text{(A.3a)}$$

where T_1 is the classical period of the motion and ξ_1 and ξ_2 are the classical turning points of the motion obtained from $p_1 = 0$.

For a longitudinal field equation (A.1) is replaced by

$$\psi_1(xyz) = \frac{1}{\sqrt{(L_y)}} e^{iyk_y} \Phi_n\left[\left(\frac{m\omega}{\hbar}\right)^{1/2}(x - X_0)\right] \phi_1(z) \quad \text{(A.4)}$$

where $X_0 = -\hbar k_y/m\omega$, Φ_n is a normalized harmonic oscillator function and $\phi_1(z)$ is the solution of (A.2) with

$$p_1^2 = 2m_1[E_1 - (n+\tfrac{1}{2})\hbar\omega_1 - V(z)]$$

For a transverse field with the junction perpendicular to the x-axis, equation (A.1) is still valid but the definition of p_1^2 in (A.2) must be changed to

$$p_1^2 = 2m_1\left[E_1 - \frac{\hbar^2 k_z^2}{2m} - \right.$$

$$\left. -\tfrac{1}{2}m_1\omega_1^2(x - X_0)^2 - V(x)\right]$$

The wave functions ψ_2 for the valence band are similar. They can be obtained from the expressions for ψ_1 by making the following replacements: $p_1 \to p_2$, where

$$p_2^2 = 2m_2[V(x) - \epsilon - E_2 - E_{2\perp}] \quad \text{(zero field)}$$

$$= 2m_2[V(z) - \epsilon - E_2 - (n' + \tfrac{1}{2})\hbar\omega_2] \quad \text{(longitudinal field)}$$

$$= 2m_2\left[V(x) - \epsilon - E_2 - \frac{\hbar^2 k_2'^2}{2m} - \right.$$

$$\left. -\tfrac{1}{2}m_2\omega_2^2(x - X_0')^2\right] \quad \text{(transverse field)}$$

APPENDIX B. CALCULATION OF MATRIX ELEMENTS

The overlap matrix element $\langle\psi_2|\psi_1\rangle$ is required only for $E_1 = E_2$ because of the δ function in equation (2.3).

For the case of zero magnetic field we thus have:

$$\langle\psi_2|\psi_1\rangle = \langle E_1, k_y', k_z'|E_1, k_y, k_z\rangle$$

$$= \delta_{k_y k_y'}\delta_{k_z k_z'}\int_{-\infty}^{\infty}\phi_2^*(x)\phi_1(x)\,dx \qquad \text{(B.1)}$$

The integral involved in equation (B.1) may be done approximately by the method of steepest descent. In this manner we readily obtain

$$\langle\psi_2|\psi_1\rangle = \delta_{k_y k_y'}\delta_{k_z k_z'}Q\exp\left[-\frac{p_0^3}{3\hbar mF}\right] \qquad \text{(B.2)}$$

where

$$Q = \left(\frac{\pi\hbar}{T_1T_2F}\right)^{1/2}\left(\frac{2m}{\epsilon}\right)^{1/2};\ \frac{1}{m} = \frac{1}{m_1}+\frac{1}{m_2}$$

$$p_0^2 = 2m[\epsilon+E_\perp];\ E_\perp = E_{1\perp}+E_{2\perp}$$

A similar result is obtained for the longitudinal case. We find

$$\langle\psi_2|\psi_1\rangle_l \simeq \delta_{k_y k_y'}\delta'_{n n'}Q\exp\left[-\frac{p_l^3}{3\hbar mF}\right] \qquad \text{(B.3)}$$

where

$$p_l^3 = 2m[\epsilon+(n+\tfrac{1}{2})\hbar\omega] \quad \omega = \omega_1+\omega_2 = \frac{eB}{mc}$$

The calculation of $\langle\psi_2|\psi_1\rangle$ for the transverse case is somewhat more involved. The method of steepest descent yields:

$$\langle\psi_2|\psi_1\rangle \simeq \delta_{k_y k_y'}\delta_{k_z k_z'}Q\times$$

$$\times\exp\left[-\frac{1}{\hbar}\int_{\eta_2}^{x_m}|p_2|\,dx-\frac{1}{\hbar}\int_{x_m}^{\xi_1}|p_1|\,dx\right] \qquad \text{(B.4)}$$

where

$$X_m = -\frac{1}{F}\left[E_1+\frac{m_2}{m_1+m_2}\epsilon\right]$$

The integrals involved in the exponent of (B.4) may be performed exactly. One obtains, for example:

$$\exp\left[-\frac{1}{\hbar}\int_{x_m}^{\xi_1}|p_1|\,dx\right] = \left\{\frac{\dfrac{2\sqrt{(a)}p_t}{\hbar}-2ax_m-b}{[b^2-4ac]^{1/2}}\times\exp\left[\frac{2\sqrt{(a)}p_t}{\hbar}\left(\frac{2ax_m+b}{b^2-4ac}\right)\right]\right\}^{\frac{b^2-4ac}{8a\sqrt{(a)}}} \qquad \text{(B.5)}$$

where

$$a = \left(\frac{m_1\omega_1}{\hbar}\right)^2,\quad b = -\frac{2m_1}{\hbar^2}[F-\hbar\omega_1 k_y],$$

$$c = k_y^2-\frac{2m_1}{\hbar^2}(E_1-E_{1z}) < 0$$

for states which tunnel appreciably,

$$p_t^2 = 2m_1[-Fx_m+\tfrac{1}{2}m_1\omega_1^2(x_m-X_0)^2-E_1+E_{1z}]$$

A similar expression is valid for

$$\exp\left[-\frac{1}{\hbar}\int_{\eta_2}^{x_m}|p_2|\,dx\right]$$

The complexity of these expressions makes it desirable to expand them in powers of the magnetic field. Such an expansion converges rapidly in a typical case, even for the largest fields available. If one desires

$$-\frac{1}{\hbar}\int_{x_m}^{\xi_1}|p_1|\,dx$$

correctly to order ω_1^2, the expression (B.5) must be expanded correctly to fifth order in ω_1, since the exponent behaves like ω_1^{-3}. One obtains

$$-\frac{1}{\hbar}\int_{x_m}^{\xi_1}|p_1|\,dx \simeq -\frac{p_0^3}{3\hbar m_1F}+$$

$$+\frac{\omega_1k_yp_0}{F^2}\left[-Fx_m-\frac{2}{3}\frac{p_0^2}{2m_1}\right]-$$

$$-\frac{m_1^2\omega_1^2}{\hbar F^3p_0}\left\{(Fx_m)^2\frac{p_0^2}{2m_1}+\right.$$

$$+\frac{4}{3}(Fx_m)\left(\frac{p_0^2}{2m_1}\right)^2+\frac{8}{15}\left(\frac{p_0^2}{2m_1}\right)^3+E_{1y}(Fx_m)^2+$$

$$\left.+4E_{1y}(FX_m)\left(\frac{p_0^2}{2m_1}\right)+\frac{8}{3}E_{1y}\left(\frac{p_0^2}{2m_1}\right)^2\right\} \qquad \text{(B.6)}$$

A similar expression is valid for

$$-\frac{1}{\hbar}\int_{\eta_2}^{x_m}|p_2|\,dx$$

The expression (B.6) may also be obtained directly by expanding $|p_1|$ in powers of ω_1 and integrating term by term. In addition to the above terms, one obtains by this method a number of small terms of order $\omega_1^{3/2}$ from the upper limit. These terms are a manifestation of the breakdown of the expansion for $|p_1|$ near $x=\xi_1$ and must be disregarded. They are in fact absent in the expansion of (B.5).

In order to obtain an approximate expression for the matrix element, we shall evaluate the terms of order ω_1 and ω_1^2 in (B.6) by using

$$p_0^2 \simeq 2m\epsilon, \quad -Fx_m \simeq \frac{m_2}{m_1+m_2}\epsilon$$

To this accuracy, the last three terms proportional to ω_1^2 in (B.6) may be dropped, and one obtains

$$-\frac{1}{\hbar}\int_{x_m}^{\xi_1}|p_1|\,dx \simeq -\frac{p_0^3}{3\hbar mF}+\frac{1}{6}\frac{\omega_1 k_y}{m_1F^2}(2m\epsilon)^{3/2}-$$

$$-\frac{3}{120}\frac{\omega_1^2}{m_1\hbar F^3}(2m\epsilon)^{5/2} \qquad \text{(B.7)}$$

The corresponding expression for

$$-\frac{1}{\hbar}\int_{\eta_2}^{x_m}|p_2|\,dx$$

is:

$$-\frac{1}{\hbar}\int_{\eta_2}^{x_m}|p_2|\,dx \simeq -\frac{p_0^3}{3\hbar m_2F}+$$

$$+\frac{1}{6}\frac{\omega_2 k_y}{m_2F^2}(2m\epsilon)^{3/2}(2+3\gamma)-$$

$$-\frac{1}{120}\frac{\omega_2^2}{m_2\hbar F^3}(2m\epsilon)^{5/2}(8+20\gamma+15\gamma^2) \qquad \text{(B.8)}$$

where $\gamma = m_2/m_1$. Substitution of (B.7) and (B.8) into (B.4) yields the following result:

$$\langle\psi_2|\psi_1\rangle_t = \langle\psi_2|\psi_1\rangle_0 \times$$

$$\times\exp\left[\frac{\lambda_1}{4}\frac{\omega k_y}{mF^2}(2m\epsilon)^{3/2}-\frac{23}{480}\lambda_2\frac{\omega^2(2m\epsilon)^{5/2}}{mhF^3}\right] \qquad \text{(B.9)}$$

where $\langle\psi_2|\psi_1\rangle_0$ is given by (B.2), and λ_1 and λ_2 are dimensionless parameters of order 1 depending on the ratio of the effective masses, $\gamma = m_2/m_1$. Explicitly

$$\lambda_1 = \frac{2}{3}\frac{(\gamma+2)}{(\gamma+1)}$$

$$\lambda_2 = \frac{4}{23}\frac{3\gamma^2+12\gamma+8}{[\gamma+1]^2}$$

Note that $\lambda_1=\lambda_2=1$ for $m_1=m_2$ and that for general γ, λ_1 and λ_2 lie in the ranges:

$$\frac{2}{3}\leqslant\lambda_1\leqslant\frac{4}{3}, \quad \frac{12}{23}\leqslant\lambda_2\leqslant\frac{32}{23}$$

APPENDIX C. EVALUATION OF SUM

The sum in equation (5.8) is of the form

$$S=\sum_{n=0}^{<\delta>}[\delta-n]^{-1/2}\exp[-2\beta(\delta-n)] \qquad \text{(C.1)}$$

where

$$\delta=\frac{E_1}{\hbar\omega}-\frac{1}{2},$$

$\langle\delta\rangle$ maximum integer $\leqslant\delta$ and

$$\beta=\frac{(2m\epsilon)^{3/2}}{\hbar mF}\frac{\hbar\omega}{2\epsilon}$$

Using the Poisson summation formula we may write

$$S=\sum_{m=-\infty}^{\infty}\exp(2\pi im\delta)\,u^{-1/2}\exp[-(2\beta+2\pi im)u]\,du \qquad \text{(C.2)}$$

If

$$2\delta\beta\simeq\frac{(2m\epsilon)^{3/2}}{\hbar mF}\frac{E_1}{\epsilon}\gtrsim 1$$

we may replace the upper limit of integration by infinity with negligible error. This condition will be

satisfied in InSb for the majority of electrons if

$$\frac{\mu_1}{\epsilon} \gtrsim \frac{1}{10},$$

i.e. if the material is reasonably degenerate. In such a case one readily finds

$$S = \left(\frac{\pi}{2\beta}\right)^{1/2}\left\{1+2\sum_{m=1}^{\infty}\left[1+\left(\frac{\pi m}{\beta}\right)^2\right]^{-1/2} \times \right.$$

$$\left. \times \cos\left[2\pi m\delta - \phi\right]\right\} \qquad \text{(C.3)}$$

where

$$2\phi = \tan^{-1}\left(\frac{\pi m}{\beta}\right)$$

REFERENCES

1. Esaki L., private communication.
2. Calawa A. R., Rediker R. H., Lax B. and McWhorter A. L., *Phys. Rev. Letters* **5,** 55 (1960).
3. Price P. J., private communication.
4. Price P. J. and Radcliffe J. M., *IBM J. Res. Dev.* **3,** 364 (1959).
5. Kane E. O., *J. Phys. Chem. Solids* **12,** 181 (1959).
6. Titchmarsh E. C., *Introduction to the Theory of Fourier Integrals*, p. 60. Clarendon Press, Oxford (1937).

Vol. 19
1961

J. Phys. Chem. Solids Pergamon Press 1961. Vol. 19, Nos. 1/2, pp. 18–28. Printed in Great Britain.

KINETICS OF DONOR REACTIONS IN OXYGEN-DOPED GERMANIUM

C. S. FULLER

Bell Telephone Laboratories, Incorporated, Murray Hill, New Jersey

(*Received* 16 *September* 1960; *revised* 1 *November* 1960)

Abstract—The kinetics of the reactions leading to the formation of donors in oxygen-doped Ge have been investigated by means of resistivity and Hall effect measurements. Reaction rates have been measured for oxygen concentrations ranging from 0·9 to $12{\cdot}0\times10^{17}$ cm^{-3} oxygen over the temperature range, 300–550°C. The apparent order of reaction is shown to increase with both temperature and oxygen concentration and to approach a limiting value of four. Although the reactions are complex in the kinetic sense, and consist of series as well as parallel reactions, both the forward and reverse reactions are shown to follow approximate first order rates over limited temperature ranges. The reaction of oxygen in the presence of copper is shown to result in the production of a neutral or paired conformation of the Cu and O atoms. The activation energy for donor generation in Cu-doped Ge is 47 kcal (2·0 eV) in excellent agreement with the activation energy for oxygen diffusion.

I. INTRODUCTION

VERY LITTLE is known about the mechanisms and kinetics of the reactions in solid solutions or about the compounds which are formed. Because the barriers to diffusion in solids are considerably higher than those in gases and liquids, it is evident that diffusion processes are expected to play a much more important role in the case of solids. Also, because diffusion is an atomic process, the reactions in solids are usually describable in terms of steps in which single atoms are added to form a product molecule. In simple systems, therefore, an investigation of the reaction kinetics in solids should prove useful, not only in providing information on the diffusion properties of reacting atoms, but also in helping to elucidate the elementary steps leading to the reaction products. As media for such reactions, the covalent semiconductors offer considerable advantages. Very pure crystals of these semiconductors are available, and both optical and electrical methods capable of measuring minute changes in solute concentrations now exist.

In the present work electrical measurements have been employed to investigate reactions of oxygen in germanium which lead to the formation and dissociation of donors. A previous paper[1] discussed the donor equilibria established when oxygen-doped Ge crystals are heated in the temperature range 300–550°C. The present work discusses the kinetics of these reactions.

Investigations relating to the kinetics of the reactions of oxygen in solution in silicon have already been reported.[2,3,4] The similarity of these reactions to those occurring in oxygen-doped Ge has also been pointed out.[5,6] It is now fairly well established[6,7,1] that in both instances oxygen undergoes a series of consecutive reactions leading to the formation of a metastable donor of the type M^*O_4, where M* represents a solvent (Ge or Si) atom at which the reactions are taking place. These reactions may be written,

$$\begin{aligned} &\text{(a)}\ M^*O + O \rightleftarrows M^*O_2 \\ &\text{(b)}\ M^*O_2 + O \rightleftarrows M^*O_3 \\ &\text{(c)}\ M^*O^3 + O \rightleftarrows M^*O_4 \end{aligned} \qquad (1)$$

The asterisk has been added to emphasize the fact that the various structures are not separate oxide phases but are present in solid solution.

It has also been shown that in Si, continuing

or side reactions occur which lead to a disappearance of the M^*O_4 donors and ultimately to silica aggregates.[7,8] Infrared investigations[9] of Si (in which oxygen reactions have been carried out) show that more than one donor is produced upon reaction and it has been postulated[2] that the products M^*O_2 and M^*O_3 in equation (1) are also donors.

The results of the present work show that the reactions of oxygen in Ge parallel those in Si very closely indeed. Also because they proceed further toward completion and because the rates of reaction are considerably higher than those in Si, more accurate data can be obtained. It is found that the kinetics of donor generation are in agreement with the reactions (1) in which, in addition to M^*O_4, the species M^*O_2 also appears to ionize as a donor. The formation of the latter is most apparent at low temperatures and low oxygen concentrations. The kinetics of the donor disappearance reaction, which occurs at higher temperatures, are also in agreement with the presence of other donor species. Although the kinetics of both the generation and disappearance reactions are complex, it is shown that they are both probably diffusion controlled, the energy of activation being the activation energy for the diffusion of oxygen.

Finally, the reactions of oxygen in the presence of Cu suggest that a neutral or internally compensated structure is formed at 350°C. Furthermore, the donor generation reaction in the presence of Cu is found to follow simple kinetics which agree with the diffusional properties of oxygen.[10]

II. EXPERIMENTAL

The Ge crystals employed in this work were grown under different partial pressures of oxygen in argon, and were the same as used in Ref. (1). The oxygen contents varied from 0·9 to 12·0 $\times$ $\times 10^{17}$ cm^{-3}. The donor concentrations† were determined from resistivity measurements at 25 $\pm$ 1°C using the mobilities given in Fig. 1 of Ref. (1). Reactions were carried out in air in furnaces controlled to within 1°C. The range of temperatures was 300–550°C. Allowance was made for heating up time which was generally 15 sec for the small specimens ($1 \times 1 \times 15$ mm^3) employed. Quenching to room temperature required less than 5 sec. The oxygen concentrations were known from infrared absorption measurements.[11]

Each reaction was preceded by a normalizing anneal to insure that the oxygen was in solution at the start of the reaction. This consisted of heating the gold-plated specimen for 1½ min at 915°C and quenching to room temperature in less than 5 sec. The gold plating served to minimize the effects of Cu contamination.

To investigate the effects of Cu, Ge specimens were copper plated, heated to 900°C for 10 min to saturate and quenched to room temperature. In the saturation step, $3{\cdot}0 \times 10^{16}$ cm^{-3} Cu were introduced.‡ The same Ge specimen (1·9 $\times$ $\times 10^{17}$ cm^{-3} oxygen) was used to investigate the effect of temperature by repeatedly reheating with Cu to 900°C and quenching before each run. Hall measurements were made on standard "bridge" specimens to determine electron mobility.

The concentrations of oxygen are believed to be accurate to within 5 per cent. This same accuracy also applies to the electron concentrations. Relative electron concentrations were determinable to better than 1 per cent. Since the donors are essentially fully ionized at 25°C and appear to possess only single energy levels, the electron concentrations are taken equal to the total donor concentrations.[1]

The data were examined by the usual procedure of plotting changes in donor concentrations against time and attempting to deduce therefrom the applicable rate expression and the order of the reaction. The results are summarized below.

III. RESULTS

When the curves showing donor generation (forward reaction) against time are examined, it is found that simple first or second order kinetics§ is followed for the majority of reactions in the range 350–470°C. Examples of such reactions are given in Ref. (1), Fig. 2. In general, however, first order kinetics is followed better than second order. Similarly for the donor dissociation

† The donors were assumed fully ionized at 25°C. See Discussion B.

‡ No effect of oxygen on the saturation value was found.

§ The terms "first order" or "second order" are used to mean simply that the fractional change in donor concentration, or 1 minus this fraction, follows the corresponding rate expression.

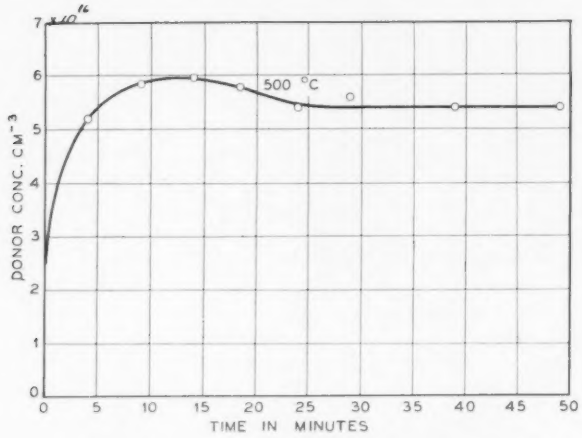

FIG. 1. Rate of donor generation at 500°C in a crystal of Ge containing $6{\cdot}0\times10^{17}$ cm^{-3} oxygen.†

(reverse reaction) the kinetics approximates first order. There are, however, also definite anomalies in the simple kinetics which are more prominent at higher temperatures and oxygen concentrations.[1] These are discussed in detail below.

(a) *Forward reaction*

That the forward reactions are complex is readily evident when curves of donor generation at high (above 470°) and at low temperature (below 350°) are examined. Fig. 1, taken from Ref. (1), shows the curve obtained at 500°C for a specimen containing $6{\cdot}0\times10^{17}$ cm^{-3} oxygen.† A single maximum (with a suggestion of a second) is evident. Similarly Fig. 2 shows curves for $3{\cdot}9\times10^{17}$ cm^{-3} and $4{\cdot}2\times10^{17}$ cm^{-3} oxygen reacted at 500°C which show distinct double maxima. The nearly horizontal

† The donor concentrations in Fig. 1 and following figures were measured at 25°C. The quench rate was rapid enough in all cases to stop the reaction in ~1 sec.

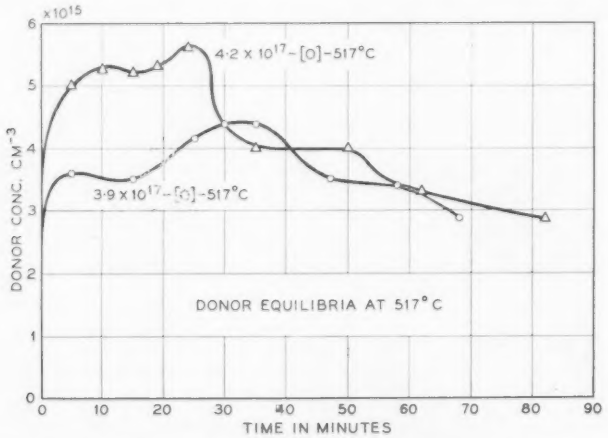

FIG. 2. Rates of donor generation at 517°C for Ge crystals containing $3{\cdot}9\times10^{17}$ cm^{-3} and $4{\cdot}2\times10^{17}$ oxygen.

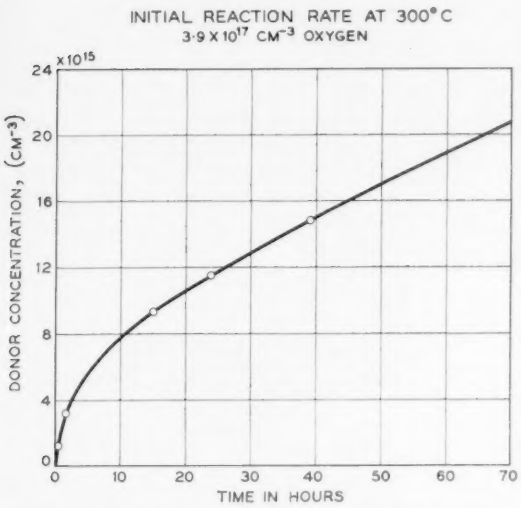

FIG. 3. Rate of donor generation at 300°C for a crystal of Ge containing $3{\cdot}9\times10^{17}$ cm^{-3} oxygen.

portions of the curves in both Figs. 1 and 2 are believed to represent donor equilibria.[1] These are also evident in Fig. 10. The final decrease in donor concentration is discussed in Section IV(d). Fig. 3 shows the initial part of the curve for a specimen containing $3{\cdot}9\times10^{17}$ cm^{-3} oxygen reacted at 300°C, and again shows deviations from simple kinetics.

To derive apparent orders for the reactions, the initial rates and the fractional life-time methods were applied.

The relevant equations are:

$$n_0 = \frac{\log R_1 - \log R_2}{\log C_1 - \log C_2} \tag{2}$$

$$n_f = 1 + \frac{\log t_1 - \log t_2}{\log C_2 - \log C_1} \tag{3}$$

where n_0 and n_f are the orders of reaction for the respective methods, R_1 and R_2 are the initial rates for oxygen contents C_1 and C_2, and t_1 and t_2 are the half-life periods for these concentrations. Such an analysis, in the case of Si, led to the concept of SiO_4 as a donor[7] and a similar behavior might therefore be expected for Ge. Fig. 4 shows plots of the initial reaction rates as a function of oxygen contents for 350, 385, 435, and 470°C. It is

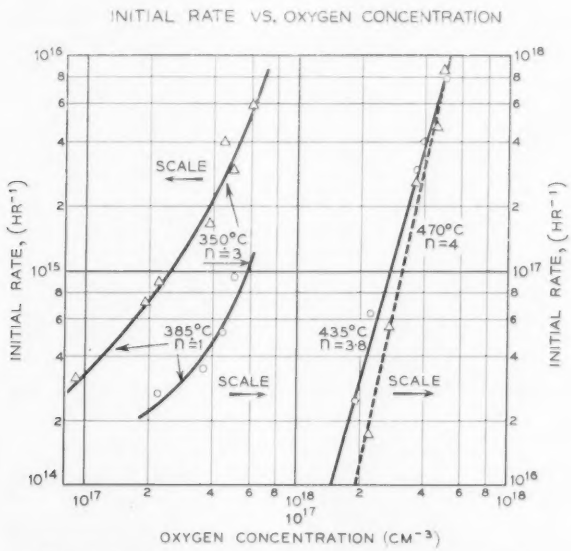

FIG. 4. Log–log plot of initial rate of reaction vs. oxygen concentration for oxygen donor generation in Ge at 350, 385, 435, and 470°C. Apparent order of reaction is indicated.

seen that the reactions, at 435°C and 470°C, suggest an apparent fourth order for the forward reactions. The reactions at the lower temperatures, especially for the low oxygen contents, give a lower order than four, thus showing the effects of the early steps in the reactions (1).

The results of the calculation of the apparent order of reaction from half life-times is shown in Fig. 5. Here again the orders for the lower temperatures are lower than those for the higher temperature (470°C) which approach 4.

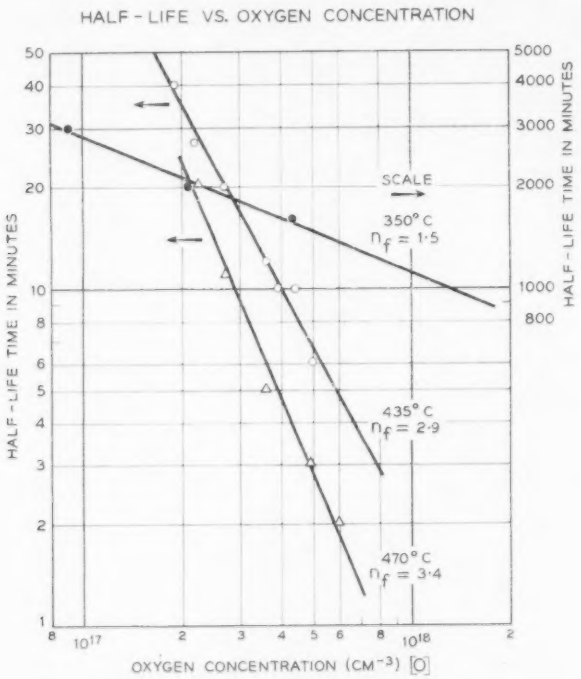

FIG. 5. Log–log plot of half-life periods vs. oxygen concentration for donor generation in Ge at 350, 435, and 470°C. Apparent orders of reaction are indicated.

As stated above, the forward reactions follow approximate first order kinetics in $(1-f)$, where f is the fraction of donors generated in a given time, over a limited temperature and oxygen content range. Apparent first order rate constants for an oxygen concentration of $4{\cdot}2\times10^{17}$ cm^{-3} were calculated and plotted against $1/T$. The curve so obtained (not produced here) showed a marked deviation from linearity. Apparent activation energies obtained from the slope of this curve varied from about 23 kcal at the higher temperature (470°C) to about 60 kcal at 400°C. Likewise, the apparent activation energies calculated from the initial rates showed a large variation with temperature; the highest value 41 kcal being given at the lower temperature (350°C) for a specimen containing $4{\cdot}2\times10^{17}$ cm^{-3} oxygen. Possible interpretations of these variations in ΔH_a are given below.

(b) *Reverse reaction*

As has been found for Si, the dissociation reactions of the donors formed from the oxygen reactions follow approximately a first order process[3] in the donor concentration. In carrying out this reaction, one starts with donor concentrations well above the equilibrium value at a given temperature and examines the rate of approach to equilibrium. However, once again deviations

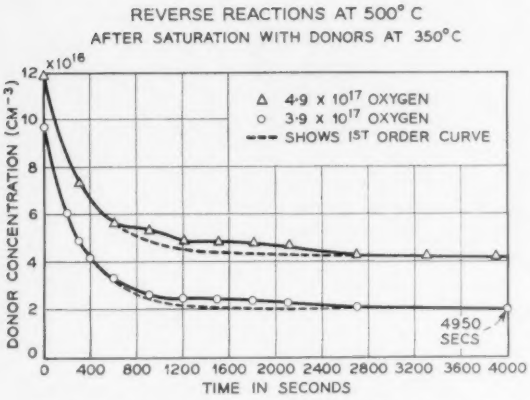

FIG. 6. Reverse reaction rate at 500°C after donor saturation at 350°C for specimens containing $3{\cdot}9\times10^{17}$ cm^{-3} and $4{\cdot}9\times10^{17}$ cm^{-3} oxygen. First order rates follow dashed lines.

from first order are evident, though not as pronounced as for the forward reactions. Fig. 6, which shows curves for $3{\cdot}9$ and $4{\cdot}9\times10^{17}$ cm^{-3} oxygen at 500°C is typical. On this figure the first order curves are shown as dashed lines. It is evident that over most of the reaction, first order kinetics is a good approximation. Fig. 7 shows a plot of the first order rate constants as obtained from dashed curves, such as shown on Fig. 7, against $1/T$ for specimens containing $4{\cdot}9\times10^{17}$ cm^{-3} oxygen. The trend of ΔH_a with temperature, while less than that found in (a), is still present, the range being from 47 to 85 kcal.

(c) *Reactions of oxygen in the presence of* Cu

Figure 8 shows the initial decrease in hole concentration and the subsequent increase in electron concentration at 350, 398, and 424°C for the same specimen of Ge containing $1{\cdot}9\times10^{17}$ cm^{-3} oxygen and $3{\cdot}0\times10^{16}$ cm^{-3} Cu. The changes of electron concentration with time, unlike the reactions in the absence of Cu, are found to follow first order kinetics in one minus the donor fraction to within

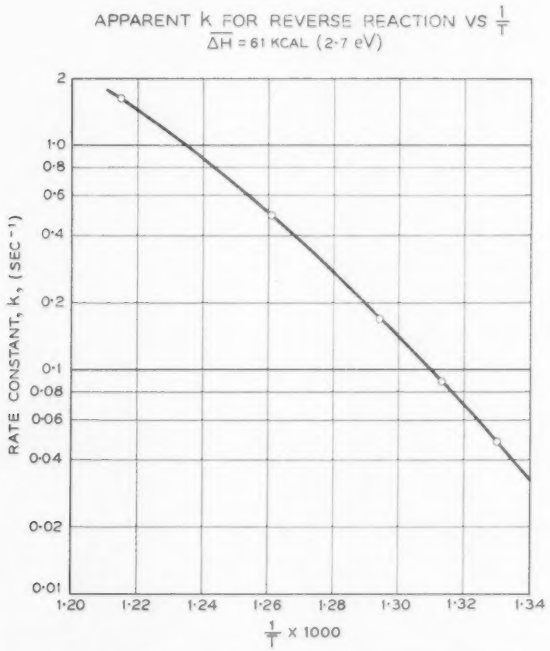

FIG. 7. Apparent first order rate constants for reverse reaction (dashed curves shown in Fig. 6) plotted against reciprocal of absolute temperature. ΔH_a varies from 47 to 85 kcal.

Vol. 19
1961

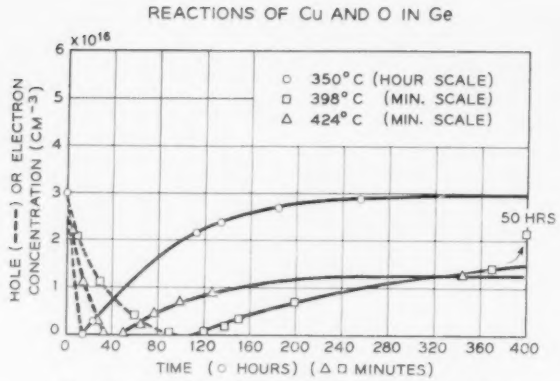
REACTIONS OF Cu AND O IN Ge
x10^16
HOLE (----) OR ELECTRON CONCENTRATION (CM^-3)
○ 350°C (HOUR SCALE)
□ 398°C (MIN. SCALE)
△ 424°C (MIN. SCALE)
50 HRS
0 40 80 120 160 200 240 280 320 360 400
TIME (○ HOURS) (△ □ MINUTES)

FIG. 8. Changes in carrier concentrations at 350, 398, and 424°C upon annealing Ge containing $3{\cdot}0\times10^{16}$ cm^{-3} Cu and $1{\cdot}9\times10^{17}$ cm^{-3} oxygen.

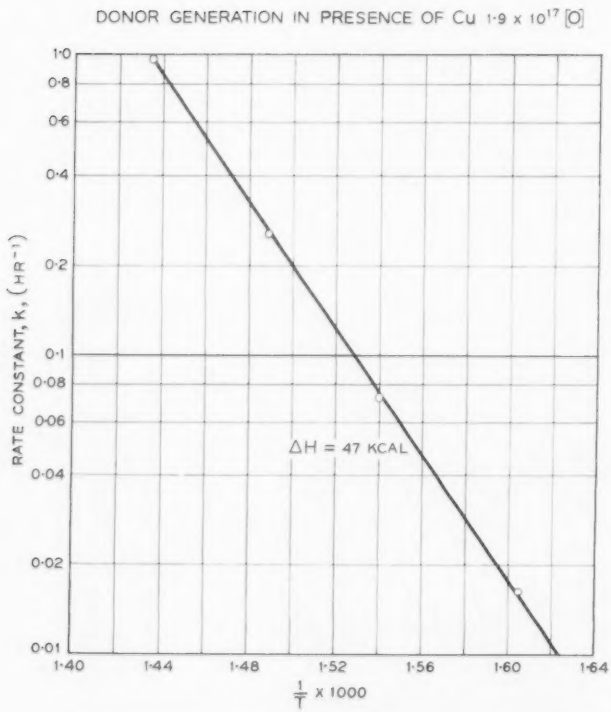

FIG. 9. Plot of rate constants derived from donor generation reaction of Fig. 8 against reciprocal of absolute temperature.

the error in the measurements. Fig. 9, which is a plot of the first order rate constants calculated from the curves in Fig. 8 (which includes a run at 375°C not shown on Fig. 8) gives a value for ΔH_a of 47 kcal and shows no trend with temperature.

It is interesting that ΔH_a calculated from the times for the *hole* concentrations to reach zero for the different temperatures, comes out 40 kcal, in fair agreement with that given above (Fig. 9).

IV DISCUSSION

(a) *Activation energies*

In the reactions of oxygen in Si it was noted that the activation energies for the forward and reverse reactions were approximately the same.[3,2] A value of 65 kcal (2·8 eV) was deduced from the reverse reaction kinetics. This value, it was pointed out,[2] is in agreement with the value found for the energy of diffusion of oxygen in Si.[13] More recently[10] a value of 60 kcal (2·6 eV) has been found from anelastic relaxation measurements. This agreement strongly suggests that the forward and reverse processes in Si are diffusion controlled. Because of the very great similarity between the reactions in Si and those in Ge, this suggests that the latter likewise are dependent on oxygen diffusion.

In the case of Ge the best value for ΔH_a appears to be that from Fig. 9, namely 47 kcal (2·0 eV). This is in good agreement with the value (2·1 eV) found from anelastic relaxation.[10]

It is interesting that the donor generation curves in the Cu experiments follow simple first order kinetics in one minus the donor fraction and yield a value of ΔH_a in excellent agreement with that from the diffusion experiments. This suggests that, in the presence of Cu, the controlling reaction causing an electrical change is that represented by the diffusion of an oxygen atom to a well-defined center.[14]

Further discussion of the reactions in the presence of Cu is given below.

(b) *Nature of the forward and reverse reactions*

No quantitative treatment of the kinetics of the forward and reverse reactions will be attempted here, but rather a qualitative discussion of the reactions. The presence of maxima (Figs. 1, 2, 5) suggests that a series of reactions of the kind shown in (1), in which at least two of the product species are donors, take place when oxygen reacts. A discussion of the analogous reactions in Si has already been given.[2] The first maximum (Fig. 1) can be understood, if it is assumed that the Ge^*O_2 species is essentially a completely ionized donor at 25°C† whereas the Ge^*O_3 is neutral or only slightly ionized as a donor. Since the Ge^*O_4 species is known to be a donor and to be essentially all ionized at 25°C,[1] the second maximum (Fig. 2) may represent a common peak due to both donors. The subsequent plateaus (which appear to represent equilibrium)[1] could then be attained by a decrease in the Ge^*O_2 and increase in the Ge^*O_3 concentrations. Other interpretations are of course possible. The reverse kinetics (Fig. 5) are also in qualitative agreement with this model. Hall effect results[15] likewise indicate the presence of several ionization energy levels assignable to separate donor species.

The assumption of two donors, with an essentially unionized intermediate species, can also explain the apparent decrease of ΔH_a with temperature for the forward reaction since at the higher temperatures, the reactions leading to Ge^*O_3 and Ge^*O_4 predominate over that leading to Ge^*O_2 and the former result in no net change in donor concentration. At lower temperatures most of the donor generation will result from Ge^*O_2 formation. The effect of temperature on rate is expected to be greater for the latter. A similar argument applies to the reverse reactions.

(c) *Reactions of oxygen in* Cu-*doped* Ge

The results shown in Figs. 8 and 9, as well as other evidence to be presented below, suggest that a reaction between oxygen and Cu occurs when both are present in Ge.‡ The results at 350°C (Fig. 8) show that, if the excess donors formed are assumed to contain 4 oxygens and do not contain Cu, two oxygen atoms per Cu are required to produce compensation or elimination of the Cu

† Recent measurements[15] indicate that the initial donor may not be fully ionized at 25°C. However, at the donor concentrations in the present experiments, the error does not affect the conclusions.

‡ A similar suggestion has been made in a recent paper by Carter J. R., Jr. and Swalin R. A., *J. Appl. Phys.* **31**, 1191 (1960). Reactions between Cu and O in Si have been postulated by G. H. Schüttke, paper presented before Electrochemical Society, Chicago, May 1–5 (1960).

Vol. 19
1961

Table 1. *Equilibrium donor generation in crystals containing oxygen and copper* (Cu = $3{\cdot}0\times10^{16}$ cm^{-3}; $T = 350°C$)

Orig. O-conc. (cm^{-3})	O-conc. in excess donors (cm^{-3})	ΔO/Cu
9×10^{16}	$3{\cdot}6\times10^{16}$	1·8
19×10^{16}	12×10^{16}	2·3
22×10^{16}	16×10^{16}	2·0

acceptors, provided no oxygen is lost in other ways. This is also indicated in crystals containing different amounts of oxygen as shown in Table 1. If it is assumed that the three acceptor levels per Cu atom observed in Ge[16] are still present after reaction to the intrinsic state (25°C), then it is necessary to postulate three donor levels per two reacted O-atoms ($Ge^*O_2^{+++}$). A comparison of observed and calculated[17] Hall mobility measurements at 77°C, however, shows that if the above holds, the Cu and Ge^*O_2 must be closely associated (see Table 2). Since other investigations[15] indicate Ge^*O_2 is singly charged, a more likely possibility is that one Cu reacts with two oxygens and Ge to form a neutral complex at 350°C.

Hall mobility calculations were made following BROOKS.[17] These were compared with experiment for a specimen of Ge reacted at 350°C in the presence of $3{\cdot}0\times10^{16}$ cm^{-3} Cu. The Ge crystal employed contained $9{\cdot}0\times10^{16}$ cm^{-3} oxygen. An effective mass of unity was used in the calculations since relative values for the mobility are sufficient for the arguments presented here. The procedure of DEBYE and KOHANE[18] was followed to convert impurity mobilities into Hall mobilities. The results are shown in Table 2.

Table 2 shows that individual (unpaired) triply-charged acceptor Cu ions are no longer present as such after reaction in the presence of oxygen. The observed mobilities in Table 2 are about one-third the values observed for other specimens (not reported here) containing comparable oxygen and electron concentrations, but essentially no Cu. These lower values may indicate that the Cu–oxygen interaction product contributes some scattering or they may be due to nonuniformities in the specimen. Likewise, the increase in mobility with reaction time shown in column 3, Table 2 may be caused by specimen inhomogeneity. However, the large discrepancy between the observed mobilities and those calculated assuming that the Cu is unpaired (columns 3 and 5, Table 2) is strong evidence for the formation of a compound of an internally compensated structure.

Since Cu in Ge is known to be in interstitial–substitutional equilibrium, a mechanism is provided whereby Cu may readily migrate interstitially to oxygen centers. This would appear more

Table 2. *Comparison of calculated and observed Hall mobilities for* $3{\cdot}0\times10^{16}$ cm^{-3} Cu *and* $9{\cdot}0\times10^{16}$ cm^{-3} O *in* Ge

Reaction temperature 350°C
Measuring temperature 77°K

Time of reaction (hr.)	Electron conc. 77°K (cm^{-3})	Obs. Hall mobility, 77°K (cm^2/V sec)	Calc. Hall mobility, 77°K (cm^2/V sec)	
			Cu "paired"	Cu "unpaired"
78	$4{\cdot}2\times10^{14}$	5570	22800	350
239	$3{\cdot}3\times10^{15}$	8200	17100	440
382	$4{\cdot}1\times10^{15}$	8690	10900	450

likely than that the oxygen atoms would migrate to the Cu acceptors, which are more dilute than the oxygen and diffuse much more slowly. Such a migration of the Cu would result in the loss of the Cu acceptors and consequently of their high scattering power for electrons as is observed.

No attempt will be made here to suggest models for the structure formed by the oxygen–copper interaction. That the association is rather strong is indicated by the fact that heating to 550°C for 20 min caused the specimen to return to only 9·0 ohm cm p-type, showing that even at this temperature, where essentially all of the donors formed from oxygen are dissociated,[1] the Cu acceptors are largely still reacted.†

Further evidence that two oxygen atoms are combined with one copper is provided by the fact that the equilibrium donor concentrations observed for the different temperatures in Fig. 8 are just those expected for a specimen containing $1{\cdot}3\times 10^{17}$ cm^{-3} oxygen, i.e. two oxygens per Cu less than the oxygen concentration known to be present. Since this applies to the 424°C curve, it confirms the findings above, namely that the oxygen–copper product is stable at this temperature.

(d) *Parallel reactions*

If the reactions of oxygen in Ge are continued long enough at temperatures which are not too low, the donors formed eventually disappear. At 470°C about ten hours are required whereas at 550°C the donors are gone after about 100 min. Similar reactions in Si have been explained as a "polymerization" in which the donors are the seat of a reaction ultimately leading to silica formation.[2] The results shown in Fig. 10 support an alternative view that, at least in the case of Ge, the donor disappearance occurs through migration of oxygen to dislocations and other points of precipitation.

In Fig. 10, the same specimen of Ge, containing $6{\cdot}0\times 10^{17}$ cm^{-3} O, was reacted at 500, 525, and 546°C until the donor loss was complete. Before each run the oxygen was dispersed by heating to 915°C for 2 min. If the time for the donor concentration to reach 2×10^{15} cm^{-3} is taken as a measure of the time for all of the oxygen to be removed into the precipitate phase, and the reciprocals of the times are plotted against $1/T$, a value of 46 kcal is obtained for ΔH_a. The closeness of this value to that for the activation energy for oxygen diffusion (47 kcal) strongly suggests that the precipitation process is diffusion-controlled. Furthermore, if a diffusion process does exist, it is possible to calculate from the value of the diffusion coefficient for oxygen at 500°C ($1{\cdot}5\times 10^{-14}$ cm^2 sec^{-1}) and the time for donor

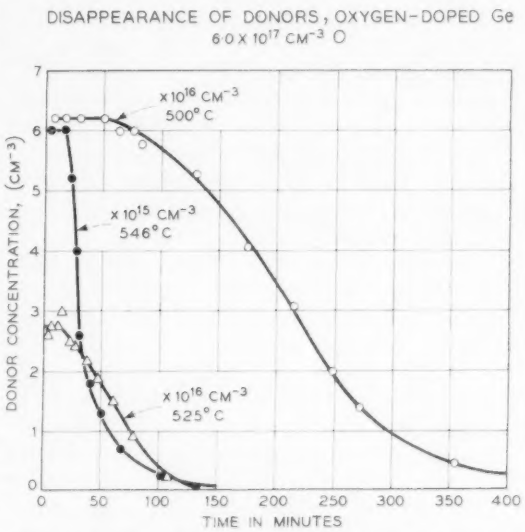

FIG. 10. Change in donor concentration with time at 500, 525, and 546°C for Ge containing $6{\cdot}0\times 10^{17}$ cm^{-3} oxygen. The initial donor rise is too fast to be shown on the time scale of the figure.

disappearance (27,000 sec) an approximate distance between precipitation centers of 4000 Å. This corresponds to a concentration of nucleation centers of about 10^{11} to 10^{12} cm^{-3}, which is not unreasonable. Optical studies on Si containing precipitated oxygen have in fact shown that considerable precipitation does occur on dislocations and similar centers.[19]

V. CONCLUSION

The present work has verified, for oxygen-doped Ge, what was known already in oxygen-doped Si, namely that the reactions of oxygen to form donors are complex in the kinetic sense and consists of probably three partial series reactions

† It is possible that the Cu and O form a precipitate phase which redissolves as the temperature is raised above about 500°C.

Vol. 19
1961

leading to a donor composed of four oxygen atoms. Evidence is presented that one of the partial reactions products is also a donor which is ionized at room temperature and one is neutral or a donor which is essentially nonionized at 25°C. The structures containing respectively 2 and 3 oxygen atoms are likely assignments for these partial reaction products.

Both the donor generation and the donor dissociation reactions follow approximate first order kinetics in the temperature ranges 350–470°C and 480–550°C, respectively. Marked deviations, however, occur; especially in the generation reaction. These are shown by qualitative arguments to be in agreement with the concept of the reactions given above. Variations with temperature and oxygen concentration of the apparent orders of the reactions as derived from initial rates and fractional life times are also shown to be in agreement with these ideas.

Activation energies derived from the approximate kinetics are found to be dependent on reaction temperature. The average value, however, agrees well with that (47 kcal) for oxygen diffusion as determined from anelastic relaxation measurements on oxygen-doped Ge.

Reactions of O in Ge containing Cu have been investigated. Evidence is given to show that two oxygen atoms per Cu atom associate or react with the Cu before the usual donors are generated. The kinetics of the latter reaction follow first order in 1 minus the donor fraction to the precision of the measurements. The activation energy (46 kcal) agrees with that for oxygen diffusion (47 kcal), thus indicating the diffusion-controlled nature of the reaction.

A study of the disappearance of donors on long reaction leads to the conclusion that a parallel reaction consuming oxygen at precipitation centers occurs in addition to the series reactions discussed above.

Acknowledgements—The author is indebted to C. D. THURMOND, W. KAISER and M. KOWALCHIK for supplying the oxygen-doped crystals employed in this work and to W. KAISER for the determinations of the oxygen concentrations. Thanks are also due F. H. DOLEIDEN and K. WOLFSTIRN for assistance with the measurements and calculations.

REFERENCES

1. FULLER C. S., KAISER W. and THURMOND C. D., *J. Phys. Chem. Solids* **16,** 161 (1960).
2. KAISER W., FRISCH H. L. and REISS H., *Phys. Rev.* **112,** 1546 (1958).
3. FULLER C. S. and LOGAN R. A., *J. Appl. Phys.* **28,** 1427 (1957).
4. FULLER C. S. and DOLEIDEN F. H., *J. Appl. Phys.* **29,** 165 (1958); *J. Phys. Chem. Solids* **13,** 187 (1960).
5. ELLIOTT G., *Nature* **180,** 1350 (1957).
6. BLOEM J., HASS C. and PENNING P., *J. Phys. Chem. Solids* **12,** 23 (1959).
7. KAISER W., *Phys. Rev.* **105,** 1751 (1957).
8. FULLER C. S., HANNAY N. B., DITZENBERGER J. A. and BUEHLER E., *Phys. Rev.* **96,** 833 (1954); *Acta Met.* **3,** 97 (1955).
9. HROSTOWSKI H. J. and KAISER R. H., *Phys. Rev. Letters* **1,** 199 (1958).
10. SOUTHGATE P. D., *Solid State Physics in Electronics and Telecommunications* Vol. I, p. 240 (edited by DÉSIRANT M. and MICHIELS J. L.). Academic Press, New York (1960).
11. KAISER W. and THURMOND C. D., *J. Appl. Phys.* (in press).
12. FROST A. A. and PEARSON R. G., *Kinetics and Mechanism*. John Wiley, New York (1953).
13. LOGAN R. A. and PETERS H., *J. Appl. Phys.* **28,** 819, 1419 (1957).
14. REISS H., FULLER C. S. and MORIN F. J., *Bell. Syst. Tech. J.* **35,** 535 (1956).
15. Unpublished results of the author and DOLEIDEN F. H.
16. WOODBURY H. H. and TYLER W. W., *Phys. Rev.* **105,** 84 (1957).
17. BROOKS H., *Advances in Electronics and Electron Physics*, Vol. VII (edited by MARTON L.). Academic Press, New York (1955).
18. DEBYE P. P. and KOHANE T., *Phys. Rev.* **94,** 724 (1954).
19. BULLOUGH R., NEWMAN R. C. and WAKEFIELD J., *Proc. Instn Elect. Engrs* May 1959.

Vol. 1
196

J. Phys. Chem. Solids Pergamon Press 1961. Vol. 19, Nos. 1/2, pp. 29–34. Printed in Great Britain.

NEUTRON DIFFRACTION INVESTIGATION OF ANTIFERROMAGNETISM IN $CrCl_3$

J. W. CABLE, M. K. WILKINSON and E. O. WOLLAN

Oak Ridge National Laboratory, Oak Ridge, Tennessee

(*Received* 13 *October* 1960)

Abstract—Neutron diffraction observations have been made on powder and single crystal samples of anhydrous $CrCl_3$ at temperatures from 298 to 4·2°K. This hexagonal layer-type crystal undergoes a transition at 16·8°K to an antiferromagnetic state in which the magnetic moments within each hexagonal layer of metal ions are aligned parallel but adjacent layers of moments are oppositely directed. The axis of spontaneous sublattice magnetization is closely perpendicular to the *c*-axis. Observations of the (003) antiferromagnetic reflection in an external magnetic field show that the antiferromagnetism can be destroyed with fields of only a few kilo-oersteds, and lead to the conclusion that a net magnetization can be produced with very small magnetic fields.

INTRODUCTION

THIS INVESTIGATION was undertaken to determine the existence of magnetic ordering in $CrCl_3$ at low temperatures. This hexagonal layer-type crystal has been the subject of several magnetic investigations[1,2] carried out from room temperature to liquid helium temperatures. The paramagnetic susceptibility of $CrCl_3$ exhibits a Curie–Weiss dependence with a positive paramagnetic Curie temperature. There is a susceptibility maximum in the vicinity of 20°K with a field dependent susceptibility below that temperature. This anomalous behavior is of the same type as that observed for the structurally similar compounds $FeCl_2$, $CoCl_2$, and $NiCl_2$, and several attempts have been made to account for this behavior in terms of proposed magnetic ordering ranging from antiferromagnetism[3,4] to two dimensional ferromagnetism.[5] Recent neutron diffraction results[6] show that $FeCl_2$ and $CoCl_2$ are antiferromagnetic at low temperatures, and that the structures consist of ferromagnetically aligned moments within each hexagonal layer but with adjacent layers coupled antiferromagnetically. It was therefore expected that the magnetic moments in $CrCl_3$ would order in the same manner with a transition temperature corresponding to the λ-type anomaly at 16·8°K in the specific heat data.[7,8]

CRYSTAL STRUCTURE

The crystal structure of anhydrous $CrCl_3$ was previously determined by X-ray methods, and a hexagonal unit cell of space group D_3^5 containing 6 molecules was reported.[9] The ions are located at the following positions: 6 Cr^{+3} at ($u\,\bar{u}\,1/3$, $2\bar{u}\bar{u}0$, $u2u\,2/3$) with $u = 8/9$ and 5/9 and 18 Cl^- at ($x, y, z+1/3; y-x, \bar{x}, z; \bar{y}, x-y, z+2/3; \bar{y}, \bar{x}, 1/3-z; y-x, y, \bar{z}; x, x-y, 2/3-z$) with $x = 8/9$, $y = 7/9$, $z = 0{\cdot}26$; $x = 5/9$, $y = 1/9$, $z = 0{\cdot}26$ and $x = 2/9$, $y = 4/9$, $z = 0{\cdot}26$. The structure then consists of hexagonal nets of chromium ions separated by two hexagonal layers of chloride ions. This is quite similar to the $CdCl_2$ type structure observed for $FeCl_2$, $CoCl_2$ and $NiCl_2$ except that here one third of the metal ion lattice positions are unoccupied. The lattice constants, $A_0 = 5{\cdot}952$ and $C_0 = 17{\cdot}47$ Å, were determined by X-ray analysis[10] for the samples used in this investigation.

SAMPLE PREPARATION

In this hexagonal layer structure the metal ion layers are tightly bound to the two adjacent chloride layers, but the groups of MCl_3 layers are held together by relatively weak van der Waal's forces. As a result stacking faults easily occur in the process of crystallization, and the

crystallographic purity of a particular sample depends upon the method of preparation. For this material the best sample was obtained by vacuum sublimation of the dehydrated salt at a temperature of 700°C. Large quantities of sublimate were prepared so that sufficient 100-mesh sample could be obtained without the necessity for grinding, a process which also has been found to introduce stacking faults in such crystals.

The $CrCl_3$ single crystals were grown from the vapor phase by sublimation of the anhydrous material in a vacuum at 950°C. The crystals obtained were in the form of thin sheets with thicknesses of only a few thousandths of an inch but with diameters as large as 1 inch. As would be expected from the two dimensional nature of the chemical bonding, the thin sheets lie parallel to the hexagonal layers of the crystal.

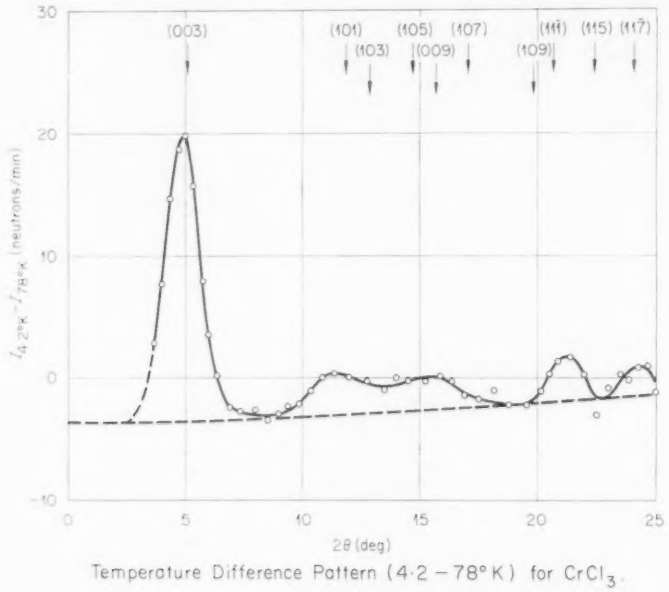

FIG. 1. Temperature difference pattern for $CrCl_3$.

EXPERIMENTAL RESULTS

Powder samples

The powder samples were sealed in cylindrical aluminum cells in a helium atmosphere and mounted in the low temperature cryostat of the neutron diffractometer. Neutron powder diffraction patterns were obtained at temperatures ranging from 298 to 4·2°K. At room temperature the pattern was typical of a paramagnetic material, and the nuclear intensities were in qualitative agreement with the known crystal structure and scattering amplitudes. Exact quantitative agreement was not obtained because of a slight crystallographic impurity and a sizeable preferred orientation effect, which was made more pronounced by the use of high packing densities in an attempt to enhance the intensities. At 4·2°K additional Bragg reflections and a decrease in the diffuse scattering were observed. These effects, due to the development of long range antiferromagnetic order, are shown in Fig. 1, where the data are presented as a difference pattern for results obtained above and below the transition temperature. Therefore, the reflections are due only to magnetic scattering; and the negative background, approximated by the dashed curve, represents the decrease in paramagnetic scattering upon ordering. To a first approximation this decrease in diffuse scattering is proportional to the square of the ordered moment and corresponds to a value of $2{\cdot}82 \pm 0{\cdot}20\ \mu_B$ (assuming the Cr^{++} form factor) in agreement with

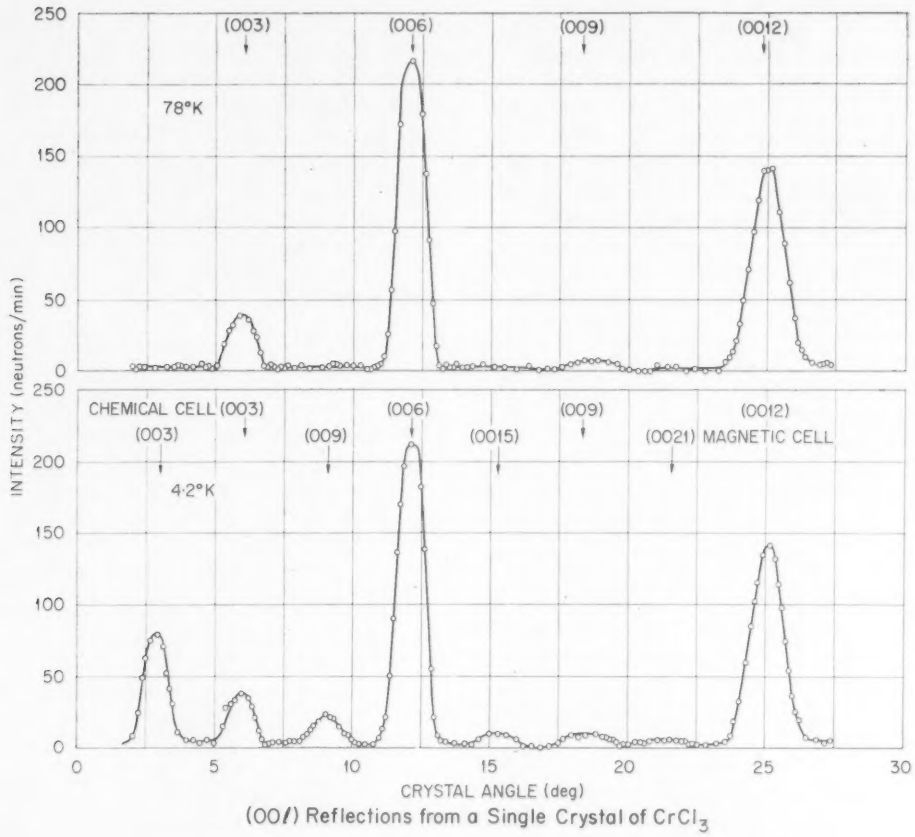

FIG. 2. The (00*l*) reflections from a single crystal of $CrCl_3$.

that expected for the Cr^{+3} ion with the oribital moment quenched.

In the pattern of Fig. 1 the indices are based on a hexagonal magnetic unit cell with the same *a*-axis and twice the *c*-axis of the chemical unit cell. The reflections indicated are those allowed for a ferromagnetic-layer structure of the $CoCl_2$ type, and qualitative agreement is observed. However, the intensities and resolution are such that the structure cannot be firmly established from these data.

Temperature studies were made in order to determine the transition temperature and the temperature dependence of the spontaneous sublattice magnetization. Sample temperatures in the range of 4·2 to 25°K were maintained by means of a heater coil located above the sample and a thermal impedance between the sample and the helium bath, and they were measured with a calibrated copper–constantan thermocouple. A Brillouin-type temperature dependence was observed for the intensity of the (003) magnetic reflection, and a Néel temperature of 17 ± 1°K was observed in agreement with the anomaly at 16·8°K in the specific heat data.

Single crystal samples

The powder data are consistent with but do not establish the ferromagnetic layer-type structure for $CrCl_3$. It was necessary to extend the investigation to single crystal samples.

The $CrCl_3$ single crystals were so small that extreme precaution had to be taken to minimize background scattering. Therefore, they were not

mounted on the low temperature goniometer,[11] but were placed between two thin aluminum plates in a cylindrical aluminum cell with the (00*l*) crystal planes perpendicular to the plane of scattering. The (00*l*) reflections from a 0·004 in. thick crystal at 78°K and 4·2°K are shown in Fig. 2. In the 78°K pattern the indices are for the hexagonal chemical cell and only the allowed reflections are observed. At 4·2°K additional (00*l*) reflections are observed and these are indexed on the magnetic cell for which the *c*-axis must be doubled.

For single crystals completely irradiated by the neutron beam the integrated intensity of an (*hkl*) reflection is given by [12]

$$E_{hkl} = \frac{KI_0 F_{hkl}^2 \exp\left(-2W\dfrac{\sin^2\theta}{\lambda^2}\right)}{\sin 2\theta} A_{hkl}$$

in which KI_0 depends on the instrumental geometry and the particular crystal under observation, F_{hkl} is the geometrical structure amplitude, the exponential is the Debye–Waller correction for thermal motion of the scattering centers, A_{hkl} is an absorption factor, and θ is the Bragg angle. For a fixed set of experimental conditions KI_0 becomes an instrumental constant which can be determined from the nuclear intensities. Since the $CrCl_3$ crystal was so thin, A_{hkl} was nearly the same for all reflections and was incorporated in the instrumental constant. Thermal corrections were made using a Debye characteristic temperature of 405°K taken from the specific heat data of HANSEN and GRIFFEL[8].

The experimentally determined values of KI_0 for the four observed nuclear reflections are plotted as a function of the chlorine positional parameter z in Fig. 3. The intersection of the curves gives the instrumental constant (130 ± 6) and the parameter ($z = 0{\cdot}2560 \pm 0{\cdot}005$) which satisfy the above expression for the observed reflections.

This value of the instrumental constant was then used in calculating the ordered moments from the intensities of the antiferromagnetic reflections. The model was that suggested by the powder data with adjacent layers of ferromagnetically aligned moments oppositely directed and the axis of magnetization directed perpendicular to the *c*-axis. In calculating the moment values given in column three of Table 1 the Cr^{+2} form factor[13] was used. The results show conclusively that the magnetic structure consists of ferromagnetically aligned moments within each hexagonal layer with adjacent layers oppositely directed. The variation of the moment values obtained at different scattering angles indicates that the Cr^{+2} form factor is not applicable to $CrCl_3$. A form factor somewhat lower at small angles and higher at the

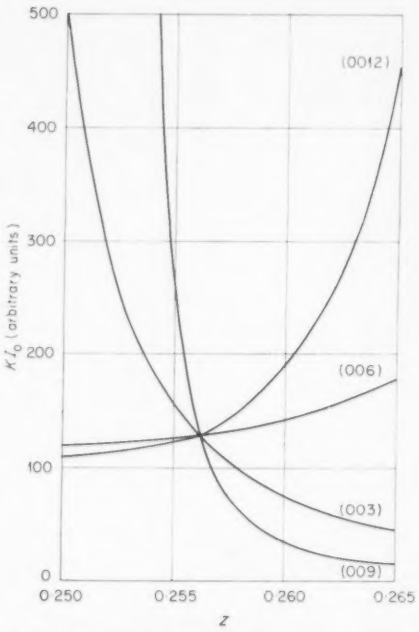

FIG. 3. The instrumental constant, KI_0, vs. the chloride ion parameter, z, for the observed (00*l*) nuclear intensities.

Table 1. *Moment values calculated from the intensities of the* (00*l*) *antiferromagnetic reflections from* $CrCl_3$

00*l*	E_{hkl}(observed)	μ/Cr^{+3} ion*
00·3	640	$2{\cdot}72 \pm 0{\cdot}10$
00·9	175	$3{\cdot}04 \pm 0{\cdot}20$
00·15	52	$3{\cdot}20 \pm 0{\cdot}40$

* Assuming the Cr^{+2} form factor.

Vol. 196

large angles would give better agreement between the moment values. Even so, the moment values obtained are close to the spin only moment for the Cr^{+3} ion.

Magnetic field effects

Among the anomalous magnetic properties of the so-called metamagnetic materials ($FeCl_2$, $CoCl_2$, $NiCl_2$, and $CrCl_3$) is the attainment of large net magnetizations with magnetic fields that accompanied by a disruption of the antiferromagnetic lattice, it is possible to observe the effect by measuring the antiferromagnetic intensities when an external field is applied. This has been done for both the powder and single crystal samples, and a typical curve is shown in Fig. 4. This curve shows the variation in the intensity of the (003) antiferromagnetic reflection from the single crystal of $CrCl_3$ with the magnetic field applied parallel to the *c*-axis and that essentially

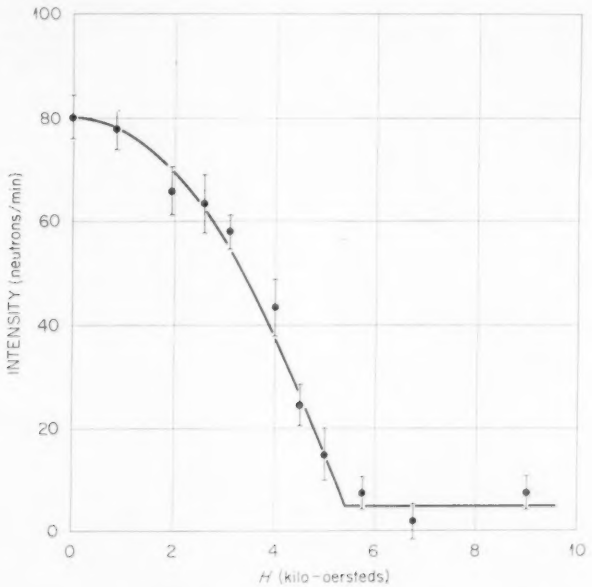

FIG. 4. The effect of a magnetic field on the intensity of the (003) antiferromagnetic reflection from $CrCl_3$. The field was applied parallel to the *c*-axis of the crystal.

are much smaller than those which would be anticipated from the Néel temperatures. Previous neutron diffraction measurements have indicated that in $FeCl_2$ and $CoCl_2$ there is a strong intralayer ferromagnetic interaction and a much weaker interlayer antiferromagnetic interaction, and that the magnetization of these materials is accomplished by overcoming only the weak antiferromagnetic interaction between the layers. For $CrCl_3$ very steep magnetization curves, similar to those of ferromagnetic materials, have been observed at liquid hydrogen[1] and liquid helium temperatures.[2] Since the magnetization is a complete disruption of the antiferromagnetic lattice is obtained with 5·4 kOe. Since in zero field the moments are directed normal to the *c*-axis these results indicate that the net magnetization observed at small fields is produced by a simple rotation of the moments into the direction of the field. If ψ is defined as the angle between the moments and the field direction (*c*-axis) then the magnetization varies as $\cos\psi$. The (003) intensity, which is proportional to the square of the component of the moment in the layer, varies as $\sin^2\psi$ and decreases rapidly as the magnetization proceeds. Within experimental error the observed

intensity variation corresponds to a linear magnetization with field up to 5·0 kOe where 93 ± 4 per cent saturation is obtained. Presumably, a much smaller field would be required for saturation if it were applied normal to the *c*-axis (i.e. within the plane of the moments). This was not possible in the apparatus used because of geometrical limitations; however, displacement of the field direction to an angle 26° from the *c*-axis lowered the field required to extinguish the (003) antiferromagnetic reflection from 5·4 to 3·4 kOe.

DISCUSSION

In the crystal structure of $CrCl_3$ each metal ion is surrounded by an octahedral arrangement of chloride ions, three in each of the adjacent layers, and by three metal ions in the same layer. The magnetic structure of $CrCl_3$ is indicative of a ferromagnetic interaction within the metal ion layers and an antiferromagnetic interaction between layers. The intralayer interaction may be due to direct exchange involving overlap of the t_{2g} cation orbitals or to indirect exchange via the anions. The relevant Cr–Cl–Cr angle of about 92° is highly unfavorable for the usual type of indirect exchange involving σ-type overlap of the e_g cation orbitals with the *p*-anion orbitals so that any indirect exchange probably involves π-type overlap of the t_{2g} cation orbitals with the *p*-anion orbitals. The large separation of the chromic ions in adjacent layers (6·15 Å) is suggestive of indirect exchange via two intervening anions for the interlayer interaction. This interaction is extremely weak as indicated by the small field required to break it down.

Acknowledgements—The authors wish to express their appreciation to D. E. LAVALLE for the preparation of the samples used in this investigation and to H. L. YAKEL and R. M. STEELE for the X-ray analyses.

REFERENCES

1. e.g. STARR C., BITTER F. and KAUFMANN A. R., *Phys. Rev.* **58,** 977 (1940); references to the earlier work are contained in this paper.
2. HENRY W. E., GRIFFEL M. and HANSEN W. N., *Proceedings of the Conference on Magnetism and Magnetic Materials, Pittsburgh, Pa., June,* 1955. AIEE, New York, p. 60 (1955).
3. LANDAU L., *Physik Z. Sowjetunion* **4,** 675 (1933).
4. SHULTZ B. H., *Physica* **7,** 413 (1940).
5. LEECH J. W. and MANUEL A. J., *Proc. Phys. Soc. Lond.* **69B,** 220 (1956).
6. WILKINSON M. K., CABLE J. W., WOLLAN E. O. and KOEHLER W. C., *Phys. Rev.* **113,** 497 (1959).
7. TRAPEZNIKOVA O., SHUBNIKOV L. and MILIUTIN G., *Physik. Z. Sowjetunion* **9,** 237 (1936).
8. HANSEN W. N. and GRIFFEL M., *J. Chem. Phys.* **28,** 902 (1958).
9. WOOSTER N., *Z. Kristall.* **74,** 363 (1930).
10. YAKEL H. and STEELE R., private communication.
11. WOLLAN E. O., KOEHLER W. C. and WILKINSON M. K., *Phys. Rev.* **110,** 638 (1958).
12. PETERSON S. W. and LEVY H. A., *J. Chem. Phys.* **20,** 704 (1952).
13. CABLE J. W., WILKINSON M. K. and WOLLAN E. O., *Phys. Rev.* **118,** 950 (1960).

Vol. 1
196

J. Phys. Chem. Solids Pergamon Press 1961. Vol. 19, Nos. 1/2, pp. 35–50. Printed in Great Britain.

THE KINETICS OF PRECIPITATION FROM SUPERSATURATED SOLID SOLUTIONS*

I. M. LIFSHITZ and V. V. SLYOZOV

Physico-Technical Institute, Kharkov, U.S.S.R.

(*Received* 10 *October* 1959)

Abstract—An analysis is made of the process whereby diffusion effects can cause the precipitation of grains of a second phase in a supersaturated solid solution. The kinetics of this type of grain growth are examined in detail. Some grains grow, only to be later dissolved; others increase in size and incorporate further grains that they encounter in so doing. This latter phenomenon of coalescence is discussed in a new "kinetic" approximation. Formulae are given for the asymptotic grain size distribution, for the number of grains per unit volume and for the supersaturation as a function of time. The effects of anisotropy, strain, crystalline order and the finite size of the specimen are allowed for. It is pointed out that for a material that can be said to be "supersaturated with vacancies", the discussion can be applied to the vacancies as solute "atoms" which cluster together to form internal cavities. The practical case of a real, finite crystal is here important, because the vacancies can in general also escape to the surface. A special analysis is made of this example, and the results are applied to the theory of sintering.

ol. 19
1961

1. FORMULATION OF THE PROBLEM

IN A supersaturated solid solution, diffusion effects may bring about the formation of grains of a new phase. Two stages of this process may be distinguished. In the first, concentration fluctuations produce nuclei of the new phase, which grow directly from the supersaturated medium. The second stage may be considered to begin when the grains thus formed have reached an appreciable size and the degree of supersaturation of the matrix has become very slight. In such circumstances the determining process is that of coalescence, i.e. the growth of large grains of the new phase by the incorporation of small ones. Fluctuation effects play a negligible part in the second stage, as new nuclei, to be of any importance, would need to be of macroscopic proportions.

The kinetics of this coalescence process are considered in what follows. Some years ago, TODES[1,2] discussed a similar phenomenon and correctly arrived at various qualitative conclusions.† Unfortunately his quantitative argument is in error and the results contain meaningless logarithmic divergencies. A satisfactory solution was first given in our paper of 1958,[4] in which the mode of arrival of the system at the asymptotic distribution of grain sizes was analysed in detail. The results of this earlier study are rederived herein by a rather different method, using the more accurate "kinetic approximation" which allows the stability of the asymptotic solutions to be examined. We also consider the effect on coalescence of various factors such as anisotropy and internal strain.

In the first instance we shall simplify matters by ignoring anisotropy and considering the grains to be spherical. The actual shape of real grains may be taken into account by adjusting certain numerical constants in the relevant formulae.

Fundamental equations

If C_∞ is the concentration of the saturated solution, and $\alpha = (2\sigma/kT)vC_\infty$ is a parameter containing the inter-phase surface tension σ and the atomic volume v of the solute, the equilibrium concentration C_R at the boundary of a grain is related to the grain radius by the usual formula:

$$C_R = C_\infty + \frac{\alpha}{R}. \qquad (1)$$

* Translated by R. D. LOWDE.

† A similar problem has also been considered by GREENWOOD[3] but not to the same extent.

The degree of supersaturation is small, so that $C-C_\infty = \Delta \ll 1$, and for the present we may ignore the interaction between grains since their dimensions are small compared with the mean distance between them. Then the diffusion current of solute across the grain boundary is given, per unit area, by*

$$j = \mathscr{D}\frac{\partial C}{\partial r}\bigg|_{r=R} = \frac{\mathscr{D}}{R}(C-C_R) = \frac{\mathscr{D}}{R}\left(\Delta - \frac{\alpha}{R}\right).$$

The radius R of the grain therefore varies with time as†

$$\frac{dR}{dt} = \frac{\mathscr{D}}{R}\left(\Delta - \frac{\alpha}{R}\right). \tag{2}$$

Thus for every value Δ of the supersaturation there exists a critical radius $R_c = \alpha/\Delta$ with which a grain is in equilibrium with the solution. If $R > R_c$ the grain grows, if $R < R_c$ it dissolves. This obvious mechanism also explains why large grains can "devour" small ones by incorporation. Both Δ and R_c themselves vary with time.

Writing Δ_0 for the initial supersaturation, $R_{c0} = \alpha/\Delta_0$ for the initial critical radius, and $T = R_{c0}^3/\alpha\mathscr{D}$, we now go over to dimensionless reduced magnitudes

$$\rho = \frac{R}{R_{c0}}, \qquad t' = \frac{t}{T}.$$

Dropping the prime on t, we obtain

$$\frac{d\rho^3}{dt} = 3\left(\frac{\rho}{x} - 1\right), \tag{3}$$

in which $x(t)$ is a dimensionless critical radius such that $x(0) = 1$. We now introduce a function $f(\rho^3, t)$ which within a factor $\frac{4}{3}\pi$ is the volume distribution function of the grains, and the rate $V_R = d\rho^3/dt$ of growth of the grains in dimension space. The unknown functions $f(\rho^3, t)$ and $x(t)$ may be determined as follows: from the equation of continuity in dimension space,

$$\frac{\partial f}{\partial t} + \frac{\partial}{\partial \rho^3}(f v_p) = 0, \tag{4}$$

while from the conservation of matter

$$Q_0 = \Delta_0 + q_0 = \Delta + q.$$

Q_0 is the total initial supersaturation, making allowance through a term q_0 for the volume of material initially in the grains. We have

$$q = \tfrac{4}{3}\pi R_{c0}^3 \int_0^\infty f\rho^3\, d\rho^3.$$

Bearing in mind that $x = \Delta_0/\Delta$, it follows that

$$\left.\begin{aligned} 1 &= \frac{\Delta_0}{Q_0}\frac{1}{x} + \kappa \int_0^\infty f\rho^3\, d\rho^3, \\ \kappa &= \tfrac{4}{3}\pi R_{c0}^3 Q_0^{-1}. \end{aligned}\right\} \tag{5}$$

A normalization to unit volume has here been performed, so that

$$n = \int_0^\infty f\, d\rho^3$$

is the number of grains per unit volume. It follows that the distribution function $F(\rho, t)$ over the dimension ρ is related to $f(\rho^3, t)$ by

$$F(\rho, t)\, d\rho = f(\rho^3, t)\, d\rho^3,$$

i.e.

$$F(\rho, t) = 3\rho^2 f(\rho^3, t).$$

2. TIME VARIATION OF THE CRITICAL DIMENSIONS AND THE ASYMPTOTIC FORM OF THE DISTRIBUTION FUNCTION IN HYDRODYNAMIC APPROXIMATION

Along an axis in dimension space representing grain volume, the point ρ^3 (which apart from a factor $\frac{4}{3}\pi$ is the volume of some given grain) moves according to the following prescription. Points to the left of $x^3(t)$ accelerate to the left, until on reaching the origin they fall out of consideration, the grain having completely dissolved. Points initially to the right of $x^3(t)$ accelerate at first to the

* The equation contains the stationary value $\partial C/\partial r$ of the concentration gradient at the grain boundary. It is easily shown that this procedure is valid if the initial supersaturation is small ($\Delta_0 \ll 1$).

† If the grains are aspherical, but in the later stages of the process grow in such a way as to preserve their shape due to an anisotropy in α, then equation (2) and all quantitative deductions from it remain correct so long as R is interpreted as $(3V/4\pi)^{1/3}$, with V the grain volume, and a, α and $\mathscr{D}$ are modified to the extent of numerical factors depending on the shape in question.

Vol. 1
1961

right; but as the degree of supersaturation falls, $x^3(t)$ increases and successively overtakes points that in the first instance were to the right of it. After being overtaken, such points begin to move in the opposite direction and finally also disappear into the origin. The motion is throughout regular in the sense that the initial order of a set of points is preserved.

Canonical form of the equations

Both the form of equation (3) and the physical meaning of $x(t)$ suggest that it would be more natural to express equations (3)–(5) in terms of a reduced volume

$$z = \frac{\rho^3}{x^3(t)}, \qquad x(0) = 1 \tag{6}$$

that compares ρ^3 with the critical volume x^3. Moreover, as $t \to \infty$, $\Delta \to 0$, so that $x(t) \to \infty$; thus $x(t)$ may be used as a measure of time. It now appears that (3), (4) and (5) take on canonical form if time is introduced through the variable

$$\tau = \ln x^3(t) \tag{7}$$

and a new volume distribution function ϕ is employed such that

$$\phi(z, \tau)\, dz = f(\rho^3, t)\, d\rho^3. \tag{8}$$

Using (6), (7) and (8), equations (3), (4) and (5) become respectively

$$\frac{\partial \phi}{\partial \tau} + \frac{\partial}{\partial z}\phi v(z, \gamma) = 0, \tag{9}$$

$$\left.\begin{aligned} \frac{dz}{d\tau} &= v(z, \gamma) = (z^{1/3} - 1)\gamma(\tau) - z, \\ \gamma(\tau) &= 3\frac{dt}{dx^3}; \end{aligned}\right\} \tag{10}$$

$$\left.\begin{aligned} 1 &= \frac{\Delta_0}{Q_0} e^{-\tau/3} + \kappa e^{\tau} \int_0^{\infty} \phi(z, \tau) z\, dz, \\ \phi|_{t=\tau=0} &= f_0(z), \qquad z|_{\tau=0} = \rho^3. \end{aligned}\right\} \tag{11}$$

If the solution of (10) under the initial condition $z|_{\tau=0} = y$ be written $z(y, \tau)$, then (11) may be expressed in terms of the initial distribution function $f_0(z)$ thus:

$$1 - \frac{\Delta_0}{Q_0} e^{-\tau/3} = \kappa e^{\tau} \int_{y_0(\tau)}^{\infty} f_0(y) z(y, \tau)\, dy. \tag{12}$$

Here $y_0(\tau)$ is the solution of $z[y_0(\tau), \tau] = 0$, i.e. the lower limit of the range of starting volumes appropriate to grains that are still undissolved at time τ.

The asymptotic solution

As it will be shown that $\phi(z, \tau)$ is asymptotically independent of $f_0(y)$, the unknown functions are now $\phi(z, \tau)$ and $\gamma(\tau)$.

The supersaturation $\Delta(t)$ decreases monotonically with time, and therefore $1/x(t)$ does the same. There are therefore only three possibilities for the asymptotic behaviour of $\gamma(\tau)$ as $\tau \to \infty$, viz. $\gamma(\tau) \to \infty$, 0 or constant. We shall show that the first two do not apply.

(i) $\gamma(\tau) \to \infty$ as $\tau \to \infty$. In this case, $x^3(t)$ varies more slowly than t. The ultimate number of grains per unit volume is associated with a rate $dz/d\tau > 0$, which implies

$$\int_0^{\infty} \phi(z, \tau) z\, dz > \text{const.} \tag{13}$$

The amount of matter in grain form at $\tau \to \infty$ will therefore be

$$q > \text{const.}\, e^{\tau} \xrightarrow[\tau \to \infty]{} \infty,$$

so that (11) is not satisfied.

(ii) $\gamma(\tau) \to 0$ as $\tau \to \infty$, i.e. $x^3(t)$ varies more quickly than t. At sufficiently large times the solution of (10) in this case is

$$\frac{dz}{d\tau} = (z^{1/3} - 1)\gamma - z \approx -\gamma(\tau) - z,$$

$$z = ye^{-\tau} - e^{-\tau} \int_0^{\tau} e^{\tau'} \gamma(\tau')\, d\tau'.$$

From the condition $z[y_0(\tau), \tau] = 0$,

$$y_0(\tau) = \int_0^{\tau} e^{\tau'} \gamma(\tau')\, d\tau' = 3t(\tau);$$

the amount of matter in grain form at $\tau \to \infty$ is

$$q = e^{\tau} \int_{y_0(\tau)}^{\infty} f_0(y) z(y, \tau)\, dy \leqslant \int_{3t}^{\infty} f_0(y) y\, dy \xrightarrow[\tau \to \infty]{t(\tau) \to \infty} 0.$$

Thus equation (12) cannot be satisfied [nor indeed equation (11)].

It follows that $\gamma(\tau)$ must tend asymptotically to some constant value γ_0, and this we now proceed to determine, together with the asymptotic form of $\phi(z, \tau)$. We first remark that at such times as $\gamma(t)$ may be put constant in equation (9), the general solution of (9) is

$$\phi(z, \tau) = \chi(\tau + \psi) \frac{1}{g(z, \gamma)},$$

with

$$g(z, \gamma) = -v(z, \gamma), \qquad \psi = \int_0^z g^{-1}(z, \gamma)\, dz,$$

and χ an arbitrary function. Substituting this result into (11) it will be seen that if the first part is to be asymptotically time-independent, χ must have the form

$$\chi(\tau + \psi) = A\, e^{-(\tau + \psi)}.$$

Thus $\phi(z, \tau)$ must tend asymptotically to

$$\phi(z, \tau) = e^{-\tau} \Phi(z, \gamma).$$

So far we have examined only the asymptotic dependence of ϕ on τ. We now turn to the determination of γ, for which we write out the asymptotic forms of equations (9)–(11):

$$-\Phi + v(z, \gamma) \frac{d\Phi}{dz} + \Phi \frac{dv}{dz} = 0; \tag{15}$$

$$\frac{dz}{d\tau} = v(z, \tau) = (z^{1/3} - 1)\gamma - z, \text{ with } \gamma = \text{const}; \tag{16}$$

$$1 = \kappa \int_0^{\infty} \Phi z\, dz. \tag{17}$$

Examination of equation (15) shows that to satisfy (17), $\Phi(z, \gamma)$ can be different from zero only in the ultimate phase of change of z; for otherwise

$$\int_0^{\infty} \Phi z\, dz$$

would be logarithmically divergent, irrespective of the detailed nature of Φ. For such a solution to exist and to be continuous and finite over the whole range of changing z, it would appear sufficient that Φ and its first derivative go to zero at some point $z = z_0$ and beyond this point join onto a constant zero. Solutions of this type can formally be found, and correspond to values of $\gamma > \gamma_0$.

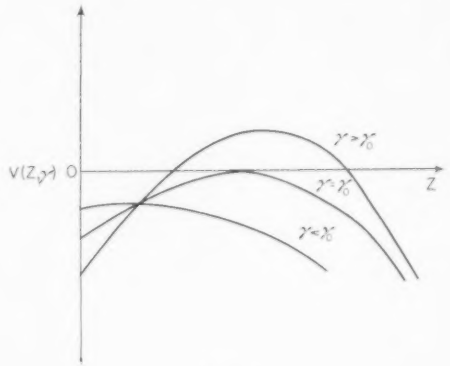

FIG. 1.

However, in Section 3 it will be shown that these solutions are unstable when the encounters between different grains are taken into account. It turns out that the only stable solution is that for which $\Phi(z, \gamma)$ and *all* its derivatives go to zero at z_0, so that to the right of z_0 the solution is identically zero. Further inspection of equation (15) now shows that the stable solution corresponds to a value of $\gamma = \gamma_0$ such that the rate of change $v(z, \gamma_0)$ has a second order zero at $z = z_0$. Using, therefore, the conditions

$$v(z, \gamma_0) = 0,$$

$$\left.\frac{dv}{dz}\right|_{z = z_0} = 0,$$

we find

$$\gamma = \gamma_0 = \frac{27}{4}; \qquad z_0 = \frac{27}{8} = \frac{\gamma_0}{2}.$$

Vol. 196

The present results may be interpreted in the light of Fig. 1, which shows $v(z, \gamma)$ as a function of z for various values of γ. If $\gamma < \gamma_0$, the representative points of all grains move to the left and disappear into the origin. The grains in existence at any given time comprise asymptotically a volume distribution in the form of an infinitely long "tail" to the initial distribution function, falling off with z faster than z^{-2}; therefore, the total amount of material in grain form tends to zero:

$$q \sim \int_{y_0(\tau)}^{\infty} \frac{1}{y^{(2+\alpha)}} y\,dy \xrightarrow[\tau \to \infty]{y_0(\tau) \to \infty} 0$$

instead of to a constant value. If on the other hand $\gamma > \gamma_0$, all grains to the right of a point z_1 move towards the point z_2, with the result* that

$$q \sim e^{\tau} \int_{z_1}^{\infty} f_0(y) z(y, \tau)\,dy$$

$$\sim e^{\tau} \int_{z_1}^{\infty} f_0(y) z_2\,dy$$

$$\sim \text{const.}\, e^{\tau} \xrightarrow[\tau \to \infty]{} \infty,$$

$$[z(y, \tau) \xrightarrow[\tau \to \infty]{} z_2, \quad y > z_1] \qquad (18)$$

this again contradicting the conditions of the problem. Thus only the case $\gamma = \gamma_0$ remains valid.

$\Phi(z, \gamma_0)$ has the form

$$\Phi(z, \gamma_0) = \begin{cases} A\, e^{-\psi(z, \gamma_0)} \dfrac{1}{g(z, \gamma_0)}, & z \leqslant z_0 = \frac{27}{8} \\ 0, & z \geqslant z_0 = \frac{27}{8} \end{cases} \qquad (19)$$

in which

$$g(z, \gamma_0) = -v(z, \gamma_0) \geqslant 0; \qquad (20)$$

$$\psi = \int_0^z \frac{dz}{g(z, \gamma_0)} = \tfrac{4}{3} \ln(z^{1/3}+3) + \tfrac{5}{3} \ln(\tfrac{3}{2} - z^{1/3}) + $$

$$+ (1 - \tfrac{2}{3} z^{1/3})^{-1} - \ln(3^3 2^{-5/2} e); \qquad (21)$$

$$A = \frac{\kappa^{-1}}{\int_0^{z_0} e^{-\psi} \dfrac{z\,dz}{g(z, \gamma_0)}} = \frac{3Q_0}{4\pi R_{c0}^3 (1{\cdot}11)} \doteqdot 0{\cdot}22 \frac{Q_0}{R_{c0}^3}.$$

Higher approximations

From a general point of view, we have found $\phi(z, \tau)$ and $\gamma(\tau)$ only in the zero approximation, this being the most interesting in practice. More accurate expressions for these quantities are derived in the appendices. Here we remark only that in the accurate equation $\gamma = \gamma_0$, all points lying to the right of the point of contact $z_0 = \frac{27}{8}$ and moving to the left are found to be unable to pass across z_0; they are, so to speak, "caught" there with the result that the quantity of matter

$$q \sim e^{\tau} \xrightarrow[\tau \to \infty]{} \infty$$

and equation (11) cannot be satisfied. The conclusion is that $\gamma(\tau)$ tends to γ_0 from below:

$$\gamma(\tau) = \gamma_0[1 - \epsilon^2(\tau)], \qquad \epsilon^2(\tau) \xrightarrow[\tau \to \infty]{} 0.$$

It follows that the "leakage" across z_0 of points approaching z_0 from the right takes place more and more slowly with the passage of time, the exact rate depending on ϵ^2, which like $\gamma(\tau)$ itself must be determined from equation (11) and the equation of motion (10).

In the next approximation, $\phi(z, \tau)$ is not zero to the right of the "blocking" point z_0, but is some function governed by the initial distribution function $f_0(z)$. However, as $\tau \to \infty$, it is increasingly dominated by its infinitely long tail and its total contribution in equation (11) tends to zero. We now see that in the region of the blocking point z_0, every initial distribution function is transformed into a unique universal function, z_0 becoming a sink for points with $z > z_0$ and a source for points with $z < z_0$. (The latter set of points have their sink at the origin.)

* Even if $\Phi(z, \gamma_0) = 0$ for $z \geqslant z_1$ at the outset, the encounters between grains treated in Section 3 produce grains in the region $z > z_1$, to which this conclusion then applies.

Vol. 19
1961

The results summarised

The basic results of this section may now be written out explicitly. The complete volume distribution function has the form

$$\phi(z,\gamma_0)=\begin{cases} Ae^{-\tau}\dfrac{e^{-\psi}}{g(z,\gamma_0)}=n(\tau)p(z,\gamma_0), & z\leqslant z_0\\ 0, & z\geqslant z_0\end{cases} \tag{22}$$

where

$$n(\tau)=\int_0^\infty \phi(z,\tau)\,dz=Ae^{-\tau} \tag{23}$$

is the number of grains per unit volume, and

$$p(z,\gamma_0)=\begin{cases}\dfrac{e^{-\psi}}{g(z,\gamma_0)}=3\cdot 2^{-5/3}e\cdot(z^{1/3}+3)^{-7/3}\left(\tfrac{3}{2}-z^{1/3}\right)^{-11/3}\exp-(1-\tfrac{2}{3}z^{1/3})^{-1}, & z\leqslant z_0\\ 0; & z\geqslant z_0\end{cases}$$

$$\left(\int_0^\infty p(z,\gamma_0)\,dz=\int_0^{z_0} p(z,\gamma_0)\,dz=1\right) \tag{24}$$

is the probability that a grain shall have a reduced volume between z and $z+dz$. Fig. 2 shows $p^*(z^{1/3},\gamma_0)=p(z,\gamma_0)\cdot(dz/dz^{1/3})$, the probability that a grain has mean dimension between $z^{1/3}=(R/x)$ and $(R/x)+d(R/x)$, as a function of $z^{1/3}$.

Further, from the fact that

$$\frac{dz}{d\psi}=z-\gamma_0(z^{1/3}-1)$$

we find

$$\overline{z^{1/3}}-1=\int_0^{z_0} e^{-\psi}\frac{z^{1/3}-1}{g(z,\gamma_0)}\,dz=[\gamma_0^{-1}e^{-\psi}z]_0^{z_0}=0, \tag{25}$$

from which it follows that

$$\bar\rho=\overline{z^{1/3}}x=x(t). \tag{26}$$

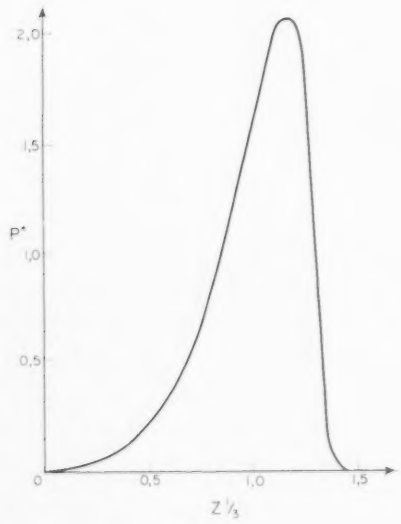

FIG. 2.

To obtain the distribution function relating to the absolute dimension ρ of the grains, we need only replace z in (22) by $[\rho^3/x^3(t)]$ and divide by

$$x^3(t)=\tfrac{4}{9}t. \tag{27}$$

Inserting the original parameters, and remembering that according to (26), $z=R^3/\bar R^3$, we obtain

$$\left.\begin{aligned} &f(R^3,t)=n(t)p(R/\bar R)\bar R^{-3},\\ &n(t)=\beta Q_0\bar R^{-3}=\mathscr{B}t^{-1}, \text{ with}\\ &\qquad\beta\doteqdot 0{\cdot}22,\ \mathscr{B}\doteqdot(2\mathscr{D}\alpha)^{-1},\\ &\bar R^3=\tfrac{4}{9}\mathscr{D}\alpha t.\end{aligned}\right\} \tag{28}$$

If measurements are to be made on a section of the material it is convenient to transform the volume distribution function $\Phi(z,\tau)$ into a distribution function over the apparent dimension r of the grains as revealed on the surface of the section.

Vol. 196

Writing $l = (r/x)$, this latter function is defined by

$$F(l,\tau)\,dl = \Phi(r,\tau)\,dr; \qquad \Phi(r,\tau) = \frac{1}{x}F\left(\frac{r}{x},\tau\right)$$

and is easily shown to be

$$F(l,\tau) = 2\int_{l_0}^{27/8} \phi(z,\tau)\left[\left(\frac{z^{1/3}}{l}\right)^2 - 1\right]^{-1/2} dz$$

(see Fig. 3).

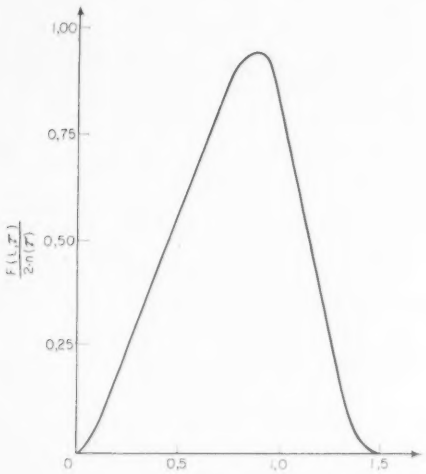

FIG. 3.

The degree of supersaturation at time t is given by

$$\Delta(t) = \frac{\Delta_0}{x(t)} = \left(\frac{2}{3}\right)^{2/3}\Delta_0 \cdot \left(\frac{T}{t}\right)^{1/3} = \lambda t^{-1/3}, \quad (29)$$

with

$$\lambda = (\tfrac{3}{2})^{2/3}(\alpha^2/\mathscr{D})^{1/3}.$$

Range of validity of the formulae

The above formulae completely determine the asymptotic distribution as a function of grain dimension and time. As shown in the appendix, they are valid when

$$1 \ll \tau^2 = (\ln x^3)^2 = 9[\ln(\bar{R}/R_{c0})]^2, \qquad \bar{R} \gg R_{c0}.$$

In this inequality, $R_{c0} = \alpha/\Delta_0$ is the initial critical radius for coalescence, corresponding to the starting supersaturation Δ_0. It will be realised that if at the outset the mean grain dimensions are of the order of the critical size ($\overline{R_0} \sim R_{c0}$), then this latter dimension must appear in the condition. However, if $\overline{R_0} \gg R_{c0}$, then the first stage of development consists in a growth of grains directly from the solution, which goes on until the degree of supersaturation has so fallen that the critical radius has caught up with the mean grain size ($\overline{R_1} \sim R_{c1}$); thereafter, strictly speaking, coalescence supervenes. In this case, R_{c1} plays the part of an initial dimension. The critical size is governed not only by the initial supersaturation, but also by

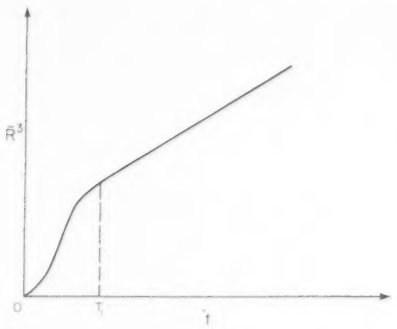

FIG. 4.

the number of grain nuclei (where this can be considered a fixed quantity). Thus if there are to begin with n_0 nuclei, and $\overline{R_0} \gg R_{c0} = \alpha/\Delta_0$, growth from the solution takes place until

$$\frac{4}{3}\pi\overline{R_1}^3 \approx \frac{\Delta_0}{n_0}.$$

In this first stage,

$$\frac{d\bar{R}^2}{dt} = 2\mathscr{D}(\Delta_0 - \tfrac{4}{3}\pi n_0\bar{R}^3) = 2\mathscr{D}\Delta_0\left[1 - \left(\frac{\bar{R}}{R_{c1}}\right)^2\right],$$

and this development occupies a time

$$t_1 \sim \overline{R_1}^2/\mathscr{D}\Delta_0.$$

The initial processes of the second stage (coalescence) have a characteristic time

$$t_0 \sim \overline{R_1}^3/\mathscr{D}\alpha \sim t_1(\overline{R_1}/R_{c0})$$

when, as in the situation discussed, $\overline{R_1} \gg R_{c0}$, i.e. $t_0 \gg t_1$. Fig. 4 shows schematically the mean dimensions as a function of time for this case.

Vol. 19
1961

Influence of other effects

We have so far ignored a number of second-order effects such as that of grain shape, crystalline order, and the elastic strain that results from a difference between the specific volumes of the grains and the matrix. These matters are examined in detail in a companion paper in the *Journal of Solid State Physics*,[5] in which we show that the qualitative conclusions of the present study are unaffected.

For instance, if the grains initially have a variety of shapes, we find that at sufficiently great times the only shape to survive is the most favourable one, which gives the greatest growth rate. All the conclusions of this Section still apply in the asymptotic situation.

Again, if the growth of a grain produces an elastic deformation of its surroundings, there will be an effect on the diffusion rate. We find[4] that this may be taken into account merely by replacing C_∞, $\mathscr{D}$ and α by certain effective values:

$$C'_\infty = C_\infty e^\gamma; \qquad \alpha' = \alpha e^\gamma; \qquad \mathscr{D}' = \mathscr{D}\beta$$

respectively, where

$$\gamma = (kT)^{-1}\left(\mathscr{E}_{II} - \mathscr{E}_I - \left[\frac{\partial \mathscr{E}_I}{\partial C}\right]_{c=0}\right);$$

$$\beta^{-1} = \int_0^1 e^{pz^3}\, dz;$$

$$p = \frac{(1+\sigma)\left[\dfrac{\partial \mathscr{E}_I}{\partial C}\right]_{c=0}}{3[(1+\sigma)+2n(1-\sigma)]}\,\frac{V}{kT}\left(\frac{\Delta V}{V}\right)^2.$$

Here $\mathscr{E}_I$ is the elastic energy per atom in the grain, $\mathscr{E}_{II}$ the same quantity in the surroundings; E is Young's modulus, and $n = E_I/E_{II}$; σ is Poisson's ratio; V is the volume per atom in the grain, and ΔV the difference between the volumes per atom of the grain and the surrounding medium.

The possibility of order in the atomic arrangement we allow for in the case where the energy required to jump an atom from one sublattice to the other is rather large, so that there can be said to exist two essentially unrelated diffusion fluxes. The flux of particles to the grain is then treated exactly as above, except that $\mathscr{D}$ is further replaced by

$$\mathscr{D}_{\text{eff}} = \frac{2\mathscr{D}_1\mathscr{D}_2}{\mathscr{D}_1+\mathscr{D}_2},$$

the suffixes 1 and 2 referring to the individual sublattices separately.

These second-order effects, therefore, call for no more than a re-expression of certain parameters in the theory. They do not alter the asymptotic grain size distribution function or influence its stability; our present solution, therefore, is universal.

3. ENCOUNTERS BETWEEN GRAINS, IN KINETIC APPROXIMATION

Equations (1) and (3) are characteristic results of applying the "hydrodynamic" approximation to our problem, while equation (10) expresses the rate of volume change $(dz/d\tau) = -g(z, \tau)$ at any time as a function of the mean supersaturation $\Delta(\tau)$. These equations, however, make no allowance for the concentration gradient near a grain that is in a state of changing volume. In fact, due to local variations of concentration the rates of volume change are not exactly equal to the mean value $-g$.

The complication thus introduced can be overcome, using the idea of "encounters" between grains. An encounter is a situation in which two or more grains find themselves separated by a distance that is less than their mean linear dimension, and either unite directly or at least undergo a diffusion interaction. The discussion may be said to introduce a "kinetic approximation".

In the treatment of Section 2, the stable asymptotic volume distribution was derived by an argument which revolved round the leaking of representative points z across a blocking point $z_0 = \frac{27}{8}$. Now encounters have the effect of carrying representative points across this barrier, and so the whole problem of their influence on the asymptotic distribution must be examined closely. This is true even if the over-all supersaturation is small and encounters are a rare phenomenon.

Treatment of encounters

In the ordinary physical space of the material we take the origin of coordinates in the middle of some chosen grain and use a reduced position

Vol. 196

vector $\boldsymbol{\zeta} = \mathbf{r}/R_c(t)$. Although the centres of the other grains are fixed in the lattice, the fact that $R_c(t) \to \infty$ means that in reduced coordinates all grains draw closer together and move radially towards the selected one. Of course, the majority of the grains disappear before reaching the origin and do not have encounters.

We also employ a reduced distribution function f and a reduced grain density $\mathcal{N}$ which refer to a unit of volume such that $\zeta^3 = 1$. They are related to the earlier quantities ϕ and n through:

$$f = R_c^3(t)\phi = e^{\tau}\phi,$$
$$\mathcal{N} = R_c^3(t)n = e^{\tau}n.$$

Since practically the whole excess of the dissolved material eventually collects into grains such that $n \sim e^{-\tau}$, $\mathcal{N}$ approaches a constant value as $t \to \infty$. It follows that the probability per unit time of an encounter in a reduced unit of volume becomes time-independent. Writing the number of encounters, per unit time per reduced volume unit, between grains of dimension in the range z to $z+dz$ and grains of dimension z' as

$$\nu = f(z')p(z, z')f(z)\,dz,$$

an encounter-probability distribution function $p(z, z')$ is defined.

$p(z, z')$ may be expressed in the form $p = w(z, z')/\tau_e$, with τ_e a characteristic time for encounters, and $w(z, z')$ a reduced volume centred around a grain z, over which the interaction with one of the grains z' may be held to occur. It is not difficult to show that to order of magnitude, $w \approx z+z'$, i.e. is given by the over-all reduced volume of the two grains. τ_e must be of the order of unity, inasmuch as all the parameters are of the order of unity both in the initial condition $z|_{\tau=0} = z_0$ and in the equation

$$\frac{dz}{d\tau} \approx -\gamma - z$$

that describes the dissolution of the lesser grain.

When two grains meet, the greater of them absorbs the lesser, and their total volume is approximately conserved. A certain fraction of the material may in fact go back into solution, but it will be obvious that nothing is essentially changed if we ignore this detail. For if the effects of encounters are to be allowed for, the first approximate equality in (18) must contain a term corresponding to the total "encounter integral"

$$\mathcal{I}_e = \tau_e^{-1}\left[\tfrac{1}{2}\int_0^z w(z-z', z')f(z-z')f(z')\,dz' - f(z)\int_0^\infty w(z, z')f(z')\,dz'\right]. \tag{30}$$

(The factor $\frac{1}{2}$ is necessary, because without it each encounter would be reckoned twice.) Taking advantage of the fact that $w(z, z')$ is symmetric with respect to a transposition of its arguments, it is easy to show that although the number of grains is reduced by encounters, the volume is conserved:

$$\int_0^\infty \mathcal{I}_e\,dz = -\tau_e^{-1}\tfrac{1}{2}\int_0^\infty f(z)\,dz\int_0^\infty w(z, z')f(z')\,dz';$$

$$\int_0^\infty \mathcal{I}_e z\,dz = 0.$$

The distribution function

Returning for the moment to equation (17), it will be observed that f is dependent on the small parameter $1/x$. To bring out more clearly its dependence on the small parameter Q_0 we introduce the function

$$\Phi = xf.$$

Using this variable, a complete set of equations controlling the system can now be written out with full allowance for encounters. The equations have the asymptotic form:

$$\frac{d}{dz}\Phi_g(z, \gamma) + \Phi = -\mathcal{I}_e$$

$$= -\frac{3Q_0}{4\pi}\tau_e^{-1}\left[\tfrac{1}{2}\int_0^z w(z-z', z')\Phi(z-z')\Phi(z')\,dz' - \Phi(z)\int_0^z w(z, z')\Phi(z')\,dz'\right], \tag{31}$$

Vol. 19
1961

$$1 = \int_0^\infty \Phi z \, dz, \qquad \gamma = \text{const.} \tag{32}$$

They may be solved by successive approximation, using the fact that $\mathscr{I}_e$ is small.

At this point we may usefully notice that both from the analysis of Section 2 and directly from physical arguments one must expect that the new considerations reduce γ below γ_0. For in the terms of the earlier discussion, grains that are carried across the barrier-point z_0 by encounters have a non-zero probability of leaking back, and this implies $\gamma < \gamma_0$. We shall now show that the zero-order approximation is equivalent to taking the solution of (31) without the first part and with $\gamma = \gamma_0$, and that this is equation (19). Indeed, the solution of the homogeneous equation with $\gamma < \gamma_0$ does not satisfy (32), as

$$\int_0^\infty \Phi z \, dz$$

is then logarithmically divergent.

If $\gamma > \gamma_0$, a solution may be constructed that is continuous and has a continuous first derivative over the whole range of z, and which is different from zero only for $z < z_1$. $g(z, \gamma) = 0$ for $z = z_1$ and z_2, $z_2 > z_1$, otherwise

$$\int_0^\infty \Phi z \, dz$$

will diverge at z_2. In the neighbourhood of $z = z_1$, $\Phi(z, \gamma)$ behaves like

$$(z - z_1)^{-[(\partial g/\partial z)_{z=z_1}^{-1}+1]} = (z - z_1)^{-[\frac{3}{2}\gamma_0^{-1}(\gamma-\gamma_0)^{-\frac{1}{2}}+1]},$$

so that for $(3\gamma_0)^{-2}+\gamma_0 > \gamma > \gamma_0$ a solution of the type mentioned is possible; it is, however, unstable in respect of the first term in equation (31), since in the next higher approximation it is

$$\Phi(z, \gamma) = \frac{e^{-\psi}}{g(z, \gamma)}\{c - \int \mathscr{I}_e[f(z', \gamma)]e^{\psi} \, dz'\}$$

and diverges at $z = z_2$. This also shows that (19) is the only stable solution of (15).

Taking, therefore, (19) as the zero-order solution, the encounter integral becomes

$$\mathscr{I}_e[\Phi] \approx \mathscr{I}_e[\Phi_0(z, \gamma_0)] = \frac{3Q_0}{4\pi}\tau_e^{-1}\mathscr{I}_0(z), \tag{33}$$

$$\mathscr{I}_0(z) = \begin{cases} \frac{1}{2}\int_0^z w(z-z', z')\Phi_0(z-z')\Phi_0(z') \, dz' - \Phi_0(z)\int_0^\infty w(z, z')\Phi_0(z') \, dz', & z \leqslant 2z_0 \\ 0, & z > 2z_0 \end{cases}$$

$$\Phi_0 \equiv \Phi_0(z, \gamma_0).$$

The method of successive approximation must consist in refining the value of

$$\frac{d}{dz}\Phi_1 g_1 + \Phi_1 = -\mathscr{I}_e[\Phi_0],$$

$$1 = \int_0^\infty \Phi_1 z \, dz.$$

In general this will lead to

$$\frac{d}{dz}\Phi_n g_n + \Phi_n = -\mathscr{I}_e[\Phi_{n-1}],$$

$$1 = \int_0^\infty \Phi_n z \, dz,$$

$$g_n = g(z, \gamma^n), \tag{34}$$

so that

$$\Phi_1 = \frac{e^{-\psi}}{g(z, \gamma_0)}\{c + \int_z^{2z_0} \mathscr{I}_e[\Phi_0(z, \gamma_0)]e^{\psi} \, dz\};$$

the convergence of

$$\int_0^\infty \Phi z \, dz$$

Vol. 196

requires $c = 0$. A refined value of γ is found from the condition

$$\int_0^\infty \Phi z \, dz = 1.$$

The desired solution of (34) is accordingly

$$\Phi(z, \gamma) = \begin{cases} e^{-\psi} g^{-1} \int_z^{2z_0} \mathcal{I}_e[\Phi_0(z', \gamma_0)] e^{\psi} \, dz', & z \leqslant 2z_0 \\ 0, & z > 2z_0 \end{cases} \tag{35}$$

$$\psi = \int_0^z g^{-1}(z, \gamma_0) \, dz.$$

(35) may be confirmed without difficulty if one remembers that $f(z, \gamma)$ and its first derivative go to zero at $z = 2z_0$, so that the first equation in (34) is satisfied over the whole range of z.

Explicitly, we have shown that in first approximation

$$\Phi = \begin{cases} \dfrac{3Q_0}{4\pi} \tau_e^{-1} e^{\Delta} A e^{-\psi} g^{-1}, & z < z_0 \\ \qquad A = \int_{z_0}^{2z_0} e^{\psi^*} \mathcal{I}_0(z') \, dz'; & \\ \dfrac{3Q_0}{4\pi} \tau_e^{-1} e^{-\psi^*} g^{-1} \int_z^{2z_0} e^{\psi^*} \mathcal{I}_0(z') \, dz'; & z_0 < z < 2z_0 \\ 0. & z > 2z_0 \end{cases} \tag{36}$$

These formulae take into account the fact that where $\Delta\gamma \ll 1$, ψ increases sharply in the neighbourhood of z_0 and thereafter varies smoothly, with $\psi^*(z, \gamma) = \psi(z, \gamma_0)$; in this condition $\Delta = \frac{3}{2}\pi(\frac{3}{4}\Delta\gamma/\gamma_0)^{-1/2}$. It follows that where $z > z_0$, $f(z) \sim Q_0$. There is, of course, a smooth transition between the two regions $z < z_0$ and $z > z_0$.

The next approximation to the distribution function may be obtained by substituting (36) back into the encounter integral; by iteration, the distribution function can be determined to any desired accuracy.

Dependence on the initial supersaturation

It is interesting to see that if in each interval $nz_0 < z < (n+1)z_0$ we retain only the terms in the lowest power of Q_0, the solution may be written

$$f(z) = Q_0^{z/z_0} \cdot \phi(z). \tag{37}$$

$\phi(z)$ in (37) can be determined within each interval; for instance, in the range $0 \leqslant z \leqslant 2z_0$ we determined it above. Physically, this type of dependence on Q_0 may be traced to the fact that the number of grains of magnitude z is continually augmented by the agglomeration of smaller grains having total volume $z_a + z_b = z$.

The form of (37) makes it apparent that to an

order of accuracy Q_0, the principal contribution in equation (34a) comes from the distribution function in the region $z < z_0$. Using this fact, we can determine the asymptotic dependence of $\Delta\gamma$ on Q_0 as follows:

$$1 = \frac{3Q_0}{4\pi}\tau_e^{-1}Ae^{\Delta}\int_0^{z_0} e^{-\psi}\frac{z}{g(z,\gamma)}\,dz. \quad (38)$$

Now because $\gamma = \gamma_0 - \Delta\gamma$ differs little from γ_0, (38) may be rewritten

$$1 = \frac{3Q_0}{4\pi}\tau_e^{-1}Ae^{\Delta}\int_0^{z_0} e^{-\psi}\frac{z}{g(z,\gamma_0)}\,dz, \quad (39)$$

whence

$$\frac{\Delta\gamma}{\gamma_0} = 12\pi^2\left[2\ln\frac{4\pi}{3Q_0} - \ln p\right]^{-2} \approx \frac{3\pi^2}{(\ln Q_0)^2} \quad (40)$$

with

$$p = A\tau_e^{-1}\int_0^{z_0} e^{-\psi}\frac{z}{g(z,\gamma_0)}\,dz \approx 1.$$

4. THE EFFECT OF CRYSTAL BOUNDARIES, AND THE THEORY OF SINTERING

The supersaturated crystal studied in Sections 1–3 was by implication unrestricted in size, and therefore contained no gross diffusion currents on a macroscopic scale. If we now remove the condition of over-all spatial uniformity, the problem is altered. The most important practical example of this more complicated situation is provided by an interphase boundary between the solution and some other phase, which might be, for instance, a crystal of pure solute, or more generally perhaps a crystal of the same phase whose precipitation is being considered. At such a boundary, the supersaturation $\Delta|_{l=0} = 0$ and macroscopic diffusion currents exist.

Vacancies

An important special case is that of a crystal supersaturated with vacancies, in which our discussion can be applied to the vacancies as solute "atoms" which cluster together to form cavities playing the part of our grains. If such a crystal has free surface, two competing processes will take place. Far from the surface, cavities will grow and coalesce according to the scheme developed in the earlier sections; on the other hand, near the border the cavities will tend to dissolve and the vacancies to diffuse to the surface. (The surface can be regarded as a cavity of infinite radius.) This dislodgment of cavities is also connected with the phenomenon of sintering.

In the remainder of this section we often refer expressly to the particular example of vacancy diffusion, although it is to be understood that the results are equally applicable to the more general case of a supersaturated solution.

Allowance for the crystal surface

Consider the situation in a half-space. Equation (3) for the grain growth and the distribution function (4) will still apply, and so will their equivalents (9) and (10). However, the conservation law $Q_0 = \Delta + q$ that underlies equations (5) and (12) must be replaced by a diffusion equation. Each point of coordinate l is now a source or sink of intensity $\partial q/\partial t$, and q is now $q(l, t)$ because the cavities are on the whole dissolving. The complete set of equations is properly

$$\frac{\partial}{\partial t}(\Delta + q) = \mathscr{D}\frac{\partial^2\Delta}{\partial l^2}, \qquad \Delta|_{l=0} = 0, \quad (41)$$

$$q = \kappa x^3(\tau)\int_{y_0(\tau)}^{\infty} f_0(y)z(y,\tau)\,dy,$$

$$z[y_0(\tau),\tau] = 0, \qquad x = \frac{\Delta_0}{\Delta(l,t)}; \quad (42)$$

in which $z(y, t)$ satisfies (10) and itself determines the form of $\Delta(l, t)$.

It will be remembered from Section 2 that the analysis led to a unique law for the decay of supersaturation [equation (29)]:

$$\Delta = \lambda t^{-1/3}.$$

This means in principle that if the asymptotic fall of the supersaturation were to be in some way retarded, however slightly, a process of limitless grain growth would set in and $q \to \infty$. Alternatively, an indefinitely small artificial increase in the rate of decay below the $t^{-1/3}$ law must fairly

Vol. 196

quickly result in the total dissolution of all grains ($q \to 0$). The mechanism of sintering is obviously related to this fact, and at least asymptotically must admit of the following discussion.

Reduction of the problem

There are, asymptotically, three fairly sharply defined regions in a supersaturated half-space:

(a) the farthest from the boundary, in a range $l_2 < l < \infty$. Here the influence of the boundary is negligible, and as with an infinite medium the supersaturation is given by (29);

(b) a region $l_1 < l < l_2$ in which the cavities (grains) have a general tendency to dissolve; and

(c) the region $0 < l < l_1$ in which there are no cavities (grains) at all, but an over-all diffusion of vacancies to the side.

The limiting distances $l_1(t)$ and $l_2(t)$ are situated well inside the crystal, and the skin layer that is free from cavities thickens continually.

Strictly speaking, equations (41) and (42) should be applied only to the intermediate region $l_1 < l < l_2$. However, it will be shown below that $(l_2-l_1)/l \ll 1$. For a first approximation we shall accordingly, consider an average depth $\zeta(t) = \frac{1}{2}(l_1+l_2)$, and by imposing some suitable boundary condition at ζ shall evaluate its magnitude and the vacancy concentration in the surface layer $0 < l < \zeta(t)$. For this purpose the intermediate region may effectively be replaced by a source of strength $Q_0(d\zeta/dt)$ at ζ, beyond which all the excess vacancies may be said to be in the cavities. Then we may say:

$$\frac{\partial \Delta}{\partial t} = \mathscr{D}\frac{\partial^2 \Delta}{\partial l^2}; \tag{43}$$

$$\Delta|_{l=0} = 0, \qquad \Delta|_{l=\zeta(t)} = \lambda t^{-1/3};$$

$$\mathscr{D}\frac{\partial \Delta}{\partial l}\bigg|_{l=\zeta(t)} = Q_0\frac{d\zeta}{dt}. \tag{44}$$

A solution of (38) is now required subject to the condition $\Delta|_{l=0} = 0$. On seeking it in the form

$$\Delta = \sum_{n=1}^{\infty} \alpha_n(t) l^n,$$

(39) gives

$$\Delta = \sum_{n=0}^{\infty} \frac{\hat{p}^n \alpha_1(t)}{(2n+1)!} l^{2n+1}, \qquad \hat{p} \equiv \frac{1}{\mathscr{D}}\frac{d}{dt}.$$

Before imposing the other two boundary conditions it is helpful to notice that $\alpha_1(t)$ is the flux of particles at the surface:

$$\alpha_1(t) = \mathscr{D}\frac{\partial \Delta}{\partial l}\bigg|_{l=0}.$$

Asymptotically, therefore, it must be a decreasing function of time, which suggests using the asymptotic form $\alpha_1(t) = B/t^s$, $(s > 0)$. Application of (42) now yields

$$\Delta = B\frac{l}{t^s}\sum_{n=0}^{\infty}(-1)^n\left(\frac{l^2}{\mathscr{D}t}\right)^n \frac{s(s+1)\ldots(s+n)}{(2n+1)!}. \tag{45}$$

As will appear shortly, $\zeta^2(t)$ is $o(t)$, that is to say

$$\zeta^2(t)/t \xrightarrow[t\to\infty]{} 0.$$

It follows that at large t the principal term in (45) is that with $n = 0$;

$$\Delta = \frac{Bl}{t^s} = \alpha_1(t)\cdot l. \tag{46}$$

Substituting now (41) into (39) we find

$$\alpha_1\zeta = \lambda t^{-1/3},$$

$$\alpha_1 = \frac{Q_0}{\mathscr{D}}\frac{d\zeta}{dt},$$

and therefore

$$\zeta = 3^{1/2}(\tfrac{3}{2})^{2/3}\frac{\bar{R}}{Q^{1/2}} = m\frac{(\mathscr{D}\alpha t)^{1/3}}{Q_0^{1/2}};$$

$$\Delta = \lambda t^{-1/3} l/\zeta = \tfrac{1}{3} m Q_0^{1/2}\alpha^{1/3} l(\mathscr{D}t)^{-2/3};$$

$$m = 3^{1/2}(\tfrac{3}{2})^{1/3} \doteq 2. \tag{47}$$

Orders of magnitude

It remains to determine the width of the intermediate region. By (43),

$$\frac{\delta\zeta}{\zeta} = \frac{\delta t}{3t} = \frac{T_d(t)}{3t},$$

Vol. 19
1961

where T_d is the time required to dissolve the largest grain to be found on the boundary at time t. Now $R_{\max} = \frac{3}{2}R_c$, and $R^3 \sim t^2$. A simple calculation shows that in the equation of motion (10), $\gamma = 3(dt/dx^3) \leqslant \frac{27}{8} < \gamma_0$. The largest grain has $z_0 = \frac{27}{8}$, and we deduce that it dissolves in a time $T_d \doteqdot \frac{1}{3}t$. Thus

$$\frac{\delta\zeta}{\zeta} \approxeq \frac{1}{9}.$$

By the same token,

$$\frac{\delta\zeta}{\bar{R}} = \frac{1}{3Q_0^{1/2}} \gg 1 \tag{49}$$

and

$$\frac{\delta\zeta}{L} = \frac{1}{3Q_0^{1/6}} \gg 1, \tag{50}$$

with L the mean distance between grains. Consequently

$$\delta\zeta \gg L \gg \bar{R}.$$

Although, therefore, the intermediate region is much thinner than the surface layer its width is considerably greater than both the mean cavity size and the mean distance between cavities (grains). The assumptions we made for equations (43) and (44) are therefore justified *post facto*.

The characteristic times associated with equation (47) are the same as those for the asymptotic equations describing coalescence in an infinite medium.

A further restriction

If the discussion for a half-space is now taken over to a specimen of finite size, as of course in practice, it must be realized that there is another condition to satisfy. For example, consider a plate-shaped layer of thickness a. Three characteristic times may be defined: that for the escape of vacancies to the surface, $T_0 \sim a^2/\mathscr{D}$; that for the growth of cavities from solution, $T_1 \sim \overline{R_1}^2/\mathscr{D}\Delta_0$ (as shown in Section 2); and the characteristic time for coalescence, $T_c \sim \bar{R}^3/\mathscr{D}\alpha$. For our picture to apply, T_0 must necessarily be much greater than T_c, so that $a^2 \gg R_1^3/\alpha$; the inequality is written in this form because the mean cavity dimensions must be those appropriate to the situation after coalescence has set in, i.e. $\bar{R} \gg R_1$. In the opposite limiting case, when $T_0 \ll T_1$, the vacancies are lost to the surface before cavities can be formed with any appreciable probability. In the intermediate situation where $a^2 \sim R_1^3/\alpha$, the exact course of events will be heavily influenced by the initial distribution function and is not amenable to a general discussion.

5. SUMMARY

1. An investigation is made of the way in which, in a supersaturated solid solution, grains of a new phase grow as the result of diffusion processes. The final stage of the process is examined in particular. A critical dimension x is determined such that large grains having dimension $\rho > x$ grow at the expense of small ones with $\rho < x$.

2. At large times t the critical dimension x tends asymptotically to depend on time as $t^{1/3}$. The degree of supersaturation correspondingly falls as $t^{-1/3}$ and the number of grains as t^{-1}.

3. A detailed picture of the law of grain growth is provided by the distribution function of grain dimensions. With the passage of time this distribution approaches a certain universal function [equations (22–24)] irrespective of the initial distribution. This function is remarkable in that the tail of the distribution towards infinity has disappeared, leaving a maximum grain size one-and-a-half times the critical dimension ($\rho_{\max} = \frac{3}{2}x$).

4. The effects of anisotropy and of the non-spherical nature of the original grain nuclei, like the effect of internal strain set up during the decay of the supersaturated solution, can all be taken into account simply by the use of "effective" parameters in place of certain quantities in the expression for the critical size. The form of the distribution function is unaffected by these considerations.

5. The process herein demonstrated for the coalescence of grains can also be applied to the study of "crust sintering". Each microscopic cavity in a specimen before sintering may be regarded as a crystal composed of vacancies. The cavities near the surface tend to dissolve as a result of their vacancies moving outwards to the boundary of the specimen, while in the depth of the material a process of coalescence goes forward essentially as in an infinite medium. The thickness of the "crust" increases with time as $\zeta \sim t^{1/3}$ [equation (47)].

APPENDIX 1. AN ACCURATE EXPRESSION FOR THE ASYMPTOTIC BEHAVIOUR OF $\gamma(\tau)$

As shown in Section 2, $\gamma(\tau) < \gamma_0$, so that we may write it

$$\gamma(\tau) = \gamma_0[1-\epsilon^2(\tau)].$$

$\epsilon(\tau)$ may be determined from the equation of motion (10):

$$\frac{dz}{d\tau} = (z^{1/3}-1)\gamma(\tau)-z$$

$$= -(z^{1/3}-\tfrac{3}{2})^2(z^{1/3}+3)-\tfrac{1}{2}\gamma_0\epsilon^2(\tau).$$

The latter term on the right has been so written because it is important only near $z = z_0 = \frac{27}{8}$. Put now for convenience $z = u^3$. Near $z = z_0$ or $u = u_0 = \frac{3}{2}$ the equation becomes

$$\frac{du}{d\tau} = -\tfrac{2}{3}(u-\tfrac{3}{2})^2-\tfrac{1}{2}\epsilon^2(\tau).$$

Changing variable to $y = (u-\frac{3}{2})/\epsilon(\tau)$ we may write this:

$$\frac{3}{2}\frac{dy}{\epsilon\, d\tau} = -y^2-\tfrac{3}{4}+\tfrac{3}{2}y\frac{d\left(\frac{1}{\epsilon}\right)}{d\tau}.$$

For the same reasons as those given in the text, the existence of a stable solution requires that in this approximation there should be a "blocking" point on the z axis and that the rate of change of z should have a second order zero at this point. This yields

$$\frac{d\left(\frac{1}{\epsilon}\right)}{d\tau} \to \frac{2}{\sqrt{(3)}}, \qquad \epsilon^2(\tau) \to \frac{3}{4\tau^2}, \qquad \tau \to \infty;$$

from which

$$\frac{3}{2}\frac{dy}{d\ln\tau} \to [y-\tfrac{1}{2}\sqrt{(3)}]^2.$$

Evidently $dy/d\tau$ does have a second order zero at the blocking point $y = y_0 = \frac{1}{2}\sqrt{3}$.

It is now apparent that at sufficiently great times,

$$\gamma(\tau) = \gamma_0(1-\tfrac{3}{4}\tau^{-2}).$$

The expression for the blocking point has been refined to

$$z_0^{1/3} = \tfrac{3}{2}+\tfrac{1}{4}\sqrt{(3)}\epsilon(\tau) = \tfrac{3}{2}+\tfrac{3}{4}\tau^{-1}.$$

By continuing with this procedure, an asymptotically accurate expansion for $\gamma(\tau)$ can be derived:

$$\gamma(\tau) = 3\frac{dt}{dx^3} = \gamma_0\left\{1-\frac{3}{4\tau^2}\left[1+\frac{1}{(\ln\tau)^2}(1+\ldots)\right]\right\},$$

and correspondingly

$$x^3 = \tfrac{4}{9}t\left[1+\frac{3}{4(\ln t)^2}(1+\ldots)\right].$$

The expansions may be broken off at any point at which the succeeding term is sufficiently small; in particular, the basic approximations $\gamma(\tau) = \gamma_0$ and $x^3 = (4/g)t$ are justified if

$$\tau^2 = (\ln x^3)^2 = (\ln \tfrac{4}{9}t)^2 \gg 1.$$

The fractional correction to γ_0 decreases swiftly with time, so that the first approximation becomes more and more accurate. It is a rather curious fact that the behaviour of the solution near the blocking point nevertheless continues to depend on just this correction.

APPENDIX 2. THE DISTRIBUTION FUNCTION IN THE REGION $z > z_0$, AND IN THE NEIGHBOURHOOD OF z_0

(i) Introduce the variable

$$\psi = \int \frac{dz}{g(z)},$$

and notice that as $z \to \infty$, $g(z) \to z$ and $z \to e^{\psi}$, i.e. $zx^3 \to e^{\tau+\psi}$. The form of the distribution function to the right of z_0 must be related to the initial distribution $f_0(\rho^3)$ over ρ^3:

$$\chi(\tau+\psi) \to f_0(\rho^3)g(\rho^3) \to f_0(zx^3)zx^3.$$

This being the case, we may determine the distribution function for $z > z_0$ from

$$\chi(\tau+\psi) \to f_0(e^{\tau+\psi})e^{\tau+\psi},$$

or,

$$\phi(z,\tau) = f_0(e^{\tau+\psi})e^{\tau+\psi}g^{-1}(z).$$

Because

$$\int_0^{\infty} f_0(z)z\,dz$$

exists, $f_0(z)$ falls off certainly faster than z^{-2}, and in fact normally is exponential in z. It follows that in the zero-order approximation, the volume probability density to the right of z_0 is zero. For

$$p(z,\tau) = \frac{\phi(z,\tau)}{n(\tau)} = f_0(e^{\tau+\psi})e^{2(\tau+\psi)}e^{-\psi}g^{-1}(z)$$

$$= f_0(p)p^2e^{-\psi}g^{-1}(z) \to 0$$

$$(p = e^{\tau+\psi} \xrightarrow[\tau\to\infty]{} \infty).$$

Of course, the probability density is non-zero to the left of z_0.

Vol. 19
1961

(ii) To derive a more accurate distribution function in the vicinity of $z = z_0 = \frac{3}{2}\tau$.

Write again for convenience $z = u^3$. Near z_0 the equation of continuity may be expressed as

$$\frac{\partial \phi}{\partial \tau} + \frac{\partial}{\partial u}\phi g(u) = 0;$$

$$g(u) = -\tfrac{2}{3}(u-\tfrac{3}{2})^2 - \tfrac{1}{2}\epsilon^2(\tau),$$

$$\epsilon^2(\tau) = \tfrac{3}{4}\tau^{-2}.$$

Changing the variable to

$$y = \tfrac{2}{3}(u-\tfrac{3}{2})\tau,$$

$$\phi(u, \tau)\, du = f(y, \ln \tau)\, dy$$

yields

$$\frac{\partial f}{\partial \ln \tau} - \frac{\partial}{\partial y} f g(y) = 0,$$

$$g(y) = (y-\tfrac{1}{2})^2.$$

The solution must be of the form

$$f \equiv f\,[\ln (\tau\, e^{\int g^{-1}(y)\, dy})].$$

We now observe that

$$\tau + \int_0^u g^{-1}(u)\, du \to \tau\, e^{\int g^{-1}(y)\, dy}$$

and

$$g^{-1}(u) \to \tfrac{2}{3} g^{-1}(y) \tau^2\, e^{\int g^{-1}(y)\, dy},$$

given that $1 \gg |u - \frac{3}{2}| \gg \epsilon^2(\tau)$. In fact

$$\tau + \int_0^u g^{-1}(u)\, du = \tau\{1 - [\tfrac{2}{3}(u-\tfrac{3}{2})\tau]^{-1}\}$$

$$= \tau(1 - y^{-1}) = \tau\, e^{\int g^{-1}(y)\, dy}.$$

Moreover at the same point $u = z^{1/3}$ the original distribution function must be given in zero order approximation by

$$f\frac{dy}{du} \to \frac{A}{\tfrac{2}{3}(u-\tfrac{3}{2})^2} \exp -\{\tau - [\tfrac{2}{3}(u-\tfrac{3}{2})]^{-1}\},$$

from which we at once obtain

$$f = A g^{-1}(y) \tau\, e^{\int g^{-1}(y)\, dy}\, e^{-\tau} \exp \int g^{-1}(y)\, dy.$$

(iii) To show that as $\tau \to \infty$, the integral contribution from the neighbourhood of z_0 becomes negligibly small.

The quantity of material accounted for in this region is

$$q_\delta = x^3 \int_{z_0-\delta}^{z_0+\delta} \phi z\, dz = z_0 e^\tau n_\delta(\tau);$$

$$n_\delta(\tau) = \int_{z_0-\delta}^{z_0+\delta} \phi\, dz, \qquad 1 \gg \delta \gg \epsilon(\tau).$$

Now from the equation of continuity,

$$\frac{dn_\delta}{d\tau} = \phi(z, \tau) g(z) \Big|_{z_0-\delta}^{z_0+\delta}$$

$$= A e^{-\tau}\, e^{-\psi(z_0-\delta)} = A e^{-\tau}\, e^{-3/2\, \delta^{-1/3}},$$

because to the right of z_0 the distribution is in the form of an infinitely long drawn out tail, which may be ignored. Thus

$$n_\delta = A e^{-\tau}\, e^{-(3/2)\, \delta^{-1/3}} + B,$$

$$q_\delta = A\, e^{-(3/2)\, \delta^{-1/3}} + B e^\tau.$$

Evidently B must be zero, since matter must be conserved. Consequently the amount of material represented in the vicinity of z_0 as $\tau \to \infty$ is

$$q_\delta = A\, e^{-(3/2)\, \delta^{-1/3}} \xrightarrow[\delta \to 0]{} 0.$$

REFERENCES

1. Todes O. M., *Zh. fiz. khim.* **20,** 7, 630 (1946).
2. Todes O. M. and Khrushchev V. V., *Zh. fiz. khim.* **21,** 3, 301 (1947).
3. Greenwood G. W., *Acta. Met.* **4,** 243 (1956).
4. Lifshitz I. M. and Slyozov T. V., *Zh. eksp. teor. fiz.* **35,** 2(8) (1958).
5. Lifshitz I. M. and Slyozov V. V., *Zh. fiz. tvyordykh tel.* (in press).

Vol. 1
196

J. Phys. Chem. Solids Pergamon Press 1961. Vol. 19, Nos. 1/2, pp. 51–53. Printed in Great Britain.

CRYSTAL STRUCTURE DISTORTIONS IN MnO_2 AND MnF_2 AT THEIR ANTIFERROMAGNETIC CURIE TEMPERATURE*

S. L. STRONG

U.S. Naval Ordnance Laboratory, Silver Spring, Maryland and Massachusetts Institute of Technology, Cambridge, Mass.

(*Received* 3 *May* 1960)

Abstract—Using a back reflection Debye powder camera, X-ray photographs were taken of MnO_2 and MnF_2 to determine the behavior of the lattice constants near the Néel temperature. It was found that on lowering the temperature the c-axis of MnO_2 expands while that of MnF_2 contracts. Examination of the results for MnO_2 and MnF_2 as well as other antiferromagnetics, shows that within a given crystal structure there is a correlation between the distortion and the spin direction.

ol. 19
1961

INTRODUCTION

One of the problems in antiferromagnetism has been the relation of the spin ordering and direction in the magnetic lattice and the lattice distortions that accompany this ordering process. These distortions are usually very small and are of the type where no discontinuity in the volume takes place. Early work[1] explained the distortions at the transition temperature (Néel temperature) in terms of the exchange integral. Thus the effect of the exchange interaction besides producing alignment of spins is to move the atoms either in contraction or expansion to lower the energy. Kanamori[2] has also treated antiferromagnetic deformations and shows that additional features besides exchange energy must be considered for certain oxides.

Experimental data have been available on antiferromagnetics with the rock salt crystal structure and also the corundum and NiAs structures. This paper presents measurements on the distortion in two compounds, MnO_2 and MnF_2, of the rutile structure.

In the Discussion we suggest an empirical correlation of the crystal distortion with the spin direction and crystal structure.

* This work has been submitted in partial fulfilment of the requirements for the degree of Master of Science at the Massachusetts Institute of Technology.

APPARATUS

The lattice parameters of MnO_2 and MnF_2 were measured using a symmetrical focusing back reflection Debye powder camera. This camera combines the high accuracy, necessary to measure the small distortions, with relatively small size, which simplifies the construction of the surrounding Dewar system. In addition to the inherent accuracy of the camera, arising from the concentration on high diffracting angles, this type of camera allows one to use a data reduction scheme[3] which minimizes errors due to film shrinkage or movement of the position of the sample.

MnO_2

Figure 1 shows the behavior of the lattice constants of MnO_2 between room temperature and 25°K. The vertical dotted line in the figure indicates the Néel temperature determined by means of magnetic susceptibility measurements. The studies by Yoshimori[4] and Erickson[5] on the magnetic structure of MnO_2 indicate that for this compound the spin moments of the manganese atoms are perpendicular to the c-axis of the crystal. Yoshimori makes the interesting interpretation that in the direction of this axis the spins form a spiral with a pitch of (7/2) c. The X-ray data combined with the above assignment of spin directions

shows that on cooling through the Néel temperature the crystal contracts along the *a*-axes.

MnF_2

Figure 2 shows the results obtained by X-ray diffraction on MnF_2 between 25° and 300°K. The dotted line indicates the Néel temperature. Combining neutron diffraction work,[5] which has assigned the spin moments in MnF_2 parallel to the *c*-axis, with the X-ray data, one finds that on cooling through the Néel temperature the distortion in MnF_2 is a contraction in the spin direction.

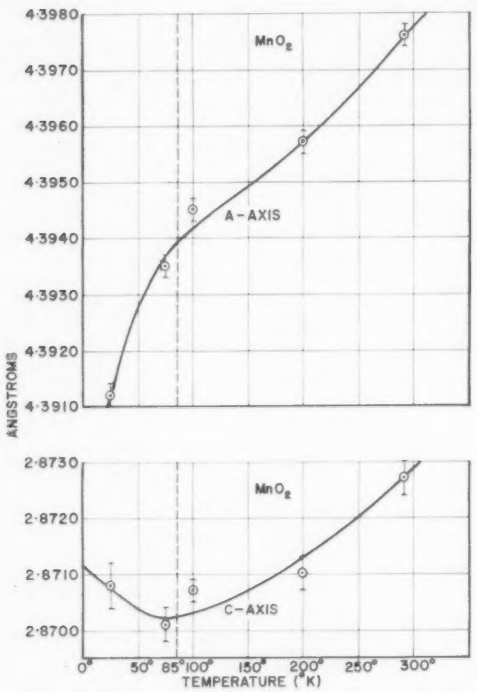

FIG. 1. Lattice constants of MnO_2 as a function of temperature.

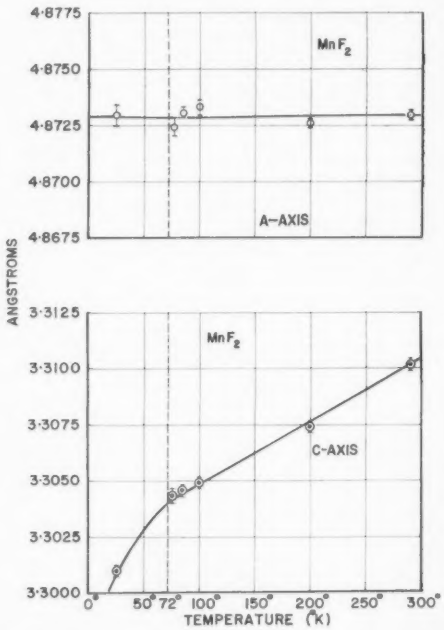

FIG. 2. Lattice constants of MnF_2 as a function of temperature.

DISCUSSION

The results found for MnO_2, MnF_2 and data available on other antiferromagnetic compounds are listed in Table 1. In the table is also listed the angular relationship between the spin direction ***S*** and the axis ***M***, which is the direction defined by the magnetic ordering. ***M*** is the vector perpendicular to sets of planes in which all spins in a given plane are parallel but the spins in neighboring planes are not parallel. In the particular cases here considered, ***M*** is unique. Included also is the distortion that takes place in the lattice parallel to the direction of the spins when the crystal is cooled through the Néel temperature.

Several regularities appear:

(1) Within a given crystal structure the sense of the distortion relative to the spin direction is always the same. For example, in the case of MnO_2 and MnF_2, both of which have the rutile structure, there is a contraction in the direction of the spins, even though in one case the spins are along the *c*-axis and in the other they are perpendicular to it.

(2) Whether the crystal expands or contracts along the spin direction depends on the point group symmetry surrounding the magnetic ion.

Vol. 1
1961

Table 1. Summary of neutron diffraction and X-ray data on antiferromagnetic compounds

Compound	Structure	Spin direction	Distortion in direction of spin	References
CrSb	Hex. NiAs	$S \parallel M$	Contracts	6, 7
FeS	Hex. NiAs	$S \perp M$	Contracts	8, 9
MnO_2	Tet. SnO_2	$S \perp M$	Contracts*	4, 5
MnF_2	Tet. SnO_2	$S \parallel M$	Contracts*	5
MnO	Cubic NaCl	$S \perp M$	Expands	10, 11
NiO	Cubic NaCl	$S \perp M$	Expands	10, 11
FeO	Cubic NaCl	$S \parallel M$	Expands	10, 13
CoO	Cubic NaCl		(See text)	10, 11
Cr_2O_3	Rh. αAl_2O_3	$S \parallel M$	Expands	14, 15
α-Fe_2O_3	Rh. αAl_2O_3	$S \parallel M$	Expands	16, 17

* Results of work reported in this paper.

(3) There is no apparent correlation between the sense of the distortion and the direction of the magnetic ordering.[1]

(4) CoO[10,11] is an exception. It violates the regularity of our classification scheme in that, though CoO is of the rock salt structure, it contracts approximately along the spin direction. KONIMARI has shown that the tetragonal deformation of CoO can reasonably be interpreted as a magnetostriction originating in the effect of the crystalline field on the orbital angular momentum of Co^{++} which is not entirely quenched in this environment.

Acknowledgements—The author would like to express his appreciation for the help received from Miss S. GREENWALD in matters concerning X-ray crystallography and from Dr. W. F. RADDLE, who performed the susceptibility measurements on MnO_2. He also wishes to thank Dr. T. R. MCGUIRE for his aid in preparing this paper.

REFERENCES

1. GREENWALD S. and SMART J. S., *Nature, Lond.* **166,** 523 (1950); *Phys. Rev.* **82,** 113 (1951).
2. KANAMORI J., *Prog. Theor. Phys. Osaka* **17,** 177, 179 (1956).
3. COHEN M., *Rev. Sci. Instrum.* **6,** 68 (1935); HESS J. B., *Acta Cryst., Camb.* **4,** 209 (1951).
4. YOSHIMORI A., *J. Phys. Soc. Japan* **14,** 807 (1959).
5. ERICKSON R. A., *Phys. Rev.* **90,** 779 (1953).
6. SNOW A. I., *Phys. Rev.* **85,** 745 (1952).
7. WILLIS B. T. M., *Acta Cryst., Camb.* **6,** 425 (1953).
8. HIRAHARA E. and MURAKAMI M., *J. Phys. Chem. Solids* **7,** 281 (1958).
9. BERTAUT F., *Bull. Soc. Franç. Minér.* **79,** 276 (1956).
10. ROTH W. L., *Phys. Rev.* **110,** 1333 (1958).
11. TOMBS N. E. and ROOKSBY H. P., *Nature, Lond.* **165,** 442 (1950).
12. ROOKSBY H. P., *Acta Cryst., Camb.* **1,** 226 (1948).
13. WILLIS B. T. M. and ROOKSBY H. P., *Acta Cryst., Camb.* **6,** 827 (1953).
14. MCGUIRE T. R., SCOTT E. J. and GRANNIS F. H., *Phys. Rev.* **102,** 1000 (1956).
15. GREENWALD S., *Nature, Lond.* **177,** 286 (1956).
16. SHULL C. G., STRAUSER W. A. and WOLLAN E. O., *Phys. Rev.* **90,** 779 (1951).
17. WILLIS B. T. M. and ROOKSBY H. P., *Proc. Phys. Soc. Lond.* **65B,** 950 (1952).

J. Phys. Chem. Solids Pergamon Press 1961. Vol. 19, Nos. 1/2, pp. 54–60. Printed in Great Britain.

REMARKS ON THE MAGNETIC PROPERTIES OF Au–Mn SYSTEM

HIROSHI SATO

Scientific Laboratory, Ford Motor Company, Dearborn, Michigan

(*Received* 16 *May* 1960)

Abstract—Au–Mn alloys show magnetic behavior which depends upon the various types of superlattice existing in this system. The comparison of the magnetic properties of Au_2Mn and Au_4Mn, however, clearly shows a difficulty of interpreting the magnetic structure of Au_2Mn, which is supposed to be helical, from competing positive and negative exchange interactions as often suggested. In both Au_4Mn and Au_2Mn, the Mn atoms form a body-centered tetragonal lattice with c/a ratio of 0·62 and 2·60 respectively. Although the first- and second-neighbor distance between Mn atoms for these two compounds are practically the same, the former is ferromagnetic but the latter is metamagnetic. The first-neighbor distance corresponds to the ferromagnetic interaction range of Mn atoms, but geometrically this alone cannot cause any cooperative alignment of spins. The second-neighbor distance, on the other hand, is too long to expect any appreciable interaction. However, it is proved that the existence of a minor interaction between the second neighbors is sufficient to produce the expected cooperative phenomena. The magnitude of such an interaction is found to be of the same order as the magnetic dipole interaction. Although, at present, it is hard to conclude what kind of interaction is operative, it is suggested that at least the difference of the magnetic behavior of Au_2Mn and Au_4Mn is explained if the magnetic dipole interaction is assumed for the weak interaction.

IN THE Au–Mn system, the following superlattices or intermetallic compounds, AuMn, Au_2Mn, Au_3Mn, Au_4Mn, have been found on the gold side of the system and their crystal structures and several other physical properties have been investigated. Among these, this system shows an

Table 1. *Magnetic properties of superlattices found in the* Au–Mn *system*

Composition	Crystal structure		Magnetic properties		
	Structure	Superlattice type	Transition point °K	θ	p_{eff}
AuMn	b.c.t. (ord.) b.c.c. (disord.)	CsCl	A 500	−150	4·9
Au_2Mn	b.c.t. (ord.)	CaC_2	A 365	450	5·05
Au_3Mn	f.c.orth. (ord.) f.c.c. (disord.)	Periodic	A 140	235	4·33
Au_4Mn	f.c.t. (ord.) f.c.c. (disord.)	Ni_4Mo	F 360	370	4·85

A: Antiferromagnetic
F: Ferromagnetic
θ: Paramagnetic Curie point
p_{eff} Effective magnetic moment deduced from the susceptibility measurement.

interesting but complicated magnetic behavior which depends upon the type of superlattice. These properties are briefly tabulated in Table 1. The analysis of magnetic properties of these compounds revealed a possibility that the magnetic dipole interaction is responsible for the cooperative spin alignment of the compounds Au_4Mn and Au_2Mn. Since the magnetic dipole interaction is usually neglected in this kind of problem because of its magnitude, it is felt to be worthwhile reporting here.

Although the crystal structures are complicated and there is a marked difference in structure between Au_4Mn and Au_2Mn as shown in Fig. 1, the distribution of Mn atoms for both structures turns out to be relatively simple and also to be similar. They both form body-centered tetragonal structures and their c/a ratios are 0·62 for Au_4Mn and 2·60 for Au_2Mn respectively as shown in Fig. 2. Furthermore, not only the nearest neighbor distances (shorter edge) for both structures are approximately the same,† (3·37 Å for

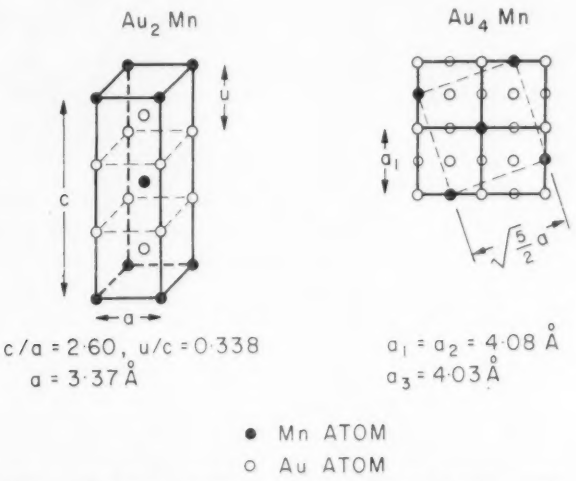

FIG. 1. The crystal structures of ordered Au_2Mn and Au_4Mn. Au_2Mn is shown with its unit cell. Au_4Mn is looked at from an [100] direction.

Ordered Au_4Mn is a superstructure based on a face centered cubic lattice and has a so-called Ni_4Mo structure.[1] This phase is ferromagnetic with a Curie point at about 360°K.[2] Ordered Au_2Mn is a superstructure based on a body centered cubic lattice and Mn atoms form a layer at every third plane.[3] This phase is antiferromagnetic with a Néel point of about 360°K. More exactly, this should be called metamagnetic.*[4] In other words, the magnetization of the crystal can be saturated by the application of the external fields of the strengths usually available. The crystal structures of these phases are shown in Fig. 1.

Au2Mn and 4·03 Å for Au_4Mn) but the second nearest neighbor distances (corner to body center of both structures) are also almost exactly the same (4·97 Å for Au_2Mn and 4·99 Å for Au_4Mn). From the resemblance both with respect to crystal structure and interatomic distance, one might think that also the magnetic properties would be similar. Nevertheless, Au_4Mn is ferromagnetic and Au_2Mn is antiferromagnetic.

As can be understood from the foregoing facts, there are several difficulties to overcome in order to understand the difference in the magnetic structure of these compounds from usual concepts.

* These words specify simply the magnetic characteristics and not the actual spin structures of the materials.

† In the sense that the both distances are in the range of the ferromagnetic interaction according to the analysis of manganese compounds and alloys.

By a usual concept, we mean that we assign a definite magnitude and sign of the interaction (exchange interaction) between magnetic moments of nearest neighbors, second nearest neighbors, etc. depending upon the distance and, upon this basis, calculate the magnetic structure. According to this concept, we must assign the same sign and magnitude of interactions for both structures not only to the nearest neighbors but also the second nearest neighbors, since the distances are the same

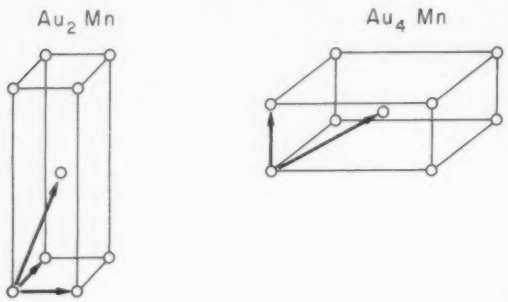

FIG. 2. The distribution of Mn atoms in the ordered Au_2Mn and Au_4Mn.

for respective pairs. Analysis of magnetic properties of many compounds or alloys of Mn as well as the analysis of the magnetic interaction in face centered cubic platinum alloys[5] shows that the interaction between Mn atoms at the nearest neighbor distance in Au_4Mn and Au_2Mn (shorter edge) should be ferromagnetic. If the interaction between edges is ferromagnetic in this kind of structure, the sign of the interaction between the corner and the body centered atoms is the essential factor to determine whether the structure is ferromagnetic or antiferromagnetic. The fact that Au_4Mn is ferromagnetic and Au_2Mn is antiferromagnetic means, therefore, the interaction cannot be taken as a kind of central force depending only on the distance between the atoms. At the same time, the relative distribution of gold atoms with respect to Mn atoms forming the corner to body center pair is quite similar. It is, therefore, hard to assume even an indirect exchange mechanism, the sign of which would have to be different for the two cases, even if we assume it to be anisotropic. It is also difficult to justify a sizable magnitude of interaction between second nearest neighboring pairs in view of their relatively long separation. In other words, although we can assign a positive interaction of reasonable magnitude for the nearest Mn pairs as explained above, the second neighbor distance (corner to center) is too long to expect any appreciable interaction. If we disregard this second neighbor interaction, the system would be either an assembly of linear chains (for Au_4Mn) or an assembly of square nets (for Au_2Mn) among each constituent of which the interaction between spins is positive. However, such systems should not show any cooperative alignment of spins as a whole which is against the experimental facts.

The second objection is, however, not really serious. It can be shown easily that in systems as above only a minor interaction between the corner and the center atoms would be enough to produce a cooperative phenomena as a whole, in other words, among the linear chains or among the square nets. Furthermore, the critical temperature would be determined by the strong interaction among the units (chains or nets) and not by the weak interaction between the corner and the center. In order to show this fact, we adopt an approximation corresponding to the molecular field treatment for this weak interaction. Let us first consider the linear chains and denote the strength of interaction between spins in the linear chain by J. The coefficient of the molecular field which acts on each atom in a chain from the other chains is called W. Using the standard technique for a linear chain,[6] we can easily get the expression for the Curie (or Néel) point T_c of the chain with interaction as shown in the Appendix:

$$1 = \left(\exp\frac{J}{kT_c}\right)\frac{J}{kT_c}\cdot\frac{2pW}{J}$$

Here, p is the magnitude of the magnetic moment. It is clear if $W \to 0$, $T_c \to 0$. However, the decrease in the Curie point is logarithmic with the ratio of W to J and, therefore, the interaction of the order of 1/1000 of J is enough to keep the Curie point to 1/3 to 1/4 of the value which is expected for a three dimensional assembly with the interaction J.

In the case of the assembly of planes, it is safe to use (at least qualitatively) the molecular field approximation for both strong and weak interaction.

Let us denote the molecular field coefficient inside the plane by W_{11} and that between the planes by W_{12}. Then the Curie point T_c of the system is given by (Appendix 2)

$$T_c = C(W_{11}+W_{12}) \qquad (2)$$

Here, C is the Weiss constant indicating the magnitude of the magnetic moment. Since $W_{11} \gg W_{12}$, T_c is solely determined by the interaction inside the plane. This is physically clear, because, in each plane, the system is cooperative (at least in this approximation and always in Ising model). Then, since each unit (the plane net) is so large the temperature fluctuation does not cause any disordering of the units of such an assembly. Therefore, the total system becomes oriented as soon as the spins inside the plane are aligned, however small the interaction between the planes may be. For the linear chain, the situation is somewhat different since each chain cannot be cooperative by itself. However, a similar argument would be employed to understand the qualitative nature.

From the discussion above, it is now clear that the total spin alignment of this system can be attained by a very small interaction between the corner and the body center atoms. If this is the case, the magnitude of this interaction can be easily determined. It has been known that Au_2Mn is metamagnetic[4] and the external field of the order of 10,000 Oe can saturate the crystal. In other words, the interaction can be overcome by an external field of the magnitude of 10^4Oe. Therefore, the magnitude of the interaction should be of the same order of magnitude as the magnetic dipole interaction. Although the existence of other kinds of interaction cannot be excluded, it is at least certain, under such a condition, that the magnetic dipole interaction plays an important role in determining the magnetic properties of this system.

If we single out the magnetic dipole interaction for the coupling of corner and center atoms, it can be shown next that the difference in magnetic structures of such system depends upon the c/a ratio. Generally, this kind of problem is quite complicated, especially in the case of ferromagnetism because of the long range nature of the interaction. However, in this case, the problem can be reduced to a much simpler one because the spins are fixed by an interaction other than the dipole interaction and are thus parallel in the planes perpendicular to c axis. (c-plane). Also we are simply interested in the difference in energy for both ferromagnetic and antiferromagnetic cases. Since the spin arrangement for both cases is exactly the same in one sublattice of the two sublattices of the body centered tetragonal lattice as can be easily visualized, the difference in energy per one atom is reduced to a problem in which we put a single dipole at a body center of a ferromagnetic simple tetragonal lattice and calculate the energy difference when the direction of the dipole is either parallel or antiparallel to the rest of the lattice (Appendix 3). It is known that this is zero irrespective of the direction of the dipole at the center if c/a equals 1. When $c/a \neq 1$, the result depends on the direction of the spin with respect to the c-axis. The calculations are similar for both cases and are shown in the Appendix 3. When the spin lies in the c-plane, the antiferromagnetic structure is more favorable than ferromagnetic case when $c/a > 1$ and vice versa. If the spin axis is parallel to the c-axis, the result is reversed. Also the energy of magnetic dipoles is two times more favorable in this case than the former case. If the spin alignment is solely determined by the magnetic dipole interaction, the spin axis would be parallel to the c-axis. However, in the present case, the spin direction would be determined by other interactions.

According to the result of the neutron diffraction the spin direction seems to lie in the c-plane at least in the case of Au_2Mn.[7] There is no experimental evidence yet for Au_4Mn. However, we can thus explain the difference of the magnetic structure between Au_2Mn and Au_4Mn by assuming that the spins lie in the c-plane for both cases. Metamagnetism can also be easily explained as above if we assume that the corner to center interaction arises mainly from the magnetic dipoles. NÉEL[8] explained the metamagnetism of Au_2Mn from the anisotropy by including a dipole type interaction between Mn layers. Therefore, the present explanation also supports NÉEL's assumptions in some sense.

The above calculation is not based on the actual magnetic structures of Au_2Mn or Au_4Mn but is simply intended to show that there can be a difference in the magnetic structure between these two compounds due to the contribution of the magnetic dipole interaction. A screw type spin

structure was indicated by a recent neutron diffraction study and was explained by competing exchange interactions between successive layers of Mn atoms.[7] This model, however, calls for isotropic interactions between spin pairs of extremely long distances. On the other hand, a simple calculation indicates that such a screw type spin structure can be stabilized also in a dipole lattice under a certain condition. This may be equivalent to the competing exchange interaction model in nature. Since it seems difficult, however, to think of an isotropic exchange interaction between such long distance pairs which satisfy the right condition for the helical structure, a highly anisotropic interaction such as the magnetic dipole interaction seems to be more plausible for the long range interaction mechanism for this system. A further experiment would be required to determine the nature of these interactions.

Acknowledgement—The author wishes to express his appreciation for stimulating discussions with Dr. A. ARROTT.

APPENDIX

1. *Assembly of linear chains with interaction*

Here we treat an assembly of linear chains with interaction. Since we are mainly interested in a relative importance of the interaction between linear chains in comparison with the interaction between spins inside the chain on the transition temperature, we adopt a molecular field approximation for the weak interaction between linear chains. Then we can single out a linear chain which is placed under a molecular field just as in Bethe's approximation of cooperative phenomena. Now let us think of a linear chain of r right spins and l left spins, $(r+l=n)$. Further, we assume, according to the usual technique, that the last spin of the chain is connected cyclicly with the first spin so that the calculation can be simplified. Practically, in the case of large values of r and l, the result is not affected by this assumption Let us first think that the r right spins and l left spins form their own rings respectively. From the r pairs of the ring of right spins, we choose to cut h pairs. Clearly, there are $\binom{r}{h}$ different ways of performing the cuts. Now, also the ring of left spins is decomposed by h cuts. Then each part of the r ring is inserted into these cuts. By doing this, we can form a ring of original number n with $g=2h$ antiparallel pairs. Since the l-ring can be cut in $\binom{l}{h}$ different ways, the total number of ways that the full ring can have g antiparallel pairs is given by:

$$G_n(r,g)=\binom{r}{h}\binom{n-r}{h} \qquad g=2h \qquad \text{(A.1)}$$

Therefore, the relative probability for specified number of r, l and h under the molecular field in the r-direction is

$$\Gamma(r,h) = C\binom{r}{h}\binom{n-r}{h}\exp\left[p(2r-n)^2\frac{W}{n}-2hJ\right]/kT \qquad \text{(A.2)}$$

Here, C is a normalization factor, W/n $(2r-n)$ is the molecular field each spin receives from the assembly of other chains and J is the energy difference for parallel and antiparallel pairs. The most probable value of r and h can be determined by

$$\frac{\partial\log\Gamma}{\partial r}=0 \text{ and } \frac{\partial\log\Gamma}{\partial h}=0.$$

With the use of Stirling's formula, the above relations can be reduced to

$$\frac{(r-h)(l-h)}{h^2}=\exp(2J/kT)$$

$$\frac{r}{l}\cdot\frac{l-h}{r-h}=\exp\left[-4\frac{p}{h}(2r-n)W\right]/kT \qquad \text{(A.3)}$$

By eliminating h from both equations, one obtains

$$\frac{m}{\sqrt{(1-m^2)}}=[\exp(J/kT)]\sinh\frac{2pWm}{kT} \qquad \text{(A.4)}$$

Here m, the relative magnetization, is defined as follows:

$$\frac{r}{n}=\frac{1}{2}(1+m);\ \frac{l}{n}=\frac{1}{2}(1-m) \qquad \text{(A.5)}$$

At high temperatures near the Curie point, m approaches 0. Expanding the equations (A.4) in powers of m and retaining only the linear term, we obtain

$$m=[\exp(J/kT)]\frac{2pWm}{kT}$$

$$=[\exp(J/kT)]\frac{J}{kT}\frac{2pWm}{J} \qquad \text{(A.6)}$$

The condition for the Curie temperature is, therefore,

$$1=[\exp(J/kT_c)]\frac{J}{kT_c}\frac{2pW}{J} \qquad \text{(A.7)}$$

It is clear from this, if $W \ll J, T_c$ approaches zero as expected. Further, it is easy to see that T_c decreases logarithmically with the ratio of W/J.

2. *Assembly of two dimensional square nets*

On the Ising model, the two dimensional square net

becomes ferromagnetic. Therefore, it is permissible to apply a molecular field approximation not only to the weak interaction between the nets but also to the strong interaction inside each net. A two sublattice model with alternate nets belonging to the same lattice is considered in this case. Then, from the molecular field theory, the Curie point T_c is determined from the following equation

$$\begin{aligned} T_c M_1 - C_1(W_{11}M_1 + W_{12}M_2) &= 0 \\ T_c M_2 - C_2(W_{21}M_1 + W_{22}M_2) &= 0 \end{aligned} \tag{A.8}$$

Here W_{11} and W_{22} are molecular field coefficients specifying the interaction between the two sublattices. C_1 and C_2 are the Weiss constants which specify the magnetic moment for the particular type of sublattice. M_1 and M_2 are the relative magnetizations of each sublattice. Then T_c is given by the condition

$$\begin{vmatrix} \left(W_{11} - \dfrac{T_c}{C_1}\right) & W_{12} \\ W_{21} & \left(W_{22} - \dfrac{T_c}{C_2}\right) \end{vmatrix} = 0 \tag{A.9}$$

From (A.9), the Curie point is

$$T_c = \tfrac{1}{2}(C_1W_{11} + C_2W_{22} + \sqrt{[(C_1W_{11} - C_2W_{22})^2 + 4C_1C_2W_{12}^2}] \tag{A.10}$$

In this case, the two sublattices are composed of identical spins and $W_{11} = W_{22}$, $C_1 = C_2$. Therefore,

$$T_c = C_1(W_{11} + W_{12}) \tag{A.11}$$

If

$$W_{12} \ll W_{11},\ T_c \fallingdotseq C_1W_{11}.$$

This means that, when W_{12} is small, T_c is determined by W_{11} only.

3. *Criterion of magnetic structures*

The body centered tetragonal structure can be divided into two equivalent interpenetrating sublattices, which we call I and II. In each sublattice, the arrangement of spins is parallel. In the case of ferromagnetism, the spin direction of I and II is the same and in the case of antiferromagnetism, I and II are antiparallel to each other. We are interested in the difference in the energy per atom between the ferromagnetic structure and the antiferromagnetic structure. For this purpose, we single out one atom from the sublattice I and calculate the energy for ferromagnetic and antiferromagnetic structure for this atom. Since the spin arrangement in I is exactly the same for both structures, the difference in the total energy per atom is found by putting that atom of I at the body center of the simple tetragonal lattice II and taking the difference in energy when the spins on II are in the same direction as the atom I and when the spins on II are antiparallel to the atom I.

At first, for the sake of simplicity, let us assume that the spins lie in the c plane and the direction of the spins is in the x-direction. In other words, it is in the direction of one edge. Then the difference in energy $E_f - E_a$ due to the magnetic dipole interaction would be

$$E_f - E_a = f(c/a) = 2\sum_{i,k,l} \frac{1}{\{(i+\frac{1}{2})^2 + (k+\frac{1}{2})^2 + (c/a)^2(l+\frac{1}{2})^2\}^{3/2}} \left\{1 - \frac{3(i+\frac{1}{2})^2}{(i+\frac{1}{2})^2 + (k+\frac{1}{2})^2 + (c/a)^2(l+\frac{1}{2})^2}\right\} \tag{A.12}$$

The lattice sum is over the entire II lattice. Here, for simplicity, we took the cube edge as the unit-length. If $c/a = 1$, this sum vanishes. In other words, $f(1) = 0$. Now, if we change c/a from unity by δ, $f(1+\delta) = f'(1)\delta + \ldots$

$$f' = \sum_{i,k,l} -\frac{\frac{3}{2}\{(i+\frac{1}{2})^2 + (k+\frac{1}{2})^2 + (c/a)^2(l+\frac{1}{2})^2\}^{1/2}2(l+\frac{1}{2})^2 c/a}{\{(i+\frac{1}{2})^2 + (k+\frac{1}{2})^2 + (c/a)^2(l+\frac{1}{2})^2\}^3}\left\{1 - \frac{3(i+\frac{1}{2})^2}{(i+\frac{1}{2})^2 + (k+\frac{1}{2})^2 + (c/a)^2(l+\frac{1}{2})^2}\right\}$$

$$+\sum_{i,k,l} \frac{1}{\{(i+\frac{1}{2})^2 + (k+\frac{1}{2})^2 + (c/a)^2(l+\frac{1}{2})^2\}^{3/2}} - 3\frac{-(i+\frac{1}{2})^2 2(l+\frac{1}{2})^2 c/a}{\{(i+\frac{1}{2})^2 + (k+\frac{1}{2})^2 + (c/a)^2(l+\frac{1}{2})^2\}}$$

The first term vanishes but the second term is positive if we put $c/a = 1$. Therefore, the sign of f depends on the sign of δ. In other words, if

$$c/a > 1,\ f > 0.$$
$$c/a < 1,\ f < 0.$$

This means that, if $c/a > 1$, the antiferromagnetic structure is more favorable than the ferromagnetic case and vice versa. This relation not only holds for small δ, but

actually also for large δ which we are interested in here.

It is also very easily proved that, by a similar calculation, the energy difference is the same as long as the spins lie in the *c*-plane. Even if the spins are perpendicular to the *c*-plane, the calculation can be done in the same way. However, the relation becomes reverse and also the energy difference is larger in this case than the former case by the factor two. Therefore, if the spin alignment is solely determined by the magnetic dipole interaction, the spin should be perpendicular to the *c*-plane.

REFERENCES

1. Watanabe D., *Acta Cryst., Camb.* **10,** 483 (1957).
2. Meyer A. J. P., *C.R. Acad. Sci., Paris* **242,** 2315 (1956).
3. Herpin A., Meriel P. and Meyer A. J. P., *C.R. Acad. Sci., Paris* **246,** 3170 (1958); Michel P., *C.R. Acad. Sci., Paris* **246,** 2632 (1958).
4. Kussmann A. and Raub E., *Z. Metallk.* **47,** 459 (1956); Meyer A. J. P. and Tagland P., *J. Phys. Radium* **17,** 459 (1956).
5. Sato H., *J. Appl. Phys.* **31,** 327S (1960).
6. Ising E., *Z. Phys.* **31,** 253 (1925).
7. Herpin A., Meriel P and Villain J., *C.R. Acad. Sci., Paris* **249,** 1334 (1959).
8. Néel L., *C.R. Acad. Sci., Paris* **242,** 1549 (1956).

Vol. 1
196

J. Phys. Chem. Solids Pergamon Press 1961. Vol. 19, Nos. 1/2, pp. 61–65. Printed in Great Britain.

VARIATION OF FIELD EFFECT MOBILITY AND HALL EFFECT MOBILITY WITH THE THICKNESS OF THE DEPOSITED FILMS OF TELLURIUM

S. K. GHOSH

Department of Physics, Indian Institute of Technology, Kharagpur

(*Received* 1 *September* 1960)

Abstract—Experimental results of the variation of conductivity, Hall mobility and field effect mobility with the thickness of the evaporated films of tellurium is reported. A tentative explanation of the experimental results is offered. The low values of Hall mobility are explained to be mainly due to the scattering of the carriers at the intercrystalline boundaries.

INTRODUCTION

THE SURFACE properties of tellurium have as yet received limited attention by experimental workers. A preliminary study of the surface by field effect experiments was first made by AIGRAIN *et al.*[1] on thin evaporated layers of tellurium deposited on mica. More recently GODEFROY[2] has made a detailed investigation of field effect on these films. From a measurement of the temperature variation of the field effect mobility, in the temperature range 77–300°K, he has calculated the energy of the surface states, to be 0·08 eV above the mid gap position, for mica–tellurium interface.

The depth of the space charge layer, in most semiconductors, is of the order of 10^{-4} to 10^{-6} cm. The effect of surface scattering on the mobility of the carriers within the space charge layer has been calculated by SCHRIEFFER[3]. The depth of the space charge layer is much smaller in comparison to the usual thickness of the experimental crystals. Hence, the mobility of the carriers in the space charge layer of one surface is independent of any changes in the opposite surface. The thickness of the films however, can be of the order of the depth of the space charge layer and we can expect an interaction between the space charge layer of the upper and lower surfaces. Thus, a measurement of the field effect mobility at the glass tellurium interface for various thicknesses of the film might yield interesting results.

This paper reports the low frequency field effect measurements on tellurium films deposited by vacuum evaporation on glass substrate. The field effect mobility at the glass–tellurium interface has been determined for films of various thickness. The corresponding measurements of Hall mobility were also made in dry atmosphere.

The film was deposited, on cleaned microscope cover slips of size 2 × 1 × 0·005 in., by vacuum evaporation; (chemically pure tellurium obtained from British Drug Houses, without any further purification, was used for the purpose). The glass plate was kept at a distance of about 8 cm from the hot filament, which ensured uniformity of film thickness; the temperature of the film and the substrate also remained practically constant during evaporation. Various thicknesses of the film could be obtained by evaporating different (weighed) quantities of tellurium. A rough estimate of the film thickness could be made by considering the spherical symmetry of the evaporated material.[4] The film thickness obtained from the weight of the deposit agreed within five per cent with that estimated by the other method.

The cleaned microscope cover slip with aquadag coatings at the two ends and provided with spring contacts was fixed on a plastic block. A thin tin foil was placed underneath the base glass plate on an insulator to form a parallel plate condenser with the tellurium film, and the whole system was

placed inside the vacuum chamber of the coating unit (Model 12E of W. Edwards & Co. London). The fresh surface of the tellurium–glass interface could then be studied immediately after evaporation and without bringing it into contact with atmosphere. The changes in conductance (ΔG) and the field effect conductance changes ($\Delta G_{\text{F.E.}}$) were measured simultaneously.

To study the changes in conductance of the film due to the applied transverse electric field the circuit used was similar to the one described by Low[5]. A block diagram of the complete experimental arrangement is as shown in Fig. 1.

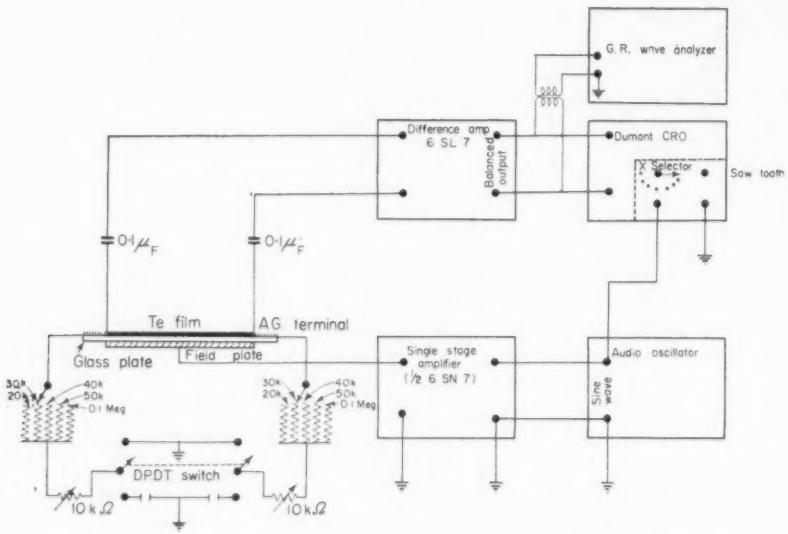

FIG. 1. Block diagram of the electrical arrangement used for the measurement of field effect conductance changes in tellurium films.

The field plate placed for the measurement of $\Delta G_{\text{F.E.}}$ was not covering the entire length of the film. To avoid pick up by the terminals it was necessary to leave out small portions of the film uncovered on both sides of the field plate. To account for the uncovered portion the proper correction was made. The corrected value of $\Delta G_{\text{F.E.}}$ can be written as

$$\Delta G_{\text{F.E.}} = \frac{\delta V(R_1+R_2+R)}{I(R_1+R_2)R^2}\left(\frac{L}{l}\right)^2 \qquad (1)$$

where R_1 and R_2 are the balancing resistances; R is the resistance of the film, I is the sweep current through the film, δV is the change in voltage recorded, L is the length of the film, and l is the length of the field plate.

The field effect mobility has been defined as

$$\mu_{\text{F.E.}} = \frac{d\Delta\sigma}{dQ} \qquad (2)$$

where, $\Delta\sigma$ is the change in surface conductivity per unit area of the surface and Q is the charge induced on unit surface area of the film. Hence,

$$\mu_{\text{F.E.}} = \frac{l^2 d(\Delta G)}{Cd(V_a)} \qquad (3)$$

where l is the length of the specimen, C is the capacity between the film and field plate, and V_a is the field voltage.

The deposited films being sufficiently thin, they could support large voltages along the sweep direction and could be made to have widths of the order of 1 cm. Hence the measurement of Hall mobility was not so difficult. However, the measurements had to be done inside an air conditioned room and in a dry atmosphere; as at times the fluctuations of room temperature and

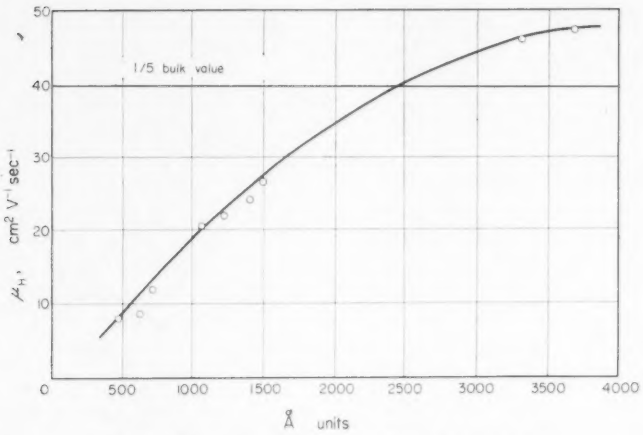

FIG. 2. Variation of Hall mobility with thickness.

the presence of high humidity made the measurements difficult and unreliable. The specimens used for Hall voltage measurement were the same films of tellurium which were just taken out of the vacuum chamber after the field effect experiments. The Hall probes were fixed by aquadag and as far as possible were adjusted to give minimum *IR* drop. A low impedance potential divider arrangement provided a source of backing voltage used to reduce the *IR* drop. The magnetic field as produced by a permanent magnet was 2200 Oe. The magnetic field could be increased to about double the value (4000 Oe) by adding soft iron pole pieces of about half the area. The Hall voltages were measured by means of a Philips d.c. electronic voltmeter of high internal impedance. The voltage due to *IR* drop was first measured when the sample was outside the magnetic field. Then it was slowly

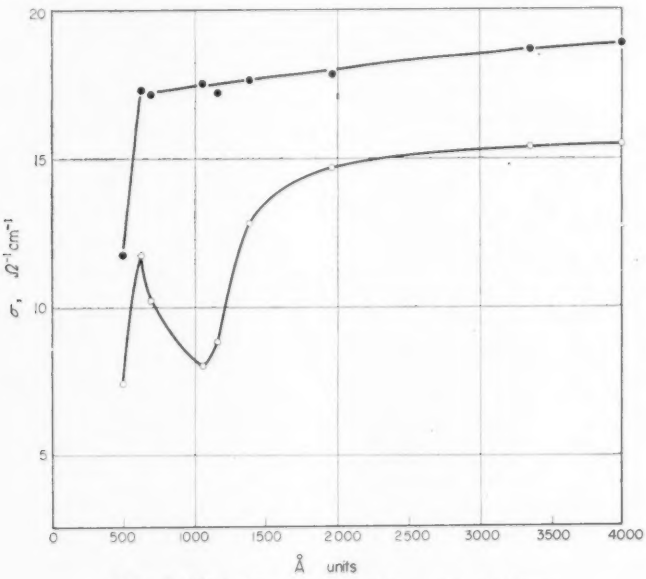

FIG. 3. Variation of conductivity with thickness.

brought in the magnetic field and the steady change in the voltmeter reading could be easily observed.

RESULTS AND DISCUSSION

Fig. 2 shows the variation of Hall mobility with the thickness of the film. The observed values of mobility in these films is much smaller than that of the bulk material. The value obtained for the film 3000 Å thick is still about one fifth that of the bulk material. The curve shows a decrease in Hall mobility with decreasing thickness.

Fig. 3 shows the variation of conductivity with the thickness of the film.

According to FUSCH and SONDHEIMER[6] the effective free path of the conduction electrons is shortened by scattering at the surfaces of the film and, when the thickness is small compared to the bulk free path, the current is mainly carried by electrons which move nearly parallel to the surface.

From a measurement of the Hall mobility in a single crystal of tellurium (obtained from the same lump from which the films were deposited) the bulk mean free path could be calculated from equation (4)

$$l = \frac{3\sqrt{(2\pi m_p kT)}}{4q}\mu_H \qquad (4)$$

where m_p is the effective mass of the hole, which has been taken equal to the mass of a free electron, μ_H is the Hall mobility as determined experimentally, k, T and q have their usual meaning. The calculation of mean free path from equation (4) yields a value of the order of 10^{-6} cm. This value of the mean free path is quite small in comparison to the thickness of the film for which the measurements have been made. The low values of mobility for such thickness of the film cannot be explained by SONDHEIMER's theory alone. However, if we consider the scattering of the carriers to occur also at the inter-crystallite boundaries, as considered by WOODS[7] for PbS films, such low values of mobility in the films can be explained.

The thinner films have a larger surface to volume ratio and are certainly more defective than the thicker ones. Hence a larger scattering of carriers is expected in thinner films resulting in a decrease of mobility with decreasing thickness of the film.

Figure 4 shows the variation of field effect mobility with the thickness of the film. The lower values of field effect mobility than Hall mobility is obviously due to the large scattering of the carriers that are made to conduct in the narrow channel of the space charge layer. It is interesting

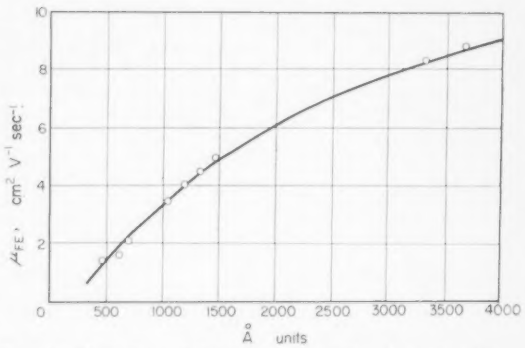

FIG. 4. Variation of field effect mobility ($\mu_{F.E.}$) with thickness.

to note that the ratio of μ_H and $\mu_{F.E.}$ remains constant (as in Fig. 5) for various thickness of the film. This result is at present not well understood. However, we may conclude that the decrease in field effect mobility with decreasing thickness of the film is due to the same reasons that cause a decrease in Hall mobility.

From the ratio $\mu_H/\mu_{F.E.}$ we can make an estimate of the surface states energy at the glass tellurium interface. The expression for the energy of surface states, as deduced by GODEFROY[2] for the case of a highly p-type material on the assumption of a single discrete energy level associated with the surface states, is as given by equation (5),

$$\frac{\mu_H}{\mu_{F.E.}} = 1+\tfrac{1}{2}\log\frac{P}{2M}+\frac{E_{G/2}-\eta}{2kT} \qquad (5)$$

where η is the energy of surface states as measured from the mid gap position at the surface, P is the acceptor density and

$$M = \left(\frac{2\pi m_p kT}{h^2}\right)^{3/2} \sim 1{\cdot}26\times10^{19}/\text{cm}^3.$$

From the data of Hall mobility and conductivity for a film 700 Å thick the calculated value of hole concentration is of the order of $3\times10^{18}/\text{cm}^3$. The

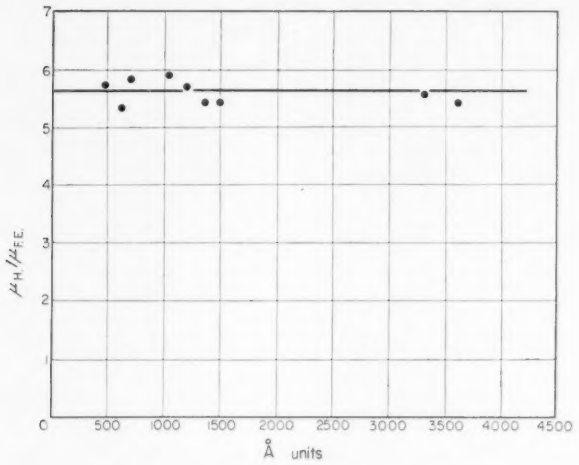

FIG. 5. Variation of $\mu/_H\mu_{F.E.}$ with thickness.

material being highly p-type the acceptor density P, in equation (5), can be taken as equal to the hole concentration. The value of this can now be calculated from equation (5) from the corresponding ratio $\mu_H/\mu_{F.E.}$ The value of η thus calculated is of the order of 0·1 eV above the middle of the forbidden energy gap. Since the value of $\mu_H/\mu_{F.E.}$ is a constant for various thickness of the film, it can be concluded that the surface states energy is a property of the tellurium glass interface and does not vary with the thickness of the film.

Acknowledgements—The author takes this opportunity to thank Professor H. N. BOSE for helpful discussions and Professor S. GUPTA and Dr. C. RAMASASTRY for encouragement.

REFERENCES

1. AIGRAIN P., LAGRENAUDIE J. and LINDART G., *J. Phys. Radium* **13,** 587 (1952).
2. GODEFROY L., *Progress in Semiconductors*, Vol. I, p. 159. Heywood, London (1956).
3. SCHRIEFFER J. R., *Phys. Rev.* **97,** 641 (1955).
4. WILLIAMS R. C. and BACKUS R. C., *J. Appl. Phys.* **20,** 98 (1949).
5. LOW G. G. E., *Proc. Phys. Soc. Lond.* B**68,** 10 (1955).
6. SONDHEIMER E. H., *Advanc. Phys.* **1,** 11 (1952).
7. WOODS J. F., *Photoconductivity Conference*, p. 636. John Wiley, New York (1956).

J. Phys. Chem. Solids Pergamon Press 1961. Vol. 19, Nos. 1/2, pp. 66–72. Printed in Great Britain.

DERIVATION OF THE BOLTZMANN TRANSPORT EQUATION FOR INELASTIC COLLISIONS

P. N. ARGYRES

Lincoln Laboratory*, Massachusetts Institute of Technology, Lexington 73, Massachusetts

(*Received* 22 *January* 1960; *revised* 2 *September* 1960)

Abstract—A quantum-mechanical derivation of the Boltzmann transport equation for inelastic collisions is given along the lines KOHN and LUTTINGER have developed for elastic collisions. It is shown that for Fermi–Dirac particles the scattering in the collision term of the transport equation is restricted to unoccupied states only, in contradistinction to the case of elastic collisions.

1. INTRODUCTION

RECENTLY, KOHN and LUTTINGER[1] have given a quantum-mechanical derivation of the Boltzmann transport equation for free electrons in solids, within the band approximation. They have considered only elastic collisions of the electrons, due to randomly distributed scattering centers. In the usual one-electron approximation and in the case of free electrons, the distribution function f_k was proven to satisfy in the lowest approximation of weak scattering the Boltzmann transport equation

$$\left(\frac{\partial f_k}{\partial t}\right)_{\text{drift}} + \left(\frac{\partial f_k}{\partial t}\right)_{\text{coll.}} = (-e/\hbar)\boldsymbol{E}\cdot\nabla_k f_0(\epsilon_k) + \sum_{k'}(w_{k'k}f_{k'} - w_{kk'}f_k) = 0 \tag{1.1}$$

A more complicated transport equation was also derived for higher orders of the scattering. $w_{kk'}$ plays the role of a transition probability per unit time from state $|k\rangle$ to $|k'\rangle$ and is given, in the first Born approximation for the scattering, by the usual expression indicated by the "golden rule" of the time-dependent perturbation procedure, namely

$$w_{kk'} = (2\pi/\hbar)\langle|V_{kk'}|^2\rangle\delta(\epsilon_k - \epsilon_{k'}), \tag{1.2}$$

where V is the interaction of an electron with the set of impurities and $\langle\ \rangle$ indicates an ensemble average over the positions of the scattering centers. $f_0(\epsilon_k)$ is the equilibrium distribution function. The derivation of (1.1) in Ref. (1) explicitly avoids any use of the repeated random phase assumption, which has been the weak point of all previous derivations.[2] In former proofs also the condition

$$\hbar/\tau \ll kT, \tag{1.3}$$

where τ is the relaxation time, was necessary for the validity of the Boltzmann equation in the approximation of weak scattering, on account of the fact that the development of the system was followed only up to short times, as allowed by the time-dependent perturbation procedure.[2] Since the procedure of KOHN and LUTTINGER deals with the long time behavior of the system, it would seem that condition (1.3) is not necessary for the validity of the Boltzmann equation in the weak scattering approximation. This point has been discussed by CHESTER and THELLUNG[3] who found that condition (1.3) is replaced by the weaker one

$$\hbar/\tau \ll \zeta = \text{Fermi energy}. \tag{1.4}$$

In an appendix of their paper, KOHN and LUTTINGER proved quite generally that in the case of elastic scattering and quantum statistics, it is always possible to derive a transport equation for the one-electron distribution function f_k which, even in the case of Fermi–Dirac statistics, is *linear* in f_k. This result was proven to be true to all orders

* Operated with support from the U.S. Army, Navy and Air Force.

in the strength of the scattering. The important point here is that the exclusion principle should be entirely ignored in the description of the scattering in the transport equation, i.e. the usual exclusion factors which restrict the transitions to unoccupied states only are not to be included. The only effect of the Fermi–Dirac statistics is to replace $f_0(\epsilon_k)$ by the Fermi–Dirac function.* From private conversations, however, it appears that this has given rise to the misunderstanding that the same is true for inelastic collisions, as e.g. in the case of scattering of the electrons by phonons. This is clearly wrong and it is easy to see that KOHN and LUTTINGER's proof breaks down for inelastic collisions.

We derive below the one-electron Boltzmann transport equation for inelastic collisions for a system of Fermi–Dirac particles and prove that the exclusion factors are indeed present in the collision term, as it is usually conjectured. This, however, proves possible only under the assumption (2.34). Apart from this particular point, which has been the motivation of this note, it is also of interest to exhibit a quantum-mechanical derivation of this important transport equation in the electron theory of solids. Thus, in this derivation no repeated random phase assumption is made and the restriction (1.3) does not appear as a condition for the applicability of the transport equation in the weak scattering approximation. This is significant for the case of lattice scattering, since condition (1.3) is not in fact satisfied for metals at high temperatures (see Ref. 2). It is expected that a study of the higher approximations would yield equation (1.4) as the condition of applicability. The following discussion will be restricted to the case of free electrons and the collisions will be treated in the lowest Born approximation.

Vol. 19
1961

* For the lowest approximation of the (elastic) scattering, it is clear that the collision term of the transport equation (1.1) *could* be written with the exclusion factors, i.e.

$$(\partial f_k/\partial t)_{\text{coll.}} = \sum_{k'} [w_{k'k} f_{k'}(1-f_k) - w_{kk'} f_k(1-f_{k'})],$$

since the bilinear terms $f_k f_{k'}$ cancel each other out on account of the fact that $w_{kk'}$, as given in this lowest approximation by (1.2), is symmetrical in k and k'. In higher orders, however, this is not possible.

2. DERIVATION OF THE TRANSPORT EQUATION

The derivation falls naturally into two parts. First, the transport equation for the distribution function R_{Nn} of the whole system (electrons and scattering system) is established. This part follows the method of KOHN and LUTTINGER[1] and it is, therefore, only briefly indicated, although enough is written down to establish a notation and demonstrate the key steps in the derivation. The second part consists in finding the transport equation for the one-electron distribution function f_k.

The system under consideration is a number of dynamically independent electrons in interaction with a scattering system, such as phonons, and an external constant electric field. Since we want to consider the case of a recoiling scattering system, we consider the Hamiltonian of the total system and take it to be

$$\tilde{H} = \tilde{H}_0 + H_s + \tilde{V} + \tilde{F}. \tag{2.1}$$

Here

$$\tilde{H}_0 = \sum_i H_0(i) = \sum_k \epsilon_k a_k^+ a_k \tag{2.2}$$

is the kinetic energy of the electrons. The summation over i goes over all electrons in the system. We take as eigenvectors $|k\rangle$ of H_0, the one-electron kinetic energy operator, the plane waves characterized by the wave vector k (the vector character of which we shall not designate explicitly), i.e. $\Omega^{-1/2}\exp(ik\cdot r)$, with corresponding energy eigenvalues $\epsilon_k = \hbar^2k^2/2m$. The spin index is entirely suppressed. In the occupation number representation, which is quite convenient for this problem, a_k^+ and a_k are the creation and destruction operators for electrons in the state $|k\rangle$ and satisfy the anti-commutation relations

$$\{a_k, a_{k'}\} = \{a_k^+, a_{k'}^+\} = 0, \qquad \{a_k^+, a_{k'}\} = \delta_{kk'}. \tag{2.3}$$

The operator representing the number of electrons in the state $|k\rangle$ is $N_k = a_k^+ a_k$ and its eigenvalues are $n_k = 0$ or 1. The eigenstates of the total kinetic energy $\tilde{H}_0$ shall be denoted, in the occupation number space, by

$$|n\rangle = |n_1 n_2 \ldots n_k \ldots\rangle,$$

the set of $\{n_k\}$ signifying the number of electrons

in each one-electron state; i.e.

$$\tilde{H}_0|n\rangle = E_n|n\rangle. \tag{2.4}$$

Clearly in this representation all N_k are diagonal and

$$E_n = \sum_k n_k \epsilon_k.$$

H_s is the Hamiltonian of the scattering system. Its eigenvectors and eigenvalues will be denoted by $|N\rangle$ and E_N respectively, i.e.

$$H_s|N\rangle = E_N|N\rangle. \tag{2.5}$$

The energy of interaction of the electrons with the scattering system is written as

$$\tilde{V} = \sum_i V(i) = \sum_{kk'} V_{kk'} a_k^+ a_{k'}. \tag{2.6}$$

$V_{kk'}$ is an operator in $|N\rangle$-space, i.e. in the space of the scattering system.

Finally, $\tilde{F}$ denotes the interaction of the electrons with the constant electric field E_α, i.e.

$$\tilde{F} = \sum_i F(i); \quad F = -eE_\alpha x_\alpha. \tag{2.7}$$

An ensemble of such systems is described by the density operator $R(t)$, which obeys the Liouville equation of motion

$$i\hbar\, dR(t)/dt = [\tilde{H}, R(t)]. \tag{2.8}$$

As an initial condition we shall assume, as in Ref. (1), that before the electric field is turned on at $t = 0$, the system is in thermal equilibrium and, therefore, the density operator is at that time

$$R(0) = R_0 = K_s K_e f_0(H_s + \tilde{H}_0 - \zeta\tilde{N} + \tilde{V}), \tag{2.9}$$

where

$$f_0(x) \equiv \exp(-x/kT) \text{ and } \tilde{N} = \sum_k N_k$$

is the operator for the total number of electrons. The normalization is taken so that

$$K_s \operatorname{tr}\{f_0(H_s)\} = K_s \sum_N f_0(E_N) = 1 \tag{2.10}$$

$$K_e \operatorname{tr}\{f_0(\tilde{H}_0 - \zeta\tilde{N})\} = K_e \sum_n f_0[\sum_k (\epsilon_k - \zeta) n_k] = 1, \tag{2.11}$$

i.e. $\operatorname{tr} R_0^{(0)} = 1$, where $R_0^{(0)}$ is the value of R_0 for $\tilde{V} = 0$. The Fermi energy ζ is chosen so that

$$\langle\tilde{N}\rangle/\Omega = K_e \operatorname{tr}\{\tilde{N} f_0(\tilde{H}_0 - \zeta\tilde{N})\}/\Omega$$

yields the desired electron concentration.

Any deviation of $R(t)$ for $t > 0$ from R_0 is then clearly of the first order in the electric field or higher. To the first order in E_α we have, therefore,

$$i\hbar\, dR(t)/dt = [\tilde{H}_0 + H_s + \tilde{V}, R(t)] - C, \tag{2.12}$$

where

$$C = [R_0, \tilde{F}]. \tag{2.13}$$

We note that R_0 and, therefore, C can be expanded in powers of $\tilde{V}$. The zeroth order of C, denoted by $C^{(0)}$, is seen to be

$$C^{(0)} = [R_0^{(0)}, \tilde{F}] = K_s K_e f_0(H_s - \zeta\tilde{N})[f_0(\tilde{H}_0), \tilde{F}]. \tag{2.14}$$

Since now operators referring to different particles commute, and

$$f_0(\tilde{H}_0) = \prod_i f_0(H_0(i)),$$

we have

$$\begin{aligned}[f_0(\tilde{H}_0), \tilde{F}] &= f_0(\tilde{H}_0) \sum_i f_0^{-1}(H_0(i))[f_0(H_0(i)), F(i)] \\ &= f_0(\tilde{H}_0) \sum_{kk'} f_0^{-1}(\epsilon_k)[f(H_0), F]_{kk'} a_k^+ a_k \\ &= f_0(\tilde{H}_0)(-ieE_\alpha)\frac{1}{kT}\sum_k \frac{\partial\epsilon_k}{\partial k_\alpha} N_k,\end{aligned} \tag{2.15}$$

the last step being a consequence of the relation

$$[f_0(H_0), F]_{kk'} = ieE_\alpha[\partial f_0(\epsilon_k)/\partial k_\alpha]\delta_{kk'}.$$

Combining equations (2.14) and (2.15) we have finally for the matrix elements in the $|Nn\rangle$ representation in which $\tilde{H}_0$ and H_s are diagonal

$$\begin{aligned}C^{(0)}_{Nn,N'n'} = \frac{eE_\alpha}{ikT}\delta_{NN'}\delta_{nn'} K_s K_e \times \\ \times f_0(E_N + E_n - \zeta\sum_k n_k)\sum_k n_k \frac{\partial\epsilon_k}{\partial k_\alpha}.\end{aligned} \tag{2.16}$$

We note that in this representation the "driving"

term in the basic equation (2.12) has diagonal matrix elements in the zeroth order in $\tilde{V}$, while the off-diagonal ones are of the first order in $\tilde{V}$. This is exactly as in the elastic scattering case.

The method of KOHN and LUTTINGER for the derivation of the transport equation from the Liouville equation (2.12) consists in the following two steps. First, equation (2.12) is solved for the off-diagonal matrix elements of $R(t)$ in terms of the diagonal ones, $R_{Nn}(t)$, in a series of successive approximations in the strength of the scattering. Then, these are inserted back in equation (2.12) for the diagonal matrix elements. Thus, an equation for the $R_{Nn}(t)$ only obtains, namely the transport equation. This procedure is most simply carried out by first transforming the differential equation (2.12) into an algebraic one. The Laplace transform is particularly convenient here, as the limiting value of $R_{Nn}(t)$ for long time, R_{Nn}, is found directly from its Laplace transform by use of Abel's theorem. Since these intermediate steps are identical to the ones of the elastic scattering case, we give only the final result. The transport equation for the steady-state distribution function of the whole system R_{Nn}, in the lowest Born approximation for the scattering, is thus found to be

$$(i/\hbar)C^{(0)}_{Nn} + \sum_{N'n'} \tilde{W}_{Nn,N'n'}(R_{N'n'} - R_{Nn}) = 0, \tag{2.17}$$

where

$$\tilde{W}_{Nn,N'n'} = (2\pi/\hbar)|\tilde{V}_{Nn,N'n'}|^2 \delta(E_{Nn} - E_{N'n'}) \tag{2.18}$$

and $C^{(0)}_{Nn} = C^{(0)}_{Nn,Nn}$ is given by (2.16).

It must be emphasized that the validity of this procedure, and consequently of the transport equation (2.17) as well, rests upon the existence of some singular properties of the matrix elements of $\tilde{V}^2$, $\tilde{V}^3$, etc., in the $|Nn\rangle$-representation, as it was demonstrated in Ref. (1) and more generally discussed by VAN HOVE[4]. Our discussion is restricted to interactions $\tilde{V}$ of this kind. In particular, for the case of electron–phonon interaction, the usual mechanism of inelastic collisions in solids, it is not difficult to prove that this indeed is the case. It is, however, convenient at this point not to specialize our discussion to the electron–phonon interaction but to proceed with a general interaction $\tilde{V}$ which is assumed to satisfy the necessary requirements. We shall discuss briefly the electron–phonon interaction at the end of this section.

Now we seek to deduce from (2.17) the transport equation for the one-electron distribution function f_k, which gives the average number of electrons in the state $|k\rangle$ under steady-state conditions. This is by definition

$$f_k = \mathrm{tr}\{N_k R\} = \sum_{Nn} n_k R_{Nn}. \tag{2.19}$$

It is worth observing that knowledge of f_k enables us to calculate only the steady-state values of physical quantities which can be represented as a sum over one-electron operators diagonal in the $|k\rangle$-representation: e.g. if

$$J_{kk'} = J_{kk}\delta_{kk'},$$

then

$$\tilde{J} = \sum_i J(i) = \sum_k J_{kk} N_k$$

and its average value for the steady-state is

$$\langle \tilde{J} \rangle = \mathrm{tr}\{\tilde{J}R\} = \sum_k J_{kk}\,\mathrm{tr}\{N_k R\} = \sum_k J_{kk} f_k.$$

In the plane wave representation the total electronic current of the system is such a physical quantity.

The transport equation for f_k is obtained by considering equation (2.17) after multiplication by n_k and summation over N and n, i.e.

$$\left(\frac{\partial f_k}{\partial t}\right)_{\mathrm{drift}} + \left(\frac{\partial f_k}{\partial t}\right)_{\mathrm{coll.}} = 0, \tag{2.20}$$

where

$$(\partial f_k/\partial t)_{\mathrm{drift}} = (i/\hbar)\sum_{Nn} n_k C^{(0)}_{Nn} \tag{2.21}$$

$$(\partial f_k/\partial t)_{\mathrm{coll.}} = \sum_{NN'}\sum_{nn'} \tilde{W}_{Nn,N'n'} n_k (R_{N'n'} - R_{Nn}). \tag{2.22}$$

The evaluation of the drift term (2.21) is quite simple. With the use of equations (2.15) and (2.16) and the well-known relations

$$\mathrm{tr}\{N_k K_e f_0(\tilde{H}_0 - \zeta\tilde{N})\} \equiv f_F(\epsilon_k) = \{1 + \exp[(\epsilon_k - \zeta)/kT]\}^{-1} \tag{2.23}$$

ol. 19
1961

$$\mathrm{tr}\{N_k N_{k'} K_e f_0(\tilde{H}_0 - \zeta\tilde{N})\} = f_F(\epsilon_k) f_F(\epsilon_{k'}), \quad (k' \neq k) \tag{2.24}$$

we see that it is given simply in terms of the Fermi–Dirac distribution function f_F, equation (2.23), namely

$$\left(\frac{\partial f_k}{\partial t}\right)_{\text{drift}} = \frac{eE_\alpha}{\hbar}\frac{1}{kT}\sum_{k'}\frac{\partial \epsilon_{k'}}{\partial k'_\alpha} \times \mathrm{tr}\{N_k N_{k'} K_e f_0(\tilde{H}_0 - \zeta\tilde{N})\}$$
$$= \frac{eE_\alpha}{\hbar}\frac{\partial \epsilon_k}{\partial k_\alpha}\frac{1}{kT} f_F(\epsilon_k)[1 - f_F(\epsilon_k)]$$
$$= (-e/\hbar)\boldsymbol{E}\cdot\boldsymbol{\nabla}_k f_F(\epsilon_k). \tag{2.25}$$

The evaluation of the collision term (2.22) is more involved. We first observe that, since $\tilde{W}_{Nn,\,N'n'}$ is symmetric in the indices $Nn, N'n'$, we can rewrite it as follows

$$(\partial f_k/\partial t)_{\text{coll.}} = \sum_{NN'}\sum_{nn'} \tilde{W}_{Nn,\,N'n'}(n'_k - n_k)R_{Nn}. \tag{2.26}$$

Now, however, $\tilde{W}_{Nn,\,N'n'}$ is given, through (2.18) and (2.6), in terms of the corresponding one-electron transition probability rate by the relation

$$\tilde{W}_{Nn,\,N'n'} = (2\pi/\hbar)\sum_{kk'}\sum_{ll'} V_{Nk,\,N'k'} V_{N'l',\,Nl}\langle n|a_k^+ a_{k'}|n'\rangle\langle n'|a_{l'}^+ a_l|n\rangle\delta(E_{Nn} - E_{N'n'})$$
$$= \sum_{k'\neq k''} W_{Nk',\,N'k''} n_{k'}(1-n_{k''})\langle \ldots n_{k'}-1 \ldots n_{k''}+1 \ldots |n'\rangle, \tag{2.27}$$

where

$$W_{Nk,\,N'k'} = (2\pi/\hbar)|V_{Nk,\,N'k'}|^2\delta(E_N + \epsilon_k - E_{N'} - \epsilon_{k'}). \tag{2.28}$$

This is a direct consequence of the properties of the creation and destruction operators. Thus (2.26) can be written

$$(\partial f_k/\partial t)_{\text{coll.}} = \sum_{NN'}\sum_{k'\neq k''} W_{Nk',\,N'k''} \times \sum_n n_{k'}(1-n_{k''})R_{Nn}\sum_{n'}(n'_k - n_k) \times \langle \ldots \underset{k'}{n} - 1 \ldots \underset{k''}{n} + 1 \ldots |n'\rangle.$$

The last sum is now easily seen to be equal to $(\delta_{k''k} - \delta_{k'k})$. Thus,

$$(\partial f_k/\partial t)_{\text{coll.}} = \sum_{NN'}\sum_{k'}\Big[W_{Nk',\,N'k}\sum_n n_{k'}(1-n_k)R_{Nn} - W_{Nk\,\,N'k'}\sum_n n_k(1-n_{k'})R_{Nn}\Big]. \tag{2.29}$$

We shall now introduce the usual assumption of statistical independence of the two subsystems and write

$$R_{Nn} = P_N\rho_n, \tag{2.30}$$

where P_N and ρ_n are the appropriately normalized distribution functions separately for the scattering system and the electrons, respectively. P_N can be any steady-state distribution appropriate to the physical situation at hand. The establishment of such a distribution is, of course, a separate problem which cannot be answered within this framework. New interactions (e.g. phonon–phonon interactions) must be considered. Here we assume that such a distribution function for the scattering system is given and we focus our attention on the problem of the determination of the steady-state distribution of the system of electrons.

It is then clear from equations (2.30) and (2.19) that the one-electron distribution function is

$$f_k = \sum_n n_k\rho_n \tag{2.31}$$

and equation (2.29) for the collision term can be written as

$$(\partial f_k/\partial t)_{\text{coll.}} = \sum_{k'}\Big[w_{k'k}\sum_n n_{k'}(1-n_k)\rho_n - w_{kk'}\sum_n n_k(1-n_{k'})\rho_n\Big], \tag{2.32}$$

where

$$w_{kk'} = \sum_N P_N\sum_{N'} W_{Nk,\,N'k'}. \tag{2.33}$$

In order to proceed further, it is necessary to know the average value of the product $n_k n_{k'} (k \neq k')$

Vol. 1
196

for the steady-state distribution ρ_n. The average value of n_k for this distribution is, of course, the one-electron steady-state distribution function f_k, equation (2.31). Now for the equilibrium distribution we know that the average value of the product $n_k n_{k'} (k \neq k')$ is equal to the product of the average values of n_k and $n_{k'}$, as we have seen in equation (2.24). We shall now *assume* that this is true also for the steady state distribution, i.e.

$$\sum_n n_k n_{k'} \rho_n = f_k f_{k'}, \quad (k \neq k'). \tag{2.34}$$

This is clearly so if the steady-state distribution ρ_n is factorable into one-electron distributions, just as the equilibrium distribution

$$\langle n|f_0(\tilde{H}_0 - \zeta\tilde{N})|n\rangle = \prod_k f_0[(\epsilon_k - \zeta)n_k]$$

is. With this basic assumption, the collision term, equation (2.32), assumes finally the commonly conjectured expression

$$(\partial f_k/\partial t)_{\text{coll.}} = \sum_{k'} [w_{k'k} f_{k'}(1-f_k) - w_{kk'} f_k (1-f_{k'})]. \tag{2.35}$$

$w_{kk'}$ is given through equations (2.33) and (2.28).

Equation (2.25), giving the drift term, and equation (2.35), giving the collision term, establish the usual Boltzmann transport equation for the one-electron distribution function f_k in the case of Fermi–Dirac particles and inelastic collisions, under the assumption (2.34). In this case, we see that the possible transitions are restricted by the exclusion factors $(1-f_k)$ to unoccupied states only.

The usual mechanism for inelastic collisions of electrons in solids is the electron–phonon interaction. In this case the one-electron scattering operator, in the usual approximation of small displacements of the ions from their equilibrium positions, is given in terms of the creation and destruction phonon operators b_q^+, b_q by

$$V = \sum_q A_q(\boldsymbol{r})(b_q + b_{-q}^+), \tag{2.36}$$

where $q = (\boldsymbol{q}, j)$ denotes collectively the phonon wave vector $\boldsymbol{q}$ and polarization index j and $A_q(\boldsymbol{r})$ is a function of q and $\boldsymbol{r}$, the exact form of which is not of importance here. The phonon Hamiltonian is

$$H_s = \sum_q \hbar\omega_q b_q^+ b_q,$$

where $\hbar\omega_q$ is the energy of the phonon q. One finds then that the quantity $w_{kk'}$, which plays the role of a transition probability rate, is given in terms of the absorption and emission probabilities for each phonon independently, namely

$$w_{kk'} = (2\pi/\hbar) \sum_q |\langle k|A_q|k'\rangle|^2 [(\bar{N}_q + 1) \times \delta(\epsilon_{kk'} - \hbar\omega_q) + \bar{N}_{-q} \delta(\epsilon_{kk'} + \hbar\omega_q)]. \tag{2.37}$$

Here

$$\bar{N}_q = \sum_N P_N N_q$$

is the average number of q-phonons when the lattice is characterized by the distribution function P_N. If the lattice is in thermal equilibrium then

$$\bar{N}_q = \bar{N}_{-q} = N_q^{(0)} = [\exp(\hbar\omega_q/kT) - 1]^{-1}.$$

Although we shall not exhibit the higher approximations in this procedure, it is essential to point out that they indeed turn out to be of higher order in the strength of the electron–phonon interaction. The dependence of these terms on the volume of the specimen is the same as that of the lowest order terms, the contributions of the intermediate states being reduced sharply on account of the well-known selection rules of the matrix elements of b_q^+ and b_q and

$$\langle k'|A_q|k\rangle \propto \delta_{k', k+q}.$$

It was pointed out before that the determination of the steady-state of the lattice is not possible within this framework. It is perhaps worthwhile to point out, however, that the previous analysis allows us to calculate the rate of change of the average number of q-phonons, F_q, due to collisions with the electrons (phonon-drag). Since

$$F_q = \text{tr}\{b_q^+ b_q R\} = \sum_{Nn} N_q R_{Nn}, \tag{2.38}$$

we have, in analogy to equations (2.26) and (2.29),

$$\begin{aligned}(\partial F_q/\partial t)_{\text{coll.}} &= \sum_{Nn} N_q \sum_{N'n'} \tilde{W}_{Nn,N'n'}(R_{N'n'} - R_{Nn}) \\ &= \sum_{NN'} \sum_{nn'} (N_q' - N_q) \tilde{W}_{Nn,N'n'} R_{Nn} \\ &= \sum_{NN'} \sum_{kk'} W_{Nk,N'k'}(N_q' - N_q) \times \sum_n n_k(1-n_{k'}) R_{Nn}\end{aligned} \tag{2.39}$$

For an interaction of the form (2.36) it is easy to see that, under the basic assumptions (2.30) and (2.34), this reduces to the form

$$(\partial F_q/\partial t)_{\text{coll.}} = (2\pi/\hbar)\sum_{kk'} |\langle k|A_q|k'\rangle|^2 \times \delta(\epsilon_{kk'}-\hbar\omega_q)[f_k(1-f_{k'})(F_q+1)-f_{k'}(1-f_k)F_q]. \tag{2.40}$$

In order to take account of the spin, the right hand member of (2.40) should be multiplied by 2.

REFERENCES

1. KOHN W. and LUTTINGER J. M., *Phys. Rev.* **108,** 590 (1957).
2. See, for example, PEIERLS R. E., *Quantum Theory of Solids.* Clarendon Press, Oxford (1956).
3. CHESTER G. V. and THELLUNG A., *Proc. Phys. Soc. Lond.* **73,** 745 (1959).
4. VAN HOVE L., *Physica* **21,** 517 (1955); **23,** 441 (1957).

Vol.
196

J. Phys. Chem. Solids Pergamon Press 1961. Vol. 19, Nos. 1/2, pp. 73–78. Printed in Great Britain.

CLOSED-SHELL ION–ION INTERACTIONS IN CALCIUM FLUORIDE*

J. R. REITZ, R. N. SEITZ and R. W. GENBERG
Case Institute of Technology, Cleveland, Ohio

(*Received* 31 *October* 1960)

Abstract—The short range ion–ion interactions in calcium fluoride are assumed to have the form

$$\phi_{ij} = A_{ij}\exp(-r/\rho).$$

By calculating the electrostatic contribution to the elastic constants of calcium fluoride and comparing the results with the experimentally observed constants, it is determined that $\rho = 0{\cdot}28 \times 10^{-8}$ cm, A_{+-} for Ca^{++}–F^- is $3{\cdot}09 \times 10^{-9}$ ergs, and A_{--} for F^-–F^- is $1{\cdot}04 \times 10^{-9}$ ergs. These results indicate that the Ca^{++}–F^- interaction is about ten times larger than the F^-–F^- interaction in this crystal. The deviation from the Cauchy relation is investigated by means of a model which allows relative motion between the sublattices making up the crystal, the model proves inadequate, however, and it is concluded that the failure of the Cauchy relation is due to a many-electron interaction between ions which cannot be approximated by a central interaction.

Vol. 19
1961

THE STUDY of defects in ionic crystals has been facilitated because many of the calculations can be carried out on a classical basis. Thus, the principal interactions to be considered in these crystals are the Coulomb interaction, the short-range repulsion of ion cores, and polarization effects. The short-range repulsive interaction between two ions is usually expressed in Born–Mayer form,

$$\phi_{ij}(r) = A_{ij}\exp(-r/\rho_{ij}), \qquad (1)$$

where r is the separation of the ions, and A_{ij} and ρ_{ij} are constants characteristic of the ion pair. The form of equation (1) is predicted theoretically from quantum mechanical calculations of the interaction between closed shell atoms, the constant A_{ij} depending primarily on the number of electron pairs in the two-atom system but also on atomic size.

From a statistical study of lattice energies and compressibilities of *alkali-halide* crystals, BORN and MAYER[1] deduced that ρ_{ij} is almost independent of ion type (i.e. $\rho_{ij} = \rho$), and they also obtained an expression for A_{ij}:

$$\phi_{ij}(r) = bc_{ij}\exp[(r_i + r_j - r)/\rho]. \qquad (2)$$

Here b and ρ are universal constants for the alkali-halide system, r_i and r_j are ionic radii, and c_{ij} is a dimensionless constant of order unity which depends on the charges on ions i and j.

It has been customary to regard equation (2) as a universal expression for the interaction between closed-shell ions, when the outer electrons are of the s, p variety. Thus, the association energies of divalent impurity–vacancy complexes in alkali-halide systems have been calculated on this basis;[2,3] these calculations have been rather successful although it should be emphasized that the experimental situation concerning impurity–vacancy association of Cd^{++} and Ca^{++} ions in sodium chloride is still in a state of flux.[4]

It is the purpose of the present paper to calculate the ϕ_{ij}'s for Ca^{++}–F^- and F^-–F^- from the measured elastic constants of CaF_2, and thereby test the validity of equation (2) under circumstances where divalent ions are involved. The geometry of CaF_2 is such that the

* Supported in part by the National Carbon Company, a division of Union Carbide Corporation, and in part by the U.S. Atomic Energy Commission.

F^-–F^- interaction should be appreciable in this crystal.

1. FORMULATION OF THE PROBLEM

The cohesive energy of calcium fluoride indicates that it is an ionic crystal consisting of doubly charged calcium ions and negatively charged fluoride ions. The electrostatic contribution to the elastic constants can be calculated, therefore, by the Ewald method.[5] In addition to the Coulomb interaction, the ions are assumed to have a short-range repulsive interaction of the form (1), with the A_{ij} and ρ_{ij} treated as disposable parameters. Strictly speaking, there is also a van der Waals interaction between ion cores; this will be discussed in Section 4 but for the moment we lump this interaction in with the ϕ_{ij}'s. In the first model to be considered, it is assumed that the state of macroscopic strain completely specifies the positions of all ions in the structure; in other words, the two fluoride sublattices are assumed to remain at the $(\frac{1}{4}\frac{1}{4}\frac{1}{4})$ and $(\frac{1}{4}\frac{1}{4}\frac{3}{4})$ positions, respectively, relative to the calcium sublattice. Under these conditions, and since the forces are central forces, the Cauchy relation is satisfied,[6] i.e. the elastic constant $C_{12} = C_{44}$.

In addition to the three elastic constants, there is also the equation of equilibrium to be satisfied. But because of the Cauchy relation, this provides only three independent equations. We assume, therefore, that ρ is independent of ion type, and we use the three equations to determine ρ, A_{+-} and A_{--}. Here A_{+-} is the repulsive interaction constant for the nearest neighbor Ca^{++}–F^- pair, and A_{--} is the constant for the next-nearest neighbor pair: F^-–F^-. Because the Ca–Ca distance is substantially larger than the F–F distance, and the Ca ionic radius apparently smaller than that of F, it appears that the neglect of ϕ_{++} is justifiable. On the basis of equation (2) one finds that ϕ_{++} is only two per cent of ϕ_{--}, although the electron density maps of CaF_2 made by Witte and Wölfel[7] do not really support this result; perhaps 10 to 15 per cent is a more reasonable estimate for ϕ_{++}/ϕ_{--}. At all events, the results of this calculation indicate that the dominant repulsive interaction in CaF_2 is the Ca–F interaction.

The present calculation depicts the crystal in the vicinity of 0°K. The low temperature elastic constants of CaF_2 which have been measured by Huffman and Norwood[8], are

$$C_{11} = 17{\cdot}4 \times 10^{11} \text{ dynes/cm}^2,$$

$$C_{12} = 5{\cdot}6 \times 10^{11} \text{ dynes/cm}^2,$$

$$C_{44} = 3{\cdot}59 \times 10^{11} \text{ dynes/cm}^2.$$

Since the Cauchy relation is obviously not obeyed, the experimental data is reinterpreted in terms of the previously defined theoretical model; the adjusted value of C_{12} and C_{44} is taken to be* $4{\cdot}60 \times 10^{11}$ dynes/cm^2. The lattice constant of CaF_2 is taken to be $a_0 = 5{\cdot}440 \times 10^{-8}$ cm.

2. ELECTROSTATIC CONTRIBUTION TO THE ELASTIC CONSTANTS

The electrostatic contributions to the elastic constants may be easily calculated with the aid of the Ewald method.[5] The Coulomb energy of the crystal per unit volume, $U_{\text{el.}}$, depends on the state of strain since the distances between atoms are functions of the strains (e_{xx}, e_{yy}, etc.). The elastic shear constant $\frac{1}{2}(C_{11}-C_{12})$ is obtained by setting e_{xx} equal to e, e_{yy} equal to $-e$, all other strains equal to zero, and differentiating twice at constant volume with respect to e:

$$\tfrac{1}{2}(C_{11}-C_{12})_{\text{el.}} = \tfrac{1}{4}(d^2U_{\text{el.}}/de^2). \qquad (3)$$

The elastic constant C_{44} is obtained by setting e_{xy} equal to e, and all other strains equal to zero. Then

$$(C_{44})_{\text{el.}} = d^2U_{\text{el.}}/de^2. \qquad (4)$$

This calculation has been checked by using two different values of the Ewald separation constant. The separation constant enters the Ewald method when the slowly convergent Coulomb series is replaced by two rapidly convergent series.

* If the failure of the Cauchy relation is due to a many-electron interaction between the ions, then the best *a priori* way of meeting the Cauchy condition appears to be a simple averaging of C_{12} and C_{44}. If the failure is due to relative motion of the sublattices making up the crystal, then it would seem more logical to take $C_{12} = C_{44} = (C_{12})_{\text{exp}}$. When the present work was initiated, we did not have the experimental results of Huffman and Norwood, but only the older room-temperature data[9] on CaF_2. According to the older experiments C_{12} was only 30 per cent larger than C_{44}; hence, the deviation from the Cauchy condition was of the same order as that of a typical alkali-halide crystal. The failure of the Cauchy relation will be discussed in more detail in Section 5.

Vol. 1
196

The results are summarized below; since the calculation is straight-forward, the details are not given:*

$$\tfrac{1}{2}(C_{11}-C_{12})_{\text{el.}} = 33{\cdot}7897\, e^2/a_0^4, \tag{5}$$

$$(C_{44})_{\text{el.}} = -12{\cdot}2046\, e^2/a_0^4. \tag{6}$$

Here e is the electronic charge and a_0 is the lattice constant.

The electrostatic contributions to the equation of equilibrium and the bulk modulus $B = \frac{1}{3}(C_{11}+2C_{12})$ are obtained by writing the total Coulomb energy in terms of the well-known Madelung constant α and differentiating with respect to a_0:

$$[\partial(VU_{\text{el.}})/\partial a]_{a=a_0} = (N_0/4)(4\alpha e^2/a_0^2), \tag{7}$$

$$B_{\text{el.}} = -(8/9)\alpha e^2/a_0^4 \tag{8}$$

Here V is the volume of the crystal containing N_0 molecules, and $\alpha = 11{\cdot}6366$ is the Madelung constant for CaF_2.

3. REPULSIVE CONTRIBUTION TO THE ELASTIC CONSTANTS

The repulsive contribution to the elastic constants may be calculated in a similar fashion. The basic interactions are taken of the form of equation (1), but because of the short-range nature of the interaction only nearest-neighbor and second nearest-neighbor (F–F) terms are included. The results are as follows:

$$\tfrac{1}{2}(C_{11}-C_{12})_{\text{rep.}} = (2/\rho a^2)\times [-(4/\sqrt{3})A_{+-}\exp(-\sqrt{(3)}a/4\rho)+ (a/2\rho-1)A_{--}\exp(-a/2\rho)], \tag{9}$$

$$(C_{44})_{\text{rep.}} = (2/\rho a^2)[(a/3\rho-8\sqrt{(3)}/9)A_{+-}\times \exp(-\sqrt{(3)}a/4\rho)-2A_{--}\exp(-a/2\rho)], \tag{10}$$

$$[\partial(VU_{\text{rep.}})/\partial a]_{a=a_0} = -(N_0/\rho)[2\sqrt{(3)}A_{+-}\times \exp(-\sqrt{(3)}a/4\rho)+3A_{--}\exp(-a/2\rho)], \tag{11}$$

$$B_{\text{rep.}} = (2/3\rho^2 a)[A_{+-}\exp(-\sqrt{(3)}a/4\rho)+ A_{--}\exp(-a/2\rho)]. \tag{12}$$

* Persons interested in the detailed formulation are referred to the report by R. N. SEITZ[10].

The parameters A_{+-}, A_{--}, and ρ have been defined in Section 1.

4. DISCUSSION OF RESULTS

Adding the electrostatic and repulsive contributions, and equating the result to the adjusted experimental values of the elastic constants of CaF_2, we obtain three independent equations for A_{+-}, A_{--}, and ρ. Their simultaneous solution yields

$$\rho = 0{\cdot}28\times10^{-8}\text{ cm},$$

$$A_{+-} = 3{\cdot}09\times10^{-9}\text{ ergs},$$

$$A_{--} = 1{\cdot}04\times10^{-9}\text{ ergs}.$$

This represents the *total* short-range interaction between ions, including the van der Waals interaction. This, perhaps, is the most useful form of the interaction energy.

But in order to compare the result obtained here with those obtained from equation (2) it is necessary to take the van der Waals terms into account explicitly. Thus, each elastic constant is considered to be made up of three parts: electrostatic, short-range repulsive, and a van der Waals term. If the van der Waals terms can be estimated, the preceding method can again be applied and the equations solved simultaneously for A_{+-}, A_{--} and ρ.

The van der Waals binding energy between two ions i and j may be expressed by

$$\psi_{ij} = -(3h/2r_{ij}^6)\alpha_i\alpha_j\nu_i\nu_j/(\nu_i+\nu_j), \tag{13}$$

where h is Planck's constant, ν_i and ν_j are the series limit frequencies of the discrete spectra of the ions i and j and α_i and α_j are the polarizabilities of the ions. Only the dipole–dipole term is considered; this contribution to the elastic constants turns out to be approximately 10 per cent of the repulsive term, and dipole–quadripole effects are expected to be an order of magnitude smaller. ν_+ is taken to be 3/4 of the third ionization potential of calcium, and ν_- is estimated to be 17·0 eV using MAYER's method[11] and the beginning of the optical absorption[12] in CaF_2 at 1220 Å. The polarizabilities are taken from TESSMAN *et al.*[13] The data are summarized in Table 1.

Since the r_{ij} depend upon the state of strain of the crystal, the contributions from equation (13) to the elastic constants may be obtained by the

Table 1. *Series limit frequencies and ionic polarizabilities in calcium fluoride*

$h\nu_+$	38·2 eV
$h\nu_-$	17·0 eV
α_+	$1{\cdot}1\times10^{-24}$ cm^3
α_-	$0{\cdot}64\times10^{-24}$ cm^3

procedure outlined in Sections 2 and 3 (see also Ref. 10). The results may be summarized:

$$2(C_{11}-C_{12})_{v\bar{d}W} \text{ or } (C_{44})_{v\bar{d}W} = -(12/\Omega r_0^6)(S_{++}a_{++}+2S_{+-}a_{+-}+2S_{--}a_{--}), \quad (14)$$

$$[\partial(VU_{v\bar{d}W})/\partial a]_{a=a_0} = (12N_0/a_0 r_0^6)(S_{++}a_{++}+2S_{+-}a_{+-}+2S_{--}a_{--}), \quad (15)$$

$$B_{v\bar{d}W} = -(28/3a_0^3 r_0^6)(S_{++}a_{++}+2S_{+-}a_{+-}+2S_{--}a_{--}). \quad (16)$$

Here $\Omega = a_0^3$ is the volume of the cubic unit cell, r_0 is the nearest-neighbor Ca^{++}–F^- distance, $a_{ij} = (3h/2)\alpha_i\alpha_j\nu_i\nu_j/(\nu_i+\nu_j)$, and S_{ij} is a lattice sum constant. For example, for $\partial(VU)/\partial a$ and B, S_{+-} is just the sum of $(r_0/r_{ij})^6$ over all fluorines in the rigid structure measured relative to a calcium, etc.; for C_{44}, S_{+-} is the sum of

$$(r_0/r_{ij})^6(7u_{ij}^2v_{ij}^2-v_{ij}^4-v_{ij}^2w_{ij}^2)/r_{ij}^4$$

over all fluorines in the rigid structure relative to a calcium, with u_{ij}, v_{ij}, w_{ij} the rectangular components of r_{ij} (see Ref. 10). The S_{ij} are given in Table 2; for $\partial(VU)/\partial a$ and B the S_{ij} were easily determined from the work of JONES and INGHAM[14], whereas for $\frac{1}{2}(C_{11}-C_{12})$ and C_{11}, the sums made directly by including terms out to the point where their numerical contribution is negligible.

Table 2. *Lattice sum constants for the van der Waals contribution to the elastic constants of the* CaF_2 *structure.*

Elastic constant	S_{++}	S_{+-}	S_{--}
$2(C_{11}-C_{12})$	0·178	−9·86	10·26
C_{44}	0·221	4·54	0·520
$\partial(VU)/\partial a$ or B	0·76222	8·8607	3·5439

The elastic constant equations are again solved simultaneously for A_{+-}, A_{--} and ρ, but this time with the van der Waals terms included as separate contributions. The results are

$$\rho = 0{\cdot}285\times10^{-8} \text{ cm},$$

$$A_{+-} = 3{\cdot}07\times10^{-9} \text{ ergs},$$

$$A_{--} = 1{\cdot}15\times10^{-9} \text{ ergs}.$$

The repulsive terms ϕ_{+-} and ϕ_{--} calculated from these values are listed in Table 3.

Table 3. *Closed shell ion–ion interactions in calcium fluoride (exclusive of the van der Waals term) in ergs.*

Interaction	From elastic constants	From Born–Mayer theory equation (2)
Ca^{++}–F^-	$0{\cdot}79\times10^{-12}$	$0{\cdot}25c_{+-}\times10^{-12}$
F^-–F^-	$0{\cdot}083\times10^{-12}$	$0{\cdot}108c_{--}\times10^{-12}$

The form of equation (2) was originally predicted by BORN and MAYER[1] from a statistical study of alkali-halide crystals. A recent study by FUMI[15], also limited to alkali-halides, gives $b = 0{\cdot}25\times10^{-12}$ ergs, $\rho = 0{\cdot}333\times10^{-8}$ cm, and the ionic radius of fluorine $= 1{\cdot}22\times10^{-8}$ cm. If we extend this model to CaF_2, then since the sum of the ionic radii should equal the Ca–F separation, we find the ionic radius of calcium to be $1{\cdot}135\times10^{-8}$ cm. The repulsive terms ϕ_{+-} and ϕ_{--} calculated from equation (2), using Fumi's parameters, are also listed in Table 3. There is really no adequate theory of the ionic charge parameters (c_{+-} and c_{--}); according to Born–Mayer theory[16] $c_{+-} = 1{\cdot}125$ and $c_{--} = 0{\cdot}75$. We conclude, therefore, that conventional Born–Mayer theory underestimates the Ca–F interaction in CaF_2 by about a factor of three, but it does give the correct order of magnitude for the F–F interaction.

Note added in proof

By conventional Born–Mayer theory, we imply the use of equation (2) together with parameters b and ρ determined from alkali-halide work. Such a procedure ignores the equilibrium relation for the crystal under

Vol. 1
1961

consideration, and it is evident that the entries in the last column of Table 3 do not satisfy the equation of equilibrium for CaF_2. An alternative procedure in the use of equation (2) is to fix only ρ in advance and determine b from the equation of equilibrium. Furthermore, the Witte–Wölfel electron density maps[7] suggest that the ionic radius of Ca^{++} is larger than that of F^- in CaF_2; this is not unreasonable since F^- is "squeezed" more in this structure than in the NaCl structure; and thus, its ionic radius may well be less than $1{\cdot}18 \times 10^{-8}$ cm. With these modifications, determining b from elementary equilibrium considerations, and allowing for a structure-dependence of the ionic radius, the Born–Mayer values for the interaction energies tend to agree more closely with the entries in column 2 of the table, although the agreement is still not perfect. We are indebted to Professor F. G. FUMI for much helpful discussion in this connection.)

5. FAILURE OF THE CAUCHY RELATION

The failure of the Cauchy relation in ionic crystals is usually attributed to a many-electron, non-central interaction between ions.[17] In CaF_2, however, there is another possibility for failure of the Cauchy relation since the state of macroscopic strain does not completely specify the positions of all ions in the structure; i.e. calcium fluoride consists of three sublattices: a calcium and two fluoride sublattices, and these can move independently during a strain. If the repulsive interactions dominate the situation, then it is reasonable to assume that each ion will adjust its position so that all of its nearest-neighbor distances are equal. This, then, is the second model we investigated for CaF_2. In hydrostatic compression and in the shear characterized by $\frac{1}{2}(C_{11}-C_{12})$, there is no difference between this model and the one discussed earlier, but for the C_{44} shear there is a difference.

Assume that the C_{44} shear takes place in the x–y plane. Then in order to keep nearest-neighbor Ca–F distances equal to one another, one of the fluoride sublattices must move in the $+z$ direction, the other in the $-z$ direction relative to the calcium sublattice.* Actually a somewhat more general model was used in the calculation: a parameter α was introduced such that when $\alpha = 1$, the nearest-neighbor Ca–F distances were all equal independent of the state of strain, and when $\alpha = 0$ the model reduced to the original model discussed in Section 1.

* A similar model was proposed by JAFFE[18] to explain the piezoelectric effect in zinc blende structures.

The result for the electrostatic contribution to C_{44} was found to be

$$(C_{44})_{\text{el}} = (-12{\cdot}2046+80{\cdot}4613\alpha)e^2/a_0^4. \tag{17}$$

The repulsive contribution contains, in addition to equation (10), terms in α and α^2. Using the actual experimental values of the elastic constants and the equation of equilibrium, we attempted to solve the four simultaneous equations for α, ρ, A_{+-}, and A_{--}. Unfortunately, we could not find a solution with reasonable values of these constants; the best approximate solution was obtained for $\alpha \approx 0$. The difficulty seems to be traced to the following situation: as α is increased from zero, the repulsive term decreases as required to make C_{44} less than C_{12}, but the electrostatic term (see equation 17) builds up so rapidly that it cancels the effect.

We conclude, therefore, that relative sublattice motion is not important in CaF_2, and that the failure of the Cauchy relation is due to a many-electron interaction between ions which cannot be approximated by a central interaction. Thus, the results of Section 4 give only the "central" part or averaged part of this interaction.

REFERENCES

1. BORN M. and MAYER J. E., *Z. Phys.* **75,** 1 (1932).
2. REITZ J. R. and GAMMEL J. L., *J. Chem. Phys.* **19,** 894 (1951).
3. BASSANI F. and FUMI F. G., *Nuovo Cim.* **11,** 274 (1954).
4. LIDIARD A. B., *Encyclopedia of Physics* (edited by FLÜGGE S.) Vol. XX, pp. 305–6. Springer Verlag, Berlin (1957).
5. EWALD P. P., *Ann. Phys.* **64,** 253 (1921); FUCHS K., *Proc. Roy. Soc.* **A153,** 622 (1936).
6. ZENER C., *Elasticity and Anelasticity of Metals*, pp. 19–20. University of Chicago Press, Chicago, Illinois (1948).
7. WITTE H. and WÖLFEL E., *Rev. Mod. Phys.* **30,** 51 (1958).
8. HUFFMAN D. R. and NORWOOD M. H., *Phys. Rev.* **117,** 709 (1960).
9. HEARMON R. F. S., *Rev. Mod. Phys.* **18,** 428 (1946).
10. SEITZ R. N., Thesis, Case Institute of Technology (1958). Also available as AEC Tech. Rep. No. 1, Contract AT(11-1)-623 (May 1958).
11. MAYER J. E., *J. Chem. Phys.* **1,** 270 (1933).
12. SCHNEIDER E. G., *Phys. Rev.* **45,** 152 (1934).

13. TESSMAN J. R., KAHN A. H. and SHOCKLEY W., *Phys. Rev.* **92,** 890 (1953).
14. JONES J. E. and INGHAM A. E., *Proc. Roy. Soc.* **A107,** 636 (1925).
15. FUMI F. G., Int. Symposium on Alkali Halides, Corvallis, Oregon (September 1959).
16. SEITZ F., *Modern Theory of Solids*, p. 82. McGraw-Hill, New York (1940).
17. LÖWDIN P. O., Thesis, Almquist and Wicksell, Uppsala, Sweden (1948).
18. JAFFE H., *Phys. Rev.* **66,** 357 (1944).

Vol. 1
1961

J. Phys. Chem. Solids Pergamon Press 1961. Vol. 19, Nos. 1/2, pp. 79–86. Printed in Great Britain.

NUCLEAR QUADRUPOLE COUPLING IN ALKALI IODIDE CRYSTALS

M. MENES* and D. I. BOLEF

Westinghouse Research Laboratories, Pittsburgh 35, Pennsylvania

(*Received* 2 *September* 1960)

Abstract—The dynamic nuclear quadrupole interaction (first derivative of the quadrupole interaction with respect to strain) has been measured for the I^{127} nucleus in crystals of CsI, RbI, KI, and NaI. These measurements were made by observing the resonant absorption of energy from an acoustic wave by the nuclear spins. Longitudinal waves propagating along a cubic axis of the crysta were used.

The observed values of the dynamic nuclear quadrupole interaction are: CsI, 1600 Mc; RbI, 615 Mc; KI, 300 Mc; NaI, 660 Mc. These values can be correlated with the chemical shift of the iodine ion in these crystals with the help of a simple model. This model, which is based on work of TOWNES and DAILEY and YOSIDA and MORIYA, attributes the quadrupole coupling and the chemical shift to the hole left in the outer p shell of the ion. This hole is due to the distortion of the ion (admixture of excited states) by the crystal surroundings. In connection with this work, the chemical shift of LiI^{127} was measured and found to be $-3{\cdot}3\times10^{-4}$.

ol. 19
1961

INTRODUCTION

NUCLEI which have an electric quadrupole moment will interact with an electric field gradient.[1,2] In many molecules and crystals, this quadrupole interaction results in a splitting of the energy states corresponding to different orientations of the nucleus. The electric field gradient is caused by an anisotropic distribution of charge around the nucleus, and in most cases is due to the electron shells surrounding the nucleus. Experimentally observed quadrupole interactions can thus be very useful in the determination of the electron density distribution in a molecule or crystal.[2,3]

The alkali halide crystals have lattices which show cubic symmetry about each nucleus. This causes the field gradient and the quadrupole interaction to vanish for the undistorted crystal. Distortion of the crystal, however, will destroy the cubic symmetry and create a field gradient. This field gradient will be a linear function of the strain in lowest order, and there will also be quadratic and higher order terms. Since both the field gradient and the strain are second rank tensor quantities, the linear relationship between them will be expressed as a fourth rank tensor similar in nature to the elastic constants tensor. The properties of this tensor are described by TAYLOR and BLOEMBERGEN, who term it the S tensor.[4] In this paper, we term this tensor the dynamic field gradient, and the resulting interaction with the nuclear quadrupole moment the dynamic quadrupole interaction.

The existence of such a dynamic quadrupole interaction has two consequences: (a) a broadening of the nuclear magnetic resonance line by random strains in the crystal, and (b) a coupling between the nuclear spins and lattice vibrations. Both of these effects have been used to estimate the magnitude of the dynamic quadrupole interaction in alkali halide crystals. In order to describe the observed results, it is useful to discuss at this point a simple theoretical model. This is the point charge model, which assumes that the electric field gradient at a nuclear position is caused by point charges at the positions of the neighboring ions. The magnitude of these charges is taken as γ times an ionic charge, where γ is an open

* Now at Polytechnic Institute of Brooklyn.

parameter. The dynamic quadrupole interaction is then due to the displacement of these charges by the distortion of the crystal.

Effects of plastic deformation of a crystal on the nuclear magnetic resonance line shape have been studied by WATKINS[5] and by OTSUKA[6]. Similar studies on mixed alkali halide crystals have been made by KAWAMURA *et al.*[7] A difficulty in this approach is presented by the estimation of the local lattice distortion due to the plastic deformation or the impurity admixture. For the case of the iodine nucleus, WATKINS estimated a value of γ of 300 in KI, while OTSUKA estimated a minimum value of 50 for the same substance.

The quadrupolar coupling between the nuclear spins and the lattice vibrations is responsible for the thermal relaxation of those nuclei possessing appreciable quadrupole moments, in particular I^{127}. At all but very low temperatures, this relaxation takes place by means of a second-order, Raman-type of process which involves two phonons having the appropriate energy difference. This Raman process depends upon the quadratic terms in the local field gradient. The relaxation process thus involves a different aspect of the dynamic quadrupole interaction, namely, a second derivative with respect to strain. This is in contrast to the line broadening discussed above and to the first order resonant phonon interaction discussed below, both of which involve a first derivative with respect to strain. A theory of thermal relaxation in ionic crystals based on the point charge model has been worked out by VAN KRANENDONK[8]. According to that model, the thermal relaxation time of I^{127} in KI at room temperature (0·018 sec) requires a value of γ of 850. More elaborate calculations, still using the point charge model, but taking into account the effect of the optical modes, have been made by WIKNER *et al.*[9] They find a γ of about 300 required by the relaxation time of KI^{127}.

The first order or resonant coupling between the nuclear spins and the lattice vibrations does not contribute to the thermal relaxation at ordinary temperatures because the number of phonon modes in the required energy range is extremely small. The coupling has, however, been observed by introducing a large density of resonant phonons in the form of an acoustic wave. Because the effective temperature of this acoustic energy is extremely high, the coupling results in an energy flow from the acoustic wave to the nuclear spin system. The effect upon the acoustic wave is a loss of intensity or attenuation, and the effect on the nuclear spin system is a departure from a thermal distribution corresponding to the crystal temperature, thus resulting in a loss of intensity or saturation of a nuclear magnetic resonance signal.

PROCTOR *et al.* have observed this nuclear spin saturation by acoustic energy.[10] PROCTOR and ROBINSON, working with NaCl, estimated the dynamic quadrupole interaction for the Na nucleus to correspond to a value of γ of 1·4. A serious problem in this method is the difficulty of knowing the acoustic energy density in the same crystal. TAYLOR and BLOEMBERGEN[4] tackled this problem by measuring the displacement due to the acoustic wave with a capacitance probe. Working also with NaCl, they obtained a value of 5 for γ of Na, and a value of 9 for the γ of Cl. JENNINGS *et al.*[11] measured the ratio of the quadrupole interaction of I to that of Na in NaI. Their results give a ratio for the respective values of γ for I and Na of 10.

The present authors measured the attenuation of an acoustic wave due to its coupling with the nuclear spin system.[12] From the observed attenuation, the magnitude of the dynamic quadrupole interaction could be determined. A value of γ of 26 was obtained for Br^{14} in KBr, and a value of 38 was found for the I^{127} nucleus in KI.

The observed values of γ for heavy halide nuclei such as I or Br are considerably larger than unity. This means that the internal electric field gradients are much larger than can be accounted for by the charges on the neighbor ions, and must thus be due to electronic charges in the ion itself. Since the closed shell configuration of the free ion is spherically symmetric, the quadrupolar interaction must be due to a deformation of the ion, i.e. to a departure from a closed shell configuration. The dynamic quadrupole interaction is then due to the change in the ion deformation when the crystal is strained.

The deformation of the ion can be ascribed to two main causes: the electric fields within the crystal and the Pauli repulsion of the neighbors. The internal field gradients resulting from the deformation of an ion by the field of an external charge have been calculated for a number of

ions.[13,14] These calculations show that the internal electric field gradient at the nuclear position is larger than that due to the external charge alone by an "antishielding" factor, $(1-\gamma_\infty)$. These results are, of course, the basis for the point charge model which we discussed, the antishielding factor $(1-\gamma_\infty)$ becoming the multiplicative factor γ. The antishielding factor may become quite large for heavy ions; calculations by WIKNER and DAS give values of 100 and 180 for $(1-\gamma_\infty)$ for Br^- and I^-, respectively.[14] The relatively large values of γ observed for the heavy halide ions are thus made plausible. The quantitative agreement, however, is not good.

An attempt to take the Pauli repulsion into account, and calculate the internal electric field gradient of an ion from its overlap with its neighbors has been made by KONDO and YAMASHITA[15]. These authors calculated the electronic charge density surrounding a nucleus from a determinantal wave function made up from ion orbitals. The overlaps were handled by a Löwdin orthogonalization. There is, however, some question as to the validity of certain approximations made in the calculation. It is also possible that this approach may not be too useful for heavy halogen ions. A calculation similar to KONDO and YAMASHITA'S gives the wrong sign for the quadrupole coupling of bromine or iodine in alkali halide molecules.

In this paper, the more phenomenological approach of YOSIDA and MORIYA[16] is used to interpret the observed quadrupole interactions in alkali-iodide crystals. This approach is similar to TOWNES and DAILEY'S treatment of alkali-halide molecules. The deformation of the electron cloud of the ion is assumed to be representable as the excitation of an electron in an outer p orbital to a higher state.* The electric field gradient at the halide nucleus is then primarily due to the hole left in the p orbital. The contribution of the excited state to the field gradient is small, as discussed by TOWNES and DAILEY[3], and is neglected.

In this theory, the amount of admixture of the excited state, λ, is left as an open parameter to be determined by comparison with the experimental data. The dynamic quadrupole coupling is then due to the variation of λ with internuclear spacing. In this paper, we assume that the variation of λ with internuclear spacing follows the same exponential law as the repulsive potential in the Born–Mayer theory of elastic constants, and the effects of the various neighbors are additive.

Since this is a phenom–ological theory, the amount of excited state admixture, λ, obtained from the quadrupole coupling should, if possible, be compared with the λ obtained from some other measurements. According to YOSIDA and MORIYA, some of the other quantities which depend upon λ and which may be used to determine it are the paramagnetic chemical shift and the indirect exchange spin–spin interaction. The chemical shift is the fractional change in the local magnetic field at the nuclear position due to the second order paramagnetism of the surrounding electrons. Since this second order paramagnetism vanishes for closed shell configurations, the chemical shift depends upon the distortion of the ion charge distribution. The observed chemical shift can thus be used to estimate this distortion, or, in terms of our model, the amount of excited state admixture λ. Since the chemical shift is easily measured, and is known for most of the crystals studied, it is a good independent check on the λ obtained from the quadrupole coupling data.

EXPERIMENTAL

Measurements of the dynamic quadrupole interaction were made on single crystals of CsI, RbI, and NaI. Results for KI have been reported previously.[12] All measurements were made using longitudinal sound waves propagating along a [100] direction of the crystal. In the notation of TAYLOR and BLOEMBERGEN (which is similar to the Voigt notation for the elastic constants tensor) this corresponds to a measurement of the S_{11} component of the dynamic field gradient tensor. (In a material having cubic symmetry, there is one other independent component of this tensor.) Since the experimental technique is described in detail in the paper on KI and KBr, only a brief sketch is given here.

In essence, the experimental method involves the measurement of the additional attenuation suffered by an acoustic wave in the material when the wave is in resonance with the precession frequency of the nuclear spins. (Because nuclear

* We describe the distortion of the halide ion as an admixture of some excited state rather than as an electron transfer (covalency) because we want to avoid being specific about the details of the admixed state.

Vol. 19
1961

transitions having a $\Delta m = \pm 2$ as well as $\Delta m = \pm 1$ are allowed by the quadrupolar interaction, a nuclear attenuation also occurs when the frequency of the acoustic wave is twice the precession frequency of the nuclear spins.) The magnitude of this attenuation can be related to the strength of the dynamic quadrupole interaction.

The sample is cut and polished so as to be mechanically resonant in the desired mode, and excited with a quartz piezoelectric transducer. In such a system, the resistive component of the transducer impedance depends upon the acoustic attenuation of the sample material. The transducer controls the marginal oscillator in a conventional n.m.r. setup. Since such an oscillator is extremely sensitive to small changes in resistance, it reacts to the small additional acoustic attenuation caused by the nuclear spins. The signal from the marginal oscillator is observed in the conventional manner with magnetic field modulation and synchronous detection.

Since many of the factors controlling the accuracy of the final result are peculiar to the method of measurement, a somewhat detailed discussion of these may be in order at this point. We divide this discussion into two parts: namely, the calculation of an acoustic attenuation coefficient from the observed signal, and the calculation of the dynamic quadrupole interaction from this attenuation coefficient. (It is possible, and even somewhat simpler, to obtain the quadrupole interaction from the ratio of absorbed acoustic power to acoustic energy density without introducing an attenuation coefficient. However, the introduction of this concept makes clearer the manner in which the energy absorption by the nuclear spins causes a change in the electrical impedance of the transducer.)

As described in Ref. (12), the resistive component of the transducer impedance is given by

$$R = \frac{\rho c}{(2a)^2} Sl\alpha.$$

This relation is derived for the case of a piezoelectric transducer having an electromechanical transformation ratio $(2a)$, driving a resonant sample having a density ρ, velocity of sound c, length l, and attenuation coefficient α. The standing wave pattern is assumed to be purely one-dimensional and to have a cross sectional area S. The change in the attenuation coefficient due to the nuclear spin absorption causes a change in the transducer resistance which is reflected by the matching network into a conductance change at the marginal oscillator terminals. The sensitivity of the oscillator to such a change was measured with a WATKINS[5] type of calibrator using a fuse bolometer as variable resistance element. The characteristics of the bolometer were obtained from bridge measurements. The electromechanical transformation ratio of the transducer was calculated from the dimensions of the latter. Values of the density of, speed of sound in, and length of the sample are known. The remaining quantity necessary for the determination of the nuclear acoustic attenuation coefficient α_n from the marginal oscillator signal is the cross-sectional area of the standing wave pattern, S. If there were no beam spreading due to diffraction, S would be equal to the driving transducer area. We assume that the effect of beam spreading is to make S larger than the transducer area, but to leave the standing wave pattern otherwise unaltered, i.e. still essentially one-dimensional and longitudinal. The value of this S is then obtained from measurements of the background attenuation of the sample and from the transducer resistance corresponding to this background attenuation. The background attenuation coefficient is measured by oscilloscopic observation of the mechanical ringing time of the sample. The transducer resistance is measured on a Q-meter. Comparison of the value of S obtained in this manner with the dimensions of the transducer and of the sample is used to check on the validity of this procedure.

The relationship between the nuclear acoustic attenuation coefficient and the dynamic quadrupole interaction in given in equations (1) and (2), respectively, for the $\Delta m = \pm 2$ and $\Delta m = \pm 1$ transitions. The constant K is a function of the nuclear spin and for I^{127} $(I = 5/2)$ has a value of $21\pi^2/1600$.

$$\alpha_n = KN(e^2Qq_1)^2 \frac{\nu^2}{\rho c^3 kT} g(\nu) \sin^4\theta \qquad (1)$$

$$\alpha_n = 4KN(e^2Qq_1)^2 \frac{\nu^2}{\rho c^3 kT} g(\nu) \sin^2\theta \cos^2\theta \qquad (2)$$

N is the number of spins per cm^3, ν is the

Vol. 196

frequency, ρ the density of the material, c the speed of sound, k Boltzmann's constant, T the absolute temperature, $g(\nu)$ is the shape function, and θ is the angle between the direction of the longitudinal strain and the main magnetic field. (e^2Qq_1) is the dynamic quadrupole interaction, eQ being the nuclear quadrupole moment and eq_1 being the first derivative of eq with respect to strain. For the orientation used in this experiment, $eq_1 = S_{11}$ of TAYLOR and BLOEMBERGEN. All of the quantities necessary to calculate e^2Qq_1 from α_n are easily obtainable with the exception of the shape function. $g(\nu)$. This shape function presents a difficulty which is present in any experiment depending upon an absolute measurement of line intensity. The problem is especially serious in the present experiment for two reasons: the relatively large quadrupole interaction which is necessary for the effect to be observable also causes the n.m.r. line to be easily broadened by strains in the material, and the particular transitions which are observed in this experiment (the so-called satellite transitions) are the ones which are the most susceptible to strain broadening. A result of this broadening is that the observed line does not contain all the transitions; some of the transitions are shifted out to such an extent that they are lost in the noise. The observed line width is therefore narrower than the actual line width. In order to obtain the actual $g(\nu)$ from the observed $g(\nu)$, we need the fraction of transitions which are included in the observed line. We obtain an estimate of this fraction by comparing the acoustic absorption line with a conventional n.m.r. line for the same sample. Since the coupling is known in the latter case, a quantitative analysis of the line is possible and the fraction of transitions represented by the n.m.r. line can be calculated. Account has to be taken of the fact that the central component of the n.m.r. line (the $\pm 1/2$ to $\mp 1/2$ transition) is missing in the acoustic line; this central component is generally easy to identify in the n.m.r. line since to first order it does not suffer any strain broadening.

Conventional n.m.r. measurements were made on all the samples used in the acoustic work, and on a crystal of LiI. (The LiI crystal was of very poor quality, and no acoustic results were obtained for it.) These measurements were used to obtain an estimate of the line loss due to broadening, as explained above, and also to obtain the value of the chemical shift for iodine nuclei in these substances. The reference for the chemical shift measurements was a crystal of KI whose shift was taken to be -1×10^{-4}. The chemical shift measurements agreed well with previous values,[17] except LiI which had not been measured before.

Acoustic data for the specimens used are given in Table 1. The values of S (the effective area of the standing wave pattern) obtained for RbI and CsI are in fair agreement with diffraction estimates. In KI the diffraction pattern is much larger than the sample cross section, and the standing wave pattern is thus limited by the sample size. The case of NaI is anomalous; the area S is smaller than the transducer area. In the NaI sample an imperfection in the crystal necessitated placing the transducer off center. This position of the transducer, as well as the imperfection, probably prevented the standing wave pattern from assuming a larger area.

RESULTS

N.M.R. results for the specimens are given in

Table 1. *Acoustic properties of specimens*

Sample	Density ρ (gm/cm^3)	Sound velocity (10^5 cm/sec)	Length l (cm)	Sample area (cm^2)	Transducer area (cm^2)	S (cm^2)	Background attenuation coeff. α_0 (cm^{-1})
NaI	3·67	2·93	1·63	2·2	0·86	0·81	0·0062
KI	3·13	2·90	1·48	1·83	0·86	1·66	0·00155
RbI	3·55	2·64	1·25	2·8	1·69	1·79	0·0105
CsI	4·51	2·29	1·22	3·98	1·83	2·90	0·0061

Table 2. N.M.R. and n.m.r.a.a. results

Sample	N (10^{22}/cm^3)	N.M.R. satellite line width (kc)	Fraction observed in sat. line (%)	N.M.R.A.A. line width (kc)	Fraction assumed in n.m.r.a.a. line (%)	Nuclear abs. coeff. α_n (10^{-8}/cm)	$\frac{e^2Qq_1}{h}$ (Mc)	Chemical shift σ (10^{-4})
LiI								−3·3
NaI	1·47	10·5	35	21·7	55	2·10	660	−1·2
KI	1·14	6·0	74	6·5	74	1·4	300	−1·0
RbI	1·01	118	90	76	45	0·281	615	−1·7
CsI	1·04	8·0	17	22	27	2·74	1600	−5·0

Table 2. The n.m.r. satellite line widths and fraction of transitions observed in the satellite components were obtained with the sample in the same orientation relative to the magnetic field as in the acoustic runs. The n.m.r. lines for all specimens except RbI were taken with relatively small field modulation, of the order of several gauss. The RbI n.m.r. line was obtained with large field modulation, 60 G. This large modulation brought out the widespread wings of the line, and increased markedly the fraction of transitions observed in the satellite lines. The acoustic lines were all observed with large field modulation, of the order of 1/2 the line width. The acoustic lines for which data are shown were all $\Delta m = \pm 2$. transitions, and the samples were oriented so that the [100] axis along which the sound waves were transmitted was perpendicular to the magnetic field, except for CsI where the angle was 57°.

The limiting factor in the accuracy of the value of e^2Qq_1 is the estimate of the fraction of transitions which are observed in the acoustic line. The situation is best for KI, where the acoustic line is relatively narrow and is almost identical in shape and width to the satellite part of the n.m.r. line.[12] Because of this, the assumed fraction of transitions included in the acoustic line was taken the same as the fraction of transitions observed in the satellite part of the n.m.r. line. In the case of the other samples, the comparison was not so simple, and a certain amount of judgment was used in estimating the fraction of transitions in the acoustic line from the n.m.r. line. This estimate is probably good to ±50 per cent, except for CsI where it should be good to within a factor of two. If we add to this the possible errors due to the n.m.r. measurements and to the acoustic measurements, we obtain confidence limits of a factor of 1·4 for the quadrupole interaction e^2Qq_1 in the alkali iodides (with a somewhat larger factor for CsI).

DISCUSSION

We interpret the experimental results on the basis of the simple phenom-ological model described in the introduction. This model assumes that the quadrupole interaction and the chemical shift of the iodine nucleus are due to the hole left in the outer p shell of the iodine ion by a partial admixture of excited states. This admixture of excited states is due primarily to the overlap of the ion with its neighbors. The lack of one $p_z(m_z = 0)$ electron in an otherwise complete shell gives rise to a field gradient which has cylindrical symmetry about the z axis and a magnitude given by $eq = (4/5)e\langle 1/r^3\rangle$, where $\langle 1/r^3\rangle$ is the expectation value of $1/r^3$ for the orbital. To obtain a dynamic quadrupole interaction, we make, following YOSIDA and MORIYA, these assumptions: (a) The effect of each neighbor ion is to cause a depletion, in amount λ, of the p orbital which overlaps most strongly with that neighbor; (b) λ is a function of the internuclear separation given by the following equation:

$$\lambda = \lambda_0 \exp\left(\frac{R_0 - R}{d}\right),$$

where R is the internuclear separation, R_0 the undistorted lattice internuclear separation, and d is the distance in the Born–Mayer relation for

Vol. 1
196

the repulsive energy, taken in this case to be 0·345 Å; (c) the effects of the various neighbors are additive. On the basis of these assumptions, one obtains for the dynamic field gradient

$$eq_1 = S_{11} = \frac{8}{5}\frac{e\lambda_0 R_0}{d}\left\langle\frac{1}{r^3}\right\rangle. \qquad (3)$$

[The derivation of this expression is straightforward for the case of a longitudinal wave moving along a crystal axis in a face-centered cubic lattice. Each pair of nearest neighbors may then be associated with a pair of p orbitals; only the internuclear distances of one pair of nearest neighbors is affected by the acoustic wave, and the relative orientations of the nearest neighbors with respect to the ion remain the same. This expression cannot be applied in a strict manner to CsI, which has a body-centered cubic structure, or to NaI, in which the next-nearest neighbor overlaps are important. In view of the simplicity of the model, however, and our lack of knowledge of the effect of changes in relative orientation (as well as internuclear separation) on λ, we apply the above expression to these two cases as well.]

The chemical shift is due to the second order paramagnetism of the electrons surrounding the iodine nucleus. The chemical shift caused by the removal of λ electrons per neighbor from the outer p shell of the halogen ion has been computed by YOSIDA and MORIYA to be:

$$\sigma = -\frac{8}{3}z\lambda\frac{\mu_B^2}{\Delta E}\left\langle\frac{1}{r^3}\right\rangle \qquad (4)$$

where z is the number of nearest neighbors, μ_B is the Bohr magneton, and ΔE is the energy of excitation to the nearest electronic state. ΔE was taken to be the energy corresponding to the fundamental absorption band.

Values of $z\lambda$, the total excited state admixture, obtained from the dynamic quadrupole interaction and from the chemical shift are given in Table 3. Also shown are some of the quantities used in obtaining these values of $z\lambda$.

These results indicate that the quadrupole coupling and the chemical shift of the iodine nucleus in alkali-iodide crystals can be explained on the basis of an admixture of excited states to the ionic configuration. As already mentioned, the detailed structure of the excited states is unimportant since both the quadrupole interaction and the chemical shift of the halogen nucleus are primarily due to the hole left in the outer p orbital. Conversely, however, the results of this experiment cannot give any information about the details of these excited states, but only about the total amount of the admixture. The quadrupole couplings of the alkali nuclei would be more informative in that respect; unfortunately, they were not measurable by the techniques used in this experiment.

REFERENCES

1. POUND R. V., *Phys. Rev.* **79,** 685 (1950).
2. The article by COHEN M. H. and REIF F. in *Solid State Physics* Vol. V. Academic Press, New York (1957), gives a good review of the subject of nuclear quadrupole interaction in solids.

Table 3. *Values of $z\lambda$, the total admixture of excited states to the* I^- *ion obtained from the dynamic quadrupole interaction and from the chemical shift. For the purposes of this calculation, the quadrupole moment of the* I^{127} *was taken as* $Q = 0{\cdot}75\times10^{-24}$ cm^2, *and* $\langle 1/r^3\rangle$ *for the outer p orbital of the* I^- *ion was taken as* 122×10^{24} cm^{-3}. *Values of* ΔE *are the first exciton peak in the fundamental band.*

	R_0 (Å)	e^2Qq_1 (Mc)	$z\lambda$(%) from e^2Qq_1	σ (10^{-4})	ΔE (eV)	$z\lambda$(%) from σ
LiI	3·00			3·3	5·7	11·2
NaI	3·23	660	8·5	1·2	5·4	4·0
KI	3·52	300	3·5	1·0	5·6	3·3
RbI	3·66	615	7·0	1·7	5·5	5·5
CsI	3·95	1600	16·5	5·0	5·6	16·5

3. TOWNES C. H. and DAILEY B. P., *J. Chem. Phys.* **20,** 35 (1951).
4. TAYLOR E. F. and BLOEMBERGEN N., *Phys. Rev.* **113,** 431 (1959). See also TAYLOR E. F., Ph.D. dissertation, Harvard University 1958 (unpublished).
5. WATKINS G. D., PhD. dissertation, Harvard University 1952 (unpublished).
6. OTSUKA E., *J. Phys. Soc. Japan* **13,** 1155 (1958).
7. KAWAMURA J., OTSUKA E. and ISHINATORI K., *J. Phys. Soc. Japan* **11,** 1064 (1956).
8. VAN KRANENDONK J., *Physica* **20,** 781 (1954).
9. WIKNER E. G., BLUMBERG W. E. and HAHN E. L., *Phys. Rev.* **118,** 631 (1960).
10. PROCTOR W. G. and TANTILLA W. H., *Phys. Rev.* **101,** 1757 (1956); PROCTOR W. G. and ROBINSON W., *Phys. Rev.* **104,** 1344 (1956).
11. JENNINGS D. A., TANTILLA W. H. and KRAUS O., *Phys. Rev.* **109,** 1059 (1958).
12. BOLEF D. I. and MENES M., *Phys. Rev.* **114,** 1441 (1959).
13. STERNHEIMER R. M., *Phys. Rev.* **105,** 158 (1957).
14. WIKNER E. G. and DAS T. P., *Phys. Rev.* **109,** 360 (1958); references to other work may be found in this paper.
15. KONDO J. and YAMASHITA J., *J. Phys. Chem. Solids* **10,** 275 (1959).
16. YOSIDA K. and MORIYA T., *J. Phys. Soc. Japan* **11,** 33 (1956).
17. SOROKIN P. P. and BLOEMBERGEN N., *Phys. Rev.* **110,** 865 (1958).

Vol.
196

J. Phys. Chem. Solids Pergamon Press 1961. Vol. 19, Nos. 1/2, pp. 87–99. Printed in Great Britain.

FIELD EMISSION FROM SILICON AND GERMANIUM; FIELD DESORPTION AND SURFACE MIGRATION

F. G. ALLEN

Bell Telephone Laboratories, Murray Hill, New Jersey

(*Received* 13 *October* 1960)

Abstract—Field desorption has been used successfully to produce clean germanium patterns in the electron field emission microscope. The field-cleaned pattern transforms upon annealing to one very similar to that obtained from silicon cleaned by heating in vacuum. Changes in impurity concentration at the surface during cleaning, heretofore a problem, are avoided by the desorption technique. Surface atom mobility becomes appreciable at ~ 250°C on clean germanium and at ~ 800°C on clean silicon. Field emission current–voltage characteristics for both clean Ge and Si are presented. The results are discussed in the light of existing theory, and the need for a theory including emission from surface states and the valence band is pointed out.

I. INTRODUCTION

ATTEMPTS to use the Müller electron field emission microscope to study clean surfaces of germanium and silicon have been made by several workers since 1952.[1]

D'ASARO[2] in 1957 obtained the first successful field emission patterns from a semiconductor with silicon emitters. Later work has confirmed the general features of his silicon patterns and the behavior of silicon tips during build-up under applied field at high temperatures.

Further work with silicon by the present author showed that the tip could be cleaned by heating alone without an applied field.[3,4] The same work and a later paper[5] showed, however, that while heating silicon to 1550°K in high vacuum did produce an atomically clean surface in the usual sense, minute amounts of boron were transferred to the surface from the glass walls of the vacuum system. This boron diffused into the silicon during heating causing *p*-type surfaces regardless of the initial bulk doping. The amount of boron involved in this effect was sometimes less than one thousandth of one monolayer and was distributed over a depth of several microns beneath the surface. At such levels it should not affect the appearance of the field emission pattern, and that it does not is borne out by recent results. However, until controlled, this effect made a meaningful study of the current–voltage characteristics of silicon or germanium impossible.

Recently at these laboratories field desorption has been used successfully in cleaning germanium for the first time. This technique avoids any such impurity change at the surface, and hence makes possible well-controlled studies on emission characteristics.

Work by PERRY and BETTLER[6] has reproduced the silicon patterns found above[3,4] using various cleaning techniques including ion bombardment, thus strengthening the evidence that these patterns represent atomically clean silicon.

Other papers on field emission from semiconductors describe work with SiC,[7] CdS and CdSe,[8,9] WC,[10] ZnS,[11] Si and Te[12] and Ge.[13,14] In no case in these papers, except for some of the work on tungsten carbide, did the authors obtain reproducible and symmetrical emission patterns in a projection microscope. The condition of the surface was thus unknown.

Several theoretical papers on semiconductor field emission characteristics have been published[1,15–19] but, as discussed below, the theory must be extended before direct comparison with data is possible.

The present paper presents the techniques that have been used and the results obtained at these laboratories in studying field emission from silicon

and germanium. While some of the most interesting quantitative work remains yet to be done, the first step—learning how to achieve reproducible patterns for both silicon and germanium—is now accomplished. Useful information about cleaning, gas adsorption, field desorption and surface migration has already been obtained.

II. PRESENT TECHNIQUES

Cutting samples

Emitters are fashioned from a single crystal in the form of a hairpin with the sharpened tip at the apex—see Fig. 1. In cutting out emitter blanks, the single crystal of silicon or germanium is first oriented by X-ray diffraction with any desired crystal axis along the emitter tip—[(100), (110) and (111) axes have all been used]—and with a known orientation in the plane perpendicular to the tip.

A set of blanks—10 to 20 at a time—of the shape shown in Fig. 1(a)–a is then sliced from a block cut with the indicated profile. The square tip is turned down to about 0·015 in. diameter by rotating the sample against a high speed diamond saw, Fig. 1(a)–b.

The samples are then cleaned thoroughly of any remaining wax or cement used to hold them during machining by boiling in nitric or sulfuric acid and rinsing in deionized water.

Etching tips

The 0·015 in. diameter cylinder is sharpened to a fine tip by electrolytic etching in a freshly-prepared 21 : 4 mixture of nitric and hydrofluoric acids, Fig. 1 (a)–(c). The same procedure applies for both silicon and germanium. The emitter tip, mounted in a lucite rod holder with a stainless steel screw contact to one leg, is held under the surface of the acid with 50 to 100 V a.c. applied. Etching currents of from 1 to 50 mA result depending on the stage of etching, the resistivity, and the temperature of the sample. Heating occurs during etching and, if not excessive, improves the etching action. A bright light is focused on the sample during etching to ensure an adequate supply of electron–hole pairs at the surface. The taper on the tip shank can be controlled by varying the fraction of time the tip is only partially below the surface. Noncircular cross sections of the tips can result from insufficient etching current allowing chemical etching to predominate, or from insufficient movement of the tip during immersion.

The etching can be interrupted for microscopic examination whenever necessary. Tip radii of 10^{-4} cm or less are needed for good results at easily attainable voltages for either thermal or field desorption cleaning. If the shank is too long and uniform the temperature drop at the tip may be too great to permit thermal cleaning; on the other hand, too large a cone angle causes the tip to blunt too rapidly during either field desorption or thermal cleaning. Cone half angles of 5°–7° are desirable.

When a tip is etched, it is rinsed in deionized water, blotted dry on filter paper and stored under cover until mounted in a tube—preferably within a few hours to minimize oxide growth. Treatments of the tip after etching to reduce the thickness of an oxide film such as by "killing" the etch with nitric acid may be desirable for easy cleaning of the tip later. Treatments to remove traces of metal impurities such as copper from the surface may also turn out to be important.

Mounting in tube

The emitter is held in molybdenum supports by molybdenum spring clamps screwed down onto the legs of the sample. [See Fig. 1(b).] This permits quick replacement of tips, and removal for optical or electron microscope observation. The grounding plate reduces spurious emission from the supporting structure.

The structure is then mounted in a conventional Pyrex field emission tube using a 1/2 in. diameter molybdenum ring anode about the tip connected electrically to a transparent tin oxide coating under the phospor screen.

The tube is evacuated with a conventional two-stage mercury diffusion pump with a liquid nitrogen trap. After bakeout for 2–4 hr at 400°C a vacuum of 2×10^{-10} mm Hg is indicated by the Bayard–Alpert type ion gauge within 8 to 12 hr.

Heating samples

The hairpin form allows heating of the tip by passing current through the legs. The cross section at the apex is smaller than elsewhere and this, together with the heat sink provided by the metal supports, allows the apex to reach the melting point while the contact points at the ends of the legs are relatively cool. This minimizes the chance of contamination from the metal supports. Brief flashing with low duty cycle improves this situation further.

Since the contact resistance between the spring clamps and the sample may be high with the sample cold, (no special doping at the contacts is used), an automatic high-voltage starting circuit is used.

Temperature measurement

Accurate temperature measurement of the sample is achieved with an optical pyrometer focussed on the apex of the tip through a viewing window in the tube. Using the appropriate emissivity corrections[20] the true temperature can be read at the melting point to ± 15°C. The temperature at the end of the tip which is too fine to resolve is then found by calculating the drop along the tip with a rough formula given in Appendix I. Since this drop is small—from 20 to 50°C at the melting point, an approximate value still yields good accuracy in absolute temperature. Prolonged heating near the melting point evaporates enough silicon so that a shutter or a separation of several inches between sample and window is advisable. Temperatures below the optical pyrometer range, when of interest, were estimated by interpolation on the temperature vs. heating current plot.

Vol. 196

(a)

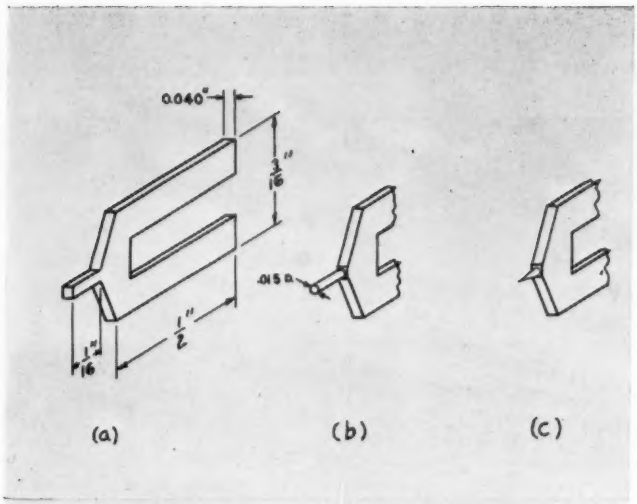

(b)

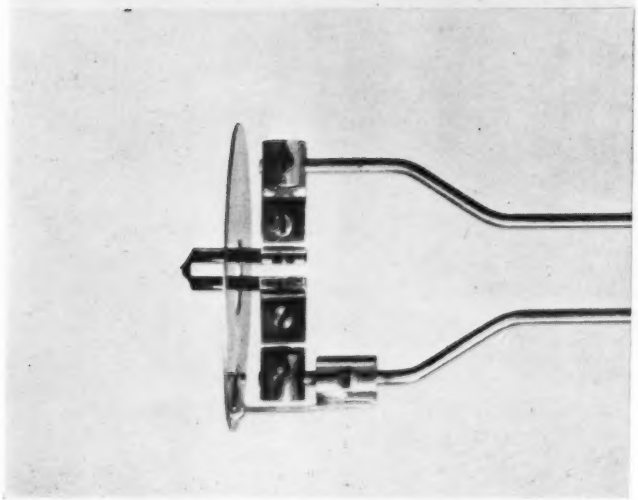

FIG. 1. (a) Details of cutting and etching tips. (b) Actual tips in mounting assembly.

[facing p. 88

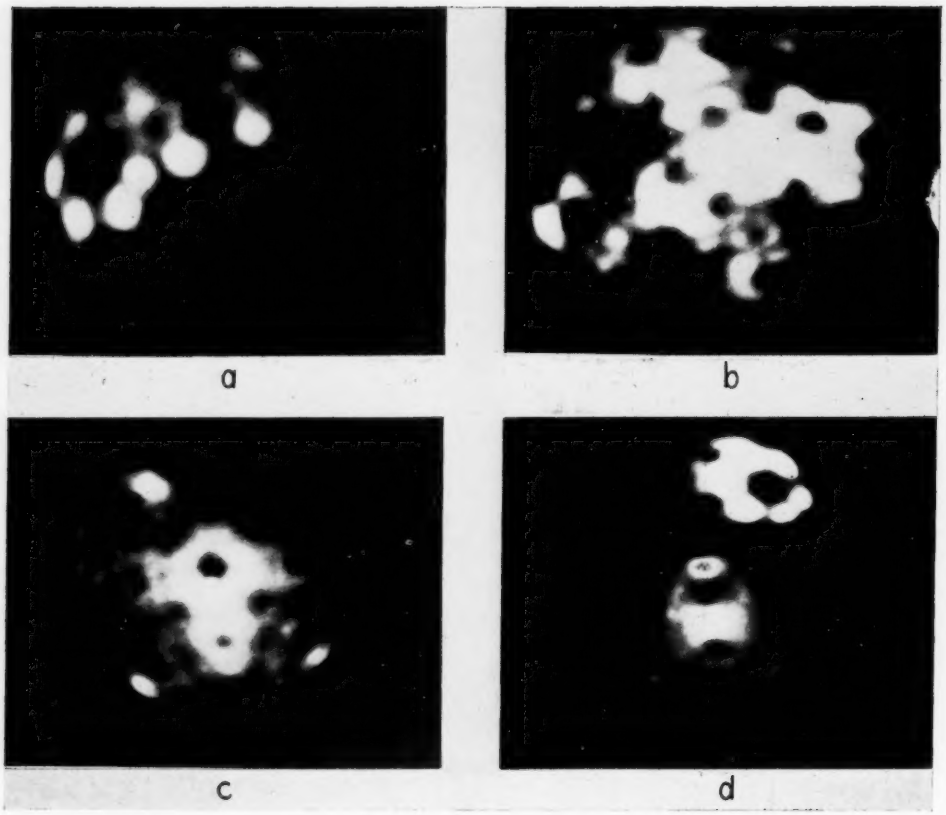

FIG. 2. Examples of the patterns from impurity crystallites found on silicon emitters during cleaning.

ol. 19
1961

(a)

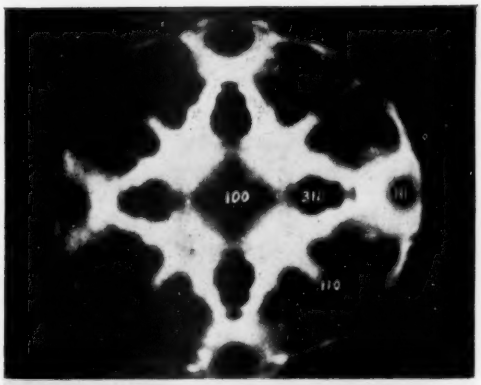

(b)

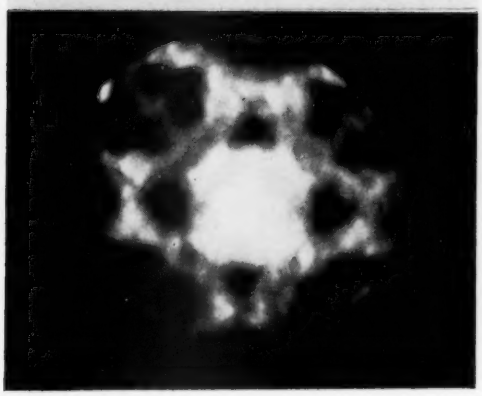

FIG. 3. Comparison of (a) thermally cleaned silicon pattern and (b) thermally annealed germanium pattern.

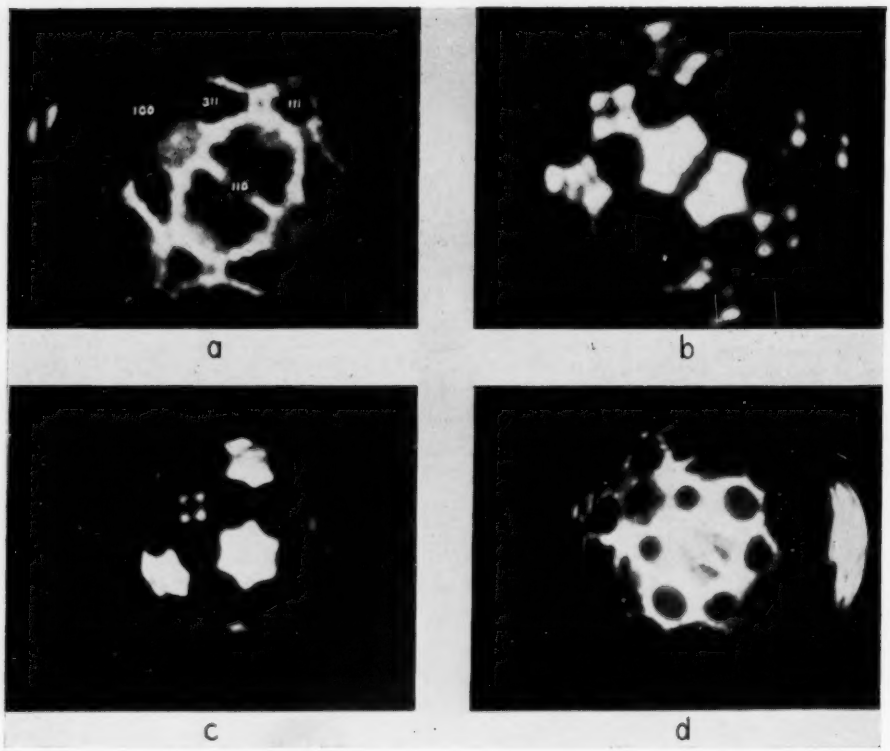

FIG. 4. Build-up of a (110) oriented silicon tip at high temperature and high field. (a) The clean pattern after flashing to high temperature with no field applied; (b) The same tip after nearly complete build-up; (c) Completely built-up tip with six (110) regions and one (100) region visible; (d) Same tip after partial annealing.

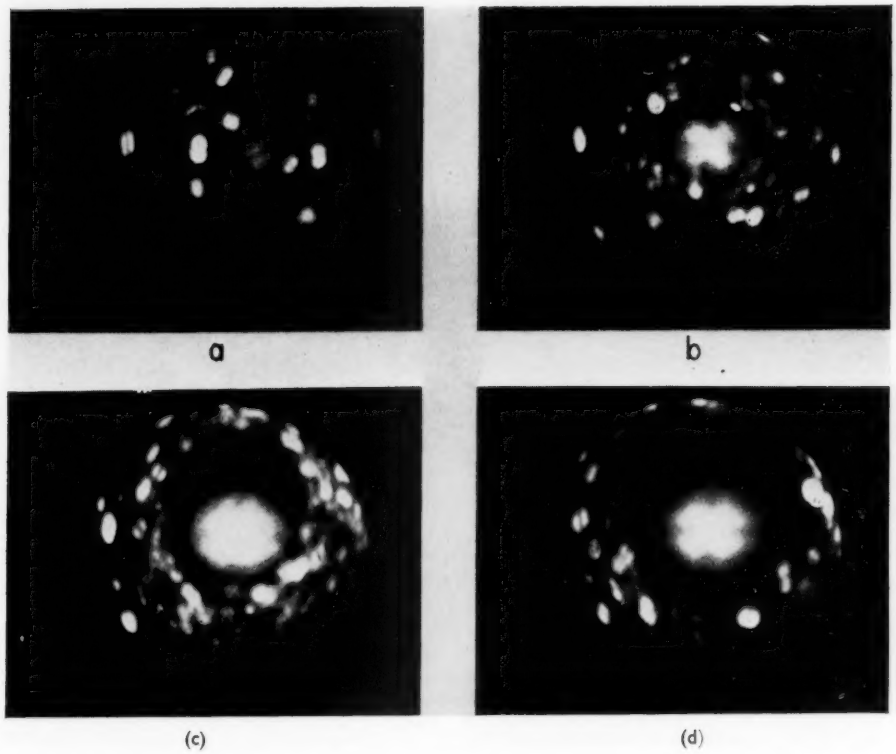

FIG 5. Field desorption cleaning of a germanium tip at room temperature. (a) Initial oxide covered surface after slight desorption. (b) Four-fold symmetry of substrate crystal emerging at center. (c) Oxide layer has receded after further desorption of whole surface. (d) Most of tip now exposed. Photos taken during cleaning.

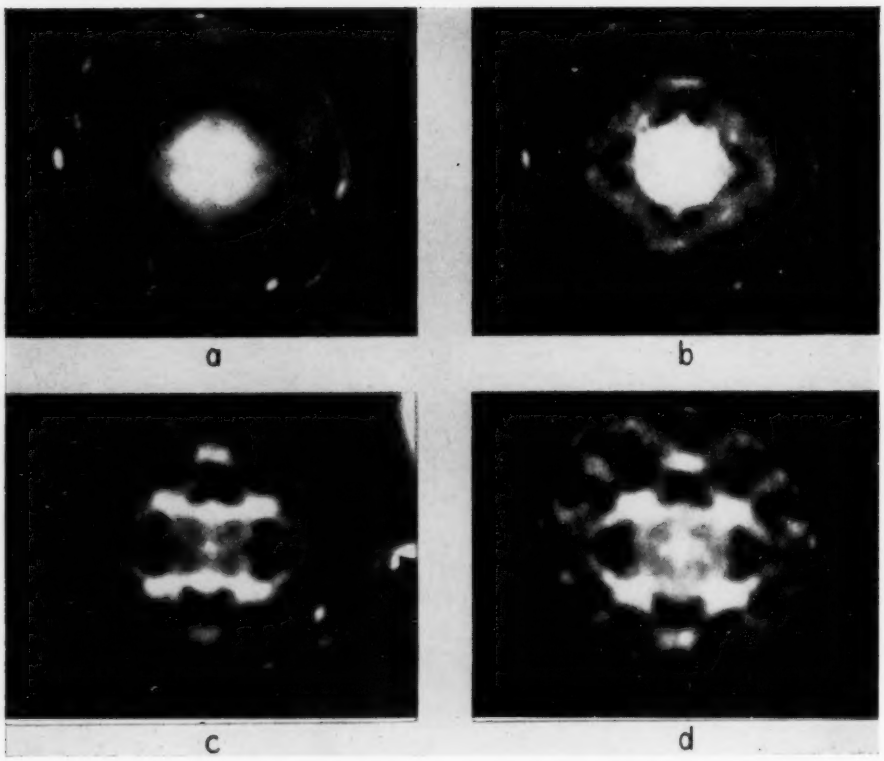

FIG. 6. The conversion of the germanium surface from the field cleaned pattern to the thermally annealed pattern. (a) Field cleaned pattern—photo taken during cleaning. (b) After heating three sec to ~ 200°C. (c) After heating five sec to ~ 280°C. (d) After heating five sec to 480°C.

ol. 19
1961

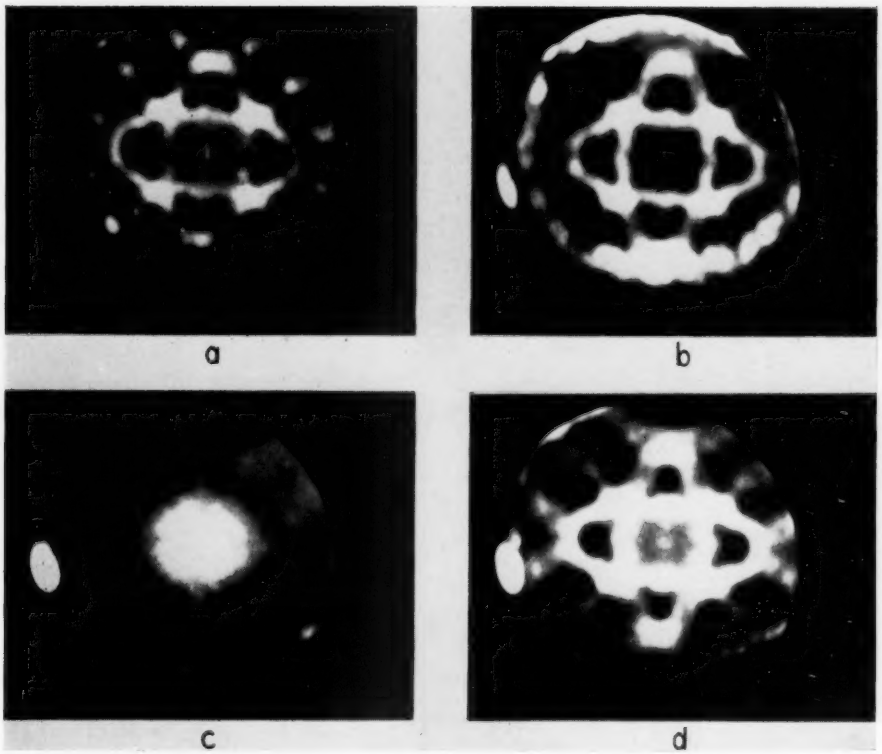

FIG. 7. Migration of oxide layer on germanium surface at high temperature. (a) After heating to 630°C. (b) After heating 30 sec at just below the melting point of 936°C. (c) After field desorption cleaning at room temperature of pattern 7(b). (d) After annealing again 15 sec at 400°C.

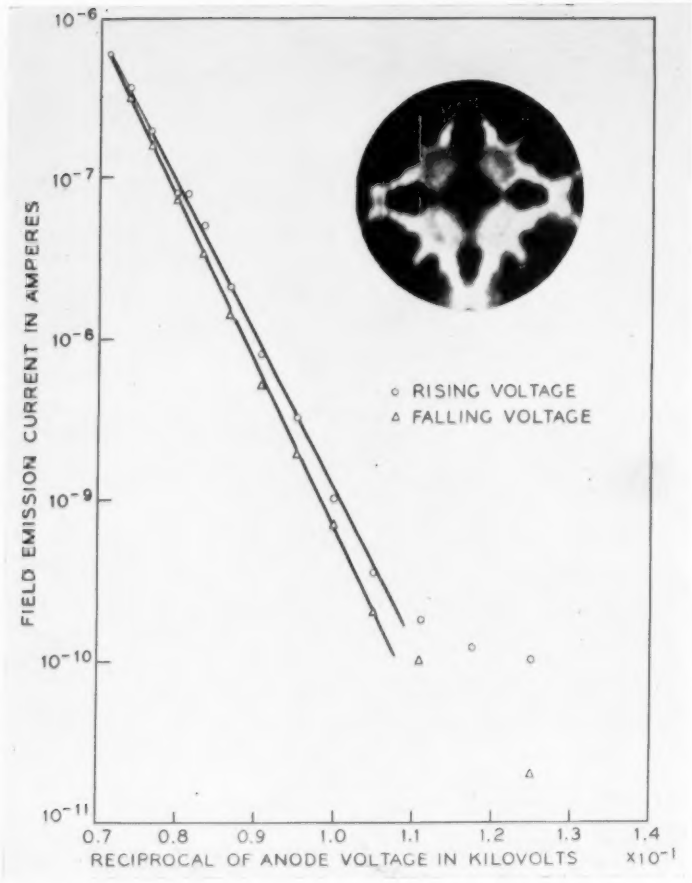

FIG. 8. Current–voltage characteristic for silicon field emission tip cleaned by heating. Photo inset shows pattern during run.

A.C. field desorption

The 60 cycle a.c. field desorption method described by COOPER and MÜLLER[21] is being used. This permits a continuous examination of the field electron emission pattern while field desorption is proceeding. Electrons are emitted each time the tip is negative with respect to the screen, field desorption occurs each time the tip is positive with respect to the screen, and the ratio of the positive to negative fields can be adjusted with the d.c. bias voltage.

A protective resistance of about 10^8 ohms is used in series with the d.c. supply to avoid tip loss by excessive emission. The a.c. voltage is supplied from a 0–44 kV r.m.s. 20 mA oil-insulated transformer. Spurious emission from the cathode structure to the Pyrex envelope has limited the maximum peak inverse voltage to about 50 kV thus far.

This a.c. desorption technique could cause fatigue failure of some specimens at stresses well below those attainable with steady applied fields. Since the reverse applied stress (see equation (1) below) during electron emission is small compared to peak stress during desorption and since the cycling frequency is only 60/sec, fatigue theory for macroscopic specimens would predict only a small reduction in strength during normal desorption times of a few minutes. Specimens with no dislocations in the tip may be entirely free of fatigue effects.

III. RESULTS ON THERMALLY CLEANED SILICON

The findings on thermally cleaned silicon field emission tips, some of which have been published elsewhere,[3,4] will be summarized here:

Initial cleaning

The surface of silicon after etching and rinsing, as first seen by field emission, is covered by a rough layer—presumably oxide—with randomly located protuding clusters loosely bound to the surface. (See Fig. 5(a) for the analogous Ge state.) There is no semblance of the underlying crystal symmetry. Little change occurs until the tip has been heated to 1200–1400°K. After several minutes of heating at these temperatures the loosely bound clusters are gone and a set of randomly oriented crystallites, each having definitely symmetrical and recognizable field emission patterns, remains.

Several apparently different species of crystallite pattern have been found repeatedly on silicon, but none has been positively identified as to chemical composition. Examples are shown in Fig. 2. (a) shows one variety, (b) shows another built-up form (high voltage and high temperature) while (c) and (d) show a pattern that can be analyzed as a tetragonal lattice. Some may be forms of SiO_2. Others may be metal oxides or silicides, such as $MoSi_2$ which has a tetragonal form, since heating the oxidized molybdenum ring surrounding the tip covers the surface with quantities of the crystallites shown in Fig. 2(b). These crystallites become mobile on the surface at 1300–1400°K and can be pulled off the tip by applying a field with the tip hot. Some of the crystallites are very tenacious and remain on the silicon surface, if no field is applied, even after heating several minutes to within about 50° of the melting point (1688°K). The number and type of these crystallites left on the tip at high temperature apparently depend on tip preparation. In a few cases, it has been possible to rid the tip of all such material by heating for only a few minutes to 1550°K with no field applied. Prolonged heating at this temperature gradually dulls the tip, however, so that it is often necessary to use a desorbing field with the tip hot to speed up the process.

The clean silicon pattern of Fig. 3(a) emerges as soon as the foreign material has left the surface. If cleaning is accomplished by heating without simultaneously applied field, this pattern is the first one sees of the clean silicon substrate. If a high desorbing field is used with the tip hot, the first sign of the clean substrate is a sudden eruption of one or several "microtips" of silicon from the substrate, seen first by D'ASARO[2] and discussed further below.

It is significant that as long as the silicon surface is covered by the above crystallites, no build-up of the surface occurs even at high fields and high temperatures. Once the surface is clean, build-up of the silicon starts at temperatures as low as 900°K.

Evidence for the atomically clean state for silicon

The clean pattern for thermally annealed silicon of Fig. 3(a) is a very distinctive one. The doubly opposed trapezoidal dark regions about the (110) poles and the series of dark spots, largest on the (311) pole and running between the (100) to the (111) poles, are prominent features. This pattern, with only minor variations, always appears as the final one after a series of cleaning treatments ending in thermal annealing.

The orientation and symmetry of the pattern have always coincided exactly with those of the substrate crystal, determined independently by

X-ray diffraction. This confirms that the surface being observed is in exact crystallographic registry with the substrate silicon.

Beyond settling this point the appearance of the electron field emission pattern cannot positively identify the surface atoms involved nor their crystal spacing and arrangement, other than their symmetry. Other evidence must be invoked to prove (a) that there is no epitaxial layer of foreign atoms arranged *on* the silicon substrate and, (b) that there is no sizable fraction of foreign atoms replacing the silicon atoms *in* the crystal surface itself. The evidence for both (a) and (b) has been presented in Ref. (4), and no new evidence has appeared to suggest that the pattern of Fig. 3(a) does not represent clean silicon.

It should be pointed out here that in order to see effects of an impurity in the surface by the electron field emission pattern, there must be either in the surface layer initially or within diffusion distance of the surface enough impurity to constitute at least a few per cent of a monolayer. The detectable limit depends on the mismatch in work function between impurity and substrate. Yet, as little as one one-thousandth of a monolayer of boron, diffused into a silicon surface for a depth to half maximum of a few microns, can radically alter the conductivity of the surface.[5] Thus the appearance of the electron field emission pattern is not nearly as sensitive an indicator of impurities as is required in many semiconductor surface studies.

Contamination and recleaning of a clean silicon tip

While initial cleaning of the silicon tip is difficult, once clean, it can be returned to the clean condition by simple flashing for a few seconds to 1500°K after contamination by all gases yet tried. Even after exposure to room air for an hour, the pattern after re-evacuation still has the symmetry of the clean substrate though obviously heavily covered with gas (probably two or three monolayers). Flashing to 1550°K for 20–30 sec restores the clean condition.

Details and temperatures for cleaning after oxygen exposure have been given elsewhere.[4]

Build-up of silicon tips at high temperature and high fields

As mentioned above, if a silicon tip is heated to 900°K or more with field emission fields applied a build-up of certain regions and an enlargement of the flats on certain planes of the tip result. A given build-up that took ~ 60 sec at 1000°K took only ~ 8 sec at 1100°K.

Figure 4 shows three stages of this build-up for a (110) oriented tip whose thermally annealed clean pattern is given in Fig. 4(a). Fig. 4(b) shows the tip of 4(a) in a nearly completely built-up condition (the built-up views were taken of the tip as frozen in at room temperature). The (110) region build-up is apparent here as a double projection from the surface. The (100) region also builds up to a lesser degree in the form of a square. The (111) flats are very large here—about twice as large as the (311) flats. Fig. 4(c) shows the completely built-up tip with six different (110) regions as hexagonal stars and one (100) square. Fig. 4(d) shows the tip of 4(c) after partial annealing. The (110) regions which built up first, have relaxed completely while the (111) and (311) flats are still enlarged.

Build-up with high fields at temperatures above 1500°K occurs very rapidly—almost explosively—and often many overlapping crystal patterns are seen at once. Apparently several "tiplets" or crystallites grow from the larger tip at once and project similar patterns on the screen. An electron microscope profile by PERRY[6] shows such a tiplet. The overlapping is explained by the fact that the electron trajectories fail to follow field lines where these are sharply curved near the tips. Each pattern is correctly oriented so that all crystallites must be part of the substrate crystal. The tiplets invariably sink back into the parent tip upon annealing without applied field.

IV. RESULTS WITH FIELD DESORPTION CLEANED SILICON

As yet this phase of the work is preliminary. One silicon tip was cleaned by a combination of room temperature field desorption and only intermediate heating (1300°K). This established that silicon can be cleaned without heating to temperatures where *p* layers form due to boron in-diffusion. The pattern resulting after annealing was the same as Fig. 3(a). While complete field desorption of this annealed pattern could not be carried out because of voltage limitations, it was established that the desorption had definitely begun to smooth

Vol. 1
196

the brightly emitting ridges, giving a lower contrast pattern.

Several attempts at cleaning silicon entirely by field desorption have failed with loss of the tip. It has been possible on several occasions to field desorb built-up portions of silicon tips, and in each case, the ratio of (negative field required for noticeable field desorption activity)/(positive field required to emit about 10^{-7} amps of electron current) was between 4·5 and 5·0.

V. RESULTS WITH FIELD DESORPTION CLEANED GERMANIUM

All attempts to clean germanium field emission tips by heating in vacuum have thus far, to the author's knowledge, failed. Presumably impurities or oxides normally left on the surface cannot be evaporated at the relatively low melting temperature of 1209°K.

Recently, however, field desorption cleaning of germanium tips at room temperature has been successfully carried out. Fig. 5 illustrates a typical sequence of steps during field cleaning of a germanium tip. The stripping action of the high field in removing the initial oxide layer and exposing the single crystal germanium substrate is clearly shown. Stripping occurs at the (100) oriented apex first where the field is the highest. After only a few minutes of stripping the four-fold symmetrical pattern of the germanium appears at the center and thereafter remains unchanged in appearance while stripping of the germanium continues. The boundary of the oxide coating moves out from the center as the stripping field is raised and the whole tip becomes more rounded. In some cases it has been possible to move this boundary back far enough from the center so that it is no longer seen in electron emission patterns.

During the stripping operation there is considerable local activity on the surface—a continual fluctuation of the grainy appearance. If the pattern is photographed without field applied the frozen-in grainy appearance is as shown in Fig. 7(c). If the ten-second exposure is taken during field cleaning the local fluctuations average out and the smooth pattern of Fig. 5(d) results. The field-cleaned germanium pattern of Figs. 5(d), 6(a), and 7(c), excluding the obvious oxide layer remaining around the periphery, is reproducible and is believed to represent an atomically clean surface. As discussed later, the very low contrast in this field emission pattern is just what is expected for the well rounded tip of a semiconductor having small variation in work function with crystal direction.

It has not yet been possible, from observing the stripping process, to determine whether atoms removed leave the surface directly from their local sites or whether they migrate over the tip surface to the apex and leave from there. The bright region at the center of the field-cleaned pattern suggests the latter.

The ratio mentioned above for silicon (the field required for noticeable field desorption)/(field required for electron emission of $\sim 10^{-7}$ A) has been measured for both the annealed and field-cleaned germanium surface, and the value always falls between 4·0 and 4·5, (at room temperature).

Annealing of field desorbed germanium surfaces

If the germanium tip is now heated slightly (always in a vacuum of $\sim 2\times 10^{-10}$ mm Hg) a drastic change in the pattern occurs as shown in Fig. 6. Fig. 6(a) shows the field-cleaned pattern. Figs. 6(b), (c) and (d) show the successive stages of change due to annealing for brief times at successively higher temperatures. It is seen that the principal change is completed after five seconds at ~ 650°K (380°C).

The annealed germanium pattern is closely analogous to thermally cleaned and annealed silicon, Fig. 3(a). Figs. 3(a) and (b) show this comparison. There are definite differences, however. There are also some changes that take place upon prolonged heating of the germanium near the melting point. The (110) regions of germanium [see Fig. 7(d)] come to resemble more and more closely the opposed trapezoids of the annealed silicon pattern. Structure around the (100) axis becomes very pronounced and does not resemble the silicon pattern at all.

One consequence of heating the germanium tip close to the melting point for several minutes is to cause the oxide sheath on the shank of the tip to migrate inwards toward the center, as shown in Figs. 7(a) (b). It is shown in Fig. 7(c) that a second field desorption cleaning at room temperature strips this sheath back from the apex again so that after a second annealing, Fig. 7(d), it is further

back than initially. The fact that this oxide sheath does not change drastically and migrates only about 10 per cent of the tip radius of $\sim 5 \times 10^{-5}$ cm in several minutes at near the melting point illustrates the difficulty in cleaning germanium by heating alone. It also shows that the oxide layer itself cannot move inward over the field-cleaned pattern during a few seconds of annealing to $\sim 280°C$.

While there is good reason to believe that the field desorbed germanium pattern of Fig. 5(d) is atomically clean (except for the contaminant sheath around the edge) the same cannot yet be said for the thermally annealed germanium pattern in Fig. 6(d). There is a possibility that the tip is coated during annealing by some contaminant. However, on five successive cyclings from the field desorbed to the annealed pattern, the latter was fairly reproducible. Also, during the annealing [Fig. 6(b)] there is no sign of a contaminant migrating over the tip surface; instead, the conversion to the annealed pattern seems to start all over the surface at once.

MELMED and GOMER[22] in 1959, photographed several emission patterns obtained with germanium whiskers grown by vacuum evaporation onto a tungsten substrate. While the patterns were distorted due to imperfect geometry, they were unquestionably very similar to the thermally annealed germanium patterns found in this work, such as Fig. 6(d).

Build-up of germanium surfaces with field and temperature

Build-up of the annealed germanium surface under high fields starts at temperatures of $\sim 400°K$—i.e. roughly the same temperature at which annealing of the surface from the field-cleaned condition begins. Build-up of the (100) oriented tip shown in Fig. 7(d) developed the bright regions already prominent around the (311) planes while the (311) and (111) flats enlarged. (See Fig. 3(a) for orientation.) The pattern could be returned again to the original annealed condition by heating a few seconds at $\sim 700°K$.

As in the case of silicon, as long as the germanium tip is covered by the oxide sheath found in the initial stages of cleaning, no build-up of the surface occurs even during prolonged exposure to high fields at just below the melting point.

Some of the properties of germanium and silicon surfaces of interest and the results of the present

Table 1. *Properties of silicon and germanium of interest in field emission, with tungsten for comparison*

Property	Silicon	Germanium	Tungsten
Melting point	1688°K (23)	1209°K (24)	3640°K
Temperature for appreciable surface migration	1000°K (This work)	450°K (This work)	1500°K (25)
Surface migration energy	~ 2 eV (This work)	~ 1 eV (estimated from this work)	2.4 eV build-up 3·1 eV anneal (25)
Evaporation rate at m.p., atomic layers/sec	300–5000 (26)	0·1–1·0 (27)	~ 1000–10,000 (27)
Temperature for cleaning in vacuum	> 1550°K (4)	> Melting point probably	> 2200°K (28)
Heat of vaporization	4·6 eV at 1550°K (26)	3·9 eV at 1150°K (26)	8·78 eV (29)
First ionization potential I	8·2 eV	7·9 eV	8·0 eV
Zero field work function ϕ	4·91 eV (100) 4·74 eV (111) (3,30)	4·7–4·8 eV (30,31)	4·5–5·0 eV (32)
Max. yield stress measured	5×10^{10} dynes/cm^2 (33)	3×10^{10} dynes/cm^2 (34)	
Dielectric constant	12·5 (35)	16·1 (35)	
Forbidden band width	1·09 eV (36)	0·66 eV (37)	
Desorption field	$1–2 \times 10^8$ V/cm (This work)	$1–2 \times 10^8$ V/cm (This work)	$5–6 \times 10^8$ V/cm (29)
Lattice spacing	5·66 Å (35) Diamond lattice	5·43 Å (35) Diamond lattice	3·16 Å b.c.c. lattice

work are included in Table 1. Comparison with tungsten is shown.

VI. CURRENT–VOLTAGE CHARACTERISTICS

There are theoretical expectations[1,16] that under certain conditions for a semiconductor the plot of log I vs. $1/V$, where I is emission current and V is anode voltage, should depart from the straight line relationship that holds for metals. We have measured this characteristic for silicon and recently for germanium. In no case where it was clear that the surfaces were clean, the vacuum good and the data reproducible, were significant departures from linearity found in this plot over the ranges studied, except at very low currents where spurious effects occurred. Data from a silicon emitter tip after high-field, high-temperature cleaning are shown in Fig. 8, and data for a germanium tip first field cleaned and then thermally annealed at $\sim 450°C$ are given in Figs. 9(a) and (b). The included photographs show the emission patterns during the runs.

One of the parameters that may be important in determining the shape of the current–voltage characteristic is the impurity concentration at the surface. The silicon sample was originally 15 ohm-cm p-type and almost certainly had a strongly p-type surface (up to 10^{19} B atoms/cm^3) due to boron in-duffusion during the heating used to clean it.[5] The field-cleaned germanium sample was originally about 10 ohm-cm n-type, and from results with a second identical sample, it can be assumed to have remained essentially unchanged both in the bulk and at the surface during the bakeout at 380°C and the field desorption.

It is thus seen that the plots for strongly p-type silicon and for n-type germanium are linear for at least three and one-half decades in current within a 20 per cent scatter in current values. The nonreproducibility of the data for silicon for rising vs. falling anode voltage is attributed to the relatively poor vacuum during the run ($\sim 2 \times 10^{-8}$ mm Hg) and the corresponding tendency of the surface to contaminate and to be altered by sputtering at high emission densities. Other Si data have not shown this effect. The irregular scatter of points above the linear plot below 10^{-10} A is attributed to spurious leakage, since, at anode voltages of several kilovolts, leakage impedances must be well over 10^{14} ohms to avoid errors. (KLEINT and FISHER[12] have recently published data for field emission from uncleaned silicon tips in which they find similar departures which they believe significant.)

The fact that the data for the field-cleaned germanium surface (10a) coincide with those of the annealed surface (10b) is coincidental. Annealing the surface after field cleaning causes the emission current (at values of $\sim 10^{-7}$ amperes) for the same anode voltage to rise by 10–20 per cent. It then falls again slightly below the original field-cleaned value when the surface is field desorbed again. Between Figs. 9(a) and (b), however, field desorption had further rounded the tip just cancelling out the enhancement of emission due to annealing.

VII. TEMPERATURE DEPENDENCE OF EMISSION

For silicon, the field emission current was found to be independent of tip temperature to within 20 per cent from room temperature up to $\sim 1200°K$ where build-up of the tip with applied field set in. This build-up was reduced by using 60 cycle a.c. applied fields, and higher temperatures can be reached using pulsed fields of short duty cycle.[38] Detailed temperature dependence of emission within this 20 per cent range, if any, has not yet been studied.

The transition between field emission and thermionic emission[39] should be of interest. The purely thermionic emission from silicon field emission samples similar to those used here was reported previously[3]; it was too small to have been observed here.

POSSIBILITY OF USING THE FIELD ION MICROSCOPE TO STUDY SILICON AND GERMANIUM SURFACES

Both silicon and germanium atoms are found to desorb at fields of only four to five times the field required to give electron emission currents of $\sim 10^{-7}$ A. MÜLLER[40] has pointed out that to get satisfactory ionization and imaging with hydrogen and helium in the ion microscope, fields of respectively ~ 5 and ~ 10 times those required for typical field electron emission currents from tungsten are needed. Since it is probable that the fields required to give the same emission from tungsten and from Ge and Si do not differ by more than

20 per cent (see below) one would predict from the above that both Si and Ge would be desorbing very rapidly during observations in the field ion microscope using helium, and slowly using hydrogen. MÜLLER[41] used silicon tips in the field ion microscope with hydrogen in 1957 and observed that though a pattern was easily visible, desorption was too rapid to permit photographing the results.

If field ion microscopy can be carried out with lower fields several interesting questions about the detailed structure on the surfaces may be answered: for example, whether or not surface atoms are displaced on some faces to satisfy dangling bonds.

IX. DISCUSSION

Appearance of thermally annealed patterns

The contrast between light and dark regions in the thermally annealed silicon and germanium patterns is considerably sharper than is normal for clean metals such as tungsten. Since emission current density depends exponentially on both local work function ϕ and local field strength, F, this contrast could be due to rapid variations over the surface in either ϕ or in local curvature (which determines the local field F).

A pattern of such sharp contrast is reminiscent of patterns from metal tips with layers present of low work function contaminants. However, as set forth above, there are good reasons for believing that no contaminant layer is involved here.

There is also evidence that the local work function of silicon and germanium faces varies less rapidly with crystallographic direction than is the case for tungsten. Results for germanium surfaces cleaned by ion bombardment[42] gave $\phi_{(100)}-\phi_{(111)} = 0{\cdot}060$ eV; $\phi_{(110)}-\phi_{(111)} = 0{\cdot}015$ eV. Those for silicon[3,43] gave $\phi_{(100)}-\phi_{(111)} = 0{\cdot}17$ eV; $\phi_{(110)}-\phi_{(111)} = 0{\cdot}12$ eV. Results of measurements on tungsten single crystals either by thermionic[32] or field emission[44] methods have given differences from 10 to 100 times larger than the above, for example, $\phi_{(110)}-\phi_{(111)} = 0{\cdot}9$–$1{\cdot}4$ eV. If this comparison can be extended to other faces, one would expect that as far as work function variation is concerned, the field emission patterns from Si or Ge would have lower contrast than that from *W*.

The high contrast of the silicon and germanium annealed patterns is therefore ascribed to rapid variations in local curvature of the surface. Evidence in support of this may be seen in the presence of dark spots at the (311), the (111) and (110) poles as well as others. These low index planes can be expected to have low surface free energy and thus to form flats, leaving ridges between them. These dark spots enlarge during build-up at high temperatures while the regions between them shrink and emit more brightly. It is noteworthy that the large flats on the (311) poles indicate this to be a very stable plane on both Si and Ge. Finally, it seems reasonable to expect a stronger variation in surface free energy with crystal direction for covalent-bonded Si and Ge than for metals like tungsten. It will be of interest to look for a variation with temperature in the difference in surface energy between different faces as discussed by HERRING[45] and manifested by a variation in flat size with temperature.[46]

Two further effects pertinent to the contrast in a field emission pattern from a semiconductor are discussed in Appendix II.

Appearance of field desorbed patterns

The field desorbed pattern for germanium (Fig. 6a) is markedly different from the annealed germanium and silicon patterns. It has the same symmetry and orientation—as it should—but the contrast between bright and dark regions is far lower and there is, if anything, a negative correlation between bright regions in the field-desorbed pattern and bright regions on the annealed pattern. There is a striking absence of round dark spots at low index crystal directions.

Since in field desorption a surface atom is desorbed as soon as the local field strength is sufficient to break its bonds to the surface, all sharp projections enhancing the field will be desorbed first leaving a smoothly rounded form. However, MÜLLER[29] and GOMER[47] have pointed out that the energy barrier for desorption may depend linearly on the difference between several other energy terms[48] and the work function, which varies over the surface. Hence, while the field desorbed tip can be expected to be free of abrupt local roughnesses, such as ridges or flats, its local curvature may vary smoothly over the surface to some extent depending on the variations in local work function. If work function variations for Si and Ge are as small as indicated by the work mentioned above, the field desorbed tip may be nearly perfectly rounded.

Vol. 196

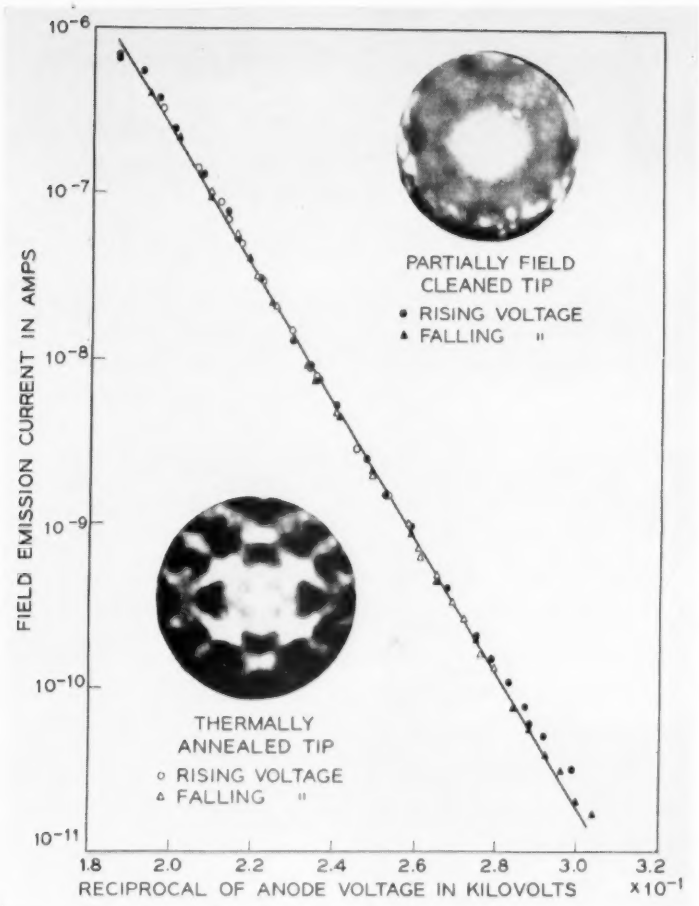

FIG. 9. Current–voltage characteristic for germanium field emission. (a) Field desorption cleaned surface before any heating. (b) After annealing at ~400°C. Photo's show patterns during runs.

[*facing p.* 94

BLANK
PAGE

Vol.
196

The appearance of the field desorbed and annealed germanium and silicon patterns is consistent with the hypothesis that the tips in the former case are smoothly rounded, while those in the latter have developed local ridges and flats to minimize surface free energy. The increase in emission for a given field after annealing is also consistent with this interpretation.

Field desorption of silicon and germanium

The tensile stress on the surface of a conductor due to an external electric field E is

$$T = E^2/8\pi \qquad (1)$$

An upper limit to the fields required for field desorption can be found from the fact that, since edge and corner atoms on the surface desorb before failure occurs in the bulk, T in (1) will be less than the yield stress of the ideal crystal. Measurements on fine whiskers have given maximum yield stresses of 5×10^{10} dynes/cm^2 for silicon[33] and 3×10^{10} dynes/cm^2 for germanium.[34] These values are believed to be close to the theoretical yield strength of the crystals at room temperature.[49] Values of E from (1) corresponding to these stresses are $\sim3{\cdot}5\times10^8$ V/cm and $2{\cdot}6\times10^8$ V/cm respectively. Desorption fields may thus be expected to be lower than this.

While direct measurements of the field strengths have not yet been made, a rough estimate can be had from the value of 4 to 5 mentioned above for the ratio (field desorption fields)/(field emission fields). If we assume the field emission fields to be comparable to those required—2 to 4×10^7 volts/cm[50]—for metals of comparable work function to Si and Ge ($\sim4{\cdot}8$ eV with no field applied and perhaps lower than this by half the energy gap of ~1 eV during field emission), we estimate the desorption fields for silicon and germanium to be 1 to 2×10^8 V/cm.

A more detailed analysis of the desorption to determine whether the Si and Ge atoms are initially desorbed as neutral atoms or ions[47] awaits further work. Since the effective work function of the semiconductor under the large desorption field (tip positive) can be expected to be only slightly larger than the clean field free value of $\sim4{\cdot}8$ eV, while the first ionization potential for both Si and Ge is close to 8 V (see Table 1), the term $I-\phi$ in GOMER's formulation should be about 3·0 V—not very different than for tungsten. The heat of evaporation has been reported by HONIG[26] to be 4·6 eV for silicon at 1550°K and 3·9 eV for germanium at 1150°K. These are significantly lower than the value of 8·78 eV cited by MÜLLER[29] for tungsten, and may explain the relative ease with which these semiconductors field desorb.

Surface migration energies

The process of surface build-up under applied field, subsequent relaxation during annealing and transformation from the field-desorbed surface to the annealed surface can all be assumed to occur by surface migration.[25,51] Assume a jumping frequency on the surface of

$$\nu = \nu_0 \exp(-Q/kT) \qquad (2)$$

where ν_0 is a natural atomic vibration frequency and Q is the activation energy for migration. (Q may be expected to vary slightly depending on which transformation is involved.[25]) Then we can estimate Q from the relative time required to accomplish a given transformation of the surface at two different temperatures.

While available data are still scanty, from the build-up and annealing rates mentioned above we estimate Q to be ~2 eV for Si and ~1 eV for Ge. For comparison, the surface migration energy of W on W has been determined by several workers to be 2·5–3·1 eV.[25]

The only other experimental evidence bearing on the surface migration temperature of silicon and germanium comes from studies of epitaxial film formation during evaporation or deposition from a vapor phase. It is to be expected that an epitaxial film can grow only at temperatures where appreciable surface mobility of the deposited atoms occurs. Epitaxial films can be grown on germanium at temperatures above 350°C[52] and on silicon at temperatures above 1100°C[53] These temperatures are in agreement with temperatures we find necessary for rapid surface migration in each case.

It should be pointed out that the type of surface transport being considered here involves removing atoms from the edge of a step. Migration of an atom already isolated on an atomically smooth plane must involve much lower energies and hence occur at correspondingly lower temperatures.

Vol. 19
1961

Theory for field emission from silicon and germanium

Theory[1,16] indicates that field emission from a semiconductor may differ from that of a metal in several respects:

(i) Due to the scarcity of charge available at the surface, the field may penetrate the semiconductor and cause potential changes (work function changes) at the surface comparable to the band gap, i.e. of 0·66 and 1·1 eV for Ge and Si, respectively. The amount of this change, its temperature dependence, and the fields at which it sets in depend strongly on a still unknown factor—the density and distribution in energy of electronic surface states on the clean surface.

(ii) The supply of electrons incident on the surface for tunnelling through the barrier, its temperature dependence and its distribution in energy may be quite different from that of a metal. Instead of originating in a conduction band filled to a depth of several volts beneath the Fermi level as in a metal, tunnelling electrons may come from the valence band, from surface states, or from a conduction band whose lower edge lies only ~0·1 eV below the Fermi level.

(iii) The image force seen by the electron outside the surface is reduced from that outside a metal by the factor α[15] where $K-1/K+1 \leqslant \alpha \leqslant 1$ in which K is the dielectric constant, and the value of α within this range is determined by the free charge available at the surface. Since K is about 12 and 16 for Si and Ge respectively, this factor is negligibly different from the metallic case in our work.

(iv) An appreciable i.r. drop may develop within the tip at high emission densities affecting emission through (i) and (ii) above as well as by alteration of field strengths just outside the tip.[8] For Si and Ge of resistivities less than 50 ohm-cm and at total emission currents of 10^{-6} A or less, effects of this sort should be negligible, and indeed no departures from linearity in the characteristic at high currents have been seen as yet in our work.

Field penetration

The penetration of the field into the surface for silicon and germanium has been treated in some detail[1] and the results need only be summarized here. If we assume no surface states, the solution of Poisson's equation at the surface shows that for samples of either Ge or Si of all normal dopings, i.e. with donor or acceptor densities of up to $\sim 3\times 10^{18}$/cm^3, the bottom of the conduction band is pulled below the Fermi level at the surface for external positive fields (tip negative) of $\geqslant 1\times 10^7$ V/cm (while the top of the valence band is pulled above the Fermi level for negative fields of $\geqslant 1\times 10^7$ V/cm). For lower dopings degeneracy occurs at only slightly lower fields. Once the valence or conduction band edge crosses the Fermi level at the surface the available state density is so high that any further realizable field can be neutralized by a further potential shift of only a few kT at room temperature.

For acceptor dopings above 3×10^{18}/cm^3, however, the surface will sustain positive fields of 10^7 V/cm without becoming degenerately n-type. The relation for the potential shift at the surface ($\Delta\Psi_s$) is then given by the Schottky exhaustion layer theory for the nondegenerate case as

$$\Delta\Psi_s = \frac{E^2}{8\pi KeN'} \tag{3}$$

where $N' = |N_D - N_A|$ is the net impurity concentration (all impurities can be assumed ionized for Ge and Si at room temperature or above) and e is the electronic charge.

Since fields of $\geqslant 10^7$ V/cm are probably necessary for appreciable field emission, we conclude that if no surface states are involved, all normally doped n- or p-type silicon or germanium samples will be degenerately n-type at the surface during field emission, while p-type samples of very high dopings should sustain at least the lower range of field emission fields without becoming degenerate.

The presence of available surface states[54] in general makes surface potential less sensitive to external fields. Thus, for a uniform density of states N_s near the Fermi level, assuming that surface state charge dominates and that all states below the Fermi level are full, all above empty, the surface potential displacement ($\Delta\Psi_s$) due to an external field E is given by

$$\Delta\Psi_s = \frac{E}{4\pi eN_s} \tag{4}$$

If $\Delta\Psi_s$ is to remain less than 0·1 eV when $E = 10^7$ V/cm, N_s from (4) must be $\geqslant 5\times 10^{13}$ states/(cm^2 eV). There is some evidence in the

Vol. 196

literature[30,55,56] that surface state densities near the Fermi level may be this high. If so, Si and Ge surfaces may remain nondegenerate throughout at least the lower range of field emission fields.

The effect of changes in surface potential caused by field penetration will be to alter the electron supply function available for tunnelling by bringing different electronic energy states close to the Fermi level, but more important, it will directly affect the height of the barrier above the Fermi level, i.e. the work function for field emission.

Electron supply function and emission probability

For the case in which the surface is degenerately n-type for the entire field emission range (low acceptor concentration and surface states unimportant) emission will certainly occur from the conduction band. The field penetration, the supply function and the emission probabilities have been treated for this case by STRATTON in equation (30),[16] and can be applied directly to Ge and Si. Except for additional exponential terms varying slowly with field, the results are essentially the same as for a metal giving a linear characteristic of log I vs. $1/V$, and the same temperature independence.

For all other cases Stratton's treatment will require modification before application to Si or Ge because it treats only the case of largely unionized donors in the bulk, assumes only one of many possible surface state distributions and neglects the possibility of emission from surface states or from the valence band. Both the temperature and field dependence of his results may be expected to be changed by such modifications. However, the general behaviour predicted of a sudden change in I followed by a linear region in the log I vs. $1/V$ plot as the field increases through the transition from surface shielding to field penetration and n-type degeneracy, should still be valid for Si and Ge. This effect will only be seen, of course, in the case that the surface states are such as to cause this transition to fall in the rather narrow range of fields observable, say $2\times10^7 < E < 4\times10^7$ V/cm. As we have seen above, in the special case that the surface state density near the Fermi level is well below 10^{13}/(cm^2 eV) and the sample is doped to $\geqslant 3\times10^{18}$ acceptors/cm^3, this transition *would* be expected to fall within this range, so that nonlinearities in the characteristic should be found.

Comparison of theory with results

The present results thus far are limited to showing that (1) log I vs. $1/V$ is linear within 20 per cent over the observable range of about four orders of magnitude in I for several samples of both silicon and germanium, and (2) the emission from silicon is temperature insensitive to within 20 per cent up to $\sim$1200 °K. Unfortunately, this permits little to be decided about the various possible situations suggested by the theory. The results are consistent with either of two interpretations. First, that the surface is degenerately n-type throughout the observable range of fields. If this is the case, nonlinearity would exist as a *decrease* in emission from the straight line relation as the applied field decreased below the observable range; this effect could perhaps be brought into the observable range by very high p-type doping. Second, the results are also consistent with a situation in which surface state densities well in excess of 5×10^{13}/(cm^2 eV) hold the surface potential clamped and insensitive to either field or temperature over the above ranges.

It should be pointed out here that some of the data of PERRY[6] taken under good experimental conditions from clean silicon emitters, show significant departures from linearity in the log I vs. $1/V$ plot. Apparently further work is again needed.

Absolute field strength determinations will assist in selecting between cases, since effective work functions during field emission can then be computed for different assumed surface state distributions. In the first case above, the work function of both silicon and germanium may be expected to be reduced below the zero-field value by some sizeable fraction of the energy gap, i.e. reduced from $\sim$4·8 eV to $\sim$4·0 eV. In the second case the work function should remain close to the zero field value of $\sim$4·8 eV.

If emission from surface states is involved, the filling time of such states may become comparable with the emission time at high emission density. This would lead to a transient change in emission after the initial application of the field with a time constant of the filling time of the fast surface

Vol. 19
1961

states, due to a change in field penetration. Pulsed emission would differ from d.c. emission.

Measurements of distribution in energy of the emitted electrons will be of great interest if they can be carried out with sufficient accuracy. In the first case above, this distribution should extend from the Fermi level down to a depth of only about 0·1 eV, while in the second, a composite distribution of electrons from both surface states and or valence band states may result.

Acknowledgements—The technical assistance of G. WOLFF in preparing samples is gratefully acknowledged. as are the many helpful conversations held with colleagues such as C. HERRING, M. LAX, J. A. BECKER and H. D. HAGSTRUM.

APPENDIX I

Temperature drop along tip

It is easily shown that for a truly conical tip heated by conduction from the base, the temperature drop due to radiation cooling will be linear along the tip as long as the drop is small relative to the absolute temperature. The amount of this drop at a distance z from the base is given by

$$\Delta T(z) \cong \frac{\epsilon\sigma \bar{T}^4}{k\alpha} z \qquad \text{(AI–1)}$$

where $\bar{T}$ is the average temperature of the tip, ϵ the total emissivity at temperature $\bar{T}$, k the thermal conductivity at $\bar{T}$, σ the Stefan–Boltzmann constant, and α the cone half angle in radians, assumed small.

While ϵ is not known for Si and Ge, it is probably between 0·2 and 0·4 (see Ref. 20 and the analogous emissivities for metals). Using values of k of respectively 0·15 and 0·20 W/(cm deg C)[57,58] for germanium and silicon, we find that the temperature drop at the end of a typical 0·05 cm tip of cone half-angle $\alpha = 5°$ would be ~18°K for germanium at 1200°K and ~35°K for silicon at 1650°K. Measurements made with a pyro-micro-optical pyrometer on actual silicon tips during heating confirm the general correctness of the above values.

APPENDIX II

Further effects relating to contrast in the field emission pattern from a semiconductor

1. *Surface state variation with crystal face.* A question pertinent to the contrast in the field emission pattern from a semiconductor is that of a possible variation of surface state density and distribution on different crystal faces. Such a variation could result in a bending of the energy bands near the surface that varies with crystallographic direction. This would not only contribute to the zero field work function variation with crystal direction, but could also result in different, and sometimes nonlinear, log I vs. $1/V$ characteristics on different faces.

2. *The smoothing of work function transitions at the surface.* The fact that an external field penetrates the semiconductor surface and causes bending of the bands implies that a work function transition must be smoothed over some region near the boundary. Roughly, one can say that for two adjacent regions whose work function difference is $\Delta\phi$ this work function smoothing will extend out from the boundary a distance d such that the external field strength $\sim\Delta\phi/2d$ is just sufficient to cause a bending of the bands comparable to $\Delta\phi$. For germanium or silicon with no surface states, fields of 10^6 V/cm bend the bands by about a tenth of a volt. Thus the boundary between two regions having $\Delta\phi = 0{\cdot}2$ V would have a smoothing width of $2d$ determined by $\Delta\phi/2d \sim 10^6$, $d \sim 10^{-7}$ cm. This would be only 1 per cent of the tip diameter for a typical crystal. With a density of surface states of $10^{13}/\text{cm}^2$ in the gap or more this effect will become smaller still, and hence, will probably not be noticed for silicon or germanium. It could, however, become important for semiconductors of high resistivity and low surface state densities.

REFERENCES

1. See, for example, ALLEN F. G., Ph.D.Thesis, Harvard University, 1955 or Cruft Laboratory Technical Report No. 237.
2. D'ASARO L. A., *J. Appl. Phys.* **29,** 33 (1958).
3. ALLEN F. G., Rochester Semiconductor Conference Proceedings, *J. Phys. Chem. Solids* **8,** 119 (1959).
4. ALLEN F. G., EISINGER J., HAGSTRUM H. D. and LAW J. T., *J. Appl. Phys.* **30,** 1563 (1959).
5. ALLEN F. G., BUCK T. M. and LAW J. T., *J. Appl. Phys.* **31,** 979 (1960).
6. PERRY R. L. and BETTLER P. C., Linfield Research Institute, Interim Technical Reports on Field Emission from Semiconductors Nos. 1–12.
7. BUSCH G. and FISCHER T., *Brown Boveri Rev.* **45,** 532 (1958).
8. APKER L. and TAFT E., *Phys. Rev.* **88,** 1027 (1952).
9. KLIMIN A. I., *Zh. tekh. fiz.* **27,** 719 (1957); *Sov. J. Tech. Phys.* **2,** 649 (1957) (English translation).
10. GOFMAN I. I., SMIRNOV B. G., SPIRIN G. S. and SHUPPE G. N., *Zh. tekh. fiz.* **27,** 2662 (1957); *Sov. J. Tech. Phys.* **2,** 2471 (1957) (English translation).
11. BERTOLDI W. and KLEINT C., *Ann. Phys., Lpz.* **4,** 388 (1959).
12. KLEINT C. and FISCHER R., *Z. Naturf.* **A14,** 753 (1959).
13. ELINSON M. I. and VASILIEV G. F., *Rad. i Elektron.* **4,** 728 (1959); *Radio Eng. and Electronics* **4,** 246 (1959) (English translation).
14. ZUBENKO Y. V., KLIMIN A. I. and SOKOLSKAYA I. L., *Sov. fiz. tverd. tela.* **1,** 1775 (1959); *Phys. Solid State* **1,** 1691 (1960) (English translation).
15. MARGULIS N., *Zh. fiz.* (*S.S.S.R.*) **11,** 67 (1947).
16. STRATTON R., *Proc. Roy. Soc.* **B68,** 746 (1955).

17. VASILIEV G. F., *Rad. i Elektron.* **3,** 151 (1958); *Radio Eng. and Electronics* **3,** 151 (1958) (English translation).
18. ELINSON M. I., *Rad. i Elektron.* **4,** 140 (1959); *Radio Eng. and Electronics* **4,** 231 (1959) (English translation).
19. GOMER R., *Field Emission and Field Ionization,* Chapter I. Harvard University Press (1960).
20. ALLEN F. G., *J. Appl. Phys.* **28,** 1510 (1957).
21. COOPER E. C. and MÜLLER E. W., *Rev. Sci. Instrum* **29,** 309 (1958).
22. MELMED A. J. and GOMER R., private communication.
23. GAYLER M. L. V., *Nature, Lond.* **142,** 478 (1938).
24. GREINER E. S., *J. Metals, N.Y.* **4,** 1044 (1952).
25. BETTLER P. C. and CHARBONNIER F. M., *Phys. Rev.* **119,** 85 (1960).
26. HONIG R. E., *J. Chem. Phys.* **22,** 1610 (1954).
27. HONIG R. E., *R.C.A. Review* XVIII, No. 2, 195 (1957), or Chart of Vapor Pressure of the Elements.
28. HAGSTRUM H. D. and D'AMICO C., *J. Appl. Phys.* **31,** 715 (1960).
29. MÜLLER E. W., *Phys. Rev.* **102,** 618 (1956).
30. GOBELI G. W. and ALLEN F. G., Second Semiconductor Surface Conference, (1959), *J. Phys. Chem. Solids* **14,** 23 (1960).
31. DILLON J. A., Jr. and FARNSWORTH H. E., *J. Appl. Phys.* **28,** 174 (1957).
32. SMITH G. F., *Phys. Rev.* **94,** 295 (1954).
33. PEARSON G. L., READ W. T. and FELDMAN W. L., *Acta. Met.* **5,** 181 (1951).
34. BREIDT P., HOBSTETTER J. N. and ELLIS W. C., *J. Appl. Phys.* **29,** 226 (1958).
35. CONWELL E. M., *Proc. Inst. Radio Engrs. N.Y.* **40,** 1327 (1952).
36. MORIN F. J. and MAITA J. P., *Phys. Rev.* **96,** 28 (1954).
37. MORIN F. J. and MAITA J. P., *Phys. Rev.* **94,** 1525 (1954).
38. DYKE W. P. and BARBOUR J. P., *J. Appl. Phys.* **27,** 356 (1956).
39. MURPHY E. L. and GOOD R. H., *Phys. Rev.* **102,** 1464 (1956).
40. MÜLLER E. W., *Ann. Phys., Lpz.* **20,** 315 (1957).
41. MÜLLER E. W., 1957 Field Emission Symposium, Pennsylvania State University; unpublished discussion.
42. ALLEN F. G. and FOWLER A. B., *J. Phys. Chem. Solids* **3,** 107 (1957).
43. DILLON J. A., Jr. and FARNSWORTH H. E., *J. Appl. Phys.* **29,** 1195 (1958).
44. MÜLLER E. W., *J. Appl. Phys.* **26,** 732 (1955).
45. HERRING C., *Structure and Properties of Solid Surfaces* (edited by GOMER R. and SMITH C. S.) Chapter I, Section III. University of Chicago Press (1953).
46. BECKER J. A., *Bell Syst. Tech. J.* **30,** 907 (1951).
47. GOMER R., *J. Chem. Phys.* **31,** 341 (1959).
48. A possible variation in heat of vaporization with crystal face should also be considered. See RIDEAL E. and WIGGINS P. M., *Proc. Roy. Soc.* **A210,** 291 (1952).
49. PEARSON G. L. and VOGEL F. L., *Progress in Semiconductors* Vol. V, to be published.
50. DOLAN W., *Phys. Rev.* **91,** 510 (1953).
51. BOLING J. L. and DOLAN W. W., *J. Appl. Phys.* **29,** 556 (1958).
52. DUNOYER J. M., *J. Phys. Radium* **12,** 602 (1951).
53. WAJDA E. S., KIPPENHAM B. W. and WHITE W. H., *IBM J. Res. Developm.* July, 1960.
54. BARDEEN J., *Phys. Rev.* **71,** 717 (1947).
55. ALLEN F. G., Ph.D. Thesis, Harvard University, 1955 or Cruft Laboratory Technical Report No. 236.
56. FOWLER A. B., *J. Appl. Phys.* **30,** 556 (1959).
57. PANKOVE J. I., *Rev. Sci. Instrum.* **30,** 495 (1959).
58. GEL'D P. V., Eighth Union Conference on Semiconductors, 1955.

J. Phys. Chem. Solids Pergamon Press 1961. Vol. 19, Nos. 1/2, pp. 100–104. Printed in Great Britain.

SCREW DISLOCATION IN CRYSTALS WITH DIAMOND STRUCTURE*

V. CELLI

University of Illinois, Urbana, Illinois

(*Received* 19 *September* 1960)

Abstract—The model of dislocation in a lattice recently proposed by MARADUDIN is modified and applied to an estimate of the strain energy of a screw dislocation in crystals with the diamond structure, in particular Si and Ge.

1. INTRODUCTION

A MODEL of dislocation has been considered by MARADUDIN[1], in which the discrete nature of an actual crystal is explicitly taken into account in the assumption of linear forces between nearest neighbors only. A complete solution for the displacements in an infinite crystal and hence the energy of a screw dislocation is obtained for two configurations (Fig. 1) which are thought to correspond to stable (I) and unstable (II) equilibrium. The difference $E_{II}-E_I$ between the energies per unit length of the two configurations is found to be exceedingly high ($6{\cdot}92\times10^7$ eV/cm, when the parameters corresponding to the case of NaCl are introduced).

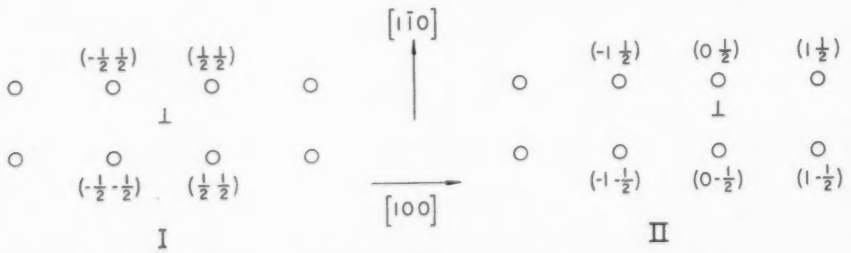

FIG. 1. Stable (I) and unstable (II) configuration of a screw dislocation in a rectangular lattice. The circles represent the intersections of atom rows with the plane of the figure.

The estimate of E_{II} however may be shown not to correspond to the actual behavior of a crystal. In fact (see Fig. 1, II) the relative displacement Δw, parallel to the dislocation line, of the two rows $(0, \frac{1}{2})$, $(0, -\frac{1}{2})$ must be one half of the Burgers vector $\boldsymbol{b}$ by reasons of symmetry. Then the two rows are in a position of unstable equilibrium with respect to each other and the mutual force vanishes. In Ref. (1) this force is implicitly assumed to vanish in setting up the equations for the displacements, but it is taken to be $Bb/2$, as given by Hooke's law with force constant B, for the purpose of calculating E_{II}. According to this, in the expression for E_{II} the term $Bb/4$, which stems from the mutual displacement of the rows $(0,\frac{1}{2})$, $(0, -\frac{1}{2})$, should be changed into $V(b/2)$, where $V(\Delta w)$ is the interaction potential between the two rows concerned. For small Δw, V can be considered elastic, but actually it is periodic with period b. It can roughly be approximated by $(bB/4\pi^2)[1-\cos$

* Supported in part by the Air Force Office of Scientific Research, through Air Force Contract AF 49–638–420.

$(2\pi\Delta w/b)$]. With the values $B = 13{\cdot}28\times10^3$ dyne/cm, $b = 3{\cdot}9456$ Å] quoted in Ref. (1) it is found that:

$$E_{II}-E_I = 6{\cdot}92\times10^7 \text{ eV/cm} - \frac{Bb}{4} + \frac{Bb}{2\pi^2}$$

$$= 0{\cdot}40\times10^7 \text{ eV/cm}.$$

Any refinement of the previous results in the case of the ionic crystals calls for taking into account the interaction between next nearest neighboring rows of ions as well as further departures from linearity in the core of the dislocation. Furthermore it has been found by HUNTINGTON *et al.*[2] that the radial displacements are essential in determining the energy of configuration II, although they are probably negligible in configuration I. In both configurations the calculation in Ref. (1) gives an upper bound for the energy of the dislocation which is probably not very close to the actual value of the energy in the crystal and one would expect this to be true *a fortiori* of the difference $E_{II}-E_I$.

2. SCREW DISLOCATION IN THE DIAMOND STRUCTURE

The model of Maradudin is likely to be better suited to discuss dislocations in crystals with the diamond structure. As a matter of fact in that case, if only nearest neighbors interactions are considered, only two microscopic constants need to be introduced and then the three macroscopic elastic constants turn out to be connected by a relation due to BORN[3], which is well substantiated for Ge[4] and to a lesser extent for Si and Group III–Group V compounds. Moreover the Peierls energy seems to be much higher than in NaCl and of the same order of magnitude obtained above for $E_{II}-E_I$.

The most probable configuration for the screw dislocation in the diamond lattice[5] is indicated in Fig. 2. Only displacements in the [110] direction, normal to the plane of the drawing, are allowed.

Let α denote the force constant associated with the radial part of the nearest neighbors interaction and β the force constant associated with the angular part. Then the force constant per atom plane for the A bond of Fig. 2 is $A = (2/3)(2\alpha+\beta)$, whereas the force constant for the B bond (see Fig. 2) is simply $B = \beta$.

The constants A and B are related to the elastic constants by the formulae:

$$c_{44} = \frac{2}{a}\times\frac{AB}{A+2B}, \quad c_{11}-c_{12} = 2\frac{B}{a} \qquad (1)$$

which are in agreement with the Born theory when A is expressed in terms of α and β.

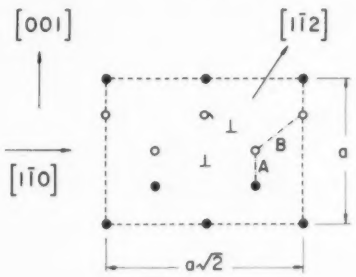

FIG. 2. Section of the cubic cell of the diamond lattice with a (110) plane. Open circles ○ denote atom rows with atoms in the plane of the figure, solid circles ● denote rows with atoms above and below that plane. A bonds connect ● with ○, B bonds connect ● with ● and ○ with ○.

To derive equation (1) we note that the macroscopic elastic energy of the unit cubic cell of edge a (see Fig. 2) for a pure shear strain e in the [110] direction, is $\frac{1}{2}c_{44}e^2a^3$ for shear in the (001) plane and $(1/4)(c_{11}-c_{12})e^2a^3$ for shear in the (110) plane. From the microscopic point of view the energy of the cell in the second case is eight times the energy of a B bond, i.e. $8\frac{1}{2}B(ea\sqrt{2}/4)^2$ whereas for shear in the (001) plane it turns out to be $e^2a^2(2AB^2+BA^2)/(A+2B)^2$.

We now write down the equations determining the displacements w_{mn1}, w_{mn2} of the two face centered cubic sublattices for the dislocation in configuration I (cf. Fig. 3). If the displacements are considered to be many-valued we have:

$$\begin{aligned} &A(w_{mn2}-w_{mn1})+B(w_{m(n-1)2}+ \\ &\quad w_{(m-1)n2}-2w_{mn1}) = 0 \\ &A(w_{mn1}-w_{mn2})+B(w_{(m+1)n1}+ \\ &\quad w_{m(n+1)1}-2w_{mn2}) = 0 \end{aligned} \qquad (2)$$

From these equations it is easy to obtain separate equations for the two sublattices. It is mathematically convenient to make a cut along the ($\bar{1}$11) plane, whose trace on the plane of Figs. 2 and

3 is $[1\bar{1}2]$, and assume that the displacements are single-valued and have a discontinuity $b = a/\sqrt{2}$ through the cut. Then the equations can be formally solved putting

$$w_{mn1} = \sum_{k=0}^{\infty} w_{mn}^{(k)}$$

and requiring the $w_{mn}^{(k)}$'s to satisfy the following equations (note that for $k = 0$, $n = \frac{1}{2}$, only the A bond is cut):

$$A(w_{(m+1)n}^{(k)} + w_{m(n+1)}^{(k)} + w_{(m-1)n}^{(k)} + w_{m(n-1)}^{(k)} - 4w_{mn}^{(k)}) +$$

$$B(w_{(m+1)(n-1)}^{(k)} + w_{(m-1)(n+1)}^{(k)} - 2w_{mn}^{(k)})$$

$$= \begin{cases} (A+B)b\delta_{m(k+\frac{1}{2})}(\delta_{n\frac{1}{2}} - \delta_{n(-\frac{1}{2})}) \\ \qquad\qquad \text{for } k = 1, 2, \ldots \\ [(A+B)\delta_{n\frac{1}{2}} - A\delta_{n(-\frac{1}{2})}]b\delta_{m\frac{1}{2}} \\ \qquad\qquad \text{for } k = 0 \end{cases}$$

By reasons of symmetry:

$$\begin{aligned} w_{mn2} &= w_{(-m)(-n)1} - b/2 \quad \text{for } n > 0 \\ w_{mn2} &= w_{(-m)(-n)1} + b/2 \quad \text{for } n < 0 \end{aligned} \tag{3}$$

The procedure is now completely analogous to that described in Ref. (1). The final expression for $n > 0$ is, apart from an additive constant:

$$w_{mn1} = \frac{b}{4\pi^2} \int_{-\pi/2}^{\pi/2} dx \int_{-\pi/2}^{\pi/2} dy \times$$

$$\frac{(A+B)(\sin y/\sin x) - Be^{i(y-x)}}{A(\sin^2 x + \sin^2 y) + B\sin^2(x-y)} e^{2i(mx+ny)} \tag{4}$$

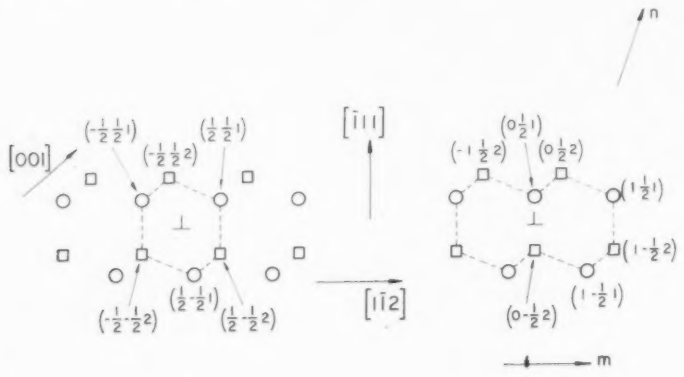

I II

FIG. 3. Stable (I) and unstable (II) configuration of a screw dislocation in the diamond lattice. The atoms of the f.c.c. sublattice labeled 1 are indicated by circles, the atoms of the sublattice 2 are indicated by squares. In I the labels m and n assume half-integer values: in II m is integer and n half-integer.

This expression is also valid for $n < 0$, provided that $b/2$ is added in order to preserve continuity. It is readily checked that (4) assumes the constant value $-b/8$ on the line $m = n$ for $n > 0$. The energy per unit length of an infinitely long cylinder of material having its axis on the dislocation line is given by

$$E = \frac{B}{2} \sum_{k=0}^{N-1} (b + w_{(k+\frac{1}{2})\frac{1}{2}1} - w_{(k+\frac{1}{2})(-\frac{1}{2})2})$$

$$= \frac{B}{2} \sum_{k=0}^{N-1} \left(\frac{b}{2} + w_{(k+\frac{1}{2})\frac{1}{2}1} - w_{-(k+\frac{1}{2})\frac{1}{2}1} \right)$$

where N is the number of atoms along the slip plane $(\bar{1}11)$.

Vol. 1
1961

Introducing expression (4), after some manipulation one finds:

$$E = \frac{Bb}{2\pi}\int_0^{\pi/2} \frac{\sqrt{C}\sin^2 Nx}{\sin x\sqrt{(1+C\sin^2 x)}}\,dx \qquad (5)$$

where $C = A/(A+2B) = c_{44}/(c_{11}-c_{12})$.

This final expression for E is formally the same as in Ref. (1), where the integral is evaluated in the limit of large N. A boundary term should be added to E, arising from the forces on the surface needed to keep the cylinder in shape. This term can be evaluated by macroscopic elastic theory[1] and it is found to be per unit length:

$$E_B = \frac{b^2}{8\pi}\sqrt{[\tfrac{1}{2}c_{44}(c_{11}-c_{12})]}\times \ln\left[\frac{\sqrt{[2c_{44}/(c_{11}-c_{12})]}}{\frac{2}{3}+\frac{1}{3}2c_{44}/(c_{11}-c_{12})}\right] \qquad (6)$$

Adding (6) to the asymptotic expression of (5):

$$E_{\mathrm{I}} = \frac{Bb}{4\pi}\sqrt{C}\left[\ln 2\gamma - \tfrac{1}{2}\ln\frac{1+C}{4} + \ln N + \tfrac{1}{2}\ln\left(\sqrt{\frac{C}{2}}\,\frac{3}{1+C}\right)\right] \qquad (7)$$

where γ is Euler's constant.

An analogous procedure can be carried out for configuration II, corresponding to unstable equilibrium. The displacements for $n > 0$ are given by:

$$w_{mn1} = \frac{b}{4\pi^2}\int_{-\pi/2}^{\pi/2}dx\int_{-\pi/2}^{\pi/2}dy\,\frac{(A+B)(\sin y/\sin x)+iA\sin y\,e^{ix}-B\cos(x-y)}{A(\sin^2 x+\sin^2 y)+B\sin^2(x-y)}\,e^{i(2m-1)x+2iny} \qquad (8)$$

Again $b/2$ must be added to (8) for $n < 0$ and w_{mn2} is found by use of equation (3). The energy is the sum of a term $V(b/2)$, due to the relative displacement of the two central rows as discussed in Section 1, and of an elastic term:

$$\frac{B}{2}\sum_{m=1}^{N}\left(\frac{b}{2}+w_{m\,\frac{1}{2}1}-w_{(-m)\,\frac{1}{2}1}\right) = \frac{Bb}{4\pi}\int_0^{\pi/2}\frac{\cos x}{\sin x}\times\frac{\cos x-\cos(2N+1)x}{\sqrt{(1+C\sin^2 x)}}\,dx \qquad (9)$$

Again this integral is formally the same as the integral evaluated in Ref. (1) for the corresponding configuration, suggesting that the result is structure-independent. The boundary correction (6 must also be added. The final result is:

$$E_{\mathrm{II}} = \frac{Bb}{4\pi}\sqrt{C}\left[\ln 2\gamma - \tfrac{1}{2}\ln\frac{1+C}{4} - \frac{1}{\sqrt{C}}\tan^{-1}\sqrt{C} + \ln N + \tfrac{1}{2}\ln\left(\sqrt{\frac{C}{2}}\times\frac{3}{1+C}\right)\right] + V(b/2) \qquad (10)$$

3. CONCLUSIONS

Formulae (7) and (10) for the elastic energy can be corrected by allowing some of the bonds in the core of the dislocation to deviate from Hooke's law. The A bonds can always be assumed to be elastic, because their deformation is small also in the core, since $A \gg B$. But for some of the B bonds the strain Δw is large enough to make the correction $V(\Delta w)-(B/2b)(\Delta w)^2$ to the elastic energy quite important. The displacements should then be recalculated in a self-consistent way, but this is hardly significant in view of the uncertainty in the form of $V(\Delta w)$ and of the neglect of radial displacements.

In configuration I four bonds are to be considered. For them

$$\Delta w = w_{\frac{1}{2}\frac{1}{2}1}-(w_{\frac{1}{2}(-\frac{1}{2})2}-b) = b/2+w_{\frac{1}{2}\frac{1}{2}1}-w_{-\frac{1}{2}\frac{1}{2}1} = (b/\pi)\tan^{-1}\sqrt{C}$$

In configuration II three couples of bonds need consideration. It is found from (8) that:

$$w_{\frac{1}{2}\frac{1}{2}2}-w_{0\,\frac{1}{2}1} = b(A/B)(\tfrac{1}{4}-\pi^{-1}\tan^{-1}\sqrt{C}),$$

$$w_{1\,\frac{1}{2}1}-(w_{1(-\frac{1}{2})2}-b) = b/\pi[(1+C^{-1})+\tan^{-1}\sqrt{C}-1/\sqrt{C}],$$

$$w_{-1\,\frac{1}{2}2}-w_{1\,\frac{1}{2}1} = (b/2\pi)[(1-C^{-1})\tan^{-1}\sqrt{C}+1/\sqrt{C}]$$

Numerical values of E_I and E_{II} can be obtained for Si, Ge and Group III–Group V compounds using the elastic constants at room temperature quoted in the review article by HUNTINGTON[4] and the value of the lattice constants given in the American Institute of Physics Handbook. $V(\Delta w)$ can be approximated by a cosine law as in Section 1. This simple assumption is sufficient to give physical meaning to all the above formulae. It has been checked that the work $Bb/2\pi^2$ needed to bring an atom in the unstable equilibrium position is smaller than the cohesive energy per bond but of the same order of magnitude.

If the expressions for the energies E_I and E_{II} are put in the form $k\ln(R/r_I)$, $k\ln(R/r_{II})$, it results that for Si: $k = 5{\cdot}06\times10^7$ eV/cm $= 1{\cdot}94$ eV/plane, $r_I = 0{\cdot}441\ a$, $r_{II} = 0{\cdot}409\ a$ and for Ge: $k = 3{\cdot}81\times10^7$ eV/cm $= 1{\cdot}52$ eV/plane, $r_I = 0{\cdot}452\ a$, $r_{II} = 0{\cdot}423\ a$.

These values of r_I and r_{II} should be considered as lower bounds to the true values. They do not represent the core radius of the dislocation in the usual sense because the quoted values for E_I and E_{II} include also the core energy of the dislocation.

The difference $E_{II}-E_I$ represents the energy barrier that the dislocation has to overcome in order to move in a pure crystal. In the present scheme $E_{II}-E_I$ has the value $0{\cdot}38\times10^7$ eV/cm or 0·15 eV/plane for Si and the value $0{\cdot}26\times10^7$ eV/cm or 0·10 eV/plane for Ge. This is consistent with experimental evidence.

Acknowledgement—It is a pleasure to thank Prof. R. THOMSON for a critical reading of the manuscript.

REFERENCES

1. MARADUDIN A. A., *J. Phys. Chem. Solids* **9**, 1 (1959).
2. HUNTINGTON H. B., DICKEY J. E. and THOMSON R., *Phys. Rev.* **100**, 1117 (1955).
3. BORN M., *Ann. Phys., Lpz.* **44**, 605 (1914). See also DE LAUNAY J., *Solid State Physics* Vol. II, p. 290. Academic Press, New York (1956).
4. HUNTINGTON H. B., *Solid State Physics* Vol. VII, p. 300. Academic Press, New York (1958).
5. VANBUEREN H. G., HORNSTRA J. and PENNING P., *Nuovo Cim. Suppl.* **7**, 646 (1958).

Vol. 1
1961

J. Phys. Chem. Solids Pergamon Press 1961. Vol. 19, Nos. 1/2, pp. 105–116. Printed in Great Britain.

SOLID SOLUTIONS OF In_2Te_3 IN Sb_2Te_3 AND Bi_2Te_3

A. J. ROSENBERG* and A. J. STRAUSS

Lincoln Laboratory,† Massachusetts Institute of Technology, Lexington 73, Massachusetts

(*Received* 29 *September* 1960)

Abstract—Solid solutions of the compositions $(Sb_2Te_3)_{1-x}(In_2Te_3)_x$, where $x \leqslant 0{\cdot}45$, and $(Bi_2Te_3)_{1-x}(In_2Te_3)_x$, where $x \leqslant 0{\cdot}25$, have been prepared in mono- or oligo-crystalline form by directional freezing. The crystals retain the hexagonal structure characteristic of Sb_2Te_3 and Bi_2Te_3, but in both cases the volume of the unit cell diminishes with increasing In concentration (measured spectrochemically). Density measurements and phase analysis prove that the mechanism of solid solution is either the direct replacement of Sb (or Bi) by In or the simultaneous replacement of Te by In and Sb (or Bi) by Te. The resistivity, Hall coefficient, and Seebeck coefficient have been measured. The In-substituted Sb_2Te_3 solutions are always *p*-type, but an inversion to *n*-type conductivity occurs in the Bi_2Te_3 alloys, particularly at high In concentrations. *The magnitude of the Hall coefficient is virtually unchanged by the introduction of* In. In the Bi_2Te_3 alloys, the carrier mobility is not strongly dependent on In content, but in the Sb_2Te_3 alloys it decreases sharply with increasing In concentration. The magnetic susceptibility is unchanged by the introduction of In. On the basis of these results, a model is proposed in which the nonbonding *s*-orbital of an In atom is transformed in the crystal into new states in the conduction band.

Information is appended on the phase diagram of the In–Sb–Te ternary system.

INTRODUCTION

THE RELATIONSHIP between chemical composition, crystal structure, and electronic properties continues to be one of the most intriguing problems in the science of the solid state. While the essential correctness of the one-electron band approximation for solids is now firmly established,[1] the theoretical apparatus is too complex to permit quantitative calculations for any but the simplest systems. On an entirely empirical level, however, a number of self-consistent correlations of properties has been evolved.[2] These correlations, which have been rationalized in terms of qualitative theories of the chemical bond, have proved to be useful in the prediction of new compounds and their electrical properties.

Where band structure calculations have been made on covalent semiconductors, it has been shown that the valence band of a crystal originates in the bonding molecular orbitals, while the conduction band is associated with antibonding molecular orbitals. The chemist has assumed that the atomic coordination in a covalent crystal reflects the symmetry of the molecular orbitals and that their symmetry in turn reflects the symmetry of the atomic orbitals from which they are derived. By determining the nature of the bonding orbitals, the chemical composition determines both the crystal structure and the general features of the band structure. By specifying the band structure (i.e. the electron capacity of the bands) and also the number of valence electrons which are available for filling the bands, the composition influences the electrical properties. In this way, an hypothetical connection is established between the composition, structure, and electrical properties.

It has been the purpose of the present study to explore a new aspect of this problem—namely, the interchange of atoms with the same nominal valence state between structures of different atomic symmetry. In particular, we have been concerned with the possible interchange of In with Sb or Bi between In_2Te_3 and Sb_2Te_3 or Bi_2Te_3. Thus, the structure and electrical properties of In_2Te_3 differ radically from those of Bi_2Te_3 and Sb_2Te_3,

* Present address: Materials Research Laboratory, TYCO Incorporated, Waltham, Massachusetts.

† Operated with support from the U.S. Army, Navy, and Air Force.

although the cations are all nominally trivalent. The most noteworthy result of this investigation has been the discovery that as much as 45 per cent of Sb in Sb_2Te_3 and as much as 25 per cent of Bi in Bi_2Te_3 may be replaced by In without altering either the crystal structure type or the charge carrier concentration of the host.[3]

EXPERIMENTAL PROCEDURES AND RESULTS

I. *Phase diagram of the* Sb_2Te_3–In_2Te_3 *pseudobinary section*

Samples of the composition, $(In_2Te_3)_x$–$(Sb_2Te_3)_{1-x}$, were prepared from the elements in their purest commercially available form and sealed in evacuated quartz ampoules fitted with reentrant thermocouple wells. The samples were melted and the freezing points determined by direct thermal analysis.

The liquidus is shown in Fig. 1, together with several solidus points obtained from the heating curves of quenched samples. The curve is quite flat in the region $0 < x < 0{\cdot}5$, and the solidus and liquidus in this region are quite close. Samples quenched from melts with $x < 0{\cdot}4$ were single phase, with the hexagonal structure characteristic of Sb_2Te_3. It was concluded tentatively that In can extensively replace Sb in Sb_2Te_3. Since Bi_2Te_3 is isomorphous with Sb_2Te_3, similar behavior was anticipated for the $(In_2Te_3)_x(Bi_2Te_3)_{1-x}$ system. This was confirmed experimentally, when single phase material with the Bi_2Te_3 structure was obtained by freezing melts with x as high as $0{\cdot}25$.

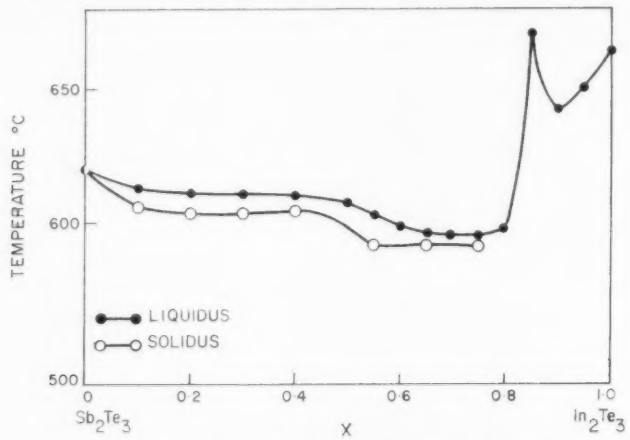

FIG. 1. Phase diagram of the Sb_2Te_3–In_2Te_3 pseudobinary system.

II. *Physical properties of* Sb_2Te_3–In_2Te_3 *and* Bi_2Te_3–In_2Te_3 *solid solutions.*

Preparation of specimens. The tendency toward the precipitation of large crystals was pronounced even in quenched samples. A simple apparatus was designed for the growth of crystals intended for physical measurements. Fifty-gram samples of the desired compositions were prepared from the elements and sealed under vacuum in 13 cm sections of 10 mm quartz tubing. The samples were placed in a vertical furnace which had a temperature gradient of about 15° per cm when the average temperature was in the range 400°C–750°C. The power input was controlled by a "Variac" auto transformer operating from a constant voltage transformer. The temperature was first raised well above the melting point of the samples. The tubes were then removed, shaken thoroughly, and returned to the furnace. The power input to the furnace was then gradually reduced by a synchronous motor turning down the "Variac" through a series of reduction gears. By this technique the samples were directionally frozen from the bottom at a slow, uniform rate without moving either samples or the furnace. Two freezing rates, 4 mm/hr and 0·2 mm/hr, were employed.

Vol. 1
1961

The samples were 5–6 cm long and 10 mm in diameter and consisted usually of several large grains from which it was possible to isolate satisfactory single crystals or bicrystals for physical measurements.

Structural analysis. The lattice parameters of powdered samples, indexed in the hexagonal system, were derived by least squares analysis of *d*-spacings obtained with a Norelco X-ray diffractometer calibrated against silicon. The variation of these parameters with indium content of the Sb_2Te_3–In_2Te_3 alloys is shown in Fig. 2. The

With increasing In concentration, the *c* parameter first increases slightly and then decreases for $x > 0{\cdot}3$; the *a* parameter, on the other hand, decreases over the whole range. The net effect is a continuous decrease in the volume of the unit cell.

In contrast to the case in the Sb_2Te_3–In_2Te_3 system, pronounced segregation of In takes place in directionally frozen ingots in the Bi_2Te_3–In_2Te_3 system. The In concentration increases by as much as a factor of three from the bottom to the top of the ingots. This observation is consistent with

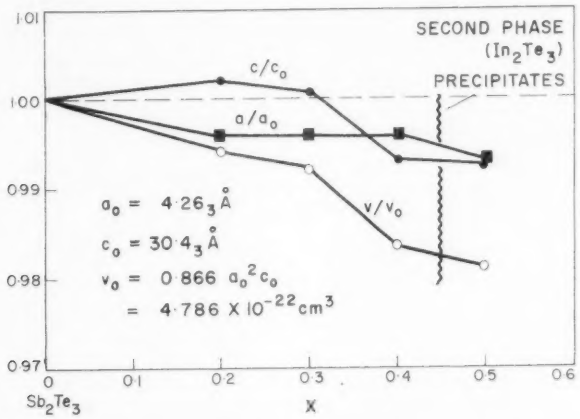

FIG. 2. Lattice parameters of Sb_2Te_3–In_2Te_3 solid solutions.

values obtained for pure Sb_2Te_3 were $a = 4{\cdot}263$ Å and $c = 30{\cdot}43$ Å, compared with the published values $a = 4{\cdot}25$ Å and $c = 30{\cdot}35$ Å.[4] The values of *x* in Fig. 1 correspond to the compositions of the solid solutions, as determined by spectrochemical analysis. The composition of each solid sample is essentially the same as that of the melt from which it was prepared, since the variation of In concentration along the length of directionally frozen ingots was less than 15 per cent. This small degree of segregation indicates that the separation of the liquidus and solidus curves is even less than shown in Fig. 1. The samples were all grown at the rate of 4 mm/hr. For this growth rate, the X-ray data show the maximum solubility of In_2Te_3 in the Sb_2Te_3 structure to be about 45 per cent. The second phase appearing in samples with larger concentrations was identified as In_2Te_3.

fragmentary thermal analysis data, which indicate a large separation between the solidus and liquidus in the phase diagram.

In Fig. 3 the variation of the lattice parameters with spectrochemically determined indium concentration is shown for two sets of Bi_2Te_3–In_2Te_3 samples grown at 4 mm/hr and 0·2 mm/hr., respectively. The lattice parameters of pure Bi_2Te_3, independent of growth rate, were found to be $a = 4{\cdot}38_8$ and $c = 30{\cdot}4_2$, compared with the published values $a = 4{\cdot}383$ Å and $c = 30{\cdot}487$ Å.[5] The variation of the lattice parameters with In concentration in the slow-grown samples is almost the same as in the Sb_2Te_3–In_2Te_3 system. The changes in the lattice parameters in the fast-grown samples, however, are significantly larger.

A further difference based on growth rate is shown in Fig. 4, where the relative intensities of

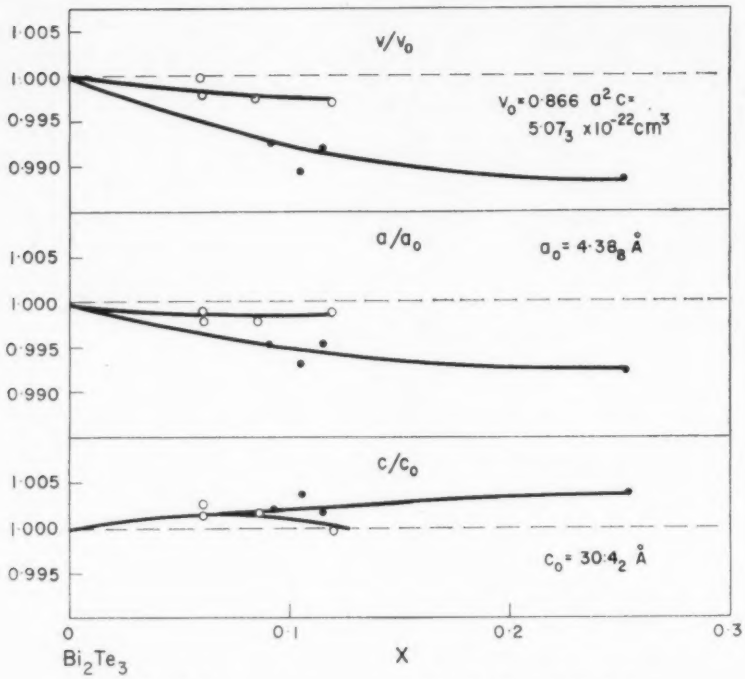

FIG. 3. Lattice parameters of Bi_2Te_3–In_2Te_3 solid solutions.

the various X-ray diffraction lines are compared. The relative intensities of the lines obtained with the slow-grown samples are the same as in pure Bi_2Te_3. In the diffraction patterns of the fast-grown samples, however, the intensities of the (0,0,6) and the (0,0,15) lines—corresponding to reflections from the cleavage plane—are anomalously high. It is well-known that when samples of an easily cleaved material are prepared for Debye–Scherer powder patterns the particles tend to be aligned, with the cleavage plane parallel to the surface of the sample holder. The intensities of the reflections from this plane then appear anomalously high. It is obvious, therefore, that the cleavage in samples of Bi_2Te_3–In_2Te_3 is facilitated by fast growth, the effect becoming even more pronounced with increasing In content. It is significant that no such effect was observed in the Sb_2Te_3–In_2Te_3 system, where the relative diffraction intensities were always the same.

Bi_2Te_3 and Sb_2Te_3 are octahedrally coordinated compounds in which sheets composed of hexagonal arrays of one atom species are stacked in five-fold layers, i.e. (—Te–Bi–Te–Bi–Te—)$_n$.[6] Although the sheets are stacked in a close-packed cubic sequence (ABCABCABC...), the spacing between sheets is variable, so that the over-all crystal symmetry is best described in the hexagonal or rhombohedral systems. The Te atoms in the central sheet of each five-fold layer are bonded to three Bi atoms in each of the adjacent sheets at a distance of 3·22 Å, the interbond angle being 85°.* Each Bi atom is bonded to three Te atoms in the central sheet and three Te atoms in a sheet bounding the layer, the bonds being 3·12 Å long at an angle of 89° 20′. The Te atoms in the sheet bounding the layer are separated by 3·57 Å at an angle of 76°. This large separation facilitates cleavage between layers.

If the stacking sequence is preserved when In is introduced, there are six degrees of freedom—three bond lengths and three bond angles—by which the lattice may be adjusted. The analysis of the Debye–Scherer patterns permits the

* The atomic positions in Sb_2Te_3 are not known.

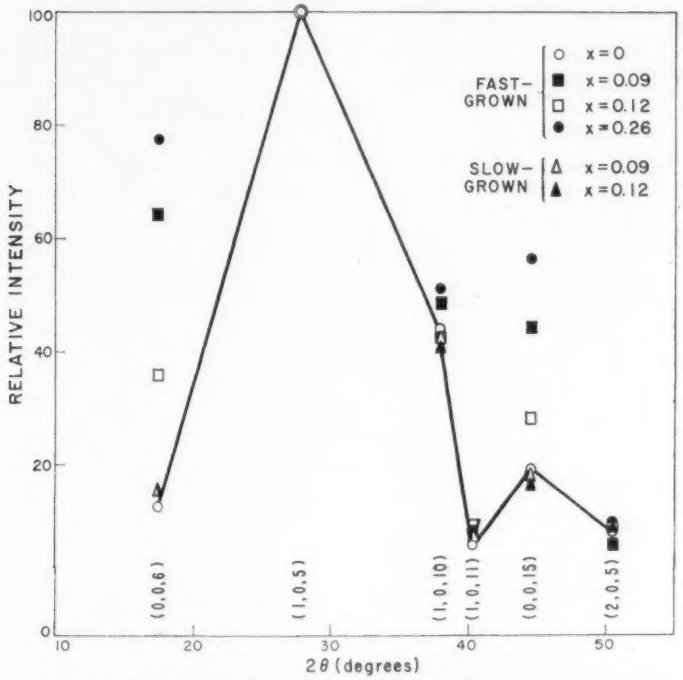

FIG. 4. Relative intensities of X-ray diffraction lines in powder patterns for Bi_2Te_3–In_2Te_3 solid solutions.

determination of only two lattice parameters, however: the a-spacing in the hexagonal system, which equals the distance between atoms in any sheet, and the c-spacing, which equals the distance between an atom in a given sheet and an atom in an equivalent sheet three layers removed. It can be shown by simple geometric arguments that if the lattice responds to the introduction of indium by a change in the bond angles only, $\partial(c/c_0)/\partial(a/a_0) \gg -3$. If, on the other hand, it responds by a change in the bond lengths only, $\partial(c/c_0)/\partial(a/a_0)=1$. According to Figs. 2 and 3 it is clear that neither of these values is consistent with the experimental results. Thus the net decline in the volume of the unit cell which accompanies the introduction of indium into the Bi_2Te_3 and Sb_2Te_3 structures must reflect a simultaneous decrease in both bond angles and bond lengths.

Density measurements. Density measurements were made by a microgravimetric buoyancy method using toluene as the liquid displaced and germanium as a standard. The density of samples weighing as little as 150 mg could be determined reproducibly to within three parts per thousand. The measured densities of pure Bi_2Te_3 and Sb_2Te_3 lie within 0·4 per cent of the values calculated from the formula weights and unit cells. The variation of density with In concentration is shown in Figs. 5 and 6 for the Sb_2Te_3 and Bi_2Te_3 solutions, respectively. It is seen that the diminution in density is much more pronounced for the fast-grown $(Bi_2Te_3)_{1-x}(In_2Te_3)_x$ samples than for the slow-grown samples.

On the assumption that the solid solutions are structurally perfect and result from the random substitution of In for Sb in Sb_2Te_3 and for Bi in Bi_2Te_3, theoretical densities were calculated from the spectrochemically determined values of the indium content and the unit cell volumes in Figs. 2 and 3. The theoretical values are shown by the dashed curves in Figs. 5 and 6.

The deviations of the experimental densities from the theoretical curve are negative in the Sb_2Te_3–In_2Te_3 system and always less than 1·1 per cent. The deviations from the theoretical curve are positive in the slow-grown Bi_2Te_3–

In_2Te_3 solutions and always less than 0·6 per cent. On the other hand, negative deviations as large as 2·5 per cent are observed in the fast-grown Bi_2Te_3–In_2Te_3 alloys.

It is believed that the difference between the properties of the fast-grown and the slow-grown crystals merely reflects an accident of crystal growth whereby microscopic voids are incorporated into otherwise perfect fast-grown crystals. The presence of such voids accounts in principle not only for the differences in density, but also for the differences in lattice parameters, X-ray diffraction intensities, and electrical behavior.

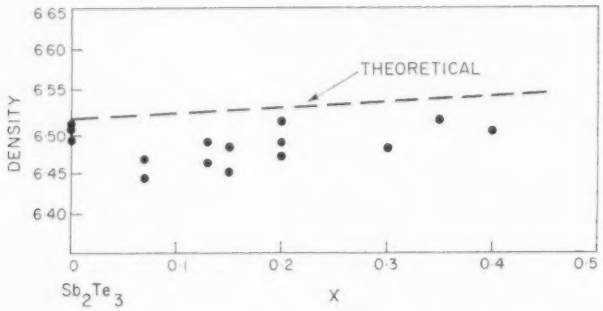

FIG. 5. Densities of Sb_2Te_3–In_2Te_3 solid solutions.

Thus the presence of small voids in layers which comprise a Bi_2Te_3 crystal (see Discussion) would enable the surrounding lattice to contract slightly in a direction normal to the *c*-axis and therefore would lessen the average *a*-spacing and increase the *c*-spacing, as observed (Fig. 3). The voids would also act as points at which crystal cleavage may be easily initiated, consistent with the anomalous variation of the diffraction intensities for fast-grown crystals. The only effect of fast growth upon the electrical properties of the solid solutions (see below) appears to be a small diminution of the carrier mobility. This is qualitatively consistent with the presence of voids, as contrasted with atomic vacancies which would be expected to have a much larger effect upon the mobility and would also affect the Hall coefficient.

The formation of such voids might be connected with the fact that the distribution coefficient of In in the Bi_2Te_3–In_2Te_3 system is much less than unity, so that large quantities of In are continuously rejected at the solid–liquid interface of a crystallizing ingot. Since the diffusion coefficients in the liquid are small, equilibrium growth conditions cannot be maintained for crystals grown at excessive rates. It would not be surprising if such crystals were structurally imperfect, while crystals grown more slowly were more nearly perfect. Although further experimental work would be required definitely to establish the existence and origin of voids, it should be noted that none of the effects which we have attributed to voids are observed for fast-grown alloys in the Sb_2Te_3–In_2Te_3 system, where the distribution coefficient of In is close to unity.

Electrical properties. The most striking electrical characteristic of the Sb_2Te_3–In_2Te_3 and Bi_2Te_3–In_2Te_3 solid solutions is the virtual independence of the Hall coefficient (i.e the free charge carrier concentration) with respect to the indium concentration.

In Table 1, the Seebeck coefficient (α), resistivity (ρ), Hall coefficient (R_H) at 8,000 G, apparent carrier concentration ($n_p = 1/eR_H$), and Hall mobility ($\mu_H = R_H/\rho$) are shown for various samples of the composition $(Sb_2Te_3)_{1-x}(In_2Te_3)_x$. All samples were *p*-type at room temperature where the measurements were made. The specimens employed were monocrystalline or oligocrystalline, and were aligned in the Hall measurements with the magnetic field normal to the cleavage plane.

With increasing In concentration there is a marked increase in the Seebeck coefficient and a still sharper rise in the resistivity. Because of experimental difficulties with samples which simultaneously exhibit high α and high ρ, measurements of

the Hall coefficient were not successful beyond $x = 0{\cdot}20$. Up to this point, however, it is seen that the increasing resistivity is due primarily to a decline in carrier mobility, since the carrier concentration remains between 4×10^{19} and 1×10^{20} cm^{-3}.

$(Bi_2Te_3)_{1-x}(In_2Te_3)_x$ system, but the point of inversion appears closer to the first-to-freeze end as x increases. At x(melt) = 0·35, the entire ingot is n-type. We attribute this result to a progressive displacement of the maximum in the solidus to the Te-rich side of the phase diagram.

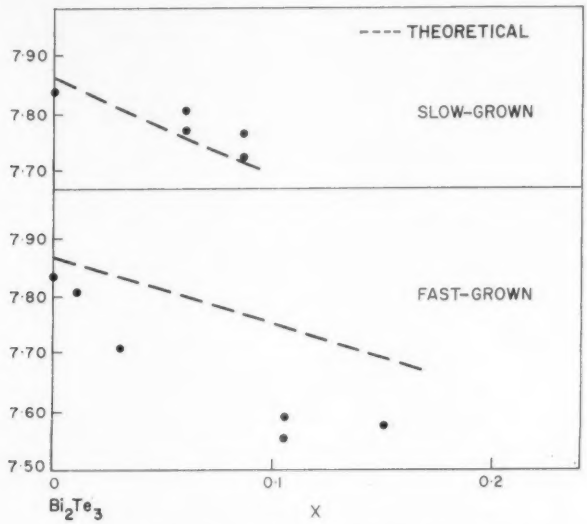

Fig. 6. Densities of Bi_2Te_3–In_2Te_3 solid solutions.

Ingots of Bi_2Te_3 grown from stoichiometric melts by directional freezing in a vertical tube exhibit p-type conductivity over most of their length, but become n-type near the end which is last to freeze. This behavior is observed because the maximum of the solidus in the Bi–Te binary section lies on the Bi-rich side of the stoichiometric composition, Bi_2Te_3.[7] A similar inversion is observed in ingots grown from melts in the

Again the striking characteristic of the $(Bi_2Te_3)_{1-x}(In_2Te_3)_x$ system is that the Hall coefficient remains near 1 cm^3/C regardless of In concentration. The properties of both p-type and n-type samples with x as high as 0·10 are compared with the properties of pure p-type and n-type Bi_2Te_3 in Table 2.

In contrast with the Sb_2Te_3–In_2Te_3 system, the mobility of the charge carriers generally does not

Table 1. *Electrical properties of solid solutions of composition* $(Sb_2Te_3)_{1-x}(In_2Te_3)_x$

x	α (μV/deg)	$\rho\times10^3$ (ohm-cm)	R_H (cm^3/C)	μ_H (cm^2/V-sec)	$n_p\times10^{-19}$ (cm^{-3})
0	+70	0·37	+0·089	250	7·2
0·07	+106	1·04	+0·064	63	9·7
0·14	+127	2·3	+0·118	28	5·3
0·20	+217	10·8	+0·149	14	4·2
0·35	+280	25·0	—	—	—

Table 2. Electrical properties of solid solutions of composition $(Bi_2Te_3)_{1-x}(In_2Te_3)_x$

x	α (μV/deg)	$\rho \times 10^3$ (ohm-cm)	R_H (cm^3/C)	μ_H (cm^2/V-sec)	$n_p \times 10^{-19}$ (cm^{-3})
p-Type					
(a) 0	+185	1·9 (0·22)	+0·46 (0·31)	240 (1410)	1·36 (2·0)
(b) 0·034	+180	6·7 (1·31)	+0·67 (1·7)	100 (1290)	0·93 (0·37)
(c) 0·061	+235	3·6 (0·48)	+0·84 (0·80)	230 (1670)	0·75 (0·78)
n-Type					
0*	−300	1·9	−0·55	290	1·1
(d) 0·10	−55	3·0 (4·7)	−0·87 (1·21)	290 (260)	0·72 (0·52)

Values outside parentheses refer to 300°K; values inside parentheses refer to 78°K. The values of x were determined by spectrochemical analysis. Sample (c) was grown at 0·2 mm/hr, while the remaining samples were grown at 3 mm/hr.

* MANSFIELD R. and WILLIAMS W., *Proc. Phys. Soc. Lond.* **72**, 733 (1958).

depend sensitively upon the In concentration. The data also indicate that the mobility is lower in fast-grown than in slow-grown crystals (compare samples (b) and (c) in Table 2). It will be noted, furthermore, that the change in Hall coefficient as the temperature is decreased is anomalous for the fast-grown crystals.

Magnetic properties. The magnetic susceptibilities of representative samples were measured at 300°K and 78°K. All samples, regardless of In concentration, were found to be diamagnetic or weakly paramagnetic with susceptibility less than 10^{-6} cm^{-3}.

DISCUSSION

In_2Te_3 crystallizes in a defect zinc blende lattice ($a_0 = 6{\cdot}15$ Å) in which 1/3 of the sites in the indium sublattice are vacant.[8] The atomic coordination is tetrahedral as in all zinc blende structures, and the structure derives its stability from the overlap of sp^3 hybrid atomic orbitals between In and Te atoms separated by 2·66 Å. Bi_2Te_3 and Sb_2Te_3 are, on the other hand, octahedrally coordinated compounds with much larger bond lengths in the totally unrelated crystal structure described above. In view of these fundamental differences, the great solubility of In_2Te_3 in Bi_2Te_3 and Sb_2Te_3 could hardly be anticipated. According to the simplest model for the solid solutions, In is substituted for Bi (or Sb) in the cation lattice of Bi_2Te_3 (or Sb_2Te_3), while the Te sublattice remains unchanged. An immediate difficulty with this model is the fact that each substitution of an In atom for a Bi (or Sb) atom deletes two electrons from the lattice. From the conventional point of view these electrons would be removed from the valence band, and the free hole concentration would rise accordingly. This, however, is contrary to experiment. Therefore, we shall consider the possibility of other models for the solid solutions.

It is conceivable, for instance, that In_2Te_3 retains its molecular integrity when it is dissolved in Sb_2Te_3 or Bi_2Te_3. Thus it could form either (A) multi-layer or (B) monolayer deposits between the layers of the host compound or (C) could arrange itself in some interstitial manner. In view of the large solubility of In_2Te_3 in the host compounds, one would expect the appearance of characteristic In_2Te_3 spacings in the X-ray patterns for case (A), a complete transformation of the X-ray patterns for case (B), and an enormous increase of density for case (C). Since none of these results is observed, it is evident that In_2Te_3 loses its identity in the host structure.

It seems certain, therefore, that the mechanism by which In enters the Bi_2Te_3 (or Sb_2Te_3) lattice is substitutional. Either In replaces Bi (or Sb) directly or In replaces Te and the same number of Te atoms enter Bi (or Sb) sites. Both models are consistent with the formation of a single, essentially undistorted phase of the Bi_2Te_3 structure type whose density agrees with the value calculated

from the stoichiometric formula $Bi_{2(1-x)}In_{2x}Te_3$ or $Sb_{2(1-x)}In_{2x}Te_3$ and the measured volume of the unit cell. In either case, however, it is still necessary to explain how the substitutions can have so little effect on the charge carrier concentrations.

It is possible, in principle, for the substitutions to be compensated by the introduction of donor defects during crystal growth. Such compensation can be excluded, however, by the following arguments. The only plausible donor defects are Te atoms on Bi (or Sb) sites, Te vacancies, and Bi (or Sb) interstitials. Vacancies or interstitials would cause a very large decrease or increase, respectively, in the crystal density, contrary to the experimental results for Sb_2Te_3–In_2Te_3 and slow-grown Bi_2Te_3–In_2Te_3 samples. They would also require a large excess of Te to accumulate during directional freezing and precipitate in the last-to-freeze section. Yet careful X-ray diffraction analysis of entire ingots which were directionally frozen from melts of the compositions $Bi_{1.8}In_{0.2}Te_3$ and $Sb_{1.2}In_{0.8}Te_3$ revealed only the hexagonal phases associated with the Bi_2Te_3 and Sb_2Te_3 lattices. This result also excludes the possibility that In replaces Bi (or Sb) and is electrically compensated by the simultaneous replacement of other Bi (or Sb) atoms by Te atoms. In this case an excess of Bi (or Sb) would have to precipitate in the last-to-freeze section.

Since the mechanism of solid solution is evidently limited either to the simple replacement of Bi (or Sb) by In or to the simultaneous replacement of Te by In and Bi (or Sb) by Te, the electrically neutral character of such replacements must be examined in terms of the fundamental properties of impurity states in compounds with Bi_2Te_3–Sb_2Te_3 structure.

According to the conventional theory of impurity states, the introduction of each indium atom should split off a doubly degenerate electron orbital from the valence band to a discrete energy level above the valence band. Therefore, even though the number of electrons in the valence band is decreased, the hole concentration could be kept constant by a compensating reduction in the number of states in the valence band—provided that the split-off states have sufficiently high ionization energy to remain unoccupied at ordinary temperatures. In the samples with highest In concentration, the split-off states (i.e. the bonding orbitals of the In atom) would comprise approximately 30 per cent of the bonding orbitals in the crystal. If they remained unoccupied, the cohesive energy would be sharply reduced, and the lattice would relax. The structural data indicate, however, that the average bond lengths are actually diminished by the substitution of In. Therefore, it is clear that the unoccupied acceptor states must originate elsewhere than from the valence band and, furthermore, that the formation of these states is associated with stronger overlap of the bonding orbitals.

Several models have been proposed for the chemical bonding in Bi_2Te_3.[9–11] Each assumes that the valence band originates in the bonding molecular orbitals, but different sets of octahedral hybrid atomic orbitals are assumed to participate in the formation of the molecular orbitals. A common feature of these models is that some or all of the atoms retain atomic-like *s*-states in their valence shells. These lie below the valence band of the crystal, and always remain filled. The electrons in these localized states contribute virtually nothing to either the chemical bonding or the electrical conductivity. The existence of such non-bonding "lone pairs" of *s*-electrons has a theoretical precedent in band structure calculations on the octahedrally coordinated semiconductor PbS, which showed that the filled *s*-orbital remains non-bonding and does not participate in the formation of the valence band.[12] There is, furthermore, considerable chemical evidence for the stability of non-bonding *s*-orbitals.[2a]

An important property associated with non-bonding *s*-orbitals is that the filled *s*-orbital on one atom repels the filled *s*-orbital on an adjacent atom and limits the approach of the two.

Consider now a purely formal model in which the six *p*-states of the In atom are equally divided between the valence band (bonding orbitals) and the conduction band (antibonding orbitals), but the two *s*-states (one orbital) are raised to an energy level well above the valence band. The three electrons of the indium atom will fill the lowest available states, i.e. the three bonding states in the valence band. Since the valence band remains filled, there is no increase in hole concentration. Since no electrons remain in the high-lying *s*-orbital, the electrostatic repulsion between adjacent atoms is reduced, and the lattice contracts

Vol. 19
1961

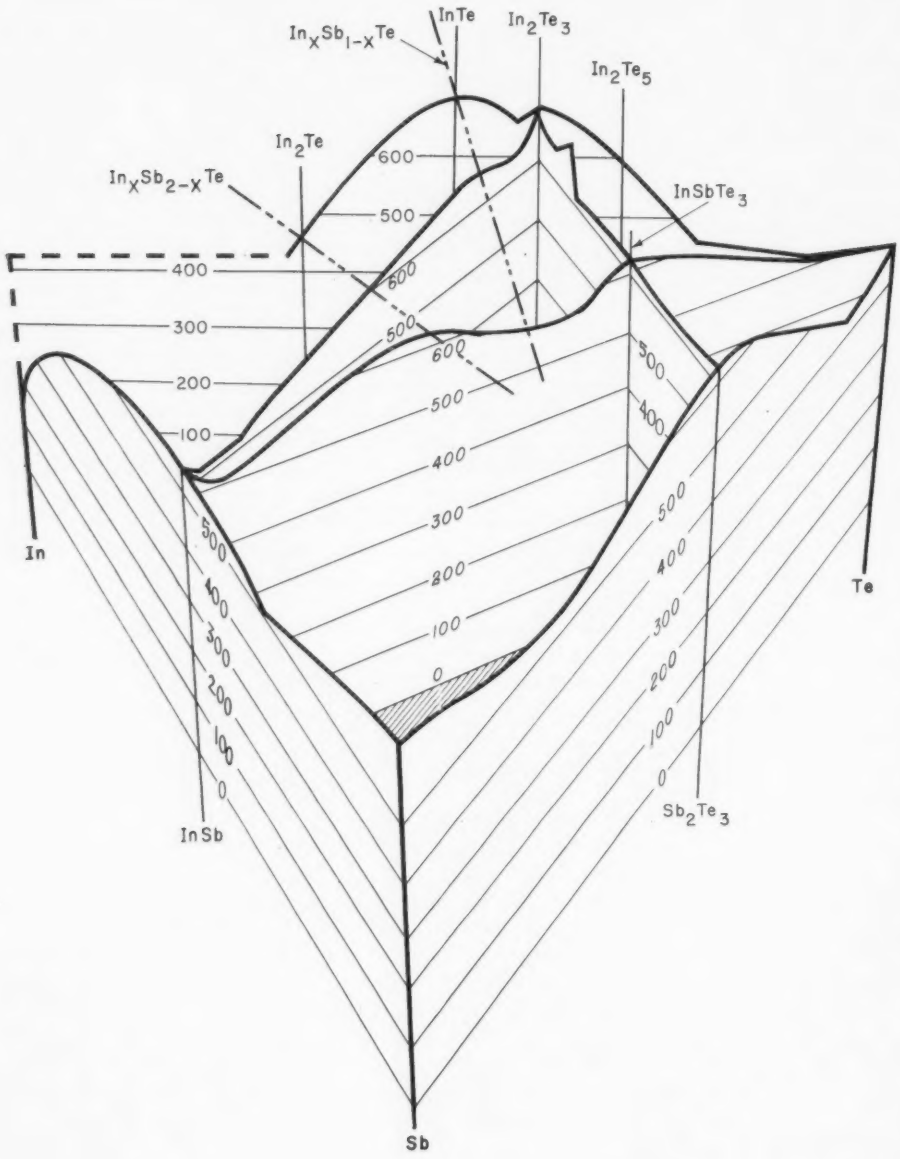

FIG. 7. Liquidus of the In–Sb–Te ternary system. The In–Te binary section is from KLEMM W. and VON VOGEL H. U., *Z. anorg. Chem.* **219,** 45 (1934). The Sb–Te section is from HANSEN M., *Constitution of Binary Alloys*, 2nd Ed., p. 1178. McGraw Hill, N.Y. (1958). The In–Sb section is from LIU T. S. and PERETTI E. A., *Trans. Amer. Soc. Metals* **44,** 539 (1952).

Vol. 1
1961

in order to take advantage of a greater overlap in the bonding orbitals.

This simple model obviously suffers from the theoretically untenable assumption that the *s*-states of an indium atom can cross over the valence band without mixing. This difficulty may be removed, however, by assuming that the two *s*- and six *p*-states of the In atom do mix, but that, under the influence of the octahedral crystal symmetry and the release of energy which accompanies lattice contraction, three largely *p*-like bonding states enter the valence band and the remaining five states are split off into the conduction band. Since the properties of *n*-type In-substituted Bi_2Te_3 do not differ greatly from those of pure *n*-type Bi_2Te_3, it must be assumed that the energy distribution of the conduction band states is such that the properties near the bottom of the band are essentially unchanged. (The *n*-type solid solutions presumably result, as in pure Bi_2Te_3,[13] from a slight excess of Te on Bi sites.)

The revised model is fundamentally acceptable and can account in principle for the salient physical characteristics of the solid solutions. Not only do the unchanging Hall coefficient and the lattice contraction find a natural explanation, but the model is not inconsistent with the weak magnetic susceptibility or the differences of charge carrier mobility in the Bi_2Te_3 and Sb_2Te_3 solutions. Thus the greater electronegativity of Sb relative to Bi will be transmitted to the Te atoms surrounding an In atom and will be reflected in a stronger polarization of the In–Te bond; it is to be expected, therefore, that the mobility will be reduced more strongly in the Sb_2Te_3 solutions.

The model is, of course, entirely formal and cannot be placed in a quantitative framework without much additional experimental and theoretical work. In its qualitative form it can be reconciled with each of the equally qualitative bonding schemes for Bi_2Te_3, but, by the same token, it does not permit a distinction between them. It is, furthermore, equally applicable whether In replaces Bi (or Sb) or In replaces Te with Te simultaneously replacing Bi (or Sb). Finally, it implies a fundamental difference between impurity states in octahedrally coordinated compounds containing non-bonding *s*-electrons and impurity states in tetrahedrally coordinated semiconductors.

APPENDIX: LIQUIDUS OF THE In–Sb–Te TERNARY SYSTEM

The liquidus curves of the sections (InSb)–Te and $(InSb)_x$–(In_2Te_3) have been determined by thermal analysis. The results are summarized in Fig. 7, which also shows the results on the Sb_2Te_3–In_2Te_3 section, described earlier, and the published binary sections.

A maximum in the over-all liquidus occurs near the composition InSbTe. This, together with other features of the liquidus, suggested that solid solutions might occur in the $In_{(12-x)}Sb_{2x}Te$ section. X-ray diffraction analysis revealed, however, that a sample quenched from a melt of the composition InSbTe consisted solely of InTe and elemental Sb. The absence of In or InSb makes it clear that Sb cannot be substituted for In in the In_2Te structure.

It was anticipated that a compound of the formula $InSbTe_2$ might be formed. This compound, which, like $AgSbTe_2$,[14] may be viewed as a derivative of SnTe, would be expected to have the rock-salt structure. Samples quenched from melts of this composition were multiphase, however, and there was no convincing X-ray evidence for the formation of a new cubic phase.

Acknowledgements—The authors are indebted to Mr. A. A. MENNA for his skilled assistance in various phases of the experimental work, to Messrs. E. P. WAREKOIS and J. W. SANCHEZ for their assistance in measuring and analyzing the X-ray diffraction patterns, and to Dr. J. B. GOODENOUGH for many stimulating discussions.

REFERENCES

1. See SLATER J. C., *J. Phys. Chem. Solids* **8,** 21 (1959).
2. For representative discussions of various aspects of this approach, see:
   (a) BURSTEIN E. and EGLI P. H., *Advanc. Electronics and Electron Phys.* **7,** 1 (1955).
   (b) GOODMAN C. H. L., *J. Phys. Chem. Solids* **6,** 305 (1958).
   (c) MOOSER E. and PEARSON W. B., *J. Electronics* **1,** 629 (1956).
   (d) FOLBERTH O. G. and WELKER H., *J. Phys. Chem. Solids* **8,** 14 (1959).
3. A preliminary acount of this work appeared in *Bull. Amer. Phys. Soc.* (ser. 2) **5,** 78 (1960).
4. DONGES E., *Z. anorg. Chem.* **265,** 56 (1951).
5. FRANCOMBE M. H., *Brit. J. Appl. Phys.* **9,** 415 (1958).
6. LANGE P. W., *Naturwissenschaften* **27,** 133 (1939); FRONDEL C., *Amer. Min.* **24,** 12 (1939).
7. SATTERTHWAITE C. B. and URE R. W., Jr., *Phys. Rev.* **108,** 1164 (1957).
8. HAHN H. and KLINGER W., *Z. anorg. Chem.* **260,** 97 (1949); WOOLLEY J. C., PAMPLIN B. R. and HOLMES P. J., *J. Less Common Metals* **1,** 362 (1959).
9. LEGRENAUDIE J., *J. Phys. Radium* **18,** 39A (1957).
10. DRABBLE J. R. and GOODMAN C. H. L., *J. Phys. Chem. Solids* **5,** 142 (1958).

11. Mooser E. and Pearson W. B., *J. Phys. Chem. Solids* **7**, 65 (1958).
12. Bell D. G., Hum D. M., Pincherle L., Sciama D. W. and Woodward P. M., *Proc. Roy. Soc.* **A217**, 71 (1953).
13. Harman T. C., Paris B., Miller S. E. and Goering H. L., *J. Phys. Chem. Solids* **2**, 181 (1957).
14. Wernick J. H., Geller S. and Benson K. E., *J. Phys. Chem. Solids* **4**, 154 (1958); **7**, 240 (1958).

Vol. 1
196

J. Phys. Chem. Solids Pergamon Press 1961. Vol. 19, Nos. 1/2, pp. 117–123. Printed in Great Britain.

A NEUTRON DIFFRACTION STUDY OF THE TEMPERATURE VARIATION OF THE SPONTANEOUS SUBLATTICE MAGNETIZATION OF FERRITES AND THE NÉEL THEORY OF FERRIMAGNETISM*†

T. RISTE‡ and L. TENZER§

Brookhaven National Laboratory, Upton, New York

(*Received* 27 *June* 1960)

Abstract—The neutron diffraction technique is used to study the temperature variation of the sublattice magnetizations of five different ferrites. Qualitative agreement with the Néel theory is obtained in all cases in the respect that the magnetization curve of the tetrahedral ions is more convex than the one due to octahedral ions. The data on magnetite are used in a quantitative analysis in terms of molecular field coefficients. It is shown that coefficients determined from conventional magnetic data do not reproduce the sublattice magnetization. This inconsistency is interpreted as an inability of the molecular field equations to take proper account of the magnetic interactions.

ol. 19
1961

1. INTRODUCTION

ACCORDING to the NÉEL theory of ferrimagnetism[1] a ferrite is a substance consisting of two non-identical magnetic substructures with negative interactions between substructures. The substructures, or sublattices as we shall call them, are constituted by the ions on tetrahedral (A) and octahedral (B) sites respectively. There are twice as many B sites as A sites, from which follows that the average net magnetic moment (M) per ion is $M = 2/3M_B - 1/3M_A$, since the AB interaction is negative. The existence of the two sublattices and their negative interaction have been conclusively proven by several types of experiments. For an excellent review of the Néel theory and the experimental verification we refer to an article by SMART[2].

It seems, however, that the possibilities offered by neutron diffraction in this connection have not been exhausted. This method has two obvious advantages. Firstly the spontaneous magnetization, i.e. the intrinsic magnetization of a domain, may be observed without saturating the crystal by applying an external field. Secondly, the sublattice magnetizations may be observed separately by looking at the reflections from certain crystallographic planes. This has been demonstrated experimentally by PICKART and NATHANS[3]. Such experiments may in the first instance give a qualitative verification of the Néel theory and may be performed without too strict requirements as to the quality of the samples. Accurate experiments on samples of high quality may further be used in a quantitative comparison with calculations based on the Néel theory.

Before going over to the experiments and their interpretation, we shall review very briefly some of the results of the Néel theory of ferrimagnetism and the theory of neutron scattering by ferrites.

2. THE NÉEL THEORY OF FERRIMAGNETISM

The Néel theory of ferrimagnetism is based on the molecular field theory. In the language of this

* Work performed under the auspices of the U.S. Atomic Energy Commission.

† Part of this work has been reported earlier, *Bull. Amer. Phys. Soc.* **2**, 127 (1957).

‡ On leave from Institutt for Atomenergi, Kjeller, Norway; now returned.

§ Deceased.

theory an ion in, say the A sublattice, is subject to molecular fields from:

(a) The B ion, characterized by the molecular field coefficient n_0. (i.e. the molecular field equals $n_0 M_B$).

(b) The other A ions, molecular field coefficient $n_0\alpha$.

Similarly an ion in the B sublattice is obviously subject to the same AB interaction characterized by n_0 and also to a BB interaction characterized by $n_0\beta$. NEEL[4] has further assumed a temperature variation of the molecular field coefficients given by

$$n = n_0(1+\gamma T). \tag{1}$$

γ is the same as the temperature coefficient of the volume expansion.

It is well known from the case of a ferromagnet that the spontaneous magnetization of a domain has its maximum value at absolute zero temperature, at which all the moments are parallel. With increasing temperature the thermal agitation makes the magnetization decrease in a way following approximately a Brillouin function. In a ferrimagnet there will correspondingly be functions which describe the temperature variation of the sublattice magnetizations. The latter functions are calculated by writing the set of linear equations resulting from the molecular fields mentioned above, and combining them with a Brillouin type equation of state. The molecular field equations are

$$H_A = (\alpha \sum M_A + \sum M_B)n, \tag{2a}$$

$$H_B = (\sum M_B + \beta \sum M_B)n, \tag{2b}$$

where H_A and H_B are the molecular fields acting on an ion in the A and the B sublattice respectively. The sums are to be taken over the number of interacting neighbours. When combined with the equation of state, the result is a pair of transcendental equations

$$M_A = M_A^0 B_{S_A}[M_A^0 H_A/(kT)] = M_A^0 B_{S_A}[u], \tag{3a}$$

$$M_B = M_B^0 B_{S_B}[M_B^0 H_B/(kT)] = M_B^0 B_{S_B}[v], \tag{3b}$$

M^0 denotes an ionic moment at absolute zero temperature and B_S the Brillouin function for spin value S. The usual way of deriving molecular field coefficients is now to match these functions to experimental curves of the temperature variation of the saturation magnetization. In doing this one must make use of an equation mentioned in the introduction:

$$M = \tfrac{2}{3} M_B - \tfrac{1}{3} M_A \tag{4}$$

By also including an external field in the molecular field equations (2) one may arrive at an expression for the paramagnetic susceptibility in terms of the molecular field coefficients. This obviously gives an alternative method for assigning numerical values to the molecular field coefficients.

SMART[2] has pointed out that the determination of the molecular field coefficients is complicated by several factors, such as: the presence of two or more kinds of magnetic ions, different magnetic properties on A and B sites for a given ion, change of ionic distribution with temperature, variations of coefficients with lattice parameters, and a number of others. Because of this the empirically determined values should be regarded with skepticism.

Even though the physical significance of such molecular field coefficients may be questioned, it may be of interest to see if the values determined by independent methods are internally consistent. PAUTHENET[5] has shown that molecular field constants determined from paramagnetic susceptibility data by FALLOT and MARONI[6] do account for the temperature variation of the saturation magnetization within 5 per cent. As a further step in investigating the consistency, we may ask if the same empirical coefficients can also account for the neutron diffraction data on sublattice magnetizations. This will be tried below in the case of magnetite.

3. NEUTRON SCATTERING BY FERRITES

In the present case we are interested in the neutrons scattered magnetically from the ions in an inverted spinel lattice. The predominant component of interest in the diffraction pattern is then constituted by the magnetic Bragg reflections. The intensity of such a reflection is given by the square of its structure factor. The structure factors of the (220), (222) and (111) reflections

then have the following forms:

$$F(220) = P_A f(220) = CM_A^0 B_{S_A}[u] f(220), \quad (5a)$$

$$F(222) = P_B f(222) = CM_B^0 B_{S_B}[v] f(222), \quad (5b)$$

$$F(111) = (P_A - 2\sqrt{P_B}) f(111). \quad (5c)$$

P denotes the amplitude for magnetic scattering in the forward direction by an isolated ion, C is a constant, and $f(hkl)$ the magnetic form factor of the reflection (hkl). In the temperature factors the Debye–Waller factor has been left out. This is, however, dealt with in Section (4c) below.

From equations (5) it is seen that the temperature variations of the (220) and (222) reflections give directly the temperature variations of the spontaneous magnetization of the A and B sublattices respectively. On the other hand, both the A and the B ions contribute to the intensity of the (111) reflection. The temperature variation of the (111) reflection has been reported earlier by McReynolds and Riste[7].

Apart from the magnetic Bragg reflections there are also weak diffuse components of magnetic origin. It has been shown elsewhere,[8] however, that these are much weaker than the Bragg reflections. At T_c, where they reach their maximum value, they still have less than one per cent of the intensity of a Bragg reflection at room temperature.

4. EXPERIMENTS

(a) *Samples*

The experiments were carried out on a natural geological specimen of magnetite (Fe_3O_4) and on some laboratory grown ferrite crystals. All of them were single crystals. A spectrographic analysis of the magnetite crystal showed that it contained less than 1 per cent of metal impurities. The laboratory grown crystals were supplied by courtesy of the Linde Air Products Company. Chemical analysis of the latter crystals showed that they were rather far from being stoichiometric, and they are consequently used only in a qualitative test of the Néel theory.

Table 1

Name of sample	Possible formula
Ni-ferrite	$(NiO)_{0.75}(FeO)_{0.25}Fe_2O_3$
(Ni+Zn)-ferrite	$(NiO)_{0.82}(FeO)_{0.15}(ZnO)_{0.03}Fe_2O_3$
Co-ferrite	$(CoO)_{0.25}(FeO)_{0.75}Fe_2O_3$
(Co+Zn)-ferrite	$(CoO)_{0.32}(FeO)_{0.48}(ZnO)_{0.20}Fe_2O_3$

The table above gives the result of the analyses in terms of approximate chemical formulae.

The crystals were all cut in the form of slabs 1 mm thick such that the (111) reflection could be measured in transmission. The $[1\bar{1}0]$ axis was mounted vertically.

(b) *Experimental arrangement*

The crystals were mounted in a quartz oven with electrical heating. The temperature could be set at any value from room temperature to about 800°C with a maximum uncertainty of 2° at the highest temperatures. In some cases the crystal was mounted in a miniature quartz oven between the poles of an electromagnet. In the latter arrangement the temperature uncertainty was as big as 4°. The wavelength of incident neutrons was 1·05 Å, and second order reflection from the monochromator was effectively removed by using a plutonium filter.

(c) *Treatment of experimental data*

We are in this connection interested in the intensity of magnetically scattered neutrons, and the intensity of the nuclear component has to be subtracted. This was done by an extrapolation to lower temperatures of the intensity above the Néel temperature. In the extrapolation process a Debye–Waller factor had to be invoked. A common Debye temperature of 470°C, which is derived from the specific heat data of magnetite, was used for all the ferrites. Measurements on the nuclear (113) reflection showed that the temperature variation was reasonably well accounted for by the Debye temperature chosen.

The magnetic intensity component obtained by this procedure must also be corrected for the temperature motion of the nuclei. In the absence of a better procedure we applied the same Debye–Waller correction. The resulting intensity, or more correctly its square root, is to be compared with formula (5).

In the abovementioned correction we have, however, neglected the influence of extinction. The effect of extinction is to flatten the curve at

lower temperatures. The extinction correction requires a knowledge of the mosaic spread. Rocking curves were taken for the different ferrites under investigation and yielded a common mosaic spread of 4–5 minutes of arc. A check on this value for the mosaic spread in magnetite was obtained by measuring the intensity ratio I_{220}/I_{440}

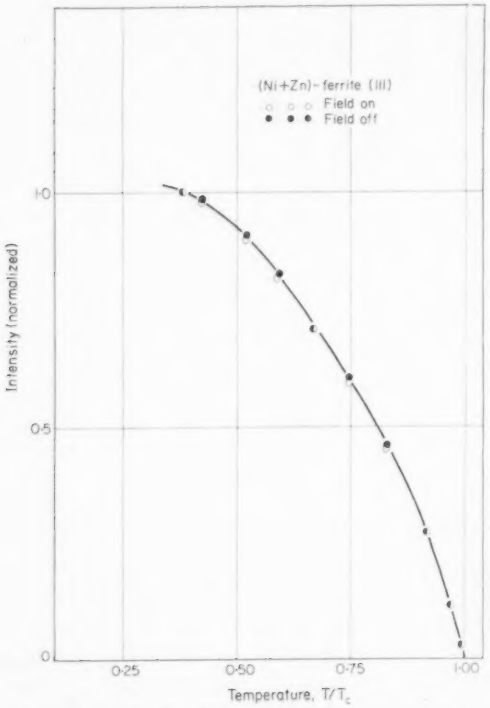

FIG. 1. Comparison between diffracted neutron intensities from unmagnetized and magnetized crystals. Magnetic field was applied normal to scattering vector, i.e. along a direction in reflecting plane. Intensities have been normalized to same value at room temperature.

for slabs of various thicknesses, ranging from 0·3 to 4 mm, and using the extinction formula given by BACON and LOWDE[9]. In the correction of the intensity vs. temperature curves we applied the extinction formula given by HAMILTON[10] which takes better account of the actual size of the crystal. It was found that the most reliable data were obtained by measuring the (111) and (222) reflections, which both diffracted in transmission, and deducing the (220) data from them. This method of deducing the (220) data was applied only in the case of magnetite. The maximum extinction corrections applied were 7 per cent on the (111) and 4 per cent on the (222) reflection.

(d) *Experimental results*

In Fig. 1 the intensity of the (111) reflection of (Ni+Zn)-ferrite is shown as a function of temperature. Two sets of values have been recorded at each temperature and both have been normalized relative to the values at room temperature. One value is measured with no field applied to the crystal, the other is observed when the crystal is

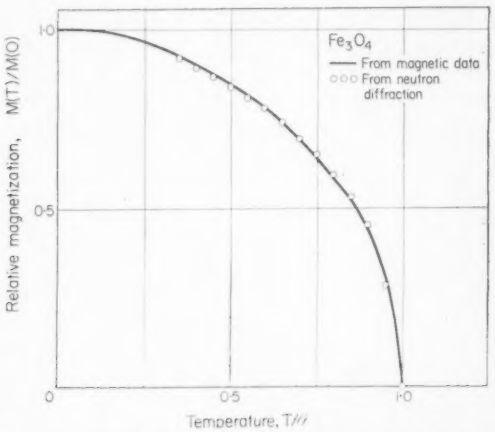

FIG. 2. Comparison between temperature variations of relative magnetization derived in two different ways. Curve is from magnetic data by PAUTHENET (Ref. 5), points from neutron diffraction data.

magnetized to saturation in the vertical direction, i.e. normal to the scattering vector. The close agreement between the two sets of values shows that the spontaneous magnetization and the saturation magnetization are equal, in other words that a field giving technical saturation does not affect the intrinsic magnetization of a domain.

In Fig. 2 the experimental data on the sublattice magnetizations of magnetite obtained from the (111) and (222) reflections have been used in synthetizing the magnetization curve by means of formula (4). The curve represents the magnetization data of PAUTHENET[5], and our experimental values have been normalized to fit the curve at room temperature. The agreement is sufficiently

Vol. 1
196

good to justify a comparison between our experimentally observed sublattice magnetizations and theoretical curves calculated by means of PAUTHENET'S molecular field coefficients.

Before proceeding to this quantitative analysis we shall give a qualitative verification of the Néel theory.

The spinel structure of ferrites is such that an A atom is surrounded by 12 B atoms and 4 A atoms, a B atom is, on the other hand, surrounded by 6 A atoms and 6 B atoms. If we make the customary assumptions that all interactions are negative, further that the AB interaction is the dominating one and the BB interaction by far the weakest one, then it follows that an A atom is subject to the strongest molecular field. It is therefore to be expected that it will be harder to disrupt the alignment of the moments on the A sites and consequently the (222) curve should lie below the (220) curve. This is indeed found to be the case, as seen from Figs. 3(a), (b), (c) and (d). The square root of the intensity has been plotted because this quantity corresponds to the sublattice magnetization.

The values of the temperature variation of the sublattice magnetizations $B_{S_A}[u]$ and $B_{S_B}[v]$ for magnetite, as deduced from the neutron diffraction data, are given in Table 2. The temperature is also given as a fraction of the paramagnetic Curie temperature θ in order to be able to compare with calculations based on PAUTHENET'S values of the molecular field coefficients. According to his paper $\theta = 869°K$. Our experimental data have been arbitrarily normalized to the theoretical values at room temperature. The table also lists two sets of Brillouin functions. In Fig. 4 we have plotted experimental and theoretical values of $B_{S_A}(u)$ and $B_{S_B}(v)$.

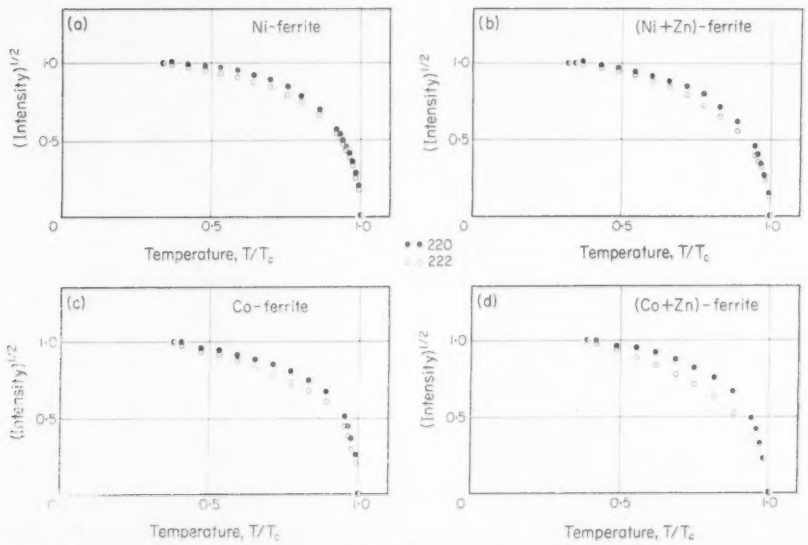

FIG. 3. Neutron diffraction data giving temperature variation of sublattice magnetizations. (220) reflection gives magnetization of ions on tetrahedral (A) sites, (222) the same for octahedral (B) sites.

5. DISCUSSION

The curves of Fig. 3 are consistent with the qualitative predictions of the molecular field theory: the sublattice, the ions of which are exposed to the strongest molecular field, will at any temperature below the Curie point have the highest degree of magnetic order. This general conclusion does not prove the correctness of the linear equations (2a) and (2b), however. Other neutron

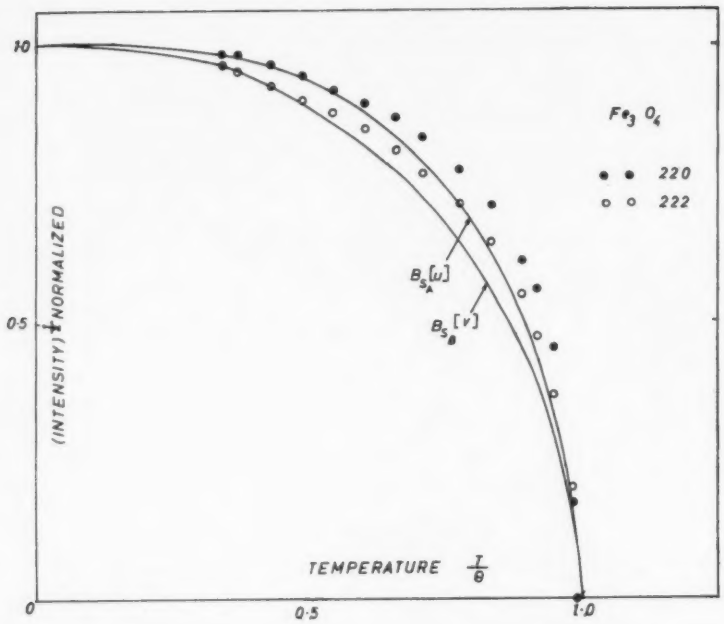

FIG. 4. Comparison between experimental and theoretical values of sublattice magnetizations of magnetite. Curves have been calculated from molecular field theory using parameters consistent with magnetic data, points represent neutron diffraction data. Filled and open circles should be compared with upper and lower curve respectively.

Vol. 19
1961

Table 2. Temperature variation of sublattice magnetizations of magnetite. Observed values are obtained from neutron diffraction data, theoretical values are calculated using parameters derived from magnetic data.

T(°K)	T/θ	$B_{S_A}[u]_{obs}$	$B_{S_B}[v]_{obs}$	$B_{S_A}[u]_{calc}$	$B_{S_B}[v]_{calc}$	$B_{1/2}$	$B_{3/2}$
298	0·341	0·982	0·962	0·982	0·962	0·995	0·975
323	0·373	0·979	0·948	0·974	0·950	0·990	0·967
373	0·431	0·962	0·923	0·957	0·922	0·977	0·949
423	0·489	0·942	0·898	0·939	0·890	0·960	0·920
473	0·547	0·912	0·875	0·912	0·853	0·935	0·891
523	0·605	0·893	0·845	0·880	0·812	0·901	0·850
573	0·662	0·868	0·806	0·838	0·772	0·856	0·805
623	0·720	0·830	0·763	0·782	0·716	0·800	0·750
673	0·778	0·772	0·711	0·713	0·646	0·728	0·675
723	0·836	0·709	0·640	0·630	0·564	0·645	0·585
773	0·894	0·608	0·547	0·525	0·464	0·524	0·480
798	0·923	0·555	0·471	0·453	0·400	0·440	0·413
823	0·951	0·453	0·367	0·360	0·316	0·335	0·310
848	0·979	0·172	0·204	0·235	0·205	0·140	0·125
858	0·990	0	0	0·160	0·160	0	0
869	1·000	0	0	0	0	0	0

diffraction data on critical scattering[8] suggest on the contrary that they must be a rather poor approximation to the real interactions.

A further test of the validity of these equations is given by the data in Fig. 4. These data have been corrected as explained above. The major corrections which had to be introduced were those due to extinction effects. In our estimate of the extinction we assumed that only secondary extinction was present and based the correction on the heavy extinction in (440) relative to (220). The empirical value of the mosaic spread arrived at by this procedure, can be applied to reflections that are either of magnetic or nuclear origin,[11] but not to reflections that have strong contributions from both components. The nuclear contribution to (111) is less than 4 per cent and an application of the same should be justified. The agreement obtained in Fig. 2 shows, however, that the (222) data are also correctly taken care of by the same procedure. The nuclear contribution to (222) is about 10 per cent.

Thus the secondary extinction must dominate, but the primary extinction[11] should show up on (220) where the nuclear and magnetic components are mixed in the ratio of three to two for a unmagnetized crystal. The (220) intensity can be arrived at in two ways, either by direct observations or from the intensities of (111) and (222). The discrepancy between the two values which we obtained in these ways, showed that the primary extinction of (220) was weak and could not be stronger than 3 per cent for the (111) and (222) reflections.

It therefore seems safe to state that the discrepancy between experimental points and theoretical curves in Fig. 4, which amounts to about 20 per cent, is of real physical significance. Fig. 4 thus implies that molecular field coefficients that match the temperature variations of the total magnetization and the paramagnetic susceptibility do not account properly for the sublattice magnetization. We have not tried to find values of the coefficients which would match our curves, but obviously these values would be inconsistent with those derived from magnetic data. This inconsistency must be due to an inability of the linear equations (2a) and (2b) to take proper account of the interactions.

Acknowledgements—The present work was done while the authors held fellowships from the Belgian American Educational Foundation (L.T.) and the Royal Norwegian Council of Scientific and Industrial Research (T.R.). The hospitality of Brookhaven National Laboratory is gratefully acknowledged. Thanks are also due to Mrs. Regina Buckley Cohen, who did most of the computation work, and to Dr. J. S. Smart for some suggestions concerning this paper.

REFERENCES

1. Néel L., *Ann. Phys., Paris* **18,** 5 (1932); *C.R. Acad. Sci., Paris* **203,** 304 (1936).
2. Smart J. S., *Amer. J. Phys.* **23,** 356 (1955).
3. Pickart S. J. and Nathans R., *Phys. Rev.* **116,** 317 (1959).
4. Néel L., *J. Phys. théor appl.* **12,** 238 (1951).
5. Pauthenet R., Thesis, Masson et Cie, Paris (1952).
6. Fallot M. and Maroni P., *J. Phys. Radium* **12,** 256 (1951).
7. McReynolds A. W. and Riste T., *Phys. Rev.* **95,** 1161 (1954).
8. Riste T., *J. Phys. Chem. Solids* **17,** 308 (1961).
9. Bacon G. E. and Lowde R. D., *Acta Cryst., Camb.* **1,** 303 (1948).
10. Hamilton W. C., *Acta Cryst., Camb.* **10,** 629 (1957).
11. Hamilton W. C., *Acta Cryst., Camb.* **11,** 585 (1958).

J. Phys. Chem. Solids Pergamon Press 1961. Vol. 19, Nos. 1/2, pp. 124–129. Printed in Great Britain.

RELATIONS BETWEEN THE ELECTRONIC PROPERTIES AND THE CHEMICAL BONDING OF $Sb_xBi_{2-x}Te_{3-y}Se_y$ SYSTEM

IWAO TERAMOTO and SHIGETOSHI TAKAYANAGI

Research Laboratory of Matsushita Electronics Corporation, Takatsuki, Osaka, Japan

(*Received* 20 *June* 1960)

Abstract—The electronic properties of $Sb_xBi_{2-x}Te_{3-y}Se_y$ were investigated. The materials were prepared by melting, quenching and annealing. It is found that y_0, the value of y for which the thermoelectric power reverses from p-type to n-type, coincides with the electrical conductivity minimum, and increases with increasing x. An explanation of the results is proposed based on a model of chemical bonding in compounds of the type $A_2^VB_3^{VI}$. The smaller value of y_0 for $x = 0$ than for $x = 1{\cdot}0$ is interpreted by taking into account the additional effect of the variation of carrier mobility with y. X-ray analysis shows that the system is a continuous solid solution with the hexagonal structure except for the region whose composition is close to Sb_2Se_3. Curves of the electrical conductivity and the thermoelectric power are discontinuous, where the admixture phases of hexagonal and orthorhombic structures are shown.

INTRODUCTION

THE semiconducting properties of Bi_2Te_3 have been known to deviate from those normally found in most of the semiconducting compounds. Thus, the rather complicated behavior of Bi_2Te_3 can be interpreted in terms of the chemical bonding. Schemes for the chemical bonding in Bi_2Te_3 have been discussed by several investigators.[1,2,3,4] The atomic arrangement in Bi_2Te_3 is believed to be a layered structure with the period of

$$Te^{(1)}-Bi-Te^{(2)}-Bi-Te,^{(1)}$$

$Te^{(1)}$ and $Te^{(2)}$ being inequivalent. The Bi–$Te^{(2)}$ bond is weaker than Bi–$Te^{(1)}$ because of the longer interatomic distance. DRABBLE and GOODMAN[3] have used this model to explain the optical energy gap of an alloy $Bi_2Te_{3-y}Se_y$, in which tellurium atoms in Bi_2Te_3 are partially replaced by more electronegative selenium. FUSCHILLO *et al.*[5] have observed that this alloy is intrinsic at the composition $y = 0{\cdot}9$, but they have given no explanation for this behavior.

It will be interesting to investigate a system in which not only is tellurium substituted for selenium but also bismuth is replaced by antimony in Bi_2Te_3. In this paper a study of the electrical conductivity and the thermoelectric power of $Sb_xBi_{2-x}Te_{3-y}Se_y$ system is presented. Since Sb_2Se_3 has a different crystal structure from the other three compounds, it is probable that there exists a limit of the solid solubility of Sb_2Se_3 in this four component system. The lattice constants and crystal structures were determined in the whole range of the system by X-ray analysis. An interpretation for the results will be proposed on the basis of the chemical bonding model for compounds of the type $A_2^VB_3^{VI}$. It is assumed that this model can be applied to the general features of similar compounds and alloys.

EXPERIMENTAL

The polycrystalline materials with the composition $Sb_xBi_{2-x}Te_{3-y}Se_y$ were prepared by melting component elements in stoichiometric proportions in sealed quartz capsules evacuated to a pressure of 10^{-5} mm Hg. The purities of these elements had been shown to be more than 99·999 per cent by spectroscopic analysis. The melt was frozen as rapidly as possible by plunging the capsule into water, and subsequently annealed at 500°C for several hours in order to achieve homogeneity. Specimens for electrical measurements were cut

from the ingot with a diamond wheel to the desired dimension and were polished on a glass plate.

The thermoelectric power, relative to two gold blocks in which copper–constantan thermojunctions (0·1 mm in diameter) were inserted, was measured with a d.c. potentiometer and a high-input impedance d.c. voltmeter. The electromotive force of the thermocouples had been calibrated at the melting point and the boiling point of water and the melting point of metallic tin. The temperature was measured by a galvanometer with an accuracy of $\pm 0{\cdot}1°C$. The specimens were disks of $2 \sim 3$ mm in thickness and 10mm in diameter. During the measurements the specimen was kept in a vacuum of 10^{-3} mm Hg. The temperature difference between the ends of the specimen was 25°C and the mean value of the temperatures at the ends was taken as the specimen temperature.

Electrical conductivity measurements were carried out by a four-point method, using a d.c. potentiometer.

Crystal structures and lattice constants were determined by the powder method with an X-ray diffractometer. The relative errors in lattice constants were within 0·01 per cent.

RESULTS

The temperature dependence of the thermoelectric power was not the same throughout all compositions of the system; however, the general features of the curves are in agreement with the results obtained by FUSCHILLO *et al.* Some typical

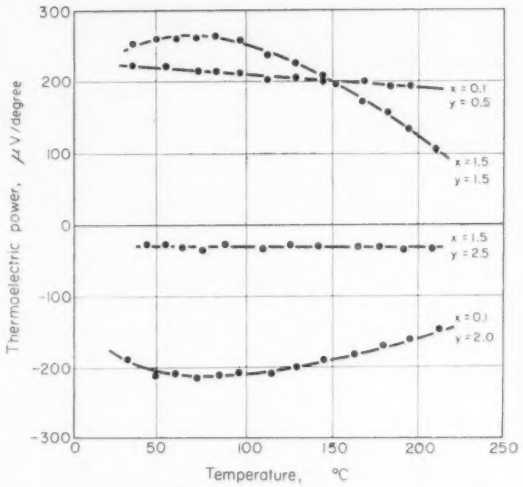

FIG. 1. Thermoelectric power of $Sb_xBi_{2-x}Te_{3-y}Se_y$ as a function of temperature.

plots of the temperature variation of the thermoelectric power are shown in Fig. 1. Fig. 2 shows the isothermal thermoelectric power vs. the composition at 50°C. The features of these curves are

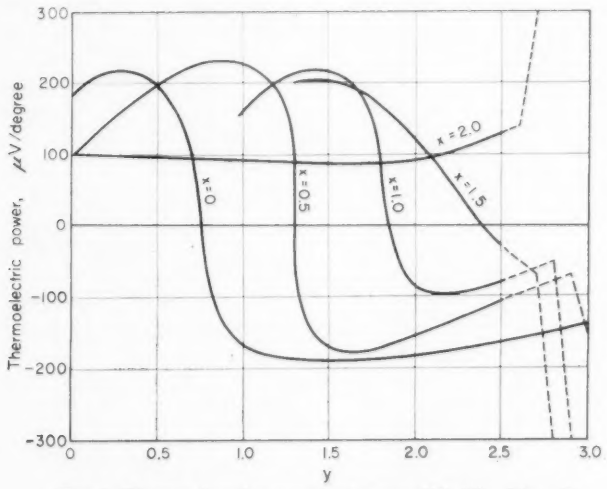

FIG. 2. Thermoelectric power isotherms of $Sb_xBi_{2-x}Te_{3-y}Se_y$ system.

similar to those for the other temperatures. These curves show that the sign of the thermoelectric power reverses from positive to negative, as y increases from zero to 3, except for the case $x = 2{\cdot}0$. y_0, the value of y for which the thermoelectric power becomes zero, is $0{\cdot}75$ for $x = 0$ ($Bi_2Te_{3-y}Se_y$). y_0 increases with increasing x as shown in the curves. In the case $x = 2{\cdot}0$, where all bismuth atoms are replaced by antimony, the sign of the thermoelectric power is always positive throughout the whole range of y from 0 to $3{\cdot}0$. At compositions in the neighborhood of $x = 2{\cdot}0$ and $y = 3{\cdot}0$, the absolute magnitudes of the thermoelectric power become extremely large, and show discontinuities with composition.

The electrical conductivity measured at room temperature for various compositions is shown in Fig. 3. These curves have minima just for the composition at which the thermoelectric power reverses sign. Curves of the electrical conductivity also have discontinuities for the compositions near $x = 2{\cdot}0$ and $y = 3{\cdot}0$. It is found that these discontinuities occur just for the same compositions as for the curves of the thermoelectric-power.

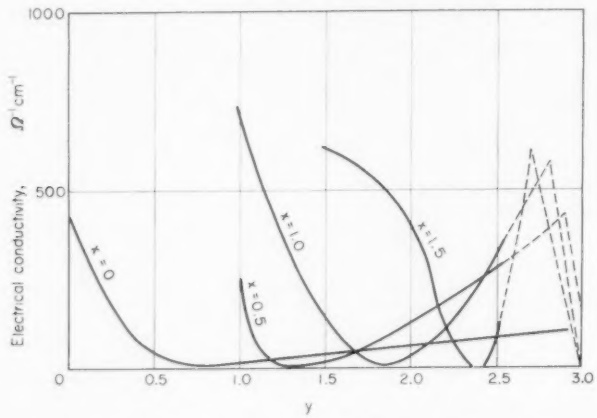

FIG. 3. Electrical conductivity isotherms of $Sb_xBi_{2-x}Te_{3-y}Se_y$ system.

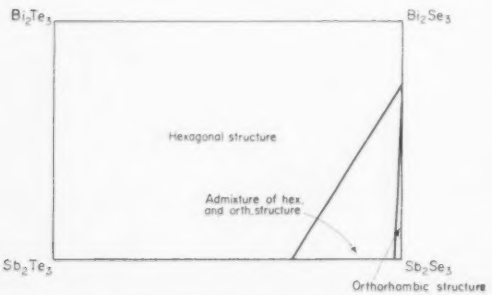

FIG. 4. Schematic diagram of the relation between the crystal structure and the composition in $Sb_xBi_{2-x}Te_{3-y}Se_y$ system.

Figure 4 is a schematic diagram showing the relation between the crystal structures obtained by X-ray analysis and the compositions in $Sb_xBi_{2-x}Te_{3-y}Se_y$. The crystal structures of the materials are either hexagonal, orthorhombic or an admixture of the two. In a wide range of compositions, except in the neighborhood of Sb_2Se_3, the structure is observed to be a hexagonal solid solution. Variations of the lattice constants with composition are shown in Figs. 5(a), 5(b) and 5(c). The lattice constants vary continuously with increasing antimony and/or selenium concentration. When the compositions are close to Sb_2Se_3, an orthorhombic solid solution appears as an admixed phase, until finally there is a pure orthorhombic phase for Sb_2Se_3. It should be noticed that the curves, both of the thermoelectric power and the

electrical conductivity show discontinuities just at the limits of solid solubility of the hexagonal structure.

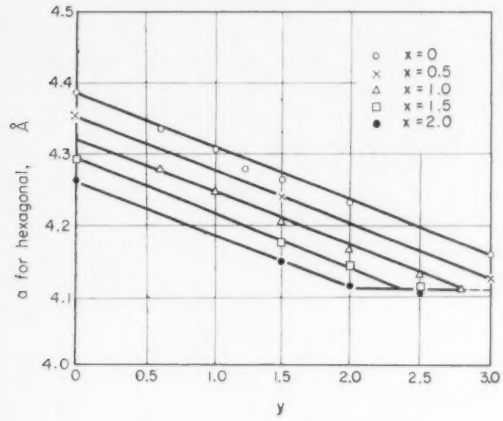

(a)

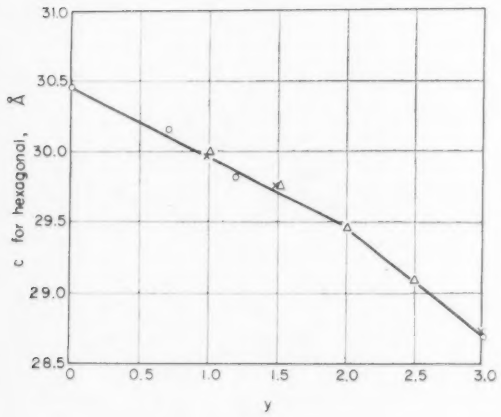

(b)

DISCUSSION

The compositions at which the curves of the thermoelectric power cross the zero-axis and those of electrical conductivity show minima, correspond to the intrinsic compositions of $Sb_xBi_{2-x}Te_{3-y}Se_y$.[5]

We shall give a general explanation of these results on the basis of chemical bonding.

The bonding model for Bi_2Te_3 proposed by DRABBLE and GOODMAN[3] leads to the expectation that a deficit of tellurium from stoichiometry may occur at the $Te^{(2)}$ sites, since $Te^{(2)}$ atoms have higher free energy than $Te^{(1)}$ atoms. It is a well-established fact[4,6] that Bi_2Te_3 grown from a melt of stoichiometric composition is always a *p*-type conductor and in order to get *n*-type it is necessary to add an excess of tellurium. From this fact, it is believed that the maximum melting point in the Bi–Te system does not occur at the stoichiometric composition of Bi_2Te_3, but rather at a bismuth-rich composition.[7] Thus, excess bismuth atoms may occupy the $Te^{(2)}$ sites and act as acceptors.

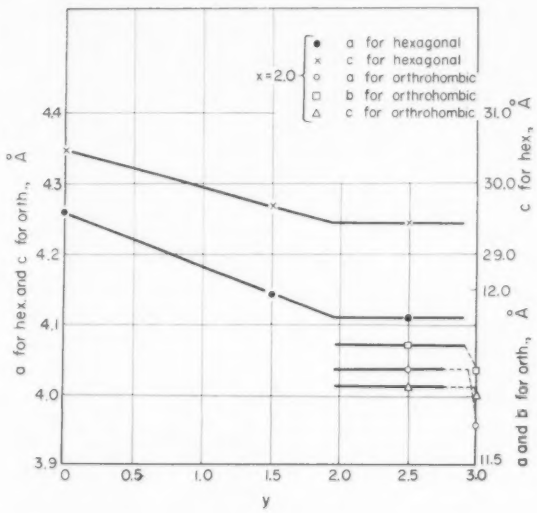

(c)

FIG. 5. Lattice constants in $Sb_xBi_{2-x}Te_{3-y}Se_y$ system.
(a) *a* for hexagonal structure
(b) *c* for hexagonal structure
(c) *a* and *c* for hexagonal structure, and *a*, *b* and *c* for orthorhombic structure.

This substitutional occupancy of the tellurium sites by bismuth atoms can be expected because bismuth and tellurium are similar in electronegativity and atomic radius. Likewise, the bismuth sites may be substitutionally occupied by the tellurium atoms when the tellurium atoms are stoichiometrically in excess and *n*-type conduction is shown.

If selenium is substituted for tellurium it is to be expected from the above model that the selenium atom will at first go into the $Te^{(2)}$ site because

selenium is more electronegative than tellurium. Thus, $Bi_2Te_{3-y}Se_y$ will be intrinsic when all the $Te^{(2)}$ atoms are replaced by selenium, since $Te^{(2)}$ sites are stabilized by the substitution with selenium. As y increases from one, the selenium atoms will go into the $Te^{(1)}$ sites making the nearest bismuth atoms more electronegative and leading to an n-type characteristic.

On the other hand, it has been observed that Sb_2Te_3 grown from a melt of stoichiometric composition is always a p-type conductor as is Bi_2Te_3. In the present investigation $Sb_xBi_{2-x}Te_3$ is a p-type conductor throughout, from $x = 0$ to 2·0. The values of electronegativity of both bismuth and antimony are 1·8 according to GORDY and THOMAS[8]. However, it is reasonable to expect that bismuth has a somewhat smaller electronegativity than antimony, since in the $Sb_xBi_{2-x}Te_{3-y}Se_y$ system, when antimony atoms are substituted for Bi, y_0 increases linearly with increasing x as shown in Fig. 6. This means that antimony, being more electronegative than bismuth, is more like tellurium in electronegativity than bismuth* and can occupy the $Te^{(2)}$ sites more easily. In any case, because of the small difference in this value between bismuth and antimony, the effect of x on the sign reversal of thermoelectric power in $Sb_xBi_{2-x}Te_{3-y}Se_y$ is not so strong as the effect of y, and the relationship between x and y_0 can be indicated by the slope in Fig. 6. Generally speaking, it can be said that the larger electronegativity of the metal component shifts the system towards p-type conduction and the larger electronegativity of the metalloid component towards n-type conduction. The above considerations lead to a prediction that y_0 will be larger in $As_xBi_{2-x}Te_{3-y}Se_y$ than in $Sb_xBi_{2-x}Te_{3-y}Se_y$ since arsenic is more electronegative than antimony, and it will be smaller in $Sb_xBi_{2-x}Te_{3-y}S_y$ than in $Sb_xBi_{2-x}Te_{3-y}Se_y$ since sulfur is more electronegative than selenium. These systems are now under investigation.

According to the above model, the value of y_0 for $x = 0$ should be 1·0 where all the $Te^{(2)}$ sites are occupied by selenium atoms. Nevertheless, the present experiment shows that $y_0 = 0{\cdot}75$, and FUSCHILLO *et al.*[5] and BIRKHOLZ[9] obtained the values 0·9 and 0·67 respectively. These values are all smaller than 1·0. This can be understood by taking into account the additional effect that hole and electron mobilities change with y. According to PUTLEY[10] the thermoelectric power is given by

$$\alpha = -\frac{k}{e}\frac{n\mu_1(2-\epsilon/kT)-p\mu_2(2-\xi/kT)}{n\mu_1+p\mu_2}$$

where α is the thermoelectric power, n and p the concentration of the conduction electrons and holes in the full band, respectively, μ_1 and μ_2 the mobility of conduction electrons and holes, respectively, ϵ the chemical potential

$$= kT\ln\left(\frac{nh^3}{2(2\pi m_1 kT)^{3/2}}\right),$$

ϵ the chemical potential for positive holes

$$= -E-\epsilon = kT\ln\left(\frac{ph^3}{2(2\pi m_2 kT)^{3/2}}\right),$$

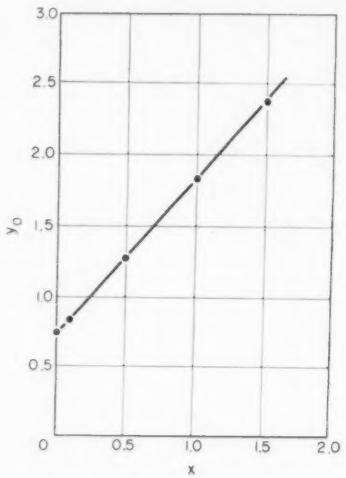

FIG. 6. Variation of y_0 (= y for the intrinsic composition) with x in $Sb_xBi_{2-x}Te_{3-y}Se_y$ system.

* GORDY and THOMAS[8] give the electronegativity values of these elements as follows,

Sb^{III}	Sb^{V}	Bi^{III}	Bi^{V}	Te	Se
1·8 ~ 1·82	2·1	1·8		2·1	2·4

The value for Bi^V was not given, but may be a little smaller than 2·1 for Sb^V.

Vol. 1
196

E the energy gap between the bands, m_1 and m_2 the effective mass of electrons and positive holes, respectively. Obviously, the carrier which has the larger product of mobility and concentration determines the sign of the thermoelectric power. JOFFE[11] has recently shown that in the Bi_2Te_3–Bi_2S_3 system the hole mobility is lowered by increasing the proportion of Bi_2S_3, and in the Bi_2Te_3–Sb_2Te_3 system, hole mobility is raised and electron mobility is lowered by increasing Sb_2Te_3. These results show that the hole mobility in $Sb_xBi_{2-x}Te_{3-y}Se_y$ will be increased with increasing x and decreased with increasing y. This additional effect of the variation in carrier mobility may be the reason why the apparent intrinsic composition of $Bi_2Te_{3-y}Se_y$ has been observed not at $y = 1{\cdot}0$ but at values of y less than $1{\cdot}0$. Impurities of component elements may also account for the distributed values from $0{\cdot}9$ to $0{\cdot}67$ even under the similar condition.

Acknowledgements—The authors wish to acknowledge the interest and the helpful discussions of Professor HAJIMU KAWAMURA.

REFERENCES

1. LAGRENAUDIE J., *J. Phys. Radium* **18,** 39 (1957).
2. MOOSER E. and PEARSON W. B., *Canad. J. Phys.* **34,** 1369 (1956).
3. DRABBLE J. R. and GOODMAN C. H. L., *J. Phys. Chem. Solids* **5,** 142 (1958).
4. MOOSER E. and PEARSON W. B., *J. Phys. Chem. Solids* **7,** 65 (1958).
5. FUSCHILLO N., BIERLY J. N. and DONAHOE F. J., *J. Phys. Chem. Solids* **8,** 430 (1959).
6. HARMAN T. C., PARIS B., MILLER S. E. and GOERING H. L., *J. Phys. Chem. Solids* **2,** 181 (1957).
7. SATTERTHWAITE C. B. and URE R. W., *Phys. Rev.* **108,** 1164 (1957).
8. GORDY W. and THOMAS W. J. O., *J. Chem. Phys.* **24,** 439 (1956).
9. BIRKHOLZ V. U., *Z. Naturf.* **13a,** 780 (1958).
10. PUTLEY E. H., *Proc. Phys. Soc. Lond.* **B68,** 35 (1955).
11. JOFFE A., *J. Phys. Chem. Solids* **8,** 6 (1959).

ol. 19
1961

J. Phys. Chem. Solids Pergamon Press 1961. Vol. 19, Nos. 1/2, pp. 130–133. Printed in Great Britain.

SOME NEW SUPERCONDUCTING COMPOUNDS

B. T. MATTHIAS, V. B. COMPTON and E. CORENZWIT

Bell Telephone Laboratories, Murray Hill, New Jersey

(*Received* 8 *August* 1960)

Abstract—The transition temperatures and crystal structures of several new superconducting compounds are reported. Some crystal structures are more favorable than others for the occurrence of superconductivity. The transition temperatures reflect the decisive influence of the valence electron concentration.

THE PURPOSE of this paper is to report several new superconducting compounds which cover a variety of crystal structures, compositions, and concentrations of valence electrons.

All the compounds except $MoGa_4$ and Y_3Bi_2 were prepared by reacting the appropriate amounts of the elements in an arc furnace under a helium or argon atmosphere. The $MoGa_4$ was prepared in fused quartz tubes at 1300°C and the Y_3Bi_2 in fused quartz tubes at 1230°C. The compositions reported are those of the mixed elements before reaction. The crystal structures were identified from Debye–Scherrer diffraction patterns. The observed intensities were compared with those calculated from the published structural data.

The superconducting transition temperatures and crystal structures are given in Table 1. The newly discovered compounds are $ThRu_2$,* Th_7Os_3 and Th_7Ir_3. $ThRu_2$ has the $MgCu_2$ type structure (C15); Th_7Os_3 and Th_7Ir_3 are isostructural with Th_7Fe_3, Th_7Co_3 and Th_7Ni_3 reported by FLORIO *et al.*[1] The powder pattern for $ZrIr_2$* is that of

* *Note added in proof:* After the present paper was completed, DWIGHT[19] reported crystal structure data for $ThRu_2$ and $ZrIr_2$. Our data are in agreement with his results.

Table 1. *Superconductivity and crystal structure data*

Compound	Transition temperature, °K	Crystal structure data				
		System	Lattice Constants a_0, Å	c_0, Å	Structure type	References to previous work
Ti_3Sb	5·8	Cubic	5·217		β-W–A15	Kjekshus[6]
Ti_3Ir	5·4	,,	5·009		,,	Geller[7]
$(V_{2\cdot67}Ir_{0\cdot33})Ir$	1·39	,,	4·794		,,	
V_3Pt	2·83	,,	4·814		,,	Geller[7]; Greenfield & Beck[8]
ZrV_2	8·8	Cubic	7·439		$MgCu_2$–C15	Wallbaum[2]; Elliott & Rostoker[3]
ZrW_2	2·16	,,	7·621		,,	Elliott & Rostoker[3]
$ZrIr_2$	4·10	,,	7·359		,,	Wallbaum[2]; Dwight[19]
$ThRu_2$	3·56	,,	7·651		,,	Dwight[19]
$ThIr_2$	6·5	,,	7·664		,,	Dwight, Downey & Conner[9]
$ZrRu_2$	1·84	Hexagonal	5·144	8·504	$MgZn_2$–C14	Wallbaum[2]
$ZrOs_2$	3·00	,,	5·219	8·538	,,	Wallbaum[2]

Vol. 1
1961

Table 1 (Contd.)

Compound	Transition temperature, °K	Crystal structure data				References to previous work
		System	Lattice Constants		Structure type	
			a_0, Å	c_0, Å		
Ti_5Re_{24}	6·6	Cubic	9·587		α-Mn–A12	Trzebiatowski & Niemiec[10]
$ZrRe_6$	7·4	,,	9·698		,,	Savitskii *et al.*[11]
$Nb_{18a/o}Re$	9·7*	,,	9·641		,,	Knapton[12]; Greenfield & Beck[8]; Niemiec & Trzebiatowski[13]
$NbOs_2$	2·52	,,	9·655		,,	Knapton[12]
$Ta_{36.2a/o}Re$	1·46*	,,	9·765		,,	Knapton[12]; Greenfield & Beck[8]; Niemiec & Trzebiatowski[13]
TaOs	1·95	,,	9·773		,,	Knapton[12]
Nb_3Os_2	1·78*	Tetragonal	9·844	5·056	σ Phase	Knapton[12]
Nb_3Ir_2	9·8*	,,	9·834	5·052	,,	Knapton[12]
Nb_5Pt_3	3·73*	,,	9·91	5·12	,,	Greenfield & Beck[8]
Th_7Fe_3	1·86	Hexagonal	9·823	6·211	D 10_2	Florio, Baenziger & Rundle[1]
Th_7Co_3	1·83	,,	9·833	6·200	,,	Florio, Baenziger & Rundle[1]
Th_7Ni_3	1·98	,,	9·885	6·225	,,	Florio, Baenziger & Rundle[1]
Th_7Os_3	1·51	,,	10·02	6·285	,,	
Th_7Ir_3	1·52	,,	10·06	6·290	,,	
Th_2Cu	3·49	Tetragonal	7·28	5·75	$CuA1_2$–C16	Murray[4]
Th_2Ag	2·26	,,	7·56	5·84	,,	Murray[4]
Th_2Au	3·08	,,	7·42	5·95	,,	Murray[4]
Ti_2Co	3·44	Cubic	11·30			Orrell & Fontana[14]; Duwez & Taylor[15]; Purdy & Parr[16]
Ru_7B_3	2·58	Hexagonal	7·465	4·715	Th_7Fe_3–D10_2	Aronnson[19]
La_3In	10·4	Cubic†	5·07		Cu_3Au–$L1_2$	Iandelli[18]
Al_3Os	5·9	Pattern not interpreted				
Y_3Bi_2	2·25					
$MoGa_4$	9·8					

* R. D. BLAUGHER and J. K. HULM (this Journal) report the transition temperature of these compounds, and with the exception of $TaRe_3$, their values are somewhat lower than those given in Table 1. The discrepancy may be due to differences in composition or to the fact that they have taken the midpoint of the transition whereas we have taken the upper onset temperature.

The difference in the reported values for the transition temperature of the α-Mn phase in the Ta–Re system is probably due to the difference in valence electron concentration. $TaRe_3$ has a valence electron concentration of 6·5 and a transition temperature of 6·78°K; whereas $Ta_{36.2a/o}$ Re has a valence electron concentration of 6·3 and a transition temperature of 1·46°K.

† This result is due to W. H. ZACHARIASEN.

the cubic Laves phase, $MgCu_2$ type (C15) and there is no evidence of the hexagonal Laves phase, $MgZn_2$ type (C14) reported by WALLBAUM[2]. ZrV_2 has the cubic Laves phase C15 type structure which agrees with the results of ELLIOTT and ROSTOKER[3] and is not the hexagonal Laves phase, C14 type, structure described by WALLBAUM[2]. The patterns of Th_2Cu, Th_2Ag, and Th_2Au were indexed using the lattice constants reported by MURRAY[4].

There are several crystal structures which are favorable for the occurrence of superconductivity. The best known seems to be the β-wolfram type (A15). All the β-wolfram compounds with suitable electron concentrations are superconducting, except V_3Au. Other common structures for superconductors are the NaCl type (B1), the $MgCu_2$ type (C15) and the $MgZn_2$ type (C14).

The CsCl type structure (B2) seems to be the least favorable of the structures investigated for superconductivity. Several compounds with this structure including MgAu, AlOs, ScPt, TiOs, and $VOs_{40\alpha/o}$ are normal down to 1·02°K in spite of favorable electron concentrations.

Several of the combinations of elements that form compounds with the β-wolfram structure will also form compounds, of different stoichiometric proportions, with the α-manganese structure or will form a sigma phase. If the electron concentration is more favorable in these structures, the superconducting transition temperature will be higher than in the corresponding β-wolfram structure. In the niobium–osmium system, for instance, $NbOs_2$ (α-Mn type—7 valence electrons) has the highest transition temperature, 2·52°K followed by Nb_3Os_2 (σ phase—6·2 valence electrons) 1·78°K, and Nb_3Os (β-W type—5·8 valence electrons) 1·05°K. The transition temperature of Nb_3Ir_2 (σ phase—6·6 valence electrons) is 9·8°K, while that of Nb_3Ir (β-W type—6 valence electrons) is 1·7°K. Occasionally it is possible to vary the electron concentration in the β-wolfram structure simply by deviating from the stoichiometric composition. For example, V_3Ir (6·0 valence electrons) is not superconducting above 1·02°K, whereas $(V_{2\cdot67}Ir_{0\cdot33})Ir$ or V_2Ir (6·3 valence electrons) becomes superconducting at 1·39°K; V_3Pt (6·3 valence electrons) becomes superconducting at 2·83°K and $(V_{2\cdot67}Pt_{0\cdot33})Pt$ or V_2Pt (6·7 valence electrons) is normal down to 1·02°K.

Quite frequently the individual superconducting nature of the constituent elements is lost entirely in a superconducting compound. For example, niobium is a superconductor above 8°K and titanium below 0·5°K; whereas, Nb_3Sb is normal down to 1°K and Ti_3Sb becomes superconducting at 5·8.* This however is consistent again with the valence electron criterion for the occurrence of superconductivity described previously.[5] However, the simple valence electron picture is very often complicated by magnetic interactions. The compounds of Fe, Co, and Ni with Th are an illustration. The maximum transition temperature in the series, that of Th_7Ni_3, occurs at an electron concentration closer to six than to five electrons per atom.

In calculating the number of valence electrons, the simplifying assumption was initially made that all the elements in the same column have the same number of electrons. Obviously, this is an oversimplification. The increasing number of superconductors makes it possible to evaluate qualitatively the relative number of contributed electrons for elements in the same column. Th_2Cu, Th_2Ag, and Th_2Au form the first complete series. Unfortunately, it is difficult to decide whether any *d*-electrons participate in this intermetallic bond and therefore whether the number of valence electrons should be counted as one or eleven. The average number of valence electrons per atom in Th_2X, where X is Cu, Ag or Au is 3·00 if X contributes one electron and 6·33 if X contributes eleven. In either case, a decrease in the superconducting transition temperature corresponds to a reduction in the number of valence electrons. Since the transition temperature varies directly with about the seventh power of the volume and inversely with the mass, Th_2Ag should have a higher transition temperature than the corresponding copper or gold compounds. However, the transition temperature of Th_2Ag is lower than that of Th_2Cu and that of Th_2Au, and therefore the number of valence electrons per atom in silver is probably less than in copper or gold. As a matter of fact this is the first superconducting compound of silver to be reported.

* We are very grateful to Dr. KEJSKHUS who pointed out to us in a private communication that Ti_3Sb forms the β-wolfram type structure (A15).

REFERENCES

1. Florio J. V., Baenziger N. C. and Rundle R. E., *Acta Cryst., Camb.* **9,** 367 (1956).
2. Wallbaum H. J., *Naturwissenschaften* **30,** 149 (1952).
3. Elliott R. P. and Rostoker W., *Trans. Amer. Soc. Metals* **50,** 617 (1958).
4. Murray J. R., *J. Inst. Met.* **84,** 91 (1955–1956).
5. Matthias B. T., *Phys. Rev.* **97,** 74 (1955).
6. Kjekshus A., Scientific paper No. 418, *The Crystal Structure of* Ti_3Sb, read at the 10th Inter-Scandinavian Chemistry Conference, Stockholm, 1959.
7. Geller S., *Acta Cryst., Camb.* **9,** 885 (1956).
8. Greenfield P. and Beck P. A., *Trans. Amer. Inst. Min.* (*Metall.*) *Engrs.* **206,** 265 (1956).
9. Dwight A. E., Downey J. W. and Conner R. A., *Trans. Amer. Inst. Min.* (*Metall.*) *Engrs.* **212,** 337 (1958).
10. Trzebiatowski W. and Niemiec J., *Roczniki Chem.* **29,** 277 (1955); *Chem. Abstr.* **49,** 15581h (1955).
11. Savitskii E. V., Tylkina M. A. and Tsyganova I. A., *Atomn. Energiya* **7,** 231 (1959); *Chem. Abstr.* **54,** 58h (1960).
12. Knapton A. G., *J. Inst. Met.* **87,** 28 (1958).
13. Niemiec J. and Trzebiatowski W., *Bull. acad. polon. sci.* **4,** 601 (1956); *Chem. Abstr.* **51,** 7280a (1957).
14. Orrell F. L. and Fontana M. G., *Trans. Amer. Soc. Metals.* **47,** 554 (1955).
15. Duwez P. and Taylor J. L., *Trans. Amer. Inst. Min.* (*Metall.*) *Engrs.* **188,** 1173 (1950).
16. Purdy G. R. and Parr J. G., *Trans. Amer. Inst. Min.* (*Metall.*) *Engrs.* **218,** 225 (1960).
17. Aronsson B., *Acta Chem. Scand.* **13,** 109 (1959).
18. Iandelli A., *Proceedings of the Symposium on Physics, Chemistry of Metallic Solutions and Intermetallic Compounds, June* 4–6, 1958, *at the National Physical Laboratory.* Paper No. 3F. Chemical Publishing Co., New York (1960).
19. Dwight A. E., *Trans. Amer. Soc. Metals.* Preprint No. 211 (1960).

ol. 19
1961

J. Phys. Chem. Solids Pergamon Press 1961. Vol. 19, Nos. 1/2, pp. 134–138. Printed in Great Britain.

SUPERCONDUCTIVITY IN THE σ AND α-Mn STRUCTURES

R. D. BLAUGHER and J. K. HULM

Westinghouse Research Laboratories, Pittsburgh, Pennsylvania

(*Received* 8 *August* 1960)

Abstract—The sigma and alpha-manganese structures formed by binary alloys between the group (V, Nb, Ta, Cr, Mo, W) and the group (Mn, Fe, Co, Ni, Ru, Rh, Pd, Re, Os, Ir, Pt) were investigated for superconductivity down to 1°K. Nineteen new superconductors were found in these two systems with the majority occurring in the sigma phase. A plot of superconducting transition temperature of the sigma phases against the average number of valence electrons per atom exhibited a maximum at approximately 6½ electrons per atom. This maximum is similar to those found for other structures by MATTHIAS, however it is displaced somewhat from the vicinity of 5 or 7 electrons per atom which MATTHIAS indicated to be characteristic of other systems. The sigma phase data therefore suggests to us that in compound formation between pairs of transition elements, the *d*-band shape is preserved to some extent and is filled at an intermediate level by the available electrons.

1. INTRODUCTION

MATTHIAS[1] has pointed out that for elements with incomplete *d*-shells, the so-called "transition" elements, superconductivity occurs in the vicinity of 3, 5 and 7 valence electrons per atom. Each of these transition temperature peaks has, on either side of it, a valley of normal behavior. This phenomenon is obviously connected with peaks in the density of states at the Fermi surface, which have also been identified in the neighborhood of Groups 3, 5 and 7 from heat capacity and other normal electronic data.[2] One possible explanation of both these effects is that the curve of density of states vs. energy in the *d*-band has the same general shape for all the transition elements. Thus as one moves across the periodic table and the *d*-band is filled up by the addition of extra electrons, the electronic properties fluctuate according to the shape of the general density of states curve. Clearly the general curve must exhibit at least three well-defined maxima to correspond with the observed electronic properties.

From the above picture it may be expected that upon mixing two transition elements in solid solution, the electronic properties will depend upon the shape of the general density of states curve between the two elements, since the *d*-band will be filled to an intermediate point. This prediction does seem to be borne out quite well by the superconducting transition temperature behavior for solid solution alloys of transition metals.[1,3,4] Unfortunately non-superconducting electronic data are almost entirely lacking for such systems.

It is of interest to examine the case in which two transition elements combine to form an intermetallic compound with a structure different from that of the parent metals. To apply the general density of states curve picture in this case would appear to be dangerous. However, there is evidence that the picture is at least roughly applicable. MATTHIAS and his co-workers[5–10] have tested a large number of β-W structure compounds for superconductivity. If one calculates for each compound an average number of valence electrons per atom based upon the valencies of the constituent elements, those compounds with close to five or seven valence electrons per atom exhibit the highest transition temperatures. One may again interpret this as a filling of the *d*-band to an intermediate point which happens to correspond to a peak in the general density of states curve.

The possibility of deducing some of the electronic properties of a compound from a knowledge of

Vol. 196

the electronic properties of the constituent elements is an attractive one. In an attempt to examine the validity of the method in further detail, we have searched for other families of transition metal compounds with superconducting members. Two such families have recently become more prominent due to advances in metallurgical techniques for dealing with refractory metals. These are the so-called "σ-phase" and the α-Mn structure.

The σ-phase is identified as a complex tetragonal structure containing 30 atoms per unit cell where the atoms are in five planes with a stacking arrangement resembling ABACA. STÜWE[11] has recently suggested that the σ-phase is an example of close sphere packing. This suggestion is important since any close packing arrangement could conceivably alter the electronic constitution of the pure components considerably, thus making any estimate of the effective valence quite difficult. The α-Mn phase is a cubic structure which is closely related to the σ-phase. SHOEMAKER *et al.*[12,13] have suggested that α-Mn is merely a high or low temperature modification of the σ-phase, which is generally unstable.

The σ and α-Mn structures formed by transition elements were studied extensively by GREENFIELD and BECK[14], who found many examples of these structures in binary systems containing a Group 5 or Group 6 metal as one component and a metal from Groups 7, 8, 9, and 10 as the other component. RAUB[15] has illustrated the formation of the σ-phase between Group 6 and Group 8 as shown in Fig. 1. Besides the σ and β-W compounds which occur in these systems, the ε hexagonal solid solution investigated by MATTHIAS is also present. Note the manner in which the σ composition shifts from one binary system to the next. This shifting of composition has led to the suggestion that the σ-phase is an electron compound.

NEVITT and BECK[16] found that most of the binary σ phases containing Mn, Fe, Co, Ni or Cr as one constituent were ferromagnetic. For this reason our superconductivity tests were confined to the σ phases formed by Nb, Mo, Ta, and W as one constituent and Ru, Rh, Pd, Re, Os, Ir, and Pt as the other. The majority of starting compositions were taken directly from GREENFIELD and BECK's work,[14] although we also employed NEVITT and DOWNEY's[17] data for osmium and iridium compounds. All of the reported σ and α-Mn structures were tested for superconductivity down to 1°K.

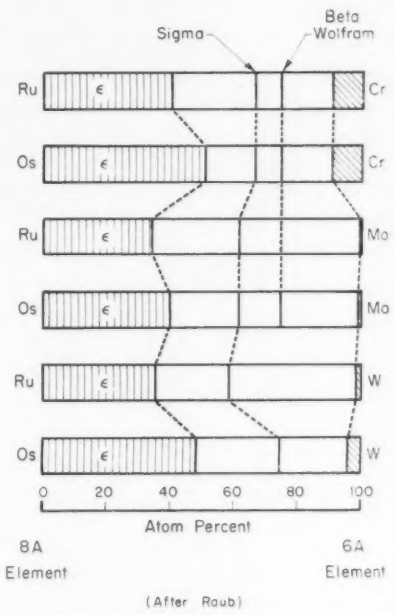

FIG. 1. Sigma phase formation between Group 6A and Group 8A.

II. EXPERIMENTAL DETAILS

The σ and α-Mn samples were prepared from starting materials containing less than one-tenth of one per cent total metallic and gaseous impurities. An arc furnace was used for preliminary melting. Homogeneity and subsequent phase formation were accomplished by annealing the samples in a specially constructed water quenching tube furnace. Annealing temperatures up to 1500°C were employed for periods of 100–150 hr at an average pressure of 3×10^{-6} mm Hg, after which the samples were quenched in water to room temperature. X-ray analysis was then performed to ensure formation of the appropriate phase. In some cases preparations had to be repeated at several compositions different from those reported in the literature in order to achieve samples which were predominantly of the desired structure.

The samples were tested for superconductivity

in an apparatus similar to that used for earlier studies on transition metal compounds by HARDY and HULM.[18] Further details on the apparatus, superconducting measurements, starting materials, melting and annealing techniques are given in another paper.[4]

III. RESULTS AND DISCUSSION

The σ phases investigated by us are shown in Fig. 2. The phases are labeled F, (ferromagnetic), S, (superconducting) and N, (normal to 1°K). The ferromagnetic Curie temperatures were taken from the work of NEVITT and BECK[16].

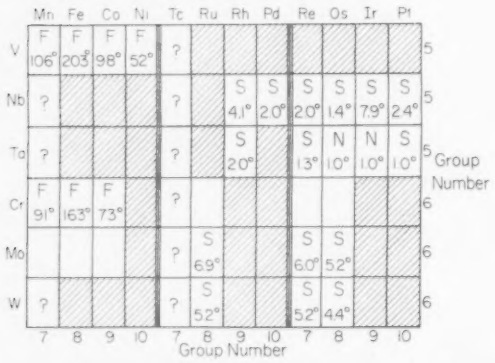
Mn Fe Co Ni Tc Ru Rh Pd Re Os Ir Pt
V F 106° F 203° F 98° F 52° ? 5
Nb ? ? S 4.1° S 2.0° S 2.0° S 1.4° S 7.9° S 2.4° 5
Ta ? ? S 2.0° S 1.3° N 1.0° N 1.0° S 1.0° 5
Cr F 91° F 163° F 73° ? 6
Mo ? S 6.9° S 6.0° S 5.2° 6
W ? ? S 5.2° S 5.2° S 4.4° 6
7 8 9 10 7 8 9 10 7 8 9 10
Group Number
Group Number

FIG. 2. Sigma phases tested for superconductivity.

The shaded regions are those systems in which, on the basis of careful tests, the σ-phase is apparently not formed. Question marks represent systems which have not been examined or where the data are insufficient to rule out σ-phase formation. Fifteen of the known σ phases were found to be superconducting with the transition temperatures shown in Fig. 2.

The four known α-Mn structures formed within the binary combinations of Fig. 2 were also investigated. All were found to be superconducting above 1°K with transition temperatures as follows:

The superconducting transition temperatures of the σ and α-Mn phases are plotted in Fig. 3 against the average number of valence electrons per atom calculated from the actual compositions of the compounds.

The transition temperatures of the known β-W compounds are plotted on the same diagram for comparison. While there is considerable scatter in the experimental points, Fig. 3 definitely gives

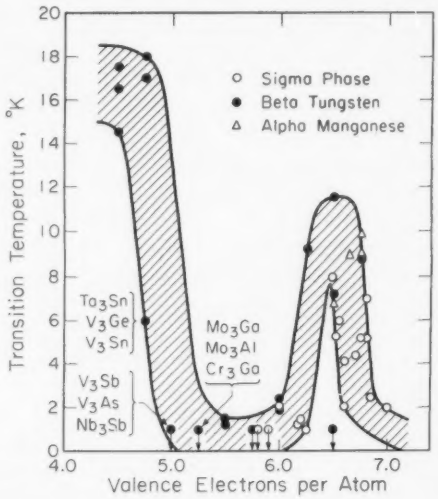

FIG. 3. Superconducting transition temperature as a function of the average number of valence electrons per atom.

an impression that for the three systems of compounds as a whole there exist maxima in T_c at approximately 4·5 and 6·5 valence electrons per atom. At the same time a minimum of T_c or even normal behavior occurs midway between the peaks and also on the upper side. The positioning of the two maxima is somewhat different from the abscissa values of five and seven electrons per atom originally proposed by MATTHIAS[1], but is in good agreement with data on solid solution alloys[4]

Nominal composition	Re_3Mo	$Re_{0.82}Nb_{0.18}$	Re_3Ta	Re_3W
T_c(°K)	9·89	8·89	6·78	9·00

and in the case of the upper peak with the data of CHANDRASEKHAR and HULM[19] for uranium compounds.

In Fig. 4 the transition temperature of many of the superconducting σ phases is plotted against the unit cell volume calculated from our determination of the individual lattice parameters. It is surprising to us that a monatomic relationship apparently exists between T_c and cell volume, a relationship which is, moreover, quite different

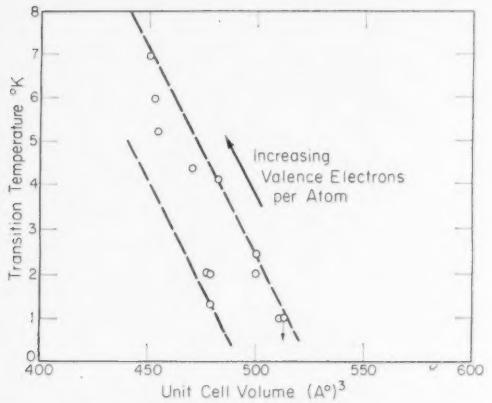

FIG. 4. Superconducting transition temperature vs. unit cell volume, sigma phases.

from the T_c–volume relationship obtained from studies of the variation of T_c with hydrostatic pressure. In the present case T_c decreases with increasing volume varying approximately as the 90th power of V. This is in direct contrast to the pressure experiments, where in most cases T_c decreases as the lattice is compressed and varies at a much lower rate, usually around the 10th power of volume.

We do not yet have a satisfactory explanation of the T_c–volume relationship of Fig. 4. It is tempting to dismiss the effect as a mere coincidence arising from the interdependence of the volume of the unit cell and the average number of valence electrons per atom. If such an interdependence really exists, it would appear to establish that the σ-phase is not one of the so-called "electron compounds". In such compounds there is supposed to be a fixed relationship between the Fermi surface and the Brillouin zone such that the average number of valence electrons per atom remains fixed in spite of changes in the value of the unit cell.

IV. CONCLUSION

Our study of the occurrence of superconductivity amongst the σ-phase and α-Mn structures indicates that these compounds show a dependence of transition temperature on average valence electron number similar to that found by MATTHIAS for the β-W system. In the σ-phase case a well-defined peak in T_c occurs at about 6·5 valence electrons per atom with a minimum of T_c or normal behavior on either side of the peak. The correlation is a rough one which breaks down in a few cases and does not allow an exact prediction of T_c.

The correlation between T_c and average number of valence electrons suggests to us that the *d*-band has the same general shape for the majority of transition metals and possesses, moreover, at least three well-defined maxima. This general shape is apparently preserved not only in the formation of solid solution alloys, for which the MATTHIAS correlation is successful, but also in the formation of intermetallic compounds such as the σ phases studied in the present work.

REFERENCES

1. MATTHIAS B. T., *Progress in Low Temperature Physics*, Vol. II. North Holland Publishing Company, Amsterdam (1957).
2. PARKINSON D. H., *Reports on Progress in Physics*, Vol. XXI. The Physical Society, London (1958).
3. MATTHIAS B. T., COMPTON V. B., SUHL H. and CORENZWIT E., *Phys. Rev.* **115,** 1597 (1959).
4. BLAUGHER R. D. and HULM J. K., *Superconductivity of the Transition Metal Alloys*, to be published.
5. MATTHIAS B. T., GEBALLE T. H., GELLER S. and CORENZWIT E., *Phys. Rev.* **95,** 1435 (1954).
6. GELLER S., MATTHIAS B. T. and GOLDSTEIN R., *J. Amer. Chem. Soc.* **77,** 1502 (1955).
7. MATTHIAS B. T., WOOD E. A., CORENZWIT E. and BALA V. B., *J. Phys. Chem. Solids* **1,** 188 (1956).
8. WOOD E. A. and MATTHIAS B. T., *Acta Cryst., Camb.* **9,** 534 (1956).
9. WOOD E. A., COMPTON V. B., MATTHIAS B. T. and CORENZWIT E., *Acta Cryst., Camb.* **11,** 604 (1958).
10. CORENZWIT E., *J. Phys. Chem. Solids* **9,** 93 (1959).
11. STÜWE H. P., *Trans. Amer. Inst. Min. (Metall.) Engrs.* **215,** 408 (1959).
12. SHOEMAKER D. P., SHOEMAKER C. P. and WILSON F. C., *Acta Cryst., Camb.* **10,** 1 (1957).

13. BRINK C. and SHOEMAKER D. P., *Acta Cryst., Camb.* **8,** 734 (1955).
14. GREENFIELD P. and BECK P. A., *J. Metals, N.Y.* **8,** 265 (1956).
15. RAUB E., *J. Less Common Metals* **1,** 3 (1959).
16. NEVITT M. V. and BECK P. A., *J. Metals, N.Y.* **7,** 669 (1955).
17. NEVITT M. V. and DOWNEY J. W., *J. Metals, N.Y.* **9,** 1072 (1957).
18. HARDY G. F. and HULM J. K., *Phys. Rev.* **93,** 1004 (1954).
19. CHANDRASEKHAR B. S. and HULM J. K., *J. Phys. Chem. Solids* **7,** 259 (1958).

Vol. 1
1961

J. Phys. Chem. Solids Pergamon Press 1961. Vol. 19, Nos. 1/2, pp. 139–146. Printed in Great Britain.

PROPERTIES OF LITHIUM HYDRIDE—III. PARAMAGNETIC RESONANCE OF COLOR CENTERS*

W. BURTON LEWIS and F. E. PRETZEL

Los Alamos Scientific Laboratory, University of California, Los Alamos, New Mexico

(*Received* 7 *October* 1960)

Abstract—Concentrations of F-centers in excess of $10^{17}/cm^3$ have been produced in single crystals of LiH by neutron irradiation at 78°K. The ESR absorption of the F-centers has been observed at $g = 2{\cdot}004 \pm 0{\cdot}001$. The saturation parameter of the ESR absorption $(T_1T_2)^{1/2}$ is close to that for F-centers in KCl. From r.m.s. line width measurements on LiH crystals of various isotopic compositions (Li^7H, Li^7D, Li^6H and Li^6D), spin densities of the F-center electron at the Li^+ and H^- sites have been estimated.

INTRODUCTION

THE PARAMAGNETIC resonance of F-centers in alkali halides has been studied extensively,[1–6] but electron spin resonance (ESR) absorption in irradiated LiH has been reported only for colloidal Li metal centers.[7] In paper II of this series,[8] optical evidence for the existence of the F-center in irradiated LiH was described, although the energy of the F band is anomalous in terms of the Ivey relation for the alkali halides. The purpose of investigating the paramagnetic resonance spectrum of irradiated LiH was threefold: (1) to confirm the assignment of the F band in the optical spectrum through the special properties of the F-center resonance; (2) to estimate the electron spin-density function at the nearest neighbor ion sites through measurements on crystals of different isotopic compositions; and (3) to detect, if possible, any additional color center species such as U- or V-centers.

The F-center resonance absorption is easily saturated, but the line width is independent of concentration and power level. The vacancy model of the F-center, which has been well established by the angular dependence of double resonance measurements,[5,6] accounts for the Gaussian line shape and width of the resonance through the nuclear hyperfine interaction of the F-center electron with the nearest-neighbor nuclei.[2] For the alkali fluorides LiF and NaF, the hyperfine structure has been partially resolved although there is not complete agreement on the interpretation of this structure.[4,6] Even its assignment to the F-center has been questioned.[9]

In LiH the observation of the F-center resonance is not hindered by the presence of other paramagnetic color centers, such as M- or V-centers or trapped hydrogen atoms, with the exception of Li metal colloid centers. The latter are not produced in significant quantities when LiH is irradiated below 80°K, whereas irradiation at room temperature yields only the colloid center resonance.[7] The species H_2^-, corresponding to the V-center in the alkali halides, and atomic hydrogen appear to be unstable with respect to the formation of H_2 in LiH at 77°K. Failure to detect a significant variation in the mean-square line width for various neutron dosages is interpreted as evidence that the ratio of M-centers to F-centers is rather small, in contrast to LORD's observations on LiF, where ratios close to unity were obtained.[10]

The absence of resolved hyperfine structure in the F-center resonance in LiH has made it necessary to study isotopic effects on the line width in order to estimate spin densities at the nearest neighbor Li^+ and H^- sites. For this reason crystals of Li^6D and Li^6H were studied as well

* Work performed under the auspices of the U.S. Atomic Energy Commission.

as normal LiH, and measurements on Li^7D were included as a check. The ratios of the hyperfine fields due to the nearest-neighbor nuclei $h(Li^7)/h(Li^6)$ and $h(H)/h(D)$ are especially favorable for this study, being 2·64 and 6·52 respectively, where h is defined by

$$h_i = \frac{16\pi\mu_i}{3g_e I_i} |\psi(i)|^2 \qquad (1)$$

except for small angular terms[11] which are shown below to be negligible. Here μ_i is the magnetic moment of nucleus i, g_e is the electron spectroscopic splitting factor, I_i is the spin of nucleus i and $\psi(i)$ is the value of the normalized F-center wave function at the nucleus i. Following KIP *et al.*,[2] the external fields at which resonant absorption occurs for a constant frequency ν are given to first order by:

$$H_0 = (h\nu/g_e\beta) - \sum_i h_i I_i^z, \qquad (2)$$

where β is the Bohr magneton, I_i^z is the net component of the nuclear spin in the direction of the field due to the ith shell of equivalent nuclei surrounding the F-center. For a cubic array of spins, one finds that the average value of h_i over all spin arrangements with a particular value of I_i^z is isotropic with respect to the external field H_0. The shape of the absorption line depends on the populations of the various I_i^z states and is approximately Gaussian, the mean-square width being given by

$$\langle(\Delta H)^2\rangle_{av} = \tfrac{1}{3}\sum_i \sum_j h_{ij}^2 I_{ij}(I_{ij}+1) \qquad (3)$$

where the summation is over the j equivalent nuclei in the ith shell.[2] The desired spin-density functions $|\psi(Li)|^2$ and $|\psi(H)|^2$ used in equation (1) are thus obtainable from the mean-square width through equation (3).

EXPERIMENTAL PROCEDURE

1. *Preparation of crystals*

The detailed procedure for the growth of LiH crystals has been described in Paper I of this series.[8] The single crystals were of optical quality except for Li^6D, which was prepared by recrystallization of a previous product, resulting in a slightly cloudy crystal due to Li_2O inclusions.

2. *Neutron irradiation of crystals*

The resonance line-width measurements were made on samples which were irradiated in the external beam of a 5 megawatt reactor at a flux of 4×10^9 n/cm² sec. In order to detect any thermally unstable paramagnetic color centers, the irradiations were carried out at 78°K in an aluminum microwave cavity mounted in a metal dewar, the lower portion of which was also aluminum. In this way the crystals were kept at constant temperature and undisturbed throughout the procedure of neutron irradiation and resonance measurement. Since the absorption half-thickness due to the large thermal neutron cross-section of Li^6 was only about 0·10 mm in Li^6H, the crystal plates containing enriched Li^6 were about 1 mm thick, an amount sufficient to absorb essentially all of the neutrons and resulting triton and α-particle fragments. The crystal plates containing natural Li were about 2 mm thick or less than two half-thicknesses.

It was also found possible to produce F-centers by other techniques. The F-centers produced at 78°K were relatively stable even at room temperature for short periods of time, so that irradiated crystals could be transferred in inert atmosphere boxes to the microwave cavity or optical crystal mount for measurements at low temperature. Over a 15 min period at room temperature, the F-center concentration decreased only about 50 per cent and much more slowly thereafter. Advantage of this stability was taken in order to observe both optical and paramagnetic resonance absorption on the same crystal before and after optical bleaching with F-band light. For this purpose crystals were irradiated near 80°K by projecting samples through the core of the reactor a number of times inside Nylon capsules which were cooled in liquid nitrogen between each pass through the reactor.

A more time-consuming technique consisted of synthesizing the crystals with small amounts of tritium and storing them in liquid nitrogen for weeks or months, but small concentrations of colloid centers and other unidentified centers were simultaneously produced by this method.

3. *Paramagnetic resonance measuremnets*

The F-center ESR absorption was measured with a spectrometer operating at about 9460 Mc

Vol. 1
1961

with frequency stabilization. The spectrometer was a reflection cavity type using a magic-tee bridge, crystal detection (MA 408B video detectors) and optimum microwave bucking. The frequency was stabilized on the sample cavity which operated in the TE_{111} mode and had a Q of about 5000 with the average sample. The power reflected from the cavity at resonance was balanced with respect to phase of the bucking power reflected from the opposite arm of the magic-tee but was slightly unbalanced in amplitude to give a signal proportional to absorption or the imaginary component of the susceptibility when the magnetic field was swept through the resonance value. The derivative of the absorption signal with respect to the field was recorded by modulating the magnetic field at 280 c/s by means of separate coils on the magnet pole faces. The magnet had a 2·0 in. gap with 8·0 in. pole faces truncated to 4·0 in. at the gap. The field was regulated to $\pm$ 0·1–0·2 G and was scanned linearly over about an 800 G or less range, which covered the *F*-center resonance as well as the resonance of an intensity reference of $CuSO_4 \cdot 5H_2O$, the scanning rate in G/in. for the recorder charts was measured by means of a proton resonance magnetometer, and g values were determined by measuring the field deviation from hydrazyl with $g = 2{\cdot}0037$ at a known frequency. The cavity frequency was measured with a calibrated cavity absorption type wavemeter.

Saturation measurements were made over a large range in power level up to 200 milliwatts by comparing the *F*-center ESR absorption derivative intensity with that of the $CuSO_4 \cdot 5H_2O$ standard with the modulation amplitude and other gain adjustments held constant. The microwave power incident on the cavity was measured with a Hewlett-Packard Model 430 C Microwave Power Meter using a precision directional coupler.

F-CENTER RESONANCE

The production of *F*-center concentrations in excess of $10^{17}/cm^3$ in LiH crystals required rather large neutron doses compared to LiF, usually 10^{12} n/cm^3 or more. Concentrations of this magnitude were necessary in order to obtain good signal-to-noise ratios for the limit of 10 G or less modulation amplitude used to avoid distortion of the line shape. On the other hand, doses greater than 2×10^{12} n/cm^3 produced a troublesome quantity of free radicals in the minute amount of cement employed in mounting the crystal specimens in the microwave cavity since the *F*-center production was not linear with neutron dose in this concentration range. The free-radical ESR absorption was scarcely detectable at the low microwave power levels used in the line-width measurements, although a small correction was usually made by saturating the *F*-center ESR signals and estimating their intensity relative to the $CuSO_4 \cdot 5H_2O$ standard at a relatively high power level where the free-radical signal was essentially unsaturated. This procedure also corrected for the colloidal Li metal resonance which frequently appeared in detectable amounts at $g = 2{\cdot}0023$. The free-radical ESR absorption consisted of two rather narrow peaks ($\sim$ 10–15 G maximum slope width) and was observed only in the normal Li crystals for which the doses were 3–4 times greater than for the enriched Li^6 crystals on account of the radiation damage being related to the Li^6 (n,α) reaction. One of these peaks was located near the center of the *F*-center resonance at G = 2·002 and was indistinguishable from the colloidal Li metal peak, while the other peak was about 110 G on the low-field side of the *F*-center.

The saturation characteristics of the *F*-center ESR absorption were studied by measuring intensities relative to a $CuSO_4 \cdot 5H_2O$ standard over a 1000-fold range of power level. Considerable variation of the saturation curve vs. microwave power among different samples was noted, but it was not possible to establish a dependence of relaxation time on concentration of *F*-centers due to (1) the limited concentration range available and (2) the difficulties in estimating absolute concentration from one sample to another because of the effect of sample geometry with respect to the variation of H_1 in the cavity. However, the longest relaxation time was observed in a sample with a high *F*-center concentration. The effect of bleaching the samples with green *F*-band light was particularly noticeable in saturation measurements. Bleached samples always saturated less readily than the same samples before bleaching, suggesting that *F* centers with longer relaxation times were preferentially bleached. This interpretation was also supported by other evidence. The saturation curves on bleached samples departed appreciably from the expression given by PORTIS[3].

$$S(w_0,H_1) \equiv (1+1/4\gamma^2H_1^2T_1T_2)^{-1/2} \quad (4)$$

When $\log(S^{-2}-1)$ is plotted vs. $\log P/P_{max}$, where P is the incident power on the cavity and P_{max} is the maximum incident power, one obtains a slope of unity for a sample having F-centers with uniform relaxation times T_1 and T_2. If the product T_1T_2 is not uniform, there will exist a region of P/P_{max} where $\log(S^{-2}-1)$ vs. $\log P/P_{max}$ has a slope less than unity. Slopes of 0·8–0·9 were obtained on bleached crystals. It was further observed that a crystal doped with Mg^{++} ions contained the largest F-center concentration after irradiation and the longest relaxation time, yet it was easily bleached until the remaining F-center concentration was undetectable (less than 2 per cent of the initial F-center concentration).

The mean value of the relaxation time product $(T_1T_2)^{1/2}$ was estimated from the average intercept of $\log(S^{-2}-1)$ vs. $\log(P/P_{max})^2$ curves for several samples. The intensity of the linearly polarized microwave magnetic field H_1 corresponding to P_{max} is obtained from the relationship below for the TE_{111}-mode cylindrical cavity.

$$(H_1)^2 = \frac{4Q_0P(1-|\Gamma|^2)}{\nu V(1-1/\chi_{11}^2)(1+\chi_{11}^2/p^2R^2)J_1^2(\chi_{11})} \quad (5)$$

where Q_0 is the unloaded or internal Q of the cavity, P is the incident power on the cavity, Γ is the voltage-reflection coefficient of the cavity, ν is the resonant frequency of the cavity, V is the volume of the cavity, $J_1(\chi)$ is the first-order Bessel function, χ_{11} is the first root of the derivative of the first-order Bessel function $J_1^1(\chi)=0$, p equals $\pi/2$, and R is D/L, the ratio of diameter to length of cavity.

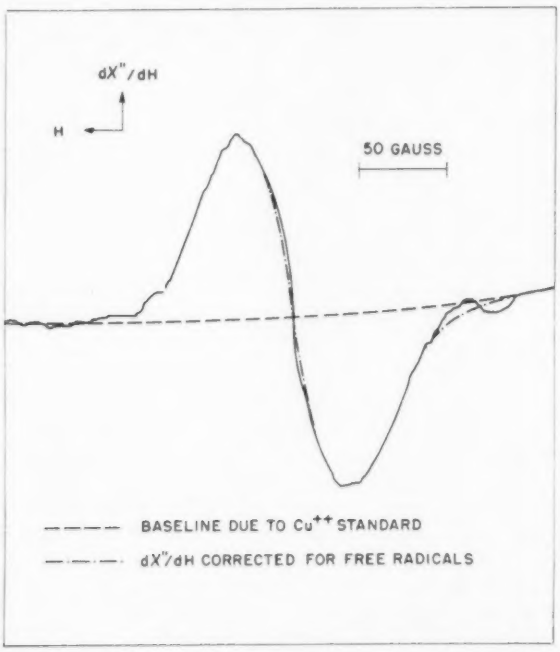

FIG. 1. The derivative of the paramagnetic resonance absorption of the F-center in Li^7H at 78°K.

The value of $(T_1/T_2)^{1/2}$ is approximately 1×10^{-5} sec in LiH at 78°K. However, the variation in $(T_1/T_2)^{1/2}$ among different specimens was about $0{\cdot}3\text{–}3\times10^{-5}$ sec. If T_1T_2 is assumed to vary inversely with the temperature, the value $1{\cdot}5\times10^{-5}$ sec is estimated for KCl at 78°K from the data of PORTIS[3].

Measurements of the mean-square line width from the recorded derivatives of the absorption intensities dX'' (corrected when necessary for impurities) vs. H were made by numerical double integration. The first integration gave the absorption intensity X'' as a function of H. The mean-square width was then obtained from the ratio of the integrals $\int X''H^2dH$ to $\int X''dH$. The average values of the mean-square line width for 2–5 absorption curves on each isotopic composition are presented in Table 1. A typical F-center absorption derivative dX''/dH vs. field curve is shown in Fig 1 for a crystal of nominal composition Li^7H.

Table 1. *Root-mean-square line widths of the F-center resonance in LiH of various isotopic compositions.*

Isotopic composition	Li^7H	Li^7D	Li^6H	Li^6D
R.M.S. width (G)	30·6	28·5	14·3	10·1

The most reliable value of the splitting factor $g = 2{\cdot}004 \pm 0{\cdot}001$ was measured on a crystal of Li^6D, which had the least line width and in which the impurity correction resulting from free-radical formation in the sample cement was nearly negligible.

IDENTIFICATION OF THE OPTICAL *F* BAND

Two intense optical absorption bands at 2·4 eV and 3·5 eV are formed in LiH crystals subjected to neutron irradiation at low temperature. The properties of these bands are described in some detail in Paper II, in which the 2·4 eV band is called the F band and the 3·5 eV band is called the V_1 band. Low temperature bleaching experiments have shown that both bands disappear together—presumably because of the mutual annihilation of the responsible F- and V_1- centers; however, significant intensity differences are obtained when bleaching occurs at high temperatures because of the different rates at which the F-centers aggregate to form M-centers and colloid and the V_1-centers produce higher V-centers. Another way to differentiate between the two optical absorption bands is to bleach a crystal containing an electron-trapping impurity to accelerate the relative rate of the destruction of F-centers during bleaching. Both of these methods have been used to identify the F band by comparisons between the bleaching of the two optical bands and the F-center ESR observed in the crystals.

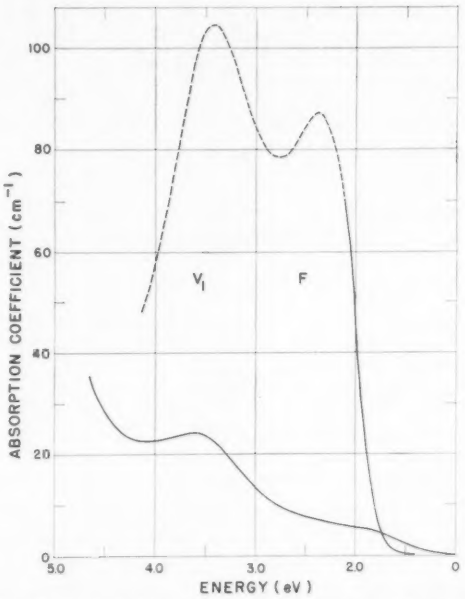

FIG. 2. Optical absorption bands formed in a Mg-doped LiH crystal exposed to 9×10^{13} n/cm² at 80–200°K. Upper spectrum taken after irradiation was too dense for direct measurement beyond 2·1 eV; the dashed portion was obtained from a thinner specimen from the same crystal. Lower spectrum was taken after a 10 min exposure to F light in the cavity at 300°K and the second ESR measurement. Both spectra were recorded at 80°K.

The procedure used in each experiment involved the low temperature neutron irradiation of crystals of "pure" and Mg-doped LiH in a 25 kW homogeneous reactor according to the procedure given in Paper II. Exposure to 9×10^{13} n/cm² generally produced $(1–3)\times10^{17}$ F-centers in the $10\times8\times1$ mm samples irradiated. After exposure the crystals were first mounted for optical absorption measurement and then transferred to the cavity with a $CuSO_4\cdot5H_2O$ intensity standard for ESR measurement. The crystals were bleached with F light from a filtered microscope lamp

focused on the sample inside the cavity for 5 to 10 min at ~ 300°K. In two cases the second ESR measurement was made before the sample was removed from the cavity for optical absorption measurement, but in one case of a "pure" LiH crystal the optical absorption measurement was made before the final ESR measurement.

In the first experiment with a "pure" LiH crystal the optical results compare to those given in curves "a" and "c" Fig. 2 in Paper II. There is not much evidence of a significant 2·4 eV band in the bleached spectrum, but a detailed analysis of the curve using the characteristics of the optical bands reported in Paper II showed that as much as $\frac{1}{4}$ of the original 2·4 eV band remained after bleaching, whereas about $\frac{1}{8}$ of the original 3·5 eV band remained. The ESR measurement made later showed that only $\frac{1}{10}$ of the *F*-centers remained after remounting the sample in the cavity. Although the agreement of ESR result with the 2·4 eV band is closer than with the 3·5 eV band, the uncertainties involved in the comparison are too large for conclusive identification of the *F* band. The experiment was repeated on another LiH crystal with variations in procedure, but the result was similar. The analysis of the curves from both of these bleaching experiments shows one important point, however, in that the absorption by the colloid, *M*, V_2, bands and at 4·5 eV on the tail of the fundamental absorption band rose during the bleaching experiments. Since only the *F*-center ESR and the 2·4 eV and 3·5 eV bands decreased during the bleaching, the possibility that any other optical absorption might be the *F* band is eliminated.

A large difference between 2·4 eV and 3·5 eV band intensities can be obtained by bleaching colored Mg-doped LiH crystals as illustrated in Fig. 9 of Paper II. The results of a study using a neutron-irradiated LiH+0·1 per cent MgH_2 crystal are shown in Fig. 2. The optical absorption of this crystal was extremely intense before bleaching and could only be followed to 2·1 eV, but the curve was completed from the spectrum of a thinner section from the same crystal. The initial spectrum corresponds to about 3×10^{18} centers/cm^3 under the 2·4 eV band and a somewhat higher concentration under the 3·5 eV band; a correspondingly intense *F*-center ESR was observed in the sample. After exposure to *F* light for 10 min at 300°K, the *F*-center ESR in the samples fell below the limit of detection which was estimated as 1/25 of the original intensity. The second spectrum of Fig. 2 with a maximum at the 3·5 eV band and a shoulder at the 1·9 eV colloid band was obtained soon after the ESR measurement. Continued bleaching removed the 1·9 eV band and produced a reduction in the 3·5 eV band, but demonstrated the absence of a significant 2·4 eV band more clearly. Analysis of the spectrum obtained after bleaching showed that the remaining concentration of centers responsible for the 3·5 eV band was at least $5{\cdot}0\times10^{17}$/cm^3 (about 1/6 of the original) compared to an estimated maximum concentration of $0{\cdot}6_5\times10^{17}$/cm^3 centers responsible for the 2·4 eV band (about 1/50 of the original concentration).

These results provide conclusive evidence that the 2·4 eV band is associated with the *F*-center ESR and that it is properly designated as the *F* band. No ESR absorption has been found to correspond to the centers responsible for the 3·5 eV band in this crystal or in others reported in Paper II; therefore, we conclude that the electron-deficient center responsible for this band is diamagnetic. We have called the 3·5 eV band a V_1 band in accordance with the model proposed by KANZIG and WOODRUFF[12] of a V_1 center consisting of a molecule trapped at an anion site.

DISCUSSION

The spin-density functions $|\psi(\mathrm{Li})|^2$ and $|\psi(\mathrm{H})|^2$ are obtained by applying equation (3) to the mean-square width data of Table 1. For the four isotopic compositions one obtains the following relations between the spin densities and the mean-square widths:

$$\mathrm{Li^7H}\langle(\Delta\mathrm{H})^2\rangle_{\mathrm{av}} = 128\pi^2\beta^2N[16{\cdot}46|\psi(\mathrm{Li})|^4+46{\cdot}80|\psi(\mathrm{H})|^4]/9$$

$$\mathrm{Li^6H}\langle(\Delta\mathrm{H})^2\rangle_{\mathrm{av}} = 128\pi^2\beta^2N[2{\cdot}249|\psi(\mathrm{Li})|^4+46{\cdot}80|\psi(\mathrm{H})|^4]/9$$

$$\mathrm{Li^7D}\langle(\Delta\mathrm{H})^2\rangle_{\mathrm{av}} = 128\pi^2\beta^2N[16{\cdot}46|\psi(\mathrm{Li})|^4+1{\cdot}470|\psi(\mathrm{H})|^4]/9$$

$$\mathrm{Li^6D}\langle(\Delta\mathrm{H})^2\rangle_{\mathrm{av}} = 128\pi^2\beta^2N[2{\cdot}249|\psi(\mathrm{Li})|^4+1{\cdot}470|\psi(\mathrm{H})|^4]/9. \quad (6)$$

Vol. 1
1961

The factors associated with the spin densities in equations (6) are $\mu^2(I+1)/I$, where μ is the nuclear moment in nuclear magnetons. The mole fractions of the Li isotopes differed appreciably from 100 per cent, so that $\langle\mu^2\rangle_{\text{av}} = \mu^2(\text{Li}^6)f(\text{Li}^6) + \mu^2(\text{Li}^7)f(\text{Li}^7)$, f being the mole fraction of a particular isotope. The Li isotopic compositions used in preparing the crystals were 92·6 per cent Li^7, 7·4 per cent Li^6 and 5·5 per cent Li^7, 94·5 per cent Li^6. The three pairs of spin-density solutions from the first three equations in (6) are fairly close together, and we have chosen their mean values $|\psi(\text{Li})|^2 = 0{\cdot}118\times10^{24}/\text{cm}^3$ and $|\psi(\text{H})|^2 = 0{\cdot}025\times10^{24}/\text{cm}^3$ as the best fit of the experimental data. The agreement obtained from the fourth equation is poor only for $|\psi(\text{H})|^2$ and results in part from the fact that the width ratio Li^7D:Li^6D is rather insensitive to this parameter and in part from the greater experimental error in the Li^6D width.

The value of $|\psi(\text{H})|^2$ is of particular interest since it is lower by a factor of 6 than the most recent results of HOLTON *et al.*[6] for $|\psi(\text{F})|^2$ in LiF. This decrease in $|\psi|^2$ at the anion site is expected from an F-center wave function of the type proposed by GOURARY and ADRIAN[13] on account of the additional terms $B_i\psi_i$ for the F^- $2s$ and $2p$ electrons in their equation (54). LORD's much smaller value of $|\psi(\text{F})|^2$[6] is not consistent with our value of $|\psi(\text{H})|^2$ for this F-center wave function. A calculation of $|\psi(\text{H})|^2$ for the GOURARY and ADRIAN wave function was not attempted because the expansion of the overlap integral used by them is a very poor approximation for the H^- ion.

The value of $g = 2{\cdot}004 \pm 0{\cdot}001$, while larger than $g_e = 2{\cdot}0023$ by more than the estimated limit of error, differs from LORD's value[4] for LiF, $g = 2{\cdot}0029 \pm 0{\cdot}0001$ by no more than the experimental error. The result of WOLGA and STRANDBERG[14] on LiF on the other hand is $g = 1{\cdot}987 \pm 0{\cdot}0004$. A small part of this discrepancy was found to arise from the difference in the second-order corrections to g applied by these authors. This has led us to re-examine the second-order correction. It is believed that both of their estimates of this correction are in error, that of LORD being too small by the factor 6·2 and that of WOLGA and STRANDBERG being too large by the factor 5·8. The latter authors assumed $I = 9$ in their term $[I(I+1)-I_z^2]$, whereas this represents the total I for only 19 of the 4096 nuclear spin states for six nearest neighbor nuclei with individual $I = 3/2$, the average value of $I(I+1)$ being 15·4 rather than 90. In LORD's expression the second-order term was summed over only one nucleus rather than all six.

The proper second-order correction can be obtained if we set up the energy matrix in the representation M_s, $m_1, \ldots, m_6$, which are the individual magnetic states of the F electron and nearest neighbor nuclei. All non-diagonal elements for H_0 along z will be zero in this representation except for $\langle M_s \pm 1,\ m_1 \mp 1,\ \ldots\ |S\cdot I|M_s, m_1, \ldots\rangle$. The frequencies to second order in $[h(\text{Li})/H_0]$ for the allowed transitions $\Delta M_s = \pm 1$, $\Delta m_i = 0$ are given by

$$\hbar\omega = g_e\beta H_0\{1 + \sum_i^6 (h_i/H_0)m_i + \sum_i^6 (h_i/H_0)^2[I(I+I)-m_i^2]/2\}. \qquad (7)$$

To obtain the second-order correction to g for Li^7H, however, the second-order term in (7) must be averaged over all 580 nuclear states corresponding to $\sum m_i = 0$. For Li^7 with $I = 3/2$, the factor $\langle I(I+I)-m_i^2\rangle_{\text{av}}$ for these states is 15·4.

The second-order correction to g from the hydride ion nuclei can be found by extending the summation in (7) to the shell of twelve nearest hydride ions. For all isotopic compositions of LiH the total second-order correction to g is considerably less than the experimental error $\pm$ 0·001. For LiF the total second-order correction, however, is $-0{\cdot}0011$ based on the recent measurements of HOLTON *et al.*,[6] which reduces even LORD's value for LiF[4] to $g = 2{\cdot}0019$. Unless one attaches special significance to HYDE's value of $g = 2{\cdot}007$, ADRIAN's interpretation of the positive Δg for LiF[15] seems unnecessary.

Acknowledgements—The authors are greatly indebted to the personnel of the Omega reactor facilities of this laboratory for their generous cooperation throughout the many crystal irradiations required by these measurements, and to Dr. P. WALDSTEIN for numerous discussions of the theory. We also thank Dr. R. J. FRIAUF for encouragement and cooperation with the preliminary experiments.

REFERENCES

1. HUTCHISON C. A., Jr. and NOBLE G. A., *Phys. Rev.* **87,** 1125 (1952).
2. KIP A. F., KITTEL C., LEVY R. A. and PORTIS A. M., *Phys. Rev.* **91,** 1066 (1953).
3. PORTIS A. M., *Phys. Rev.* **91,** 1071 (1953).
4. LORD N. W., *Phys. Rev.* **105,** 756 (1957).
5. FEHER G., *Phys. Rev.* **105,** 1122 (1957).
6. LORD N. W., *Phys. Rev. Letters* **1,** 170 (1958); HOLTON W. C., BLUM H. and SLICHTER C. P., *Phys. Rev. Letters* **5,** 197 (1960).
7. DOYLE W. T., INGRAM D. J. E. and SMITH M. J. A., *Phys. Rev. Letters* **2,** 497 (1959); GUERON M. and RYTER C. H., *Phys. Rev. Letters* **3,** 338 (1959).
8. PRETZEL F. E., RUPERT G. N., MADER C. L., STORMS E. K., GRITTON G. V. and RUSHING C. C., *J. Phys. Chem. Solids* **16,** 10 (1960) (Paper I); PRETZEL F. E. and RUSHING C. C., *J. Phys. Chem. Solids* **17,** 232 (1961) (Paper II).
9. HYDE J. S., *Phys. Rev.* **119,** 1483 (1960).
10. LORD N. W., *Phys. Rev.* **106,** 1100 (1957).
11. ZELDES H., TRAMMEL G. T., LIVINGSTON R. and HOLMBERG R. W., *J. Chem. Phys.* **32,** 618 (1960).
12. KÄNZIG W. and WOODRUFF T. O., Jr., *J. Phys. Chem. Solids* **9,** 70 (1959).
13. GOURARY B. S. and ADRIAN F. J., *Phys. Rev.* **105,** 1180 (1957).
14. WOLGA G. J. and STRANDBERG M. W. P., *J. Phys. Chem. Solids* **9,** 309 (1959).
15. ADRIAN F. J., *Phys. Rev.* **107,** 488 (1957).

Vol. 1
1961

J. Phys. Chem. Solids Pergamon Press 1961. Vol. 19, Nos. 1/2, pp. 147–154. Printed in Great Britain.

ELECTRICAL AND OPTICAL PROPERTIES OF InAs–In_2Te_3 ALLOYS

J. C. WOOLLEY, B. R. PAMPLIN and J. A. EVANS

Department of Physics, University of Nottingham, England

(*Received* 25 *July* 1960)

Abstract—The production of suitable InAs–In_2Te_3 alloys by annealing and by directional freezing methods is considered and the relevance of the second method to the phase diagram of the system is discussed. The results of measurements of Hall effect, conductivity, thermoelectric power and infra-red absorption are given for the whole composition range, and values of carrier density n, mobility μ and optical energy gap E_g are obtained. It is seen that the behaviour is similar to that of InSb–In_2Te_3 alloys in that the InAs rich alloys are highly degenerate having $n \approx 5 \times 10^{19}/cm^3$ and explanations of this behaviour in terms of solubility of tellurium in InAs or of the band structure of InAs are discussed. The variation of μ with composition and hence possible scattering mechanisms and types of conduction occurring in the alloys are considered. Assuming certain scattering effects, attempts are made to use the values of thermoelectric power in conjunction with the measured values of E_g to determine the variation of intrinsic energy gap throughout the composition range.

1. INTRODUCTION

In_2Te_3 has a defect zinc blende structure with one lattice site in three on the A sub lattice vacant, (or alternatively a defect antifluorite A_2B structure with two lattice sites in three on the A sub lattice vacant[1]). Thus, when In_2Te_3 is alloyed with a normal $A^{III}B^{V}$ zinc blende type compound such as InSb or InAs, the resulting alloy will have some A sub lattice sites vacant, the exact fraction being determined by the composition of the alloy. The electrical properties of such alloys may therefore be of interest in that a controlled number of lattice vacancies can be introduced into the alloy.

In a recent paper[2] the properties of alloys formed by solid solution of In_2Te_3 in InSb have been discussed. In that case the range of composition available to measurement is limited to the available range of solid solution of approximately 15 mol. per cent In_2Te_3* for alloys annealed close to the solidus of the system. As has been shown previously[3] in the case of the InAs–In_2Te_3 system solid solution is obtained throughout the whole range of composition. Thus the limitations of the InSb–In_2Te_3 system do not apply in this case and hence it is possible to investigate the variation of the various semiconductor parameters over a much wider range of composition and to investigate the gradual transition from the normal type semiconductor InAs to the defect structure In_2Te_3.

The present paper reports an investigation of some properties of this alloy system. The alloy system GaAs–Ga_2Se_3 should show similar behaviour[3] and recently NASLEDOV and FELTIN'SH[4] have reported electrical measurements on these alloys. Unfortunately, measurements of conductivity and thermo-electric power only and not of Hall effect were made in this work and so the usefulness of the results is somewhat limited, as separate values of number of carriers and mobility cannot be determined.

2. PREPARATION OF SPECIMENS

The In_2Te_3 was prepared from indium of 99·999 per cent purity and commercial high purity tellurium which had been purified by repeated distillation. Some of the initial measurements were made

* In calculating mol. percentage in systems composed of one $A^{III}B^{V}$ compound and one $A_2^{III}B_3^{VI}$ compound, the molecules have been taken as $A_3^{III}B_3^{V}$ and $A_2^{III}B_3^{VI}$, i.e. the percentage is strictly the percentage of B^{V} and B^{VI} atoms on the B sub lattice.

on specimens using InAs of rather high carrier concentration, but the InAs used in the majority of the work was of good purity having approximately 3×10^{16} carriers/cm^3. Some of the alloys were prepared from the two compounds by melting together the required amounts under vacuum, the resulting ingots then being annealed at a suitable temperature to obtain a good equilibrium condition. The annealing temperatures lay in the range 650°C to 800°C, the actual value in each case being determined by the composition of the alloy concerned. As has been shown previously[3] there is evidence of a closed miscibility gap in this system, and hence it was necessary to anneal each alloy at a temperature above the miscibility gap limit but below the solidus, neither of these curves having as yet been accurately determined. The majority of the specimens were annealed for some 6 or 7 weeks and X-ray photographs then showed that good single phase conditions had been attained in all alloys except those lying in the range 10–35 mol. per cent In_2Te_3, where a blurring of the lines in the X-ray photograph showed that even after this time of annealing these particular alloys were still partly inhomogeneous.

It had already been noted during the initial X-ray work[3] that it was very difficult to attain equilibrium with alloys in this composition range and the results in that case were based on slightly inhomogeneous alloys. The results obtained during the present work tend to indicate that the mean lattice parameter curve shown previously[3] is probably too high in this range but is correct beyond 35 mol. per cent In_2Te_3. This will be discussed elsewhere when further crystallographic work has been carried out.

A second method used to produce suitable alloys was to directionally freeze a suitable ingot. This technique has been very useful in alloys of two $A^{III}B^{V}$ compounds[5] since, provided the rate of freezing is sufficiently slow to obtain good equilibrium conditions, the alloy composition varies continuously along the ingot giving a useful range of composition in a single ingot. The problem in the case of InAs–In_2Te_3 alloys was that the appropriate section of the ternary diagram As–In–Te is not truly pseudobinary as shown by the behaviour in the miscibility gap and therefore it was not certain that sections cut from the directionally frozen ingot would be alloys on the InAs–In_2Te_3 section of the ternary diagram. Nevertheless an ingot of length 17 cm and mean composition 66 mol. per cent In_2Te_3 was directionally frozen so that there was a temperature gradient of approximately 5°C/cm. along the ingot and the freezing surface travelled along the ingot at about 1·5 cm/day. Sections were taken from positions at 1·7, 5·0, 14·0 cm along the ingot and chemically analysed, and these were found to have compositions of the form $x In_3As_3 (1-x) In_2Te_3$ within a limit of 1 per cent. Also sections from various points along the ingot were X-rayed and found to show the zinc blende structure associated with InAs–In_2Te_3 alloys.[3] It was therefore assumed that the solidus–liquidus area of the InAs–In_2Te_3 system shows pseudo-binary behaviour and that all cross sections cut from the ingot represented stoichiometric InAs–In_2Te_3 alloys. Such sections were used for measurements, the composition of the section being found by determining the lattice parameter and comparing this with the previous results for this system[3] and with the chemically analysed specimens mentioned above. In some of these sections the high angle X-ray lines were found to be just split into two lines indicating that some sections of the ingot had cooled into the top of the closed miscibility gap. This effect appeared to be quite small, however, and the results from all specimens were found to be in good agreement with those obtained from the lump annealed ingots.

3. METHODS OF MEASUREMENTS AND RESULTS

Conductivity and Hall coefficient were investigated for alloys of various compositions. For alloys containing less than 50 mol. per cent In_2Te_3 measurements were made over a range of temperature from liquid air to room temperature, while for alloys with more than 50 mol. per cent In_2Te_3 the conductivity became so low at low temperatures that only room temperature measurements were made. The methods used for the measurements were the same as those described previously for the InSb–In_2Te_3 alloys.[2] Optical measurements were also made on all alloys to determine the value of optical energy gap E_g at room temperature and again the method was the same as described previously.[2]

For alloys of less than 70 mol. per cent In_2Te_3 measurements were made of thermoelectric power

Vol. 1
1961

over the temperature range from liquid air to room temperature. A conventional apparatus was used for these measurements, the temperature gradient being produced by means of a heat source consisting of a heating coil wound on a solid copper cylinder and coated with alumina and a heat sink in the form of a copper block. On either side of the specimen and insulated from both source and sink by thin sheets of mica two copper electrodes were placed. Set into these were two calibrated chromel alumel thermocouples used to obtain the temperature difference ΔT across the specimen, and a lead was taken from each electrode to the potentiometer to determine the potential

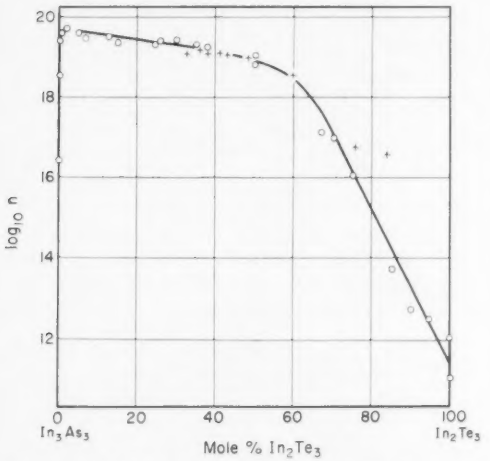

FIG. 1. Variation of room temperature carrier concentration n with composition.

° Annealed specimens. + Directionally frozen specimens.

ΔV across the specimen. The whole apparatus was enclosed in either a tubular furnace or in a vacuum flask to provide the required ambient temperature. $\Delta V/\Delta T$ was taken as the thermoelectric power at the ambient temperature, ΔT being usually of the order 5°C. This was the thermoelectric power relative to copper, but in all cases the correction for this was assumed to be negligible.

For the alloys for which electrical measurements were made over a range of temperature (i.e. those with less than 50 mol. per cent In_2Te_3) it was found that the values of conductivity σ and Hall coefficient R_H and hence the derived Hall mobility

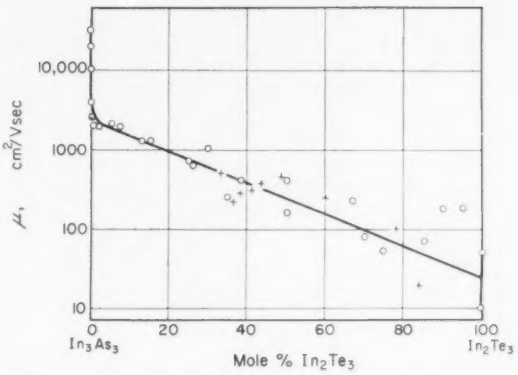

FIG. 2. Variation of room temperature electron mobility μ with composition.

° Annealed specimens. + Directionally frozen specimens.

μ were practically independent of temperature. In all such cases the carrier concentration n as determined from the Hall coefficient was greater that $10^{19}/cm^3$ indicating the material to be highly degenerate. In order to compare the values of

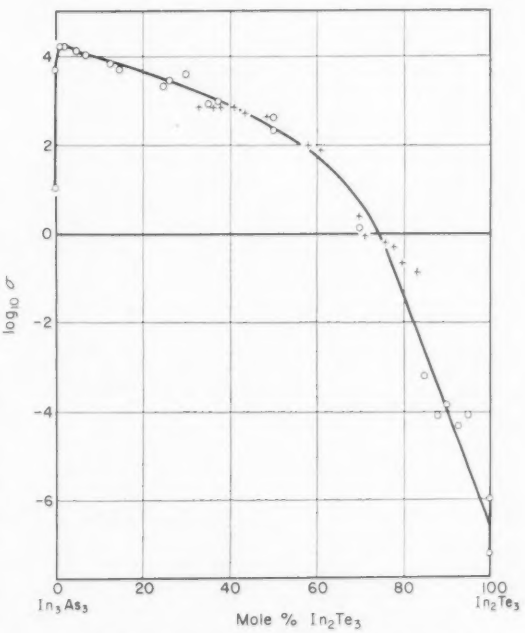

FIG. 3. Variation of room temperature conductivity σ with composition.

° Annealed specimens. + Directional frozen specimens.

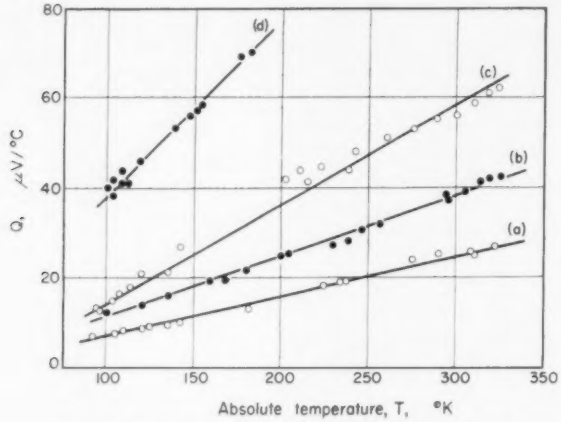

FIG. 4. Variation of thermoelectric power Q with temperature for typical specimens.
(a) 15 mol. per cent In_2Te_3 (c) 49 mol. per cent In_2Te_3
(b) 37·5 mol. per cent In_2Te_3 (d) 69 mol. per cent In_2Te_3

n, μ and σ for the various compositions, it was therefore necessary to consider only the room temperature values and the variations of room temperature values of n, μ and σ with composition are shown in Figs. 1–3. The two points shown on each graph for In_2Te_3 itself represent the values for ordered and disordered state of the compound.

The variation of thermoelectric power Q with temperature for a number of typical specimens is shown in Fig. 4. It was found that for all alloys investigated, Q was directly proportional to the absolute temperature T. This is as expected in degenerate material and the value of Q/T can be directly related to the height of the Fermi

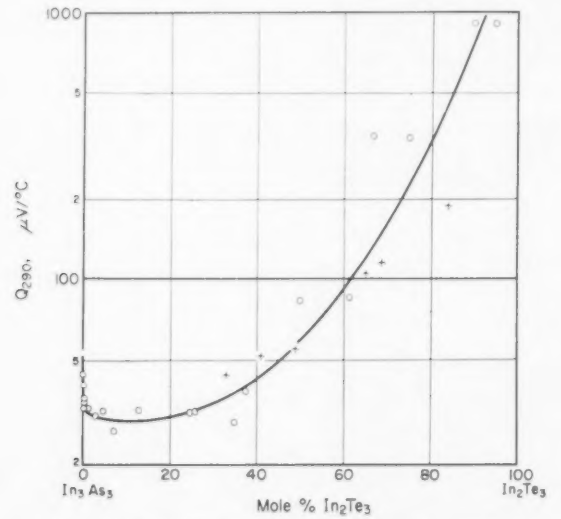

FIG. 5. Variation of room temperature thermoelectric power Q_{290} with composition.
° Annealed specimens. + Directionally frozen specimens.

level in the conduction band. The variation of the room temperature value of $Q(Q_{290})$ with composition is shown in Fig. 5 where the value of Q_{290} is given for alloys ranging from pure InAs to 90 mol. per cent In_2Te_3. The form of this curve is very similar to that for the GaAs–Ga_2Se_3 alloys[4] over the range 0–70 mol. per cent Ga_2Se_3. In the latter case beyond 70 mol. per cent the value of Q falls and becomes negative because of the p-type behaviour of Ga_2Se_3.

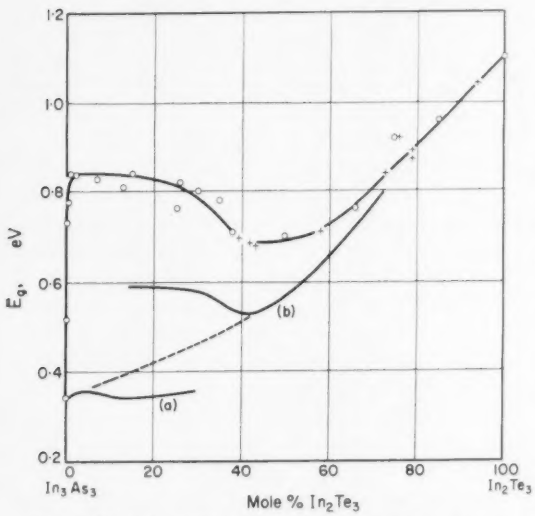

FIG. 6. Variation with composition of room temperature optical energy gap E_g and values of intrinsic energy gap E_{g0} calculated for different values of scattering coefficient s.

(a) $s = +\frac{1}{2}$ (b) $s = -\frac{1}{2}$

° Annealed specimens. + Directionally frozen specimens.

In Fig. 6 the variation of optical energy gap E_g is shown as a function of composition. It is seen that in the range from 0–60 mol. per cent In_2Te_3 where the material is highly degenerate, the results show a very considerable filling of the conduction band and the optical measurements do not give the intrinsic energy gap. In the range from 5 to 35 mol. per cent In_2Te_3 there is some spread in the experimental points. Three factors contribute to this effect. Firstly, as the level to which the conduction band is filled depends upon the carrier concentration there will be a real variation from one specimen to another depending upon the value of n in each case. Secondly, with the large carrier concentration in this range, the resulting free carrier absorption will be large and hence the accuracy in determination of E_g will be less here than elsewhere. Finally, as already indicated the alloys in this range were inhomogeneous to some extent and this factor can affect the shape of the absorption vs. wavelength curve and hence the determination of E_g. Thus the values of E_g in this range are only approximate.

4. DISCUSSION

The results for alloys of low In_2Te_3 content are very similar to those for the InSb–In_2Te_3 system,[2] where solid solution is limited to 15 mol. per cent In_2Te_3, and to the conductivity measurements in the GaAs–Ga_2Se_3 system.[4] Thus as In_2Te_3 is added to InAs the value of n rises rapidly and reaches a maximum of $5\times10^{19}/cm^3$ at 2 mol. per cent In_2Te_3. It then drops slowly reaching a value of $8\times10^{18}/cm^3$ at 50 mol. per cent In_2Te_3. As indicated previously,[2] it would appear that initially when In_2Te_3 is added to InAs (or InSb) the In and Te atoms enter the lattice without leaving lattice vacancies and the Te atoms in the As lattice act as donors. As the concentration of Te is increased some lattice vacancies appear and beyond 2 mol. per cent In_2Te_3 each In_2Te_3 molecule added causes the associated vacancy on the In lattice. On this basis the maximum carrier concentration of $5\times10^{19}/cm^3$ would be determined by the limit of solid solution of Te in InAs. A second possible explanation can be put forward however if it is suggested that the maximum observed value of n of $5\times10^{19}/cm^3$ is determined by the band structure of InAs. On this basis it would be postulated that solid solution of Te continues beyond the value corresponding to 5×10^{19} carriers/cm^3 but that the resulting electrons enter the conduction band in a region where they have considerably larger effective mass than the electrons at the normal band minimum and hence would contribute very little to the Hall coefficient and would not be effectively observed. Two factors which possibly favour this second explanation can be cited. Firstly, the results of adding In_2Se_3 to InAs and to InSb[6] give maximum values of n of $6\times10^{19}/cm^3$ and $9\times10^{18}/cm^3$ respectively which are very similar to the values when In_2Te_3 is added to the compounds. Secondly, for every

three Te atoms giving electrons in the conduction band there will be one lattice vacancy less than the number expected from the stoichiometric formula and this should cause a small increase in density. Unfortunately specimens with less than 37 mol. per cent were found to contain numerous blowholds which render density measurements inaccurate. At higher percentage and particularly for the directionally frozen ingot the specimens were more uniform and hence density measurements were made on various samples. The values obtained appeared to be nearly 1 per cent higher than those expected from the values of lattice parameter and stoichiometric formulae. It was considered, however, that this difference probably lay within the limits of experimental error. Until further evidence is available it is difficult to decide which of the postulated explanations is more correct.

The variation in the n vs. composition curve for alloys with more than 50 mol. per cent In_2Te_3 is very large and as seen from Fig. 1 the room temperature value of n falls from $4\times10^{18}/cm^3$ at 50 mol. per cent In_2Te_3 to approximately $5\times10^{11}/cm^3$ for In_2Te_3 itself. While the return to a stoichiometric condition could explain a fall of two or three orders of magnitude in n, corresponding to the rise in n from the value at InAs to that at 5 mol. per cent In_2Te_3, the much larger change in n of seven orders of magnitude needs further explanation. Various factors have to be considered in discussing this large change. Firstly, bearing in mind the suggestions of JOFFE[7], ZENER[8], and others it is possible that the normal ideas of conduction cannot be applied to In_2Te_3 and that "hopping" conduction must be considered. If this is so, it is not certain that the value of n obtained here from Hall data can be correlated with the values obtained for the more normal substance such as InAs and the high percentage InAs alloys. If it is assumed that the value of n has its normal significance, it is necessary to explain this very large fall in carrier concentration. In this range of composition the energy gap has such a value that we are dealing with impurity carriers at room temperature. An obvious suggestion is that the donor levels are depressed as In_2Te_3 is added and the impurity activation energy is therefore increased. A factor of 10^7 in carrier concentration could be explained by a change in position of donor levels from approximately 0·01 eV below the conduction band, a value typical of normal $A^{III}B^{V}$ compounds, to the centre of the forbidden gap in In_2Te_3 itself. Such an effect could explain the very low carrier concentration observed in In_2Te_3.[9]

Because of the nature of In_2Te_3 however, other explanations are possible for the very low carrier concentration observed in this compound. With the preparation described above, it would be expected from experience with other intermetallic compounds that the In_2Te_3 would contain impurities of the order $10^{17}/cm^3$ or more, and that some reasonable proportion of these would act as donors or acceptors. But as has been shown, In_2Te_3 will take into solid solution both $A^{III}B^{V}$ compounds such as InAs and $A^{II}B^{VI}$ compounds such as CdTe[10] and for low percentages of these substances the ideal stoichiometry may be lost. Thus it is possible that small amounts of elements from the 2nd, 3rd, 4th, 5th or 6th columns of the periodic table can be accommodated in the lattice, and by suitable loss or gain of lattice vacancies the electron concentration can remain at a value of 4 electrons per site. With such an electron distribution, no donors or acceptors would be present in the lattice and no impurity levels, in the usual semiconductor sense, would occur. An important factor in this case is the possibility, as yet unconfirmed,[1] that In_2Te_3 has a defect antifluorite rather than a defect zinc blende structure. It this were the case, the presence of the enantiomorphous fluorite sites would give even more flexibility in the lattice to accommodate impurity atoms.

If the behaviour of In_2Te_3 is as described above, the very rapid fall in n over the range of alloys from 50 mol. per cent In_2Te_3 to In_2Te_3 itself can be looked upon as a gradual transition from the normal impurity behaviour of the InAs rich alloys to the effectively intrinsic behaviour of In_2Te_3.

The variation of mobility μ with composition (Fig. 2) shows that μ falls very rapidly from 30,000 for InAs to 2000 at 2 mol. per cent In_2Te_3 and then falls more slowly to a value between 10 and 50 for In_2Te_3. Various scattering mechanisms can be postulated to explain this reduction in μ, but such a discussion must be linked with the considerations of the alloying effects given above. Over the first few per cent of In_2Te_3 the predominant scattering effect could be due to ionized tellurium atoms or to neutral tellurium atoms and

lattice vacancies in the lattice. It is of interest to note that up to 15 mol. per cent In_2Te_3 a logarithmic plot (Fig. 7) shows that μ varies approximately as $N^{-1/3}$ where N represents the concentration of In_2Te_3. The same type of result was obtained with the InSb–In_2Te_3 alloys. At higher concentrations of In_2Te_3 the scattering is almost certainly due to the presence of lattice impurities and at such high densities that alloy scattering is relevant. In this range the possibilities of antifluorite structure and "hopping" conduction become important. Some further evidence on scattering mechanisms may be obtained from a consideration of the thermoelectric effects.

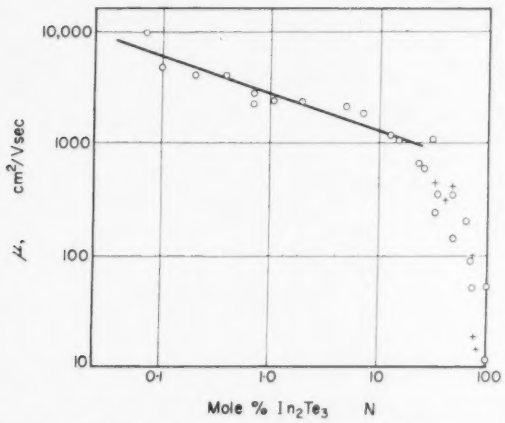

FIG. 7. Variation of $\log_{10}\mu$ with $\log_{10}N$ where N is In_2Te_3 concentration.

° Annealed specimens. + Directionally frozen specimen.

As indicated above for degenerate material the thermoelectric power Q is found to be directly proportional to the absolute temperature T, and the value of Q/T can be used to determine the height of the Fermi level (ζ) above the conduction band minimum. The appropriate equation[11] is

$$Q = -\frac{k}{e}\frac{\pi^2}{2}\frac{kT}{\zeta}\left[1+\frac{2}{3}\left(\frac{E}{\tau}\frac{d\tau}{dE}\right)_{E=\zeta}\right]$$

and if it is assumed that

$$\tau \propto E^s$$

then

$$Q = -\left(\frac{3+2s}{6}\right)\frac{\pi^2k^2T}{e\zeta}$$

A determination of (ζ) from Q thus requires a knowledge of s which depends upon the particular scattering mechanism concerned. The two mechanisms expected to predominate are ionized impurity scattering at low In_2Te_3 content and alloy scattering at higher In_2Te_3 content. Thus values of ζ have been calculated from the mean Q vs. composition curve assuming that $s = -\frac{1}{2}$ for alloy scattering[12] and $s = +\frac{1}{2}$ for ionized impurity scattering,[13] and these values of ζ subtracted from the optical values of E_g. The resultant values should approximate to the intrinsic energy gap E_{g0}, and these are plotted in Fig. 6. In the range 40–70 mol. per cent In_2Te_3 the values of E_{g0} obtained by assuming $s = -\frac{1}{2}$ are consistent with the values of E_g from 70–100 mol. per cent In_2Te_3, in which range the carrier concentration is so small that the optical value is the intrinsic gap. Also, using $s = +\frac{1}{2}$, the values of E_{g0} at low In_2Te_3 concentrations are in good agreement with the intrinsic gap for InAs itself. Thus it would appear correct to assume that alloy scattering is predominant in the range 40–70 mol. per cent In_2Te_3 and ionized impurity scattering for compositions from InAs to approximately 5 mol. per cent In_2Te_3. It cannot be seen from these results what values of E_{g0} apply in the range 5–40 mol. per cent In_2Te_3, but it seems unlikely that in this range either of the plotted E_{g0} curves are applicable. Probably no single scattering mechanism predominates, but that alloy scattering increasingly dominates over ionized impurity scattering.

With highly degenerate material the value of ζ can be used to determine an effective mass (m_n) of the conduction electrons, the equation

$$n = \frac{8\pi}{3}\frac{(2m_n)^{3/2}}{h^3}\zeta^{3/2}$$

giving a "density of states" effective mass. If the values of ζ for alloys containing up to 3 mol. per cent In_2Te_3 are used in this way values for m_n lying between 0·08 m_0 and 0·09 m_0 are obtained, (m_0 being the free electron mass). For alloys of In_2Te_3 content rather higher than this the values of ζ are not known but from Fig. 6 a rough estimate can be made, shown by the dotted line, and this indicates values of m_n similar to those for the lower percentage alloys. As the values are almost three times the accepted value for non-degenerate InAs it

appears that the InAs band shows considerable deviation from parabolic form at these values of electron concentration. The values obtained here are consistent with the values calculated by STERN[14] using a KANE type[15] model for InAs.

In alloy systems of this type the possibility of ordering at various special compositions should be considered. An investigation of the possible types of ordering in this case[16] indicates that the most probable percentages at which ordering may occur are 75 mol. per cent In_2Te_3, 50 mol. per cent In_2Te_3 and 37·5 mol. per cent In_2Te_3 where the formulae of the alloys would be $In_3 \square AsTe_3$, $In_5 \square As_3Te_3$ and $In_7 \square As_5Te_3$ respectively (where $\square$ indicates a lattice vacancy). No direct X-ray evidence has been obtained at any of these compositions but some evidence in the case of the 75 mol. per cent In_2Te_3 alloy may be obtained from the optical data, for Fig. 6 shows the values of E_g at this percentage significantly above the mean curve for E_g values in this range. It is of interest to note that in an analogous system InAs–In_2Se_3 ordering at the 75 mol. per cent In_2Se_3 composition has been reported.[17]

Acknowledgements—The authors are indebted to Professor L. F. BATES for the facilities of his laboratory. The work described forms part of an investigation carried out for the Admiralty.

REFERENCES

1. WOOLLEY J. C., PAMPLIN B. R. and HOLMES P. J. *J. Less Common Metals* **1,** 362 (1959).
2. WOOLLEY J. C., GILLETT C. M. and EVANS J. A., *J. Phys. Chem. Solids* **16,** 138 (1960).
3. WOOLLEY J. C. and SMITH B. A., *Proc. Phys. Soc. Lond.* **72,** 867 (1958).
4. NASLEDOV D. N. and FELTIN'SH I. A., *Soviet Phys. Solid State* **1,** 510 (1959).
5. WOOLLEY J. C., EVANS J. A. and GILLETT C. M., *Proc. Phys. Soc. Lond.* **74,** 244 (1959).
6. WOOLLEY J. C. and KEATING P. N., to be published.
7. JOFFE A. F., *J. Phys. Chem. Solids* **8,** 6 (1959).
8. ZENER C., *J. Phys. Chem. Solids* **8,** 26 (1959).
9. WOOLLEY J. C. and PAMPLIN B. R., to be published.
10. WOOLLEY J. C. and RAY B., *J. Phys. Chem. Solids* **15,** 27 (1960).
11. BARRIE R. and EDMOND J. T., *J. Electronics* **1,** 161 (1955).
12. NORDHEIM L., *Ann. Phys., Lpz.* **9,** 607 (1931).
13. SCLAR N., *Phys. Rev.* **104,** 1548 (1956).
14. STERN F., *Bull. Amer. Phys. Soc.* (ser. 2) **4,** 28 (1959).
15. KANE E. O., *J. Phys. Chem. Solids* **1,** 249 (1957).
16. PAMPLIN B. R., *Nature, Lond.* **188,** 136 (1960).
17. GORYUNOVA N. A. and RADAUTSAN S. I., *Soviet Phys. Tech. Phys.* **3,** 1762 (1958).

J. Phys. Chem. Solids Pergamon Press 1961. Vol. 19, Nos. 1/2, pp. 155–166. Printed in Great Britain.

THE ROLE OF PHONONS IN PARAMAGNETIC RELAXATION*†

B. W. FAUGHNAN‡ and M. W. P. STRANDBERG

Department of Physics and Research Laboratory of Electronics, Massachusetts Institute of Technology, Cambridge, Massachusetts

(*Received* 27 *September* 1960)

Abstract—The coupled spin–lattice-bath system is investigated under conditions of microwave power saturation and the conditions for the existence of a steady-state nonthermal equilibrium phonon distribution are determined. The spin–lattice-bath equations are solved numerically for a few special cases involving a nonequilibrium distribution of phonons. The results of an experiment designed to detect the presence of nonequilibrium phonons are reported. No indication of the presence of such phonons was found. The experiments were performed using Cr^{3+} impurities in MgO, Al_2O_3 and $K_3Co(CN)_6$ and at $T = 4{\cdot}2°K$ and 2°K. The sensitivity of the experiment was such that for ruby a phonon temperature rise of $\Delta T = 0{\cdot}005T$ could have been observed. Finally, the validity of the theory, in view of the experimental results, is discussed.

INTRODUCTION

ACCORDING to current theories of thermal relaxation in paramagnetic crystals,[1,2] the electron spin–lattice relaxation is a direct process at low temperatures. That is, the spin-flip is accompanied by the creation of a single phonon whose frequency is equal to the resonant frequency of the paramagnetic transition.[1] If the phonons in contact with spins are assumed to remain at the bath temperature, then the spin–lattice relaxation is a simple exponential decay. However, at liquid helium temperatures, the spin specific heat is very much larger than the phonon specific heat, and so we would expect a rise in "phonon temperature" at least in a frequency band centered about the paramagnetic resonant frequency. A negligible temperature rise would be expected only in the event that the phonon lifetime is sufficiently short to allow a rapid transfer of energy from the phonons in contact with the spins to the rest of the phonon spectrum and the surrounding bath.

GIORDMAINE *et al.*[3] proposed a theory of spin–lattice relaxation at liquid helium temperatures in which the total rate of relaxation is limited by lattice-bath relaxation. In their theory, the spin–lattice relaxation time is assumed shorter than the observed relaxation time. In addition, the frequency range $\Delta\nu$ of phonons in contact with the spins is very much greater than the spin resonance line width. The limiting relaxation time is the time it takes for these "hot phonons" to diffuse to the surface of the paramagnetic crystal, their transport to the surface being interrupted by absorption and re-emission by interaction with the paramagnetic spins. STRANDBERG[4] has derived equations relating spins, phonons and temperature bath, which obtain, when the finite phonon specific heat is taken into account. Here no assumption is made about the phonon bandwidth $\Delta\nu$. The loss of energy from this phonon band is described by a single phonon relaxation time and allows for energy loss to the rest of the phonon spectrum and directly to the bath. BLOEMBERGEN *et al.*[5] have explained the experiments of GIORDMAINE *et al.*, as well as saturation effects in three-level masers[6]

* This work is based on a thesis submitted to the Massachusetts Institute of Technology in partial fulfillment of the requirements for the degree of Doctor of Philosophy in Physics.

† This work was supported in part by the U.S. Army (Signal Corps), the U.S. Air Force (Office of Scientific Research, Air Research and Development Command), and the U.S. Navy (Office of Naval Research).

‡ Now at RCA Laboratories, Princeton, New Jersey.

in terms of cross-relaxation effects. Nevertheless, they estimate that even with the spin energy spread out over the entire phonon spectrum and a surface thermal contact of unity, a small (0·3°K in his example) lattice temperature rise could be expected. DRANSFELD[7] and SHIREN and TUCKER[8] have tried to detect a rise in phonon temperature in ruby, but without success. SHIREN and TUCKER estimate that a rise in phonon temperature ΔT of 0·2°K at $T = 1{\cdot}8$°K would have been observable. ANDERSON[9] has considered the spin–phonon problem and compared it with trapped resonant radiation in gases. He shows that the phonon linewidth will be equal to the spin linewidth and proposes a combination of phonon diffusion and spin–spin interaction to explain spin–lattice relaxation.

SCOPE OF THIS PAPER

(1) In this paper we study the coupled spin–lattice-bath system and determine under what conditions a steady-state nonequilibrium phonon distribution will exist. The effect of such a phonon distribution on the observed spin relaxation is also investigated.

(2) We report an experiment similar to that described by SHIREN and TUCKER, designed to detect a rise in temperature of phonons in contact with a saturated spin transition. The experiment involved two microwave cavities with a paramagnetic crystal placed between them and extending into each cavity. Excited phonons would be detected only if they traverse the crystal from the "saturating cavity" to the "detecting cavity". The experiment was performed using ruby and also Cr^{3+} impurities in MgO and in $K_3Co(CN)_6$ as paramagnetic crystals. The sensitivity was such that in the case of ruby, a temperature rise $\Delta T = 0{\cdot}005T$ could have been detected. However, no such temperature rise was observed.

(3) The validity of the theory presented here is discussed in the light of the experimental results.

THE SPIN–PHONON BATH EQUATIONS

For simplicity, we assume only two spin levels, Then the energy transfer from spins to lattice leads to the equation[4]:

$$\frac{d}{dt}(N_i - N_j) = 2\rho(\nu_{ij})[N_i A_{ij}\langle M_{ij}+1\rangle - N_j A_{ij}\langle M_{ij}\rangle] \tag{1}$$

where

N_i = number of spins in excited state
N_j = number of spins in ground state
$\langle M_{ij}\rangle$ = number of phonons with frequency ν_{ij}
$\rho(\nu_{ij})$ = density of phonon states at frequency ν_{ij}
A_{ij} = induced transition probability for spin flip with emission or absorption of a phonon.

We now assume that only phonons in a frequency range $\Delta\nu$ centered about the spin resonant frequency interact directly with the spins. Furthermore, it is assumed that the loss of phonons from this frequency interval, apart from interaction with the spins, can be described by a single relaxation time. This includes both direct absorption by the temperature bath, and scattering into other lattice modes. Then the equation for the decay of phonons with time is

$$\frac{d}{dt}\langle M_{ij} - M_{ij}^0\rangle = \frac{-1}{2\rho(\nu_{ij})\Delta\nu}\frac{d}{dt}(N_i - N_j) - \frac{\langle M_{ij} - M_{ij}^0\rangle}{T_{\mathrm{ph}}} \tag{2}$$

where

$\Delta\nu$ = bandwidth of phonons interacting directly with spins
T_{ph} = lifetime of those phonons with frequencies within bandwidth $\Delta\nu$ of ν_{ij}.

These two equations are the coupled spin–lattice equations. To simplify them, we introduce the following quantities:

$$x = \frac{N_i - N_j}{N_i^0 - N_j^0} \qquad y = \frac{\langle M_{ij} - M_{ij}^0\rangle}{\langle M_{ij}^0 + 1/2\rangle}$$

where

N_i^0, N_j^0 are the values of N_i, N_j at thermal equilibrium,

and

$N_i^0 + N_j^0 = N_i + N_j = N_s$ = total number of spins.

Vol. 1
196

The spin–lattice equations become

$$\frac{dx}{dt} = \frac{1}{T_{sp}}[1-x-xy]$$
$$\frac{dy}{dt} = b\frac{dx}{dt} - y/T_{ph} \tag{3}$$

where

$$b = \frac{1}{\langle M_{ij}^0 + 1/2\rangle} \times \frac{N_j^0 - N_i^0}{2\rho(\nu_{ij})\Delta\nu}$$
$$\approx \frac{N_s}{4\rho(\nu_{ij})\Delta\nu}\left(\frac{h\nu_{ij}}{kT}\right)^2 \quad \text{for } \frac{h\nu_{ij}}{kT} \ll 1$$
$$T_{sp} = \frac{1}{\langle 2M_{ij}^0 + 1\rangle \rho(\nu_{ij}) A_{ij}}$$

A further substitution is convenient for studying these equations. Let

$$v = 1-x, \quad w = \frac{1}{\sigma}y, \quad \sigma = b/a, \quad a = T_{sp}/T_{ph}$$

The equations become, with time measured in units of T_{sp},

$$\frac{dv}{dt} = -v + \sigma w(1-v) \tag{5}$$

$$\frac{dw}{dt} = a[(v-w) - \sigma w(1-v)] \tag{6}$$

We now draw some conclusions from these equations:

(i) If $\sigma \ll 1$, the solution of (5) yields a simple exponential decay for v. Thus, the size of σ is a measure of how important the nonthermal phonon distribution is in leading to a departure of the spin system from simple exponential relaxation.

(ii) The steady-state solution of the spin–lattice equations with a resonant r.f. magnetic field present shows that w has a maximum value of unity.

Therefore

$$(y)_{max} = \frac{\langle M_{ij} - M_{ij}^0\rangle}{\langle M_{ij}^0 + 1/2\rangle} = \sigma$$

Writing this in terms of temperature with

$$\langle M_{ij}^0\rangle = \frac{1}{\exp\left(\frac{h\nu_{ij}}{kT}\right) - 1} \approx \frac{kT}{h\nu_{ij}}$$

for

$$\frac{h\nu_{ij}}{kT} \ll 1$$

yields

$$\left(\frac{T_{ph} - T_B}{T_B}\right)_{max} = \sigma$$

where

T_{ph} = temperature of excited phonons

T_B = temperature of surrounding liquid helium bath.

Therefore even when the spin temperature is infinite (or very large) and thus describes complete r.f. saturation of the spins, the phonons in contact with the spins will never rise above the temperature

$$T_{ph} = (\sigma+1)T_B$$

(iii) σ is an important parameter in the theory and can be given a simple meaning, that is

$$\sigma = \frac{C_{sp}/T_{sp}}{C_{ph}/T_{ph}}$$

where

C_{sp} = spin specific heat

C_{ph} = specific heat of phonons in contact with spins.

To show this for $h\nu_{ij}/kT \ll 1$, we note that

$$C_{sp} = \frac{dE}{dT} = \frac{h\nu}{2}\frac{d}{dT}(N_i^0 - N_j^0)$$
$$= k\frac{N_s}{4}\left(\frac{h\nu_{ij}}{kT}\right)^2$$
$$C_{ph} = h\nu\frac{d}{dT}\rho\langle M_{ij}\rangle\Delta\nu = k\rho\Delta\nu$$

Therefore

$$C_{sp}/C_{ph} = \frac{N_s}{4\rho(\nu_{ij})\Delta\nu}\left(\frac{h\nu_{ij}}{kT}\right)^2 = b$$

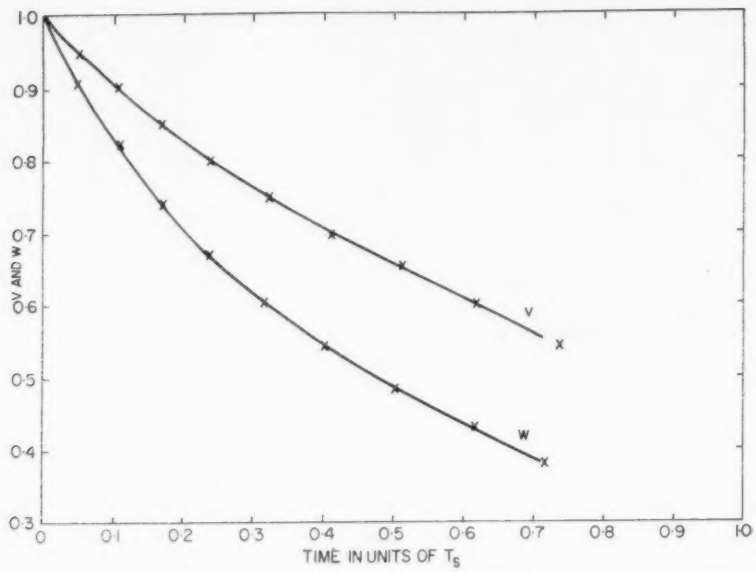

FIG. 1. Numerical solution of the spin–lattice-bath equations for $\sigma = 1$, $a = 10^3$. Solid lines represent exact numerical solution, crosses the approximate solution.

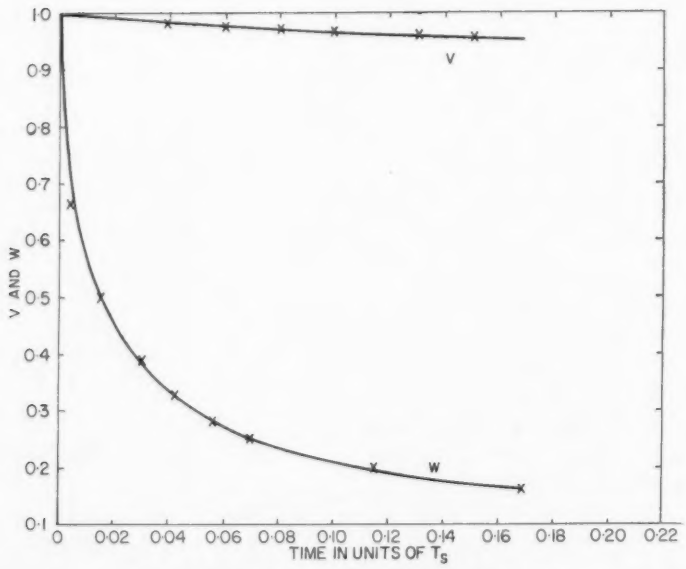

FIG. 2. Same as Fig. 1 except $\sigma = 100$, $a = 10^3$.

(iv) If $a \gg 1$, which is physically reasonable, then the spin–lattice equations can be solved approximately. We have $(1/a)\, dw/dt \approx 0$ and equation (6) becomes

$$w = \frac{v}{1+\sigma(1-v)} \tag{7}$$

Putting this into (5) yields

$$\frac{dv}{dt} = \frac{-v}{1+\sigma(1-v)} = -w \tag{8}$$

The results are shown in Figs. 1 to 3. The approximate solution agrees quite well with the numerical solution. Inspection of equation (10) shows that a large σ will lead to a longer observed spin–lattice relaxation time, for a function that departs from a simple exponential decay.

ESTIMATE OF a, b, σ

For $\nu = 9{\cdot}2$ kmc/s, $T = 4{\cdot}2°\mathrm{K}$, $\Delta\nu = 50$ Mc/s and assuming a Debye spectrum for $\rho(\nu)$ we obtain

$$b = 0{\cdot}6\, C\theta_D^3$$

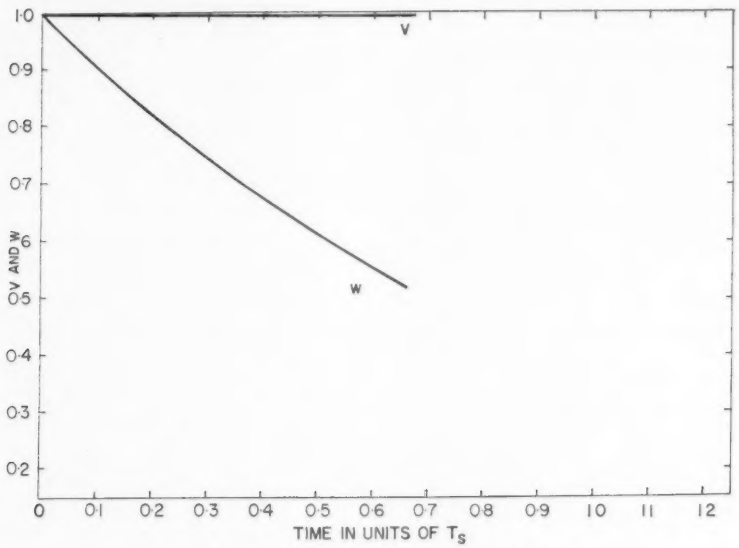

FIG. 3. Same as Fig. 1 except $\sigma = 10^3$, $a = 2$.

Equation (8) has the solution

$$t = (1+\sigma)\ln\frac{1}{v} - \sigma(1-v) \tag{9}$$

or if it is inverted,

$$v = \exp[-t/(1+\sigma)]\exp(1-v)[\sigma/(1+\sigma)] \tag{10}$$

The initial conditions for saturation at $t = 0$ are $v = w = 1$. Equations (5) and (6) have been solved numerically for the three following cases:

(1) $\sigma = 1$, $\quad a = 10^3$

(2) $\sigma = 10^2$, $\quad a = 10^3$

(3) $\sigma = 10^3$, $\quad a = 1$

where

C = concentration of paramagnetic ions
θ_D = Debye temperature.

For the ruby crystal,

$$C = 10^{-4} \quad \theta_D = 980°\mathrm{K} \quad b \approx 6 \times 10^4$$

For T_{sp} we use the measured spin–lattice relaxation time, $T_{sp} = 3 \times 10^{-2}$ sec. The proper value for T_{ph} will be discussed more fully below. For the present estimate we assume $T_{ph} = 10^{-6}$ sec. Then

$$a = \frac{T_{sp}}{T_{ph}} = 3 \times 10^4$$

and so

$$\sigma_{\text{ruby}} \approx 2$$

A σ of 2 would not have a marked effect on the spin–lattice relaxation time, but would lead to a phonon temperature of three times the bath temperature.

For the MgO crystal, $C = 0{\cdot}5 \times 10^{-5}$, $\Delta\nu \approx 12$ Mc/s, $\theta_D \approx 10^3$ and $b = 10^4$ at $T = 4{\cdot}2°$K.

If we assume the same value for a as for ruby, we obtain

$$(\sigma)_{\text{MgO}} \approx 0{\cdot}4$$

PHONON LIFETIME

Of the quantities appearing in the expression for σ, the one whose magnitude is most in doubt is T_{ph}, the phonon lifetime. We consider now some of the mechanisms that limit this lifetime.

(i) *Phonon–phonon collisions*

This will be the only term in an otherwise ideal crystal of infinite extent. It is due to the anharmonic part of the lattice potential energy. At liquid helium temperatures it leads to a very long lifetime. An approximate calculation can be made with the aid of equations found in an article by KLEMENS[10]. With suitable approximations, the following expression for T_{ph} is obtained:

$$T_{\text{ph}} = 1{\cdot}5 \times 10^{-20} \frac{\rho v^5}{\gamma^2} \frac{1}{\nu T^4}$$

where

ρ = density of crystal
v = velocity of sound
γ = Gruneisen coefficient
ν = Frequency of phonon considered
T = temperature.

This gives the lifetime of a phonon whose frequency ν is low compared with other phonons present in the crystal. The most serious approximation is the neglect of crystal dispersion. However, equation (11) will give a lower limit on the lifetime.

For Al_2O_3, $\rho = 4{\cdot}0$ g/cm^3, $v = 7{\cdot}6 \times 10^5$ cm/sec, $\gamma = 3$

Therefore

$$T_{\text{ph}} = 0{\cdot}6 \times 10^{-3} \text{ sec.}$$

A similar result is obtained for MgO. VAN VLECK[11] has carried out a similar calculation and also obtains a long relaxation time. It is interesting that recent experiments on hypersonic wave in quartz[12,13,14] indicate a very long lifetime for microwave phonons in quartz at 4·2°K.

(ii) *Crystal impurities*

The contribution of various types of impurities to phonon scattering is more difficult to estimate, especially since little is known about the number and type of impurities in the crystals used in our experiments. KLEMENS[10] has derived a formula for the phonon lifetime when it is limited by scattering from point imperfections:

$$T_{\text{ph}} = \frac{v^3 G}{3\pi a^3 \omega^4}$$

where

v = velocity of sound
G = 1/impurity concentration
a = interatomic distance
ω = angular frequency.

Putting in numbers for the crystals we used and assuming $G = 10^4$, we obtain $T_{\text{ph}} = 0{\cdot}1$ sec.

This is a very long lifetime. The true lifetime because of imperfections is probably much shorter than this.

(iii) *Boundaries*

For crystals whose dimensions are only a few millimeters, phonon absorption and scattering at the boundary may limit the phonon lifetime. Thermal conductivity experiments on ruby[15] indicate a phonon mean-free path limited only by diffuse scattering at the boundaries for a rod a few millimeters in diameter. However, the mean-free path calculated in this way would be for phonons with frequency approximately ten times greater than X-band microwave phonons, $\nu = 9$ kMc/s.

Let r^2 = power reflected at boundary per phonon collision
v = velocity of sound in crystal
P_0 = initial power in phonon wave packet
P = power in phonon wave packet after time t,

then

$$P = r^{2n} P_0 = P_0 e^{-t/T}$$

Vol. 1
196

where

$$n = t/t_0 \text{ and } T = t_0/\ln\left(\frac{1}{r^2}\right)$$

An upper limit will be set by the degree of acoustical match between the crystal and the helium bath. In this case

$$r^2 = \left(\frac{Z_c - Z_H}{Z_c + Z_H}\right)^2$$

where

Z_c = acoustical impedance of crystal
Z_H = acoustical impedance of liquid helium
$Z = \rho V$.

For a ruby crystal in liquid helium,

$\rho_c = 4{\cdot}0$ gm/cm^3
$\rho_H = 0{\cdot}125$ gm/cm^3
$v_c = 7 \times 10^5$ cm/sec
$v_H = 2 \times 10^4$ cm/sec

Taking $l = 2$ mm, $t_0 = 0{\cdot}3 \times 10^{-6}$ sec, we obtain

$T_{\text{ph}} = 0{\cdot}75 \times 10^{-4}$ sec.

Phonons at 9 kMc/s have a wavelength of about 8000 Å. If the crystal surfaces are not polished, there may be some diffuse scattering. If 25 per cent of the power is lost by diffuse scattering at the surface, then the phonon lifetime becomes 10^{-6} sec. This is probably a reasonable value and has been used in our estimate of σ.

PHONON TRANSPORT IN PARAMAGNETIC CRYSTALS

Suppose we have the following experimental situation. A crystal containing paramagnetic spins is in the form of a parallelepiped with square cross section of area l^2 and length L, where $L \gg l$. The crystal is divided into three regions. Regions I and III form cubes of volume l^3 at the two ends of the crystal, and region II comprises the central portion. Assume that phonons are generated uniformly in region I. Some of these phonons will traverse region II and enter region III. We would like to know what is the average number of phonons in region III. We examine two different situations.

(i) There is no attenuation of phonons in the interior of the crystal, but all phonons that reach a surface are lost.

(ii) Region II contains paramagnetic spins in equilibrium with the lattice. These spins can absorb and re-emit phonons. Again, all phonons reaching a surface are lost. These two examples represent extreme cases so that the number of phonons in region III as calculated in (i) and (ii) will be a lower limit.

Case (i). Here only those phonons initially travelling in a direction contained within the solid angle subtended by the face of region III with the center in region I will reach region III. If this solid angle is denoted by $d\omega$ then $d\omega = (l/L)^2$, and the average number of phonons in region III is

$$n_{\text{III}} = n_{\text{I}} \frac{1}{4\pi}\left(\frac{l}{L}\right)^2$$

For the crystals used in our experiments,

$$l = 2{\cdot}2 \text{ mm} \quad L = 6{\cdot}6 \text{ mm}$$

and

$$\frac{1}{4\pi}\left(\frac{l}{L}\right)^2 \approx 0{\cdot}01$$

Case (ii). A beam of phonons is incident on the left face of region II. If the mean-free path of a phonon, because of spin–phonon interaction is small compared with the length of the crystal, then the problem can be described by a diffusion equation in which the diffusion constant is given by $D = (1/3)v\lambda$, where λ = phonon mean-free path from phonon–spin interaction. The solution of the diffusion equation for this case is

$$n_{\text{III}} = n_{\text{I}}(0{\cdot}64)\exp -\left(\frac{\pi L}{l}\right)$$

$$\frac{n_{\text{III}}}{n_{\text{I}}} = 6 \times 10^{-5} \text{ for } L/l = 3$$

In addition to the diffusion flux into region III, there will be the unscattered part of the incident primary beam of phonons which gives a contribution to n_{III},

$$n_{\text{III}} = n_{\text{I}} \exp(-L/\lambda)$$

ESTIMATE OF DIFFUSION CONSTANT

The attenuation calculated above could place a severe limitation on the possibility of transmitting

phonons down a crystal rod. Therefore, an estimate of the phonon mean-free path is desirable.

Let

W = transition probability for a spin flip and the creation or destruction of a phonon

$$W = \Delta N_s N_{\rm ph} W^0$$

where

ΔN_s = difference in spin population between upper and lower states

$N_{\rm ph}$ = number of phonons in frequency band

W^0 = transition probability per spin per phonon.

For ruby

$$v = 7\times 10^5 \text{ cm/sec.}$$
$$T_{\rm sp} = 3\times 10^{-2} \text{ sec.}$$
$$b = 6\times 10^4$$

so that

$$\lambda \approx 3{\cdot}5 \text{ mm}$$

and

$$\exp(-L/\lambda) \approx e^{-2} \approx 0{\cdot}1$$

For the MgO crystal, the phonon mean-free path will be longer because of the smaller value of b.

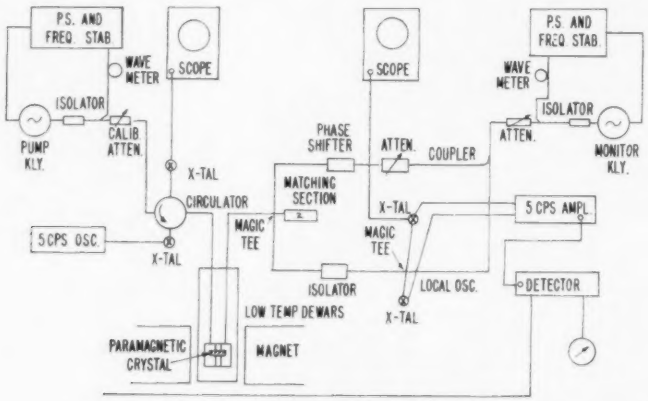

FIG. 4. Block diagram of experimental apparatus.

Then

$$T_{\rm sp} = \frac{1}{W/\frac{1}{2}\Delta N_s}$$

and

$$T_{\rm ph} = \frac{1}{W/N_{\rm ph}}$$

Therefore

$$T_{\rm ph} = T_{\rm sp}\left(\frac{N_{\rm ph}}{\frac{1}{2}\Delta N_s}\right) = \frac{1}{b}T_{\rm sp}$$

The phonon mean-free path is

$$\lambda = vT_{\rm ph} = \frac{vT_{\rm sp}}{b}$$

THE EXPERIMENT

A block diagram of the experimental arrangement is shown in Fig. 4. The paramagnetic crystal is placed between two identical TE_{101}-mode rectangular X-band microwave cavities. The region containing the crystal between the two cavities forms a waveguide beyond cutoff and provides about 40 db of isolation between the two cavities. In one cavity a paramagnetic transition is saturated, while the same spin transition is monitored in the second cavity. If nonequilibrium phonons are created via spin–lattice relaxation in the saturating cavity and are transported through the crystal, then their presence will be detected by their effect on the resonance absorption in the detecting cavity. To increase the detection sensitivity, the saturating power is amplitude-modulated at 5 c/s. The monitoring klystron is set on resonance

and the detected signal is passed through a 5 c/s narrow-band amplifier and a phase-sensitive detector with a time constant of 30 sec. A low modulating frequency is used so that the spin system can follow the amplitude variation of the r.f. power.

SENSITIVITY OF THE EXPERIMENT

Let

$$k = Q_0/Q_e, \qquad \kappa = Q_0/Q_m$$

where

Q_0 = quality factor of the cavity
Q_e = external Q
Q_m = crystal magnetic Q

Then the reflection coefficient of the monitor cavity is

$$\gamma^2 = \left(\frac{1+\kappa-k}{1+\kappa-k}\right)^2$$

If the phonons in the monitoring end of the crystal have an a.c. component, the observed κ will be

$$\kappa = \kappa_0 + \kappa_1 \cos \omega t$$

and the detected signal will be proportional to k_1 which is defined as

$$\kappa_1 = \frac{\Delta T}{T}\kappa_0$$

$$\Delta T \ll T$$

and ΔT is the time-variant temperature variation. If, on the other hand, the magnetic field is modulated over the whole linewidth, the detected signal will be proportional to κ_0. If the signal-to-noise ratio of the resonance signal for full linewidth mololation is S/N, then the minimum detectable temperature rise will be

$$\left(\frac{\Delta T}{T}\right)_{\min} \approx \frac{1}{(S/N)}$$

For the experiments with MgO and ruby, it was found that $S/N \approx 10^3$.
Therefore

$$\left(\frac{\Delta T}{T}\right)_{\min} \approx 0{\cdot}005$$

with a mean deviation of 1/5 in ΔT.

L*

RESULTS

(i) MgO. The Cr^{3+} impurity ion concentration was approximately 10^{18} spins/cm^3. The sample size was $2{\cdot}2 \times 2{\cdot}2 \times 10$ mm, with 5 mm distance between the two cavities. The isolation between cavities was measured to be 43 db, whereas the power required to reduce the resonance signal by one half was 33 db below the maximum saturating power used, or approximately $0{\cdot}5 \times 10^{-6}$ W. Therefore, the maximum leakage power which enters the monitor cavity by direct microwave leakage is $(P_l)_{\max} = 0{\cdot}1\, P_{\text{sat}}$. The leakage power will not be directly detected by the 5 c/s amplifier because it mixes incoherently with the local oscillator. Rather, its effect will be felt through partial saturation of the monitor resonance. It

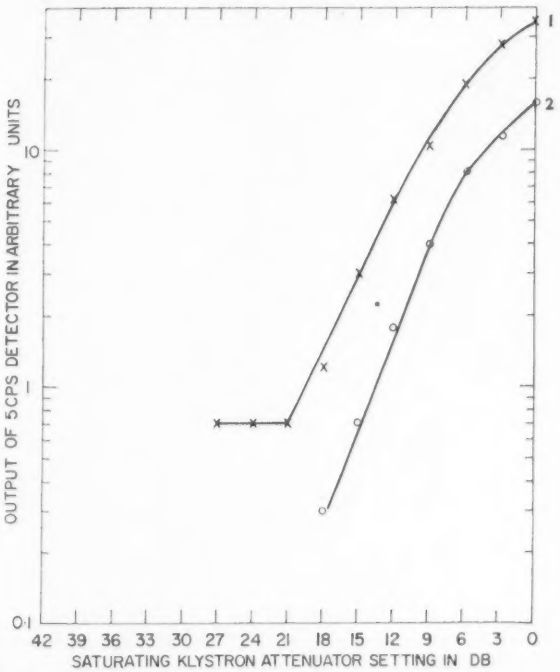
OUTPUT OF 5CPS DETECTOR IN ARBITRARY UNITS
10
1
0·1
1
2
42 39 36 33 30 27 24 21 18 15 12 9 6 3 0
SATURATING KLYSTRON ATTENUATOR SETTING IN DB

FIG. 5. Phonon-detection experiment using Cr^{3+} impurities in MgO. Main isotropic Cr^{3+} line is used. $H = 3255$ G (approximately), parallel to c-axis of crystal. $\nu = 9{\cdot}2$ kMc/s, $T = 4{\cdot}2$°K. Two runs are shown, labeled 1 and 2. The flat portion of run 1 at low saturating klystron power is equal to the experimental error.

will contribute a detected signal of the form:

$$\kappa_l = \frac{1}{1+P_l/P_{\text{sat}}}\kappa_0 \approx \frac{P_l}{P_{\text{sat}}}\kappa_0 \text{ for } P_l \ll P_{\text{sat}}$$

For large saturating power, this term may be greater than the one arising from phonon transport. However, by reducing the saturating power one can make this term small, and still have sufficient power to saturate the resonance in the saturating cavity. Thus, what one expects is a detected signal which decreases linearly with saturating power and then levels off when the effect on nonequilibrium phonons is felt. Fig. 5 gives curves for two runs, showing detected signal against saturating power for an MgO sample. No leveling-off is observed within the experimental error. These curves indicate that saturation takes place at a lower power level than that expected from the measured saturation power and isolation between cavities. From the runs made on MgO, we estimate for a minimum $\Delta T/T$

$$\left(\frac{\Delta T}{T}\right)_{\text{min}} = 0{\cdot}01$$

or

$$(\Delta T) < 0{\cdot}04°\text{K at } T = 4{\cdot}2°K$$

(ii) *Ruby*. The results of two runs taken with a ruby crystal of dimensions $2{\cdot}2\times2{\cdot}2\times10$ mm are shown in Fig. 6. The chromium line in ruby (a

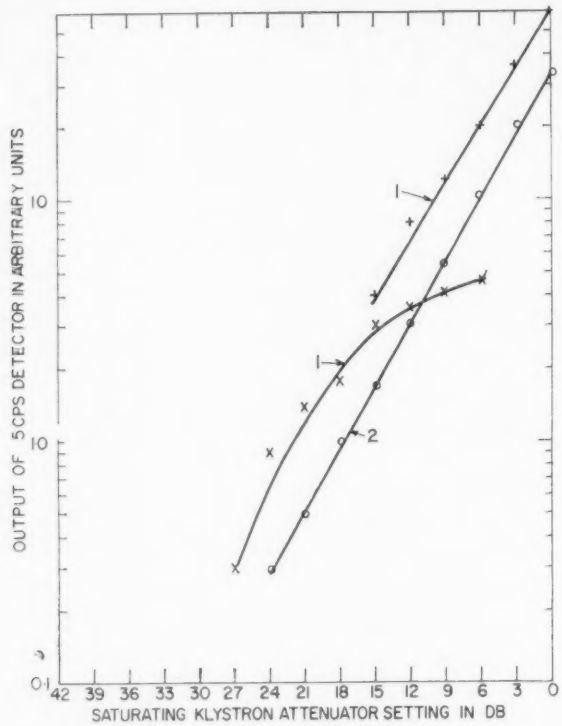

FIG. 6. Phonon-detection experiment using Cr^{3+} impurities in Al_2O_3. $H = 2172$ G, 55° with respect to c-axis. $f = 9{\cdot}2$ kMc, $T = 4{\cdot}2°$K. The leveling-off of the lower portion of run 1 is due to saturation of the phase-sensitive detector. The upper portion of run 1 is obtained from the output of the 5 c/s amplifier.

Vol. 1
1961

superposition of absorption by $M_s = \pm 3/2 \rightarrow \pm 1/2$) has a shorter relaxation time than the chromium line in MgO, so that for maximum saturation power there is no indication of saturation in the monitor resonance. Also, since the $1/Q_m$ for ruby is three times greater than for MgO, the sensitivity is somewhat increased. Again there is no indication of phonon transport through the crystal. Here we estimate that

$$\left(\frac{\Delta T}{T}\right)_{\min} = 0{\cdot}005$$

$$(\Delta T) < 0{\cdot}02°\text{K at } T = 4{\cdot}2°K$$

The experiment was also tried at $T = 2°$K and for H parallel to the c-axis with similar results. Both the ruby and MgO crystals were polished to increase the amount of specular reflection from the boundaries.

(iii) $K_3Co(CN)_6$. Several different concentrations of Cr^{3+} impurities were used, namely 0·03, 0·01, 0·001.

In the first experiment, a sample of dimensions $3 \times 5 \times 10$ mm was placed between a circular TE_{111}-mode cavity within a coaxial TE_{113}-mode cavity. The r.f. magnetic fields were orthogonal. The c-axis was parallel to the d.c. magnetic field. At $H = 2200$ G, the (1–3) and (3–4) transitions are degenerate, and have different r.f. selection rules. The (1–3) transition was saturated in the coaxial cavity and the (3–4) resonance traced out in the circular cavity. No phonon effect was observed, that is, the resonance traced out in the circular cavity was independent of saturation of the resonance in the coaxial cavity. Then a crystal with 0·01 Cr concentration and dimensions $2{\cdot}2 \times 2{\cdot}2 \times 10$ mm was used for a run in which the rectangular cavities and the 5 c/s amplifier, but no phase-sensitive detector, were used.

Again no effect was observed. In this case we estimate that

$$\frac{\Delta T}{T} < 0{\cdot}05$$

DISCUSSION

No evidence of nonequilibrium phonons was found with all three crystals in this experiment. This is rather surprising in view of the theory presented earlier. For example, for ruby we expect $\Delta T/T \approx 1$ in the saturating cavity, with a decrease in the monitoring cavity of not more than a factor of 10. Yet we find $\Delta T/T \ll 0{\cdot}005$, which is more than 10 times smaller than we would reasonably expect. Ruby and MgO should be very favorable crystals for producing a nonthermal phonon distribution. They both have very high Debye temperatures and σ is proportional to θ_D^3. We now discuss some possible reasons for the lack of a nonequilibrium phonon distribution.

1. *Density of phonon states.* We have assumed a Debye distribution and since θ_D is so large for ruby and MgO, it leads to very few phonon states in the microwave region. If a small fraction of the total crystal vibrations available have another distribution that favors lower energy states, then the number of phonon states in contact with the spins might be much larger.

In fact, it has been elegantly demonstrated that no three-dimensional crystal can have a density of eigenstates as simple as that given by the Debye spectrum.[16,17] Frequency extrema and saddle points give rise to maxima in the density of states well below the maximum frequency. We do not suggest that a maximum in the density of states could exist at as low a frequency as 10^{10} c/s but the density of photon states at microwave frequencies will be underestimated when a spectrum as greatly oversimplified physically and analytically, as a Debye spectrum is used.

2. *Incorrect spin–lattice relaxation theory.* For example, it may be that the spins can give their energy to other phonon states besides those centered about the resonance linewidth. Actually, our assumption of only two spin states is incorrect, since there are four energy levels in a spin 3/2 system. If one pair of levels is saturated, the relaxation can occur by transitions to the other spin states if the matrix elements are favorable. This will reduce the energy transferred to the lattice at the saturating frequency. Although this will reduce σ somewhat, it does not explain the large discrepancy found in our experiments, since according to our present understanding[2] the pumped transitions have allowed matrix elements coupling them to the lattice.

3. *Phonon relaxation time shorter than expected.* None of the known phonon scattering mechanisms lead to a phonon lifetime short enough to explain our results. In fact, our assumed value of

$T_{ph} = 10^{-6}$ sec is quite a bit shorter than the experimentally observed phonon lifetime in quartz at the same frequency.[12,13,14] T_{ph} would have to be about 10^{-7} sec to explain our experimental results.

The first two explanations seem the most probable. It is probably too much to expect that all low-frequency lattice modes have a Debye frequency distribution. There may be a number of low frequency localized modes, for example, or a small fraction of the total number of modes may be distributed according to a Debye distribution, but with small θ_D. With regard to the second suggestion, there is no direct evidence, but it is well known that there are many aspects of spin–lattice relaxation that are unexplained[17] and the possibility of a broad coupling to the lattice modes cannot be overlooked. Finally, the experiments on the saturation of paramagnetic impurities in quartz and MgO by hypersonic waves show that much more power is required to saturate the spins than would be calculated on the basis of present spin–lattice relaxation theory.[2]

REFERENCES

1. VAN VLECK J. H., *Phys. Rev.* **57,** 426 (1940).
2. MATTUCK R. D. and STRANDBERG M. W. P., *Phys. Rev.* **119,** 1204 (1960).
3. GIORDMAINE J. A., ALSOP L. E., NASH F. R. and TOWNES C. H., *Phys. Rev.* **109,** 302 (1958).
4. STRANDBERG M. W. P., *Phys. Rev.* **110,** 65 (1958).
5. BLOEMBERGEN N., SHAPIRO S., PERSHAM P. S. and ARTMAN J. D., *Phys. Rev.* **114,** 445 (1959).
6. STRANDBERG M. W. P., DAVIS C. F., FAUGHNAN B. W., KYHL R. L. and WOLGA G. J., *Phys. Rev.* **109,** 1088 (1958).
7. DRANSFELD K., *Bull. Amer. Phys. Soc.* (ser. 2) **3,** 324 (1958).
8. SHIREN N. S. and TUCKER E. B., *Phys. Rev. Letters* **2,** 206 (1959).
9. ANDERSON P. W., *Phys. Rev.* **114,** 1002 (1959).
10. KLEMENS P. G., *Solid State Physics* Vol. VII, p. 1. Academic Press, New York (1958).
11. VAN VLECK J. H., *Phys. Rev.* **59,** 730 (1941).
12. BOMMEL H. and DRANSFELD K., *Phys. Rev. Letters* **2,** 298 (1959).
13. JACOBSEN E. H., *Phys. Rev. Letters* **2,** 249 (1959).
14. BOMMEL H. and DRANSFELD K., *Phys. Rev.* **117,** 1245 (1960).
15. BERMAN R., *Proc. Roy. Soc.* **208A,** 90 (1951).
16. VAN HOVE L., *Phys. Rev.* **89,** 1189 (1953).
17. PERETTI J., *J. Phys. Chem. Solids* **12,** 216 (1960).

Vol. 1
196

J. Phys. Chem. Solids Pergamon Press 1961. Vol. 19, Nos. 1/2, pp. 167–169. Printed in Great Britain.

DEVIATIONS FROM STOICHIOMETRY IN MnO AND FeO

D. M. SMYTH

Sprague Electric Company, North Adams, Mass.

(*Received* 6 *October* 1960)

Abstract—Deviations from stoichiometry in divalent oxides containing cation vacancies such as MnO and FeO are treated according to a simple mass action approximation which predicts that the composition should vary with the sixth root of the oxygen pressure for large deviations from stoichiometry and with the square root of the oxygen pressure close to the stoichiometric composition. Published data for MnO and FeO are in excellent agreement with the predictions.

A RECENT paper by DAVIES and RICHARDSON[1] describes the deviations from stoichiometry in MnO for temperatures from 1500 to 1650°C in oxygen atmospheres of 10^{-7} to 10^{-2} atm. The composition ranges from $MnO_{1.000}$ to $MnO_{1.045}$ and the system appears to be analogous to the FeO system as described by DARKEN and GURRY[2]. The main differences in the two systems are that stoichiometric FeO is not stable, and the latter deviates from stoichiometric proportions to a much greater extent.

DAVIES and RICHARDSON consider that the deviations from stoichiometry in MnO are due to cation vacancies, as has been shown for FeO. The experimental data are treated by a technique of disorder thermodynamics attributed to WAGNER[3] which fits the data in the composition range $MnO_{1.000}$ to $MnO_{1.005}$. The lack of agreement between theory and experiment for more oxygen rich compositions is assumed by them to be due to changes in the cation vacancy activity coefficient.

In this paper, these data have been evaluated according to another thermodynamic treatment developed by the Wagner school[4] and extended by KRÖGER and VINK[5], and good agreement between theory and experiment are attained up to the maximum deviations from stoichiometry reported without involving changes in activity coefficient. The FeO data of DARKEN and GURRY have been similarly treated with equally good agreement.

The deviations from stoichiometry can be considered in terms of the following pseudochemical equilibrium:

$$\tfrac{1}{2}O_2 \rightleftharpoons Mn_{vac}^{++} + 2(\oplus) + MnO \qquad (1)$$

where Mn_{vac}^{++} is a cation vacancy and $(\oplus)$ is an electron hole in the valence band. The mass action expression for this equilibrium is:

$$[Mn_{vac}^{++}][(\oplus)]^2 = KP_{O_2}^{1/2} \qquad (2)$$

where the brackets denote the concentration of the enclosed species, P_{O_2} is the oxygen pressure in atm, and K is a function of temperature. The standard state is taken as the perfect stoichiometric lattice with a filled valence band and empty conduction band.

For small deviations from disorder, one must also consider the thermal disorder reactions:

$$Mn_{vac}^{++} + Mn_{int}^{++} \rightleftharpoons O \qquad (3)$$

and

$$e^- + (\oplus) \rightleftharpoons O \qquad (4)$$

where Mn_{int}^{++} is an interstitial cation and e^- is an electron in the conduction band. Defects in the oxide sublattice can almost certainly be neglected. For compositions sufficiently far from stoichiometry the disorder will result almost completely from reaction (1) and the concentrations of Mn_{int}^{++} and e^- may be neglected.

In this range:

$$[(\oplus)] = 2[Mn_{vac}^{++}] \equiv 2v \qquad (5)$$

and equation (2) becomes

$$4v^3 = KP_{O_2}^{1/2} \tag{6}$$

and

$$v \propto P_{O_2}^{1/6} \tag{7}$$

Thus the concentration of cation vacancies, which is equal to $x/1+x$ in MnO_{1+x} should be proportional to the sixth root of the oxygen pressure. FeO can be treated analogously.

In the region of very small deviations from stoichiometry, the concentration of electron holes due to thermal disorder (reaction 4) will become significant and eventually predominant. The relationship between the concentration of cation vacancies and of electron holes given in equation (5) will no longer be valid, the latter being constant at a given temperature. In this case the mass action expression for reaction (1) reduces to

$$v \propto P_{O_2}^{1/2} \tag{8}$$

which is essentially the relation derived by DAVIES and RICHARDSON and which agrees with the experimental results between the compositions of $MnO_{1.000}$ and $MnO_{1.005}$.

MnO

The data of DAVIES and RICHARDSON show no temperature effect over the range studied; thus the data for each P_{O_2} have been averaged irrespective of temperature. The average composition as a function of P_{O_2} has then been fitted to equation (7) by the method of least squares with the following results:

(a) For oxygen pressures in the range 10^{-7} to 10^{-2} atm ($MnO_{1.0056}$ to $MnO_{1.0444}$).

$$v \propto P_{O_2}^{1/5.61} \tag{9}$$

(b) For oxygen pressures in the range 3.16×10^{-7} to 10^{-2} atm ($MnO_{1.0081}$ to $MnO_{1.0444}$).

$$v \propto P_{O_2}^{1/6.07} \tag{10}$$

Thus the agreement is excellent over the latter range of composition. Apparently reaction (4) is not negligible for compositions below $MnO_{1.008}$.

FeO

The data of DARKEN and GURRY are somewhat more difficult to evaluate because both temperature and P_{O_2} have large influences on the composition. When the data are plotted as log P_{O_2} against $1+x$ (expressing the composition as FeO_{1+x}) the experimental points fall on a series of straight lines having the ratio CO_2/CO as the parameter (the oxygen pressure was experimentally adjusted by this ratio and the temperature, and was calculated using the equilibrium data implicit in the DARKEN and GURRY paper). Thus each line connects a series of points taken at different experimental temperatures. Points along these lines at 1100°, 1200°, 1300°, and 1400° were found by interpolation from the actual experimental temperatures and the resulting points fall on straight lines with these temperatures as the parameter.* This gives the required information: composition vs. P_{O_2} at constant temperature and this is shown in Table 1.

The data at each temperature were then fitted to equation (7) by the method of least squares taking $[Fe^{++}_{vac}]$ as $x/1+x$. The results are shown in Table 2.

* This plot clearly shows that all of the data of DARKEN and GURRY for $CO_2/CO = 2.23$ are in error in that P_{O_2} is too high by about 65 per cent for the entire set.

Table 1. *Oxygen pressure in equilibrium with* FeO_{1+x}

$1+x$	1100°C	1200°C	1300°C	1400°C
1·060	9.45×10^{-14} atm	2.13×10^{-12} atm	3.28×10^{-11} atm	4.60×10^{-10} atm
1·080	2.82×10^{-13}	6.60×10^{-12}	1.00×10^{-10}	1.32×10^{-9}
1·100	8.55×10^{-13}	2.03×10^{-11}	3.00×10^{-10}	3.84×10^{-9}
1·120	2.55×10^{-12}	6.20×10^{-11}	9.05×10^{-10}	1.11×10^{-8}
1·140	7.73×10^{-12}	1.91×10^{-10}	2.73×10^{-9}	3.20×10^{-8}
1·160	2.32×10^{-11}	5.90×10^{-10}	8.20×10^{-9}	9.35×10^{-8}

Vol. 1
1961

The average agreement within 5 per cent over the entire experimental range is satisfactory. It appears that even for the compositions of least disorder, i.e. $FeO_{1\cdot05}$, the thermal defect concentrations are insignificant.

Table 2. Calculated values of m in $v \propto P_{O_2}^{1/m}$

Temperature	m	per cent deviation from $m = 6$
1100°	6·32	5·3
1200	6·40	6·7
1300	6·31	5·2
1400	6·08	1·3
Average	6·28	4·7

The extensive equilibrium data of SANBONGI[6] on the Fe–O system have been analyzed with similar results. The Fe_3O_4–FeO phase boundaries reported by SCHENCK[7] are in agreement with the data of DARKEN and GURRY and of SANBONGI and can be included in this analysis.

DISCUSSION

The deviations from stoichiometry for the composition ranges $MnO_{1\cdot008}$ to $MnO_{1\cdot044}$ and $FeO_{1\cdot05}$ to $Fe_{1\cdot17}$ are proportional to the sixth root of the oxygen pressure as predicted by a simple mass action analysis. A previous statistical mechanical treatment of the FeO system by TAKEUCHI and IGAKI[8] does not use the mass action approximation and is thus more rigorous at the expense of being much less direct.

The theoretical analysis of their data for MnO by DAVIES and RICHARDSON neglects electronic defects and implies a proportionality between the stoichiometric deviation and $P_{O_2}^{1/2}$. Such a proportionality will be valid only in the range where the concentration of electron holes due to deviations from the stoichiometric composition is negligible compared to that due to thermal disorder. Thus the DAVIES and RICHARDSON analysis is only valid for small deviations from stoichiometry, whereas the treatment outlined in this paper is valid for larger deviations. There is thus no need to invoke large changes in the cation vacancy activity coefficient to explain the failure of the DAVIES and RICHARDSON treatment in the range of large deviations from the ideal composition. The data of SANBONGI on the FeO system extend to smaller defect concentrations than do the data of DARKEN and GURRY, and in the former case the cation vacancy concentration is also roughly proportional to $P_{O_2}^{1/2}$ for compositions having oxygen contents less than that of $FeO_{1\cdot05}$.

The dependence of composition on oxygen pressure obeys the mass action prediction much more accurately than has generally been found for the pressure dependence of electronic conduction.[9] This is to be expected since the composition is a function only of the activity of defects whereas the conductivity is a function of both defect activity and mobility; the latter is not necessarily independent of concentration.

REFERENCES

1. DAVIES M. W. and RICHARDSON F. D., *Trans. Faraday Soc.* **55,** 604 (1959).
2. DARKEN L. S. and GURRY R. W., *J. Amer. Chem. Soc.* **67,** 1398 (1945).
3. WAGNER C., *Thermodynamics of Alloys.* Addison, Wesley Press Inc., Cambridge, Mass. (1952).
4. WAGNER C., *Z. Phys. Chem.* **32B,** 447 (1936).
5. KRÖGER F. A. and VINK H. J., *Solid State Physics* Vol. III, p. 307. Academic Press, New York (1956); KRÖGER F. A. and VINK H. J., *J. Phys. Chem. Solids* **5,** 208 (1958).
6. SANBONGI K., *Sci. Rep. Res. Inst. Tohoku Univ.* **1,** 213 (1949).
7. SCHENCK R. and DINGHAM T., *Z. anorg Chem.* **166,** 113 (1927).
8. TAKEUCHI S. and IGAKI K., *Sci. Rep. Res. Inst. Tohoku Univ.* **4,** 164 (1952).
9. WAGNER C. and KOCH E., *Z. Phys. Chem.* **B32,** 439 (1936); BAUMBACH H. and WAGNER C., *Z. Phys. Chem.* **B24,** 59 (1934).

LETTER TO THE EDITOR

Preparation of single crystals of $Zn_xCd_{1-x}Sb$ by interruption of free crystallization of the melt

(*Received* 26 *July* 1960)

ACCORDING to their equilibrium diagrams,[1] semiconducting antimonides of cadmium and zinc do not crystallize congruently during the cooling of the melt. In the case of CdSb the metastable compound Cd_3Sb_2 is formed first, while the compound ZnSb is formed by the peritectic reaction between Zn_4Sb_3 and the melt. In order to get pure CdSb and ZnSb, polycrystalline samples have to be subjected to long and careful heat treatment.[2]

Other methods could be used to obtain these materials directly. If the crystallization is initiated by inoculation with a stable solid phase, CdSb will crystallize from the melt, held in the temperature interval between its stable melting point and the metastable freezing point of Cd_3Sb_2. ZnSb could be produced by the crystallization from the melt, whose liquidus point was lowered under the peritectic temperature by the addition of antimony.

Compounds CdSb and ZnSb, both having an orthorhombic structure, form a continuous series of mutual solid solutions $Zn_xCd_{1-x}Sb$.[3] The same methods can be used for the preparation of crystals of these solid solutions. Their final composition, however, does not depend only on the composition of the melt, but also on the temperature of crystallization. Based on the discussion above it is possible to prepare single crystals of the system $Zn_xCd_{1-x}Sb$ by current methods,[4–7] or they can be obtained in the form of platelets, as it is described below.

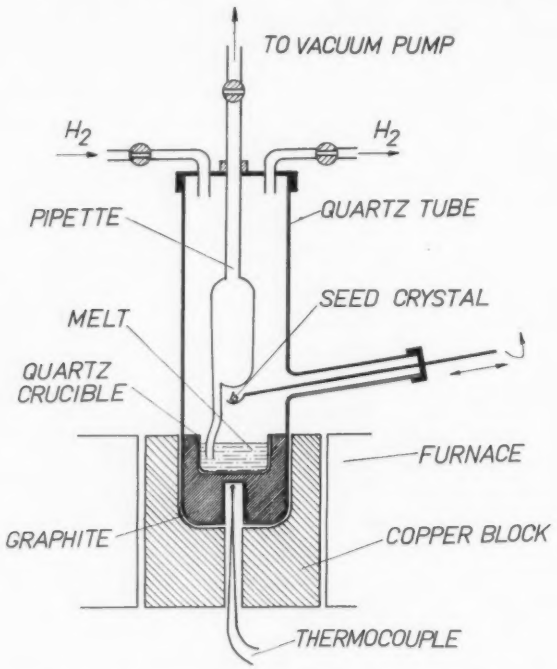

FIG. 1. Apparatus for preparation of single crystals in the form of platelets.

The apparatus, schematically shown in Fig. 1,

allows the temperature to be held constant with satisfactory accuracy. The melt is placed in a quartz crucible, imbedded in graphite. The narrow tube of a quartz pipette can reach the bottom of the crucible. A device for throwing a seed crystal into the melt is attached to the outer wall of the apparatus. The interior of the apparatus is filled with purified and dried hydrogen at an overpressure of a few mm Hg. A tube with an observation window is also attached (not drawn in the figure).

The following procedure was followed in our experiments: material, prepared separately by melting of very pure components in an evacuated sealed tube, is remelted in the crucible of the apparatus. The pipette is then inserted into the bottom of the crucible. After constant temperature is reached, the seed crystal is thrown on the surface of the melt.

Around the place where the seed crystal touched the melt, crystals of equilibrium phase begin to grow. After a few minutes the process of crystallization is interrupted by swabbing off the remaining melt into the pipette. This is done by means of a vacuum pump, after shutting off the hydrogen inlet and outlet valves. The critical moment for sucking the rest of the melt out of the crucible happens when outlines of the platelets in the form of distinct rays on the surface of the melt are seen. In that time there is about 10–15 per cent solidified.

In the manner described, single crystals of both binary compounds CdSb, ZnSb, and also of solid solutions $Zn_xCd_{1-x}Sb$ of various compositions were obtained. Some platelets reached the dimensions of $15 \times 10 \times 1{\cdot}5$ mm. Though the platelets grow, as was observed, by the gradual growing of needles oriented in parallel, with [001] in the axis of the needle, every plate with the orientation (010) was a perfect crystal. Supposing that only a small part of the melt crystallizes, the composition of the crystals $Zn_xCd_{1-x}Sb$ corresponds to the equilibrium diagram ZnSb–CdSb and is exactly determined by the temperature which is kept constant during the process.

As compared with the large single crystals prepared by other methods, the crystals obtained in the manner described show greater perfection of mosaic structure, higher mobility of current carriers, and lower absorption of the infrared.

Institute of Technical Physics K. Šmirous
Czechoslovak Academy of Sciences
Prague

References

1. Hansen M., *Constitution of Binary Alloys.* McGraw Hill, New York (1958).
2. Justi E., Neumann G. and Schneider G., *Z. Phys.* **156,** 217 (1959).
3. Toman K., *J. Phys. Chem. Solids* **11,** 342 (1959).
4. Šmirous K. and Vrchovská V., *Czech. J. Phys.* **10,** 674 (1960).
5. Stevenson M. J., *Bull. Amer. Phys. Soc.* (ser. 2) **5,** 177 (1960).
6. Andronik J. K. and Kot M. V., *F.T.T. Akad. nauk SSSR,* **2,** 1128 (1960).
7. Kot M. V. and Kretsu I. V., *F.T.T. Akad. nauk SSSR,* **2,** 1250 (1960).

BOOK REVIEW

P. R. AIGRAIN: **Electronic Processes in Solids.** The Technology Press of Massachusetts Institute of Technology and John Wiley, New York, 1960. 67 pp. with 13 figs., 32*s*.

THIS SHORT book is one of the series of Technology Press Research Monographs. It is based on eight lectures given at the Massachusetts Institute of Technology in 1957 by Professor PIERRE R. AIGRAIN of Ecole Normale Supérieure, Paris. It was prepared by R. J. COELHO and G. ASCARELLI of the Department of Physics, Massachusetts Institute of Technology. The book gives a condensed presentation of the theory of electric conduction in solids. The first half of the book deals with some general material in the electron theory of solids. It begins with a discussion of the crystal Hamiltonian and the adiabatic approximation. This is followed by a treatment of the lattice vibration and phonon scattering. Then the electron wave function is considered. Hartree and Hartree–Fock equations are discussed briefly. Bloch wave functions are introduced, and there is a section on the $\boldsymbol{k} \cdot \boldsymbol{p}$ perturbation method of treating a wave function in terms of the wave functions for $k = 0$. The problem of perturbed potential is treated by using the Wannier formalism, and the concept of effective mass is inferred from the wave equation for the perturbed problem. The second half of the book concerns specifically the theory of conduction. After discussing briefly the Boltzmann equation, a different and somewhat unusual approach is used. A vector mean free path is introduced in terms of the energy gain of the electrons in the applied field, and the current density is shown to involve a mean free time which is a tensor relating the mean free path and the velocity. Various scattering mechanisms are then considered. Two sections are devoted to the scattering of electrons by phonons. The calculation of scattering by ionized impurities is outlined. Scatterings by neutral impurity and by dislocations and carrier–carrier scattering are discussed qualitatively. The book ends with a section on the high field conduction phenomena.

This monograph is by nature a treatise intermediate between a review article and a regular book. The discussions are highly condensed and many steps in the mathematical developments are only indicated. There are some errors in the equations but these are mostly trivial and fairly obvious. The statement that the phonon drag effect is responsible for the T^5 dependence of the resistivity of metals at low temperature seems to be misleading. On the whole, the material is very well organized and clearly presented. It should be useful for those who wish to obtain an appreciation of the elements of the theory without being burdened by the details. Those who are familiar with the subject may also find it interesting to read this clear and concise account which contains some fresh points of view.

H. Y. FAN

Vol. 1
1961

J. Phys. Chem. Solids Pergamon Press 1961. Vol. 19, Nos. 3/4, pp. 173–180. Printed in Great Britain.

NEUTRON SCATTERING FROM ISOTROPIC LATTICES

R. SUBRAMANIAN

Atomic Energy Establishment Trombay, Bombay

(*Received* 17 *October* 1960)

Abstract—To study theoretically the scattering of neutrons from a solid, one normally uses the Debye model for the lattice vibrations. Here we have taken a model based on the Born von Karman theory of lattice vibrations and applied it to the above problem. Some of the integrals involved cannot be evaluated analytically and we have therefore computed them on the T.I.F.R. electronic computer. The results are presented here with particular reference to neutron scattering from beryllium and magnesium. The agreement with experimental data is very good for cold and thermal neutron scattering from the crystals at room temperature but not so good for other crystal temperatures and higher neutron energies.

1. INTRODUCTION

CALCULATIONS of the inelastic scattering cross-section of thermal neutrons from isotropic or near isotropic lattices are usually made on the basis of the Debye model of a solid. A better approach would be to use the Born von Karman theory of the lattice spectrum. We assume the lattice to be completely isotropic, so that the dispersion relation is the same in all directions, and we take this to be the same as for a linear chain of equally spaced mass points, each point carrying the same mass and with interaction confined between nearest neighbours. This model has been applied to the neutron scattering problem by KOTHARI[1]. BARBER and MARTIN[2] have used the same model to calculate the specific heat of aluminium as a function of temperature and they find that the theory gives a better fit with experimental data.

The theory of neutron scattering based on the Born von Kármán model involves integrals which are too complicated to be solved analytically except in a few limiting cases. We have therefore programmed for these integrals and evaluated them[3] on the T.I.F.R. electronic computer.[4] Taking the particular cases of beryllium and magnesium, we present here some results for (i) the partial scattering cross-section $\sigma(E_1 \rightarrow E_2)$, for a neutron of energy E_1 being scattered into energy E_2, (ii) total scattering cross-section $\sigma(E_1)$ and (iii) the mean energy of the scattered neutrons, for various neutron energies and scatterer temperatures. The incoherent approximation[5] has been used and generally we have calculated the first term of the Placzek expansion[6] so that some multiphonon contribution is also taken into account.

2. SCATTERING CROSS SECTION

In the incoherent approximation, the first term of the Placzek expansion gives a cross-section*[1]

$$\sigma^1(E_1 \rightarrow E_2) = [4(S+s)/\pi^3 M] \times [\xi_{0L}^{-1} a^{-1/2}\{f_{3/2}(x, a, b) + a f_{1/2}(x, a, b)\} + 2\xi_{0T}^{-1}(\alpha a)^{-1/2}\{f_{3/2}(\alpha x, \alpha a, \alpha b) + \alpha a f_{1/2}(\alpha x, \alpha a, \alpha b)\}] \quad (1)$$

where

$$f_{n/2}(x, a, b) = (a+x)^{n/2}\left(\coth\frac{x}{2b} - 1\right)(\sin^{-1}x)^2 x^{-1}(1-x^2)^{-1/2} \quad (2)$$

S is the coherent and s the incoherent bound scattering cross-section; $M = m/m_0$ is the ratio of scatterer mass to the neutron mass, ξ_{0L} and ξ_{0T} are respectively the energies of longitudinal and transverse phonons corresponding to the maximum wave-vector f_0. The other symbols are defined by

$$x = \xi/\xi_{0L}, \quad a = E_1/\xi_{0L}, \quad b = k_0 T/\xi_{0L} = T/\theta_L$$
$$\alpha = \xi_{0L}/\xi_{0T} = \theta_L/\theta_T \quad (3)$$

* Notation used is the same as in Ref. (1) which may be consulted for details.

where ξ is the energy of a phonon, T the temperature of the scatterer, k_0 the Boltzmann constant and θ_L, θ_T are the 'characteristic' temperatures for longitudinal and transverse vibrations respectively. The total scattering cross-section would be given by

$$\sigma^1(E_1) = \int \sigma^1(E_1 \to E_2)\, dE_2 \tag{4}$$

$$= [4(S+s)/\pi^3 M][a^{-1/2}\{I_{3/2}(a, b) + aI_{1/2}(a, b)\} + 2(\alpha a)^{-1/2} \times \{I_{3/2}(\alpha a, \alpha b) + \alpha a I_{1/2}(\alpha a, \alpha b)\}] \tag{5}$$

where

$$I_{n/2}(a, b) = \int_{\max(-a, -1)}^{1} f_{n/2}(x, a, b)\, dx. \tag{6}$$

The integrals $I_{n/2}(a, b)$ have been evaluated for $n = 1, 3, 5$ and 7 and for $0 \leqslant a, b \leqslant 2{\cdot}0$ at an interval of $0{\cdot}2$ for both a and b, (and also for $a = 0{\cdot}1$). The detailed results are given in an internal report[3] (which can be obtained on request), and here we give only some values of $I_{1/2}$ and $I_{3/2}$ in Tables 1 and 2, respectively.

The mean energy of neutrons after scattering is

$$\overline{E_2} = \frac{1}{\sigma^1(E_1)} \int \sigma^1(E_1 \to E_2) E_2\, dE_2, \tag{7}$$

which in the present case reduces to

$$\overline{E_2} = \frac{1}{\sigma^1(E_1)} [4(S+s)/\pi^3 M] \times [\xi_{0L} a^{-1/2}\{I_{5/2}(a, b) + aI_{3/2}(a, b)\} + 2\xi_{0T}(\alpha a)^{-1/2}\{I_{5/2}(\alpha a, \alpha b) + \alpha a I_{3/2}(\alpha a, \alpha b)\}]. \tag{8}$$

Table 1. Values of $I_{1/2}(a, b)$ for various a and b. $[I_{1/2}(a, 0) = 0]$

b \ $a \to$	0	0·2	0·4	0·8	1·0	1·2	1·6	2·0
0·2	0·0861	0·1441	0·2392	0·6652	1·3202	2·1537	3·0854	3·7771
0·4	0·4834	0·6382	0·8360	1·4865	2·2841	3·2618	4·4000	5·2620
0·6	1·0506	1·3218	1·6413	2·5658	3·5578	4·7416	6·1641	7·2581
0·8	1·6825	2·0772	2·5254	3·7411	4·9465	6·3604	8·0965	9·4456
1·0	2·3436	2·8651	3·4450	4·9595	6·3870	8·0416	10·1047	11·7194
1·2	3·0200	3·6700	4·3834	6·2006	7·8545	9·7558	12·1528	14·0386
1·4	3·7056	4·4850	5·3327	7·4550	9·3381	11·4892	14·2243	16·3845
1·6	4·3968	5·3064	6·2889	8·7178	10·8317	13·2349	16·3107	18·7472
1·8	5·0919	6·1320	7·2499	9·9863	12·3321	14·9888	18·4070	21·1214
2·0	5·7898	6·9607	8·2142	11·2587	13·8373	16·7486	20·5104	23·5036

Table 2. Values of $I_{3/2}(a, b)$ for various a and b values. $[I_{3/2}(a, 0) = 0]$

b \ $a \to$	0	0·2	0·4	0·8	1·0	1·2	1·6	2·0
0·2	0·0429	0·0768	0·1332	0·3820	0·6571	1·1977	2·7886	4·8547
0·4	0·3279	0·4954	0·7153	1·3881	1·9293	2·7826	5·1029	8·0101
0·6	0·7614	1·1164	1·5596	2·7949	3·6861	4·9555	8·2528	12·2899
0·8	1·2522	1·8153	2·5043	4·3543	5·6264	7·3505	11·7175	16·9926
1·0	1·7692	2·5496	3·4946	5·9826	7·6497	9·8458	15·3242	21·8859
1·2	2·3000	3·3025	4·5089	7·6472	9·7166	12·3938	19·0057	26·8797
1·4	2·8389	4·0664	5·5374	9·3332	11·8092	14·9729	22·7310	31·9324
1·6	3·3829	4·8373	6·5748	11·0327	13·9180	17·5717	26·4842	37·0225
1·8	3·9304	5·6129	7·6182	12·7414	16·0379	20·1837	30·2562	42·1377
2·0	4·4804	6·3918	8·6660	14·4565	18·1654	22·8051	34·0414	47·2708

Vol. 1
196

3. LIMITING CASE

In the case of cold neutron scattering $a \ll 1$, from solids at temperature greater than their Debye temperature, $b \geqslant 1$, one can evaluate the integrals $I_{n/2}$ analytically. Because of general interest in this problem we shall now discuss this limiting case $a \ll 1$, $b \geqslant 1$. Since the algebra involved is rather long, we shall indicate the method of evaluating the integrals and give the final results.

In the limit under consideration, we expand the coth function as a power series in $x/2b$. Further the range of integration is divided into two parts, one from $-a$ to a and another from a to 1. In the first range we expand $(a+x)^{n/2}$ as a power series in x/a whereas in the second range we use a power series expansion in terms of a/x. If we write

$$I_{n/2} = P_{n/2} + Q_{n/2} \tag{9}$$

then the first integral gives

$$P_{n/2}(a, b) = 8[2^{n/2}a^{(n+2)/2}b/(n+2)] \times \left[1 - \frac{na}{2(n+4)b} + \ldots\right] \tag{10}$$

whereas the second one, in terms of $y = \sin^{-1}x$, becomes

$$Q_{n/2}(a, b) = \int_{\sin^{-1}a}^{\pi/2} y^2 \sin^{n/2}y \, dy \times \left[-\frac{\sin^2 y}{45(2b)^3} - \frac{na \sin y}{90(2b)^3} + \frac{1}{6b} + \left(\frac{na}{12b} - 1\right)\frac{1}{\sin y} + \left(2b - \frac{na}{2} + \frac{n(n-2)a^2}{48b}\right)\frac{1}{\sin^2 y} + \ldots\right] \tag{11}$$

To integrate this further we make use of the following result[7]

$$y^2 = \pi^2/4 - (8/\pi) \times \cos y\{a_0 + a_1 \sin^2 y + a_2 \sin^4 y + a_3 \sin^6 y + \ldots\} \tag{12}$$

where

$$a_0 = \frac{\pi^3}{32} = 0{\cdot}968946,$$

$$a_1 = \frac{\pi^3}{64} - \frac{\pi}{8} = 0{\cdot}091774,$$

$$a_2 = \frac{\pi}{48}\left(\frac{9\pi^2}{16} - 5\right) = 0{\cdot}036105,$$

$$a_3 = \frac{\pi}{64}\left(\frac{5\pi^2}{8} - \frac{259}{45}\right) = 0{\cdot}020270.$$

Terms involving powers of sin and a cos function can be directly integrated, whereas terms containing powers of only sin function can be evaluated in terms of the beta function

$$B(m, n) = 2\int_0^{\pi/2} \sin^{2m-1}\theta \cos^{2n-1}\theta \, d\theta = \Gamma(m)\Gamma(n)/\Gamma(m+n). \tag{13}$$

After some straightforward, though rather lengthy calculation, one arrives at the result

$$Q_{n/2}(a, b) = \left[-\frac{A_{4,n}}{45(2b)^3} - \frac{naA_{2,n}}{90(2b)^3} + \frac{A_{0,n}}{6b} + \left(\frac{na}{12b} - 1\right)A_{-2,n} + \left(2b - \frac{na}{2} + \frac{n(n-2)}{48}\frac{a^2}{b}\right)A_{-4,n}\right] \tag{14}$$

where

$$A_{m,n} = (\pi^2/8)B\left(\frac{m+n+2}{4}, \frac{1}{2}\right) - \frac{16}{\pi}\left(\frac{a_0}{m+n+2} + \frac{a_1}{m+n+6} + \frac{a_2}{m+n+10} + \frac{a_3}{m+n+14} + \ldots\right) \tag{15}$$

Since the coefficients $A_{m,n}$ do not involve either the energy or the temperature variable, these can first be calculated. Then it is simple to find $Q_{n/2}$ for

Table 3. Constants used in the calculations, for the metals beryllium and magnesium

	Mg	Be
a	3·2029 Å	2·2810 Å
c	5·2000 Å	3·5760 Å
V/N	$23{\cdot}0982 \times 10^{-24}$ cm^3	$8{\cdot}0563 \times 10^{-24}$ cm^3
d	2·295 Å	1·615 Å
C_{0L}	$5{\cdot}858 \times 10^5$ cm/sec	$12{\cdot}36 \times 10^5$ cm/sec
C_{0T}	$3{\cdot}070 \times 10^5$ cm/sec	$8{\cdot}179 \times 10^5$ cm/sec
$\theta_L = \xi_{0L}/k_0$	389·6°K	1168·1°K
$\theta_T = \xi_{0T}/k_0$	204·2°K	773·0°K
$(S+s)$	3·7 barns	7·54 barns
M	24·32	9·02

d is the average particle separation in the lattice. C_{0L} and C_{0T} are the limiting velocities for longitudinal and transverse waves respectively. The other symbols have been defined in the text.

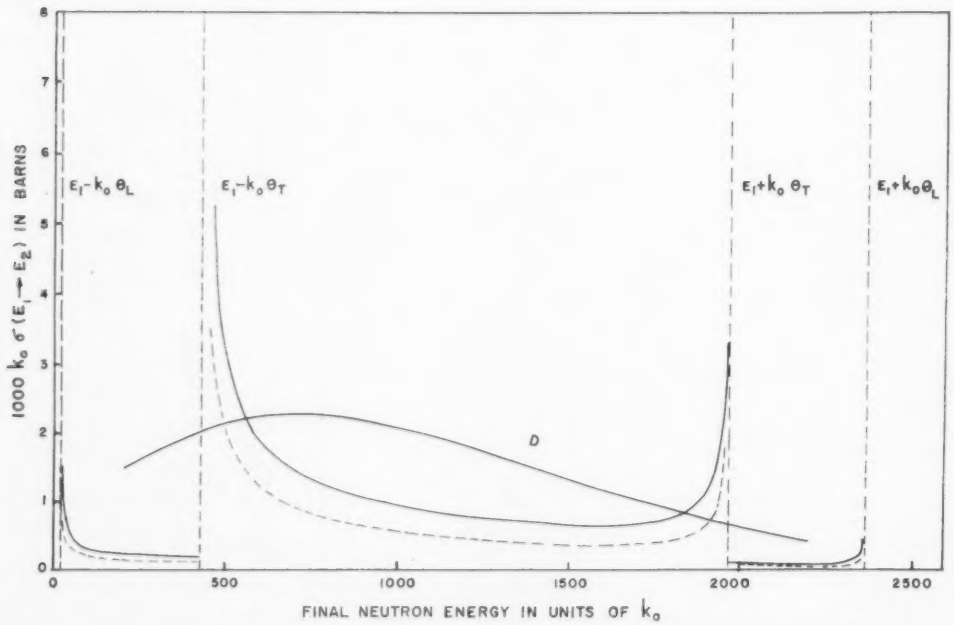

FIG. 1. The partial scattering cross-section $\sigma^1(E_1 \rightarrow E_2)$ plotted, after multiplying by 1000 k_0, as a function of the final neutron energy E_2 for $E_1 = 1200\ k_0$, for beryllium at a temperature of 300°K. The dashed lines represent the one-phonon results. The corresponding curve for 1000 $k_0 \times \sigma^1(E_1 \rightarrow E_2)$ on the Debye model is indicated by D.

any given a and b. The results obtained by using the formulae (9), (10), (12) and (15) agree with the earlier results obtained by direct integration to within a few per cent.

4. RESULTS AND DISCUSSION

The above model has been used to study neutron scattering from beryllium and magnesium metals both of which have a hexagonal close packed structure and have fairly isotropic elastic properties. Lattice parameters[8] a (this should not be confused with $a = E_1/\xi_{0L}$) and c and other constants needed in the calculations are given in Table 3.

Using these constants in equations (1) and (2) we have calculated the partial scattering cross-sections $\sigma^1(E_1 \to E_2)$ for beryllium at 300°K and for neutrons of initial energy $E_1 = 1200\ k_0$ and $30\ k_0$. The results* are shown in Figs. 1 and 2 respectively. In Fig. 1 the dashed line gives the one phonon results. For comparison, we have calculated $\sigma^1(E_1 \to E_2)$ for beryllium at 300°K and for $E_1 = 1200\ k_0$ on the Debye model[5] (curve D of Fig. 1) retaining the first term of the Placzek expansion. This gives results which are very different from those obtained on the present model. The Debye model gives a broad maximum as compared to two sharp maxima at $E_2 = E_1 \pm k_0\ \theta_T$ (besides two other minor maxima at $E_2 = E_1 \pm k_0\ \theta_L$) given by the present model. This is to be expected, since in our model the cross-section depends directly on the form of the frequency distribution function[1] $g(\xi)$ [see equation (4.14) of Ref. (5)]. It is easy to see that the peaks in Figs. (1) and (2) correspond to the singularities of $g(\xi)$ which is very different from the $g(\xi)$ of the Debye model. The mean energy of the scattered neutrons on the Debye model is nearly $1005\ k_0$ whereas on the present model it is near $955\ k_0$.

For a scatterer of large M, the main contribution

* In plotting we have multiplied $\sigma^1(E_1 \to E_2)$ by $1000\ k_0$, so that the units of the product are barns.

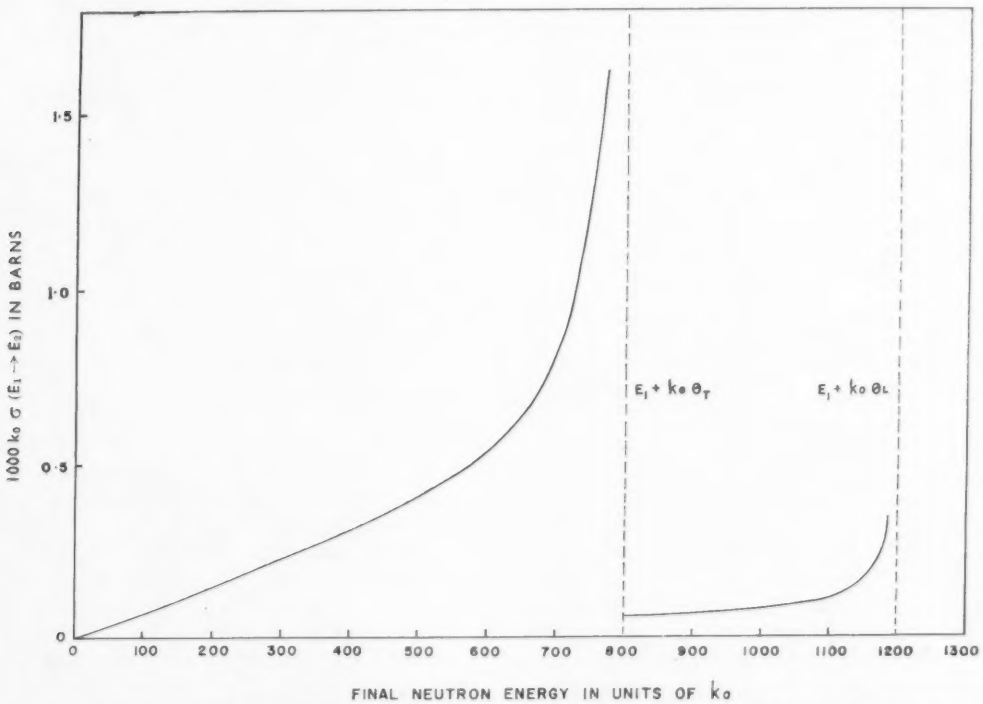

FIG. 2. The partial scattering cross-section $\sigma^1(E_1 \to E_2)$ plotted, after multiplying by $1000\ k_0$, as a function of the final neutron energy E_2, for $E_1 = 30\ k_0$, for beryllium at a temperature of 300°K.

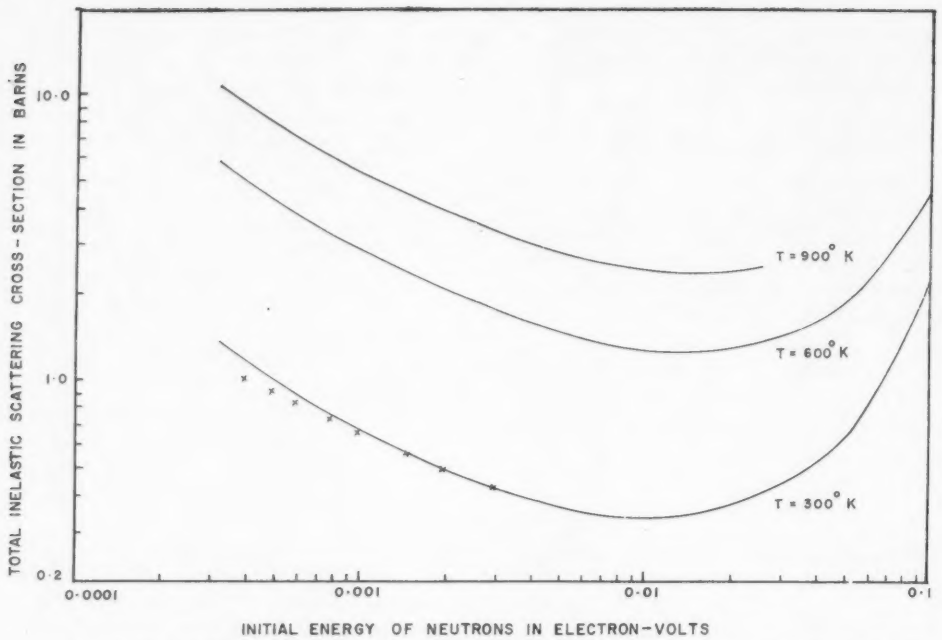

FIG. 3. Total inelastic scattering cross-section of neutrons as a function of the initial neutron energy for beryllium at different temperatures. The experimental data, after subtracting the absorption part, are indicated by crosses.

to the scattering cross-section comes from the first term of the Placzek expansion. The contribution of two phonon processes in the energy and temperature range of interest is also comparatively small since that again varies as $1/M^2$. (Higher phonon processes will contribute even less.) In such a case one observes that the energy dependence of the differential scattering cross-section for neutrons scattered at 90° is the same as for the integrated (over angle) cross-section

$$\left(\frac{d^2\sigma^1}{dE_2\, d\Omega}\right)_{\theta=90^\circ} = \frac{1}{4\pi}\sigma^1(E_1 \to E_2).$$

It should therefore be possible to decide at least qualitatively between various models of lattice vibrations by studying the energy distribution of neutrons scattered at 90° for a polycrystalline sample. On the present model one expects two peaks roughly at $E_2 = E_1 \pm k_0\,\theta_T$, whereas on the Debye model one would expect only a flat distribution.

In Fig. 3, the total inelastic scattering cross-section in beryllium is plotted as a function of initial neutron energy for different temperatures. Comparison with experiment[9,10] can only be made in the cold neutron region since we have not considered the elastic scattering contribution. The frequency distribution affects only the Debye–Waller factor in the case of elastic scattering and hence this cross-section is not very sensitive to the frequency distribution assumed. The calculations on the Debye model have been made by BHANDARI[11]. At $T = 300$°K the agreement with experimental data is good. (For comparison, one must subtract the absorption cross-section $\sigma_{abs.}$ from experimental values. For beryllium, $\sigma_{abs.} =$ 10 mbarns at 2200 m/sec). At a beryllium temperature of 900°K, the experimental value[10] of the inelastic scattering cross-section is nearly 6 barns whereas the value on the present model is 5·8 barns. Detailed calculation of the total one-phonon scattering cross-section has also been made on the present model using equation (24) of

Vol. 1
1961

Table 4. Comparison of the inelastic scattering cross-section of neutrons in beryllium obtained on the present model with Bhandari's values

T	E_1/k_0 (°K)	Values on the present model (barns)		Bhandari's values (barns)	
		$\sigma_1(E_1)$	$\sigma^1(E_1)$	σ_1	$\sigma_1+\sigma_2$
900°K	10	4·0867	5·7751	3·871	5·082
300°K	10	0·6342	0·7303	0·735	0·750
	30	—	0·4560	0·495	0·512
	300	—	0·4142	0·420	0·480
	900	—	1·3562	1·101	1·271
	1200	1·3853	2·2254	1·515	1·810

σ_1 and σ_2 are the one-phonon and two-phonon scattering cross-sections respectively.

Ref. (1), for an initial neutron energy of 10 k_0, at the two beryllium temperatures of 300°K and 900°K and for 1200 k_0 at 300°K. In Table 4 these results are compared with the values obtained by retaining only the 1st term of the Placzek expansion and also with the one and two phonon cross-sections of BHANDARI[11]. For low values of neutron energy and crystal temperature, the contribution of the second and higher terms of the Placzek expansion to the scattering cross-section is small and the detailed calculation gives values which are very close to the values of $\sigma^1(E_1)$. Also these values

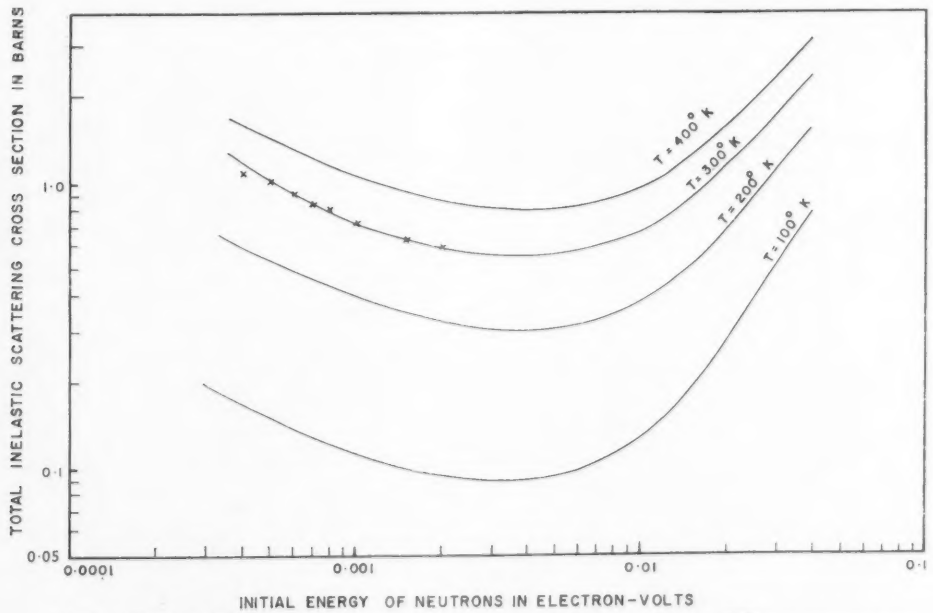

FIG. 4. Total inelastic scattering cross-section of neutrons in magnesium at different temperatures as a function of the initial neutron energy. Crosses represent the experimental data after subtracting the absorption part.

agree well with Bhandari's values. But, for large neutron energies and high temperatures, the exponent of the Debye–Waller factor becomes large, and the first Placzek term cannot be expected to give correct values, especially for substances like beryllium which have low M values.

The total inelastic scattering cross-section of neutrons in magnesium is represented in Fig. 4. The experimental points[9] are marked as crosses. (Absorption cross section of neutrons in magnesium is 63 millibarns for a neutron velocity of 2200 m/sec.) Here the agreement with experimental values is very satisfactory at a magnesium temperature of 300°K. Even at high energies, the first Placzek term will give good values because of the comparatively large mass of magnesium.

Acknowledgements—The author is indebted to Dr. L. S. KOTHARI for the suggestion of this problem and for useful discussions. He also wishes to thank Dr. R. NARASIMHAN, Messrs K. S. KANE and M. M. DOSABHAI of the Computer Group of the Tata Institute of Fundamental Research for their valuable help in programming for the calculations.

REFERENCES

1. KOTHARI L. S., *Phil. Mag.* **4,** 1325 (1959).
2. BARBER S. W. and MARTIN B., *J. Phys. Chem. Solids* **9,** 198 (1959).
3. SUBRAMANIAN R., internal report (unpublished).
4. NARASIMHAN R., *Proc. Indian Acad. Sci.* **52**A, 47 (1960).
5. KOTHARI L. S. and SINGWI K. S., *Solid State Physics* Vol. VIII, p. 109. Academic Press, New York (1959).
6. PLACZEK G., *Phys. Rev.* **93,** 895 (1954).
7. DWIGHT H. B., *Tables of Integrals and other Mathematical Data*, p. 84. Macmillan Company, New York (1957).
8. PEARSON W. B., *A Handbook of Lattice Spacings and Structures of Metals and Alloys.* Pergamon Press (1958).
9. HUGHES D. J. and SCHWARTZ R. B., USAEC Report No. BNL–325 (1958).
10. HUGHES D. J., *Pile Neutron Research.* Addison-Wesley Publishing Co., Cambridge, Mass. (1953).
11. BHANDARI R. C., *J. Nucl. Energy* **6,** 104 (1957); also unpublished work.

Vol. 1
1961

J. Phys. Chem. Solids Pergamon Press 1961. Vol. 19, Nos. 3/4, pp. 181–188. Printed in Great Britain.

TRANSITION TO THE HIGH FIELD LIMIT IN THE ZEEMAN SPECTRA OF GERMANIUM DONORS*

W. S. BOYLE

Bell Telephone Laboratories, Murray Hill, New Jersey

and

R. E. HOWARD†

Carnegie Institute of Technology, Pittsburgh, Pennsylvania

(*Received* 17 *October* 1960)

Abstract—An experimental and theoretical study of the connection between the low field Zeeman spectra and high field photoionization spectrum of donor impurities in germanium is presented. It is shown that at high fields the absorption maxima that occur in the photoionization spectrum correspond to transitions to Landau levels which are bound by a coulomb force to the parent donor impurity. As the magnetic field is decreased some of the lines in the photoionization spectrum remain sharp and pass into Zeeman lines while others have no small field counterpart. These are metastable and become increasingly diffuse with decreasing field.

ol. 19
1961

INTRODUCTION

THE ZEEMAN spectra of the levels introduced into a semiconductor by an impurity have been studied by several observers.[1,2,3,4] In general, at low fields the spectra obtained experimentally agree very well with those expected from the hydrogen model. The effective mass and its anisotropy in the band nearest the impurity level are reflected directly in the spectra obtained. This in some cases leads to a more complicated spectrum than in the atomic case but can be used to determine the effective mass parameters of the electron band in question.

A feature of some interest is that the equivalent fields that can be obtained experimentally are much larger than in the case of atomic spectra. By equivalent field we mean that field which leads to the same spectroscopic splitting when measured in Rydbergs of the two systems. This arises from the small effective masses that occur in certain semiconductors; in germanium for example, with the field normal to a low mass direction, the Zeeman splitting at 20 kG of a $2p$ state is comparable to the binding energy at zero field.

It has also been found that the photoionization spectrum shows pronounced periodic structure in a magnetic field.[3] This was ascribed to the periodic variation of the density of states in the continuum of the band when the band is broken up into a series of Landau sub-bands by the magnetic field.[5] This leads to an increased absorption coefficient for photon energies where transitions from the ground state of the impurity to the bottom of each Landau sub-band occur. The period obtained experimentally agreed quite well with this model. However the ionization energy of the impurity deduced by extrapolation differed considerably from that predicted by the effective mass theory. In addition, the first two oscillations in the absorption coefficient showed fine structure which was inexplicable from the model based on transitions to free Landau levels and it was assumed that these arose from bound Landau levels split off from the continuum by the coulomb perturbation of the impurity level. HOWARD and HASEGAWA[6,7] have now shown that the absorption

* Work supported in part by the Office of Naval Research.

† Present address: National Bureau of Standards, Washington, D.C.

coefficient at a Landau edge is finite and continuous as a function of photon energy and that in the limit of infinite fields the matrix elements for optical transitions from the ground state of the impurity to the continuum Landau states become vanishingly small, and in this limit all transitions are to the bound Landau levels. In this paper we will show both by experiment and theory how the Zeeman spectra change with increasing magnetic field and how the high field bound Landau levels are connected to the low field Zeeman levels.

1. THEORY

(a) *Donor levels*

In the experiment to be discussed the field was oriented so as to make an equal angle with the symmetry axis of each of the conduction band ellipsoids; thus each state described in an effective mass approximation is fourfold degenerate. The absence of an axis of rotational symmetry, however, makes a complete effective mass description of these states difficult. We shall therefore consider the relatively simple case where the field is oriented along one of the conduction band symmetry axes and discuss levels associated with the conduction band minimum that lies on this axis. Because of the large ratio of the longitudinal to the transverse effective masses of electrons in germanium, the effect of a field component perpendicular to a symmetry axis upon effective mass energy levels is small. Hence we may expect the following discussion to provide a basis for an understanding of at least the qualitative features of the data.

We assume a uniform field H in the longitudinal direction which we take along the z axis. The appropriate effective mass hamiltonian describing the donor electron may be written

$$\mathscr{H} = \mathscr{H}_0 + \mathscr{H}_1, \tag{1.1}$$

where,

$$\mathscr{H}_0 = \frac{1}{2m_t}\left[\left(p_x - \frac{eH}{2c}y\right)^2 + \left(p_y + \frac{eH}{2c}x\right)^2\right], \tag{1.2}$$

and

$$\mathscr{H}_1 = \frac{p_z^2}{2m_1} - \frac{e^2}{\kappa\sqrt{(x^2+y^2+z^2)}}. \tag{1.3}$$

Here m_t, m_1 and κ are the transverse and longitudinal effective masses and the static dielectric constant respectively. These parameters have the following values for germanium:

$$m_1 = (1{\cdot}6 \pm 0{\cdot}008)m_0, \quad m_t = (0{\cdot}0813 \pm 0{\cdot}002)m_0,$$
$$\kappa = 16.$$

The energy levels of the above hamiltonian have been discussed in the limiting cases of very small and of very large magnetic field strengths. The hydrogenic solutions for zero field were treated by KOHN[8], while HAERING[9] considered their first order Zeeman splitting. In the other limit (where the field is so strong that the coulomb term in the hamiltonian may be treated as a perturbation), YAFET *et al.*[10] have shown that the following are good approximate eigenfunctions and become exact in the limit $H \to \infty$:*

$$\Psi_{N,M,\mu}(x, y, z) = \Phi_{N,M}(x, y) f_{N,M,\mu}(z), \tag{1.4}$$

where

$$\mathscr{H}_0\Phi_{N,M}(x, y) = (N+1/2)\hbar\omega_t\Phi_{N,M}(x, y),$$
$$N = 0, 1, 2 \ldots \infty,$$
$$M = N, N-1 \ldots -\infty. \tag{1.5}$$

Here $\omega_t = eH/m_tc$. The energies $(N+1/2)\,\hbar\omega_t$ are the so-called Landau energies. M is the quantum number of the angular momentum in the z direction. (Note $M \leqslant N$). Explicitly

$$\Phi_{N,M}(\rho, \phi) = (-1)^N N![2^{(1-M)}\pi N!(N-M!)]^{-1/2} \times$$
$$\frac{1}{\lambda}\left(\frac{\rho}{\lambda}\right)^{-M} L_N^{-M}(\rho^2/2\lambda^2)\exp(-\rho^2/4\lambda^2)\exp iM\theta, \tag{1.6}$$

where

$$\lambda^2 = \hbar c/eH,$$

and

$$L_N^M(x) = \frac{1}{N!}x^M \exp x \frac{d^N}{dx^N}(X^{N-M}\exp -x).$$

* These functions were also used by WALLIS and BOWLDEN[5].

The functions $f^{(z)}_{N,M,\mu}$ satisfy the equation

$$-\frac{1}{2m_1}\frac{d^2 f_{N,M,\mu}(z)}{dz^2}+V_{N,M}(z)f_{N,M,\mu}(z)= \epsilon_{N,M,\mu}f_{N,M,\mu}(z), \tag{1.7}$$

where

$$V^{(z)}_{N,M}=-\frac{e^2}{\kappa}\frac{\int|\Phi_{N,M}(x,y)|^2\,dxdy}{\sqrt{(x^2+y^2+z^2)}}. \tag{1.8}$$

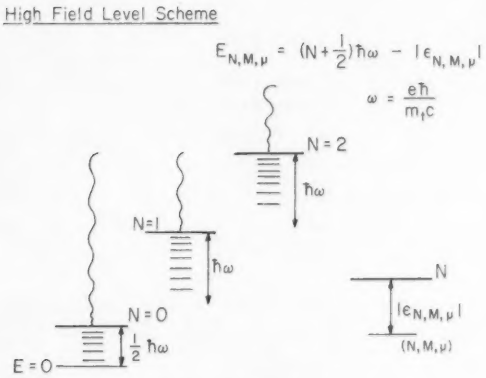

FIG. 1. High field level scheme.

Equation (1.7) has an infinite number of discrete solutions for which $\epsilon_{N,M,\mu}<0$, $\mu=0,1,2\ldots$, and a continuum solution for which $\epsilon_{N,M,\mu}>0$. The total energy of a state (N, M, μ) measured from the zero field ionization edge is given by

$$E_{N,M,\mu}=(N+1/2)\hbar\omega_t+\epsilon_{N,M,\mu}. \tag{1.9}$$

A diagram of the level scheme is shown in Fig. 1. Associated with each Landau edge N, there are an infinite number of bound states pulled down by the coulomb potential, and also a continuum solution. It may be shown that for each pair $(N, M,)\epsilon_{N,M,0}$ becomes negatively infinite as $-(\log H)^2$, $(H\to\infty)$. All other discrete $\epsilon_{N,M,\mu}$, however, approach finite negative values in this limit.

(b) *Connection between high and low field states*

Over most of the range of the present measurements the field strength corresponds to neither of the limits considered above. It is, therefore, particularly instructive to investigate how the zero field hydrogenic levels go over into levels described in the high field approximation as the field strength is increased. Such correspondence can be easily found from the following considerations.* The hamiltonian (1.1) is invariant under inversion and under rotation about the z axis; hence P and M are good quantum numbers for all field strengths.

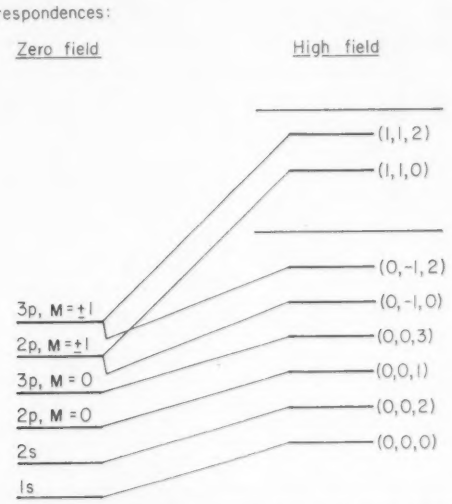

FIG. 2. Correspondence between low and high field states. The parity of a state (N, M, μ) is even or odd when $M+\mu$ is respectively even or odd.

Since there is no other symmetry operation under which $\mathscr{H}$ is invariant, levels having the same values of P and M cannot be degenerate; i.e. two such levels cannot "cross" as the field strength is varied. Using this principle we have constructed the correspondence scheme shown in Fig. 2 for a few of the low-lying levels.

More generally, it is easy to see that the above no-crossing principle implies that the high field states with $\epsilon<0$ divide themselves into two classes: those that do and those that do not correspond to zero field bound states. The former states are those for which $N=0$, and also those for

* Our discussion here is closely similar to that of KOHN and LUTTINGER[11] on the connection between states described in the hydrogenic and in the "adiabatic" limits.

which $N > 0$, $N = M$. No such correspondence exist for the remaining high field states (those for which $N > 0$, $N > M$). This division may also be seen from another point of view. All states ($\epsilon < 0$) for which $N > 1$ are degenerate with continuum states. Of these, states with $N = M$ are degenerate only with continuum states of small values of M. Hence matrix elements of the coulomb term in the hamiltonian, which might mix these states with the continuum, vanish. On the other hand those states for which $N > M$ are connected, for finite field strengths, to the continuum by a non-vanishing matrix element of the coulomb term in the hamiltonian. Therefore the class of high field states that correspond to zero field states are truly discrete; the

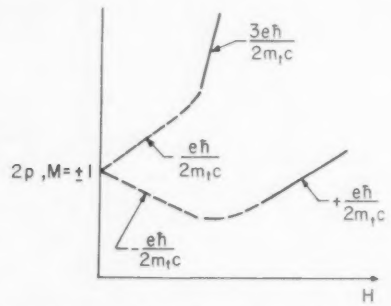

FIG. 3. Qualitative dependence of $2p$, $M = \pm 1$ states on field strength.

class of high field states that do not correspond to zero field states are metastable and have a finite probability of decaying into the continuum. Because of this, we would expect an optical transition to one of the metastable states to appear broadened, and to eventually disappear as the field strength is lowered. A transition to one of the truly discrete states, on the other hand, should appear sharp down to zero field.

(c) $2p$, $M = \pm 1$ *levels**

We have sketched in Fig. 3 the qualitative behavior of the $2p$, $M = \pm 1$ levels as a function of field strength. In a small field, the energies of these levels measured from their positions at zero field are given by the equation

$$E_{2p,M=\pm 1} = \pm \tfrac{1}{2}\hbar\omega_t \qquad (1.10)$$

* These are the usual hydrogenic states where we use M to denote the magnetic quantum number.

Therefore, the initial slopes of the $M = \pm 1$ levels as functions of H are $\pm(e\hbar/2m_tc)$ respectively. For high fields, we have the correspondences

$$2p,\ M = +1, \rightarrow (1, 1, 0),$$
$$2p,\ M = -1, \rightarrow (0, -1, 0),$$

and the limiting energies

$$E_{1,1,0} = 3/2\hbar\omega_t - \text{const.}\ (\log H)^2 \qquad (1.11)$$
$$E_{0,-1,0} = 1/2\hbar\omega_t - \text{const.}\ (\log H)^2. \qquad (1.12)$$

The slopes of the $2p$, $M = \pm 1$ levels, therefore, change continuously from their initial values to the limiting values $\frac{3}{2}(e\hbar/m_tc)$ and $+\frac{1}{2}\times e\hbar/m_tc$ respectively.

2. OPTICAL TRANSITIONS: ABSORPTION AT LANDAU EDGES

Only excited states for which $M = \pm 1$ or 0 can be reached from the ground state by optical dipole transitions. If we assume a high field description, transitions are then allowed to continuum states above each Landau level, to discrete states beneath the level $N = 0$, to both discrete and metastable discrete states beneath the $N = 1$ level and to metastable discrete states beneath Landau levels for which $N > 1$.

The intensity of transitions to states in the immediate neighborhood of a Landau edge has been a question of considerable interest. WALLIS and BOWLDEN[5] assumed that continuum states at a Landau edge could be described in a Born approximation. This is equivalent to neglecting the effect of the coulomb term in the hamiltonian upon these states. Accordingly they calculated that the absorption coefficient becomes infinite, (for $\Delta M = \pm 1$, and in the absence of broadening), at wavelengths corresponding to transitions from the ground state to Landau levels. Upon this basis, they predicted peaks in the absorption spectrum at such wavelengths.

Recently, however, it has been shown that the effect of the coulomb perturbation upon transitions to continuum states near Landau edges is of critical importance.[6,7,12] It can be shown that if the coulomb perturbation is properly taken into account, the infinities in the absorption coefficient are removed. The absorption coefficient as a function of photon energy becomes finite and continuous at a Landau edge. Further, the magnitude of

Vol. 1
1961

the absorption per unit energy at a Landau edge tends to zero in the limit $H \to \infty$. In this limit, however, transitions to bound states beneath Landau edges become intense.

In view of these results, we should expect that transitions to states at Landau edges do not appear prominently in the magneto-optic absorption spectrum, but rather that intense peaks in the spectrum correspond to transitions to bound states well separated from Landau edges. We shall see that the experiment supports this interpretation.

3. EXPERIMENTAL RESULTS AND INTERPRETATION

All the data presented here was obtained from a germanium sample with $1{\cdot}5 \times 10^{15}$ arsenic impurity atoms per cm^3 and 0·05 cm thick. This is a considerably lower concentration than that used in the previous experiments and leads to much better defined lines in the region of the spectrum near the ionization edge. Both the magnetic field and the direction of propagation were along a [100] crystal axis.

Monochromatic radiation from a grating spectrometer was introduced through the bottom of the cryostat. Immediately before reaching the sample the beam was split with a half mirror. A large fraction of this beam passed through the sample and then a bolometer detector; the remainder was monitored by a second similar detector. In this way an accurate normalizing spectrum was obtained. This procedure was found to be necessary even in the flushed system because of the difficulty in removing residual and fluctuating water vapor absorption. Care was taken to reduce strain broadening by etching at least 4×10^{-3} cm from the sample, and thermal stresses were reduced by attaching the sample to the cold finger at only one end. The helium bath temperature was 1·5°K and the sample temperature was estimated from the resistance of the control bolometer to be not more than 0·5°K above this.

(a) $2p$, $M = \pm 1$ *levels*

(i) *Field dependence.* Fig. 4 shows the Zeeman splitting of the zero field $2p$, $M = \pm 1$ levels up to field strengths of 30·2 kG. The experimental curves agree qualitatively with those of Fig. 3, except that at the highest experimental field strengths the $2p$, $M = -1$ level has only just begun to turn upwards.

We have attempted to calculate in some detail the field dependence of the $2p$, $M = \pm 1$ levels. We have neglected the component of the magnetic field perpendicular to the [1, 1, 1] direction and have described the electron by the hamiltonian (1.1) containing an effective field H' equal to the component of the field strength H parallel to the [1, 1, 1] direction i.e. $H' = H/\sqrt{3}$. It may be shown that within the effective mass approximation, the energy computed by this procedure is correct to first order in H; it is correct to all orders in H if the ratio $m_t/m_l \to 0$. For donor electrons in germanium $m_t/m_l = 0{\cdot}05$. Hence we expect our approximations to be good, at least qualitatively, over the whole range of the experiment.

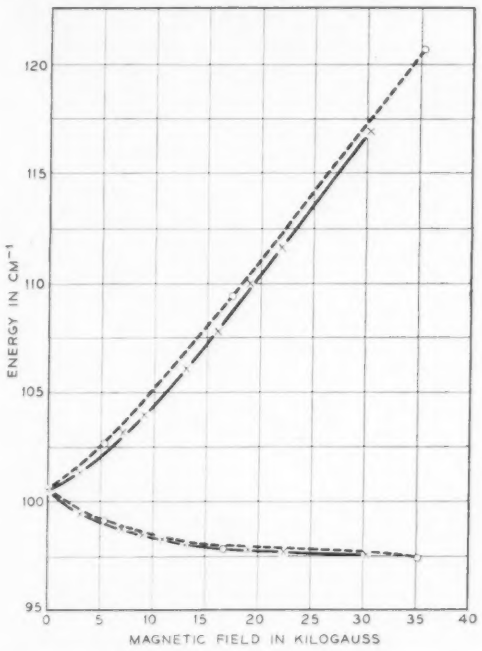

FIG. 4. $2p$, $M = \pm 1$ levels: the full lines are drawn through the measured values indicated; the dotted lines represent a variational calculation of these levels. The zero field measured and calculated energies have been placed in coincidence.

For the $2p$, $M = 1$ state, a two-parameter variational function of the proper symmetry is

given by

$$\Psi_{1,1,0}(\rho, \phi, z) = \left(\frac{\epsilon_2^2}{2\lambda'^2\sqrt{\pi}}\right)\left\{\frac{\epsilon_1^2}{2\pi\lambda'^2}\right\}^{1/4} \rho \times$$

$$\exp -[\epsilon_2^2\rho^2+\epsilon_1^2 z^2]/4\lambda'^2 \exp i\phi \qquad (3.1)$$

Here $\lambda' = \hbar c/eH'$. The appropriate variational function for the $2p$, $M = -1$ state, $\Psi_{0,-1,0}$, is identical except that $\exp i\phi$ is replaced by $\exp -i\phi$. The variational parameters ϵ_1 and ϵ_2 are determined from the condition that $(\Psi_{1,1,0}, \mathscr{H}'\Psi_{1,1,0}) \equiv \langle E'_{1,1,0}\rangle$ be a minimum. ($\mathscr{H}'$ is the hamiltonian (1.1) containing the effective field H'.) It is clear that the variational energies for the $2p$, $M = 1$ and the $2p$, $M = -1$ states, viz. $\langle E'_{1,1,0}\rangle$ and $\langle E'_{0,-1,0}\rangle$, are related at all field strengths by the equation

$$\langle E_{1,1,0}\rangle - \langle E_{0,-1,0}\rangle = \hbar\omega'_t, \qquad (3.2)$$

and

$$f_{0,-1,0;+} = (E_{0,-1,0} - E_0)|\langle 0, -1, 0|x+iy|0\rangle|^2, \qquad (3.4)$$

respectively, where E_0 is the ground state energy. The matrix elements appearing in these expressions are equal. Hence the ratio of the intensities is given by

$$\frac{f_{0,-1,0;+}}{f_{1,1,0;-}} = \frac{E_{0\,-1\,0} - E_0}{E_{1,1\,0} - E_0} = 1 - \frac{\hbar\omega'_t}{(E_{1\,1,0} - E_0)} \qquad (3.5)$$

This predicts that for $H' > 0$, transitions to the $M = +1$ state are more intense than those to the $M = -1$ state. This is observed experimentally. For the field strength $H = 19$ kG, the ratio of the transmission minimum of the $2p$, $M = -1$ state to that of the $2p$, $M = +1$ state is found from equation (3.5) to equal 0·89. The observed value is 0·82.

Table 1

H, kG	H', kG	$\hbar\omega'_t$, cm^{-1}	$\langle E'_{1,1,0}\rangle$, cm^{-1}	$\langle E'_{0,-1,0}\rangle$, cm^{-1}
0	0	0	−11·4	−11·4
5·20	3	3·50	− 9·31	−12·81
17·3	10	11·66	− 2·58	−14·24
34·6	20	23·32	8·64	−14·68

where

$$\omega'_t = eH'/m_t c.$$

Results of this calculation for several field strengths are listed in Table 1. Here the variational energies are measured from the zero field ionization edge. The zero field energy is about 10 per cent higher than the value $-12{\cdot}9$ cm^{-1} calculated by KOHN[8].

In Fig. 4, we have put the experimental and calculated zero field energies (now measured from the ground state) into coincidence. The fit of the calculated and experimental curves is seen to be in good qualitative agreement. This justifies our neglect of the perpendicular field component.

(ii) *Relative intensities.* The intensities of transitions from the ground state to the $2p$, $M = \pm 1$ and $M = -1$ states are proportional to the oscillator strengths.[5]

$$f_{1,1,0;-} = (E_{1\,1,0} - E_0)|\langle 1, 1, 0|x-iy|0\rangle|^2, \qquad (3.3)$$

(b) *Higher energy levels*

The spectra of Fig. 5 show the relative transmission plotted against photon energy for field strengths H equal to 0, 19·0 and 30·2 kG. In Fig. 6, the photon energies at which transmission minima occur are plotted against field strength. The lines labelled (3) and (4) on this figure are easily identifiable since they go back smoothly to the $3p$, $M = \pm 1$ zero field states. In the region above 3 kG the $3p$, $M = -1$ state becomes hard to resolve because of its proximity to the more intense $2p$, $M = +1$ peak, however at the largest fields the $3p$, $M = -1$ line should be resolved and we are unable to explain its absence. Calculation of the field dependence of the $3p$ states has not been made because of the complexity of the appropriate

Vol. 1
1961

variational trial functions. It should be noticed, however, that as for $2p$, $M = 1$ level, the slope of the $3p$, $M = +1$ level continually increases as a

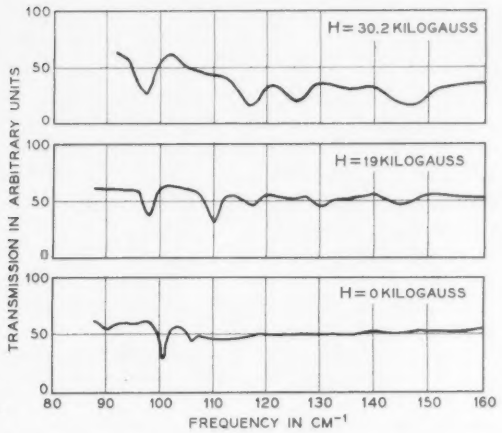

FIG. 5. Relative transmission coefficients as a function of frequency for $H = 0$, 19 and 30·2 kG.

function of H, reaching a value of about 0·7 cm^{-1}/kG at the highest field strengths. This value is still considerably less than the limiting slope $\frac{1}{2}\sqrt{3} \times eh/m_t \times 1/\sqrt{3} = 1{\cdot}01$ cm^{-1}/kG.

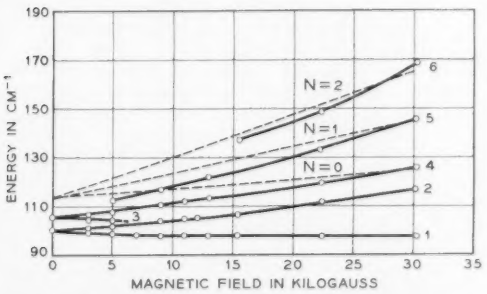

FIG. 6. Minima in the transmission coefficient plotted as a function of field strength. The straight lines in the figure are the plots of the Landau edges $I+(N+1/2)\hbar\omega_c$ for $N = 0$, 1, and 2.

No clear correspondence to any zero field states appears for any of the states higher than $3p$, $M = 1$. We have, however, estimated the energy of the metastable state (2, 1, 0) i.e. the lowest $M = 1$ state associated with the Landau edge $N = 2$, for the field strength $H = 30$ kG ($H' = 17{\cdot}3$ kG). For this purpose the following one-parameter variational trial function was chosen:

$$\Psi_{2,1,0}(\rho, \phi, z) = \left(\frac{\epsilon^2}{2\pi\lambda'^2}\right)^{1/4} \times \exp -(\epsilon^2 z^2/4\lambda'^2)\Phi_{2,1}(\rho, \phi),$$

where $\Phi_{2,1}(\rho, \phi)$ is given by equation (1.6).

Again $\lambda'^2 = \hbar c/eH'$. For $H = 30$ kG we find

$$\langle E'_{2,1\,0} \rangle = \tfrac{5}{2}\hbar\omega'_t - 21{\cdot}0 \text{ cm}^{-1} = 29{\cdot}6 \text{ cm}^{-1}.$$

This is the energy of the (2, 1, 0) state measured from the zero field ionization edge. The donor ionization energy as found from the zero field data using KOHN's calculations of the zero field energy levels, is 113 cm^{-1}. Hence the energy of the (2, 1, 0) state measured from the ground state is 142·6 cm^{-1}. On the basis of this result, we should identify the strong transmission minimum that occurs at about 146 cm^{-1} for $H = 30$ kG as due to a transition to the (2, 1, 0) state, and hence label line (5) on Fig. 6 as corresponding to such transitions for weaker fields. In our estimate of the energy of the (2, 1, 0) state, we have again neglected the field component perpendicular to the [1, 1, 1] direction. This probably introduces a more serious error than in the corresponding calculation for the (1, 1, 0) state: it tends to underestimate the energy.

We have not attempted any calculations for levels lying along line (6). We should guess, however, by analogy with lines (4) and (5) that these states are the lowest $M = 1$ states associated with $N = 3$, i.e. they are states that correspond to the high field metastable state (3, 1, 0). Our interpretation of states on lines (5) and (6) as metastable states associated with Landau edges $N = 2$ and $N = 3$ respectively is consistent with the following observations: (1) these states broaden and eventually fail to be resolved as the field strength is decreased. This is characteristic of metastable states as discussed in Section 2(b). (2) The slopes of the lines (5) and (6) as a function of H are, at the highest field, about 1·6 cm^{-1}/kG and 2·1 cm^{-1}/kG respectively. These are less than but nearly equal to the limiting slopes of bound states beneath the $N = 2$ and $N = 3$ edges of $5/2(e\hbar/m_t c) \times 1/\sqrt{3} = 1{\cdot}8$ cm^{-1}/kG and $7/2(e\hbar/m_t c) \times 1/\sqrt{3} = 2{\cdot}5$ cm^{-1}/kG respectively.

4. THE IONIZATION ENERGY

There appears to be no simple way of finding the zero-field ionization energy from the magneto-optic absorption data, contrary to the expectations of previous work.[3] There, the magneto-optic absorption spectrum measured at two field strengths was analyzed on the assumption that strong transmission minima corresponded to transitions to states at Landau edges. But the present measurements of the absorption minima as a function of field strength indicate that this assumption is not correct.

In Fig. 6, we have plotted the "cyclotron" Landau energies $I+(N+1/2)\hbar\omega_c$, where I is the zero field ionization energy which is taken equal to 113 cm^{-1}. ω_c is the cyclotron frequency $eH/m_c c$ where the cyclotron mass m_c is equal to 0·13 m_0 for electrons in germanium.* It is observed that for H equal to the highest field strengths lines (4), (5), and (6) just intersect the Landau edges $N = 0$, 1 and 2 respectively. We believe that this is fortuitous. At lower field strengths and also, if our interpretation of these lines is correct, at higher field strengths, there is no strong absorption in the neighborhood of Landau edges. At a field strength of 30 kG, the bound states to which lines (4), (5) and (6) correspond lie at a spacing of about $\hbar\omega_c = 22$ cm^{-1} beneath their associated Landau edges ($N = 1$, 2, 3 respectively). That this is to be expected for the (2, 1, 0) state was shown by our variational estimate.

It would be possible to find the ionization energy from the magneto-optic data by carrying out a very careful energy level calculation (of say the $2p$, $M = 1$ state) as a function of field strength. As in our rough calculation, we would compute the energy of a state relative to the ionization edge. A comparison of this value with the measured value would yield the ionization energy. This, of course, is similar to the procedure used in finding the ionization energy from zero-field data, and, therefore, appears to have no special advantages over the zero field method apart from providing a rather searching check. These remarks only apply, of course, to semiconductors where well defined zero field spectra can be obtained and there are probably many instances in other materials where information can be obtained only from such magneto-optic experiments.

* Note that the "effective field" Landau energy $e\hbar/2m_t c \times H/\sqrt{3} = 0{\cdot}34\,H$ cm^{-1} and the "cyclotron" energy $(e\hbar/2m_t c)H = 0{\cdot}36\,H$ are closely equal. In the limit $m_t/m_l \to 0$, they become identical.

Acknowledgements—The authors would like to thank D. H. HASEGAWA, Professor W. KOHN and Professor R. SMOLUCHOWSKI for many valuable suggestions. They wish also to express their appreciation to Professor J. M. RADCLIFFE and Professor J. C. PHILLIPS for a critical reading of the manuscript.

REFERENCES

1. LAX B., PUFF R. D. and KLEINER W. H., *Bull. Amer. Phys. Soc.* **3,** 31 (1958).
2. FAN H. Y. and FISHER P., *J. Phys. Chem. Solids* **8,** 270 (1959).
3. BOYLE W. S., *J. Phys. Chem. Solids* **8,** 321 (1959).
4. ZWERDLING S., BUTTON K. J. and LAX B., *Phys. Rev.* **118,** 975 (1960).
5. WALLIS R. F. and BOWLDEN H. J., *J. Phys. Chem. Solids* **7,** 78 (1958).
6. HOWARD R. E. and HASEGAWA H., to be published.
7. HASEGAWA H. and HOWARD R. E., to be published.
8. KOHN W., *Solid State Physics* Vol. V, p. 286. Academic Press, New York (1957).
9. HAERING R. R., *Canad. J. Phys.* **36,** 1161 (1958).
10. YAFET Y., KEYES R. W. and ADAMS E. N., *J. Phys. Chem. Solids* **1,** 137 (1956).
11. KOHN W. and LUTTINGER J. M., *Phys. Rev.* **98,** 915 (1955).
12. LOUDON R., doctoral thesis, University of Oxford, *Some Problems Connected with the Spectra of Atoms in Solids.*

Vol. 1
1961

J. Phys. Chem. Solids Pergamon Press 1961. Vol. 19, Nos. 3/4, pp. 189–197. Printed in Great Britain.

ETUDE SPECTROPHOTOMETRIQUE DES SPECTRES CONTINUS DE Cu_2O A DIVERSES TEMPERATURES

J. B. GRUN, M. SIESKIND et S. NIKITINE

Laboratoire de Spectroscopie et d'Optique du Corps Solide, Institut de Physique, Strasbourg (France).

(*Received* 27 *July* 1960)

Abstract—The absorption of samples of different thicknesses (from 10 to 180 μ) of synthetic Cu_2O has been measured at different temperatures (293°K, 249°K, 169°K, 104°K, 77°K, 20°K, 4°K). The yellow series of Cu_2O has been studied previously.[1] In this paper measurements in different parts of the spectrum where the absorption is continuous are reported. The red continuum is situated on the low energy side of the yellow series, the yellow continuum on the high energy side. Both are well described by ELLIOTT's[2] theory of indirect and forbidden transitions. The red continuum is probably an indirect transition with phonon creation and annihilation to the first exciton state $n = 1$. At high temperatures, the yellow series disappears and is replaced by a continuum which is characteristic for a forbidden band to band transition. The "yellow" continuum corresponds to the continuous absorption on the high energy side of the series limit.

Résumé—La courbe d'absorption de lames minces (10 à 182 μ d'épaisseur) de cuprite synthétique a été mesurée à différentes températures (293°K, 249°K, 169°K, 104°K, 77°K, 20°K, 4°K). La série "jaune" a fait l'objet d'un précédent mémoire.[1] Dans la présente étude, on a examiné les deux régions d'absorption continue situées de part et d'autre de la série jaune: "l'absorption continue rouge", qui se trouve du côté des petits nombres d'onde par rapport à la série jaune et "l'absorption continue jaune", qui suit la série jaune vers les grands nombres d'onde. Ces absorptions continues peuvent être expliquées dans le cadre de la théorie d'ELLIOTT des transitions excitoniques interdites et indirectes[2]: "l'absorption continue rouge" est formée, vers les petits nombres d'onde, de deux fonds continus qui représentent les deux spectres de transitions indirectes vers le premier niveau excitonique, l'un correspondant à la création, l'autre à la destruction d'un phonon. Vers les grands nombres d'onde, un troisième fond continu apparaît aux hautes températures. "L'absorption continue jaune" correspond au spectre continu qui suit la série hydrogénoïde de raies dans les transitions interdites.

INTRODUCTION

UNE ETUDE spectrophotométrique de l'absorption de Cu_2O dans la région spectrale de la "série jaune" nous a permis d'apporter des arguments nouveaux pour l'interprétation de cette série.[1] Il semble subsister peu de doutes sur l'attribution de cette série à des transitions excitoniques interdites (ou de deuxième classe) prévues par la théorie d'ELLIOTT[2].

Or, le spectre d'absorption de Cu_2O présente deux régions d'absorption continue situées de part et d'autre de la série jaune. Nous appellerons "absorption continue rouge" la partie du spectre qui se trouve du côté des grandes longueurs d'onde de la série jaune et "absorption continue jaune" celle qui suit la série jaune vers les petites longueurs d'onde et qui précède la série verte.

L'absorption continue rouge présente le caractère de transitions indirectes dont la possibilité est prévue par la théorie d'ELLIOTT[2]. L'absorption continue jaune est prévue par la théorie des transitions interdites.[2] Une étude spectrophotométrique des deux spectres continus était nécessaire pour permettre une comparaison des données expérimentales avec la théorie. Cette étude fait l'objet de ce mémoire.

1. TRANSITIONS INTERDITES

Spectre de raies de deuxième classe

La théorie d'ELLIOTT prévoit, en plus des

transitions permises correspondant à la règle de sélection $\boldsymbol{k} = 0$ et $\Delta\boldsymbol{k} = 0$, où $\boldsymbol{k}$ est le vecteur d'onde, des transitions interdites correspondant aux règles de sélection $\Delta\boldsymbol{k} = 0$, $\boldsymbol{k} \neq 0$ mais petit. Dans ce cas, la théorie prévoit que l'on doit observer une série hydrogénoïde de raies, dans laquelle la première raie manque.

$$\nu = \nu_\infty - \frac{R_e}{n^2} \text{ avec } \begin{matrix} n = 2, 3, 4 \ldots \\ n \neq 1 \end{matrix} \qquad (1)$$

ν est le nombre d'onde exprimé en cm^{-1} et ν_∞ la limite de la série. La théorie prévoit la valeur des intensités d'oscillateur f de ces raies. Leur étude a fait l'objet d'un article récent.[1]

Spectre continu de deuxième classe

(a) Quand n devient grand dans la formule (1), les raies de la série se recouvrent et forment un spectre que nous appellerons pseudo-continu, alors que $\nu < \nu_\infty$. La théorie montre que, dans cette partie du spectre, le coefficient d'absorption K est donné par la formule :

$$K = cte\ [1+(\nu-\nu_\infty)/R_e]\nu \qquad (2)$$

(b) Quand $\nu > \nu_\infty$, la théorie prévoit que l'absorption est continue. Elle correspond à des transitions de bande à bande d'un type interdit et l'absorption doit être faible. Dans cette partie du spectre, le coefficient d'absorption doit varier selon la formule suivante :

$$\begin{aligned} K &= cte\ \nu(1+\alpha^2)\alpha\ e^{\pi\alpha} E^{3/2}/sh\pi\alpha \\ \text{où } E &= ch(\nu-\nu_\infty) \\ \text{et } \alpha &= \left(\frac{R_e}{\nu-\nu_\infty}\right)^{1/2} \end{aligned} \qquad (3)$$

Il est facile de voir que lorsque E devient grand,

$$K \propto E^{3/2} \qquad (4)$$

Les deux spectres continus (a) et (b) se raccordent pour $\nu = \nu_\infty$.

2. TRANSITIONS INDIRECTES

La théorie prévoit, par ailleurs, que des transitions peuvent également avoir lieu pour $\Delta\boldsymbol{k} \neq 0$. Ces transitions sont couplées avec une création ou une destruction de phonons. Elles contribuent à former un spectre continu.

Supposons, pour fixer les idées, que le maximum de la bande de valence corresponde à $\boldsymbol{k} = 0$ et le minimum de la bande de conduction à $\boldsymbol{k} = \boldsymbol{k}_0$. Appelons $\nu_{\boldsymbol{k}_0}$ le nombre d'onde du phonon de vecteur d'onde $\boldsymbol{k}_0$ susceptible d'être créé ou annihilé lors d'une transition. La théorie montre que l'on doit s'attendre à l'apparition de deux spectres de transitions indirectes vers le premier niveau excitonique $n = 1$, l'un correspondant à la création, l'autre à la destruction d'un phonon.

Le coefficient d'absorption dans ce spectre doit être de la forme :

$$\begin{aligned} K &= K_1 + K_2 \\ \text{où} \begin{cases} K_1 &= C(\nu-\nu_g+\nu_{\boldsymbol{k}_0}+R_e)^{1/2}N \\ K_2 &= C(\nu-\nu_g-\nu_{\boldsymbol{k}_0}+R_e)^{1/2}(N+1) \end{cases} \end{aligned} \qquad (5)$$

$ch\nu_g = E_g$ représente la différence d'énergie entre le bas de la bande de conduction (pour $\boldsymbol{k} = \boldsymbol{k}_0$) et le haut de la bande de valence (pour $\boldsymbol{k} = 0$).

C est une constante indépendante de la température.

N est le nombre de phonons présents dans le cristal à la température T.

$$N = \frac{1}{\exp(ch\nu_{\boldsymbol{k}_0}/kT)-1} \qquad (6)$$

Les coefficients d'absorption K_1 et K_2 peuvent s'écrire plus simplement :

$$\begin{cases} K_1 = C(\nu-\nu_1)^{1/2}N \\ K_2 = C(\nu-\nu_2)^{1/2}(N+1) \end{cases} \qquad (7)$$

où ν_1 et ν_2 correspondent aux deux bords des spectres continus. Par ailleurs, $\nu_2 - \nu_1 = 2\nu_{\boldsymbol{k}_0}$

Ainsi, les formules (7) donnent, pour une température donnée :

$$K_i^2 \propto (\nu-\nu_i) \quad \text{où } i = 1 \text{ ou } 2 \qquad (8)$$

D'autre part, les formules (7) peuvent s'écrire en fonction de la température :

$$p_1 = \frac{K_1}{(\nu-\nu_1)^{1/2}} = C\frac{1}{\exp(ch\nu_{\boldsymbol{k}_0}/kT)-1} \qquad (9a)$$

Vol. 1
196

$$\text{où} \begin{cases} p_1 = C\dfrac{kT}{ch\nu_{k_0}} \text{ pour } T \text{ grand} \\ p_1 = C\exp(-ch\nu_{k_0}/kT) \text{ pour } T \text{ petit} \end{cases}$$

$$p_2 = \frac{K_2}{(\nu-\nu_2)^{1/2}} = C\left[\frac{1}{\exp(ch\nu_{k_0}/kT)-1}+1\right]$$

$$\text{où} \begin{cases} p_2 = C\left[\dfrac{kT}{ch\nu_{k_0}}+1\right] \text{ pour } T \text{ grand} \\ p_2 = C[\exp(-ch\nu_{k_0}/kT)+1] \text{ pour } T \text{ petit} \end{cases} \quad (9b)$$

Nous avons étudié plusieurs lames cristallines d'épaisseurs variables (10, 30, 100 et 182 μ) aux températures suivantes : température ordinaire (293°K), température d'ébullition du chlorure de méthyle (249°K), de l'éthylène (169°K), du méthane (104°K), de l'azote (77°K), de l'hydrogène (20°K) et de l'hélium (4°K). Le montage utilisé a été décrit dans un précédent mémoire.[1]

Par suite de leur faible absorption, les échantillons les plus minces (10 μ) permettent d'observer l'ensemble du spectre d'absorption (Fig. 1).

A la température ordinaire, on observe seulement "l'absorption continue rouge". Elle est formée de deux fonds continus, limités vers les petits nombres d'onde par deux bords nets, puis d'un troisième

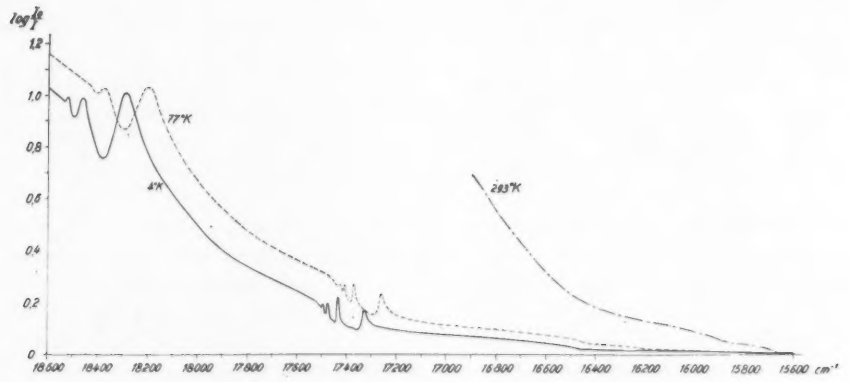

FIG. 1. Absorption d'une lame de Cu_2O de 10μ d'épaisseur.

On voit que, lorsque T est petit, p_1 tend vers zéro, alors que p_2 tend vers C. Lorsque T est grand, les deux quantités varient linéairement avec T.

La théorie prévoit également l'apparition de spectres excitoniques de transitions indirectes vers les niveaux excitoniques plus élevés ($n > 1$), mais leur intensité relative décroit comme $1/n^3$. Enfin, à la limite de la série des niveaux excitoniques, l'absorption varie comme E^2.

3. DESCRIPTION QUALITATIVE DE L'ABSORPTION

Nous avons mesuré l'absorption de la cuprite, afin de la comparer aux données précédentes.

fond continu dont la courbure est l'inverse de celle des deux précédents.

Aux basses températures, le premier fond continu rouge, situé vers les petits nombres d'onde, disparaît progressivement lorsque la température s'abaisse, tandis que le suivant reste. Ensuite, apparaît la série jaune—trois raies à 77°K, quatre à 4°K—suivie d'un palier dû probablement au recouvrement des raies de la série. On observe, après la limite de la série, "l'absorption continue jaune" et la série verte.

Les échantillons les plus épais (182 μ) sont fortement absorbants et permettent ainsi l'étude, avec plus de précision, de l'absorption continue rouge (Fig. 2).

Nous allons donc, tout d'abord, étudier "l'absorption continue rouge". Nous montrerons qu'on peut l'attribuer à des transitions excitoniques indirectes. Puis, nous examinerons si "l'absorption continue jaune" correspond aux transitions interdites prévues par la théorie d'ELLIOTT.

coefficient d'absorption K_1^2 du premier fond continu rouge en fonction du nombre d'onde ν (Fig. 3). On a obtenu une droite. Ceci nous a permis de prolonger ce premier continuum vers les grands nombres d'onde et de déduire, de l'absorption totale, l'absorption $K_2 = K - K_1$ du

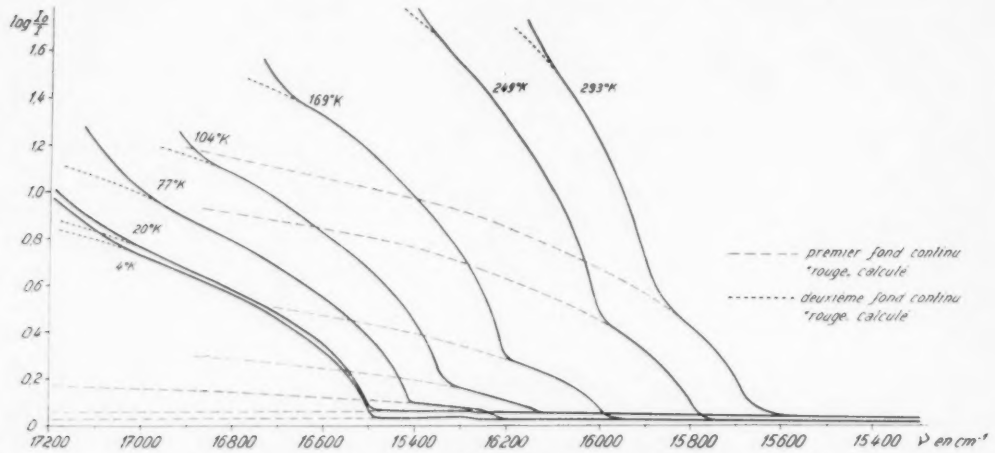

FIG. 2. Absorption d'une lame de Cu_2O de 182μ d'épaisseur à différentes températures.

4. ETUDE DE L'ABSORPTION CONTINUE ROUGE

Données expérimentales

On a, tout d'abord, étudié les deux premiers fonds continus rouges à partir des courbes d'absorption d'échantillons épais. Nous donnons en exemple les courbes obtenues avec des échantillons de 182 μ d'épaisseur (Fig. 2).

On a tracé la courbe de variation du carré du deuxième fond continu rouge (Fig. 2). On a tracé la courbe de variation de K_2^2 en fonction de ν (Fig. 4). La courbe est également une droite.

Les deux droites ainsi obtenues coupent l'axe des ν respectivement en ν_1 et ν_2. Ce sont les bords des deux fonds continus. Nous avons représenté leur déplacement avec la température (Fig. 5).[3] On constate que l'écart entre les deux bords reste

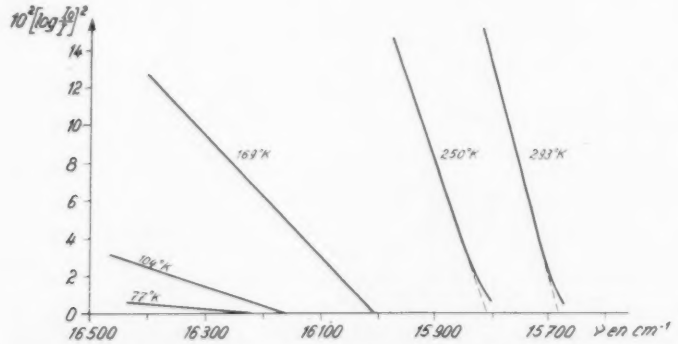

FIG. 3. Carré de la densité optique du 1er fond continu "rouge" à différentes températures d'un échantillon de 182μ d'épaisseur.

Vol. 1
1961

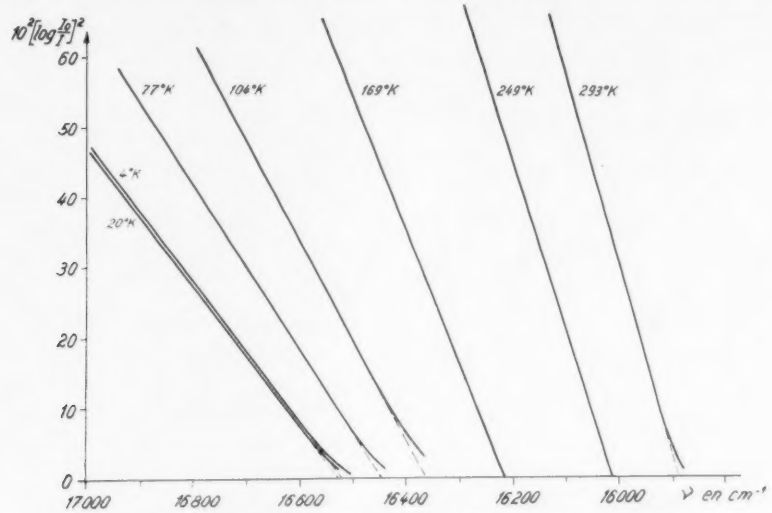

FIG. 4. Carré de la densité optique du 2ème fond continu "rouge" à différentes températures d'un échantillon de 182μ d'épaisseur.

constant. On en déduit le nombre d'onde des vibrations du réseau ν_{k_0} qui intervient dans l'absorption. $\nu_{k_0} = 104\ \text{cm}^{-1}$.

On a ensuite évalué les coefficients expérimentaux $p_1 = K_1/(\nu-\nu_1)^{1/2}$ et $p_2 = K_2/(\nu-\nu_2)^{1/2}$ à différentes températures (Figs 6 et 7). On remarque qu'aux très basses températures, p_1 tend vers zéro tandis que p_2 tend vers une constante et qu'aux températures plus élevées, p_1 et p_2 varient linéairement avec T.

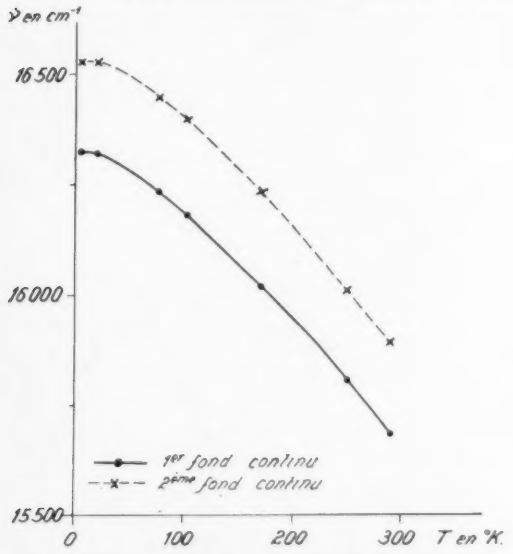

FIG. 5. Variation thermique des deux bords limitant les "fonds continus rouges".

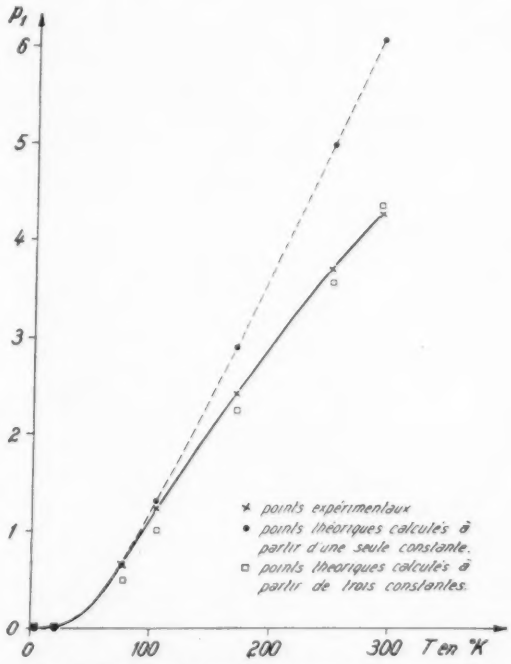
p1
points expérimentaux
points théoriques calculés à partir d'une seule constante.
points théoriques calculés à partir de trois constantes.
T en °K

FIG. 6. Variation thermique de $p_1 = K_1/(\nu-\nu_1)^{1/2}$.

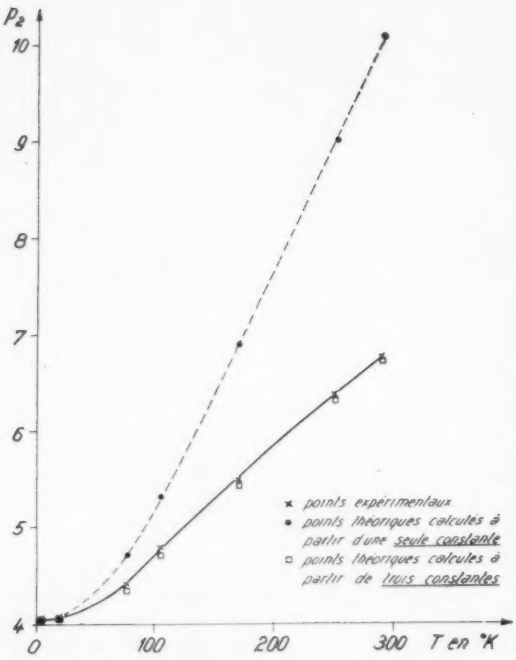

FIG. 7. Variation thermique de $p_2 = K_2/(\nu - \nu_2)^{1/2}$.

Aux basses températures, après ces deux fonds continus, se situe vers les grands nombres d'onde, la série jaune. A la température ordinaire, par contre, on observe un nouveau fond continu. Pour l'étudier, on doit utiliser des échantillons minces de 10 μ d'épaisseur par exemple (Fig. 1), les échantillons épais absorbant trop.

On peut prolonger le deuxième fond continu rouge vers les grands nombres d'onde et déduire, de l'absorption totale, l'absorption K_3 de ce nouveau fond continu. Il présente une courbure inverse de celle des précédents et si l'on trace la variation de $K_3^{1/2}$ en fonction de ν, on obtient encore une droite (Fig. 8).

*Comparaison de ces données expérimentales avec la théorie d'*ELLIOTT

Nous avons, tout d'abord, montré que les carrés des coefficients d'absorption expérimentaux des deux premiers fonds continus rouges varient linéairement avec le nombre d'onde ν, comme ELLIOTT le prévoit pour les transitions excitoniques indirectes (voir formule (5)).

D'autre part, nous avons tracé les courbes expérimentales de variation de p_1 et p_2 avec la température. Comparons-les avec les courbes théoriques (9a) et (9b).

Les deux courbes théoriques se déduisent l'une de l'autre par une translation C. Leurs parties linéaires pour T grand ont la même pente et pour $T = 0$, on a :

$$p_2 = p_1 + C = C$$

Nous avons pu, expérimentalement, évaluer la

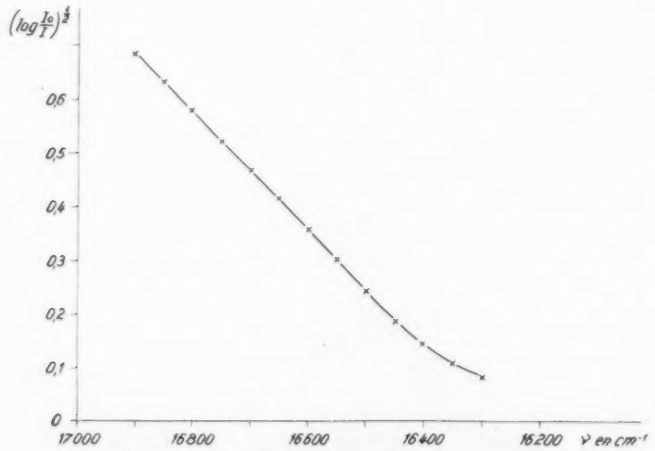

FIG. 8. Racine carrée de la densité optique du "fond continu rouge" à la température ordinaire (293°K)—échantillon de 10μ d'epaisseur.

Vol. 1
1961

constante C ($C = 4{,}05$ pour $T = 0$) et en déduire les courbes théoriques correspondantes (Figs. 6 et 7). On voit qu'elles ne coïncident pas avec les courbes expérimentales, surtout dans la partie linéaire pour T grand où l'on remarque que les courbes expérimentales n'ont pas la même pente.

Pour représenter les courbes expérimentales, nous avons été obligés d'introduire trois constantes différentes C_1, C_2 et C_3 dans les lois théoriques :

$$\begin{aligned} p_1 &= C_1 N \\ p_2 &= C_2 N + C_3 \end{aligned} \qquad (10)$$

La loi théorique d'ELLIOTT donne donc l'allure générale de la variation de p_1 et de p_2 avec la température.*

Enfin, le troisième fond continu rouge observé à la température ordinaire correspond à l'absorption de bande à bande.

La théorie d'ELLIOTT des transitions excitoniques indirectes permet donc d'expliquer, d'une manière satisfaisante, la forme de "l'absorption continue rouge" et sa dépendance de la température. Les deux premiers fonds continus rouges représentent l'absorption des deux spectres

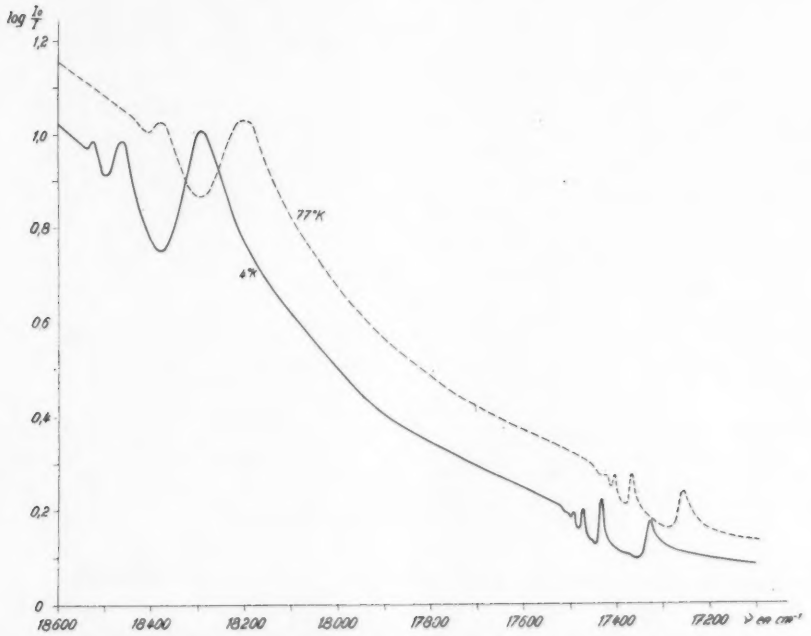

FIG. 9. Absorption continue jaune d'une lame de Cu_2O de 10μ d'épaisseur.

On a évalué expérimentalement ces constantes:

$$C_1 = 6{,}49$$
$$C_2 = 1{,}82$$
$$C_3 = 4{,}05$$

On a tracé les courbes théoriques correspondant à ces constantes. On est arrivé à un excellent accord avec les valeurs expérimentales pour les deux fonds continus (Figs. 6 et 7).

de transitions indirectes vers le premier niveau excitonique $n = 1$, l'un correspondant à la création, l'autre à la destruction d'un phonon.

---

* *Note ajoutée sur épreuves*: Au Congrès International sur les Semiconducteurs de Prague (September 1960), ELLIOTT a montré que dans les formules (7) c devait être variable avec T et que ceci pouvait amener un meilleur accord entre la théorie et l'expérience. Ces calculs d'ELLIOTT sont basés sur des hypothèses qui ont été vérifiées par des mesures récentes des auteurs.

La distance entre leurs deux bords est donc égale à deux fois la fréquence des phonons. Les absorptions correspondant aux niveaux excitoniques plus élevés n'ont pas été observées expérimentalement. Mais, le troisième fond continu rouge représente l'absorption de bande à bande à haute température, quand les raies excitoniques disparaissent.

5. ETUDE DE L'ABSORPTION CONTINUE JAUNE

L'étude des facteurs d'intensité d'oscillateur des raies de la série jaune a permis de montrer qu'il s'agissait d'un spectre de raies de deuxième classe, correspondant à des transitions directes faiblement interdites. Il était intéressant de comparer la forme de l'absorption continue située après la raie avec celle prévue par la théorie des transitions interdites [voir formule (4)]. Nous avons donc étudié l'absorption de lames de Cu_2O de faibles épaisseurs entre les séries "jaune" et "verte". Nous donnons à titre d'exemple les courbes d'absorption obtenues avec des échantillons de 10 μ d'épaisseur (Fig. 9).

On observe, immédiatement après les raies de la série jaune, un palier qui peut correspondre à la superposition des autres raies de la série, de nombre quantique $n > 5$. Mais, il est très difficile de l'étudier en détail car il est peu étendu.

Ce palier est suivi d'une absorption continue qui se prolonge jusque vers la série verte. On obtient son absorption propre K_4 en déduisant l'absorption continue rouge de l'absorption totale. D'après la théorie des transitions interdites, $K_4^{2/3}$ doit varier linéairement avec ν, loin de la limite de la série. On a donc tracé la courbe expérimentale de variation de $K_4^{2/3}$ en fonction de ν (Fig. 10). C'est une droite, mais sur un domaine peu étendu. Il semble que les raies de la série verte soient dissymétriques comme les raies de la série jaune et qu'elles perturbent fortement ce fond continu d'absorption.

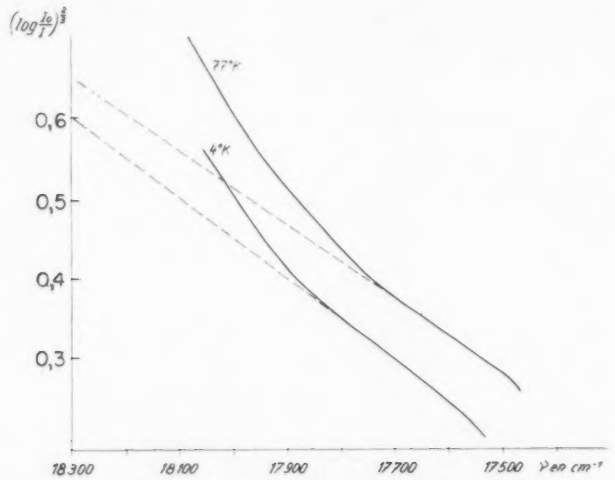

FIG. 10. Puissance 2/3 de la densité optique du "fond continu jaune"—échantillon de 10μ d'épaisseur.

CONCLUSION

Cette étude nous a fourni des données sur "les absorptions continues jaune et rouge". Elle complète notre étude précédente sur la série "jaune".

On a pu montrer que l'absorption continue rouge est due à des transitions indirectes[4]. Les deux premiers fonds continus représentent les deux spectres de transitions indirectes vers le premier niveau excitonique, l'un correspondant à la création, l'autre à la destruction d'un phonon. Le carré de leur coefficient d'absorption varie linéairement avec le nombre d'onde ν et leur variation avec la température concorde qualitativement avec la théorie. Le troisième fond continu

représente l'absorption de bande à bande. La racine carrée de son coefficient d'absorption varie linéairement avec le nombre d'onde ν.

D'autre part, nous avons montré précédemment que la série jaune correspond à un spectre de deuxième classe, à des transitions faiblement interdites. L'absorption continue jaune correspond à la forme théorique du fond continu, qui doit suivre les raies dans les transitions interdites, mais elle est rapidement perturbée par la série verte. Ce fait est un argument nouveau en faveur de l'interprétation du spectre de la cuprite comme spectre excitonique de deuxième classe.

BIBLIOGRAPHIE

1. Nikitine S., Grun J. B. et Sieskind M., *J. Phys. Chem. Solids* **17,** 292 (1961).
2. Elliott R. J., R.R.E. Memorandum, N, p. 1342 (1957); *Phys. Rev.* **108,** 1384 (1957).
3. Nikitine S., Sieskind M. et Perny G., *C.R. Acad. Sci., Paris* **238,** 1987 (1954).
4. Gross E. F. et Pastrnyak I., *Fiz. tverdogo tela* **1,** 518 (1959).

ol. 19
1961

J. Phys. Chem. Solids Pergamon Press 1961. Vol. 19, Nos. 3/4, pp. 198–217. Printed in Great Britain.

A STUDY OF ENERGY-LOSS PROCESSES IN GERMANIUM AT HIGH ELECTRIC FIELDS USING MICROWAVE TECHNIQUES

A. F. GIBSON, J. W. GRANVILLE and E. G. S. PAIGE

Royal Radar Establishment, Malvern

(*Received* 1 *August* 1960)

Abstract—At room temperature, measurements have been made of the absorption and phase shift of microwaves (34·75 kMc) in germanium to which a high electric field is applied. The mobility and dielectric constant have been deduced from these measurements and we find, (i) that the mobility at the microwave frequency is intermediate between the mobility (V/E) and the slope mobility (dV/dE) obtained from the variation of carrier velocity with electric field and (ii) that the contribution of the free carriers to the dielectric constant is negative at zero field but becomes positive for high electric fields. These effects have been interpreted in terms of an energy relaxation process.

A theory of the mobility and dielectric constant under the conditions of the experiment is developed; initially an elementary, phenomenological approach is taken, but finally a more refined theory is given which includes specific scattering processes (optical and acoustical phonons). A relationship between mobility and dielectric constant predicted by theory is found to be obeyed by electrons but not by holes. A detailed investigation of electrons reveals that a parameter deduced from the experimental observations (II), and analogous to an energy relaxation time, agrees with theoretical prediction with regard to magnitude but not with regard to field dependence. Possible reasons for this discrepancy are given.

From the dielectric constant data at zero field an effective mass is deduced. For electrons the comparison of this mass with the conductivity mass reveals no increase between 4°K and 300°K within the experimental error (15 per cent). For holes evidence is presented that the relaxation times of light and heavy holes are not identical at 300°K and that there is a significant increase in the effective mass between 4°K and 300°K.

I. INTRODUCTION

When an electric field is applied to a conductor, the current carriers (electrons or holes) are accelerated, gaining energy and momentum from the field. In germanium of low impurity content, and at room temperature, the excess energy and momentum is dissipated almost exclusively by interaction with the acoustical and optical modes of vibration of the lattice. In such collisions energy and momentum must be conserved. Except in the case of a carrier which, having an energy comparable with that of an optical phonon, interacts with an optical phonon, the fractional change in carrier momentum per collision considerably exceeds the fractional change in energy. Hence if the rates of energy and momentum loss by carriers can be described by simple relaxation times τ_ε and τ_m it follows that $\tau_\varepsilon > \tau_m$. Since τ_ε is comparatively large, the application of a high electric field to germanium or silicon leads, in equilibrium, to a substantial rise in carrier energy or "temperature" above the lattice temperature. τ_m decreases, though slowly, with increasing carrier energy and hence the carrier mobility decreases. This leads to the "saturation" of the carrier drift velocity at high fields, which has been studied in germanium by a number of authors.[1–5] Attempts have been made, using a variety of techniques, to estimate the carrier temperature in germanium as a function of electric field,[6–9] but significant discrepancies exist between the results of different approaches.

One approach to the study of high-field effects

has been based on measurements of the absorption of microwave radiation by germanium to which a high electric field is applied. ARTHUR *et al.*[10] showed that the absorption decreased markedly when an external (essentially d.c.) field was applied and similar results have been obtained by DOUSMANIS (private communication). An analogous technique has been used by MORGAN[11] and by SEEGER[12]. The experiments to be described in this paper are similar, though more detailed, than those of ARTHUR *et al.* and our results are in qualitative but not quantitative agreement with the latter. ARTHUR *et al.* argued that, as the externally applied and r.f. electric fields were parallel, and $\omega\tau_m \ll 1$, the absorption should be proportional to the slope mobility, dv/dE. It would appear that the above conditions are necessary but not sufficient since we find that the absorption is generally greater than that given by the slope mobility. In addition to absorption (and therefore conductivity) measurements, we have measured the free carrier contribution to the dielectric constant as a function of electric field. Here a new situation is observed, namely that the free carrier contribution is negative at zero and low electric fields, but becomes positive at high fields. Our results can be explained by the effect of a finite energy relaxation time which is large compared with τ_m. Measurements have been made on *n*- and *p*-type germanium, and in less detail on silicon, at a frequency of 34·75 kMc/s. At this frequency we find that $\omega\tau_\varepsilon \sim 1$ so that the experimental results yield, as a function of electric field, the value of τ_ε, (or a comparable parameter, see Section 5), and the carrier effective temperature.

The description of energy-loss processes by an energy relaxation time, τ_ε, is extremely convenient and is in many ways analogous to the description of carrier recombination processes by a single-valued minority-carrier lifetime. It does, not however, give any direct information on the nature of the energy-loss processes—any more than lifetime measurement gives any direct information on the nature of the recombination centres involved. Furthermore, the concept of a relaxation time implies that the average energy loss per collision is proportional to the excess energy of the carrier, which is justified only for acoustical and not optical mode scattering. On the other hand in a more rigorous treatment of carrier scattering at high electric fields the underlying physical model may be obscured. With these considerations in mind the paper is arranged as follows; in the next section (Section 2) we develop a simple quantitative theory of the conductivity and dielectric constant in terms of τ_ε by solving a pair of coupled differential equations describing the time dependence of the energy and momentum of the carriers. In this model, the energy distribution of the carriers is assumed to be a delta function and τ_ε and τ_m are assumed to be functions of energy only. The experimental method and results are described in Section 3, and compared with this simple theoretical approach in Section 4. Values of the mean carrier energy and energy relaxation times as functions of electric field are deduced from this model. In Section 5 we develop a more sophisticated model which assumes that the energy distribution of the carriers is Maxwellian and that scattering is by acoustical and optical phonons. Some of the results obtained from the simpler model of Section 2 are still applicable in this approach, which facilitates the comparison of theory and experiment. Our main conclusions are brought together, with a summary, in Section 6.

2. AN ELEMENTARY THEORY OF THE CONDUCTIVITY AND POLARIZABILITY DUE TO FREE CARRIERS IN A HIGH ELECTRIC FIELD

The contribution of the free carriers to the constants which characterize the propagation of electromagnetic radiation through a semiconductor in thermal equilibrium are well known.[13] The conductivity, σ, is given by

$$\sigma = \frac{Ne^2}{m}\left\langle \frac{\varepsilon\tau_m}{1+\omega^2\tau_m^2} \right\rangle \frac{1}{\langle\varepsilon\rangle}. \qquad (2.1)$$

The polarizability, α, and hence the dielectric constant, is given by

$$\alpha = -\frac{Ne^2}{m}\left\langle \frac{\varepsilon\tau_m^2}{1+\omega^2\tau_m^2} \right\rangle \frac{1}{\langle\varepsilon\rangle}. \qquad (2.2)$$

N, e, ε and m are the concentration, charge, kinetic energy and mass of the carriers respectively and ω is the angular frequency of the electromagnetic radiation. The brackets indicate that the appropriate averaging procedure over the Maxwellian energy distribution has been performed. When a

large d.c. electric field is applied to the semiconductor the thermal equilibrium is destroyed. In this section we shall derive expressions for σ and α under this condition. We shall pursue an elementary, phenomenological, approach in the hope of giving a clear insight into the physical processes which affect σ and α. This approach leads us to make certain assumptions which are invalid for germanium, yet we shall find in Section 5 that some of the relations derived here are more general than the assumptions made would indicate.

There are three basic assumptions:

(1) The constant energy surfaces in $\boldsymbol{k}$ space are spherical for both electrons and holes.

(2) The free carrier distribution is monoenergetic.

(3) The energy and momentum relaxation times are functions of the energy only and can be expressed in the form ε^n where n is a constant.

The net rate of change of momentum of free carriers in an electric field $\boldsymbol{E}$ is given by

$$\frac{d(m\boldsymbol{v})}{dt} = e\boldsymbol{E} - \frac{m\boldsymbol{v}}{\tau_m} \tag{2.3}$$

where $\boldsymbol{v}$ is the drift velocity of the carrier. The first term on the right hand side of equation (2.3) is the rate of gain of momentum from the electric field and the second term is the rate of loss of momentum to the lattice. With a d.c. field applied, equation (2.3) has, of course, a steady state solution.

$$\boldsymbol{v}_0 = \frac{e}{m}\tau_{m_0}\boldsymbol{E}_0 = \mu_0\boldsymbol{E}_0$$

where the subscript 0 indicates the d.c. field values both here and subsequently.

We shall write the equation for the net rate of change of energy in the form

$$\frac{d\varepsilon}{dt} = e\boldsymbol{v}\cdot\boldsymbol{E} - \frac{\varepsilon-\varepsilon_L}{\tau_\varepsilon}, \tag{2.4}$$

where ε_L is the thermal equilibrium energy of the carriers.* The first term on the right hand side is the rate of gain of energy from the field and the second term is the rate of loss of energy to the lattice. If τ_ε is independent of energy, then we have defined it in such a way that, when the electric field is switched off at a time $t = 0$,

$$\varepsilon(t)-\varepsilon_L = [\varepsilon(0)-\varepsilon_L]\exp(-t/\tau_\varepsilon),\ t \geqslant 0,$$

and we are clearly justified in terming τ_ε the energy relaxation time. However, we shall allow $1/\tau_\varepsilon$ some energy dependence and shall loosely continue to call τ_ε the energy relaxation time.

Equations (2.3) and (2.4) are coupled because τ_m and hence $\boldsymbol{v}$ are functions of the energy of the carriers.

In the experiment to be described the microwave field $\boldsymbol{E}_1$ was always parallel to and much smaller than $\boldsymbol{E}_0$, thus we can divide ε and $\boldsymbol{v}$ into two terms, $\varepsilon = \varepsilon_0 + \Delta\varepsilon$ and $\boldsymbol{v} = \boldsymbol{v}_0 + \Delta\boldsymbol{v}$ when the second terms are always very much less than the first. Since all the vector quantities are colinear we shall simplify the following equations by dropping the vector notation. Writing the energy dependence of τ_m and τ_ε as

$$\tau_m = a\,\varepsilon^{-n_1} \text{ and } \tau_\varepsilon = b\varepsilon^{-n_2}$$

where n_1 and n_2 are constants, we have, to a good approximation,

$$\left.\begin{aligned} \tau_m &= \tau_{m_0}\left[1-n_1\frac{\Delta\varepsilon}{\varepsilon_0}\right] \\ \text{and}\qquad \tau_\varepsilon &= \tau_{\varepsilon_0}\left[1-n_2\frac{\Delta\varepsilon}{\varepsilon_0}\right]. \end{aligned}\right\} \tag{2.5}$$

Substituting these relations in equations (2.3) and (2.4) we obtain

$$\frac{d\Delta v}{dt} = \frac{eE_1e^{i\omega t}}{m} - \frac{\Delta v}{\tau_{m_0}} - n_1\frac{v_0}{\tau_{m_0}}\frac{\Delta\varepsilon}{\varepsilon_0} \tag{2.6}$$

and

$$\frac{d\Delta\varepsilon}{dt} = ev_0E_1e^{i\omega t} + e\Delta vE_0 - \frac{\Delta\varepsilon}{\tau_{\varepsilon_0}}\left[1+n_2\frac{(\varepsilon_0-\varepsilon_L)}{\varepsilon_0}\right] \tag{2.7}$$

In these equations we have neglected second order terms, viz $(\Delta v)^2$, $\Delta vE_1/E_0$, and we have used the steady state solutions of equations (2.3) and (2.4). Equation (2.6) represents the rate of change of incremental velocity due to the presence of the microwave field. The first two terms would give the total effect of the microwave field if it did not change the energy of the free carriers, hence Δv would then be given by an equation of the same form as (2.1). The third term is due to the effect on the steady state value of τ_m of the change of carrier energy produced by the microwave field, and equation (2.7) represents the rate of change of incremental energy due to this field. In equation (2.7), the first two terms give the first order change in the rate of gain of energy due to superposition of the microwave field on the d.c. field while the third term gives the change in the rate of energy loss including the change of the steady state value of τ_ε.

If we eliminate $\Delta\varepsilon$ from (2.6) and (2.7) and solve the resulting equation for Δv we obtain for the

* The implication that the rate of change of energy loss is proportional to the increase in energy of the carriers is only valid for acoustical phonon scattering—departures from this will influence the value of τ_ε.

Vol. 1
196

complex conductivity, σ^*, which is related to Δv by $\sigma^* = Ne\Delta v/(E_1 e^{i\omega t})$,

$$\sigma^* = \frac{-\sigma_0}{P\left(1+\frac{\tau_{m_0}}{\tau_{\varepsilon_0}}\left[1+n_2\frac{(\varepsilon_0-\varepsilon_L)}{\varepsilon_0}\right]\right)}\left\{\frac{\phi^+/\tau'_{\varepsilon_0}+\omega^2}{(\phi^+)^2+\omega^2}+\frac{\phi^-/\tau'_{\varepsilon_0}-\omega^2}{(\phi^-)^2+\omega^2}\right.$$
$$\left.+i\omega\left[\frac{\phi^+-1/\tau'_{\varepsilon_0}}{(\phi^+)^2+\omega^2}+\frac{\phi^-+1/\tau'_{\varepsilon_0}}{(\phi^-)^2+\omega^2}\right]\right\} \tag{2.8}$$

where

$$\phi^+ = (P+1)\left\{\frac{1}{2\tau_{m_0}}+\frac{1}{2\tau_{\varepsilon_0}}\left[1+n_2\frac{(\varepsilon_0-\varepsilon_L)}{\varepsilon_0}\right]\right\},$$

$$\phi^- = (P-1)\left\{\frac{1}{2\tau_{m_0}}+\frac{1}{2\tau_{\varepsilon_0}}\left[1+n_2\frac{(\varepsilon_0-\varepsilon_L)}{\varepsilon_0}\right]\right\},$$

$$P^2 = 1-\frac{4\tau_{m_0}}{T}\left(1+\frac{\tau_{m_0}}{\tau_{\varepsilon_0}}\left[1+n_2\frac{(\varepsilon_0-\varepsilon_L)}{\varepsilon_0}\right]\right)^{-2},$$

$$\tau'_{\varepsilon_0} = \tau_{\varepsilon_0}\left[1+(n_2-n_1)\frac{(\varepsilon_0-\varepsilon_L)}{\varepsilon_0}\right]^{-1},$$

and

$$T = \tau_{\varepsilon_0}\left[1+(n_2+n_1)\frac{(\varepsilon_0-\varepsilon_L)}{\varepsilon_0}\right]^{-1}, \tag{2.9}$$

The first pair of terms of (2.8) give σ and represent the in-phase motion of the carriers, the second pair of terms give the polarizability and represent the out of phase motion of the carriers. If the thermal equilibrium condition is imposed on (2.8) by putting $\varepsilon_0 = \varepsilon_L$, then it reduces to relations which are essentially the same as (2.1) and (2.2).

We shall now put equation (2.8) into a simpler form by making approximations which are reasonable for germanium under the conditions of the experiment. They are (i) that $(\omega\tau_m)^2 \ll 1$ and (ii) that $\tau_\varepsilon \gg \tau_m$. Since $\omega = 2{\cdot}18\times10^{11}$ radians sec^{-1} and $\tau_m < 10^{-12}$ sec, the lattice being at 300°K in the present experiment, it is clear that (i) is satisfied. As pointed out in the introduction, condition (ii) is valid for all the carriers except the small fraction which have an energy comparable with an optical phonon and moreover are scattered by an optical phonon. Therefore condition (ii) is probably valid for the carrier distribution as a whole. Then

$$\sigma = \sigma_0\left(1-2n_1\frac{(\varepsilon_0-\varepsilon_L)}{\varepsilon_0}\frac{T}{\tau_{\varepsilon_0}}\frac{1}{(1+\omega^2T^2)}\right) \tag{2.10}$$

and

$$\alpha = -\sigma_0\left\{\tau_{m_0}-2n_1\frac{(\varepsilon_0-\varepsilon_L)}{\varepsilon_0}\frac{T^2}{\tau_{\varepsilon_0}}\frac{1}{(1+\omega^2T^2)}\right\} \tag{2.11}$$

From (2.10) it can be shown that when $(\omega T)^2 \to \infty$, $\sigma = \sigma_0$ and when $(\omega T)^2 \ll 1$, $\sigma = Ne(dv/dE)$. When ωT is between these two extreme conditions we can deduce T from conductivity measurements alone,

$$T = \frac{1}{\omega}\left(\frac{\mu-(dv/dE)_0}{\mu_0-\mu}\right)^{1/2} \tag{2.12}$$

where the relation $\sigma = Ne\mu$ has been used. We shall find in Section 5 that the form of the relationships (2.10) and (2.11) is retained in a more refined theory. Furthermore, the parameter T, while its definition is modified, remains the significant parameter in the sense that the value of $(\omega T)^2$ relative to unity determines what is observed.

Finally we restate the physical origin of the terms which appear in σ and α. Since we assume $(\omega\tau_{m_0})^2 \ll 1$, the first term in both (2.10) and

(2.11) is the normal expression for conductivity and polarizability but for the fact that the microwave field is interacting with a steady state τ_{m_0} determined by E_0. The other terms arise from the modulation of τ_m due to the change in energy of the free carriers—this is resolved into an in-phase modulation and an out-of-phase modulation which can be of comparable magnitude if $\omega T \sim 1$. The in-phase modulation of τ_m results in the second term in the σ while the out-of-phase modulation of τ_m contributes to α. It is of interest to note that since τ_{m_0} is small relative to T there is a possibility of the free carriers giving a positive contribution to the dielectric constant. In this statement we have anticipated that n_1 is positive as indeed it should be, since impurity scattering is negligible in the samples on which the experiments to be described were performed.

3. EXPERIMENTAL TECHNIQUES AND RESULTS

The conductivity and dielectric constant of a solid may be determined at microwave frequencies in a variety of ways. We have measured the transmission properties (attenuation and phase shift) of a section of waveguide partially filled by a sample of germanium. The theoretical relationships between the measured quantities and the dielectric constant and conductivity are described in Section 3.2, following a description of the apparatus in 3.1. In Section 3.3 we discuss the sources of error inherent in this method and estimate their magnitude. Finally some typical experimental observations are presented.

3.1 *Sample preparation and microwave apparatus*

Samples of germanium or silicon in the form of thin flat plates were mounted through axial slots about 0·3 mm wide cut in the centre of the broad faces of 7 mm × 3·5 mm rectangular guide, in the same manner as those of ARTHUR *et al.*[10] The sample was insulated from the guide by thin P.T.F.E. film, glued to the guide walls. Outside the guide, contact was made by alloying $n+$ or $p+$ non-injecting connections along the entire length of the slice, and tests showed that these connections had no significant effect on the transmission properties of the partially filled guide.

The specimen and slotted guide formed part of one arm of a conventional microwave bridge with a calibrated phase shifter and attenuator in the other arm. The bridge was isolated from the klystron oscillator by a ferrite isolator and at the measurement frequency (34·75 kMc/s) no component, other than the two magic T's, had a standing wave ratio greater than 1·02.

As the external field had to be applied to the sample in the form of short pulses to avoid heating, the following cycle of operations was found convenient. (1) Pulse applied to switch on klystron. (2) 0·25 to 0·5 μsec later, pulse of 0·5 μsec duration applied to sample. (3) 0·25 to 0·5 μsec after cessation of sample field pulse, klystron switched off. The bridge could then be balanced to give zero output with any given field across the sample, the quiescent period of the klystron serving as a convenient "zero power" indicator. Two 20 Mc bandwidth amplifiers and a Tektronix 545 Oscilloscope were used to amplify and display the pulses.

3.2 *Microwave propagation*

The transmission properties of any medium (in the present case a section of waveguide partially filled with germanium) can be characterized by a phase constant n' and an absorption constant k defined by

$$n' = \frac{\phi\lambda_0}{360x} \text{ and } k = 0{\cdot}23\,\frac{A\lambda_0}{4\pi x} \qquad (3.1)$$

where λ_0 is the free space wavelength, ϕ is the phase shift in degrees, A is the absorption in dB's in a sample of length x in the propagation direction and the factor $0{\cdot}23 = \log_e(10)/10$. In terms of n' and k the power reflection coefficient, R, and the phase shift on reflection, ψ, are given by

$$R = \frac{(n'/n_0-1)^2+k^2/n_0^2}{(n'/n_0+1)^2+k^2/n^2} \qquad (3.2)$$

and

$$\tan\psi = \frac{2k/n_0}{(k/n_0)^2+(n'/n_0)^2-1} \qquad (3.3)$$

where n_0 is the phase constant of the adjoining medium, namely empty rectangular waveguide in which the absorption is zero. n_0 is given by

$$n_0 = \sqrt{[1-(\lambda_0/2a)^2]} \qquad (3.4)$$

where a is the width of the broad face of the guide.

The relationship between the propagation constants n' and k of a partially filled guide and the dielectric constant and r.f. conductivity of the germanium or silicon sample may be obtained by extending the calculations of MARCUVITZ[14] to include a lossy dielectric. Our samples extended completely across the narrow dimension of the guide but occupied only a relatively small fraction of the width of the guide. Under these conditions the relationship between n' and k on the one hand, and the dielectric constant ϵ and conductivity σ on the other, is given by

$$\frac{\tan[\frac{1}{2}(a-d)\sqrt{(\beta^2+\gamma^2)}]}{\sqrt{(\beta^2+\gamma^2)}} = \frac{\cot\left[\frac{d}{2}\sqrt{(\epsilon\beta^2+\gamma^2)}\right]}{\sqrt{(\epsilon\beta^2+\gamma^2)}} \qquad (3.5)$$

where

$$\beta = \frac{4\pi}{\lambda_0}, \gamma^2 = \beta^2(k^2 - n'^2 + 2in'k),$$

$$\epsilon = \frac{\epsilon'}{\epsilon_0} - i\frac{\sigma}{\omega\epsilon_0},$$

ϵ_0 is the permittivity of free space, and d is the width of the sample in the broad ("a") dimension of the waveguide.* Equation (3.5) reduces to more familiar forms on simplification. For example, when $d = 0$ (empty guide) the real and imaginary parts of (3.5) yield

$$\left.\begin{aligned} k &= 0 \\ \text{and} \qquad n' &= \sqrt{[1-(\lambda_0/2a)^2]} \end{aligned}\right\}$$

which is equation (3.4) above. When $d = a$ (completely filled guide) equation (3.5) reduces to

$$\left.\begin{aligned} 2n'k &= \sigma/\omega\epsilon_0 \\ \text{and} \qquad n'^2 - k^2 &= \epsilon'/\epsilon_0 + (\lambda_0/2a)^2 \end{aligned}\right\}. \quad (3.6)$$

Equations (3.6) are standard results given in any textbook of optics. For all values of d, k is approximately proportional to σ and independent of ϵ' while n' is proportional to ϵ' and independent of σ. In our experiments, however, the application of an external field to the sample produces a large change in σ and a relatively small change in ϵ'. The second order variation in n' with σ, ϵ' being held constant, must therefore be taken into account. It is of interest to note then that equations (3.6) predict that n' increases monotonically as σ increases when ϵ' is constant but when $d \ll a$ equation (3.5) predicts that n' decreases as σ increases until very large values of σ are reached. This rather surprising prediction was examined experimentally and confirmed.

3.3 *Sources of experimental error*

For comparison between theory and experiment it is found that the absolute value of the conductivity is never required, so some potential sources of error are eliminated; the same is not true of the dielectric constant, which immediately implies that less reliance can be placed on values derived from it. Furthermore, the free carrier contribution to the dielectric constant is comparatively small (at most 20 per cent) whereas the free carriers are responsible for almost all the absorption.

The significant sources of error may be classified into three groups, namely observational errors in attenuation and phase shift, errors in deriving σ and ϵ' from the attenuation and phase shift, and observational errors in other required quantities, e.g. the d.c. conductivity as a function of applied electric field.

3.3.1. *Attenuation and phase shift measurements.* For a given sample, the attenuation and phase shift could be determined at all electric fields with a reproducibility of better than 2 per cent. By comparison, non-uniformity of sample resistivity and errors in the measurement of sample dimensions could be more important. Most samples were 0·2 mm wide and 5–9 mm long, the width being measured to $\pm$ 1μ. All samples were checked as regards uniformity of resistivity and rejected if the non-uniformity exceeded 2 or 3 per cent.

3.3.2 *Derivation of σ and ϵ' from experimental data.* To obtain ϕ and A (equation 3.1), the observed phase shift and attenuation must be corrected for end effects and multiple reflections in the sample. One advantage of the use of thin samples is that the reflection coefficient, R, is small so that these corrections are also small. Thus the power loss by reflection, estimated from equation (3.2), was usually about 0·6 dB. The residual absorption was typically 15–20 dB at zero applied field, falling to about 3 dB at the highest field. Similarly the observed phase shift was corrected for phase shift on reflection (and hence transmission) at the interfaces of the medium. This correction was estimated using equation (3.3) and was equal to or less than 6° compared with a total phase shift of about 400° and a total change in phase shift, on applying the external field, of about 50°.

Equation (3.5) was checked experimentally as far as possible by the use of samples of various resistivities and dimensions. The equation does not take account of any effects due to the slots cut in the guide walls or due to the presence of the insulating P.T.F.E. film. It was found that the presence of the latter had a marked effect, reducing the apparent conductivity and dielectric constant of all samples by about 10 per cent, though the relative values of the conductivity of samples in the range studied (1 to 50 Ω cm) remained substantially unaltered. As already remarked, absolute values of the conductivity are fortunately not required for a comparison between theory and experiment but this effect cannot be neglected in an analysis of the data derived from measurement of the dielectric constant.

3.3.3 *D.C. conductivity data.* The d.c. conductivity or mobility is obtained by simply noting the current as a function of the applied electric field, and the slope mobility, dv/dE is deduced graphically from this result. Small errors in the conductivity can be very important in the determination of dv/dE, and it is unlikely that this quantity can be relied upon to better than 5 or 10 per cent, particularly at high fields.

3.4 *Experimental results*

Some typical experimental results are shown in Figs. 1, 2 and 3. Fig. 1 shows smoothed mobility data for an 8·77 mm long n-type sample and for an 8·09 mm long p-type sample, together with the appropriate d.c. and slope mobilities. Figs. 2 and 3

* We are indebted to Dr. P. N. Butcher, of this establishment, for the derivation of equation (3.5). It has been solved numerically by Miss R. Hensman.

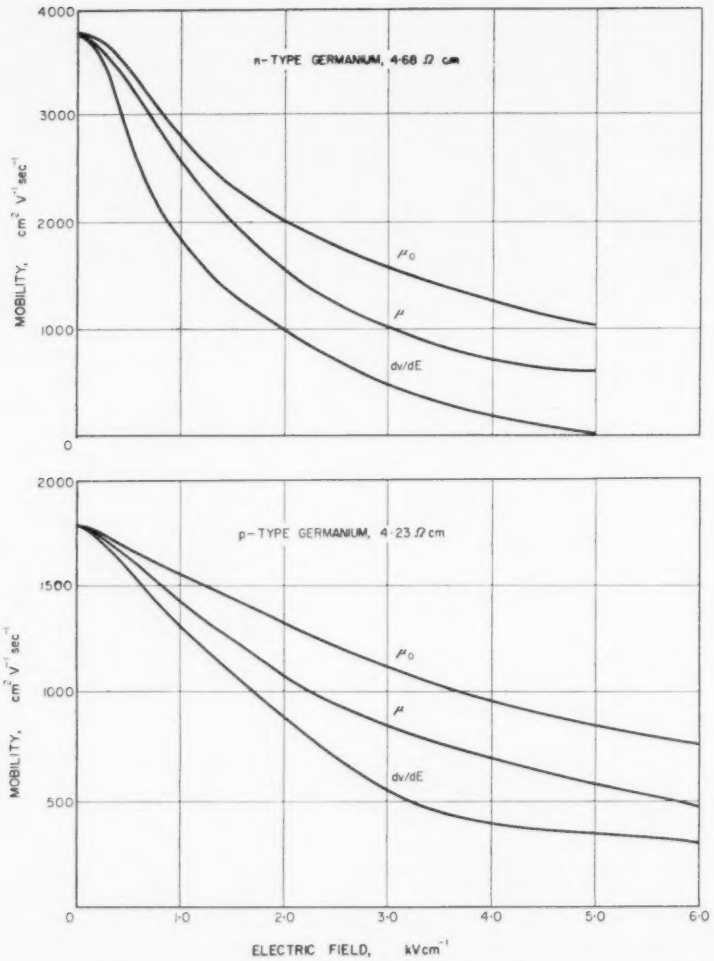

FIG. 1. Experimental values of mobility, slope mobility and r.f. mobility as a function of applied electric field for *n*- and *p*-type germanium.

show the dielectric constants of the same samples, together with the average dielectric constant deduced from 12 intrinsic germanium samples measured under identical conditions. As explained in Section 3.3.2 above, no significance should be attached to the low value of the dielectric constant of the intrinsic material and only relative values should be considered.

Inspection of Fig. 1 shows immediately that μ lies almost midway between μ_0 and (dv/dE), and hence $\omega\tau_\varepsilon \sim 1$. Similarly Figs. 2 and 3 show that the free carrier contribution to the dielectric constant is negative at low electric fields but becomes positive at high fields. This result is in qualitative accord with the prediction from equation (2.11). A quantitative analysis of these results, which are representative, forms the subject matter of the following sections.

4. PRELIMINARY ANALYSIS OF THE EXPERIMENTAL RESULTS

In this section we shall divide the analysis of

Vol. 1
1961

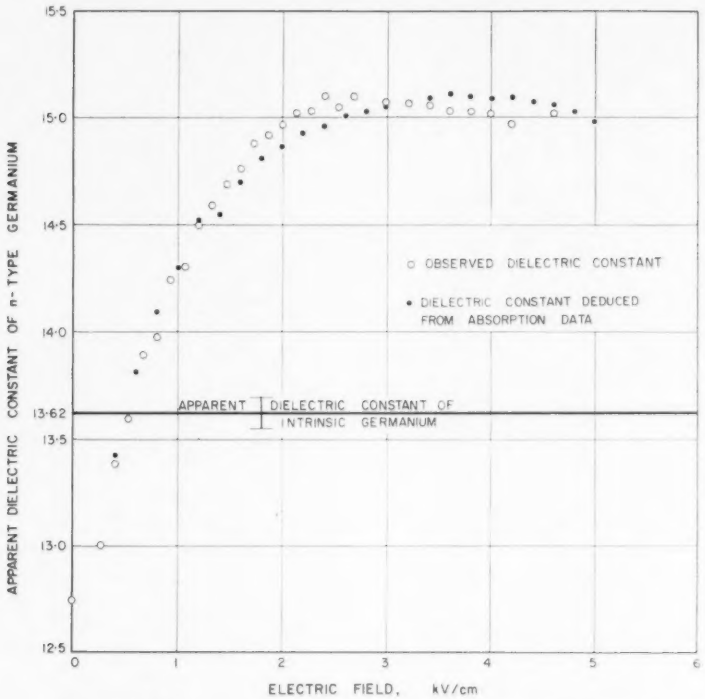

FIG. 2. Dielectric constant of n-type germanium as a function of applied electric field. ○ Experimental observation. ● Predicted dielectric constant from r.f. conductivity data of same sample, as explained in text. Only difference values and not absolute values of dielectric constant significant.

the mobility and dielectric constant data into two parts. The first part will be concerned with the zero-field observations from which conductivity masses of holes and electrons can be deduced using formally correct expressions. In the second part the high-field results will be analysed in terms of the elementary theory of Section 2.

4.1 *Analysis of zero-field data: the effective masses*

Exact expressions for the zero field conductivity and dielectric constant have been given by equations (2.1) and (2.2). From these we can write the effective mass

$$m = \frac{\Delta\epsilon}{\sigma}\frac{e}{\mu}\frac{\langle\varepsilon\tau_m\rangle^2}{\langle\varepsilon\tau_m^2\rangle\langle\varepsilon\rangle}, E_0 = 0, \qquad (4.1)$$

by using the fact that $(\omega\tau_m)^2 \ll 1$. Here $\Delta\epsilon$ is the free-carrier contribution to the dielectric constant and it is obtained from Figs. 2 and 3 by subtracting the dielectric constant of intrinsic material from that of the doped sample, then applying a correction ($\leqslant 5$ per cent) for the intrinsic carrier contribution.

The factor $\langle\varepsilon\tau_m\rangle^2[\langle\varepsilon\tau_m\rangle\langle\varepsilon\rangle]^{-1}$ can be evaluated in two ways; (a) by assuming $\tau_m \propto \varepsilon^{-\lambda}$ hence the averaging factor becomes $\Gamma^2(\frac{5}{2}-\lambda)/[\Gamma(\frac{5}{2}-2\lambda)\Gamma(\frac{5}{2})]$ or (b) from the ratio of Hall to drift mobility

$$\langle\varepsilon\tau_m\rangle^2[\langle\varepsilon\tau_m^2\rangle\langle\varepsilon\rangle]^{-1} = B\mu/\mu_H, H \to 0,$$

where B is a ratio of effective masses. B has been defined by HERRING[15] for electrons in germanium while for holes $B = DF/E^2$, these quantities having been defined by LAX and MAVROIDES[16]. Values of B deduced from cyclotron resonance observation are presented in Table 1 together with μ_H/μ values obtained by MORIN[17] at 275°K.

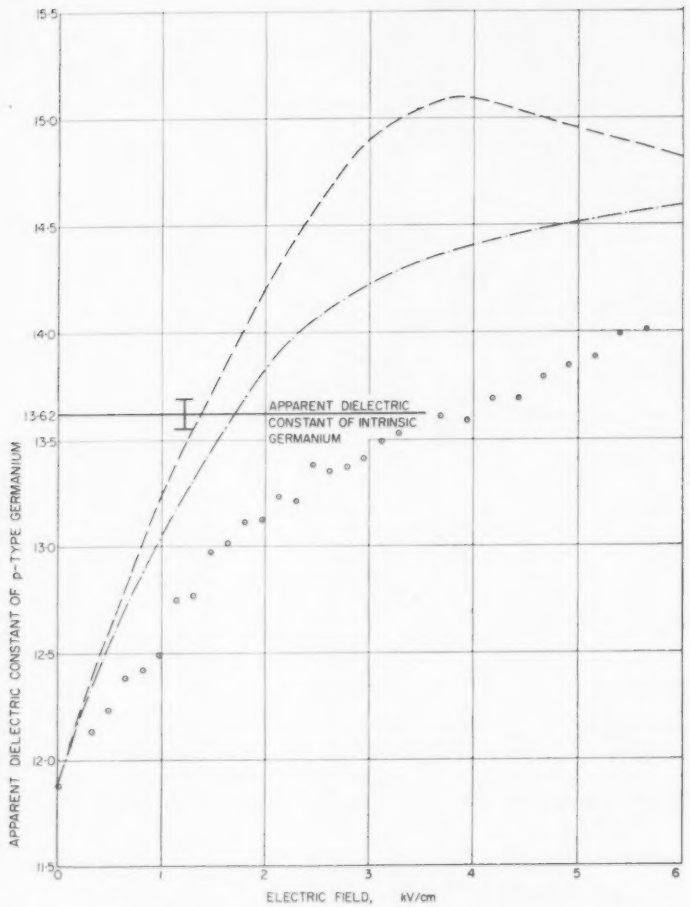

FIG. 3. Dielectric constant of p-type germanium as a function of applied electric field. ⊙ Experimental observations. – – – Predicted dielectric constant from r.f. conductivity data assuming τ_ε single valued. – · – · – · Predicted dielectric constant from r.f. conductivity data assuming two values of τ_ε, as explained in text.

The averaging factor has been calculated by both methods, assuming $\lambda = \frac{1}{2}$ for the calculation from the relaxation time (acoustical phonon scattering). Taking the mobility of electrons as 3800 $cm^2\ V^{-1}\ sec^{-1}$ and the mobility of holes as 1900 $cm^2\ V^{-1}\ sec^{-1}$ the values of mass given in Table 1 were obtained.

The conductivity masses can be deduced from cyclotron resonance observations made at 4°K.

For electrons,

$$m_e = 3\left[\frac{1}{m_\parallel} + \frac{1}{m_\perp}\right]^{-1} \tag{4.2}$$

where $m_\parallel$ and $m_\perp$ are the effective masses parallel and perpendicular to the symmetry axis of an ellipsoidal constant energy surface in the conduction band. For holes,

$$m_h = (m_{DH}^{3/2} + m_{DL}^{3/2})\left[\frac{m_{DH}^{3/2}}{m_H} + \frac{m_{DL}^{3/2}}{m_L}\right]^{-1} \tag{4.3}$$

Vol. 1
1961

Table 1

Carrier	B	μ_H/μ	$\dfrac{\langle\varepsilon\tau_m\rangle^2}{\langle\varepsilon\tau_m^2\rangle\langle\varepsilon\rangle}$		m/m_0		m/m_0 (4°K)
			μ_H/μ	$\tau_m \propto \varepsilon^{-1/2}$	μ_H/μ	$\tau_m \propto \varepsilon^{-1/2}$	
Electron	0·784	1·05	0·75	0·85	0·13 ± 0·02	0·14 ± 0·02	0·12
Hole	1·76	1·76	1·00	0·85	0·59 ± 0·12	0·50 ± 0·10	0·23

where m_D is the density of states mass—the subscripts L and H referring to light and heavy holes respectively. These relationships are subject to assumptions concerning the relaxation times. This limitation applies also to the value of the averaging factor.

We are concerned, in fact, with three sets of masses; (i) masses deduced from cyclotron resonance observations which are dependent only on the band structure, (ii) conductivity masses, m_σ, defined by equation (2.1), which depend for electrons on the anisotropy of τ_m and for holes on the relative magnitude and energy dependences of τ_{mL} and τ_{mH}, and (iii) the masses deduced from equation (4.1), which we shall call the polarizability masses, m_α, which also depend on τ_m but in a different way to the conductivity masses.

HERRING and VOGT[18] have presented evidence that τ_m for optical and acoustical phonon scattering is isotropic for electrons, so a comparison can be made between the polarizability mass and the conductivity mass deduced for cyclotron resonance observations[19] and given in the final column of Table 1. Within the experimental error both masses are the same, showing that the effective masses are unchanged in the temperature range 4°K to 300°K.

A similar comparison for holes (Table 1) shows a difference of a factor of approximately two between m_α at 300°K and m_σ at 4°K. However, m_α and m_σ are only the same if the relaxation times of the two types of holes are identical. If the τ_m's do not have the same magnitude then m_α is greater than m_σ deduced for (4.3). For example, if $\tau_{mL}/\tau_{mH} = 3$, m_α is 15 per cent greater than m_σ. This example demonstrates that m_α is rather insensitive to the assumptions concerning τ_m which, together with the experimental evidence of BEER and WILLARDSON[20] that $\tau_{mL}/\tau_{mH} \sim 1$ at 77°K and 195°K, leads us to believe that a significant part of the difference between m_α (300°K) and m_σ (4°K) is due to a change of mass with temperature. Nevertheless, the total difference between these two masses cannot be attributed to a change in the conductivity mass for the following reason. It is known that no increase in the cyclotron resonance masses occurs between 4°K and 65°K.[21] Furthermore it would appear that the mobility of holes scattered only by phonons follows the familiar $T^{-2\cdot3}$ law above, but not below, this temperature.[22] Hence the conductivity mass cannot increase by more than 60 per cent between 65°K and 300°K to be consistent with this data. We conclude, therefore, that a significant increase in the conductivity mass does occur but that this is not observed unambiguously in the microwave experiment due to complications introduced by unequal relaxation times.

4.2 *Analysis of high field data. The energy relaxation time*

4.2.1 *Comparison of dielectric constant and conductivity data.* To facilitate comparison of the results with the theory of Section 2 we re-write equations (2.10), (2.11) and (2.12) in the form:

$$\mu = \mu_0\left[1 - \frac{QT}{1+\omega^2T^2}\right] \tag{4.4}$$

$$\frac{\Delta\epsilon'}{\epsilon_0} = \frac{-\sigma_0}{\epsilon_0}\left[\tau_{m_0} - \frac{QT^2}{1+\omega^2T^2}\right] \tag{4.5}$$

$$T = \frac{1}{\omega}\left(\frac{\mu-(dv/dE)_0}{\mu_0-\mu}\right)^{1/2} \tag{4.6}$$

where Q has been written in place of $2n_1(\varepsilon_0-\varepsilon_L)/\varepsilon_0\tau_{\varepsilon_0}$.

This procedure has been adopted because the theoretical interpretation of Q depends on the detailed assumptions made in the model but the form of equations (4.4) and (4.5) is not sensitive to the energy loss mechanism and remains unchanged in the more sophisticated model discussed in Section 5.

It is clear from inspection of the above equations that, if τ_{m_0} is known, it should be possible to deduce the dielectric constant as a function of electric field from the mobility data. The value of τ_{m_0} can be found immediately at zero applied field and to determine its value at other field strengths we assume that τ_{m_0} is simply proportional to μ_0. The comparison of the dielectric constant and the mobility depends only on this assumption and is, of course, independent of the interpretation of τ_m discussed in the previous section. At high fields $\tau_{m_0} \ll QT^2/1+\omega^2T^2$ so that the comparison becomes insensitive to the value of τ_{m_0}.

The predicted and observed dielectric constants for the n- and p-type samples are shown in Figs. 2 and 3 respectively. It will be seen that the agreement for electrons is excellent. There is, however, a substantial discrepancy for holes.

We cannot explain this discrepancy in terms of τ_{m_0} since τ_{m_0} would have to *increase* by a factor of nearly 5 with increasing field. In all likelihood, the values of T for light and heavy holes are unequal. Then equations (4.4) and (4.5) should be written as the sum of two terms and, as $(T_1+T_2)^2 \neq T_1^2+T_2^2$ no agreement would be expected. To indicate the magnitude and sign of this modification to the simple theory we have assumed that the energies and indices n_1 and n_2 of the light and heavy holes at any electric field are equal. Hence

$$\frac{\tau_{\varepsilon_1}}{\tau_{\varepsilon_2}} = \frac{T_1}{T_2} = \frac{\mu_{0_2}}{\mu_{0_1}}.$$

Using this expression and assuming that the light holes represent 4 per cent of the total density[19] we predict the second theoretical dielectric constant curve shown in Fig. 3. This curve is at least nearer to and, more significantly, has the same shape as the experimental curve, but it must be admitted that the assumption of equal energies is not very realistic. If no simplifying assumptions are made, insufficient data is available to solve the resulting equations.

4.2.2 *Analysis of conductivity data for n-type germanium.* In view of the difficulties encountered with p-type germanium and described above we shall now restrict our attention to n-type material.

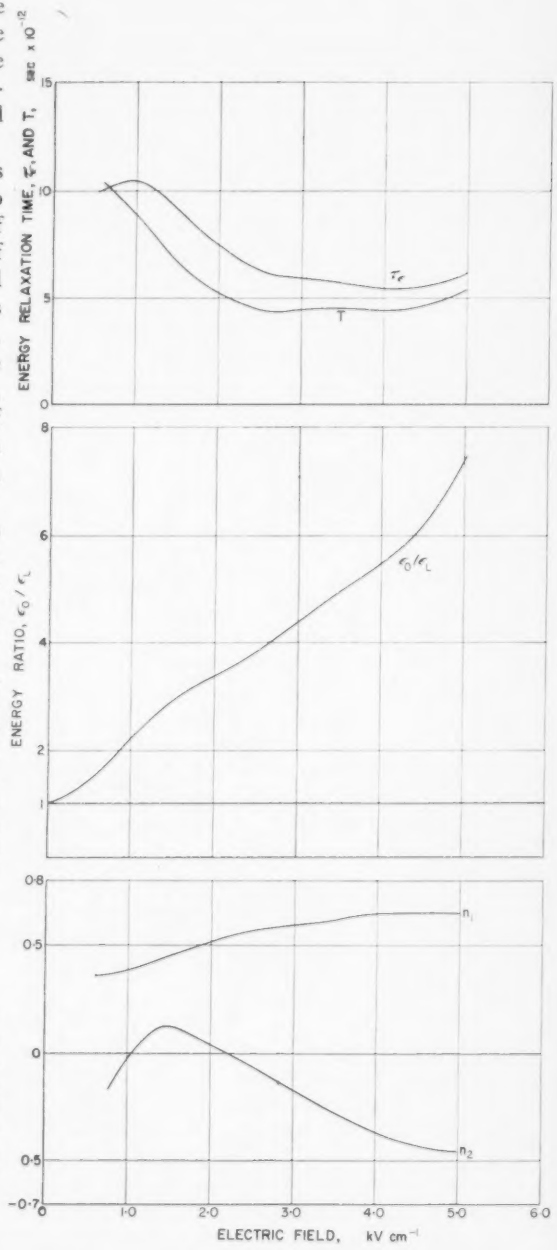

FIG. 4. Values of T, τ_ε, $\varepsilon_0/\varepsilon_L$, n_1 and n_2 for n-type germanium deduced from conductivity data using theory developed in Section 2.

Vol. 1
1961

Using the equations developed in Section 2 we can deduce the values of ε_0, τ_{ε_0}, T, n_1 and n_2 from the experimental data and these are given as functions of the electric field in Fig. 4. In spite of the use of an over-simplified model, the values deduced are in surprisingly good agreement with the predictions of the theory of Section 5 based on acoustical and optical mode scattering and a Maxwellian carrier energy distribution. In particular we find that n_1 is about 0·5 at low fields, characteristic of acoustical mode scattering, but increases slowly when optical mode scattering becomes important. The deduced carrier energies, or rather the ratio $\varepsilon_0/\varepsilon_L$, may be compared with the temperatures deduced in Section 5 and given in Fig. 5. Again surprisingly good agreement between the simple and more sophisticated model is obtained. The latter agreement encourages us to believe that τ_{ε_0}, which is simply related to ε_0, represents a good, if artificial, description of the energy loss processes occuring at high electric fields and justifies the use of the simple model in device applications. A final word should be added about the value of n_2 which is obtained from the small difference of large quantities and is therefore very inaccurate. It does, however, vary in sympathy with the variation of τ_{ε_0} with ε_0, which indicates the internal consistency of the data.

5. THE ENERGY RELAXATION PROCESS IN TERMS OF OPTICAL AND ACOUSTICAL PHONON SCATTERING

In the preceding sections we have demonstrated that a relaxation process occurs in germanium at high electric fields which affects the conductivity and phase at microwave frequencies. As an initial step we have set up a simple theory in which the relaxation process is interpreted as an energy relaxation phenomenon (Section 2), and find (Section 4) that this simple theory gives a semi-quantitative description of the observations. In this section we shall present a more refined theory for the energy relaxation process. In particular we shall consider specific scattering mechanisms and shall assume that the free carriers have a Maxwellian energy distribution.

5.1 *Theory*

It is well known that, for fields below 6 kV cm^{-1} at least, the interaction of free carriers with both optical and acoustical phonons is important; collisions with acoustical modes dominate the momentum balance equation while optical modes dominate the energy balance equation. The incorporation of these scattering mechanisms, together with the use of a Maxwellian energy distribution, presents a more realistic approach and will enable comparisons to be made between the observed relaxation times and those predicted from theory incorporating parameters from other observations. Impurity scattering is not considered because it is unimportant in the samples used; the inclusion of such additional scattering mechanisms in the following theory is straightforward.

We assume that the distribution for the free carriers, f, in an electric field is given by

$$f(\boldsymbol{V},\boldsymbol{v},T) = N\left(\frac{m_D}{2\pi kT}\right)^{3/2} \exp\left(-m|\boldsymbol{V}-\boldsymbol{v}|^2/2kT\right) \tag{5.1}$$

where N and T are the concentration and temperature of the carriers, $\boldsymbol{V}$ the free carrier velocity and k is Boltzmann's constant. Such a distribution function, Maxwellian and displaced in momentum space by $m\boldsymbol{v}$, has been used by FROHLICH and PARANJAPE[23] and STRATTON[24] and, as they point out, only exists when electron–electron (e–e) collisions predominate. By adopting (5.1) as the distribution function we have chosen to base our calculations on the simplest of the quantitative theories of hot electrons;[24] it has the additional advantages of giving analytical expressions for the final expressions and gives relationships which parallel the relationships of Section 2 very closely—it is, in fact, unnecessary to reinterpret physically the various terms that arise. While (e–e) scattering does not predominate in the specimens used in this experiment, we cannot assume (e–e) scattering effects are negligible. Calculations of the mobility of hot electrons neglecting (e–e) scattering give results which are close (within 10 per cent) to values calculated assuming a large amount of (e–e) scattering.[25] Thus, since we do not know the extent of (e–e) scattering but know that the mobility is insensitive to it, we feel that the choice of basing our calculations on the simpler theory is justified at this stage.

We shall use an isotropic mass and assume that

it is independent of energy; it is identified with the conductivity mass of the carrier. We shall return to a discussion of this simplification in Section 5.2.

When (e–e) scattering predominates over other scattering processes in the exchange of momentum and energy, the rate of change of momentum and rate of change of energy are given by

$$Nm\frac{d\boldsymbol{v}}{dt} = Ne\boldsymbol{E}$$

$$-\int_0^\infty \boldsymbol{V}\left\{\left(\frac{\partial f}{\partial t}\right)_{\text{ac}}+\left(\frac{\partial f}{\partial t}\right)_{\text{op}}\right\}d^3V \qquad (5.2)$$

write the distribution function in the form

$$f(\boldsymbol{V},\boldsymbol{v},T) = f_0+f_1\cos\theta,$$

where

$$f_0(\varepsilon,T) = N\left(\frac{m_D}{2\pi kT}\right)^{3/2}\exp\left(-\frac{\varepsilon}{kT}\right)$$

$$f_1(\varepsilon,\boldsymbol{v},T) = \frac{m}{kT}f_0|\boldsymbol{V}||\boldsymbol{v}|$$

and

$$\cos\theta = \boldsymbol{V}\cdot\boldsymbol{E}/|\boldsymbol{E}||\boldsymbol{V}|.$$

Then STRATTON shows that

$$\left(\frac{\partial f_0}{\partial t}\right)_{\text{ac}} = \frac{1}{mV}\frac{\partial}{\partial\varepsilon}\left\{\frac{4\varepsilon^2 m_D S^2}{L_{\text{ac}}kT_L}\left(f_0+kT_L\frac{\partial f_0}{\partial\varepsilon}\right)\right\},$$

$$\left(\frac{\partial f_1}{\partial t}\right)_{\text{ac}} = -\frac{f_1}{\tau_{\text{ac}}} = -f_1\frac{(2\varepsilon/m)^{1/2}}{L_{\text{ac}}},$$

$$\left(\frac{\partial f_0}{\partial t}\right)_{\text{op}} = \frac{f_0 2\varepsilon}{mV(2N_L+1)L_{\text{op}}}[(N_L+1)\exp(-\gamma)-N_L]$$

$$\times\left([1+h\nu/\varepsilon]^{1/2}-[1-h\nu/\varepsilon]^{1/2}\exp\gamma\right),$$

$$\left(\frac{\partial f_1}{\partial t}\right)_{\text{op}} = -\frac{f_1}{\tau_{\text{op}}} = -f_1\frac{(2\varepsilon/m)^{1/2}}{L_{\text{op}}}\left\{\frac{N_L[1+h\nu/\varepsilon]^{1/2}+(N_L+1)[1-h\nu/\varepsilon]^{1/2}}{2N_L+1}\right\},$$

and

$$N\frac{d(\tfrac{3}{2}kT)}{dt} = Ne\boldsymbol{v}\cdot\boldsymbol{E}$$

$$-\int_0^\infty \varepsilon\left\{\left(\frac{\partial f}{\partial t}\right)_{\text{ac}}+\left(\frac{\partial f}{\partial t}\right)_{\text{op}}\right\}d^3V, \qquad (5.3)$$

where $(\partial f/\partial t)_{\text{ac}}$ and $(\partial f/\partial t)_{\text{op}}$ are the rates of change of the distribution function due to scattering by acoustical phonons and optical phonons respectively. [c.f. STRATTON[24] equations (3.1) and (3.2)]. A condition which is always satisfied is that $mv^2/2kT \ll 1$, since even if we go to the extreme of equating v to the saturated drift velocity yet maintaining T at the lattice temperature, it is satisfied. This condition allows us to

where L_{ac} is the energy independent mean free path for scattering by acoustical phonons, L_{op} is the energy independent mean free path which can be defined for the scattering of high energy carriers ($\varepsilon \gg h\nu$) by optical phonons, T_L is the temperature of the lattice, S is the velocity of longitudinal sound waves, and $\gamma = h\nu/kT$ where $h\nu$ is the energy of the optical phonon. N_L is the number of excited optical modes,

$$N_L = [\exp(h\nu/kT_L)-1]^{-1}.$$

The terms representing the emission of an optical phonon, containing the factor $(1 - h\nu/\varepsilon)^{1/2}$, should be set equal to zero for $\varepsilon < h\nu$. The density of states mass, m_D, has been introduced into the factor which represents the inelasticity of acoustical phonon scattering.

Vol. 19
1961

For a d.c. field producing a drift velocity $\boldsymbol{v}_0$ and an electron temperature T_0 equations (5.2) and (5.3) become

$$e\boldsymbol{E}_0-\boldsymbol{A}_p-\boldsymbol{O}_p=0, \tag{5.4}$$

$$e\boldsymbol{v}_0\cdot\boldsymbol{E}_0-A_\varepsilon-O_\varepsilon=0, \tag{5.5}$$

where $$\boldsymbol{A}_p=\left(\frac{32}{9\pi}\right)\frac{e\boldsymbol{v}_0}{\mu_{\rm ac}}\left(\frac{T_0}{T_L}\right)^{1/2},\quad A_\varepsilon=\left(\frac{32}{9\pi}\right)\frac{3eS^2}{\mu_{\rm ac}}\left(\frac{T_0}{T_L}\right)^{3/2}\left(1-\frac{T_L}{T_0}\right)\frac{m_D}{m},$$

$$\boldsymbol{O}_p=\left(\frac{32}{9\pi}\right)\frac{e\boldsymbol{v}_0}{2\mu_{\rm op}(2N_L+1)}\left(\frac{T_0}{T_L}\right)^{1/2}\left\{\frac{I_{3/2}(\gamma)}{3}\,([N_L+1]e^{-\gamma}+N_L)+\frac{\gamma}{2}I_{1/2}(\gamma)([N_L+1]e^{-\gamma}-N_L)\right\}$$

and $$O_\varepsilon=\left(\frac{32}{9\pi}\right)\frac{3ehv}{4m\mu_{\rm op}}\left(\frac{T_0}{T_L}\right)^{1/2}I_{1/2}(\gamma)\frac{[(N_L+1)e^{-\gamma}-N_L]}{(2N_L+1)}.$$

The integrals $I_n(\gamma)$ are defined in terms of Bessel functions in the appendix, and

$$\mu_i=4eL_i/[3(2\pi mkT_L)^{1/2}],\ i=\text{ac, op.}$$

The zero field mobility for acoustical modes deduced from (5.4) is

$$[\mu_{\rm ac}]=(9\pi/32)\mu_{\rm ac},$$

where the square brackets imply that the averaging procedure used to determine the mobility assumes predominant (e–e) scattering.

As in Section 2, the drift velocity due to the combined d.c. and microwave fields is written as two terms $v=v_0+\Delta v$,† and here we assume we can write $T=T_0+\Delta T$ where Δv and ΔT are the incremental drift velocity and carrier temperature resulting from the microwave field. These relations are substituted in (5.2) and (5.3), and after integrating, neglecting second order terms viz. $(\Delta v)^2$, $(\Delta v\Delta T)$, (ΔvE_1) etc. and using the steady state relations (5.4) and (5.5) we obtain

where the functions $H(\gamma)$ and $G(\gamma)$ are defined in terms of the integrals I_n in the appendix. This pair of coupled differential equations is identical in form to (2.6) and (2.7) and it follows that the resulting σ^* has the same form as (2.8).

We shall now consider three conditions which, if satisfied, enable us to write σ^* in a simplified form:

(i) $mv_0^2/2kT\ll 1$, this, as we noted when expanding (5.1), is a condition which always holds.

(ii) $(\omega\tau_m)^2\ll 1$, this is valid at all fields in the present experiment (see Section 2).

(iii) $$1/\tau_m\gg\left(\left\{\frac{3-T_L/T}{1-T_L/T}\right\}\frac{A_\varepsilon}{2}+\{G(\gamma)-\tfrac{3}{2}\}O_\varepsilon\right)\frac{1}{\frac{3}{2}kT}.$$

This is very similar to the condition $1/\tau_m\ll 1/\Pi$ where Π^{-1}, a parameter defined below, is essentially $1/\tau_\varepsilon$. The condition becomes $\tau_m\ll\tau_\varepsilon$ which has been shown to be valid (see Sections 2 and 4). Using these three conditions we obtain

$$m\frac{d\Delta v}{dt}=eE_1e^{i\omega t}-\frac{\Delta v}{v_0}(A_p+O_p)-\frac{\Delta T}{T_0}(\tfrac{1}{2}A_p+\{H(\gamma)-\tfrac{5}{2}\}O_p) \tag{5.6}$$

and

$$\tfrac{3}{2}k\frac{d\Delta T}{dt}=ev_0E_1e^{i\omega t}+e\Delta vE_0-\frac{\Delta T}{T_0}\left(\frac{(3-T_L/T_0)}{(1-T_L/T_0)}\frac{A_\varepsilon}{2}+\{G(\gamma)-\tfrac{3}{2}\}O_\varepsilon\right) \tag{5.7}$$

† The vector notation will be omitted since the d.c. field and the microwave field vectors are colinear.

$$\mu = \mu_0\left(1 - \frac{2v_0}{\frac{3}{2}kT_0}(\tfrac{1}{2}A_p + \{H(\gamma) - \tfrac{5}{2}\}O_p)\frac{\Pi}{1+\omega^2\Pi^2}\right) \tag{5.8}$$

and

$$\varkappa = -Ne\mu_0\left(\frac{m\mu_0}{e} - \frac{2v_0}{\frac{3}{2}kT_0}(\tfrac{1}{2}A_p + \{H(\gamma) - \tfrac{5}{2}\}O_p)\frac{\Pi^2}{1+\omega^2\Pi^2}\right) \tag{5.9}$$

where

$$\Pi^{-1} = \left\{v_0(\tfrac{1}{2}A_p + \{H(\gamma) - \tfrac{5}{2}\}O_p) + \left(\frac{(3 - T_L/T_0)}{(1 - T_L/T_0)}\frac{A_\varepsilon}{2} + \{G(\gamma) - \tfrac{3}{2}\}O_\varepsilon\right)\right\} \Big/ \tfrac{3}{2}kT_0 \tag{5.10}$$

As the ω is lowered $\mu \to (dv/dE)_0$, hence from equation (5.8) we have

$$\Pi = \left(\frac{\mu - (dv/dE)_0}{\mu_0 - \mu}\right)^{1/2}\frac{1}{\omega} \tag{5.11}$$

(c.f. equation 2.12).

If R is the ratio of the strength of the interaction between an electron and optical phonon to the strength of the interaction between an electron and acoustical phonon, then we can define

$$L_{ac}/L_{op} = (2N_L + 1)Rh\nu/kT_L$$

(c.f. STRATTON[24], equation 4.1a). Using this relation μ_{op} can be eliminated from the foregoing equations. From the steady state equations (5.4) and (5.5) we have

$$\frac{1}{\mu_0} = \frac{1}{[\mu_{ac}]}\left(\frac{T_0}{T_L}\right)^{1/2}(1 + RF_p(\gamma)) \tag{5.12}$$

and

$$v_0E_0 = \frac{3S^2}{[\mu_{ac}]}\left(\frac{T_0}{T_L}\right)^{3/2}(1 - T_L/T_0)(1 + RF_\varepsilon(\gamma)), \tag{5.13}$$

and from (5.10) and (5.11) we obtain

$$\left(\frac{\mu_0 - \mu}{\mu - (dv/dE)_0}\right)^{1/2}\omega = \left\{\frac{ev_0^2}{[\mu_{ac}]}\left(\frac{T_0}{T_L}\right)^{1/2}(\tfrac{1}{2} + \{H(\gamma) - \tfrac{5}{2}\}RF_p(\gamma)) + \frac{3eS^2}{[\mu_{ac}]}\left(\frac{T_0}{T_L}\right)^{3/2}[\tfrac{1}{2}(3 - T_L/T_0) + (1 - T_L/T_0)\{G(\gamma) - \tfrac{3}{2}\}RF_\varepsilon(\gamma)]\right\}\frac{1}{\tfrac{3}{2}kT_0} \tag{5.14}$$

where $RF_p(\gamma) = O_p(\gamma)/A_p(\gamma)$

and $RF_\varepsilon(\gamma) = O_\varepsilon(\gamma)/A_\varepsilon(\gamma)$.

We have already noted that Π and the parameter T of Section 2 (not to be confused with temperature) are determined in an identical manner from the experimental observations. Physically they are, of course, the same quantity but have somewhat different definitions dependent on the details of the theory. Thus the equation for Π, (5.12), reduces to that for T, (2.9), if we neglect optical modes and recast the acoustical mode terms on the basis of a monoenergetic distribution.

5.2 *Comparison between theory and experiment*

Before making a detailed comparison between the theory and the experimental observations it is worthwhile pointing out that the relationship between the phase and the absorption [(4.4) and (4.5)] remains valid. Thus the discrepancy, mentioned in Section 4.2, between the phase and absorption data for holes remains, which implies that the theory is inadequate to deal with holes. Since the phase and absorption data are consistent for electrons of about the same concentration as the holes, it would appear that the presence of two types of holes is an essential feature not incorporated in the theory. We may conclude that the transitions between light and heavy hole states and the energy and momentum exchanges between light and heavy holes are not sufficiently rapid, for the carrier concentrations with which we are dealing, for both types of holes to be characterized by a single temperature and a single mean velocity in the high field transport problem. In

Vol. 1
1961

fact it is generally accepted that the relaxation time for transfer from the heavy to light hole states (τ_{HL}) is $\sim(m_{DH}/m_{DL})^{3/2}\tau_m$[26] where τ_m is the momentum relaxation time.[16] A typical value of τ_m gives $\tau_{HL} \sim 10^{-11}$ sec which introduces a further complication since $(\omega\tau_{HL}) \sim 1$, and this presents the possibility of additional relaxation effects.

In the light of these conclusions regarding holes we shall attempt a detailed comparison between theory and experiment only for electrons, though it should be mentioned that the above conclusions concerning holes do not affect the deduction of effective masses from the zero-field observations.

5.2.1 *The magnitude of* Π. In order to calculate the magnitude of Π we must first of all consider the value of R. Assuming no increase in the effective mass of the electron, R can be estimated from the variation of the lattice mobility with temperature. This procedure gives a value of R of 0·14,[27] which we take to be an upper limit since any increase in mass will lower the value estimated in this way.* We have taken values of R of 0·14, $\frac{1}{2}\times 0{\cdot}14$ and $\frac{1}{4}\times 0{\cdot}14$. The range of values of R is terminated at 0·035 because, as we shall see, this value leads to some consistency between equations (5.12) and (5.13).

Besides knowing R we see from equation (5.14) that it is essential to know T_0 as a function of E_0 to be able to predict Π. To obtain $T_0(E_0)$ and to calculate Π we proceed as follows: (i) take one of the values of R—this enables a value of $[\mu_{ac}]$ to be calculated from the zero field lattice mobility, (ii) calculate T_0 from the value of μ_0 at a given field (equation 5.12), (iii) calculate T_0 from the value of v_0E_0 at a given field (equation 5.13), (iv) calculate the values of Π^{-1} for the two electron temperatures predicted. Throughout, the optical mode energy is taken as 0·0375 eV.[28] The resulting temperatures as a function of field calculated by methods (ii) and (iii) are shown in Fig. 5; limits placed on the field co-ordinate reflect the experimental error in determining μ_0 and v_0E_0. The temperatures obtained by method (ii) for the various values of R are sufficiently close for them to be represented by a single curve in Fig. 5. The greater sensitivity of v_0E_0 to R arises from the effectiveness of optical modes in the energy loss process. It is clear from Fig. 5 that for a value of R of about 0·035 the T_0's calculated by methods (ii) and (iii) are the same within the experimental error over a large part of the field range. In Fig. 6 the predicted values of Π^{-1} are plotted against the electric field; limits due

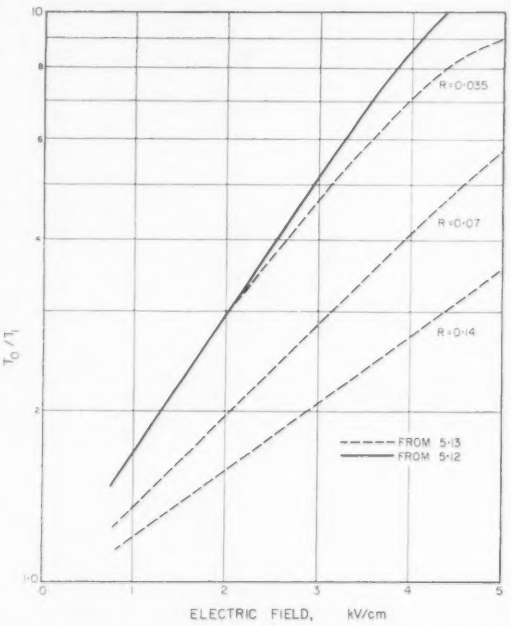

FIG. 5. The variation of the reduced electron temperature with electric field.

to experimental errors can readily be transferred from Fig. 5 to this figure. The trend is for a decrease of the predicted Π^{-1} with increasing electron temperature. The decrease arises because optical phonon emission causes the greatest fractional change in energy when the carrier has an initial energy just in excess of the energy of the optical mode—the fractional change in energy decreases as the carrier energy increases above this value and causes Π^{-1} to decrease. Even at zero field, optical modes are dominant because the mean carrier energy is $\frac{3}{2}kT_L \sim h\nu$ for $T_L =$ 300°K. (For a lattice temperature of 77°K there is a marked decrease in the predicted value of

* Although we find the m for electrons is constant within the experimental error, the mobility is strongly dependent on m, $\mu\alpha[mm_D^{3/2}]^{-1}$, which in turn makes the calculated value of R very sensitive to changes in m.

Π^{-1} as the electric field tends to zero so that Π^{-1} passes through a maximum when the mean carrier energy is about $h\nu$.)

In comparing the observed with the predicted values of Π^{-1} we note that although the observed Π^{-1} does not have the expected field dependence it does fall within the range of predicted values of Π^{-1}. Since we believe that R lies between 0·14 and 0·03 we are encouraged by this degree of agreement. In fact we see from Figs. 5 and 6 that a dependences of Π^{-1}. In the light of this we list and examine some of the approximations and simplifications we have made which are known to be invalid.

(a) the effective mass is isotropic,

(b) the (ε, $\boldsymbol{k}$) surface is parabolic (effective mass independent of ε), and

(c) (e–e) scattering predominates over other scattering mechanisms and determines the form of the distribution function.

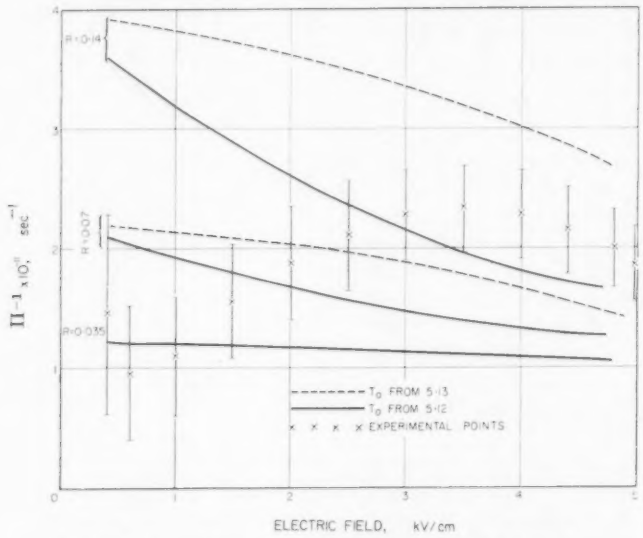

FIG. 6. The variation of the theoretically predicted and experimentally observed values of Π^{-1} with electric field.

value of R about 0·035 leads to internal consistency between μ_0, v_0E_0 and Π, as given by equations (5.12)–(5.14), up to a field of between 1·5 kV cm^{-1} to 2 kV cm^{-1}. This value of R leads to higher values of T_0 than those predicted from $R = 0{\cdot}14$, c.f. STRATTON[27], PAIGE[8] and Fig. 5; it also implies that optical modes are not entirely responsible for the departure from a $T_L^{-1{\cdot}5}$ law for lattice mobility. (This conclusion is in agreement with BROWN'S[29] deductions.)

5.2.2 *The variation of* Π^{-1} *with field.* Although the theory we have presented is more refined than that given in Section 2 it is clear that it is not capable of interpreting the details of the experimental observations, notably the field

(a) It is well known that electrons in germanium populate four equivalent minima in $\boldsymbol{k}$ space, where the constant energy surfaces are ellipsoidal in shape. The ellipsoids are so orientated that if $\boldsymbol{E}$ is in the ⟨100⟩ direction the accelerative mass is the same in each valley (the conductivity mass) and no special effects arise due to the presence of several valleys since the electrons in each valley are under identical conditions. For other directions of the electric field the situation is more complicated,[8,25] yet with the lattice at room temperature the drift velocities as a function field for various orientation differ by less than 5 per cent.[30] It appears, therefore, that our use of an isotropic mass—taken to have the value of the conductivity mass—is a good approximation for electrons. However, a feature of the multivalley model which might conceivably manifest itself in the microwave experiment is a relaxation process associated with the transfer of electrons from one valley to another. An estimate of the intervalley relaxation time, τ_{if}, based

on low temperature data,[8,31] makes it plausible that $\omega\tau_{ij} \sim 1$ for some range of electric field. Such an effect would clearly be orientation dependent (zero for $\boldsymbol{E}$ in the $\langle 100 \rangle$ direction) and requires a difference of electron temperature between the valleys. The orientations of the samples used in the experiment we have described are unknown, but we have concluded, from an examination of data on a large number of samples and from BROWN'S[29] observations that no significant orientation effect is observed. Also calculations of the temperature difference between valleys[8] supports the conclusion that this type of relaxation process is unimportant under the conditions of the present experiment.

(b) Since the electrons acquire high energies in the electric field they may have populated both regions of the valleys where the $(\varepsilon, \boldsymbol{k})$ surfaces are not parabolic and energy minima other than the $\langle 111 \rangle$ minima at the edge of the Brillouin zone. In fact since a value of $R = 0{\cdot}035$ leads to consistency between the velocity field curve and Π up to fields between $1{\cdot}5\ \mathrm{kV\ cm^{-1}}$ and $2\ \mathrm{kV\ cm^{-1}}$, we should predict that the electrons attain a mean energy of 0·10 eV in this field range. As the band at $\boldsymbol{k} = 0$ is 0·14 eV above the minima at the edge of the zone and as, presumably, the parabolic $(\varepsilon, \boldsymbol{k})$ relation within the 111 valleys breaks down at about this energy, we are led to expect significant deviations from the theory of 5.1 at fields in excess of $2\ \mathrm{kV\ cm^{-1}}$.*

(c) As stated at the beginning of this section, (e–e) scattering does not affect significantly the predicted values of the mobility. A sensitivity to R implies some sensitivity to the detailed form of the distribution function and it is possible, therefore, that Π may be more influenced by (e–e) scattering than the mobility.

We conclude, therefore, that the most likely reason for the disagreement between theory and experiment is that at fields as low as $2\ \mathrm{kV\ cm^{-1}}$ regions of $\boldsymbol{k}$ space are populated in which the average effective mass is dependent upon energy either through departures from the parabolic $(\varepsilon,\boldsymbol{k})$ relationship within the $\langle 111 \rangle$ valleys or through population of the $\boldsymbol{k} = 0$ minimum. Besides the direct effect of variation of effective mass on the mobility, the corresponding changes in the density of states mass can have pronounced effects on the relaxation times. Furthermore, relaxation processes between the edge and centre of the zone become possible. Some uncertainty in this interpretation is introduced by the unknown extent of the influence of (e–e) scattering on Π, though as we have noted there is evidence that (e–e) scattering effects on the mobility are small.

* STRATTON[27] has previously pointed out that the band edge at $k = 0$ may become populated.

6. SUMMARY AND CONCLUSIONS

Experimentally it has been observed that the absorption of microwave radiation by silicon and germanium in the presence of a high electric field is not proportional to either the mobility μ_0, or the slope mobility $(dv/dE)_0$, in the high field. The measurement of the phase shift of the microwaves in germanium due to an applied field showed the unexpected result that at high fields the free carrier contribution to the dielectric constant becomes positive. It is apparent that some relaxation process is operative which we associate with the large departure from the thermal equilibrium.

We have interpreted the relaxation process as giving what is essentially an energy relaxation time. Using a very elementary theory we have shown that such a relaxation process can account in a qualitative way for both the absorption and phase observations. The relaxation times for germanium are about $1/\omega$ while those for silicon are about $2/\omega$ $(1/\omega = 4{\cdot}58 \times 10^{-12}\ \mathrm{sec})$. A relationship is established between the r.f. mobility and dielectric constant, which is also given by a more realistic theory. This relationship is verified experimentally for electrons in germanium but it is found not to hold for holes.

It is concluded that, since the free carrier concentration in both the n- and p-type samples were much the same, an interpretation of the high-field transport properties of holes in germanium which does not take into account the existence of both light and heavy holes is inadequate.

A more refined theory for the interpretation of the observations is set up which includes optical and acoustical phonon scattering. It enables a comparison to be made between the relaxation time obtained from the experiment with that deduced from theory. There is agreement between the observed and predicted magnitude of the relaxation time for electrons in germanium, but the predicted variation with electric field is not observed. This discrepancy is discussed in the light of the simplifying assumptions made in the theory. It is concluded that a reason for the discrepancy is that at fields greater than about $2\ \mathrm{kV\ cm^{-1}}$ the energy minimum at $\boldsymbol{k} = 0$ becomes populated and probably the energy of carriers within the $\langle 111 \rangle$ minima has risen to such an extent that the parabolic $(\varepsilon,\boldsymbol{k})$ relationship breaks down. This

conclusion is somewhat tentative since we are uncertain as to the effects that would be produced if we took (e–e) scattering into account correctly, though there is some indication that these effects would not be large.

An important feature of this experiment is that it demonstrates the necessity of care in the interpretation of high-field microwave experiments. In particular the microwave measurements of small deviations from Ohm's law[29] and the high-field experiments of MORGAN[11] and SEEGER[12] must be reassessed. In addition to the energy relaxation time, it has been pointed out that the relaxation time for a heavy to light hole transition and the relaxation time for inter-valley transitions could be of the same order as $1/\omega$. It is possible that under suitable conditions effects due to these processes might be observed in a microwave experiment similar to the one we have presented.

From the dielectric constant at zero field, values of the conductivity mass of both electrons and holes have been obtained. Within the experimental error the conductivity mass of electrons is unchanged between 4°K and 300°K, while the conductivity mass of holes appears to increase by a factor of about two. It has been emphasized that care is needed in interpreting this apparent increase in mass since it can be influenced by the relative values of the relaxation times of light and heavy holes. It is concluded that a significant increase in the conductivity mass does occur and that the relaxation times of light and heavy holes are not identical.

Acknowledgements—The authors would like to thank Dr. T. P. MCLEAN for his critical comments on the manuscript and to acknowledge many helpful discussions with Mr. R. M. GARNHAM concerning the microwave system. The paper is published by permission of the Controller of H.M. Stationery Office.

APPENDIX

We shall define certain integrals which are required for the solution of the steady state equations (5.4) and (5.5) as well as for the time dependent equations (5.6) and (5.7)

The integrals are of the form

$$I_{n,m}(\gamma) = \int_0^\infty dx\, e^{-x} x^n (x+\gamma)^m$$

though, for brevity, $I_{n,n}$ is written I_n in the text. By integration by parts the integrals $I_{n,m}$ can be written in terms of $I_{n,n}$. $I_{n,n}$ can then be evaluated from the following relations:

$$I_{1/2,1/2}(\gamma) = \gamma/2 \exp(\gamma/2) K_1(\gamma/2)$$

$$I_{3/2,3/2}(\gamma) = 3(\gamma/2)^2 \exp(\gamma/2) K_2(\gamma/2)$$

$$I_{5/2,5/2}(\gamma) = 15(\gamma/2)^3 \exp(\gamma/2) K_3(\gamma/2)$$

where the $K_{(i)}(\gamma/2)$ is the modified Bessel function of the second kind. (In STRATTON's[27] notation, $J(\gamma) = I_{1/2,1/2}(\gamma)$.)

In the solution of the time dependent equations certain combinations of these integrals appear which are, in terms of the I_n's,

$$H(\gamma) = \frac{I_{3/2}(\gamma)}{I_{1/2}(\gamma)} \left\{ \frac{\frac{2}{5}\frac{I_{5/2}(\gamma)}{I_{3/2}(\gamma)} - 5 + \gamma \tanh\left(\frac{\gamma_L - \gamma}{2}\right)}{\frac{2}{3}\frac{I_{3/2}}{I_{1/2}} + \gamma \tanh\left(\frac{\gamma_L - \gamma}{2}\right)} \right\}$$

and

$$G(\gamma) = \frac{1}{3}\frac{I_{3/2}(\gamma)}{I_{1/2}(\gamma)} \left\{ \frac{3\gamma I_{1/2}(\gamma)}{2I_{3/2} \tanh\left(\frac{\gamma_L - \gamma}{2}\right)} + 1 \right\}$$

REFERENCES

1. SHOCKLEY W., *Bell Syst. Tech. J.* **30,** 990 (1951).
2. RYDER E. J., *Phys. Rev.* **90,** 766 (1953).
3. GUNN J. B., *J. Electronics* **2,** 88 (1956).
4. GIBSON A. F. and GRANVILLE J. W., *J. Electronics* **2,** 259 (1956).
5. PRIOR A. C., *J. Phys. Chem. Solids* **12,** 175 (1960).
6. PAIGE E. G. S., *Proc. Phys. Soc. Lond.* **72,** 921 (1958).
7. CONWELL E., *J. Phys. Chem. Solids* **8,** 234 (1959).
8. PAIGE E. G. S., *Proc. Phys. Soc. Lond.* **75,** 174 (1960).
9. BOK J., *Solid State Physics in Electronics and Telecommunications* Vol. 1 Part 1, p.475. Academic Press, New York (1960).
10. ARTHUR J. B., GIBSON A. F. and GRANVILLE J. W., *J. Electronics* **2,** 145 (1956).
11. MORGAN T. N., *J. Phys. Chem. Solids* **8,** 245 (1959).
12. SEEGER K., *Phys. Rev.* **114,** 476 (1959).
13. SMITH R. A., *Semiconductors*, p. 216. Cambridge University Press (1959).
14. MARCUVITZ N., *Waveguide Handbook*. Radiation Laboratory Series Vol. 10, p. 388.
15. HERRING C., *Bell Syst. Tech. J.* **34,** 237 (1955).
16. LAX B. and MAVROIDES J. G., *Phys. Rev.* **100,** 1650 (1955).

17. MORIN F. J., *Phys. Rev.* **93,** 62 (1954).
18. HERRING C. and VOGT E., *Phys. Rev.* **101,** 944 (1956).
19. DEXTER R. N., LAX B. and ZEIGER H. J., *Phys. Rev.* **104,** 637 (1956).
20. BEER A. C. and WILLARDSON R. K., *Phys. Rev.* **110,** 1286 (1958).
21. BAGGULEY D. M. S., POWELL J. A. and TAYLOR D. J., *Proc. Phys. Soc. Lond.* **A.70,** 759 (1957).
22. MCLEAN T. P. and PAIGE E. G. S., submitted to *J. Phys. Chem. Solids*; BROWN D. M. and BRAY R., *Bull Amer. Phys. Soc.* **5,** 194 (1960).
23. FROHLICH H. and PARANJAPE B. V., *Proc. Phys. Soc. Lond.* **B69,** 21 (1956).
24. STRATTON R., *Proc. Roy. Soc.* **242,** 355 (1957).
25. YAMASHITA J. and INOUE K., *J. Phys. Chem. Solids* **12,** 1 (1959).
26. BROOKS H., *Electronics and Electron Physics* **7,** 87 (1955).
27. STRATTON R., *J. Electronics and Control* **5,** 157 (1958).
28. BROCKHOUSE B. N. and IYENGER P. K., *Phys. Rev.* **111,** 747 (1958).
29. BROWN M. A. C. S., following paper.
30. PRIOR A. C., private communication.
31. WEINRIECH G., SANDERS T. M. and WHITE H. G. *Phys. Rev.* **114,** 33 (1959).

ol. 19
1961

J. Phys. Chem. Solids Pergamon Press 1961. Vol. 19, Nos. 3/4, pp. 218–227. Printed in Great Britain.

DEVIATIONS FROM OHM'S LAW IN GERMANIUM AND SILICON

M. A. C. S. BROWN

Royal Radar Establishment, Malvern, Worcs.

(*Received* 8 *June* 1959; *revised* 11 *July* 1960)

Abstract—The deviation from Ohm's law in germanium and silicon at high electric fields has been measured by a microwave method at room temperature. It has been found that this deviation depends on the type and resistivity of the material, and also on the orientation of the electric field with respect to the crystallographic axis. Small deviations from the well-known quadratic variation with electric field have been observed. The quantity measured has been related to the steady-state deviation from Ohm's law by an expression involving the energy relaxation time of the carriers and the period of the microwave frequency used. Agreement with the experimental values for the steady state deviation from Ohm's law has been obtained by using a theory which considers scattering by both acoustical and optical modes, combined with a postulated increase in the effective masses of the free carriers.

I. INTRODUCTION

AN EXPLANATION of the departure from Ohm's law at high electric fields, which occurs in silicon and germanium, was put forward by SHOCKLEY[1]. The basis of the explanation is that the mean energy of the free carriers is raised as the electric field is increased, so altering the energy-dependent relaxation time. GUNN[2] has shown that at sufficiently low values of the electric field, E, the steady state mobility, μ_0, is given by

$$\mu_0 = (\mu_0)_{E=0}(1-\beta E^2) \qquad (1)$$

where β is a quantity which depends on the rate at which energy is lost by the free carriers. The relationship given by equation (1) has previously been studied experimentally by ARTHUR *et al.*[3]. When acoustical mode scattering is the only scattering mechanism, SHOCKLEY's theory predicts the following value of β.

$$\beta = \frac{3\pi}{64}\frac{(\mu_0^2)_{E=0}}{C^2}, \qquad (2)$$

where C is the velocity of longitudinal sound waves in the material. This assumption implies that the dependence of the zero-field mobility on the lattice temperature, T, if the effective mass of the carrier remains constant, is of the form

$$(\mu_0)_{E=0} \propto T^{-1.5}. \qquad (3)$$

In both germanium and silicon the zero-field mobilities of holes and electrons show a more rapid variation with temperature than predicted by equation (3); furthermore, the experimentally determined value of β in n-type germanium is about 50 times smaller than that predicted from equation (2).

More recent calculations by STRATTON[4], YAMASHITA[5] and CONWELL[6] on n-type germanium have taken into account the effect of scattering by optical phonons; these calculations were independent but are essentially similar, and for convenience we have chosen to follow that by STRATTON. He chooses an amount of optical-mode scattering sufficient to give the known mobility–temperature law for n-type germanium i.e. $(\mu_0)_{E=0} \propto T^{-1.66}$. His value for β, calculated for combined optical and acoustical modes, agrees closely with the experimental result due to ARTHUR *et al.* which is quoted by GUNN[8].

The method of ARTHUR *et al.*[3] is to observe the change in the absorption of microwave power in a germanium specimen, the change being caused by the application of a large pulsed electric field

to the specimen. They then argue that the microwave absorption is proportional to the slope mobility of the carriers in the germanium; thus the change in slope mobility can be measured as a function of electric field strength. This argument is justified if both the energy and momentum relaxation times of the free carriers are much less than the period of oscillation of the microwave field. More recent work by GIBSON *et al.*[9] has shown that this assumption is incorrect since the energy relaxation time of the carriers is almost equal to the period at the microwave frequency used. Thus the quantity measured by ARTHUR *et al.*[8] which we write as β', must be corrected in order to obtain the true value of β as defined in equation (1).

The measured quantity β' may be defined by the following equation

$$\mu = (\mu_0)_{E=0}(1-\beta' E^2), \tag{4}$$

where μ is in fact the mobility measured at field strength E when using the microwave method. The relation between μ and μ_0 is given by GIBSON *et al.*[9] (equation 5.11) as

$$\Pi = \frac{1}{\omega}\left(\frac{\mu-\left(\frac{dv}{dE}\right)_0}{\mu_0-\mu}\right)^{1/2}, \tag{5}$$

where ω is the angular frequency of the microwave power and $(dv/dE)_0$ is the slope mobility of the carriers measured by a d.c. method, that is, measured when the carriers are in a steady state. Π has the dimensions of time and is closely related to the energy relaxation time of the carriers. The relation between β, β', ω and Π can be obtained from equations (1), (4) and (5) and is given by

$$\beta' = \beta\frac{(3+\omega^2\Pi^2)}{3(1+\omega^2\Pi^2)} \tag{6}$$

It is interesting to observe that the limits of β' are $\frac{1}{3}\beta$ and β for $\Pi = \infty$ and $\Pi = 0$ respectively. The latter case corresponds to the assumption made by ARTHUR *et al.*[3] which allows one to replace the measured quantity β' by β directly. Values of Π have been determined experimentally[9] and will be used in the calculation of β.

This paper describes measurements of β' made with both *n*-type and *p*-type germanium and silicon of resistivities between 4 and 25 ohm cm; with the electric field applied in ⟨100⟩ and ⟨111⟩ crystallographic directions. The main purpose was to discover if the modification brought about by including optical mode scattering could be applied to *p*-type germanium and to silicon and further to see if β varied with carrier density or crystal orientation.

2. EXPERIMENTAL DETAILS

The apparatus is basically the same as that used by ARTHUR *et al.*[3]. The specimen, in the form of a thin slice (thickness $d = 0{\cdot}18$ mm) is positioned in fine slots which run longitudinally in the centre of the broad faces of 8 mm waveguide. A reflex klystron is used to supply about 15 mW of microwave power which is incident on the specimen, and the large electric field, E, is applied to the specimen in the form of 1 μsec pulses. This causes a change in the absorption of the specimen, which is observed, by means of a microwave detector and video amplifier, as a small signal voltage, ΔV, on the oscilloscope. After matching the waveguide on the detector side of the specimen, any power, A_R, reflected by the specimen is measured using a standing-wave meter. The insertion loss, A_I, due to the specimen is determined by pulsing the power from the klystron off for 1 μsec, this produces a signal V_1. The specimen is then removed and a precision microwave attenuator adjusted to give the same signal. The absolute absorption of the specimen, A_0, is then given by

$$A_0 = (A_\varepsilon - A_D).$$

It follows from equation (4) that

$$\frac{\Delta A}{A_0} = 3\beta' E^2, \tag{7}$$

in which ΔA, the change in absorption, can easily be expressed in terms of ΔV and V_1. It is convenient at this stage to deal directly with the measured quantity, β', rather than a complicated and hence obscure function of β', namely β.

Since we were hoping to observe small changes in β', associated with orientation or resistivity of the specimen, some effort was made to improve the sensitivity of the apparatus and also to check

the basic assumptions made in its use. A possible source of error occurs in the use of the microwave crystal detector. If G is the gain of the video amplifier and oscilloscope, and is independent of signal level, the observed signal voltage V, for a microwave power P incident on the crystal, is given by

$$V = GP^{x/2}, \tag{8}$$

where in general x is not constant but varies with P. The crystal law, as expressed by equation (8), is measured and used directly to convert signal ΔV into attenuation ΔA. When the crystal law is taken into account equation (7) becomes after some manipulation.

$$3\beta' E^2 = \frac{\dfrac{20}{x}\log_{10}\left(1+\dfrac{\Delta V}{V_1}\right)}{A_0} \tag{9}$$

where x is the slope of the crystal detector at the particular signal voltage V being observed. Accurate measurement of the sometimes large ratio $V_1/\Delta V$ is made possible by use of a carefully calibrated attenuator at the input to the video amplifier.

Measurement of the 1 μsec voltage pulse by using a d.c. calibrated resistive attenuator and oscilloscope was considered inaccurate, and a system was devised to calibrate the oscilloscope. Two techniques were used, both of which employed a thermionic high-voltage rectifier: the first was essentially a peak rectifying meter using a calibrated electrostatic voltmeter as the indicator; the second used the valve in series with a sensitive galvanometer which was the null indicator in a d.c. potentiometer. Both methods must be corrected for positive ion current in the rectifier. The accuracy of the field pulse measurement is believed to be within 2 per cent in the range 200–600 V and within 5 per cent outside this range.

All measurements were made at room temperature. The specimens were ground and then etched in CP4, and L–H junctions were made to one end of the specimen to prevent minority carrier injection.

3. EXPERIMENTAL RESULTS

Equation (9) is used to calculate the value of β' from the absorption data. A graph of

$$\log_{10}\left[\frac{20}{x}\log_{10}\left(1+\frac{\Delta V}{V_1}\right)\right]$$

plotted against $\log_{10}E$ should have a slope of 2, this being the power to which E is raised. However it was found in practice that the slope is not always exactly equal to 2 and thus we have arbitrarily decided to determine all values of β' at a given low value of field, namely 100 V cm^{-1}, and to assume that true quadratic behaviour does exist.

Figure 1 shows all the results for β' plotted against the resistivity of the specimens. It is noticeable that there is a factor of 100 between the magnitude of β' for n-type germanium and for p-type silicon. In fact β is proportional to the square of the zero-field mobility of the appropriate carrier [see for instance equation (2)], which is the main factor accounting for this large difference. For the same reason we should expect to see a slight increase of β with increasing resistivity and Fig. 1 does show this for the germanium samples. The average experimental values for β' are summarized in Table 1 (the results have been normalized with respect to $(\mu_0^2)_{E=0}$ to a value appropriate to 4 Ω cm material) together with experimental values for Π[9] and values for β calculated by using equation (6). In all the experiments $\omega = 2{\cdot}2\times10^{11}$ sec^{-1}.

We shall now consider second order effects shown in Figs. 1 and 4; Fig. 1 shows that in n-type germanium $\beta'_{111} > \beta'_{100}$, whereas in n-type silicon $\beta'_{100} > \beta'_{111}$ and the difference between them increases noticeably with resistivity. For p-type materials there is no evidence for orientation effects.

As we have said above the deviation from zero-field mobility is not always quadratic with respect to field strength, and in particular, for n-type germanium, the mobility is given empirically, in the range 100 V cm^{-1} to 400 V cm^{-1}, by the equation

$$\mu = (\mu_0)_{E=0}(1-\beta' E^{2+y}), \tag{10}$$

where y is small and may be negative. Fig. 4 shows $2+y$ plotted against the resistivity of the n-type germanium specimens. There is a noticeable dependence on resistivity and orientation, and

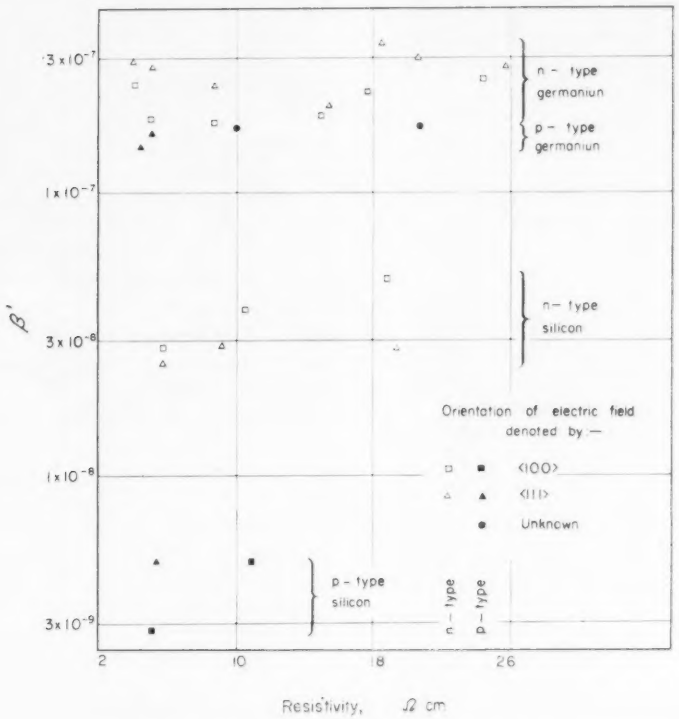

FIG. 1. Experimentally determined values of β' for germanium and silicon plotted against the resistivity of the specimens. Results are shown for the electric field in the ⟨100⟩ and ⟨111⟩ crystallographic directions.

Table 1

Material	Orientation of electric field	Experimental values of $\beta'(V^{-2}\,cm^2)$	Experimental values of Π(sec)	Calculated value for $\beta(V^{-2}\,cm^2)$
n-type germanium	⟨100⟩	$(2{\cdot}0\pm0{\cdot}3)\times10^{-7}$	$6\pm3\times10^{-12}$	$(3{\cdot}5\pm1{\cdot}4)\times10^{-7}$
	⟨111⟩	$(2{\cdot}6\pm0{\cdot}3)\times10^{-7}$		
p-type germanium	—	$(1{\cdot}6\pm0{\cdot}2)\times10^{-7}$	$5\pm2{\cdot}5\times10^{-12}$	$(2{\cdot}3\pm1{\cdot}0)\times10^{-7}$
n-type silicon	⟨111⟩	$(2{\cdot}7\pm0{\cdot}5)\times10^{-8}$	$8\pm4\times10^{-12}$	$(5{\cdot}4\pm2{\cdot}6)\times10^{-8}$
	⟨100⟩	$>2{\cdot}7\times10^{-8}$		
p-type silicon	—	$(4{\cdot}0\pm2{\cdot}0)\times10^{-9}$	$6{\cdot}5\pm3{\cdot}2\times10^{-12}$	$(7{\cdot}9\pm5{\cdot}3)\times10^{-9}$

although there is a large scatter of points on the graph, the measurement is inherently more accurate than that of β' because the absolute absorption, A_0, does not have to be considered.

4. DISCUSSION

The results will now be discussed in two parts:

(i) comparison of experimental and theoretical values of β,
(ii) second order effects.

4.1 *Comparison of β with theory*

In this section we shall attempt not only to obtain agreement between theoretical and experimental values of β using the theory of STRATTON[4], but also to obtain for each material the correct law giving the variation of mobility with temperature and a good approximation to the observed variation of mobility with electric field strength.

Initially we have followed the procedure of STRATTON, that is, to choose an amount of optical mode scattering sufficient to give the known law for the variation of mobility with temperature. The amount is specified by a parameter R,* which we have determined by the solution of an equation of the form

$$\left[\frac{\mu_0(R, 300°\mathrm{K})}{\mu_0(R, 100°\mathrm{K})}\right]_{E=0} = \left(\frac{300}{100}\right)^{-n}, \qquad (11)$$

where n is the appropriate power. No attempt has been made at curve fitting. The value of R is then used to calculate β and is also used to determine the variation of steady-state mobility with electric field strength. The results are summarized in Table 2 together with other parameters used.

Table 2 shows that all the theoretical values for β are lower than the experimental values, in particular, that for p-type germanium is low by a factor of 4. The alternative value of $\theta_0 = 430°\mathrm{K}$ for n-type silicon is taken to represent the temperature of an inter-valley phonon, since HARRISON[11] has suggested that optical mode scattering is forbidden in n-type silicon and that inter-valley scattering is a more likely process. However, with $\theta_0 = 430°\mathrm{K}$ the limiting value of power that is obtainable for the mobility temperature law is 2·43 which occurs as R tends to infinity. The observed power law for n-type silicon is $\mu \propto T^{-2\cdot5\pm0\cdot1}$ according to LUDWIG and WATTERS[12] and LONG and MEYERS[13] though PUTLEY and MITCHELL[14] find $\mu \propto T^{-2\cdot0}$. Using the values of R shown in Table 2, the variation of mobility with electric field strength has been calculated using STRATTON's theory, and the results have been compared with the experimental curves due to PRIOR[15]. In each case there is a similar marked disagreement between theoretical and experimental curves: the theoretical curve does not deviate sufficiently from Ohm's law at low fields and then saturates too much at high fields. Agreement can be obtained for each case by using values for R which are an order of magnitude smaller than those shown in Table 2. However, if this is done, it is impossible to obtain the powers required for the mobility temperature laws. Therefore, to obtain consistency between the available experimental data a new variable, such as the effective mass, must be introduced.

It has been shown[28] that the zero-field mobility of free carriers is inversely proportional

* In the notation of STRATTON R is given by:
$R = (\mu_{aA}/\mu_{0A})/\gamma_0 N_0(2+\gamma_0+0\cdot25\gamma_0^2)$

Table 2

Material	Experimental value of β(V^{-2} cm^2)	m^*/m_0	Optical-phonon temperature θ_0(7) (10)	Mobility–temperature power law	R	Theoretical value of β(V^{-2} cm^2)
n-type Ge	$(3\cdot5\pm1\cdot4)\times10^{-7}$	0·12	430°K	1·66	0·19	$1\cdot5\times10^{-7}$
p-type Ge	$(2\cdot3\pm1\cdot0)\times10^{-7}$	0·27	430°K	2·33	7·4	$3\cdot4\times10^{-8}$
n-type Si	$(5\cdot4\pm2\cdot6)\times10^{-8}$	0·27	680°K	2·5	2·0	$2\cdot0\times10^{-8}$
			430°K	2·43	$\to\infty$	$1\cdot5\times10^{-8}$
p-type Si	$(7\cdot9\pm5\cdot3)\times10^{-9}$	0·37	680°K	2·7	3·1	$2\cdot7\times10^{-9}$

to the carrier effective mass to the power 5/2. Thus, part of the large temperature dependence of mobility could be due to a small change in the effective mass with change in temperature. Many experiments[16,17–23] have been carried out on germanium and silicon which result in estimates of the effective masses of the carriers at temperatures above 4°K. While some of these experiments suggest that the effective masses remain constant, (within the limits of experimental error) up to room temperature, many others indicate that the shown that the mass of the hole remains constant between 4°K and 100°K and for this reason we have somewhat arbitrarily taken 100°K as our lowest limit of temperature and assumed in every case that the effective mass determined at 4°K also holds at 100°K.

Results are presented in Figs. 2 and 3 for germanium and silicon respectively. In each case the two limiting experimental values for β, have been taken, and by using STRATTON's theory a range of values for R and fractional mass increases

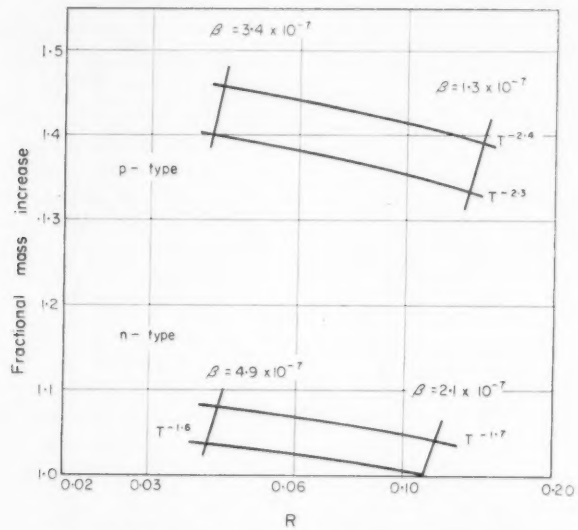

FIG. 2. Values of R and fractional mass increase between 100°K and 300°K which satisfy the experimental limits of β and mobility temperature laws for n- and p-type germanium.

effective masses increase, though there is disagreement about the precise magnitude of the increase. One of the most recent results for germanium is due to GIBSON *et al.*[9] which gives a possible increase of a few per cent in the effective mass of the electron and a definite increase of between 40 and 100 per cent in the effective mass of the hole. We have therefore postulated that the effective masses of all the carriers with which we are concerned increase, in the temperature range 100°K to 300°K, above the values shown in Table 2 which we assume to hold at 100°K. In the particular case of p-type germanium BAGGULEY *et al.*[27] have have been found which satisfy these values of β. It is now assumed that the change in zero-field mobility with temperature has two components, one due to change in effective mass, the second due to the effect of lattice scattering. Then one may calculate as before a range of values for R and for the fractional mass increase which satisfy the known experimental limits for the laws giving the variation of mobility with temperature. For p-type materials it is assumed that both light and heavy holes increase in mass by equal proportions. The four intersecting curves of Figs. 2 and 3 define the experimental limits of R and the fractional

mass increase in the range 100°K to 300°K. It should be noticed that the absolute value of effective mass appears only in the expression for β. Thus, if it is found that the values of effective mass quoted in Table 2 do not hold at 100°K, then the curves for β in Figs. 2 and 3 will need to be moved vertically by the appropriate factor, which as can be seen will not greatly affect the results obtained.

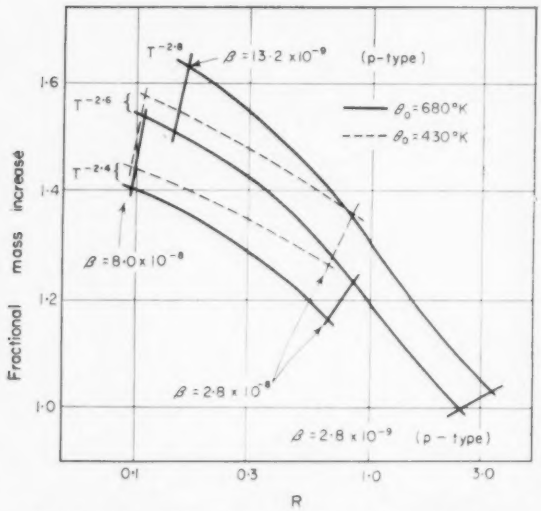

FIG. 3. Values of R and fractional mass increase between 100°K and 300°K which satisfy the experimental limits of β and mobility temperature laws for n- and p-type silicon. For n-type silicon the result is shown for two optical phonon temperatures, 430°K and 680°K.

Figure 2 shows that in the case of germanium where the possible errors in β are relatively small and the variation of mobility with temperature is well known, we deduce, for electrons, an increase in the effective mass of (4 ± 2) per cent in the range 100°K to 300°K, and for holes an increase in the effective mass of (40 ± 5) per cent in the temperature range 4–300°K, since for holes we also have the result of BAGGULEY *et al.*[27]; these results are in qualitative agreement with those of GIBSON *et al.*[9].

Figure 3 shows the results for silicon; for this material the errors in β are larger. For n-type silicon since there is some doubt about both the mobility variation and the value of the optical-phonon temperature, the results are plotted for $\theta_0 = 430$°K and $\theta_0 = 680$°K; the mobility law for p-type silicon has been taken as $(\mu_0)_{E=0} \propto T^{-2\cdot7-0\cdot1}$ in accord with experimental determinations.[12, 14, 24] With regard to the increase of effective mass for silicon we consider that the increase is (40 ± 20) per cent in the temperature range 100°K to 300°K for both electrons and holes. The lower possible value for the effective mass of holes has been disregarded because the value for R required is much too large to give an agreement between theoretical and experimental figures for the variation of mobility with electric field.

The variation of mobility with electric field has been calculated using STRATTON's theory with the following values of R: 0·06 and 0·1 for n- and p-type germanium, 0·2 and 0·5 for n- and p-type silicon. The effective masses used were as shown in Table 2 but increased by the percentages indicated above, though we were very conscious that the effective masses are likely to change at high electric field strengths. Agreement with the experimental curves[15] can be obtained in each case to within about 20 per cent except for n-type germanium. In this case, values of R between 0·04 and 0·06 will give agreement but theoretical and experimental curves begin to diverge at about 2kV cm^{-1} and, for the latter value of R, exceed a difference of 20 per cent at about 5kV cm^{-1}. The lower value, $R = 0{\cdot}04$, is in substantial agreement with GIBSON *et al.*[9].

4.2 *Interpretation of second order effects*

The second order effects, which we have detailed in Section 3, may arise in three ways:

(i) due to the assumption, made in the derivation[4] of β, that E is very small.
(ii) due to the inadequacy of the simple model used, e.g. overestimation of the degree of carrier–carrier scattering.
(iii) due to the variation of the quantity Π with carrier concentration or with the strength or orientation of the electric field in the crystal.

With regard to the first point, we have incorporated the next term in the series used by STRATTON to obtain β, and have obtained an equation of the form

$$\mu_0 = (\mu_0)_{E=0}(1-\beta_1 E^2+\beta_2 E^4) \qquad (12)$$

Vol. 1
1961

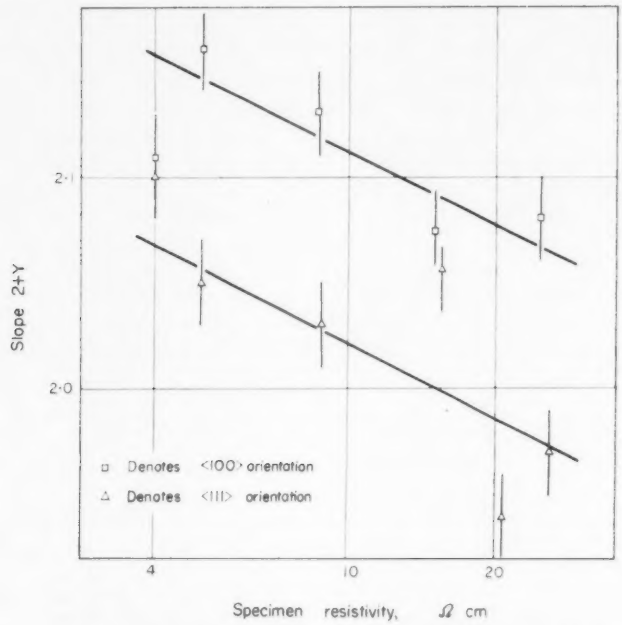

FIG. 4. The exponent, $2+y$, of the electric field observed from the absorption data for n-type germanium is plotted, for the two orientations of electric field, against specimen resistivity. The quantity y is a measure of the variation of β' with electric field.

in which both β_1 and β_2 are slowly varying functions of E. Calculations show that this correction predicts a variation which should be observed as a power law $E^{1\cdot97}$ in the range 100–400 V cm^{-1}. However the results presented in Fig. 4 show that the exponent of E may be as high as 2·16. If β is independent of electric field strength then this effective variation of β' with electric field could be explained by a decrease in Π as electric field strength increases. Unfortunately the experimental results[9] for Π are not sufficiently accurate in this low field region to determine if this is in fact happening.

Considering now orientation effects, SASAKI *et al.*[25] have demonstrated that in the presence of an electric field, the average energy of free carriers in different valleys will differ, and consequently the populations of the valleys will also differ. If the electric field is applied in the $\langle 100 \rangle$ direction in n-type germanium, the four valleys are symmetrical with respect to the field. Thus no change in population will occur and the value of β obtained should tend to that given by the simple model. When the field is applied in the $\langle 111 \rangle$ direction, however, a change in valley populations will occur and in such a direction as to give a lower average mobility; this will be observed as a high value of β. As shown in Fig. 1 for n-type germanium $\beta'_{111} > \beta'_{100}$. For silicon, the valleys lie along the $\langle 100 \rangle$ directions in the crystal and thus we would expect β_{100} to be greater than β_{111}; in fact we observe that $\beta'_{100} > \beta'_{111}$. From these two results for n-type material it seems likely that Π is not a rapidly varying function of orientation.

With regard to the results in Fig. 4, we can offer no positive reason why the power laws are so much greater than 2·0, or why they vary with resistivity, but we can explain the variation with orientation. We have considered the results for the $\langle 100 \rangle$ direction to be a standard, in which, as stated, all valleys will be at the same effective temperature.

One may easily interpret the results for the ⟨100⟩ direction, at a particular resistivity, as an experimental relationship between mobility and electron temperature. For the ⟨111⟩ direction of the electric field in germanium it is possible to estimate the number and temperature of the carriers in the different valleys, and the manner in which these quantities change with electric field strength, by use of the calculation by PAIGE[26]. If one now applies the experimental relationship between mobility and electron temperature obtained when the electric field is in the ⟨100⟩ direction, to the valleys which have different temperatures and populations when the electric field is in the ⟨111⟩ direction, a simple calculation gives the lower values of slope, $2+y$, that is observed.

The remarkable increase of β'_{100} with resistivity for *n*-type silicon (see Fig. 1) is presumably due to an electron–electron scattering mechanism and may be an indication that inter-valley scattering is more important than optical-phonon scattering in this material.

5. CONCLUSIONS

(1) Values of β' have been measured for *n*- and *p*-types germanium and silicon, and by using a measured quantity Π, values of β have been deduced from these values of β'.

(2) Good agreement between the optical-mode theory of STRATTON[4] and the three experimental results, namely, the deduced value of β, the variation of mobility with temperature, and the variation of mobility with electric field strength, can only be obtained by assuming an increase in the effective mass of the appropriate carrier between 100°K and 300°K for both germanium and silicon.

(3) The increases in effective masses are believed to be:

holes, germanium (40 ± 5) per cent between 4°K and 300°K.

electrons, germanium (4 ± 2) per cent between 100°K and 300°K.

electrons and holes, silicon (40 ± 20) per cent between 100°K and 300°K.

(4) Variations of β' with orientation have been observed in *n*-type materials which could be explained qualitatively by changes in valley populations.

(5) Variations of β' with electric field strength have been observed in *n*-type germanium which depend on orientation and resistivity of the specimens.

(6) Due to the necessary introduction of the quantity Π it has not been possible to make specific statements about β which was the original intention of the work. The evidence tends to show that β is a function of orientation and may be a function of electric field strength and carrier concentration.

Acknowledgements—I am indebted to my colleagues at R.R.E. for supplying the crystals used and also to Drs. A. F. GIBSON and E. G. S. PAIGE for much helpful advice and discussion on this work. The paper is published with the permission of the Controller, H.M. Stationery Office.

REFERENCES

1. SHOCKLEY W., *Bell Syst. Tech. J.* **30,** 990 (1951).
2. GUNN J. B., *Progress in Semiconductors* **2,** 216 (1957).
3. ARTHUR J. B., GIBSON A. F. and GRANVILLE J. W., *J. Electronics* **2,** 145 (1956).
4. STRATTON R., *J. Electronics and Control* **5,** 157 (1958).
5. YAMASHITA J., *Phys. Rev.* **111,** 1529 (1958).
6. CONWELL E., *J. Phys. Chem. Solids* **8,** 234 (1959).
7. BROCKHOUSE B. N. and IYANGER P. K., *Phys. Rev.* **111,** 747 (1958).
8. GUNN J. B., *Progress in Semiconductors* **2,** 230 (1957).
9. GIBSON A. F., GRANVILLE J. W. and PAIGE E. G. S., preceding paper.
10. BROCKHOUSE B. N., *Phys. Rev. Letters* **2,** 254 (1959).
11. HARRISON W. A., *Phys. Rev.* **104,** 5, 1281 (1956).
12. LUDWIG G. W. and WATTERS R. L., *Phys. Rev.* **101,** 1699 (1956).
13. LONG D. and MEYERS J., *Phys. Rev.* **115,** 5, 1107 (1959).
14. PUTLEY E. H. and MITCHELL W. H., *Proc. Phys. Soc. Lond.* **72,** 193 (1958).
15. PRIOR A. C., *J. Phys. Chem. Solids* **12,** 2 175 (1960).
16. BENEDICT T. R. and SHOCKLEY W., *Phys. Rev.* **89,** 1152 (1953).
17. GOLDEY J. M. and BROWN S. C., *Phys. Rev.* **98,** 1761 (1955).
18. MACFARLANE G. G., MCLEAN T. P., QUARRINGTON J. E. and ROBERTS V., *Phys. Rev.* **108,** 1377 (1957).
19. MACFARLANE G. G., MCLEAN T. P., QUARRINGTON J. E. and ROBERTS V., *Phys. Rev.* **111,** 1245 (1958).
20. BOYLE W. S., *J. Phys. Chem. Solids* **8,** 321 (1959).
21. GEIST D., *Naturwissenschaften* **45,** 33 (1958).
22. CARDONA M., Thesis. Tech. Report No. HP5, Harvard University (1959).

23. STUBB T., Thesis, State Institute for Tech. Research, Finland (1958).
24. LONG D., *Phys. Rev.* **107,** 672 (1957).
25. SASAKI W., SHIBUYA M., MIZUGUCHI K. and HATOZAMA G. N., *J. Phys. Chem. Solids* **8,** 250 (1959).
26. PAIGE E. G. S., *Proc. Phys. Soc. Lond.* **75,** 174 (1960).
27. BAGGULEY D. M. S., POWELL J. A. and TAYLOR D. J., *Proc. Phys. Soc. Lond.* **A70,** 759 (1957).
28. BLATT F. J., *Solid State Physics* Vol. IV, p. 334. Academic Press, New York (1957).

ol. 19
961

J. Phys. Chem. Solids Pergamon Press 1961. Vol. 19, Nos. 3/4, pp. 228–229. Printed in Great Britain.

THE ELECTRICAL RESISTIVITY OF $ZrZn_2$*

C. E. OLSEN

Los Alamos Scientific Laboratory of the University of California, Los Alamos, New Mexico

(*Received* 28 *October* 1960)

Abstract—Electrical resistivity measurements on the ferromagnetic intermetallic compound $ZrZn_2$ between 2·2°K and 295°K fail to show an anomaly at the ferromagnetic transition such as are observed in other ferromagnetic elements and compounds. A possible mechanism is considered for this behavior.

INTRODUCTION

FERROMAGNETISM in $ZrZn_2$ was first detected by MATTHIAS and BOZORTH[1]. Because of the unusual properties of the compound, neutron diffraction measurements were made by ABRAHAMS[2]. He did not detect any localized moments larger than 0·2 Bohr magnetons.

Therefore, it became of interest to compare the electrical behavior of $ZrZn_2$ to that of other ferromagnetic elements and compounds.[3]

EXPERIMENTAL PROCEDURE

The specimen used for the measurements was a single crystal in the form of a rough prism $5{\cdot}1 \times 3{\cdot}1 \times 2{\cdot}9$ mm. The direction of the resistivity measurement was parallel to one of the 110 axes. The resistance measurements were made potentiometrically using standard four terminal methods.

The current contacts were made by spring loaded hollow brass cylinders. The insulated spring loaded potential contacts pass through the center of these cylinders. An air core solenoid surrounded the specimen holder. The cryostat, electrical measuring circuit, and the techniques used are described in a previous report.[4]

EXPERIMENTAL RESULTS

The results of the measurements are shown in Fig. 1. The resistivities are uncorrected for thermal expansion. The specific resistivity at 295·6°K is calculated to be 535 microhm cm. The relative resistivity appears to be reliable to 0·3 per cent. The specific resistivity, because of irregular specimen shape appears to be reliable to 10 per cent.

The rapid fall in the resistivity below 6°K appears to come from tantalum inclusions in the sample arising from the bomb in which the specimen was prepared. At 3·96°K this was indicated by current dependent resistivities when the sample was subjected to magnetic fields less than 200 Oe.

Longitudinal magnetoresistivity measurements at 3·96 and 19·52°K with fields up to 1000 Oe (the highest obtainable in the apparatus) showed resistivity changes of 0·1 per cent or less. Application of magnetic fields in the neighborhood of the Curie point showed no greater resistivity changes.

The resistivity was measured through the Curie point six times. Within limits of experimental error, no evidence was found for a resistivity anomaly at the magnetic transition (35°K).

Comparison of the temperature–resistivity behavior and the high specific resistivity (535 microhm cm at 295·6°K, 55·2 microhm cm at 3·96°K) with that of USi_2 (2836 microhm cm at 298°K, 1219 microhm cm at 3·96°K) suggest that $ZrZn_2$ exhibits a spin disorder resistivity. Furthermore, the results show that this spin disorder resistivity does not disappear at the Curie point. In magnetic materials such as are cited in the references, large local moments exist. Alignment of these local moments are responsible for the removal of the spin disorder resistivity. Since no such local moments exist in $ZrZn_2$, one would not

* Work performed under the auspices of the Atomic Energy Commission.

Vol. 19
1961

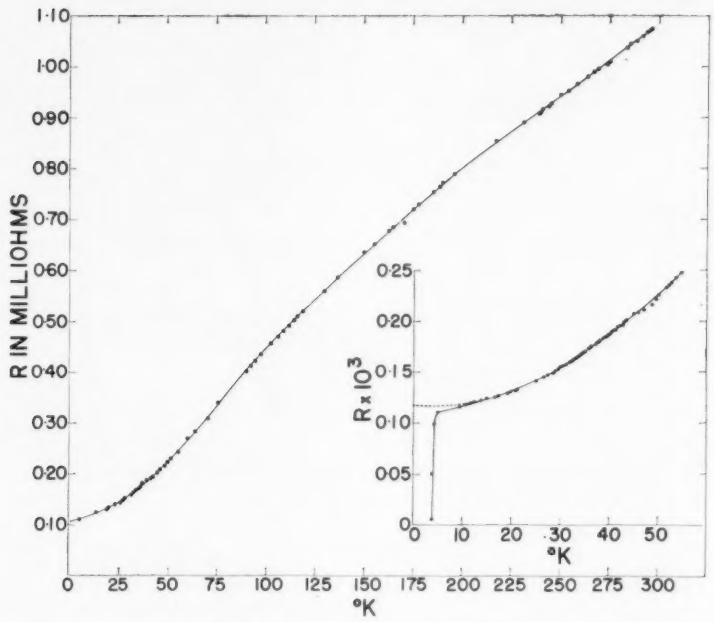

FIG. 1. The resistance of the $ZrZn_2$ crystal as a function of temperature.

anticipate any anomaly at the Curie point of the material.

Acknowledgements—The author would like to thank Bell Telephone Laboratories and Dr. J. W. NIELSEN and E. DEARBORN for the loan of the crystal; also the author would like to acknowledge the helpful discussions of Dr. B. T. MATTHIAS, consultant to this Laboratory.

REFERENCES

1. MATTHIAS B. T. and BOZORTH R. M., *Phys. Rev.* **109,** 604 (1958).
2. ABRAHAMS S. C., *Z. Kristallogr.* **112,** 427 (1959).
3. For reviews and references see: rare earth elements: SPEDDING F. H., LEGVOLD S. and JENNINGS L. D., *Progress in Low Temperature Physics* Vol. II, pp. 368–393. North Holland Publishing Co., Amsterdam (1957); for transition group elements: WEISS R. J. and MAROTTA A. S., *J. Phys. Chem. Solids* **9,** 302 (1959); compounds and elements: COLES B. R., *Advanc. Phys.* **7,** 40 (1958); europium: CURRY M. A., LEGVOLD S. and SPEDDING F. H., *Phys. Rev.* **117,** 953 (1960); dysprosium: HALL P. M., LEGVOLD S. and SPEDDING F. H., *Phys. Rev.* **117,** 971 (1960); samarium and europium: OLSEN C. E., U.S. Atomic Energy Commission LASL 240621 p. (1960); uranium digermanide: OLSEN C. E., *J. Appl. Phys.* **31,** 340S (1960).
4. OLSEN C. E., U.S. Atomic Energy Report LASL-2406 21 p. (1960).

J. Phys. Chem. Solids Pergamon Press 1961. Vol. 19, Nos. 3/4, pp. 230–234. Printed in Great Britain.

THE DIFFUSIVITY OF CARBON IN SILICON

R. C. NEWMAN and J. WAKEFIELD

Research Laboratory, Associated Electrical Industries, Aldermaston Court, Aldermaston, Berkshire

(*Received* 14 *November* 1960; *revised* 5 *December* 1960)

Abstract—Radioactive ^{14}C has been diffused into silicon at temperatures in the range 1070–1400°C. From the resulting distributions of activity, the diffusion coefficient is deduced to be:

$$D = 0{\cdot}33 \exp\left(\frac{-2{\cdot}92 \pm 0{\cdot}25 \text{ eV}}{kT}\right) \text{cm}^2/\text{sec}$$

The surface concentration increases with increasing temperature, the largest value being about 10^{18} atoms/cm^3 at the highest temperature employed of 1402°C.

1. INTRODUCTION

RECENT electron diffraction studies have shown that the lattice structure of at least part of the precipitated second phase found in silicon crystals after annealing at high temperatures[1,2] is consistent with that of silicon carbide. The kinetics of the precipitation process are governed by diffusion, and hence, it is necessary to know both the diffusivity and solubility of carbon in silicon.

Neither of these quantities has been determined directly before although the solid solubility at the melting point of silicon has been estimated by DASH[3,4] to be about 10^{18} atoms/cm^3 or less (he measured a carbon solubility of 3×10^{18} atoms/cm^3 in the melt and presented some evidence for segregation). This solubility is, however, about an order of magnitude smaller than the carbon content of some of our crystals inferred from the electron diffraction evidence,[2] our estimate being closer to the value of 10^{19} atoms/cm^3 given by PAPAZIAN and WOLSKY[5].

The main purpose of this paper is to describe the measurement of the diffusivity of carbon in silicon; in addition, some further information concerning the solubility is obtained from the measured surface concentrations. A radio-tracer technique with either barium carbonate or acetylene as a source of ^{14}C was used in these experiments.

2. EXPERIMENTAL TECHNIQUE

The silicon used in these experiments was cut from ingots pulled from a quartz crucible under high vacuum.[6] The resistivity was greater than 100 ohm cm and the dislocation density was about 10 lines/cm^2. The samples were in the form of discs about 1·5 cm in diameter and 1 mm in thickness; both (111) and (100) orientations were used. The faces were ground on a fine grade carborundum paper to produce plane parallel faces. The samples were then given a light etch in a mixture of 50 per cent hydrofluoric and 50 per cent nitric acids to remove surface damage.

In most experiments the sample, together with 5–10 mg of barium carbonate which had a specific activity of 23 mc/m mole, was sealed into an evacuated silica tube. At high temperatures barium carbonate decomposes and the $^{14}CO_2$ thus generated reacts with the silicon to form a relatively thin coating of $Si^{14}C$ which acts as a surface source of carbon. When acetylene was used, the sample was first placed in a silica tube which was evacuated to a pressure of about 10^{-4} mm Hg. Acetylene was then introduced to a pressure of about 1–5 mm Hg and the tube was sealed off. On heating, acetylene reacts with silicon and a surface coating of silicon carbide is again formed.

The use of acetylene had the advantage that

Vol. 1
1961

no other metallic impurity was present in the system. However, the maximum specific activity of acetylene which was readily available was only about 5 mc/m mole; it will become apparent later that this reduced activity compared with barium carbonate was a serious limitation, and the use of the latter source provided the simplest technique for obtaining the highest surface concentration of active carbon in the silicon.

After the heat treatment the layer of silicon carbide was removed by grinding, and the surface activity of the sample was determined directly with a thin end window Geiger counter. Further layers of silicon were then removed by grinding on carborundum paper and the activity was measured at each stage. The thickness of the layer removed was measured with a precision dial gauge to an accuracy of $\pm 2\,\mu$. With this technique it is necessary to know the absorption coefficient α of the β-particles in silicon (see Section 3). Some measurements were made with our experimental arrangement in which the β-particles were absorbed by various known thicknesses of aluminium foils. These measurements gave a value of α of 600 cm^{-1} in agreement with the value calculated from previous data.[7]

The efficiency of the counting system was determined using samples with a known quantity of active carbon atoms on their surfaces. For this purpose known weights of stearic acid with a given specific activity were dissolved in a given volume of benzene; a small quantity of solution was then dropped onto the surface of standard silicon slices and the benzene was allowed to evaporate. This technique produced fairly uniform coatings of stearic acid, the thickness of which was much less than 1 μ and hence all self-absorption corrections were negligible. The counting efficiency was thus found to be 6·4 ± 0·3 per cent. In the calibration experiments all the active carbon was on the silicon surface and the above efficiency is enhanced by the back-scattering[7] from the silicon by about 15 per cent. In the diffused samples the carbon was embedded in the silicon and β-particles originating from depths of more than 20 μ contributed to the measured counting rate (see Section 3). Under these conditions, a reduced backscattering factor should apply and the actual counting efficiency E was estimated to be about 5·8 per cent.

3. THEORY

It is assumed that the surface concentration of carbon rapidly attains its equilibrium value C_s which then remains constant. The total concentration (active plus non-active) of carbon in the silicon resulting from diffusion from the source is then given by:

$$C(x) = C_s \operatorname{erfc} \frac{x}{2\sqrt{(Dt)}} \qquad (1)$$

where D is the diffusion coefficient, t is the time of heating and x is the distance into the sample measured from the surface ($x = 0$).

We now consider the counting rate $R(x_0)$ (counts/min) to be expected after grinding away a thickness x_0 of the sample. The number of particles dN emitted per minute from a sheet of thickness dy at a depth y below the new surface is:

$$dN = \frac{3{\cdot}7 \times 10^{-12} ZA}{n} C(x_0+y)\, dy \qquad (2)$$

where Z is the specific activity of the source material in mc/m mole, n is the number of carbon atoms per molecule in this material and A is the surface area of the specimen (taken equal to the area of the mask immediately above the sample). The efficiency for detecting these particles will be reduced by the factor $\exp(-\alpha y)$ compared with that given in the previous section due to the self-absorption in the silicon; the contribution to the counting rate from this layer is thus:

$$dR = E \exp(-\alpha y)\, dN \qquad (3)$$

We substitute for $C(x_0+y)$ from equation (1), and integrate equation (3) and obtain:

$$R(x_0) = \frac{3{\cdot}7 \times 10^{-12} Z \,.\, A \,.\, E \,.\, C_s}{n\alpha} \times \left[\operatorname{erfc} \frac{x_0}{2\sqrt{(Dt)}} - \exp(\alpha^2 Dt + \alpha x_0) \times \operatorname{erfc}\left(\frac{x_0}{2\sqrt{(Dt)}} + \alpha\sqrt{(Dt)} \right) \right] \qquad (4)$$

4. RESULTS

The counting rate as a function of thickness removed from the surface of a typical specimen is shown in Fig. 1, where barium carbonate was used

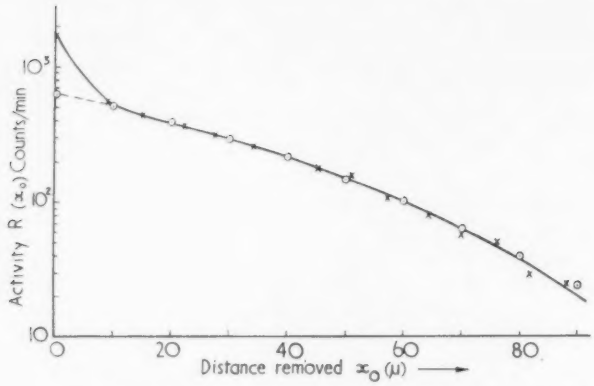

FIG. 1. Variation of counting rate with the thickness of material removed by grinding. Specimen heated at 1150°C for 168 hr; mask area 0·96 cm².

× Experimental points.

⊙ Theory with $R(0) = 630$ and $\sqrt{(Dt)} = 33\ \mu$

as the source. It is seen that there is a rapid drop in counting rate over the first 10–15 μ removed and then the rate of change is much reduced. The experimental points for x_0 greater than about 15 μ agree with the variation predicted by equation (4) with $\sqrt{(Dt)} = 33\ \mu$ and $R(0) = 630$ counts/min. The enhanced counting rate close to the surface was found to be due to small quantities of silicon carbide which had not been removed by the initial grinding. Autoradiographs showed that this silicon carbide was often embedded in grooves running along $\langle 0\bar{1}1 \rangle$ directions.[8] It is thus clear that the experimentally observed value of the counting rate at $x_0 = 0$ is artificially high and the true value of $R(0)$ can only be ascertained by a curve fitting procedure. The value of C_s may be determined with the aid of equation (4), once the values of D and $R(0)$ have been found. The disadvantage of using low-activity acetylene is that the counting rate rapidly drops below the background rate (20 counts/min) as layers are ground from the surface, and the observations over the first 15 μ cannot be utilized because of the surface erosion. Determinations of the diffusion coefficient from experiments using acetylene were thus liable to considerable error; values obtained were, however, in reasonably good agreement with those obtained when barium carbonate was used as the source.

Experiments were carried out at various temperatures in the range 1070°C to 1400°C and the

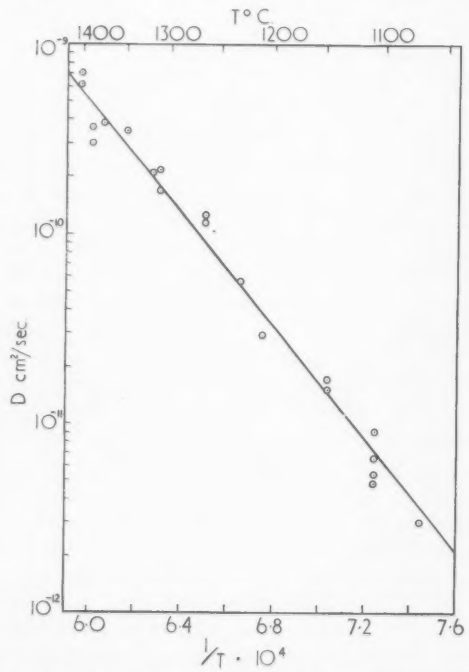

FIG. 2. Variation of the diffusion coefficient with reciprocal temperature.

Table 1. *Experimental values of diffusion coefficient and surface concentration*

Temp, °C	Time, hr	D, cm²/sec	$R(0)$*, min^{-1}	C_s, cm^{-3}
1402	1·0	$6{\cdot}3\times10^{-10}$	4000	$1{\cdot}5\times10^{18}$
1402	1·0	$7{\cdot}1\times10^{-10}$	3300	$1{\cdot}1\times10^{18}$
1390	3·0	$3{\cdot}7\times10^{-10}$	1800	$4{\cdot}8\times10^{17}$
1390	3·0	$3{\cdot}0\times10^{-10}$	1750	$4{\cdot}9\times10^{17}$
1375	2·0	$3{\cdot}9\times10^{-10}$	1000	$2{\cdot}9\times10^{17}$
1375	2·0	$3{\cdot}9\times10^{-10}$	1000	$2{\cdot}9\times10^{17}$
1350	3·9	$3{\cdot}5\times10^{-10}$	1170	$3{\cdot}0\times10^{17}$
1320	7·0	$2{\cdot}1\times10^{-10}$	950	$2{\cdot}4\times10^{17}$
†1314	10·2	$2{\cdot}2\times10^{-10}$	900	$2{\cdot}1\times10^{17}$
1314	15·8	$1{\cdot}7\times10^{-10}$	1300	$3{\cdot}0\times10^{17}$
1264	25·0	$1{\cdot}2\times10^{-10}$	400	$8{\cdot}9\times10^{16}$
1264	24·0	$1{\cdot}3\times10^{-10}$	450	$1{\cdot}0\times10^{17}$
1231	26·0	$5{\cdot}6\times10^{-11}$	400	$1{\cdot}0\times10^{17}$
1231	26·0	$5{\cdot}6\times10^{-11}$	615	$1{\cdot}6\times10^{17}$
1210	64·0	$3{\cdot}0\times10^{-11}$	360	$8{\cdot}6\times10^{16}$
1210	64·0	$2{\cdot}4\times10^{-11}$	720	$1{\cdot}8\times10^{17}$
1150	168·0	$1{\cdot}5\times10^{-11}$	625	$1{\cdot}4\times10^{17}$
1150	168·0	$1{\cdot}7\times10^{-11}$	530	$1{\cdot}5\times10^{17}$
†1109	309·0	$6{\cdot}6\times10^{-12}$	305	$7{\cdot}3\times10^{16}$
†1109	309·0	$5{\cdot}2\times10^{-12}$	320	$7{\cdot}9\times10^{16}$
1109	309·0	$4{\cdot}8\times10^{-12}$	270	$6{\cdot}7\times10^{16}$
1109	309·0	$9{\cdot}1\times10^{-12}$	235	$5{\cdot}3\times10^{16}$
1070	403·0	$3{\cdot}0\times10^{-12}$	600	$1{\cdot}6\times10^{17}$
‡1200	112·0	$2{\cdot}6\times10^{-11}$	100	$1{\cdot}9\times10^{17}$
‡1200	112·0	$2{\cdot}2\times10^{-11}$	86	$1{\cdot}7\times10^{17}$
‡1250	43·0	$5{\cdot}0\times10^{-11}$	—	—

* Standardized to mask area A of 0·74 cm².

† Plastically deformed prior to heating.

‡ Acetylene as source of ^{14}C.

time of heating was arranged to give measureable counting rates at depths of about 60 μ or greater. The results are shown in detail in Table 1. During the heating, particularly at the highest temperatures, a few samples were slightly deformed; this is not thought to alter the diffusion rates, since no detectable change was observed between dislocation-free samples and others which were heavily plastically deformed prior to the diffusion.

Figure 2 shows the variation of D with temperature from which we obtain:

$$D = 0{\cdot}33 \exp\left(-\frac{2{\cdot}92\text{ eV}}{kT}\right) \text{cm}^2/\text{sec} \quad (5)$$

We consider the error on the activation energy to be $\pm$ 0·25 eV.

5. DISCUSSION

There are possible objections to the use of equation (1), since the silicon samples used in the experiments contained some non-active ^{12}C. Out-diffusion of this carbon would lead to a surface concentration which would decrease with time. Moreover, if its concentration was above the solubility limit at the temperature of the experiment, precipitation would occur and some active carbon would be incorporated into the precipitate particles. However, since the observed distribution could be fitted to equation (4) extremely well, it is concluded that the above effects are relatively unimportant.

The measured values of the diffusion coefficient and the activation energy for diffusion are similar to those found for impurities which are known to

diffuse substitutionally[9]; D is, however, several orders of magnitude smaller than the values found for impurities which diffuse interstitially. It is therefore concluded that carbon occupies substitutional sites in silicon. This would be in accord with the fact that up to the present no characteristic absorption band in the infra-red has been attributed to carbon in single crystals of silicon.*

In general the measured values of the surface concentrations, given in Table 1, increase with increasing temperature up to 1402°C where a value of $1{\cdot}5 \times 10^{18}$ atoms/cm^3 is found. The actual solubilities will be somewhat greater than these values due to the presence of spurious non-active carbon. If DASH's value for the solubility in the melt is taken as 3×10^{18} atoms/cm^3 then the value of the segregation coefficient of carbon between liquid and solid silicon is close to unity. A true solubility in the solid less than this last figure would indicate a eutectic alloy system (with $k < 1$), but a higher figure between 3×10^{18} and 10^{19} indicated by electron diffraction observations would suggest a peritectic system ($k > 1$). Further work is now in progress in an attempt to resolve this problem.

* We have found an absorption peak at 12·2 μ in polycrystalline silicon which can be interpreted as due to β-silicon carbide which is thought to lie in the grain boundaries.[10] This is a possible explanation of a similar absorption band found recently by BALKANSKI *et al.*[11].

Acknowledgements—Thanks are due to D. J. MAULE and J. H. NEAVE for experimental assistance and to R. L. ROUSE for his encouragement. Thanks are also due to Dr. T. E. ALLIBONE, C.B.E., F.R.S., Director of the Laboratory, and to the Admiralty for permission to publish this paper.

REFERENCES

1. BULLOUGH R., NEWMAN R. C., WAKEFIELD J. and WILLIS J. B., *J. Appl. Phys.* **31,** 707 (1960).
2. NEWMAN R. C., *Proc. Phys. Soc. Lond.* **76,** 993 (1960).
3. DASH W. C., *J. Appl. Phys.* **30,** 459 (1959).
4. SCACE R. I. and SLACK G. A., *J. Chem. Phys.* **30,** 1551 (1959).
5. PAPAZIAN H. A. and WOLSKY S. P., *J. Appl. Phys.* **27,** 1561 (1956).
6. BILLIG E. and GASSON D. B., *J. Sci. Instrum.* **35,** 360 (1958).
7. CALVIN M., HEIDELBERGER C., REID J. C., TOLBER B. M. and YANKWICH P. F., *Isotopic Carbon.* John Wiley, New York (1949).
8. NEWMAN R. C. and WAKEFIELD J., *Proceedings of the International Conference on Solid-State Physics in Electronics and Telecommunications, Brussels,* p. 318 (edited by DESIRANT M. and MICHIELS J. L.). Academic Press, New York (1958).
9. REISS H. and FULLER C. S., *Semiconductors* (edited by HANNAY N. B.) p. 244. Reinhold, New York (1959).
10. WILLIS J. B., unpublished work.
11. BALKANSKI M., NAZAREWICZ W. and SILVA E., *C.R. Acad. Sci., Paris* **251,** 1277 (1960).

Vol. 1
1961

J. Phys. Chem. Solids Pergamon Press 1961. Vol. 19, Nos. 3/4, pp. 235–250. Printed in Great Britain.

MESSUNGEN DER ELEKTRISCHEN LEITFÄHIGKEIT UND DES HALLEFFEKTS AN ZnO-KRISTALLEN UND IHRE DEUTUNG DURCH STÖRBÄNDER

G. BOGNER

Institut für Angewandte Physik der Universität Erlangen, Erlangen, Deutschland

(*Received* 26 *September* 1960)

Zusammenfassung—Um den Einfluss definierter Zusätze auf die in unbehandelten ZnO-Kristallen vorliegende *n*-Leitung zu prüfen, wurden Hallspannung und elektrische Leitfähigkeit im Temperaturbereich von 63 bis 700°K gemessen. Als Versuchsmaterial dienten undotierte, nachträglich mit Sauerstoff behandelte Kristalle und solche mit Zusätzen von Indium und Kupfer. Die Wirkung der Zusätze konnte durch geeignete Modellvorstellungen über deren Einbau ins ZnO erklärt werden. Das Temperaturverhalten der gemessenen Grössen wurde unter der Annahme von Donatorenbändern und makroskopischen Inhomogenitäten gedeutet. Aus den an nachträglich mit Sauerstoff behandelten und Kupfer dotierten Kristallen gewonnenen Ergebnissen, lässt sich die Aktivierungsenergie des diskreten Donatorenniveaus abschätzen, das im Grenzfall der kleinsten gemessenen Leitfähigkeiten für die *n*-Leitung in diesen Kristallen verantwortlich ist.

Abstract—Investigating the influence of defined foreign additions on *n*-conduction of untreated ZnO-crystals, Hall voltage and electrical conductivity have been measured from 63–700°K. Crystals were used as grown or after heating in an O_2-atmosphere or with indium and copper additions. The effect of impurities could be explained by a suitable model of their incorporation in ZnO. The temperature dependence of the measured quantities was discussed in terms of impurity band conduction and macroscopic inhomogeneities. From the results of oxygen treated and copper doped crystals the activation energy of the discrete donor level can be estimated, which defines the temperature dependence of the conductivity in crystals with a low donor concentration.

EINLEITUNG

FRÜHERE Messungen der elektrischen Leitfähigkeit und des Hallkoeffizienten an ZnO-Kristallen ohne absichtlichen Zusatz[1] haben ergeben, dass das Temperaturverhalten der gemessenen Grössen (Meyersche Regel) nicht erklärt werden kann bei Annahme eines einfachen Halbleitermodells, das nur ein Donatorenniveau enthält. Es wurde deshalb angenommen, dass das Temperaturverhalten durch eine Reihe unbekannter Donatoren-Zustände verursacht wird, und es war nicht möglich, Aussagen über die Donatorenkonzentrationen, die Donatoren-Ionisierungsenergien und die effektiven Elektronenmassen in solchen Kristallen zu gewinnen.

HUTSON[2] und RUPPRECHT[3] umgingen diese Schwierigkeit dadurch, dass sie die Halleffektsmessungen an Kristallproben mit Zusätzen definierter Donatoren (H_2, Zn, in gewissen Grenzen auch Indium) ausführten. Es wurden dabei Kristalle mit niedriger Ausgangsleitfähigkeit verwendet und die Donatorenkonzentration so hoch gewählt, dass die durch sie erzeugten Ladungsträgerkonzentrationen bei Zimmertemperatur mindestens um eine Grössenordnung höher als die des Grundmaterials waren. Das Temperaturverhalten der gemessenen Grössen konnte damit einem bekannten Donator zugeschrieben werden und wurde mit Hilfe des einfachen Halbleitermodells analysiert.

In der vorliegenden Arbeit wird über Messungen der Hallspannung und der elektrischen Leitfähigkeit berichtet, die an undotierten, nachträglich mit Sauerstoff behandelten und an Kristallen mit Zusätzen von In und Cu ausgeführt wurden, sowie über die aus Leitfähigkeit σ und

Hallkoeffizient R_H berechnete Hallbeweglichkeit. Für die Analyse des Temperaturverhaltens der gemessenen Grössen wurden kompliziertere Halbleitermodelle verwendet: Annahme von Donatorenbändern und Berücksichtigung makroskopischer Inhomogenitäten.

HERSTELLUNG DER KRISTALLE UND IHRE KONTAKTIERUNG

Die Einkristalle wurden hergestellt durch eine Dampfphasenreaktion zwischen Zink und Sauerstoff bei 1350°C, wie sie bei SCHAROWSKY[4] zum ersten Mal beschrieben wurde. Der Einbau von Indium und Kupfer erfolgte während des Kristallwachstums nach einem bei BOGNER und MOLLWO[5] beschriebenen Verfahren. Die nachträgliche Sauerstoffbehandlung undotierter Kristalle wurde in einem Quarzrohr bei 20 atm. O_2-Druck und Temperaturen von 850 und 1050°C durchgeführt. Die Behandlungszeit war dabei jeweils mindestens doppelt so gross, wie die mit Hilfe der von v. BERNUTH[6] gemessenen O_2-Diffusionskonstanten berechnete Sättigungszeit.

Die bei den Messungen verwendeten Kristalle hatten die Form hexagonaler Prismen. Ihre Länge betrug 5–10 mm, ihr Durchmesser 0,2–0,7 mm. Die spezifische elektrische Leitfähigkeit undotierter Kristalle bei Zimmertemperatur betrug 5×10^{-2}–7 $ohm^{-1}\,cm^{-1}$. Nach Sauerstoffbehandlung wurde eine Leitfähigkeit von 8×10^{-3}–5×10^{-2} $ohm^{-1}\,cm^{-1}$ festgestellt. Die in dieser Arbeit vermessenen Kristalle mit In-Zusatz hatten Leitfähigkeiten bei 20°C zwischen 10 und 60 $ohm^{-1}\,cm^{-1}$, während sie bei Cu-dotierten Kristallen je nach Zusatz zwischen 10^{-3} und 10^{-1} $ohm^{-1}\,cm^{-1}$ variierten.

Da bei Kristallen mit kleinen Leitfähigkeiten mit Kontaktschwierigkeiten zu rechnen war, die sich besonders bei tiefen Temperaturen bemerkbar machen, wurden die Kristalle für die Messungen der elektrischen Leitfähigkeit und der Hallspannung mit 2 Stromzuführungselektroden an den Enden und 4 rechteckigen, auf 2 gegenüberliegenden Kristallseiten paarweise angeordneten, im Vakuum aufgedampften Leitfähigkeits- bzw. Hallelektroden aus Gold versehen (Abb. 1). Um sperrfreie Kontakte zu erhalten, wurden vor dem Aufdampfen der Au-Elektroden, die Kristalloberflächen im Vakuum kurze Zeit atomarem Wasserstoff ausgesetzt. Atomarer Wasserstoff erzeugt Anreicherungsrandschichten auf ZnO, die im Vakuum längere Zeit erhalten bleiben[7]. Die Sperrfreiheit der Au-Elektroden wurde durch Verifizierung des Ohmschen Gesetzes bei verschiedenen Temperaturen nachgewiesen.

APPARATIVER AUFBAU

Die Apparatur bestand im wesentlichen aus einem selbstgebauten Elektromagneten und einem zylindrischen Vakuumgefäss aus Messing.

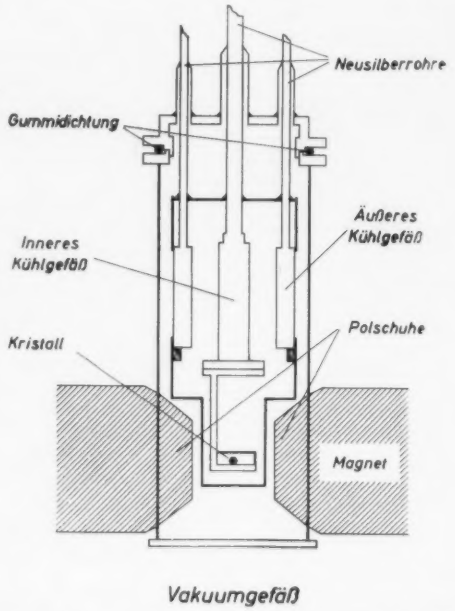

ABB. 2. Vakuumgefäss mit Tieftemperatur-Messeinsatz.

Der Magnet war so konstruiert, dass er das Vakuumgefäss von aussen umschloss. Die Polschuhe wurden im Inneren des Gefässes fortgeführt (Abb. 2). Sie waren nicht fest mit dem Vakuumgefäss verbunden, sondern auswechselbar. Breite des Luftspaltes und Polschuhflächen konnten also verändert werden. Im vorliegenden Fall betrug die Luftspaltbreite 35 mm und die Polschuhfläche 5×5 cm^2. In diesem Raum wurde eine Kraftflussdichte von 8200 G erreicht.

In das Vakuumgefäss konnten je nach Wahl des Temperaturbereiches (oberhalb oder unterhalb Zimmertemperatur) zwei verschiedene Messeinsätze eingebracht werden (Abb. 2). Die

Vol. 19
1961

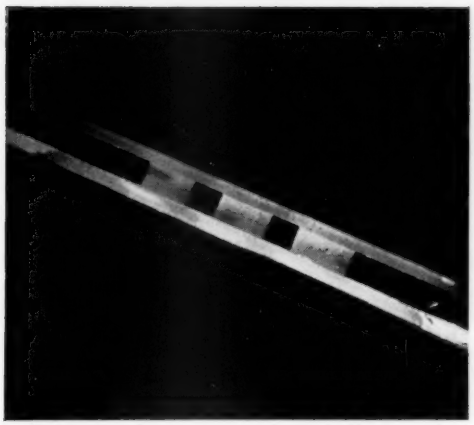

ABB. 1. ZnO-Kristall mit Stromzuführungs- und Hall-elektroden aus Gold. (Vergrösserung 16 fach).

[*facing p.* 236

BLANK
PAGE

Vol.
196

Messeinsätze unterschieden sich in ihrem Aufbau wenig voneinander. Sie bestanden aus einer Deckplatte, die das Vakuumgefäss verschloss, und an der mittels Neusilberrohren zwei konzentrische Kupferbehälter befestigt waren. An den inneren Behälter war die Grundplatte mit der Kristallhalterung montiert. Beim Tieftemperatureinsatz konnten durch Einfüllen bestimmter Mengen flüssiger Luft in das Innengefäss beliebige Temperaturen zwischen 300 und 90°K eingestellt werden. Durch Abpumpen der flüssigen Luft wurden Temperaturen bis zu 63°K erreicht. Beim Hochtemperatureinsatz enthielt das Innengefäss eine Heizung, die es ohne weiteres ermöglichte, Temperaturen von 700°K zu erreichen. Das Aussengefäss, das je nach Temperaturbereich mit flüssiger Luft oder Wasser beschickt wurde, diente zur Wärmeabschirmung.

Die Kristallhalterung erfolgte in beiden Fällen auf die gleiche Art (Abb. 3). Durch diese Elektrodenanordnung wurde ein Brechen der Kristalle praktisch ausgeschlossen. Die 6 Elektroden wurden an den Stellen mit dem Kristall in Berührung gebracht, wo sich die aufgedampften Au-Elektroden befanden. Um für Tieftemperatur-Messungen gute Kontakte zu erhalten, wurden über letztere noch kleine Kondensatoren (0,01 μF : 440 V) entladen. Die Temperatur der Kristalle wurde mit Hilfe eines Manganin–Konstantan-Thermopaares, das an einer Stromzuführungselektrode befestigt war, gemessen.

MESSANORDNUNG UND MESSTECHNIK

Das Vakuum betrug bei Hochtemperaturmessungen etwa 10^{-6} Torr, bei Tieftemperaturmessungen bis zu 10^{-7} Torr. Um störende Oberflächeneffekte auszuschliessen, wurden die Kristalle vor jeder Messreihe abgeätzt und im Vakuum mindestens 1 Stunde auf Temperaturen bis zu 400°C gehalten.

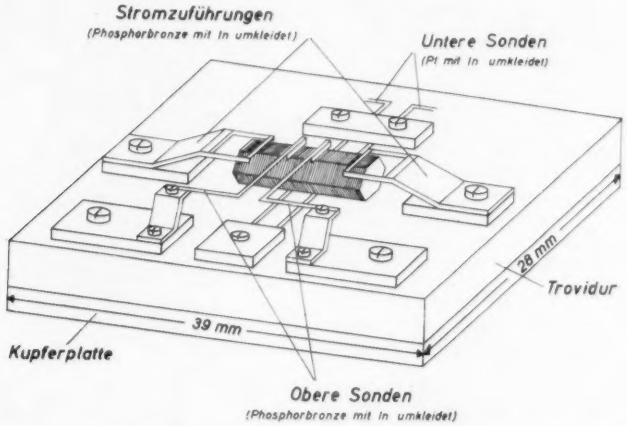

ABB. 3. Kristallhalterung bei Tieftemperatur-Messeinsatz. (Der Kristall ist stark vergrössert gezeichnet). Beim Hochtemperatureinsatz waren die Halterungen für die 6 Elektroden, durch eine dünne Glimmerfolie isoliert, direkt auf die Cu-Grundplatte aufgeschraubt. Obere Hallsonden und Stromzuführungsbügel bestanden dabei aus Wo-Draht, der mit Pt-Kontakten versehen war. Die unteren Hallsonden bestanden aus Pt-Drähten.

Die Messung der elektrischen Leitfähigkeit wurde in jedem Fall mit Hilfe von 2 Strom- und 4 Spannungselektroden (Sonden) durchgeführt. Dabei war je ein Paar von Spannungssonden auf 2 gegenüberliegenden Kristallseiten im Abstand von etwa 0,5 mm angebracht. Die Sondenspannungen wurden mit einem Elektrometerverstärker (Schwingkondensator) der Fa. Frieseke u. Höpfner gemessen. Zur Berechnung der Leitfähigkeit wurde das arithmetische Mittel der beiden Sondenspannungen verwendet.

Die Hallspannung wurde über den 2 etwa

0,5 mm voneinander entfernten Hallstrecken gewonnen. Kleine Hallspannungen (10^{-3} bis 10^{-5} V) wurden in Belastung der Hallstrecke mit einen Galvanometer-Kreis gemessen. Hallspannungen $> 10^{-3}$ V wurden mit dem Elektrometerverstärker gemessen. Um störende Temperatureffekte auszuschliessen, wurde die Hallspannung in jedem Fall für beide Richtungen des Magnetfeldes gemessen. Ferner wurde bei sämtlichen Leitfähigkeits- und Hallspannungsmessungen die Stromrichtung kommutiert. Die Stromstärken durch die Kristalle waren im verwendeten Temperaturbereich stets so bemessen, dass eine Erwärmung der Kristalle durch Joulsche Wärme ausgeschlossen war.

Für die Hallspannung von Proben mit Sechseck-Querschnitt gilt[3]:

$$U_H = \frac{2}{3} \times R_H \frac{J \times B}{a}$$

R_H = Hallkonstante, J = Stromstärke, B = magn. Kraftflussdichte, a = Länge einer Sechseckseite.

Mit Hilfe dieser Formel wurde aus den gemessenen Hallspannungen die Hallkonstante berechnet. Da die gemessene Hallspannung wesentlich vom Verhältnis Sondenbreite/Kristalldurchmesser abhängt und die aufgedampften Au-Elektroden eine Breite von 0,2–0,3 mm aufwiesen, mussten die Hallspannungen mit Korrekturfaktoren versehen werden, die der Arbeit von RUPPRECHT[3] entnommen wurden. Aus den korrigierten Spannungswerten wurde dann R_H bestimmt.

Für die Hallbeweglichkeit gilt : $\mu_H = R_H \times \sigma$.

Für die Berechnung von μ_H wurden die arithmetischen Mittel der an 2 gegenüberliegenden Seiten gemessenen Leitfähigkeiten und der an beiden Hallstrecken bestimmten Hallkonstanten verwendet. Das war bei der Längsinhomogenität, die manche Kristalle zeigten, unerlässlich.

MESSERGEBNISSE

(a) *Kristalle mit Indium-Zusatz*

Die reziproke Hallkonstante zeigt eine relativ geringe Temperaturabhängigkeit, die bei grösseren Donatorendichten überhaupt verschwindet (Abb. 4). Sie durchläuft bei Kristallen mit kleinem Donatorengehalt nach anfänglichem Abfall bei höheren Temperaturen ein Minimum, um nach tieferen Temperaturen hin wieder langsam anzusteigen. Für Kristall d wird die reziproke Hallkonstante bei tiefen Temperaturen wieder konstant. Das Minimum wird umso tiefer und seine Lage immer mehr nach tiefen Temperaturen hin verschoben, je kleiner die Donatorenkonzentration ist.

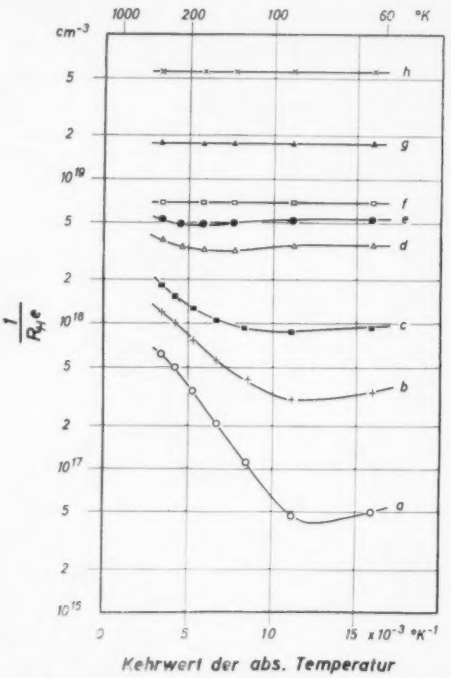

ABB. 4. Reziproke Hallkonstante In-dotierter Kristalle als Funktion der abs. Temperatur.

Die In-Konzentration der Kristalle variiert zwischen 9×10^{17} In-Atome/cm³ (Kristall a) und $5{,}5 \times 10^{19}$ In-Atome/cm³ (Kristall h). Grösste Aktivierungsenergie E_D = 0,044 eV (Kristall a). (Die Kristalle f, g und h wurden von RUPPRECHT[3] vermessen).

Die elektrische Leitfähigkeit wird bei kleinen Donatorenkonzentrationen mit abnehmender Temperatur kleiner und nähert sich bei tiefen Temperaturen einem konstanten Wert (Abb. 5). Die Temperaturabhängigkeit wird umso geringer, je grösser die Donatorenkonzentration ist und wird Null, wenn $N_D > 2 \times 10^{19}$ In-Atome/cm³ ist.

Die Hallbeweglichkeit bei Zimmertemperatur

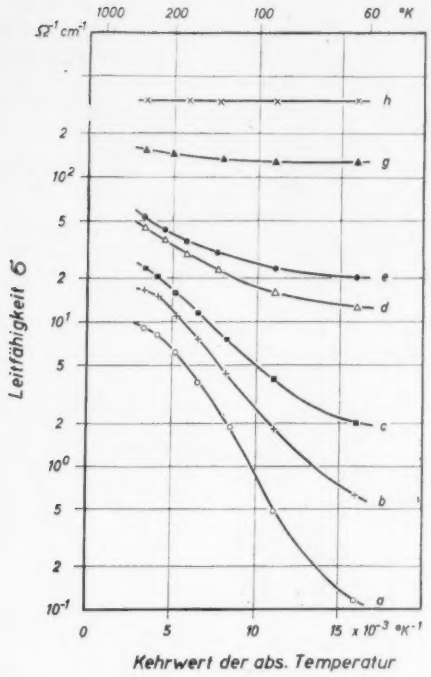

ABB. 5. Elektrische Leitfähigkeit In-dotierter Kristalle als Funktion der abs. Temperatur.

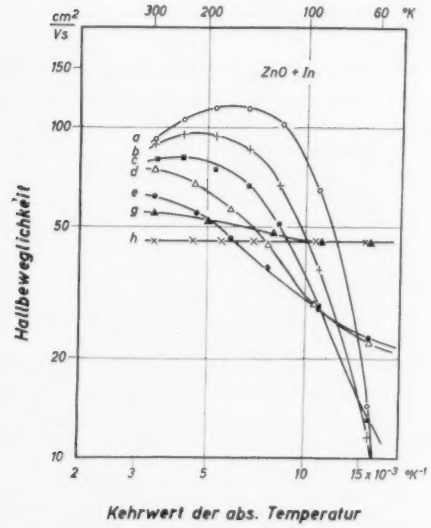

ABB. 6. Hallbeweglichkeit der in Abb. 4 und 5 gemessenen In-dotierten Kristalle als Funktion der abs. Temperatur.

nimmt mit steigender Donatorenkonzentration ab (Abb. 6). Für Indiumkonzentrationen $> 4\times10^{19}$ cm^{-3} wird sie unabhängig von der Donatorendichte etwa 45 cm^2/Vs. (Letzteres geht aus Messungen von Kristallproben mit entsprechend hohen In-Konzentrationen hervor, von denen einfachheitshalber nur die Ergebnisse der Probe h in den Abbildungen 5–7 dargestellt sind). Die Beweglichkeitskurven der schwächer dotierten Kristalle zeigen bei tiefen Temperaturen einen steilen Abfall, der etwa

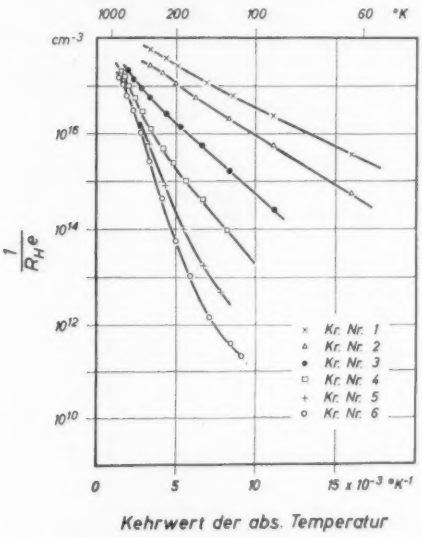

ABB. 7. Reziproke Hallkonstante undotierter Kristalle als Funktion der abs. Temperatur.

proportional $T^{+3,5}$ ist. Mit zunehmender Donatorenkonzentration sinkt die Temperaturabhängigkeit von μ_H und wird bei den höchsten Donatorenkonzentrationen ($> 4\times10^{19}$ cm^{-3}) Null. Die Hallbeweglichkeit von Kristallen mit mittlerer In-Konzentration strebt bei den zur Verfügung stehenden tiefen Temperaturen ebenfalls einem konstanten Wert zu. Ein äusserst bemerkenswerter Befund ist die Tatsache, dass sich die Hallbeweglichkeitskurven bei tiefen Temperaturen überschneiden. Die Hallbeweglichkeiten von Kristallproben mit hohem Störstellengehalt sind also bei tiefen Temperaturen höher, als die Beweglichkeiten von Kristallen mit kleinerem Störstellengehalt. Dieser experimentelle Befund steht

offensichtlich im Widerspruch zu früheren theoretischen Vorhersagen.[8,9]

(b) *Kristalle ohne Zusatz und mit nachträglicher Sauerstoffbehandlung.*

In Abb. 7 ist die reziproke Hallkonstante gegen den Kehrwert der absoluten Temperatur für eine Reihe von undotierten und unbehandelten Kristallen aufgetragen. Die Ladungsträgerkonzentration bei Zimmertemperatur und der Temperaturkoeffizient der $1/R_He$-Kurven variieren in einem

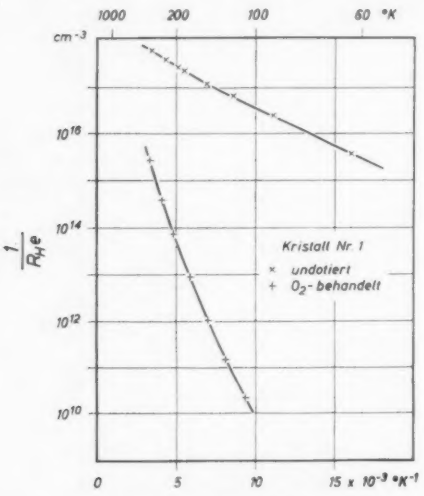

ABB. 8. Reziproke Hallkonstante vor und nach Sauerstoffbehandlung als Funktion der abs. Temperatur. Obere Kurve : Kristall undotiert.
Abtrennarbeit $E_D = 0{,}06$ eV
Untere Kurve : Kristall nach 360 h bei 850°C und 20 atm. Sauerstoff.
Abtrennarbeit $E_D = 0{,}39$ eV
Die Abtrennarbeit wurde für die untere Kurve aus dem Hochtemperaturteil derselben gewonnen.

grossen Bereich. Der Temperaturkoeffizient der reziproken Hallkonstanten ist umso kleiner, je grösser die Ladungsträgerkonzentration der betreffenden Probe ist.* Die Ladungsträgerkonzentration bei Zimmertemperatur liegt für die verschiedenen Kristalle zwischen 2×10^{15} und 6×10^{17} Elektronen/cm³.

* Dieser Zusammenhang wird in der Literatur häufig qualitativ als Meyersche Regel bezeichnet.

Durch eine hinreichend lange Sauerstoffbehandlung bei Temperaturen von 850°C und 1050°C und Sauerstoffdrucken > Partialdruck der Luft, wird die Elektronenkonzentration der Kristalle bei Zimmertemperatur stark, u.U. um 1–2 Grössenordnungen herabgesetzt, der Temperaturkoeffizient von $1/R_He$ wird ebenfalls stark vergrössert (Abb. 8,9). Die relative Herabsetzung der Elektronenkonzentration bei $T = 300$°K und die relative Vergrösserung des Temperaturkoeffizienten von $1/R_He$ werden umso

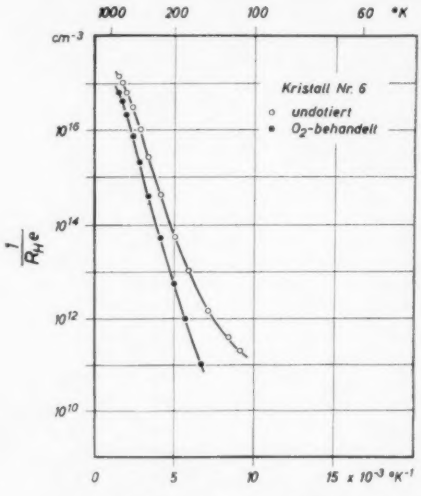

ABB. 9. Reziproke Hallkonstante vor und nach O_2-Behandlung. Kristall Nr. 6 war 450 h bei 850°C und 20 atm. Sauerstoff behandelt worden ; undotiert : $E_D = 0{,}39$ eV: O_2-behandelt : $E_D = 0{,}46$ eV.

geringer, je kleiner die Ausgangselektronenkonzentration bei $T = 300$°K der betreffenden Kristalle ist. Dabei zeigen Kristalle mit kleiner Ausgangsleitfähigkeit unter denselben Bedingungen eine tiefere Elektronenkonzentration und einen grösseren Temperaturkoeffizienten als solche mit höherer Ausgangsleitfähigkeit. Die untere Grenze der bei mit Sauerstoff behandelten Kristallen gemessenen Elektronenkonzentrationen bei Zimmertemperatur liegt bei einigen 10^{14} Elektronen/cm³, die obere Grenze der gemessenen Abtrennarbeiten bei 0,47 eV. Aus den Kurven kann man weiter entnehmen, dass die reziproke Hallkonstante besonders bei tiefer leitenden

Vol. 1
1961

Kristallen einen temperaturabhängigen Temperaturkoeffizienten aufweist, derart, dass bei tiefen Temperaturen der Temperaturkoeffizient abnimmt.

Da sich der Temperaturverlauf der elektrischen Leitfähigkeit praktisch nicht von dem der reziproken Hallkonstante unterscheidet, wurden die Messungen der elektrischen Leitfähigkeit hier nicht explizit angeführt, sondern sind nur in den berechneten Hallbeweglichkeiten enthalten.

(c) *Kristalle mit* Cu-*Zusatz*

Das während des Wachstums in die ZnO-Kristalle eingebaute Kupfer hat augenscheinlich eine ähnliche Wirkung wie nachträglich in undotierte Kristalle eindiffundierter Sauerstoff. Es verursacht eine starke Herabsetzung der Konzentration der Leitungselektronen und hat eine merkliche Vergrösserung des Temperaturkoeffizienten von $1/R_{He}$ zur Folge (Abb. 12). Der Effekt wird umso stärker, je grösser die eingebaute

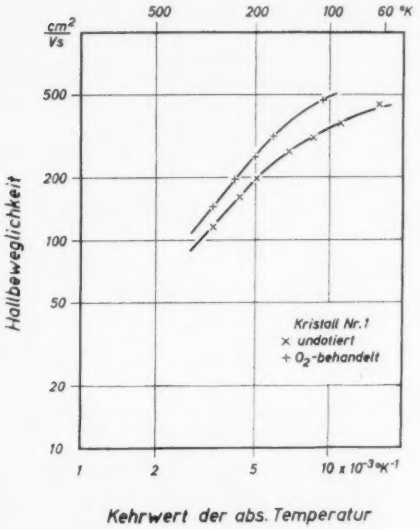

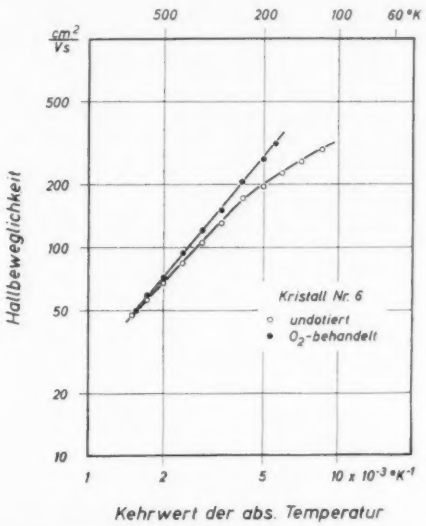

ABB. 10 und 11. Hallbeweglichkeit vor und nach Sauerstoffbehandlung der in Abb. 8 und 9 gemessenen Kristalle als Funktion der abs. Temperatur.

Die Hallbeweglichkeit wächst bis etwa 200°K bei abnehmender Temperatur mit $T^{-\alpha}$ wobei α zwischen 1,2 und 1,7 bestimmt wurde (Abb. 10,11). Bei tieferen Temperaturen nimmt die Steigung der μ_H-Kurven langsam ab. Bei den meisten Kristallproben hatte die Sauerstoffbehandlung eine geringe Erhöhung der Beweglichkeit bei tieferen Temperaturen und einen leichten Anstieg des Temperaturkoeffizienten im Gebiet der Zimmertemperatur zur Folge (Abb. 10, 11). Es wurden aber auch Kristalle vermessen, bei denen kein Unterschied der Beweglichkeit im undotierten und O_2-behandelten Zustand festgestellt werden konnte. Eine Abnahme der Beweglichkeit nach Sauerstoffbehandlung trat in keinem Fall auf.

Kupfermenge ist. Diese variierte zwischen $2{,}5 \times 10^{17}$ und $3{,}5 \times 10^{18}$ Cu-Atome/cm³.* Die kleinsten bei Zimmertemperatur gemessenen Elektronenkonzentrationen liegen bei 10^{14} Elektronen/cm³, die grösste Abtrennarbeit beträgt 0,49 eV. Der Temperaturkoeffizient von $1/R_{He}$ nimmt bei tiefen Temperaturen ab.

Die Absolutwerte und der Temperaturverlauf der Beweglichkeit entsprechen etwa den bei

* Die in dieser Arbeit angegebenen Cu- und In-Konzentrationen wurden spektralanalytisch von Herrn Dr. E. GOLLING im Forschungslabor der Siemens-Schuckert-Werke Erlangen bestimmt. Ich möchte ihm an dieser Stelle nochmals meinen herzlichen Dank aussprechen.

undotierten und O_2-behandelten Kristallen erhaltenen Ergebnissen (Abb. 13). Die Beweglichkeit variiert im Gebiet der Zimmertemperatur ebenfalls näherungsweise mit $T^{-3/2}$. Das Temperaturverhalten scheint im zugänglichen Temperaturbereich nicht merklich von der Cu-Konzentration abzuhängen.

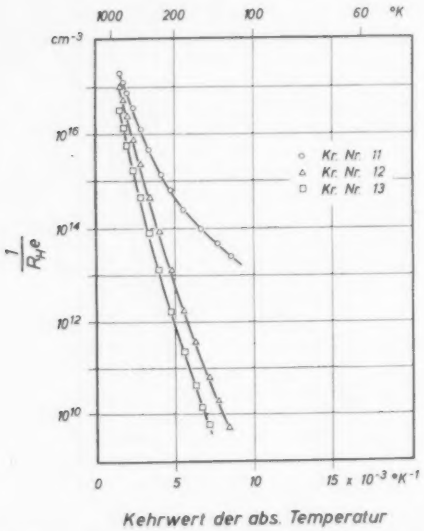

ABB. 12. Reziproke Hallkonstante von Kristallen mit Cu-Zusatz als Funktion der abs. Temperatur.

Kr. Nr.	Cu-Gehalt	Abtrennarbeit E_D
11	$2{,}5 \times 10^{17}$ Cu-Atome/cm³	0,33 eV
12	$1{,}1 \times 10^{18}$ Cu-Atome/cm³	0,45 eV
13	$3{,}0 \times 10^{18}$ Cu-Atome/cm³	0,49 eV

Die Abtrennarbeit E_D wurde aus dem Hochtemperaturteil der Kurven gewonnen.

DISKUSSION

Die experimentellen Ergebnisse, der vorangegangenen Abschnitte lassen sich nicht mit Hilfe des einfachen Halbleiter-Modells erklären, in welchem der Strom durch eine Sorte von Ladungsträgern in einem Leitungsband getragen wird.

Zur Erklärung der Effekte sind kompliziertere Modelle erforderlich. Diese Modelle haben alle gemeinsam, dass der Strom durch mindestens 2 parallellaufende Leitungsmechanismen getragen wird. Das Ausmass, in welchem die verschiedenen Mechanismen an der Leitung teilhaben, ändert sich mit der Temperatur. An solchen Modellen sind im einzelnen zu nennen:

1. Das Störbandmodell, d.h. Leitung ist nicht nur im normalen Leitungsband möglich, sondern auch in einem Störband, das durch Störstellen gebildet wird (z.B. BALTENSPERGER[10]).
2. Ein Modell, das makroskopische Inhomogenitäten berücksichtigt.

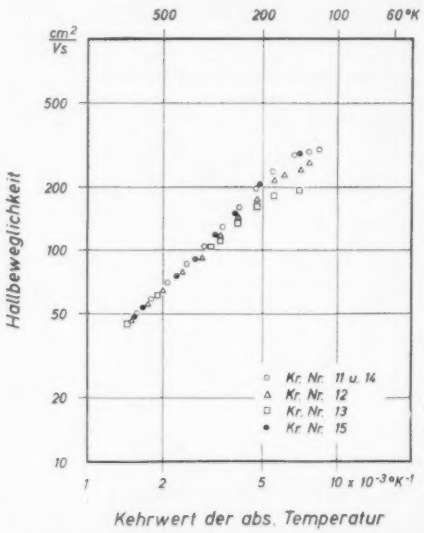

ABB. 13. Hallbeweglichkeit von ZnO-Kristallen mit Cu-Zusatz als Funktion der abs. Temperatur. (Angabe der Cu-Konzentrationen der Kristalle 11, 12 und 13 im Text der Abb. 12).

Kr. Nr. 14: $3{,}5 \times 10^{17}$ Cu-Atome/cm³
Kr. Nr. 15: $1{,}5 \times 10^{18}$ Cu-Atome/cm³

3. Ein Modell, bei welchem Änderungen der Leitfähigkeit an der Kristalloberfläche, z.B. durch adsorbierte Gase, berücksichtigt werden oder das Zustände, die durch Versetzungen hervorgerufen worden sind, einschliesst.

Bei der im folgenden gegebenen Deutung der vorliegenden Ergebnisse werden nur Modell 1 und 2 verwendet. Mit der Wirkung einer besonderen, durch Gasadsorption geschaffenen Oberflächenleitfähigkeit ist praktisch nicht zu rechnen, da die verwendeten Kristalle vor den Messungen

Vol. 1
196

bei 10^{-6} Torr einige Stunden Temperaturen von 200–400°C ausgesetzt waren. Ebenso ist die Konzentration der durch Versetzungen hervorgerufenen Zustände sicher zu gering (nach THOMAS[11] etwa 10^{14} cm^{-3}), um bei den vorliegenden Donatorenkonzentrationen eine Rolle zu spielen.

(A) *Kristalle mit Indium-Zusatz*

Es gilt als ziemlich sicher, dass das während des Kristallwachstums zugesetzte Indium substitutionell ins Grundgitter des ZnO eingebaut wird und dort als Donator sein überschüssiges 3 Valenzelektron abgibt.[11] Optische und elektrische Messungen haben ergeben, dass das Indium homogen über den Kristall verteilt ist, sodass nicht mit einer Wirkung von makroskopischen Inhomogenitäten zu rechnen ist. Wir werden deshalb in der nachfolgenden Diskussion das Störbandmodell verwenden.

Die spektralanalytisch bestimmten In-Konzentrationen der gemessenen Kristalle lagen zwischen 9×10^{17} und 6×10^{19} Indium-Atome/cm^{-3}. Beim CdS, einem seiner Struktur nach dem ZnO sehr verwandten Verbindungshalbleiter, hat man bei ähnlich hohen Donatorenkonzentrationen zur Deutung der experimentellen Ergebnisse das Störbandmodell verwendet (KRÖGER *et al.*[12]) Bei den Elementhalbleitern Ge und Si wird schon bei viel kleineren Donatorenkonzentrationen die Existenz von Störbändern angenommen (z.B. CONWELL[13]). Der bei höheren Donatorenkonzentrationen beobachtete Effekt, dass die Aktivierungsenergie der Donatoren gegen Null geht, wird auf eine Überlappung des Donatorenbandes mit dem Leitungsband zurückgeführt.

Wie sich im folgenden herausstellen wird, lassen sich die experimentellen Befunde der Indium-dotierten ZnO-Kristalle ebenfalls recht gut durch die Annahme eines Donatorenbandes unterhalb des Leitungsbandes erklären.

(1) *Reziproke Hallkonstante.* Für den Fall, dass noch keine Überlappung zwischen Donatorenband und Leitungsband vorliegt, also bei nicht allzugrossen Donatorenkonzentrationen, liefert das 2-Bandmodell folgenden Ausdruck für die reziproke Hallkonstante[13]:

$$\frac{1}{R_H e} = \frac{(n_1\mu_1+n_2\mu_2)^2}{n_1\mu_1\mu_{1H}+n_2\mu_2\mu_{2H}} \qquad (1)$$

Dabei sind:

n_1 bzw. μ_1 Ladungsträgerkonz. bzw. Beweglichkeit in Band 1 (Leitungsband)

n_2 bzw. μ_2 Ladungsträgerkonz. bzw. Beweglichkeit in Band 2 (Donatorenband)

μ_H = Hallbeweglichkeit, μ = Driftbeweglichkeit der Leitungselektronen.

Im allgemeinen gilt: $\mu_1 > \mu_2$; $\mu_H/\mu = f$, liegt zwischen 1 und 2 und hängt vom jeweiligen Streuprozess ab. (Im Entartungsfall gilt $\mu_H/\mu = 1$)

Ferner ist: $n_1+n_2 = N_D$ wobei N_D die Donatorenkonzentration ist. Wenn gleichzeitig Akzeptoren vorhanden sind, gilt $n_1+n_2 = N_D-N_A$.

Bei hohen Temperaturen gilt: $n_1\mu_1 \gg n_2\mu_2$ und es folgt:

$$\frac{1}{R_H e} = \frac{1}{f_1}\times n_1 \qquad (2)$$

d.h. bei hohen Temperaturen wird die Leitung praktisch völlig vom Leitungsband getragen, da fast alle Elektronen im Leitungsband sind.

Differenziert man den Ausdruck für die reziproke Hallkonstante (Gl.1) nach der Temperatur, so erhält man für $1/R_H e$ ein Minimum. Macht man die vereinfachenden Annahmen, dass $\mu_1/\mu_2 = b$ nicht temperaturabhängig ist, und dass $\mu_{1H}/\mu_1 = \mu_{2H}/\mu_2 = \mu_H/\mu = 1$, dann findet man das Minimum bei der Temperatur, für die gilt:

$$n_1 = \frac{1}{1+b}\times(N_D-N_A) \rightarrow n_1\mu_1 = n_2\mu_2 \qquad (3)$$

Das Minimum der reziproken Hallkonstanten liegt also ungefähr bei der Temperatur, für die die Leitfähigkeit des Donatorenbandes gleich der des Leitungsbandes wird.

Für die reziproke Hallkonstante beim Minimum gilt:

$$\left(\frac{1}{R_H e}\right)_{\text{Min}} = (N_D-N_A)\times\frac{4b}{(b+1)^2} \qquad (4)$$

Wie in der nachfolgenden Diskussion der Beweglichkeitsmessungen noch gezeigt wird, wächst $b = \mu_1/\mu_2$ mit abnehmender Donatorendichte.

Gl. (3) und (4) bestätigen damit das experimentelle Ergebnis, dass die Minima der reziproken Hallkonstanten umso tiefer sind und sich nach

umso tieferen Temperaturen hin verschieben, je kleiner die Donatorenkonzentration der jeweiligen Probe ist. Es muss also ein umso grösserer Prozentsatz der z.B. bei Zimmertemperatur im Leitungsband vorhandenen Elektronen ins Donatorenband herunterfallen, bevor die Donatorenbandleitung gleich der des Leitungsbandes wird, je kleiner die Leitfähigkeit in den Donatorenzuständen ist. Bei noch tieferen Temperaturen wird die Leitung schliesslich ganz vom Donatorenband übernommen, da n_2 gleich (N_D-N_A) wird. $1/R_He$ bleibt dann konstant (Kristall d!). Die Tatsache, dass bei Proben mit einer Donatorenkonzentration $N_D > 5\times10^{18}$ In-Atome/cm^3 keine Temperaturabhängigkeit von $1/R_He$ mehr festzustellen ist, zeigt, dass für solche Donatorenkonzentrationen die Überlappung des Donatorenbandes mit dem Leitungsband einsetzt und somit die Aktivierungsenergie E_D gegen Null geht.

(2) *Hallbeweglichkeit.* Das Temperaturverhalten von μ_H wird in dem einfachen 2-Bandmodell gegeben durch die Gleichung:

$$\mu_H = R_H\times\sigma = \frac{n_1\mu_1\mu_{1H}+n_2\mu_2\mu_{2H}}{n_1\mu_1+n_2\mu_2} \qquad (5)$$

Dabei gilt wieder: $n_1+n_2 = N_D-N_A$, und im allgemeinen: $\mu_1 > \mu_2$.

Für hohe Temperaturen gilt: $n_1 \gg n_2 \rightarrow \mu_H = \mu_{1H}$

Für tiefe Temperaturen gilt: $n_2 \gg n_1 \rightarrow \mu_H = \mu_{2H}$

Bei hohen Temperaturen wird also die gemessene Hallbeweglichkeit durch die Beweglichkeit im Leitungsband dargestellt. Sie steigt bei Kristallen mit kleinerer Dotierung (Kristalle a,b) bei abnehmender Temp. zunachst noch an (Gebiet der Gitterstreuung). Die Abhängigkeit von μ_{1H} bei Zimmertemperatur von der Dotierung zeigt deutlich, dass hier auch schon Störstellenstreuung vorliegt.

Bei tiefen Temperaturen geht μ_H über in die für das Donatorenband charakteristische Beweglichkeit μ_{2H} und ist dann temperaturunabhängig (Fermistatistik?). Der Übergang erfolgt bei umso höheren Temperaturen, je grösser die Störbandleitung, also die Donatorenkonzentration ist. Bei den Kristallen d, e und g liegt der Übergang noch im zur Verfügung stehenden Temperaturbereich.

Bei Kristallen mit kleinerem Donatorengehalt (Kristalle a, b, c) übernimmt das Störband die Leitung erst bei Temperaturen, die unterhalb der Messgrenze von 63°K liegen, der Übergang konnte bei diesen Kristallen also nicht mehr experimentell erfasst werden. Es ist aber möglich, mit Hilfe der Gl. (4) und den experimentell bestimmten Werten $(1/R_He)_{\mathrm{Min}}$, $N_D-N_A \approx n$ (300°K) und μ_{1H}, die Störbandbeweglichkeit μ_{2H} näherungsweise zu berechnen. Die Ergebnisse dieser Näherungsrechnung sind in der letzten Spalte der Tabelle 1 aufgeführt:

Tabelle 1. *Zusammenhang zwischen der Differenz aus Donatoren- und Akzeptorenkonzentration* N_D-N_A *und der Donatorenbandbeweglichkeit* μ_{2H}

Kristall	N_D-N_A, cm^{-3}	μ_{2H}, cm^2/V sec
a	9×10^{17}	1,5
b	$1{,}7\times10^{18}$	4,1
c	$2{,}5\times10^{18}$	7
d	4×10^{18}	28

Diese Werte können natürlich wegen der verwendeten Modellvorstellung und den vereinfachenden Annahmen nur als Orientierungswerte gelten.

Nach dem experimentellen Temperaturverlauf von μ_H ist bei den Kristallen a,b,c auf jeden Fall eine Störbandbeweglichkeit $\mu_{2H} < 10$ cm^2/V sec zu erwarten. Kristall d strebt einem Tieftemperaturwert der Hallbeweglichkeit von etwa 20 cm^2/V sec zu, in guter Übereinstimmung mit dem berechneten Wert.

Die aus dem 2-Bandmodell berechneten Werte für μ_{2H} bestätigen die zunächst anomal erscheinende Tatsache, dass Kristalle mit höherer Donatorenkonzentration bei tiefen Temperaturen eine grössere Hallbeweglichkeit haben als solche mit geringerer Donatorendichte. Bei tiefen Temperaturen wird die Leitung im Kristall durch das Donatorenband getragen. Ein grösserer Donatorengehalt hat eine zunehmende Überlappung der Elektronenwellenfunktionen benachbarter Donatoren zur Folge und damit eine Verbreiterung des

Donatorenbandes. Die Störbandbeweglichkeit ist umso grösser, je breiter das Störband ist, was der allgemeinen Vorstellung entspricht, dass die effektive Masse mit zunehmender Bandbreite kleiner wird.

Aus den Beweglichkeitskurven der Kristalle g und h geht hervor, dass für In-Konzentrationen $N_D > 10^{19}$ Atome/cm^3 die Beweglichkeit keine Temperaturabhängigkeit mehr zeigt. Bei so hohen Konzentrationen sind Donatoren- und Leitungsband weitgehend verschmolzen. μ_1 und μ_2 sind nicht mehr unterscheidbar und es gilt über den ganzen Temperaturbereich : $\mu_1 = \mu_2$. Bei diesen hohen Konzentrationen ist wegen Entartung keine Temperaturabhängigkeit der Beweglichkeit mehr zu erwarten.

Da die 2-Bandformel zu viele Variable enthält, ist es nicht möglich, eine quantitative Angabe über den Temperaturverlauf von μ_H im Gebiet wo $n_1\mu_1 \approx n_2\mu_2$ zu geben, also z.B. den experimentellen Befund eines $T^{+3,5}$-Gesetzes bei kleinen Indium-Dotierungen quantitativ zu erklären. Dagegen ist eine qualitative Erklärung des relativ steilen Abfalls der Beweglichkeitskurven bei tiefen Temperaturen und schwacher Dotierung möglich. Man muss dabei folgendes berücksichtigen : (a) $\mu_1 \gg \mu_2$: (b) der Ausdruck für die Beweglichkeit (Gl.5) enthält die temperaturabhängigen Elektronenkonzentrationen und Beweglichkeiten der beiden Bänder.

Das Temperaturverhalten der Leitfähigkeit σ (Abb. 5) wird bestimmt durch die eben diskutierten Temperaturabhängigkeiten von μ_H und $1/R_He$.

(B) *Kristalle ohne Zusatz, mit Sauerstoff behandelte Kristalle und Kristalle mit* Cu-*Zusatz.*

(1) *Reziproke Hallkonstante von undotierten und* O_2*-behandelten Kristallen.* Wie aus den gemessenen $1/R_He$-Werten hervorgeht, liegen die bei höheren Temperaturen an undotierten Kristallen bestimmten Elektronenkonzentrationen beträchtlich über den spektralanalytisch bestimmten Zusatzkonzentrationen von Fremdatomen.[5] Diese kommen also als Donatoren nicht in Frage.

Mit Hilfe eines von SECCO und MOORE[14,15] angegebenen chemischen Analysenverfahrens wurde der in ZnO vorhandene stöchiometrische Metallüberschuss bestimmt. Als Mittelwert vieler Analysen ergab sich für unbehandelte Kristalle eine Überschusskonzentration von 8×10^{17} Atome/cm^3. Durch die Analyse wurden nur solche Metalle nachgewiesen, die eine kleinere Elektronenaffinität als Wasserstoff haben. Spektralanalytische Bestimmungen aller in Frage kommenden Fremdatome (überschüssiges Zn wird dabei nicht erfasst) ergaben im Mittel eine Fremdzusatzkonzentration, die viel kleiner als 8×10^{17} Atome/cm^3 war.

Die relativ grosse n-Leitung undotierter ZnO-Kristalle beruht also mit grosser Wahrscheinlichkeit auf der Wirkung eines stöchiometrischen Überschusses von Zn in ZnO. Es sind dabei grundsätzlich 2 Arten von Donatoren möglich. Zn-Atome auf Zwischengitterplätzen (Zn_0) und Sauerstofflücken, die mit 2 Elektronen besetzt sind ($O_{\square}^{=}$). Wir nehmen an, dass es sich bei den in dieser Arbeit vermessenen Kristallen in der Hauptsache um 2-fach mit Elektronen besetzte Sauerstofflücken handelt. Für diese Annahme sprechen Untersuchungen über den Zusammenhang zwischen Lumineszenz und elektrischer Leitfähigkeit,[16] ferner die weiter unten diskutierte Wirkung des während des Kristallwachstums ins ZnO eingebauten Kupfers.

Im folgenden wird also vorausgesetzt, dass im gemessenen Temperaturbereich nur eine Sorte von Donatoren, nämlich 2-fach mit Elektronen besetzte Sauerstofflücken $O_{\square}^{=}$, eine Rolle spielt. Die aus den $1/R_He$-Kurven (Abb. 7, 8, 9) durch Extrapolation nach $1/T = 0$ abgeschätzten Donatorenkonzentrationen liegen zwischen einigen 10^{17} und 10^{18} cm^{-3}. Die Tatsache, dass der Temperaturkoeffizient der reziproken Hallkonstante von undotierten und O_2-behandelten Kristallen umso kleiner ist, je grösser die Leitfähigkeit der Proben ist, lässt vermuten, dass auf Grund verschiedener Konzentrationen ein und deselben Donators in den Kristallen verschieden breite Donatorenbänder vorliegen. Je grösser die Donatorenkonzentration ist, umso kleiner wird der Abstand zwischen oberer Kante des Donatorenbandes und unterer Kante des Leitungsbandes. Dieser Abstand stellt die Aktivierungsenergie der Donatoren dar und bestimmt den Temperaturkoeffizienten von $1/R_He$.

Von der Wirkung der Sauerstoffbehandlung kann man sich folgendes Bild machen : Sauerstoff diffundiert in den Kristall und füllt die Sauerstofflücken im Anionengitter, die mit 2 Elektronen besetzt sind. Dadurch wird ein Teil der Donatoren vernichtet, die Breite des Donatorenbandes

verkleinert und die Elektronenkonzentration im Leitungsband herabgesetzt. Für dieses Modell spricht die bei den meisten Kristallen gefundene Beweglichkeitszunahme nach Sauerstoffbehandlung (Verminderung der Streuung an Störstellen). Dieser Befund spricht gegen die Annahme, dass ein wesentlicher Teil des Sauerstoffs im Zwischengitter als Akzeptor die Wirkung der Donatoren kompensiert (vgl. auch (16)).

Die $1/R_He$-Kurven undotierter und sauerstoffbehandelter Kristalle zeigen, dass der Temperaturkoeffizient der reziproken Hallkonstante temperaturabhängig ist. Besonders tieferleitende Kristalle zeigen bei tiefen Temperaturen eine kontinuierliche Abnahme des Temperaturkoeffizienten von $1/R_He$. Sauerstoffbehandlung hat sowohl im Hoch- wie im Tieftemperaturgebiet eine Zunahme des Temperaturkoeffizienten zur Folge. Mit grosser Wahrscheinlichkeit ist das kontinuierliche Abbiegen von $1/R_He$ in der Hauptsache auf die Wirkung makroskopischer Inhomogenitäten in der Konzentration ein und desselben Donators, nämlich zweifach mit Elektronen besetzter Sauerstofflücken, zurückzuführen. Nach Messungen mit Hilfe einer Potentialsondenmethode weisen besonders Kristalle mit niedriger Leitfähigkeit in Längs- und Querrichtung Bereiche mit grösserer und kleinerer Leitfähigkeit auf. Diese Befunde sind in Übereinstimmung mit Lumineszenz- und Leitfähigkeitsmessungen von Herrn Prof. E. MOLLWO[17]. Inwieweit geringe Konzentrationen von Zwischengitter-Zink und Fremdatomen mit kleiner Aktivierungsenergie eine Rolle spielen, kann nicht entschieden werden.

Der Einfluss makroskopischer Inhomogenitäten quer zur Stromrichtung auf den Verlauf von $1/R_He$ wird durch ein bei KRÖGER *et al.*[12] diskutiertes Modell erfasst. Der Kristall ist dabei aus zwei verschiedenen in sich homogenen Bereichen aufgebaut. Dieses Modell liefert eine reziproke Hallkonstante, die in komplizierter Weise von den Geometrieverhältnissen und den elektrischen Eigenschaften der Teilbereiche abhängt. Nimmt man für die Teilbereiche geeignete Werte an, so liefert eine Diskussion der massgebenden Formel[12] folgende Aussage: Bei hohen Temperaturen dominiert der Kristallbereich mit dem grösseren Temperaturkoeffizienten (Bereich 1), bei tiefen Temperaturen der Bereich mit dem kleineren Temperaturkoeffizienten (Bereich 2).

Dieses Verhalten kommt bei den gemessenen $1/R_He$-Kurven deutlich zum Ausdruck.

Im einzelnen ergibt sich:

$$\frac{1}{R_He} \approx A_1 \frac{n_1}{f_1} \tag{6}$$

für hohe Temperaturen

$$\frac{1}{R_He} \approx A_2 \frac{n_2}{f_2} \tag{7}$$

für tiefe Temperaturen. n_1 bzw. n_2 sind die Elektronenkonzentrationen in Bereich 1 bzw. 2, f ist das Verhältnis der Beweglichkeiten μ_H/μ (vgl. weiter oben). Im Falle der Nichtentartung gilt: $f_1 = 3\pi/8$ und $f_2 \approx 2$. A_1 bzw. A_2 sind Geometriefaktoren. Sie enthalten die Bruchteile des Gesamt-Kristallquerschnittes, die der tieferleitende Bereich (1) bzw. der höherleitende Bereich (2) einnimmt.

Die Tatsache, dass die makroskopischen Inhomogenitäten höchstwahrscheinlich nur von verschiedenen Konzentrationen ein und desselben Donators herrühren und dass verschiedene Kristallbereiche trotzdem verschiedene Temperaturkoeffizienten haben, deutet darauf hin, dass in den einzelnen Kristallbereichen Donatorenbänder von verschiedener Breite vorliegen. Diese bestimmen dann in einem speziellen Temperaturbereich das Temperaturverhalten von $1/R_He$, während sie in einem anderen Temperaturbereich nicht mehr wirksam sind.

Auf Grund der Inhomogenitäten und der daraus resultierenden komplizierten Form der Hallkonstante ist es nicht möglich, eine für den ganzen Kristall geltende Aktivierungsenergie E_D zu gewinnen. Man muss sich besonders bei den Kristallen mit kleiner Leitfähigkeit auf das Hochtemperaturende der $1/R_He$-Kurven beschränken, denn nur dort erhalten wir eine Beziehung von der Form:

$$\frac{1}{R_He} \sim \frac{1}{f_1} \times n_1$$

wobei

$$n_1 = (N_C^0)^{1/2} \times (N_{D1} - n_1)^{1/2} \times \left[\frac{m_{\mathrm{eff}1}}{m_0}\right]^{3/4} \times D^{-1/2} \times \exp(-E_{D1}/2kT) \tag{8}$$

N_C' = effektive Zustandsdichte des Leitungsbandes

N_{D1} = Donatorendichte des tiefstleitenden Kristallbereiches

m_{eff1} bzw. m_0 ist die effektive bzw. freie Elektronenmasse

D ist die sog. Donatoren-Entartung und hat gewöhnlich den Wert 2.

Diese Gleichung gestattet die Berechnung der Aktivierungsenergie für das Hochtemperaturgebiet von $1/R_He$. Hier ist auch der Temperaturkoeffizient in den meisten Fällen über einen relativ grossen Temperaturbereich konstant, sodass bei der Bestimmung von E_{D1} keine allzugrossen Fehler möglich sind. Ferner ist in dem verwendeten Temperaturbereich (E_{D1} wurde zwischen $1/T = 3$ und $1/T = 4\times 10^{-3}°K^{-1}$ bestimmt) keine grosse Änderung von f_1 mit der Temperatur zu erwarten, da sich in diesem Bereich der Streumechanismus wenig ändert.

Die aus dem Hochtemperaturbereich von $1/R_He$ gewonnene Aktivierungsenergie E_{D1} gehört zu dem Kristallbereich mit der jeweils kleinsten Donatorenkonzentration. Da in den einzelnen Kristallbereichen Donatorenbänder vorliegen, bezeichnet E_{D1} jetzt allgemein den Energieabstand zwischen oberer Kante des schmalsten vorliegenden Donatorenbandes und unterer Kante des Leitungsbandes.

Eine Auswertung der Gl. (8) nach E_{D1} mit Hilfe von $n_1 \sim f_1/R_He$ macht eine genaue Kenntnis von N_{D1} nötig. Da der Sättigungscharakter der $1/R_He$-Kurven bei hohen Temperaturen noch nicht sehr ausgeprägt ist, kann N_{D1} nur sehr ungenau abgeschätzt werden und wir müssen deshalb zu einer Vereinfachung der Gl. (8) greifen: Da n_1 bei $T = 300°K$ noch keine Sättigung zeigt, können wir annehmen, dass in der Umgebung von $T \leq 300°K$ gilt:

$N_{D1} \gg n_1$:

Damit ergibt sich aus Gl. (8):

$$\frac{f_1}{R_He} = A_1 n_1 = A_1 \times \left(N_C^0 \frac{N_{D1}}{2}\right)^{1/2} \times \left[\frac{m_{eff1}}{m_0}\right]^{3/4} \times \exp(-E_{D1}/2kT) \qquad (9)$$

Mit Hilfe der Gl. (9) kann nun E_{D1} bestimmt werden (vgl. Abb. 15).

(2) *Reziproke Hallkonstante von* Cu-*dotierten Kristallen.* Zum Einbau des Kupfers in ZnO wurde folgende Modellvorstellung entwickelt: Wir nehmen an, dass das Cu zunächst als einwertiges Kation in das Grundgitter des ZnO eingebaut wird und dort ein 2-wertiges Zn-Ion ersetzt. Der

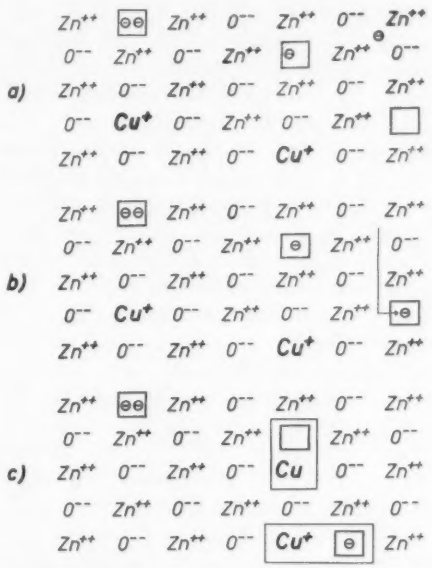

ABB. 14. Atomistisches Bild zum Einbau von Kupfer in ZnO mit Sauerstofflücken. (a) Zeigt einen neutralen Donator $O_{\square}^{-}$, einen ionisierten Donator $O_{\square}$ plus Leitungselektron, zwei im Gitter eingebaute Cu^+-Ionen mit zugehöriger Sauerstofflücke $O_{\square}$. (b) Folgt aus (a) durch Einfang des Leitungselektrons durch die Sauerstofflücke. (c) Folgt aus (b) durch Assoziation der Cu^+-Ionen mit den einfach besetzten Sauerstofflücken. Für die dadurch entstehenden Assoziate werden zwei Darstellungen gegeben.

Kupfereinbau hat aus Gründen der Elektroneutralität die Bildung zusätzlicher Sauerstofflücken zur Folge, die zu den durch Zn-Überschuss geschaffenen noch hinzukommen. Für den Einbau kann man folgende Reaktionsgleichung ansetzen:

$$(1-2\epsilon)Zn^{++}O^{--} + \epsilon Cu_2^+O^{--} \rightleftharpoons Zn^{++}_{(1-2\epsilon)}Cu^+_{2\epsilon}O^{--}_{(1-\epsilon)}O_{\square\epsilon}$$

Dabei bedeutet $O_{\square}$ eine leere Sauerstofflücke im Anionengitter. $2x$ Cu-Ionen erzeugen also x leere Sauerstofflücken (Abb. 14a). Diese x leeren Sauerstofflücken reagieren mit x 2 fach mit

Elektronen besetzten Sauerstofflücken nach folgender Reaktionsgleichung (Abb. 14b):

$$x\mathrm{O}_{\square} + x\mathrm{O}_{\square}^{--} \rightleftharpoons 2\,x\,\mathrm{O}_{\square}^{-}$$

Wir nehmen an, dass keine beliebige Verteilung von Cu^+ und einfach besetzten Sauerstofflücken im ZnO vorliegt, sondern dass das Cu^+ mit den vorhandenen einfach besetzten Sauerstofflücken ($O_{\square}^{-}$) assoziiert (Abb. 14c). Assoziation einer einfach besetzten Sauerstofflücke mit Cu^+ bedeutet, dass die Aufenthaltswahrscheinlichkeit des Elektrons am Cu^+ grösser ist als an den umgebenden Zn^{++}-Nachbarn, mit anderen Worten, das Cu liegt praktisch neutral im Grundgitter des ZnO vor. Jedem Cu-Atom ist eine leere Sauerstofflücke zugeordnet. Durch den Einbau von $2\,x$ Cu-Atomen verschwinden also x ursprünglich vorhandene Donatoren.

Dieses Modell wird gestützt durch elektrochemische Überlegungen. Aus den Ergebnissen mit undotierten ZnO-Kristallen weiss man, dass bei den verwendeten Herstellungsbedingungen für das ZnO[4,5] keine vollständige Oxydation des Zn-Dampfes erreicht wird. Stöchiometrischer Überschuss von Zn! Die Herstellung der Cu-dotierten Kristalle erfolgte unter den gleichen Bedingungen. Es wurden Zn und geringe Mengen von Cu gleichzeitig verdampft, das Dampfgemisch oxydiert und zwar bei der gleichen Temperatur und demselben Sauerstoffdruck wie im Falle der nichtdotierten Kristalle. Aus der Tatsache, dass Cu eine grössere Elektronenaffinität als das Zn besitzt,[18] müssen wir schliessen, dass bei der offensichtlich nicht vollständigen Oxydation das Cu hauptsächlich als neutrales Cu im ZnO vorliegt.

Nach dem oben entwickelten Modell hat Cu also keine Donatoren kompensierende, sondern ebenso wie der Einbau von Sauerstoff eine Donatoren vernichtende Wirkung. Dass Cu zu wesentlichem Bruchteil neutral ins Zwischengitter eingebaut wird, kann ausgeschlossen werden, da es dort als Donator wirken und die Leitfähigkeit erhöhen müsste. Das steht im Gegensatz zu den experimentellen Befunden.

Eine Analyse der $1/R_{He}$-Kurven ist mit den gleichen Annahmen wie im Fall der undotierten und O_2-behandelten Kristalle möglich. Auf Grund makroskopischer Querinhomogenitäten, die Cu-dotierte Kristalle aufweisen, hat man es wieder mit einer komplizierten Form der reziproken Hallkonstanten zu tun, wie sie bei KRÖGER *et al.*[12] gegeben ist. Die Temperaturabhängigkeit des Temperaturkoeffizienten von $1/R_{He}$ kann wieder mit verschieden breiten Donatorenbändern in den einzelnen Kristallbereichen erklärt werden. Die Aktivierungsenergie wurde ebenfalls aus dem Hochtemperaturende der $1/R_{He}$-Kurven mit Hilfe der Gl. (9) berechnet.

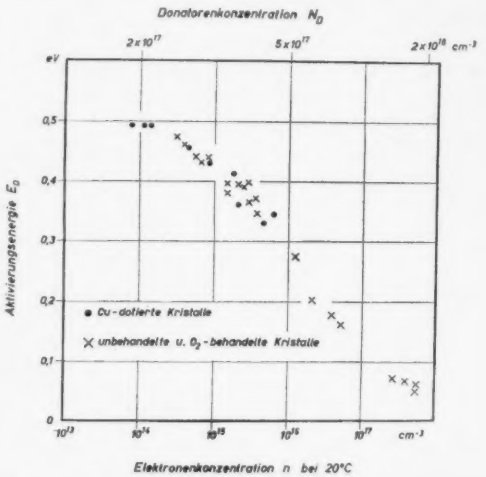

ABB. 15. Zusammenhang zwischen der Elektronenkonzentration bei Zimmertemperatur und der nach Gl. (9) berechneten Aktivierungsenergie E_D für unbehandelte, O_2-behandelte und Cu-dotierte Kristalle. Die angegebenen Donatorenkonzentrationen N_D wurden durch Extrapolation der Hochtemperaturwerte der $1/R_{He}$-Kurven gewonnen.

In Abb. 15 wurden die so berechneten Aktivierungsenergien aller gemessenen undotierten, sauerstoffbehandelten und Cu-dotierten Kristalle gegen die Elektronenkonzentration bei Zimmertemperatur aufgetragen. Wir sehen, dass bei Kristallen mit Cu-Zusatz und solchen mit nachträglicher Sauerstoffbehandlung zu den gleichen Elektronenkonzentrationen bei 20°C die gleichen Aktivierungsenergien gehören. Dies ist ein Argument für die Richtigkeit der oben gemachten Modellvorstellung über den Cu-Einbau in ZnO. Hiernach soll ja das Cu ebenso wie der Einbau von Sauerstoff donatorenvernichtend wirken.

Die grössten Aktivierungsenergien liegen bei etwa 0,5 eV (Abb. 15). Nach unseren Vorstellungen

Vol. 1
1961

stellt diese Energie etwa den Abstand des diskreten Donatorenniveaus der 2-fach mit Elektronen besetzten Sauerstofflücke vom unteren Rand des Leitungsbandes dar. Dann ist es möglich, die Donatorenbandbreiten für höhere Donatorenkonzentrationen näherungsweise anzugeben. Für Donatorenkonzentrationen die grösser als 10^{18} cm^{-3} sind, ergeben sich Bandbreiten von etwa 1 eV und darüber.

Wie man aus Abb. 15 weiter entnimmt, entspricht der Erniedrigung der Donatorenkonzentration um etwa eine Zehnerpotenz eine Verminderung der Elektronenkonzentration (bei 20°C) um etwa 4 Zehnerpotenzen. Der Grund hierfür ist die starke Zunahme der Aktivierungsenergie mit abnehmender Donatorenkonzentration und der daraus folgende geringere Dissoziationsgrad der Donatoren.

(3) *Hallbeweglichkeit von undotierten, O_2-behandelten und* Cu-*dotierten Kristallen.* Bei einer Analyse des Temperaturverlaufs der gemessenen Hallbeweglichkeiten dieser Kristalle, muss den makroskopischen Inhomogenitäten Rechnung getragen werden, die besonders Kristalle mit kleiner Leitfähigkeit in Längs- und Querrichtung aufweisen.

Wie oben beschrieben, wurde versucht, die Wirkung der Längsinhomogenitäten dadurch zu vermindern, dass für die Berechnung der Hallbeweglichkeit die arithmetischen Mittel der an zwei Kristallseiten gemessenen Leitfähigkeiten und der an zwei Hallstrecken gewonnenen Hallkonstanten verwendet wurden. Ferner wurden Kristalle mit relativ guter Längshomogenität ausgesucht.

Um den Einfluss der makroskopischen Inhomogenitäten quer zur Kristall-Längsachse auf den Temperaturverlauf der Hallbeweglichkeit zu erfassen, muss man wieder das bei KRÖGER *et al.*[12] angegebene Modell beachten. Eine Diskussion der aus diesem Modell resultierenden Formel für die Hallbeweglichkeit[12] ergibt folgende Aussage: Bei hohen Temperaturen wird die Hallbeweglichkeit durch die Bereiche mit kleiner Donatorenkonzentration bestimmt, während bei tiefen Temperaturen die Bedeutung der Bereiche mit grösserer Donatorenkonzentration erheblich zunimmt.

Die Tatsache, dass die meisten Kristalle nach Sauerstoffbehandlung im Gebiet der Zimmertemperatur und darunter eine etwas grössere Beweglichkeit haben, als im unbehandelten Zustand, deutet darauf hin, dass durch den eindiffundierten Sauerstoff Lücken im Anionengitter aufgefüllt wurden, was einer Verminderung der Störstellenstreuung entspricht. Die dabei auftretenden Änderungen sind gering und können u.U. durch Messfehler verfälscht werden. Es sind aber auch nur kleine Effekte zu erwarten, da sich die Donatorenkonzentrationen bei Sauerstoffbehandlung nicht um Grössenordnungen ändern (vgl. Abb. 15).

Die Beweglichkeit ändert sich im Gebiet der Zimmertemperatur mit $T^{-\alpha}$, wobei α etwa 1,5 ist, was darauf hinweist, dass in diesem Temperaturgebiet hauptsächlich mit Streuung am akustischen Zweig der Gitterschwingungen zu rechnen ist.[19] Die Tendenz, dass ein Grossteil der Kristalle nach Sauerstoffbehandlung im Gebiet der Zimmertemperatur ein etwas grösseres α als im unbehandelten Zustand aufweist, kann so erklärt werden, dass bei den undotierten Kristallen Bereiche mit so hohen Donatorenkonzentrationen vorliegen, dass im Gebiet der Zimmertemperatur nicht allein die Streuung an Gitterschwingungen, sondern bereits die Streuung an ionisierten Störstellen[20] eine Rolle spielt. Diese Streuung an ionisierten Störstellen ist auch für das Abbiegen der Beweglichkeitskurven bei tiefen Temperaturen verantwortlich zu machen. Durch Sauerstoffbehandlung wird die Donatorenkonzentration verringert, sodass der Anteil der Störstellenstreuung am Gesamtstreuprozess im Gebiet der Zimmertemperatur abnimmt.

Die experimentellen Befunde, dass die Absolutwerte und der Temperaturverlauf der Beweglichkeit von Cu-dotierten Kristallen etwa den bei undotierten und O_2-behandelten Kristallen erhaltenen Ergebnissen entsprechen und im zugänglichen Temperaturbereich nicht merklich von der Cu-Konzentration abzuhängen scheinen, deuten darauf hin, dass Cu nicht als geladene Störstelle im ZnO vorliegt. Dies ist ein weiteres Argument für die Richtigkeit der von uns gemachten Modellvorstellung über den Einbau von Cu in das ZnO.

Anerkennungen—Herrn Professor Dr. E. MOLLWO danke ich aufrichtig für die Anregung zu dieser Arbeit und für sein stets förderndes Interesse bei ihrer Durchführung.

Die Arbeit wurde durch Leihgaben der Deutschen Forschungsgemeinschaft unterstützt.

LITERATUR

1. HARRISON E., *Phys. Rev.* **93,** 52 (1954).
2. HUTSON A. R., *Phys. Rev.* **108,** 222 (1957).
3. RUPPRECHT H., *J. Phys. Chem. Solids* **6,** 144–154 (1958).
4. SCHAROWSKY E., *Z. Phys.* **135,** 318 (1953).
5. BOGNER G. und MOLLWO E., *J. Phys. Chem. Solids* **6,** 136–143 (1958).
6. v. BERNUTH G., Erlanger Diplomarbeit, (1959) unveröffentlicht.
7. HEILAND G., *Z. Phys.* **148,** 15 (1957).
8. MOTT N. F., *Proc. Camb. Phil. Soc.* **32,** 281 (1936).
9. JOHNSON A. und LARK-HOROVITZ K., *Phys. Rev.* **71,** 374 (1947).
10. BALTENSPERGER W., *Phil. Mag.* **44,** 1355 (1953).
11. THOMAS D. G., *J. Phys. Chem. Solids* **9,** 31–42 (1958).
12. KRÖGER F. A., VINK H. J. und VOLGER J., *Philips Res. Rep.* **10,** 39 (1955).
13. CONWELL E. M., *Phys. Rev.* **103,** 51 (1956).
14. SECCO E. A. und MOORE W. J., *J. Chem. Phys.* **26,** 942–948, (1957).
15. BOGNER G., Erlanger Diplomarbeit (1956), unveröffentlicht.
16. Proceedings of the International Conference on Semiconductor Physics, Prague 1960. Demnächst erscheinend.
17. HEILAND G., MOLLWO E. und STÖCKMANN F., *Solid State Physics* Vol. VIII, p. 191. Academic Press, New York (1959).
18. HOLLEMAN A. F. und WIBERG E., *Lehrbuch der Anorganischen Chemie.* Walter de Gruyter, Berlin (1958).
19. SHOCKLEY W., *Electrons and Holes in Semiconductors.* Van Nostrand, New York (1951).
20. DEBYE P. P. und CONWELL E. M., *Phys. Rev.* **93,** 693 (1954).

Vol. 1
196

J. Phys. Chem. Solids Pergamon Press 1961. Vol. 19, Nos. 3/4, pp. 251–260. Printed in Great Britain.

THE IONIZATION BEHAVIOR OF DONORS FORMED FROM OXYGEN IN GERMANIUM

C. S. FULLER and F. H. DOLEIDEN

Bell Telephone Laboratories, Incorporated

Murray Hill, New Jersey

(*Received* 21 *December* 1960)

Abstract—Hall and conductivity measurements have been made on a series of oxygen-doped Ge crystals in which donors were formed by oxygen aggregation. Three donor energy levels ($\sim 0{\cdot}2$, $0{\cdot}04$ and $0{\cdot}017$ eV) are found in partially reacted crystals. The shallowest level ($0{\cdot}017$ eV) alone appears to be left on complete reaction and is therefore attributed to the donor containing 4 oxygen atoms. The other two levels are attributed to donors containing fewer oxygens. In particular there is good evidence favoring the assignment of the $0{\cdot}2$ eV level to the donor containing two oxygens. The concentration of the $0{\cdot}04$ eV donor level is found to depend on temperature and time in a manner which suggests an internal rearrangement of the oxygen atoms. The energetics of this process have been studied and an attempt made to account for the results on the basis of an equilibrium between two forms of the donor. The bearing of the results on the reaction kinetics is discussed.

ol. 19
1961

1. INTRODUCTION

WHEN germanium containing oxygen in solution is heated in the temperature range 300–600°C, donors are formed.[1] Depending upon the temperature, donor equilibria are reached which are able to be described in terms of a donor "molecule" consisting of four oxygen atoms.[2, 3] The equilibrium results are consistent with the donor having one level which is almost completely ionized at room temperature. Infrared investigations[4] as well as kinetics studies,[5] however, indicate that donors containing less than four oxygen atoms form during the initial stages of the reaction and suggest that a species which is neutral or partly ionized at room temperature is present during part of the reaction. The presence of intermediate donor species has also been postulated for the analogous reactions in silicon.[6] Also infrared investigations[7] in silicon show the presence of a variety of donor energy levels, suggesting that several different donors are present in oxygen-doped Si during reaction at 430°C.

It is the purpose of the present paper to investigate the donors formed by the reaction of oxygen in Ge by means of Hall effect measurements and to compare the results with those obtained from the equilibrium, kinetics, and infrared work mentioned above.

An attempt to determine the ionization energy of donors formed by the reaction of oxygen in Ge was made by BLOEM *et al.*[2] Their results indicated that more than one donor or a multi-levelled donor was present. Our results show that more than one donor is produced during the reaction. The changes in the Hall curves, both during the donor generation and the donor dissociation reactions,[5] have been explored further. Of particular interest is the finding that a donor formed early in the reaction is capable of a reversible transformation with temperature. At fixed temperatures a relaxation of the donor resulting in reduced ionization is observed. This relaxation phenomenon is discussed in detail below.

2. EXPERIMENTAL

A. *Materials and procedure*

The oxygen-doped Ge crystals employed in this work were the same as employed in the previous investigations.[3, 5] The oxygen concentrations

were determined by infrared absorption measurements.[8] Three different oxygen concentrations were studied: $2{\cdot}2\times10^{17}$ cm^{-3}, $3{\cdot}9\times10^{17}$ cm^{-3} and $4{\cdot}9\times10^{17}$ cm^{-3}. In addition to the above, a crystal containing $4{\cdot}0\times10^{16}$ cm^{-3} In and $7{\cdot}0\times10^{17}$ cm^{-3} in results attributable to the quench procedure was noted except that these crystals behaved more uniformly in the Hall measurements. Hall effect and conductivity were measured after reaction for different times at 300°C and at 350°C

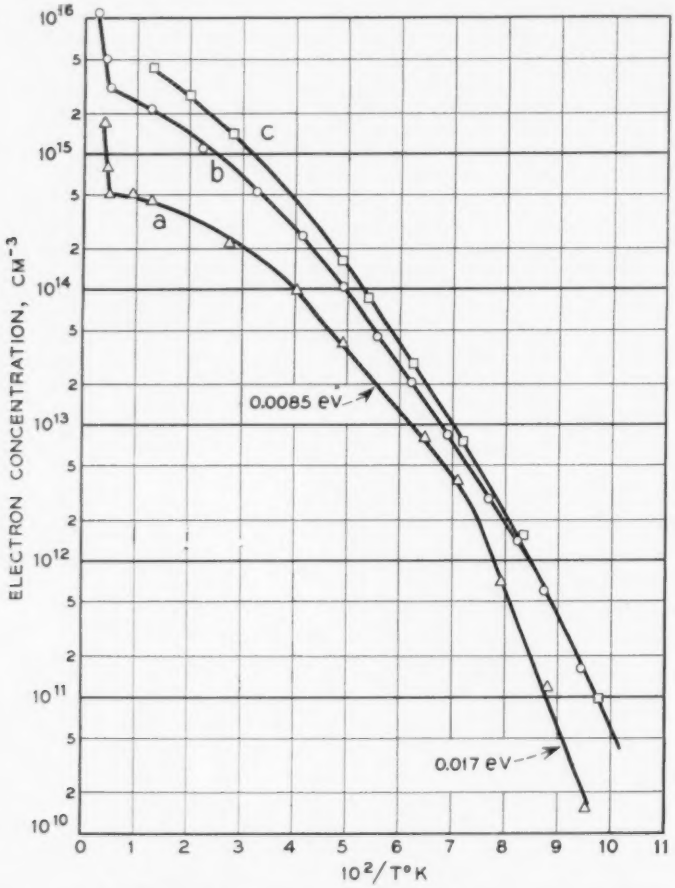

FIG. 1. Electron concentration vs. $1/T$ for $2{\cdot}2\times10^{17}$ cm^{-3} O reacted at 300°C.

(a) Slow run on specimen reacted 3 hr.
(b) Slow run on specimen reacted 66 hr.
(c) Quenched run on specimen shown in (b).

oxygen was examined after reaction to near intrinsic *n*-type in order to search for deep donor levels.

Oxygen-doped crystals were examined "as grown" and after a heat-quench procedure[3] applied to the gold-plated specimens. No difference

including one specimen ($3{\cdot}9\times10^{17}$ cm^{-3} O) reacted to complete equilibrium (1500 hr). One series of measurements was made approaching equilibrium from the reverse direction at a temperature of 500°C. Reaction temperatures were controlled to 1°C.

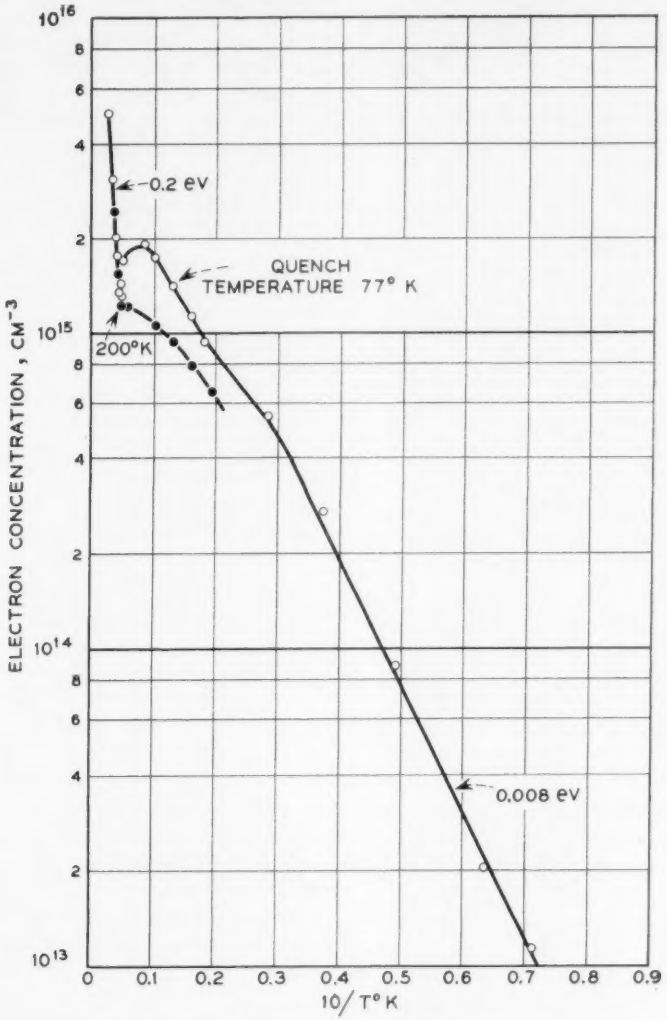

FIG. 2. Electron concentration vs. $1/T$ for a crystal containing $2{\cdot}2 \times 10^{17}$ cm^{-3} O showing the effect of quenching. The donors in this specimen were formed by heat-treatment received during growth.

B. *Electrical measurements*

All Hall effect and conductivity measurements were made on standard bridges[9] cut from the central portions of the doped crystals. Runs in liquid H_2 and liquid He were made to establish the lowest donor levels. Quenching experiments were performed by plunging the bridges and the mount into liquid nitrogen (77°K) after initial measurement at room temperature. The relaxation measurements were made by rapidly raising the quenched specimens to the desired temperature from liquid nitrogen temperature and measuring the change in Hall voltage with time at constant temperature.

Calculations of the electron concentration were made in the usual manner assuming $\mu_H/\mu_D = 1$. Ionization energies were determined by plotting $nT^{-3/2}$ vs. $1/T$ for the In-doped crystal ($n \ll N_A$ and $nT^{-3/4}$ for the oxygen-doped crystals ($n \gg N_A$). The latter plots provided one-half the ionization energy of the donor.

3. RESULTS

A. *Determination of donor levels*

In order separately to determine the ionization levels of the different oxygen-containing species, Hall effect measurements were carried out on specimens reacted under different conditions. Fig. 1 shows the results of runs made at 300°C on the crystal containing $2{\cdot}2 \times 10^{17}$ cm^{-3} O. Curve (a) was obtained after 3 hr, curve (b) after 66 hr and curve (c) is a re-run on curve (b) after quenching the specimen from 300°K to 77°K. It is seen that the electron concentration is markedly increased in the high temperature region by quenching from room temperature. This phenomenon is treated in detail in paragraph B below. Returning to curve (a) we note several slopes. The initial slope yields an ionization energy of 0·2 eV.* The next lower linear portion gives an energy of 0·0085 eV. This is believed to represent one-half the true level (0·017 eV) which appears at still lower temperatures. There is also an inflection in the curve just below 50°K. This has not been indicated in Fig. 1, but is evident on Fig. 2 and in particular on Fig. 3 as a 0·04 eV level. In the latter the 0·017 eV level has been compensated by adding indium.

There are present, therefore, three distinct donor levels, ~0·2, 0·04 and 0·017 eV in specimens which are only slightly reacted. It is tempting to assign these to the donors containing two, three and four oxygen atoms, respectively. However, as we shall see below, there are difficulties with this assignment.

B. *Donor relaxation*

We wish next to discuss the quenching phenomenon shown by curve (c) Fig. 1. Fig. 2 shows Hall results for the crystal containing $2{\cdot}2 \times 10^{17}$ cm^{-3} oxygen. The donors in this crystal were formed by heat treatment received during growth. It is noted that as the temperature is decreased from 300°K, a steep linear decrease in n occurs. This is the same process referred to above in connection with Fig. 1. The slope of the line, taken after correction for the shallow levels, is again about 0·2 eV.

At about 200°K an abrupt change to a second slope occurs. The lower curve (Fig. 2) was obtained upon *slow* cooling from 300°K. However, if the specimen was rapidly quenched in liquid N_2 (77°K) from 300°K, the upper curve was obtained. Decreasing the temperature below 77°K showed the presence of a shallow level corresponding to 0·016† eV. In Fig. 2, which includes only part of the data, the slope is halved because it is assumed that $n > N_A$. Fig. 2 like Fig. 1 also shows indication of a second level coming in between 25 and 50°K.‡ Results discussed below indicate that the energy corresponding to this level is about 0·04 eV. It is the concentration of this level which appears to be increased on quenching.

Of particular interest is the behavior of the upper curve in Fig. 2 when the temperature is increased above the quench temperature (77°K). As noted, a strong decrease in n occurs in the temperature range near 200°K. In fact, n is found to decrease at *constant temperature* in this region and this will now be described in detail in connection with Fig. 3.

The results in Fig. 3 were obtained on a Ge crystal which was doped both with indium ($4{\cdot}0 \times 10^{16}$ cm^{-3}) and with oxygen ($7{\cdot}0 \times 10^{17}$ cm^{-3}). The crystal was given the "heat-quench treatment" to insure that all oxygen was in the dissociated state and in solution initially. It was then reacted for 7 hr at 350°C, after which the resistivity at 25°C was 1·7 ohm cm n-type. The Hall effect

* A rather large error is present because it is necessary to subtract levels of lower ionization energy. Also because these lower energy levels prevent investigation of the deep level into the truly linear portions of the Hall curves, the value of 0·2 eV must be regarded as a lower limit. Since n is very likely greater than N_A, it is possible that this energy level is actually 0·4 eV.

† This is believed to be the 0·017 eV level mentioned earlier, within the error of measurement.

‡ This portion of the curve cannot be accounted for by assuming a single energy level. It can be fitted by assuming it is a composite of the 0·017 and 0·04 eV levels using an effective electron mass of 0·5 m_0.

was then run on this sample according to the following procedure: Referring to Fig. 3, the continuous curve shows the path followed when the measurements were made slowly, especially slowly in the neighborhood of 200°K. The dashed curves represent runs made after quenching to 77°K and raising the temperature as described above. Three relaxation runs made at constant

The relaxation curves shown on Fig. 3 follow first order kinetics within the error in the experiments. A plot of the corresponding rate constants against $1/T$ (Fig. 4) gives an activation energy of $6{\cdot}6 \pm 0{\cdot}8$ kcal (0·29 eV). A possible interpretation of this result will be given below.

Figure 3 also shows the same effect found in Fig. 2, namely that quenching results in the

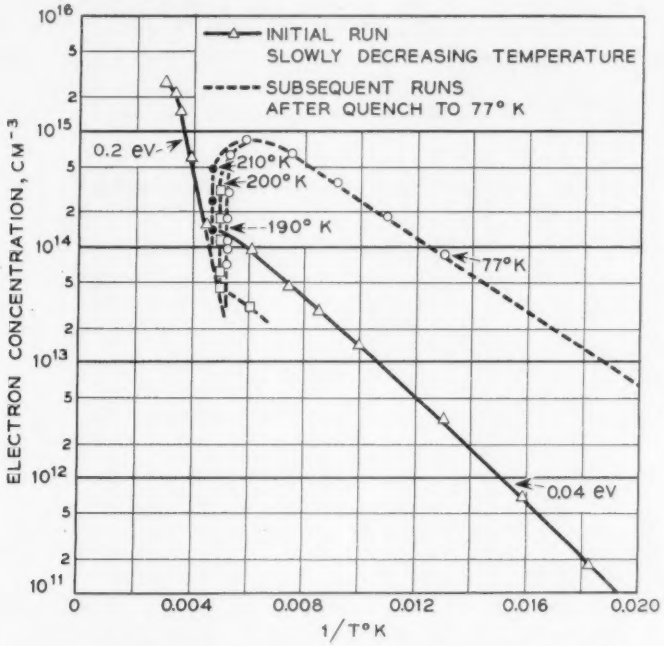

FIG. 3. Electron concentration vs. $1/T$ for crystal containing $4{\cdot}0 \times 10^{16}$ cm^{-3} In and $7{\cdot}0 \times 10^{17}$ cm^{-3} O after 7 hr at 350°C. Continuous curves show paths for slow cooling. Dashed lines show paths below and above quench point (77°K). Vertical dashed lines show relaxations at constant temperatures. Point at 164°K was obtained after relaxation at 200°K.

temperature are shown: 190, 200, and 210°K ($\pm 0{\cdot}3$°K). All of these runs, it will be observed terminate on the "steep" or "0·2 eV line".* At the end of the 200°K run, measurements made lowering the temperature, followed the dashed line to 164°K.

appearance of an enhanced concentration of the 0·04 eV level. The slope of 0·04 eV, as determined from Fig. 3, was obtained from a plot of $nT^{-3/2}$ vs. $1/T$ since N_A in this specimen is known to be very much greater than n.† The concentration of this level is dependent on the temperature from which

* The value of 0·2 eV found for this specimen which contains $4{\cdot}0 \times 10^{16}$ cm^{-3} In can be made to agree with that of Fig. 1 only if it is assumed that the In and O react to reduce N_A below n (see footnote * on p. 254).

† The slope of the "quenched" curve in Fig. 3 could not be obtained satisfactorily on account of the incidence of impurity conduction at low temperatures.

the quench to 77°K is made as well as on the rate of quench.

A comparison of the unquenched with the quenched results on Fig. 1 (curves (b) and (c) respectively), shows that the two coincide within error of measurement over the low temperature portions. This indicates that only one level, which we now identify as the 0·04 eV level, is involved in the transformation and that the lower level (0·017 eV) is unaffected.

It is found, furthermore, that the increase in n upon quenching passes through a maximum with a deep-lying donor level ($\geqslant 0{\cdot}2$ eV). Further discussion of this topic is given below.

C. *Dependence of Hall results on extent of forward reaction*

The approximate kinetics of the forward reaction (donor generation), based on room temperature resistivity measurements, have already been described.[5] Further information is furnished by the Hall measurements shown in Fig. 5 for the crystal containing $3{\cdot}9\times10^{17}$ cm^{-3} O, reacted at 300°C. Fig. 5 shows curves for reaction

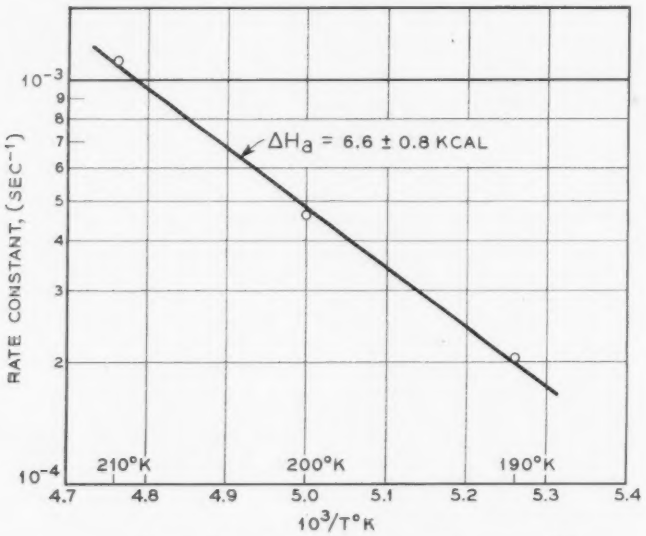

FIG. 4. Plot of relaxation rate constants vs. $1/T$.

time of reaction, as does the 0·2 eV donor concentration. However, in no case has more than 3×10^{15} cm^{-3} increase in n been observed at 77°C. Finally, the electron mobility has been observed to decrease upon quenching by an amount which can be explained by an increase in scatterers comparable to n. Similarly, a corresponding decrease in mobility occurs upon relaxation. These results suggest that a donor corresponding to a maximum concentration of about 4×10^{15} cm^{-3} is present at *room temperature* in specimens reacted to some intermediate stage, and that this donor has the special property of transforming with decreasing temperature to a structure which is neutral or has

times of 1, 4, 25, 89, 202, 561 and 1500 hr. The latter curve for 350 instead of 300°C, was obtained on a separate specimen. The reactions at 300 and 350°C are essentially both irreversible so that the 350°C curve may be taken as the complete reaction.[5] It is to be noted that as the reaction proceeds, the concentrations of the donors responsible for the lower levels, 0·04 and 0·017 eV, (given approximately by the extrapolation of the horizontal curves in Fig. 5) steadily increase, whereas, the donor represented by the deep level (0·2 eV) at first increases and then, if allowance is made for the donors of lower ionization energy, decreases.

Vol. 1
1961

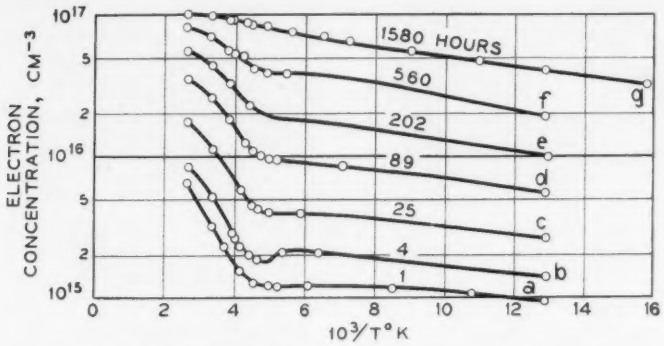

FIG. 5. Effect of extent of the forward reaction at 300°C for crystal containing $3{\cdot}9 \times 10^{17}$ cm^{-3} oxygen. Times of reaction are indicated. Uppermost curve is for reaction at 350°C (see text). The reaction times in hours are shown opposite each curve.

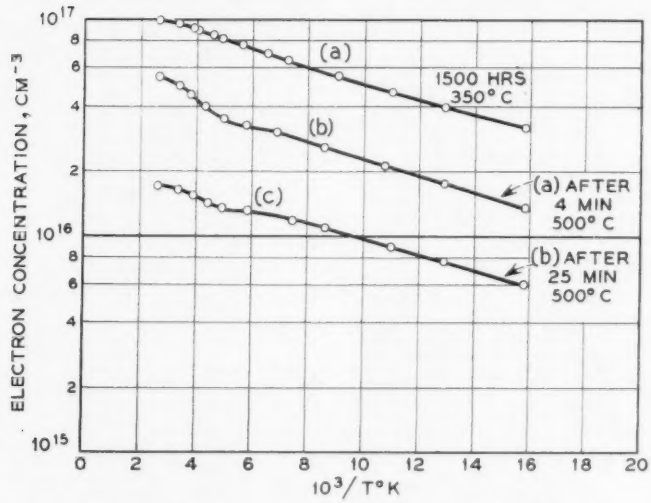

FIG. 6. Effect of extent of reverse reaction at 500°C on the "steep slope".

(a) $3{\cdot}9 \times 10^{17}$ cm^{-3} O after 1500 hr reaction at 350°C (curve g Fig. 5).
(b) Specimen shown in (a) after 4 min at 500°C.
(c) Specimen shown in (b) after 25 min at 500°C.

Figure 5 shows further that (1) the initial donor formed, presumably Ge*O_2 (Ref. 5) corresponds to the deep (0·2 eV) level, (2) as required by the series nature of the reactions, this donor goes through a concentration maximum during the reaction, (3) the lower energy donors increase in concentration progressively with reaction, finally becoming equal to 1/4 the original oxygen concentration.[3]

* As in Ref. (5) the asterisk is employed to designate the fact that the radicals are solutes and not separate oxide phases.

D. *Dependence of Hall results on reverse reaction*

The crystal shown in Fig. 5, which had been reacted to completion ($1{\cdot}0\times10^{17}$ cm^{-3} donors) at 350°C, was heated for 4 min and then for 25 min more at 500°C. The Hall results are shown in Fig. 6, in which curve (g) of Fig. 5 has been reproduced (curve a). It is noted that the steep portion is regenerated to some extent in curve (b) (4 min heat) but decreases in curve (c) (25 min heat). A detailed investigation of this behavior, which would be required in order to understand the detailed kinetics,[5] has not been made. The results indicate, however, that the donor species corresponding to the deep level (0·2 eV) is produced during both the generation and the dissociation reactions. Also, as in the donor generation reaction, the concentration of this species goes through a maximum, i.e. a temporary build-up of the Ge*O_2 donor occurs upon dissociation. This is further discussed below.

4. DISCUSSION

A. *Interpretation of donor levels*

As already mentioned above, there is ample evidence that the 0·2 eV level corresponds to the donor composed of two oxygen atoms. A donor having a deep-lying level has been recently reported[10] in epitaxial films of Ge on a single crystal Ge substrate and attributed to interstitial Ge atoms. In view of the results given here and the behavior of the level upon heat treatment as given in Ref. (10), it seems most likely that the reported level is to be attributed to O in the Ge layer.

Similarly the 0·017 eV level reasonably can be attributed to the donor containing four O atoms. It cannot, however, be excluded that this level (or one indistinguishably close to it) may not also arise from the structure containing three O atoms (See discussion below).

The level, found at 0·04 eV in the indium-doped crystal containing oxygen, and which shows the relaxation phenomenon on quenching, is more difficult to account for. The fact that the concentration of this level passes through a maximum upon reaction suggests it is associated in some way with the 0·2 eV level which behaves similarly. The relatively small concentration of this level, even in reacted specimens of crystals containing $4{\cdot}4\times10^{17}$ cm^{-3} O, also seems to preclude that it can be assigned to the species containing three oxygen atoms. One possibility is that it is a stereoisomer of the Ge*O_2 structure. We discuss this further in the next paragraph.

B. *Donor relaxation*

The donor relaxation phenomenon related to the 0·04 eV level is of particular interest. The explanation of this phenomenon is not known. Several facts, however, suggest that a reversible transformation with temperature occurs. Because of the rather high activation energy for the transformation, it is rather easy to quench-in the high-temperature (0·04 eV) form of the donor.

Similarly, the quenched-in form changes readily into the low-temperature form when the temperature is raised towards 200°K. With slow cooling the change ceases rather abruptly near 200°K. The latter fact suggests that when kT falls below about 170 cal (0·008 eV) the high-temperature form becomes locked-in. This energy is of the same order of magnitude as the tunnelling energy for oxygen between interstitial sites in Ge[11] and suggests that such tunnelling is prerequisite to the donor transformation.

The large value of the activation energy for oxygen diffusion[12] of 46 kcal (2·0 eV) precludes the change as being due to the movement of oxygen atoms over diffusion barriers. Hence, we conclude that the transformation is of the nature of a molecular rearrangement. The first order nature of the change also argues in favor of an internal rearrangement.

The detailed nature of the rearrangement is of course open to conjecture. One possibility is that, as already suggested, the Ge*O_2 species can exist in two forms. If the oxygen atoms occupy interstitial sites it is conceivable that reduced thermal energy may allow bond formation to take place between the oxygens. Atoms trapped in the low-energy well (corresponding to the tunnelling energy) may be prevented from transforming below ~200°K on this account. It should be pointed out, however, that the present results are not specific to a given structure. They could for example be due to oxygens not bonded to a common Ge atom.

The possibility that the 0·2 eV level may represent the heat of transformation rather than a

Vol. 1
196

donor ionization energy has been considered. This assumption, however, has to be dismissed because of the limit to the concentration of the high-temperature donor form which can be quenched-in. This limit is much less than the concentration of the 0·2 eV, for example, in the curves (a) to (g) of Fig. 5. In addition, equilibrium constants calculated for the two donor forms on the basis of the above assumption do not reproduce the observed curves as a function of temperature.

The ionization energy corresponding to the low-temperature form of donor has not been determined. This form could in fact be a deep-lying donor or an electrically neutral structure.

The model presented is consistent with the "bonded" form of donor having the higher ionization energy since the energy of the electrons in the system might be expected to be lower in this state. The possibility of a peroxide-type of linkage has been suggested.[13]

C. *Bearing of the results on reaction kinetics*

In a previous paper[5] the approximate kinetics of the donor formation and dissociation reactions have been discussed. It is evident from the more detailed knowledge of the donor ionization levels presented above that a quantitative treatment of the kinetics of the reactions still presents a formidable task. A brief discussion of the effect of the present results on previous ideas, however, is desirable.

It has generally been assumed in past treatments of the kinetics[6, 5] that the slow step in the series of reactions was the formation of the Ge^*O_4 donor. The approximate first order nature of the donor generation and dissociation reactions can be accounted for in this way.[6] While these assumptions may hold for reaction at higher temperatures, the curves of Fig. 6 suggest that at 300°C, the Ge^*O_2 species does not come to equilibrium rapidly, since the 0·2 eV level increases in concentration continuously with time up to at least 200 hours. No simplifying assumptions about the partial reactions appear justified under these circumstances and first order kinetics is then a poor approximation. Until the kinetics of the partial reactions are better understood it seems fruitless to attempt a more quantitative evaluation.

One of the features to be explained is the occurrence of maxima in the rate curves (Ref. 5). One possibility, suggested in Ref. (5), is that the Ge^*O_3 is a neutral or slightly-ionized donor so that its formation from Ge^*O_2 would result in a net decrease in over-all donor concentration. Another possibility is that both the Ge^*O_3 and Ge^*O_4 are easily ionized donors (i.e. they would be indistinguishable by means of the Hall measurements) and that the Ge^*O_2 initially formed dissociates later in the reaction in order to supply atomic oxygen for the formation of the higher molecular donors. At present, therefore, it is not clear where the species Ge^*O_3 fits into the reaction scheme and more work will be required using optical as well as electrical means of investigation before this question can be satisfactorily answered.

5. CONCLUSIONS

The present study of the reaction of oxygen by means of Hall and conductivity measurements confirms the previous findings that intermediate compounds containing less than four oxygen atoms are formed during the reaction. The structure containing four oxygens, Ge^*O_4, itself is a shallow donor. Its energy is believed to be 0·017 eV. Two deeper ionization energies are observed (0·04 eV and 0·2 eV) which are possibly related to the other intermediates (Ge^*O_2 and Ge^*O_3). The 0·2 eV donor level is reasonably associated with the Ge^*O_2 structure. Little evidence for a Ge^*O_3 structure is obtained from the electrical measurements.

A reversible change in donor properties with temperature has been observed. This transformation is shown to be of the nature of an internal rearrangement of oxygen atoms in the structure of a specific donor which it is suggested may be Ge^*O_2. It is shown that the changes observed are reasonably explained by movements (tunnelling) of the oxygen atoms without mounting diffusion barriers.

Hall results taken during the course of the oxygen aggregation reactions at 300°C show that the concentration of the donor responsible for the deep level (0·2 eV) at first increases and then decreases with extent of reaction. Likewise, the amount of the transformable donor (0·04 eV) passes through a maximum as the reaction proceeds towards completion. Dissociation of the

"stable" Ge^*O_4 donor at 500°C results immediately in the formation of considerable concentrations of the 0·2 eV donors. On continued reaction these disappear and the equilibrium donors are made up mostly of those having the shallow levels.

Acknowledgements—The authors are indebted to M. KOWALCHIK, W. KAISER and C. D. THURMOND who were responsible for growing the crystals employed in this investigation. Thanks are also due to KATHERINE WOLFSTIRN for help with the figures and calculations, J. P. MAITA for aiding with the Hall measurements and to H. J. HROSTOWSKI, H. REISS and N. B. HANNAY for useful discussions.

REFERENCES

1. ELLIOTT G., *Nature, Lond.* **180,** 135 (1959).
2. BLOEM J., HAAS C. and PENNING P, *J. Phys. Chem. Solids* **12,** 22 (1959).
3. FULLER C. S., KAISER W. and THURMOND C. D., *J. Phys. Chem. Solids* **17,** 301 (1961).
4. KAISER W., private communication.
5. FULLER C. S., *J. Phys. Chem. Solids*, in press.
6. KAISER W., FRISCH H. L. and REISS H., *Phys. Rev.* **112,** 1546 (1958).
7. HROSTOWSKI H. J. and KAISER R. H., *Phys. Rev. Letters* **1,** 199 (1958).
8. KAISER W. and THURMOND C. D., *J. Appl. Phys.* **32,** 115 (1961).
9. PEARSON G. L. and SUHL H., *Phys. Rev.* **83,** 768 (1951).
10. RUTH R. P., MARINACE J. C. and DUNLAP W. C., Jr., *J. Appl. Phys.* **31,** 995 (1960).
11. HROSTOWSKI H. J. and ALDER B., *J. Chem. Phys.* **33,** 980 (1960).
12. SOUTHGATE P. D., *Solid State Physics* Vol. I, p. 240. Academic Press, New York (1960).
13. Suggestion of HROSTOWSKI H. J.

Vol. 1
196

J. Phys. Chem. Solids Pergamon Press 1961. Vol. 19, Nos. 3/4, pp. 261–264. Printed in Great Britain.

THE EFFECT OF PRESSURE AND TEMPERATURE ON THE ABSORPTION EDGES OF THREE SILVER HALIDES*

A. S. BALCHAN and H. G. DRICKAMER

Department of Chemistry and Chemical Engineering, University of Illinois, Urbana, Illinois

(*Received* 19 *December* 1960)

Abstract—The effect of pressure to 160 kilobars, combined with temperature to 400°C has been measured on the absorption edge of AgCl, AgBr, and AgI. The behavior of AgCl and of AgBr is nearly identical. In the low pressure (f.c.c.) phase there is a red shift with pressure at low temperature. At high temperature the edge shifts blue with increasing pressure. A possible explanation in terms of the defect structure is proposed. The high pressure phase shows a normal red shift with pressure at all temperatures. The behaviour of AgI in the f.c.c. phase is anomalous both at room temperature and at elevated temperature.

THE CONTINUED effects of pressure to 160 kilobars and temperature to 400°C on the absorption edges of silver chloride, bromide, and iodide, was determined. The experimental techniques have been previously described[1,2,3]; the latest revised pressure calibration[4] was used. The silver halides used were from the same crystals used in the room temperature work.[2] The results for both the NaCl (f.c.c.) and CsCl (s.c.) phases of the three compounds are illustrated in Figs. 1, 2 and 3. The room temperature shift of the edge in all cases was obtained from the data of SLYKHOUSE[2].

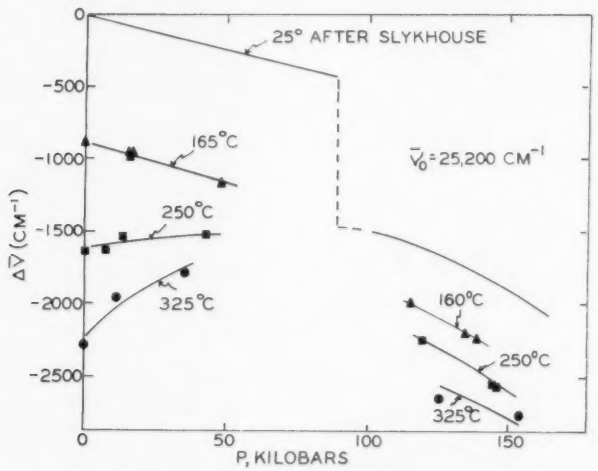

FIG. 1. Absorption edge of AgCl shift with pressure and temperature.

In the cases of the chloride and bromide, the

* This work was supported in part by the U.S. Atomic Energy Commission Contract AT(11-1)-67, Chemical Engineering Project 5.

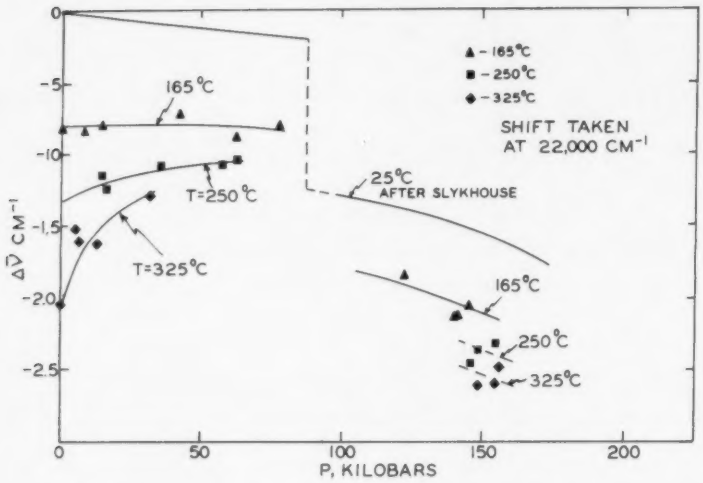

FIG. 2. Absorption edge of AgBr shift with pressure and temperature.

results are quite similar. At room temperature, the edge in both phases showed a shift toward lower energy with increasing pressure. At higher temperatures, the pressure shift in the sodium chloride phase of the bromide and chloride exhibited a reversal in sign, the magnitude of the reversal increasing with increasing temperature. Shift of the iodide in the sodium chloride phase was to higher energies with increasing temperature, with little or no trend toward reversal of the pressure shift.

In all silver halide "isobars", when a certain temperature was reached, an irreversibility was noticed, the displacement of the room temperature edge (upon cooling) from the initial value being greater than that due to a simple pressure loss on

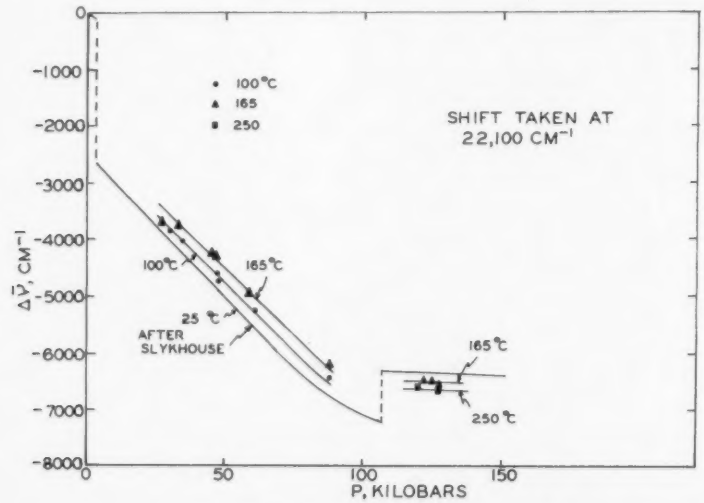

FIG. 3. Absorption edge of AgI shift with pressure and temperature.

heating. In the case of the iodide, the effect was quite severe, and a temperature of 165°C was the highest that could be reached reversibly. The irreversibility was probably associated with the flow of the sodium chloride from the center of the pellet, and subsequent reduction in effective cross-section of the sample, as it was noticed that the degree of irreversibility was directly proportional to the pressure loss at a given temperature and pressure. The effect on the iodide may have been due in part to the phase transition at 145°C.

The results given here are measurements after which the edge upon cooling of the sample was found to return to its value at room temperature; in short, all reversible results.

The shifts observed were relatively independent of wavelength, over a range of about 3000 cm^{-1}, but the data for all runs on a particular compound were taken at one value of wavelength (corresponding to an absorption coefficient of about 30 cm^{-1}).

The results of URBACH[5] show that in the long wavelength region of the edge (up to about 450 mμ in AgBr and 385 mμ in AgCl) the logarithm of the absorption coefficient is a linear function of wavelength (with a slope of $-1/kT$ in the case of the bromide). From this URBACH concludes that the absorption in this region is directly related to the thermal energy. Further measurements[6,7] indicate that this absorption is not an impurity effect.[8] The large effect of high temperatures on the pressure shift of the bromide and chloride in this work also leads to the conclusion that the absorption processes are due to a thermally-controlled mechanism.

Two possible reasons for the unusual behavior of the NaCl phase of the chloride and bromide at high temperatures can be proposed:

1. Let it be assumed that the long wavelength absorption consists primarily of the indirect transition u, that is, a transition from the valence band at the zone boundary to the conduction state at $\bar{k} = 0$. Then the blue shift with pressure at high temperatures would occur if either the conduction band shifted toward higher energies and the valence band remained relatively fixed, or the valence band became narrower faster than the conduction band shifted toward lower energies. Both of these alternatives seem improbable in view of results obtained in this laboratory on the fundamental absorption of other simple lattices. These invariably show a broadening of the bands with pressure.

2. The absorption at high temperature is caused by the defect structure of the crystal. As it has been proposed that the absorption is not associated with impurities, the defects concerned are probably thermally induced. Work in this laboratory on the effect of pressure on the optical absorption of imperfections has shown that a shift toward higher energies of this absorption with pressure is not unusual. In addition it has been shown that the equilibrium concentration of vacancies (predominantly Frenkel defects)[9,10,11,12] in the silver halides is quite high as the melting point is approached (about 2 atomic per cent).

In the high pressure (presumably CsCl) phase of the chloride and bromide, the pressure shift appeared quite regular with increasing temperature, the direction being toward lower energies with increasing temperature. There is no indication here of the reversal in sign of the pressure shift as exhibited by the NaCl phase. The data on the bromide in the high pressure phase is of necessity sparse, because of the difficulties in controlling the amount of sodium chloride extrusion, and hence the center pressure, at the higher temperatures. Data in the high pressure phase of the chloride were fortunately less erratic.

The regularity in the high pressure phase lends weight to the second hypothesis above. In the close-packed simple cubic phase, the energy required to produce a Frenkel defect would be quite high, and a much lower concentration of these defects would be expected than in the NaCl structure.

The shift of the edge with increasing temperature toward higher energies in the NaCl phase of silver iodide is anomalous with respect to the other halides, as is the room temperature shift. These facts appear to indicate that a different transition is occurring in the low-wavelength tail than in the other halides. In the high pressure phase, however, the pressure shifts at all temperatures resemble those in the bromide and chloride, with a steady displacement toward lower energy with increasing temperature. The anomalous blue shift across the high pressure transition shows a decrease in magnitude as the temperature is increased, and it is likely that the shift will reverse

ol. 19
1961

sign at about 300–350°C. Because of the large irreversibility accompanying the heating of the iodide in the NaCl phase to greater than 165°C, this effect could not be observed. It appears that the unusual blue discontinuity at room temperature may indeed be simply due to an oddity in the band structure, which becomes resolved at a high temperature.

Acknowledgements—The authors would like to thank Dr. F. C. BROWN of the Department of Physics for the AgBr crystal, and both Dr. BROWN and Dr. F. SEITZ for helpful discussions. Mr. A. S. BALCHAN would like to acknowledge assistance from a Consolidation Coal Company Fellowship and from an Autoclave Engineers Fellowship.

REFERENCES

1. FITCH R. A., SLYKHOUSE T. E. and DRICKAMER H. G., *J. Opt. Soc. Amer.* **47,** 1015 (1957).
2. SLYKHOUSE T. E. and DRICKAMER H. G., *J. Phys. Chem. Solids* **7,** 210 (1958).
3. BALCHAN A. S. and DRICKAMER H. G., *Rev. Sci. Instrum.* **31,** 511 (1960).
4. DRICKAMER H. G., *Rev. Sci. Instrum.*, in press.
5. URBACH F., *Phys. Rev.* **92,** 1324 (1957).
6. MOSER F. and URBACH F., *Phys. Rev.* **102,** 1519 (1956).
7. GILLEO M. A., *Phys. Rev.* **91,** 534 (1953).
8. BROWN F. and SEITZ F., *Photographic Sensitivity*, Vol. II (1957).
9. TELROW J., *Ann. Phys. Lpz.* **5,** 61, 71 (1949).
10. BERRY C. R., *Phys. Rev.* **82,** 422 (1951).
11. STRELKOW P. G., *Phys. Z. Sowjetunion* **12,** 77 (1937).
12. ZEITEN W., *Z. Phys.* **145,** 125 (1956).

Vol. 1
196

J. Phys. Chem. Solids Pergamon Press 1961. Vol. 19, Nos. 3/4, pp. 265–280. Printed in Great Britain.

ELECTRICAL RESISTIVITY CHANGES IN ANNEALED Cu_3Au ABOVE THE CRITICAL TEMPERATURE

A. C. DAMASK,* Z. A. FUHRMAN and E. GERMAGNOLI†

Laboratori C.I.S.E., Milano, Italy

(*Received* 21 *November* 1960)

Abstract—Changes in electrical resistivity of Cu_3Au which occur above the critical temperature have been studied in detail, both at temperature and after quenching. In general it has been found that the time required to establish a new equilibrium resistivity is several hours, and over the range of T_c to 700°C this time varies only by a factor of about three. The rates of changes at temperature are for the most part exponential, and a law for the behavior has been obtained. The changes occuring after quenching are much more complex. When the temperature is increased and an isothermal curve is obtained by quenching the wire after each time at temperature, there is a sudden increase of resistivity followed by a monotonic decrease. When the temperature is lowered, only a monotonic decrease is observed. These curves do not fit any simple kinetic equation. The final values of these resistivities obtained from the quenching data give two equilibrium states of resistivity, and a transition between them is observed at 600°C as suggested by other experimenters. When the lower of these two equilibrium resistivity states is established there is no longer a discontinuity in the electrical resistivity when the critical temperature is crossed. Only a single equilibrium state of resistivity was observed at temperature, however, and some possible effects of quenching are discussed.

1. INTRODUCTION

THE CLASSICAL theory[1] of short-range order has been developed on the basis of quasi-chemical theory, in which only the nearest neighbor interaction energy is considered. X-ray diffraction measurements on Cu_3Au have verified a more refined calculation of the magnitude of short-range order vs. temperature, but not quite in detail.[2] In addition to this lack of complete agreement between theory and experiment, there are other observations which seem to prevent a full understanding of the behavior of Cu_3Au above the critical temperature, T_c. Electron diffraction, for instance, has shown a persistance of satellite spots about the superlattice position well above the critical temperature, and these have been interpreted by RAETHER[3] in terms of domains of order, which in general are not reconcilable with the classical theory. Other investigations have revealed some anomalies in the physical properties of Cu_3Au above the critical temperature. One of the earliest observations was by SYKES and EVANS[4] who noted a hysteresis of electrical resistivity about T_c. BORIE and WARREN[5] measured the diffuse X-ray scattering of quenched samples and found more short-range order in the samples quenched from 620°C and 695°C than from 530°C. KUCZYNSKI *et al.*[6] found anomalies in several physical properties of quenched rods of this alloy, although their work contains the self-criticism that the quenching rate of large samples was probably not fast enough.‡ HIRABAYASHI *et al.*[7] repeated the heat release measurements and disputed the findings of KUCZYNSKI *et al.*, but reported that samples quenched from above 600°C seemed to contain more order than those quenched from below.

Some of these anomalies in the quenched samples can perhaps be explained by the motion of excess single or divacancies either during or

* Supported by a U.S. Secretary of Army Fellowship. Permanent Address: Pitman–Dunn Laboratories, Frankford Arsenal, Philadelphia, Pennsylvania.

† Laboratori C.I.S.E. and Istituto di Fisica del Politecnico, Milano, Italy.

‡ See footnote Ref. (6), p. 653.

after the quench, and this view is supported by experiments[6,8] which showed that the rate of decrease of electrical resistivity below the critical temperature increased with higher quenching temperatures. FEDER and NOWICK[9] have shown that the rate of growth of the superlattice reflection below the critical temperature increases with increasing quench temperature, which can also probably be explained in part by the excess vacancies which have been quenched in.

This simple interpretation in terms of excess vacancies is somewhat confused, however, by the observation of DUGDALE[10] that the longer a sample is held at 600°C before quenching, in the range of 0 to 340 hr, the faster is its rate of ordering below T_c.

Some other data from measurements of resistivity seem to point out that excess vacancies cannot be entirely responsible for the behavior observed in quenched specimens. DAMASK[11] quenched wires of Cu_3Au in water and found that the resistivity decreased with increasing quench temperature from T_c until about 500°C, at which temperature the resistivity began to increase, although quenching strains prevented the extension of these measurements to higher temperatures. The calculation of GIBSON[12] predicted that the residual electrical resistivity of Cu_3Au should decrease steadily with decreasing short-range order and the observed increase above 500°C was too large to be explained by quenched-in vacancies alone. SCHÜLE[13] repeated these measurements with foils, confirmed the findings of DAMASK, and further showed that the resistivity continued to increase from 500°C up to about 800°C. SCHÜLE also performed Hall coefficient measurements which resulted in the same shape of curve, i.e. a decrease above T_c followed by an increase above 500°C. This increase of Hall coefficient above 500°C indicates that all of this increase of resistivity cannot be assigned to excess vacancies but must reflect some state of the alloy.

These various phenomena indicate an insufficient knowledge of the effect of the motion of vacancies and divacancies in quenched alloys. Furthermore the above quoted phenomena which were observed at temperature cannot be so easily dismissed in terms of defects. For this reason the present investigation was made of the resistivity of Cu_3Au both at temperature and after quenching. An air quenching technique for heated wires was used which had previously been successfully employed for the quenching-in of vacancies in copper.[14] Although the quenching rate of this method, of the order of 1 sec, was relatively slow, this rate could be changed by simply varying the wire diameter. The technique has the virtue of excellent reproducibility for repeated quenchings, because of the elimination of drastic quenching in water.

It should be stated at the outset that the relatively simple behavior which was hoped for was not observed, but rather resistivity changes of considerable complexity were found, which are difficult to interpret in terms of the accepted properties of short-range order.

2. MEASURING TECHNIQUES

The Cu_3Au specimens were wires* whose diameters were 0·2, 0·07, and 0·04 mm: the most extensively used specimens were 0·2 and 0·07 mm in diameter, although similar results were obtained with the 0·04 mm diameter. Wires were sealed within a brass container, provided with electrical contacts, which was evacuated for the at temperature measurements, and filled with 1·1 atm of argon, previously purified by circulation through Ca–Mg alloy, for the quenching experiments. Typical quenching times in the argon atmosphere were 3 sec for 0·2 mm diameter wires and 1 sec for 0·07 mm diameter wires. These time intervals were those required for the wires to cool until their temperatures exceeded room temperature by less than a few per cent of the initial temperatures. In order to achieve a good uniformity of temperature along the major part of the wires, which were heated electrically, the 0·07 and 0·04 mm specimens were 12 cm long and the 0·2 mm specimens were 30 cm long. Previous tests of this technique[14,15] showed that end effects for these relations of length to diameter were confined within 4 per cent of the total length.

The measurements of resistivity during isothermal and isochronal annealings were performed at room temperature after quenching. The changes of resistivity were measured by comparing the

* Two different batches were used: one was the alloy of Ref. (11) and the other was supplied by Sigmund Cohn Corp.

voltage drops across the quenched specimen and a dummy sample, while absolute values of resistivity were obtained by comparing the voltage drops across the specimen and a standard resistor, and the reported ratios $\Delta\rho/\rho_0$ have an accuracy of about 10^{-4}. The explored interval of temperature ranged between T_c (388°C) and 870°C. The preliminary treatment of the wires consisted of 2–3 hr annealing at high temperature.

At temperature measurements were carried out *in vacuo* in order to avoid small fluctuations of wire temperature which could arise from convection phenomena close to the hot wires if the annealings were performed in an argon atmosphere. Because of the necessity of using a vacuum the times required to achieve temperature equilibrium after decreasing the temperature were of the order of 5 min. For reasons which will become apparent in the next section the following procedure was adopted for the at temperature measurements. The wire to be investigated and a dummy sample were simultaneously annealed at high temperature and thereby put into the same equilibrium state at a temperature T_1. Then the dummy specimen was annealed for several hours at a temperature T_2 to allow it to reach the corresponding equilibrium state. The temperature of the specimen to be measured was suddenly changed from T_1 to T_2 and the difference in resistivity between the two wires was continuously measured by means of a bridge circuit. Although the changes in resistivity of the specimen during the $T_1 \rightarrow T_2$ transition could be measured by this method, the absolute values of resistivity cannot be accurately determined because of the difficulty of measuring with precision the small amount of power required to heat the wire. After the few minutes required for the thermal transient of the specimen wire to end, the temperature difference of the two wires is estimated to be less than 2°C. This small temperature difference was achievable in spite of the changing resistivity of the specimen by having relatively large standard resistors arranged in series with each of the two wires in the bridge circuit.

The temperature calibration was made by

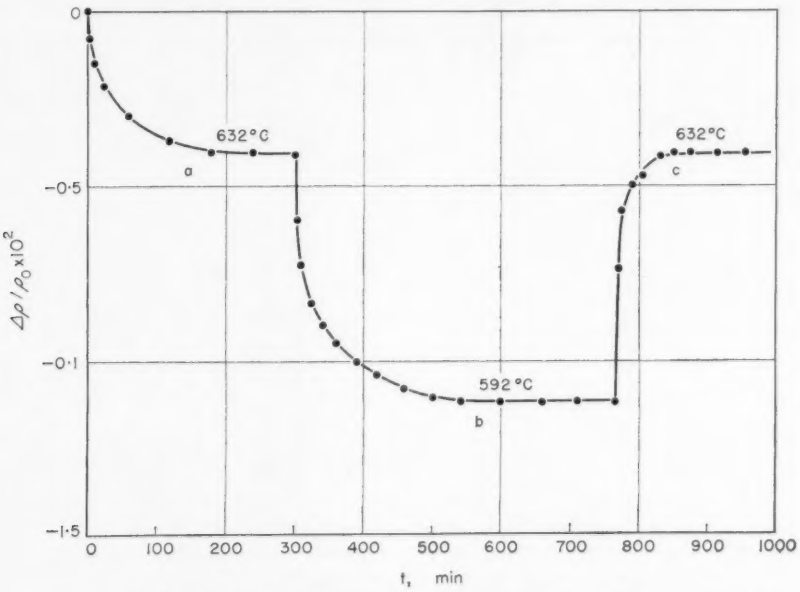

FIG. 1. Typical isothermal curves for a 0·2 mm Cu_3Au wire. Specimen annealed for 3 hr at 750°C, then brought successively to 632°C and to 592°C, and back to 632°C. Resistivity measured at room temperature after quenching.

placing a coil of 0·2 mm wire 1 meter in length in a vacuum furnace whose temperature was uniform within 0·5°C and constant within ± 0·2°C. The wire was held for several hours at each of many temperatures from T_c to 760°C during both an ascending and a descending temperature program. The result was one curve which could be resolved into two straight lines intersecting at about 580°C. The corrresponding slopes were $6{\cdot}9 \times 10^{-9}$ Ω cm/deg for the lower temperature region, and $8{\cdot}5 \times 10^{-9}$ Ω cm/deg for the higher temperature region. This break in slope at 580°C was reported by KUCZINSKI *et al.*[6], and the ratio of the present slopes is the same as the ratio of slopes reported by them. For this diameter wire and for the other diameters used, the temperature in all of the following experiments was estimated from the resistance.

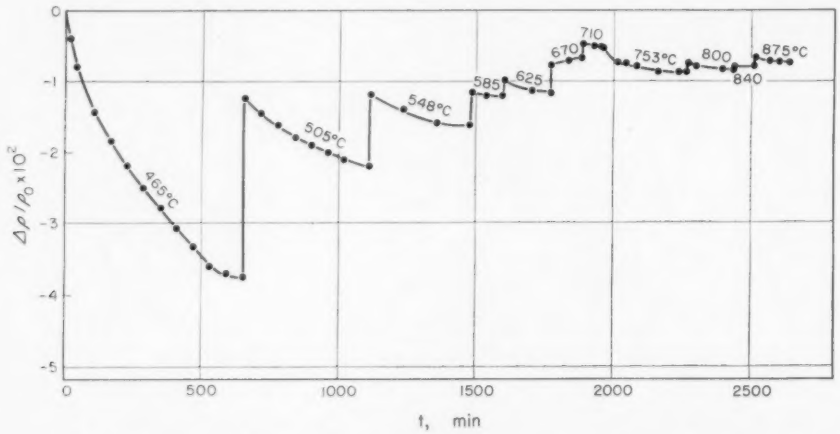

FIG. 2. Isothermal curves with ascending temperatures. 0·07 mm specimen preliminarily annealed at 890°C. Resistivity measured at room temperature after quenching.

3. EXPERIMENTAL RESULTS

(a) *Quenching experiments: isotherms*

A specific example of the general procedure which was performed with many wires will first be described. A 0·2 mm wire was annealed at 750°C for several hours and quenched. Then it was brought to a lower temperature T_1 and quenched after a few minutes of annealing at that temperature. The wire was then returned to the temperature T_1, held for some minutes and quenched again. This procedure was repeated and the resistivity was measured at room temperature after each quench. Typical results are shown in the first decay portion, curve a, of Fig. 1. After the last quench at T_1 the wire was brought to a lower temperature T_2 and the same procedure repeated. The result is shown by the second decay portion, curve b, of Fig. 1. After the last point at T_2 was obtained the wire was brought back to T_1 and the procedure was repeated. It can be seen from curve c, Fig. 1, that the resistivity returns to essentially the final value which was obtained in the first decay portion of Fig. 1. This kind of experiment was repeated, and similar results and magnitudes of change were obtained with 0·07 and 0·04 mm wires for temperatures ranging between T_c and 700°C. It was found, however, that if T_2 is selected as higher than T_1, at first there is a sudden increase in resistivity, and subsequent measurements show the same type of decay exemplified by curves a and b of Fig. 1. If the wire is then brought to other temperatures, each of which is higher than the previous one, an essentially similar behavior is observed, at least for temperatures lower than about 600°C. This is shown in Fig. 2. If T_2 is lower than T_1, and all the subsequent temperatures are lower than the previous ones, the observed behavior is the one shown in Fig. 3.

It was desired to examine the nature of the above described sudden increases in resistivity with

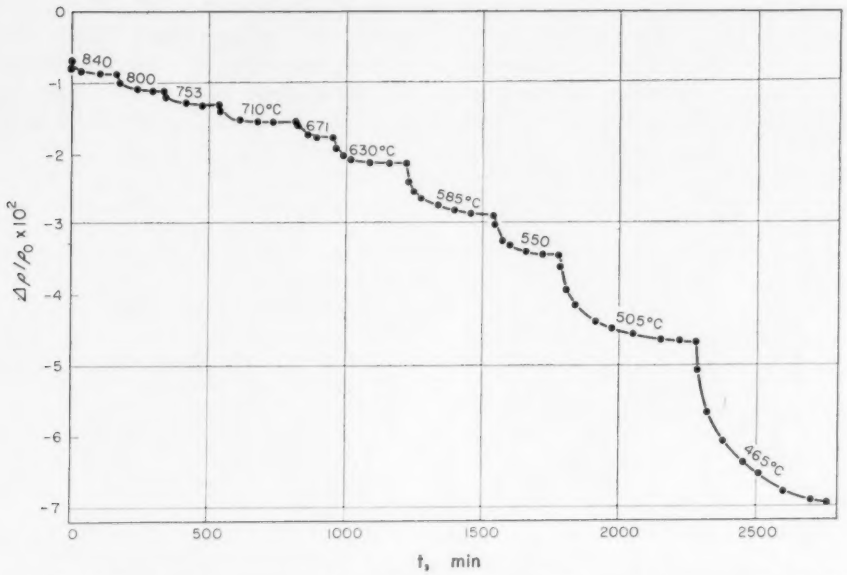

FIG. 3. Isothermal curves with descending temperatures. The same specimen as in Fig. 2.

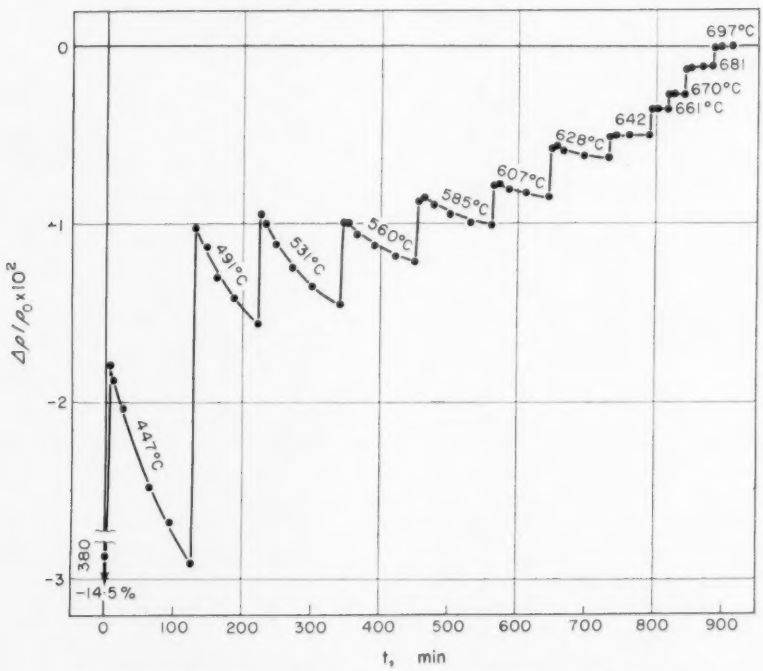

FIG. 4. Isothermal curves with ascending temperatures. 0·2 mm specimen preliminarily annealed at 750°C and partially ordered below the critical temperature.

increasing temperature in more detail. A large number of specimens was used and in general two types of behavior were observed. The first type is shown in Fig. 4 (in the curve shown the specimen was first annealed for a few hours below the critical temperature). The sudden increases in resistivity followed by a decay were observed at temperatures lower than about 640°C. The second type of behavior is illustrated in Fig. 5; the essential differences are that around 600°C a large decrease in resistivity occurs and that thereafter the phenomenon of sudden increase in resistivity followed by a decay continues with increasing temperature. The large decrease occurring around 600°C was observed to take place in several different ways in different samples; for example, a normal type of decay, as the ones shown in Fig. 1, would be in progress when a sudden drop in resistivity occurred, or the resistivity would decrease by oscillating irregularly. The decrease seems to occur in a narrow range of temperatures, above 560°C and below 620°C. No patterns of the difference between Fig. 4 and Fig. 5 were obtained: these different behaviors were found seemingly at random with different diameters of wires and with adjacent pieces of wire which had the same previous heat treatment. It should be noted that in these observations the wires were not held to the completion of the resistivity decay at the temperatures below 600°C, and each curve was made with a different temperature history. It is not known if this has an effect on whether or not the decrease appears, although Fig. 2, in which the decays are essentially complete, still shows the sudden increases below 600°C but no drop in resistivity around 600°C.

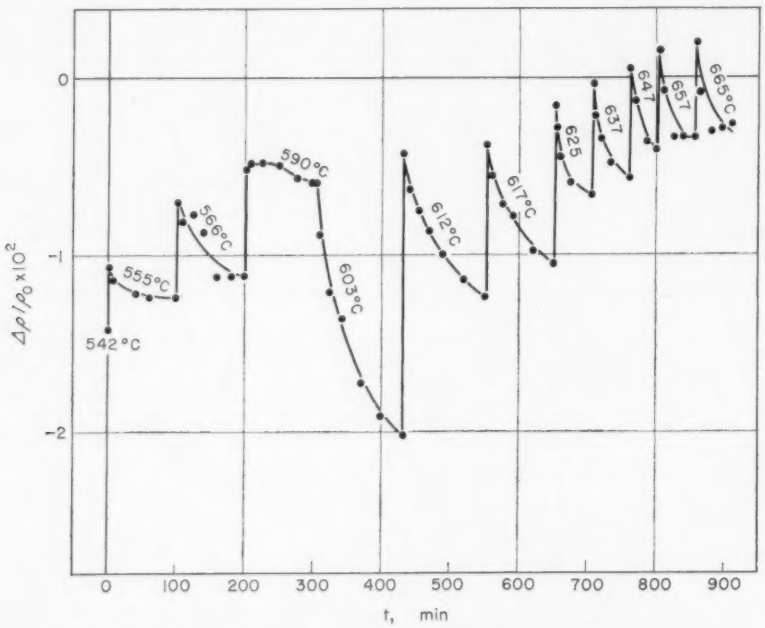

FIG. 5. Isothermal curves with ascending temperatures. 0·2 mm specimen preliminarily annealed at 750°C and brought into an equilibrium state at 542°C.

It was necessary to investigate in detail the phenomenon of the sudden increase in resistivity which occurred after an increase in temperature. The following features were observed:

(1) The occurrence of the sudden increase is at all temperatures independent of the time the sample was held at temperature before the first quench. The times examined were in

Vol. 1
1961

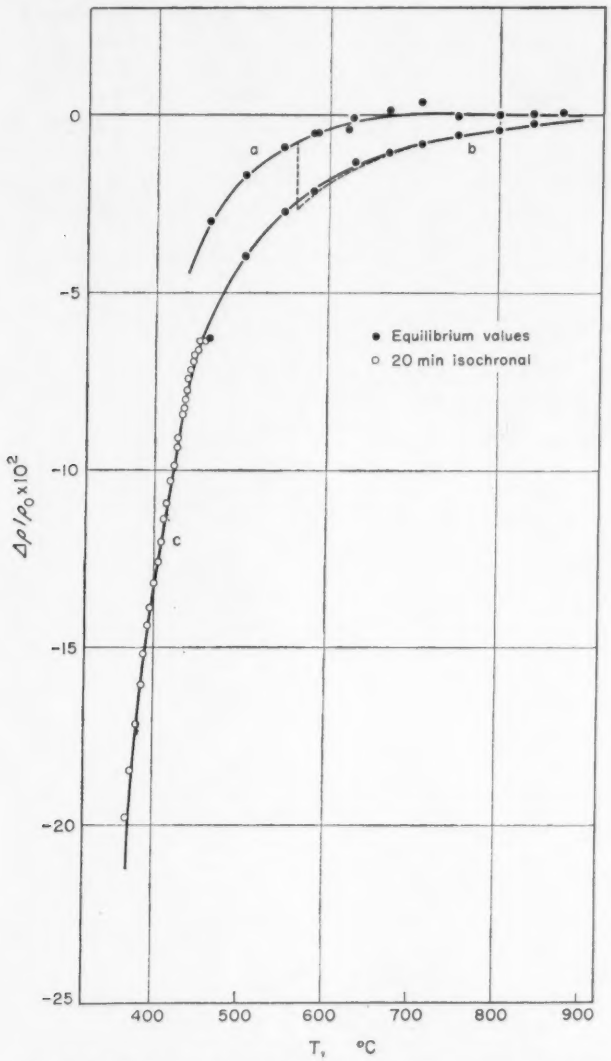

FIG. 6. Equilibrium values of resistivity vs. temperature for a 0·07 mm specimen (curve a deduced from Fig. 2 and curve b from Fig. 3). ○ Values of resistivity from a 20 min isochronal curve, performed with both descending and ascending temperatures.

the range of 1 min to 8 hr. The absolute value of the height of the sudden increase could not be obtained accurately because the evaluation of the initial resistivity required extrapolation of the curve at the preceding temperature, but the approximate magnitude is the same for all the examined times.

(2) The excess of the resistivity at the peak over the resistivity after the completion of the decay appears to be independent of the amount of time spent at the preceding lower temperature.

(3) The sudden increases of resistivity were found to be independent of the value of the

previous temperature. The increases of temperature ranged between 4 and 50°C; the effect of temperatures increases outside of this range was not studied.

(4) The amount of the sudden increase of resistivity after the first quench was observed to depend on the diameter of the wire; the smaller the diameter the smaller the sudden increase. For instance, the magnitude of the sudden increase in resistivity for the 0·2 mm wire was about a factor of three larger than that for the 0·04 mm diameter wire.

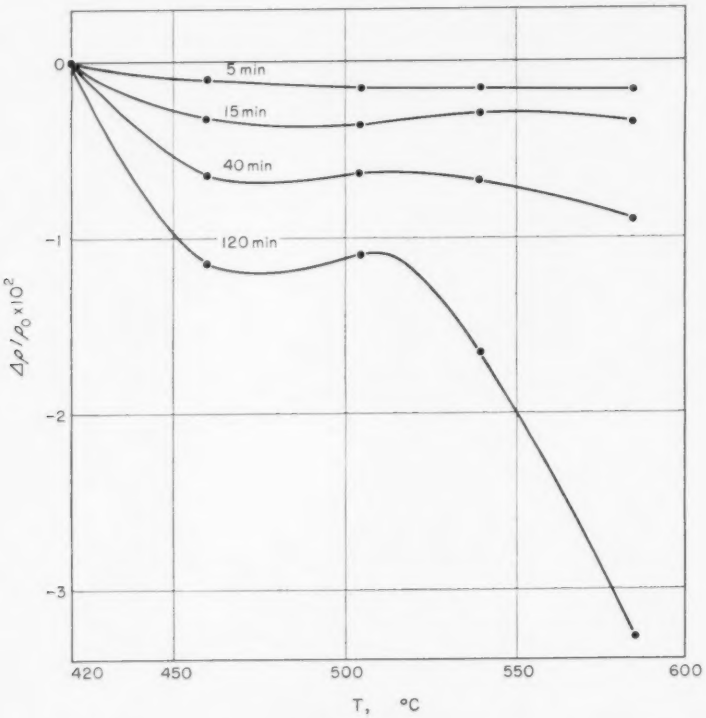

FIG. 7. Isochronal curves obtained with a 0·07 mm specimen, with the same temperature history before the initial point.

The final values of the resistivity, from curves given in Fig. 2 and Fig. 3, are plotted as solid circles vs. temperature in Fig. 6, the upper curve, labeled a, being the one obtained from the increasing temperature curves of Fig. 2, and the lower curve, labeled b, being the one obtained from the decreasing temperature curves of Fig. 3. The vertical dashed line gives the approximate magnitude of the decrease of resistivity around 600°C which occurred in a number of specimens exhibiting the phenomena like that of Fig. 5. The further dashed line is obtained from the lowest values of resistivity, averaged over a number of specimens, achieved by the successive decay curves above 600°C, as those shown in Fig. 5. It was also observed that in general the sudden increases at higher temperatures after the drop at 600°C were of the right magnitude to bring the corresponding initial resistivities to values in line with curve a of Fig. 6.

The curves obtained by quenching do not clearly obey any simple kinetic law. The closest comparison obtained was with a second order reaction, and the curves with decreasing temperature obey this law somewhat better than the ones

obtained from the decay following an increase in temperature.

(b) *Quenching experiments: isochronals*

Because the experiments of others, discussed in the introduction, were performed with samples held for different amounts of time above the critical temperature, it seemed desirable to perform isochronal annealings in order to see the effect of the decrease in resistivity which could occur around 600°C, indicated by the dashed curve in Fig. 6. After annealing at 750°C a wire was held for 5 min each at a series of increasing temperatures below T_c. This caused a decrease of resistivity due to the development of long-range order which was greater than the changes which will be shown. A 5 min isochronal curve was then made at temperatures above T_c. After having completed this isochronal curve, an annealing of several hours at 750°C was performed. Then the procedure was started again; the final temperature at which the wire was held for 5 min was 420°C,

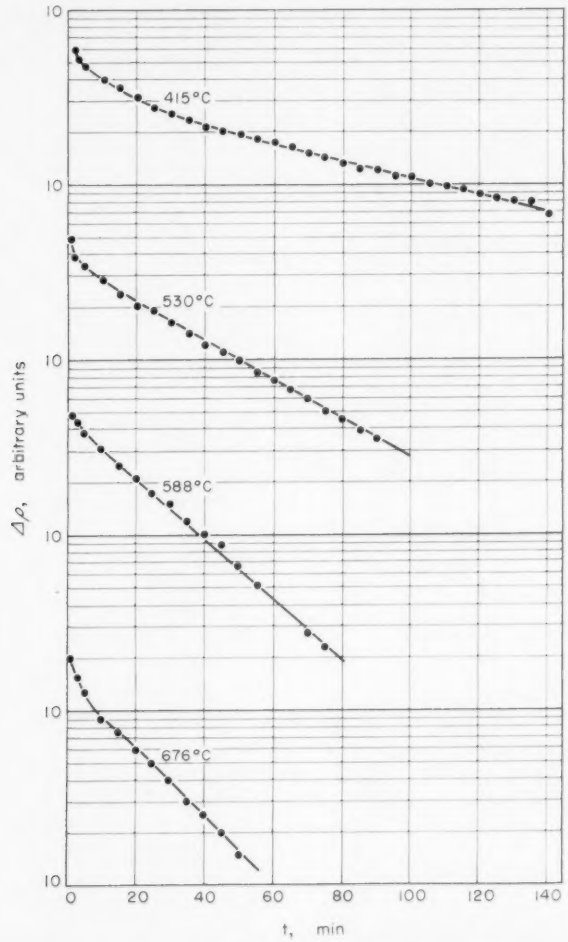

FIG. 8. Isothermal changes of resistivity at temperature. 0·2 mm wire cooled from 728°C to the indicated temperatures.

and a 20 min isochronal curve was made for the higher temperatures. In a similar way the other isochronal curves shown in Fig. 7 were performed. The 120 min isochronal clearly shows the tendency

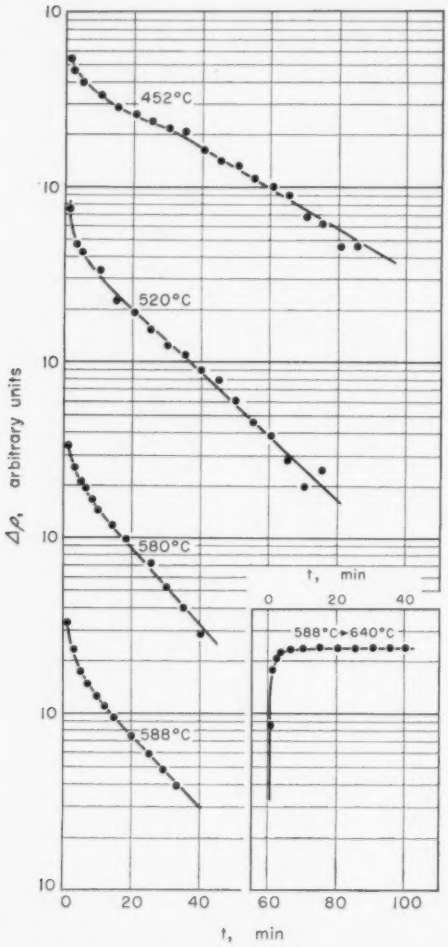

FIG. 9. Isothermal changes of resistivity at temperature. 0·2 mm wire cooled from 640°C to the indicated temperatures. The insert shows the rate of return to the initial state.

for the resistivity decrease indicated by Fig. 5 and by the dashed portion of Fig. 6.

In all these experiments a discontinuity of resistivity was observed at T_c, in agreement with all previous work.

Figure 6 seems to indicate, however, that two different states of resistivity of this alloy can be obtained by quenching. It was therefore desired to see if the discontinuity of resistivity occurred at the critical temperature if one passes through it from higher temperature after the lower equilibrium curve b of Fig. 6 was achieved. Because the resistivity changes or slight oxidation of the wire could alter the temperature calibration by a few degrees, a 20 min isochronal was carried out at two degree intervals, to insure coming within 1° of T_c (388°C), from the lowest temperature of curve b of Fig. 6, i.e. the equilibrium part marked by solid circles, to a temperature well below the critical temperature. It is seen from Fig. 6 that the minimum temperature was 365°C. This isochrone is shown in the lower temperature portion of the curve, marked with open circles and labeled c. After the final point was completed, the same isochronal annealing was performed with ascending temperatures. This ascending isochrone essentially superposed the descending isochrone shown. It is therefore seen from Fig. 6 that not only was a discontinuity not observed in the descending section of the curve, but that the expected discontinuity at the critical temperature was no longer observed in the ascending curve. After the wire was annealed at 870°C for 2 hr and partially ordered below T_c, an ascending isochronal curve showed the expected discontinuity at the critical temperature.

After the ascending isochrone was complete, but before the wire was reannealed at 870°C, some isothermal curves were made with ascending temperatures while the wire was still in the lower equilibrium state, curve b, of Fig. 6. These isotherms showed a sudden increase to an equilibrium value as in the third portion, curve c, of Fig. 1, and not the overshoot followed by decay shown in Figs. 2, 4, and 5.

(c) *At temperature experiments*

The procedure used for the at temperature measurements has been described in Section 2. Most of the at temperature data were taken with three initial equilibrium temperatures: 728°C, 640°C and 528°C. Typical examples of the curves which were obtained at temperature are shown in Figs. 8, 9 and 10. The latter portions of all these curves indicate an exponential decay, and therefore

the data are plotted semilogarithmically. The scale of resistivity is shown in arbitrary units because the transient after changing the temperature of the wires prevented accurate normalization. All the

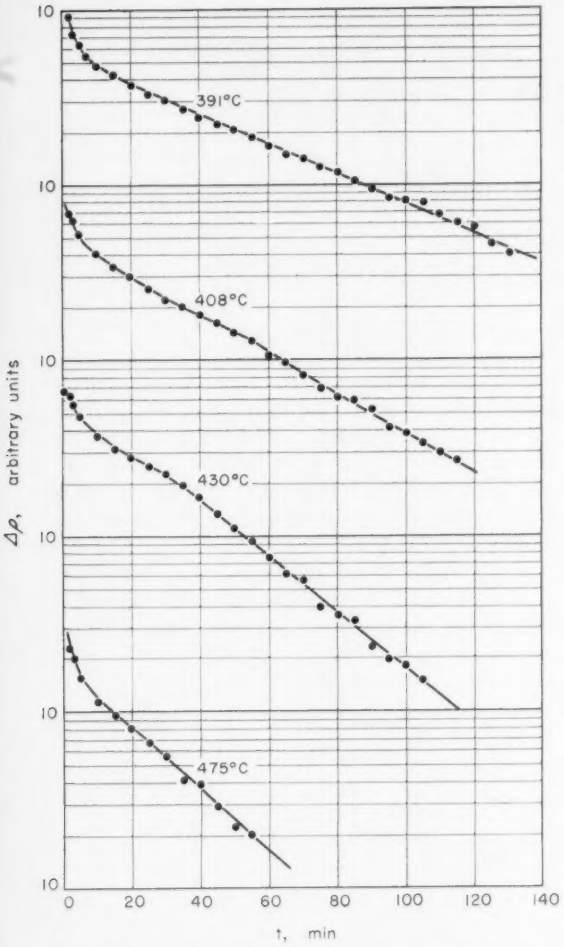

FIG. 10. Isothermal changes of resistivity at temperature. 0·2 mm wire cooled from 528°C to the indicated temperatures.

magnitudes of decreases in resistivity are of the same order however (about 0·5 to 1 per cent), and the curves are shown in the figures with one logarithmic cycle displacement.

The initial curvatures are in part due to the thermal transient, which was shown to be complete in about 5 min in copper wires of the same diameter; however, most of the initial curvatures persist to times longer than 5 min. Another anomaly is that most of the curves obtained from 528°C show the peculiar inflection around 30 min indicated by the 430°C curve of Fig. 10. An occasional curve from 640°C (indicated by the 452°C curve of Fig. 9) shows the same inflection point. Furthermore the inflection point never occurs at annealing temperatures above 500°C, and none of the curves from 728°C exhibit an inflection point.

After each of the curves the time to return to the initial high temperature state was also measured, and a typical example is shown by the insert in Fig. 9. The general feature is that the increase to the steady state value is very rapid and none of the overshoots observed in the quenching curves is present. The same magnitudes and rates of change occur in the other wire diameters.

The curves of Figs. 8, 9 and 10 show a general trend in behavior in the sense that the lower the annealing temperature the longer the characteristic time of the exponential portion. Table 1 lists the characteristic times measured from the slopes of the exponential parts of all the curves taken from these three initial temperatures.

Two important features can be observed: one is that the changes of the characteristic times over a range of 300°C is on the average about a factor 2–3, and on the extreme about a factor of 4; the second is that many irregularities exist with respect to the dependence of characteristic times on temperature. In fact, if one tries to plot the logarithms of the characteristic times vs. $1/T$ in the usual method with an Arrhenius equation, the result is a wide scatter of points over half a logarithmic cycle in time. This is shown in Fig. 11. The experimental points can only suggest that the limits which can be assigned are 0–6 kcal/mol for the slope and about 50–1500 sec for the τ_0 intercept. Although it is conceivable that some transformation could be taking place with such a small activation energy, the abnormally large value of τ_0 which apparently persists over a 300°C range suggests that these values of the constants should not be used to interpret the behavior of the system. The essential constancy of the τ values suggests a temperature dependent activation energy which

Table 1. Measurements with three initial temperatures: characteristic times calculated from curves like Figs. 8, 9 and 10 at different annealing temperatures.

728°C		640°C		528°C	
T°C	τ, sec	T°C	τ, sec	T°C	τ, sec
680	$1{\cdot}32 \times 10^3$	588	$1{\cdot}38 \times 10^3$	488	$2{\cdot}34 \times 10^3$
676	1·47	580	1·32	475	1·68
639	1·20	528	2·52	452	3·72
612	1·89	520	1·56	430	1·80
588	1·80	452	2·58	426	2·28
580	1·56			421	2·82
540	1·74			408	2·28
538	2·58			403	3·66
521	1·92			393	3·06
510	1·17			391	3·48
475	2·94				
415	5·88				

could be factored into separate terms. Since the meaning of the resulting equation remains speculative, this factored form will be discussed in the next section.

4. DISCUSSION

In an extension of the quasi-chemical theory IIDA[16] has shown that for small changes in short-range order the rate of return to equilibrium should be approximately exponential with the rate constant of the Arrhenius equation. Normal behavior of this type has been demonstrated in the α-brass system in both resistivity[17] and lattice parameter kinetics,[18] and it is therefore not unreasonable to expect the same type of behavior in other short-range ordering systems. However when the expected characteristic times for short-range order changes in Cu_3Au are calculated in the same way and compared with the observed times, surprising differences are immediately evident. If the mean

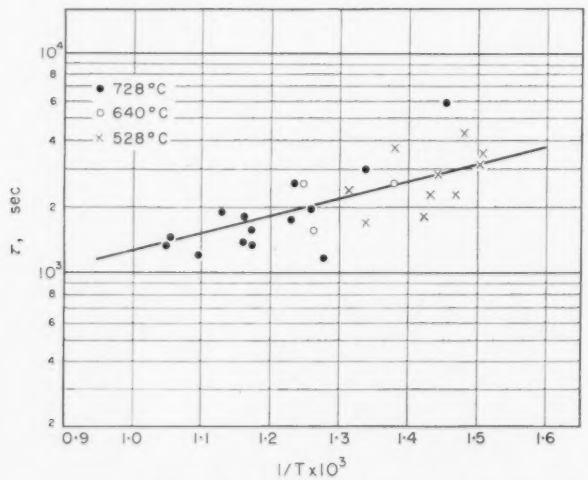

FIG. 11. Characteristic times of Table 1 vs. $1/T$. For the derivation of the curve see text.

atomic jump time is calculated from the Arrhenius equation

$$\tau = \tau_0 \exp [H/kT] \qquad (1)$$

with $\tau_0 = 10^{-13}$ sec and $H = 2{\cdot}03$ eV (46·7 kcal/mol), the value derived for Cu_3Au below the critical temperature by FEDER *et al.*[19] from the kinetics present experiment, 3×10^3 sec. No such arguments can be used to compare the observed factor of 3 change of time in the 300° range of observations given in Table 1 with the factor of 10^4 expected from the above simple calculation.

The temperature dependence of the activation energy mentioned in the preceding section is

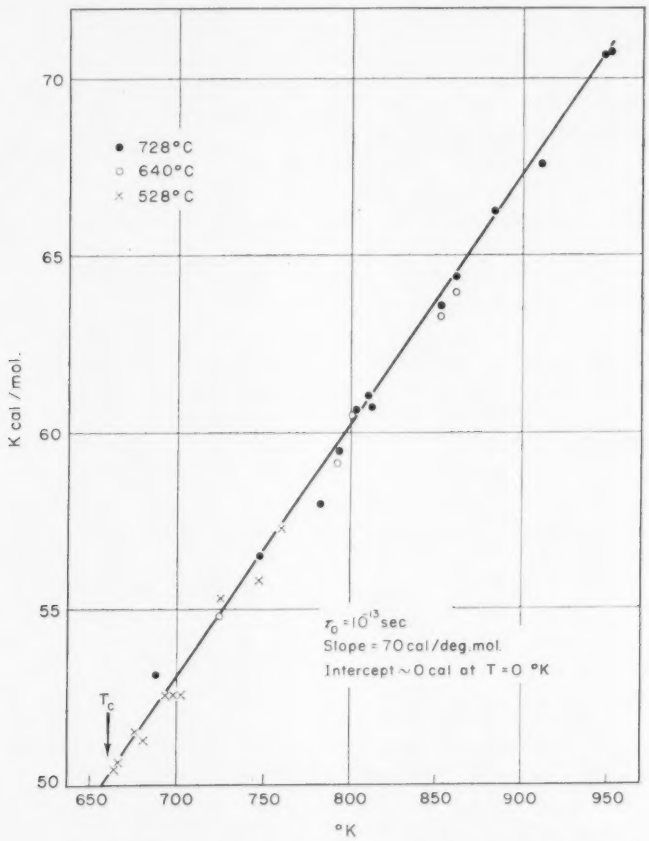

FIG. 12. Plot of activation energies vs. temperature calculated from the data of Table 1, assuming $\tau_0 = 10^{-13}$ sec.

of resistivity,[20] Young's modulus,[21] and lattice parameter changes,[19] the result is $\tau = 10^2$ sec at 400°C and $\tau = 2{\cdot}5 \times 10^{-3}$ sec at 700°C. Since it is expected that the degree of short-range order is changed by a few atomic jumps, it can be argued that the τ_0 used is in error by an order of magnitude and thus the calculated value at 400°C, 10^2 sec is actually compatible with the times observed in the examined in the following manner. τ_0 is held fixed at 10^{-13} sec and the Arrhenius equation is used to calculate H from the values of Table 1. The results are plotted in Fig. 12. The value of 50 kcal/mol at the critical temperature in this plot compares reasonably well with the value 46·7 kcal/mol calculated by FEDER *et al.*[19] and is therefore considered not to be coincidence. It

suggests, rather reasonably, that one of the terms to be factored is the activation energy for the interchange of atoms in this system. If the correction term for the degree of order is ignored and this activation energy held constant for temperatures below T_c, the equation of Fig. 12 can then be written as

$$\tau = \tau_0 \exp\left[\frac{50{,}000+70(T-T_c)}{RT}\right] \qquad (2)$$

and this can be rearranged into the form

$$\tau = A \exp\,[B/RT] \qquad (3)$$

where $A = \tau_0 \exp\,[70/R] = 2{\cdot}1 \times 10^2$ sec and $B = 50{,}000 - 70\ T_c \cong 3{\cdot}6$ Kcal/mol. These values give the line through the data of Fig. 11. However, although the internal agreements suggest that this method of factoring is correct, the meaning of equations (2) and (3) is not clear. It can of course be argued that the temperature dependent part of the exponent in equation (2) can be changed to an order dependent term, except that the magnitude of change seems to be too high. Also it is recognized that this equation can be rearranged into

$$\tau = \tau_0 \exp\left[\frac{70}{R}\left(1-\frac{T_c}{T}\right)+\frac{50{,}000}{RT}\right] \qquad (4)$$

so that the extra contribution appears as a changing entropy term. However, since this entropy term increases by about a factor of 10^4 between 400°C and 700°C it is felt that such a large variation could only arise from a changing configurational entropy. It should be recalled that configurational entropy involves the logarithm of the ratio of the number of atomic sites to the number of equivalent sites, and that the implication of equation (4) is that the structure is becoming less random with increasing temperature by a considerable amount. Such a conclusion does not seem warranted on the basis of present knowledge. Thus, although the treatment of the data is internally consistent, the meaning of equation (2) or its other forms is obscure.

Although an interpretation of the at temperature effects in terms of the above arguments might be possible, it is difficult to explain the observations of the quenching experiments. Since the sudden increase with increasing temperature is a function of the wire diameter and independent of the time before quenching, it is apparent that this increase is a result of the quench itself. Two factors which could be considered are the motion of excess vacancies and the motion of dislocations. The motion of excess vacancies would be such as to increase the order which would decrease the resistivity, and therefore they cannot account for the sudden increase. The more reasonable possibility is that the quenching strains cause dislocation motion which disorders the sample, thereby suddenly increasing the resistivity. However, although each quench is identical, it is seen from the data that apparently only the first quench causes this increase. If disordering by dislocation motion through a short-range ordered region is postulated, then each subsequent quench should produce at least the same value of resistivity, if not a higher one, and not the monotonically decreasing resistivity which was observed.

Rather than introducing some new concept such as a phase change to explain this behavior we prefer to attempt an interpretation on the basis of some existing experimental observations which suggest that two dimensional domains of order may exist above the critical temperature.

First we point out that RAETHER[3] observed domains by electron diffraction from T_c to 525°C, and assigned a possible structure to them in his interpretation. WATANABE and IWASAKI[22] suggested that there are other possible interpretations of RAETHER's data, but all interpretations require domains with different types of order. Second, although the surface energy would seem to be unreasonably high for two dimensional growth, two dimensional platelets of order on the (100) planes have been invoked by CHIPMAN[23] to explain his X-ray observations below T_c. If the surface energy is not a problem there seems to be no immediate reason why these platelets could not form on other planes including the (111) glide planes, and we now suggest that the passage of dislocations would destroy all except those on the glide planes. One obvious requirement to the proposal of platelet domains is that they have either very small dimensions or be of such a state of internal disorder as to render them invisible to X-rays above T_c, and to electron diffraction above 525°C.*

* It is interesting to note that CHIPMAN and RAETHER independently suggest a domain size of the order of 10 atomic spacings.

If these platelets are confined to the glide planes by the passage of dislocations during the first quench they would probably continue to grow on these planes so that subsequent dislocation passage would not affect them. This would account for the fact that only the first quench results in a large increase of resistivity. Since the rate of atomic interchange is very fast, a sudden increase in temperature could alter both the equilibrium state of domains and their internal order, and growth of domains could begin on other planes which would have to be destroyed again. This would explain the sudden increase every time the temperature is raised. If the temperature is lowered, however, the growth of the pre-established domains could continue on the glide planes without growth on the other planes which would explain the decrease of resistivity when the temperature is lowered. A return to the previous temperature should then only disrupt the new growth and yield the phenomena observed in Fig. 1. Such a structure of stacks of platelets on parallel planes could probably go into long-range order without first being completely destroyed. This ability would account for the lack of discontinuity in resistivity at the critical temperature in Fig. 6. The absence of the overshoot of resistivity with increasing temperature when the specimen is in the state defined by curve b of Fig. 6 would indicate that a stable growth on the glide planes has been established without growth in other directions and dislocation passage has nothing to destroy. The absence of the overshoot in the at temperature observations probably is a result of the slow temperature change which occurs when the wire is in a vacuum, and therefore there is not sufficient internal strain to cause much dislocation motion.

Since the proposed model is on the basis of domains it would suggest that the forms of equations (2) and (4) are both partly correct, and that the extra term in the exponent includes both a changing ordering energy and a changing configurational entropy.

The temptation to pursue the proposed model in explaining the rest of the observations will be resisted at the present time because it is highly speculative and needs supporting data, particularly diffraction and isothermal specific heat studies. Curves a and b of Fig. 6 are not understood, nor is it known how to get from one to the other except by the complicated program followed in this work. We are currently studying the thermal history dependence of these states with the aim of finding the simplest way of producing them. The data shown do support the conclusions of Refs. (5), (6) and (7) that a sharp change occurs in this alloy around 600°C, although on the resistivity scale this change is relatively small. The observations also show that under some, as yet unknown, conditions this change will be observed, but sometimes not.

It should be recalled that the observations at temperature showed only one value of resistivity with no anomalous changes and the expected resistivity discontinuity at the critical temperature. Except for the change in slope of resistivity vs. temperature mentioned in Section 2, all of the at temperature behavior was quite regular. The quenching data therefore indicate, both by differences of behavior and kinetics, that a measurement of a property of this alloy quenched to room temperature is not the same as a measurement at temperature.

Inspection of curve 3 recalls that any model to be proposed must account for at least a 7 per cent decrease in resistivity above the critical temperature; if curve 3 had been extended to lower temperatures, this resistivity decrease would probably be even larger as indicated by curve c of Fig. 6. Present theoretical knowledge of resistivity of ordering alloys relegates electrical resistivity to secondary importance as a measuring technique, since by itself it proves nothing positive and can only substantiate the findings by other techniques. However the writers feel that one positive conclusion can be drawn from these resistivity measurements, and it is that the present understanding of the details of short-range order in Cu_3Au is not satisfactory.

Acknowledgement—Appreciation is expressed to Miss C. Di Pietro for her assistance in making some of the measurements.

REFERENCES

1. Nix F. C. and Shockley W. M., *Rev. Mod. Phys.* **10,** 1 (1938).
2. Cowley J. M., *Phys. Rev.* **77,** 669 (1950).
3. Raether H., *Z. angew. Phys.* **4,** 53 (1952).
4. Sykes C. and Evans H., *J. Inst. Met.* **58,** 255 (1936).

5. BORIE B. and WARREN B. E., *J. Appl. Phys.* **27,** 1562 (1956).
6. KUCZYNSKI G. C., DOYAMA M. and FINE M. E., *J. Appl. Phys.* **27,** 651 (1956).
7. HIRABAYASHI H., NAGASAKI S. and KŌNO H., *J. Appl. Phys.* **28,** 1070 (1957).
8. BRINKMAN J. A., DIXON C. E. and MEECHAN C. J., *Acta Met.* **2,** 38 (1954).
9. FEDER R. and NOWICK A. S., *Phys. Rev.* **98,** 1152(A) (1955).
10. DUGDALE R. A., *Phil. Mag.* **1,** 537 (1956).
11. DAMASK A. C., *J. Phys. Chem. Solids* **1,** 23 (1956).
12. GIBSON J. B., *J. Phys. Chem. Solids* **1,** 27 (1956).
13. SCHÜLE W., Thesis, Max Planck Institut für Metallforschung, Stuttgart (1957).
14. AIROLDI G., BACCHELLA G. L. and GERMAGNOLI E., *Phys. Rev. Letters* **2,** 145 (1959).
15. ASCOLI A., ASDENTE M., GERMAGNOLI E. and MANARA A., *J. Phys. Chem. Solids* **6,** 59 (1958).
16. IIDA S., *J. Phys. Soc. Japan* **10,** 769 (1955).
17. DAMASK A. C., *J. Appl. Phys.* **27,** 610 (1956).
18. FEDER R., NOWICK A. S. and ROSENBLATT D. B., *J. Appl. Phys.* **29,** 984 (1958).
19. FEDER R., MOONEY M. and NOWICK A. S., *Acta Met.* **6,** 266 (1958).
20. BURNS F. P. and QUIMBY S. L., *Phys. Rev.* **97,** 1567 (1955).
21. WEISBERG L. R. and QUIMBY S. L., *Phys. Rev.* **110,** 338 (1958).
22. WATANABE D. and IWASAKI H., private communication. Although it is not suggested that Cu_3Au behaves in detail as other ordering alloys, the reader who is interested in a recent study of domains above the critical temperature is referred to the work on Cu_3Pd by WATANABE D., *J. Phys. Soc. Japan* **14,** 436 (1959).
23. CHIPMAN D. R., *J. Appl. Phys.* **27,** 739 (1956).

Vol. 1
196

J. Phys. Chem. Solids Pergamon Press 1961. Vol. 19, Nos. 3/4, pp. 281–290. Printed in Great Britain.

A.C. POLARIZATION EFFECTS IN THE IONIC CONDUCTIVITY OF POTASSIUM CHLORIDE CRYSTALS

A. R. ALLNATT* and P. W. M. JACOBS

Department of Chemistry, Imperial College of Science and Technology, London, S.W.7, England

(*Received* 23 *March* 1960; *revised* 15 *November* 1960)

Abstract—Measurements of a.c. capacitance and resistance have been made on single crystals of pure potassium chloride, and on potassium chloride containing up to $7{\cdot}0 \times 10^{-3}$ mole ratio of strontium chloride. The dependence of capacity on frequency, crystal thickness, temperature, and impurity content has been interpreted in terms of blocking of the charge carriers at the electrodes. However, the observed capacities are 10^3 to 10^4 times greater than those predicted by the theory of FRIAUF.

1. INTRODUCTION

THE IONIC conductivity of the alkali and silver halides, and of the halides containing small amounts of divalent cation impurities has been extensively studied in recent years. Such measurements yield information concerning the number and mobility of the Schottky and Frenkel defects responsible for the conduction, and also concerning the interactions between divalent impurities and cation vacancies.[1] It has long been known that polarization effects are often observed when measurements of d.c. conductivity are made. The current flowing under a constant applied potential decreases with time, reaching a steady value after a period varying from less than a minute to several hours.[2] More recently FRIAUF[3] has found polarization effects in the a.c. conductivity of silver bromide. The frequency-dependent capacity and resistance observed by FRIAUF were attributed to the finite rate of discharge of the charge carriers at the electrodes. The migrating carriers thus accumulate at the electrodes forming a space charge which gives rise to the additional capacity and resistance observed. Similarly, when a d.c. field is applied the space charge at the electrodes manifests itself as a "polarization voltage" which opposes the applied field and so reduces the effective field within the crystal. However, it has been realized that blocking of charge carriers at internal boundaries in the crystal could produce similar a.c.[4] and d.c.[5] effects. The unambiguous assignment of the cause of polarization effects has thus not always been possible. The purpose of this paper is to describe measurements of a.c. polarization phenomena in the conductivity of potassium chloride, both pure and containing small amounts of strontium chloride, over a wide range of temperature using platinum electrodes. These results will be compared with the only theory extant at present, that due to FRIAUF[3].

2. EXPERIMENTAL PROCEDURE

Single crystals of potassium chloride containing amounts of strontium chloride up to $7{\cdot}0 \times 10^{-3}$ mole ratio were grown *in vacuo* from Analar reagent chemicals by the Stockbarger method. The materials were pretreated at 100, 200, 300 and 500°C by a mixture of purified hydrogen chloride gas and nitrogen gas in a manner similar to that described by GARDNER *et al.*[6]. Single crystals of pure potassium chloride were also grown in air by the Kyropoulos method. No differences between the two batches of crystals were detected in the electrical measurements. Specimens were cleaved to rectangular parallelopipeds. The doped specimens were 3 to 4 mm thick with faces 10×10 mm. Pure crystals were cleaved to the same cross sectional area but the thickness was varied from

* Present Address: Institute for the Study of Metals, University of Chicago, Chicago 37, Illinois, U.S.A.

1 to 5 mm. The strontium contents were determined by X-ray fluorescence spectra or flame spectrophotometry with an accuracy of 5 per cent or better.[7] The specimens were held between platinum foil electrodes resting on insulating discs of recrystallized alumina. In some cases additional electrodes were applied by evaporation of platinum *in vacuo*. The electrodes and crystal were held under light compression applied from ventional variable ratio-arm Wheatstone bridge, which incorporated a Wagner earth to balance any stray capacities to earth. The measurements give the equivalent parallel resistance and capacity of the sample. Considerable care was exercised in the selection and the shielding of the components to avoid spurious effects. Sources of error are the capacity due to the unshielded length of leads inside the cell, and a small residual capacity, due

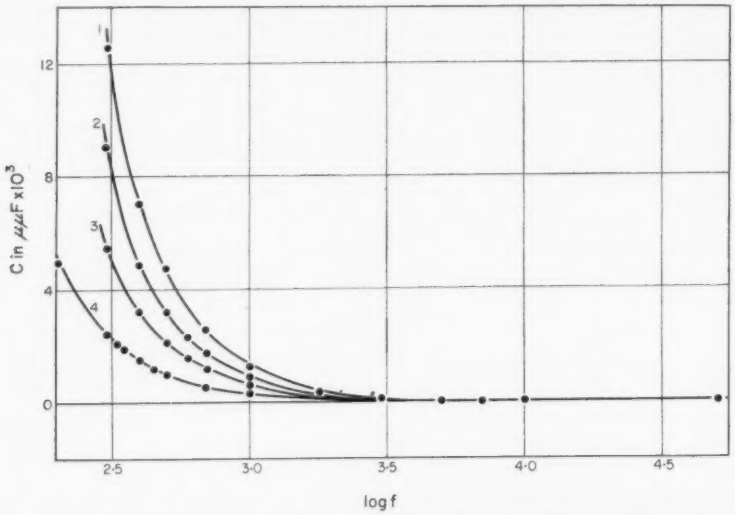

FIG. 1. Polarization capacity (in $\mu\mu F \times 10^3$) as a function of frequency for a KCl crystal containing $9{\cdot}7 \times 10^{-4}$ mole ratio $SrCl_2$. $2L = 0{\cdot}345$ cm; $A = 0{\cdot}803$ cm^2. Curve 1, 691°C; curve 2, 667°C; curve 3, 639°C; curve 4, 591°C.

springs situated outside the furnace. The temperature was measured by means of two thermocouples formed by welding a 13 per cent platinum–rhodium thermocouple wire to the back of each platinum electrode at its centre.

At the start of an experiment the apparatus was evacuated to 10^{-6} mm at room temperature and a gentle stream of purified nitrogen was passed thereafter. When no additional electrodes had been applied the temperature was first raised to 690–700°C for a period of one hour. This sufficed to perfect the contact between electrodes and crystal because of the slight plasticity of the crystal at high temperatures. Except where otherwise stated the measurements were made with the temperature descending after such an anneal.

The a.c. measurements were made with a conto imperfect winding and shielding of the balancing arm resistors, which caused the absolute value of the capacity to be in error by an amount which depended slightly on the resistance measured. However, at 50 kc the magnitude of the polarization capacity measured was negligibly small compared with the values at lower frequencies (Fig. 1). The capacity at 50 kc, which also included the geometric capacity of the sample was therefore subtracted from the values at lower frequencies. Using this procedure, polarization capacities greater than $10\mu\mu F$ could be measured with an accuracy of 1 to 2 per cent. The resistance could be measured to 0·1 per cent. Measurements were made in the range 300 to 50,000 c/s, and the performance of the bridge was extensively checked using standard components.

Vol. 196

Vol. 19
1961

3. EXPERIMENTAL RESULTS

Reproducibility

The conductivity of pure potassium chloride in the intrinsic range was within 10 per cent of the values of PHIPPS and PARTRIDGE[8]. The average value of the activation energy using data from six different runs was 44·9 ± 0·7 kcal in the temperature range 530–680°C. The capacities and conductivities were always unchanged if the crystal was held overnight at the temperature of measurement, except for the most heavily doped crystal. Here, the capacity increased irreversibly by 5 per cent at 636°C, while the conductivity remained unchanged. When the temperature of a pure crystal was cycled between 634 and 675°C for two days the capacities were reproducible to ± 5 per cent. However, after cooling to 548°C the capacity of a pure KCl crystal at 659°C was found to be 10 per cent lower. Measurements on a crystal with evaporated platinum electrodes (run 4c) gave much larger changes on thermal cycling. After the passage of d.c. current through pure KCl in the range 683–520°C, the capacity at 632°C was found to be 22 per cent lower than before this treatment.

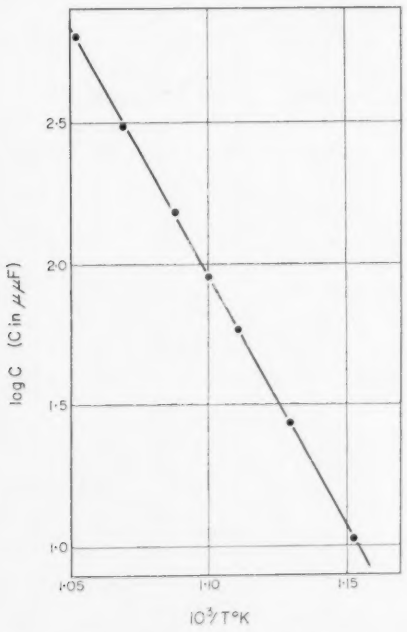

FIG. 2. The logarithm of the polarization capacity at 300 c/s in $\mu\mu$F as a function of T^{-1} for a KCl crystal with platinum foil electrodes. ($2L$ = 1·625 mm, A = 1·023 cm².)

Frequency dependence of the capacity

The capacity frequency measurements are summarized in Tables 1 and 2. The plots of log C vs. log f were always accurately linear and it is the slopes of these lines which are designated "frequency slope" in the tables. The slopes are recorded in the order in which the points were taken.

Temperature dependence of the capacity

The plot of log C vs. T^{-1} at 300 c/s was linear within experimental error for runs on pure potassium chloride without applied electrodes (Fig. 2). The slopes recorded in Table 3 refer to measurements made with descending temperature. For the impure crystals the plots of log C vs. T^{-1} were generally curved, as shown in Figs. 3 and 4. The reason for the greater scatter of the points in Fig. 3c is not known.

Dependence on thickness

The capacity at 300 c/s and 636°C of pure potassium chloride crystals is shown as a function of crystal thickness in Fig. 5. The straight line has been drawn with a slope of -2, thus verifying the relation $C \propto L^{-2}$.

Dependence on applied voltage

The capacity at 678°C in pure potassium chloride was independent of applied voltage in the range 0·28 to 3·0 V. The measurements on the impure crystals were made with applied potential differences of 100 mV up to 10^4 ohms and 800 mV up to 10^6 ohms. Changing the voltage by a factor of 2 again produced no change in the capacity.

Polarization resistance

A careful search revealed no frequency dependence of the resistance of pure potassium chloride. Only in the most heavily doped crystal ($7{\cdot}0 \times 10^{-3}$ mole ratio of strontium chloride) was the resistance a function of frequency. A typical graph showing this is given in Fig. 6. The polarization conductance was obtained in the same way as the polarization capacity, i.e. by subtraction of the value of $1/R$ at 50 kc from its value at lower frequencies. Plots of log $[-\Delta(1/R)]$ vs. log f were

Table 1. Frequency dependence of the polarization capacity in pure potassium chloride. The numbers given at each temperature are the slopes of the plot of log C vs. log f

Run number	Frequency slope at the temperature (°C)						Mean slope
16	685 1·68	656 1·68	632 1·63				1·66
7*	639 1·47	674 1·68	636 1·51	614 1·28	659 1·52	632 1·45	1·49
10	677 1·74	663 1·71	646 1·72	636 1·61	627 1·68		1·69
4c	(evaporated platinum electrodes) 591 1·23	608 1·24	627 1·20	592 1·19			1·22
4d	(evaporated platinum electrodes) 587 1·20	604 1·24	625 1·27	639 1·28			1·25
9	(silver paint electrodes) 697 1·48	674 1·53	656 1·56				1·52

* Annealed for 10 days in presence of electrodes.

Table 2. Frequency dependence of the polarization capacity in potassium chloride containing strontium chloride

Mole ratio Sr:K	Frequency slope at the temperature (°C)								Mean Slope
$14{\cdot}2\times10^{-5}$	688 1·71	660 1·72	637 1·74	613 1·76	586 1·73	559 1·75	534 1·73	513 1·70	1·73
$20{\cdot}3\times10^{-5}$	686 1·66	667 1·69	646 1·70	622 1·70	601 1·67	582 1·67	561 1·65	534 1·66	
$20{\cdot}3\times10^{-5}$			512 1·67	482 1·70					1·68
$53{\cdot}6\times10^{-5}$	689 1·75	662 1·75	635 1·75	610 1·76	570 1·71	544 1·70	509 1·68	454 1·76	1·73
$96{\cdot}8\times10^{-5}$	691 1·90	667 1·90	639 1·88	615 1·87	591 1·89	566 1·86	538 1·84	514 1·85	
$96{\cdot}8\times10^{-5}$		494 1·88	465 1·93	438 1·91	418 1·93	391 1·86			1·88
696×10^{-5}		685 1·79	661 1·80	636 1·81	639 1·82	613 1·81	583 1·80		1·80

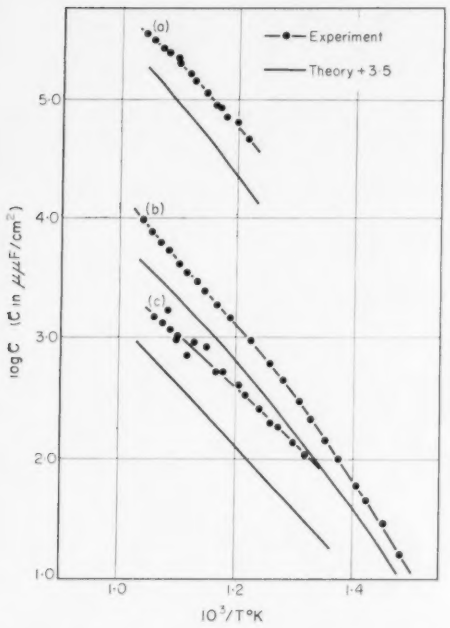

FIG. 3. Capacity at 300 c/s in $\mu\mu$F/cm^2 of Sr-doped crystals as a function of T^{-1}. Mole ratio Sr^{++}:K^+ for a is 696×10^{-5}, for b is $53{\cdot}6 \times 10^{-5}$ and for c is $14{\cdot}2 \times 10^{-5}$. The lines without points have been obtained by adding 3·5 to the calculated values of log C. Measurements on the most heavily doped crystal were limited to the temperature range in which the Sr^{++} remains completely in solution: at lower temperatures some precipitation of $SrCl_2$ occurs.

linear; the slopes are given in Table 4 in the column headed frequency dependence.

4. DISCUSSION

Polarization at the electrodes resulting from a finite rate of discharge of the charge carriers has been discussed theoretically by JAFFÉ[9,10] and FRIAUF[3].

The differential equations relating the concentrations of positive (p) and negative (n) charge carriers to the electric field E are

$$\frac{\partial p}{\partial t} = -\mu_p \frac{\partial (pE)}{\partial x} + D_p \frac{\partial^2 p}{\partial x^2} + k_1(c_0^2 - pn)$$

$$\frac{\partial n}{\partial t} = \mu_n \frac{\partial (nE)}{\partial x} + D_n \frac{\partial^2 n}{\partial x^2} + k_1(c_0^2 - pn)$$

$$\frac{\partial E}{\partial x} = \frac{4\pi e}{\epsilon}(p - n) \qquad (1)$$

where μ and D denote mobility and diffusion coefficients respectively, and c_0 is the equilibrium concentration of each species. The rates of formation and recombination of defects have been combined into the single rate constant k_1. The Einstein relation

$$\mu/D = e/kT$$

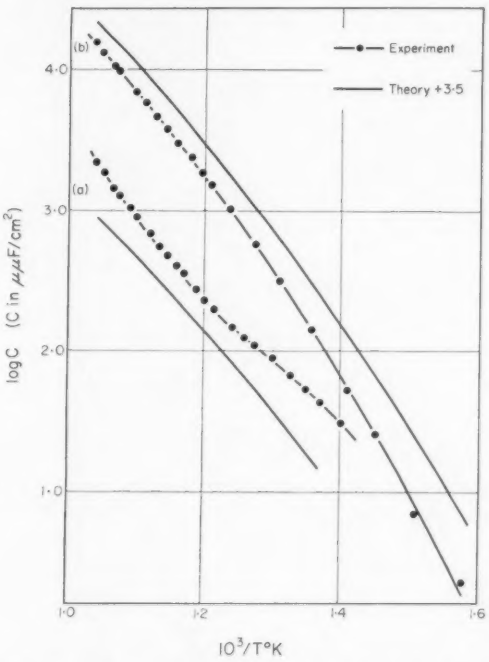

FIG. 4. Capacity at 300 c/s in $\mu\mu$F/cm^2 of Sr-doped crystals as a function of T^{-1}. Mole ratio Sr^{++}:K^+ is $20{\cdot}3 \times 10^{-5}$ for a and $96{\cdot}8 \times 10^{-5}$ for b. The lines without points have been obtained by adding 3·5 to the calculated values of log C.

is assumed for both species. JAFFÉ has given the d.c. solution to these equations assuming that the field is homogeneous and that the formation and recombination terms can be neglected. A solution for alternating applied fields has been obtained by FRIAUF. In order to linearize the equations he assumed that the applied voltage V may be expressed by

$$V(t) = V_0 + V_1 \exp jwt \qquad (a)$$

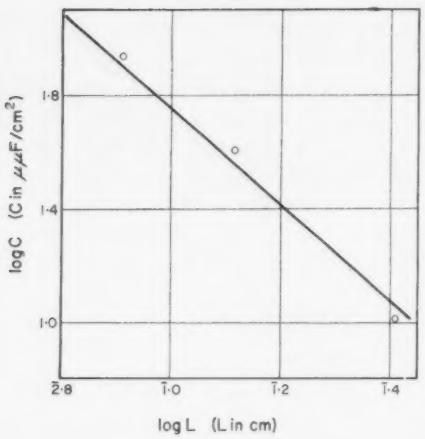

FIG. 5. Dependence of polarization capacity at 300 c/s on thickness for pure KCl at 636°C. The solid line is of slope −2 as predicted by the theory.

from which it follows that

$$p(x, t) = p_0(x_1) + p_1(x) \exp jwt$$

$$p_0(x) = c_0,\ n_0(x) = c_0,\ E_0(x) = 0. \qquad \text{(b)}$$

For certain limiting cases of the boundary conditions the results take relatively simple forms. When both charge carriers are completely blocked at the electrodes, that is when

$$i_p(\pm L, t) = 0 \text{ and } i_n(\pm L, t) = 0, \qquad (2)$$

$$C = C_0/[1+(\omega\tau)^2]$$

$$-\Delta(1/R) = 1/[1+(\omega\tau)^2]R_0 \qquad (3)$$

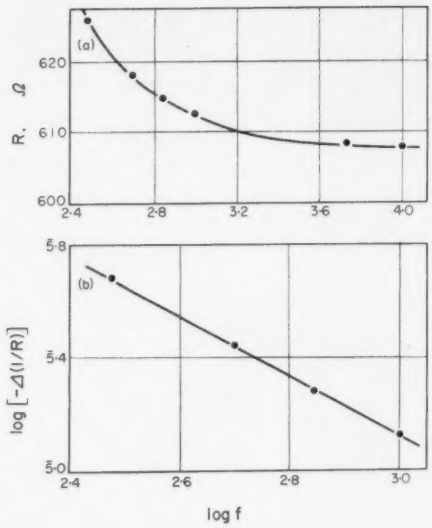

FIG. 6. Frequency dependence of resistance at 583°C of KCl containing 7×10^{-3} mole fraction of $SrCl_2$. (a) R vs. $\log f$. (b) $\log [\Delta-(1/R)]$ vs. $\log f$.

where

$$R_0 = 2L/[e(\mu_p+\mu_n)c_0] = 2L/\sigma$$

$$C_0 = \epsilon\alpha/4\pi\sqrt{2}$$

$$\tau = R_0C_0 \text{ and } \alpha^2 = 4\pi e^2c_0/\epsilon kT$$

As implied by the boundary conditions (2) the origin has been placed at the centre of a crystal of length $2L$.

The equations for the cases when positive carriers are free and negative carriers blocked $(\infty, 0)$, and positive carriers blocked and negative ones free $(0, \infty)$ have also been given by FRIAUF[3],

Table 3. Temperature dependence of polarization capacity in pure KCl

Run number	E(kcal/mole)	E(eV)	Temperature range (°C)
16	84·8	3·68	686–594
7	76·3	3·31	675–590
10	80·1	3·47	676–594
Mean value	80·4	3·49	
4c (ascend)	52·1	2·26	590–529
4c (descend)	58·0	2·51	627–572
4d (ascend)	67·3	2·92	639–569
9	73·2	3·18	697–636

Table 4. *Polarization conductance at* 300 *c/s for a* KCl *crystal containing* $SrCl_2$ *in the mole ratio* Sr : K = 696×10^{-5}. ($A = 0{\cdot}748$ cm^2; $2L = 0{\cdot}549$ cm)

Temperature (°C)	$-\Delta(1/R)$ at $f = 300$ c/s	$\frac{\omega C}{-\Delta(1/R)}$ at $f = 300$ c/s	Approximate frequency dependence
685	$1{\cdot}844 \times 10^{-4}$	2·64	
661	$1{\cdot}369 \times 10^{-4}$	2·70	1·26
639	$1{\cdot}169 \times 10^{-4}$	2·61	1·24
583	$4{\cdot}93 \times 10^{-5}$	2·45	1·07

and the equation for the impurity region where only cation vacancies produced by immobile divalent impurity ions are present, has been derived by NIMOMIYA and SONOIKE[4]. For comparison with our results, it is convenient to eliminate the diffusion coefficients from these equations in terms of the total conductivity and the transport number t_n and t_p, giving

$$\omega C = \frac{\sigma^{3/2}}{\sqrt{2}L^2} \times \frac{t_n^{3/2}}{(2t_p)^{1/2}} \left(\frac{kT}{Ne^2}\right)^{1/2} \times \frac{1}{\omega^{1/2}}$$

$$= -\Delta\left(\frac{1}{R}\right) \qquad (\infty, 0) \qquad (4)$$

$$\omega C = \frac{\sigma^{3/2}}{2\sqrt{2}L^2} \left(\frac{kT}{Ne^2}\right)^{1/2} \times \frac{1}{\omega^{1/2}}$$

$$= -\Delta\left(\frac{1}{R}\right) \qquad \text{(Impurity region)} \qquad (5)$$

Possible criticisms of the theory are the neglect of non-linear terms (justified if $eV_1 \ll kT$), the neglect of the static space charge[12] in the d.c. solution (b) above and the fact that rectification effects are not included.

We consider first the results for runs with no applied electrodes. The mean value of the slopes of the plots of log C vs. log f is 1·62 for pure potassium chloride. This is in moderate accord with the value 1·50 predicted for the $(0, \infty)$ and $(\infty, 0)$ cases (equation 4). Log C vs. T^{-1} curves were calculated from the observed conductivity using equations (3), (4) and (5), the transport numbers being obtained from the diffusion data of LAURENT and BENARD[11]. The results are summarized in Table 5. A value of zero for the blocking parameter means that the charge carrier concerned is completely blocked while a value of ∞ indicates that it is completely unblocked. The activation energy observed is in accord with the $(0, \infty)$ case although the order of magnitude of C is nearer that for $(\infty, 0)$. Blocking of both carriers is excluded by the value of the frequency slope.

Table 5. *Summary of theoretical and experimental results for polarization capacity in pure* KCl (*for* $2L = 0{\cdot}161$ cm, *as in run* 10, *and* $f = 300$ c/s, $T = 636$°C)

Value of the blocking parameter for		C ($\mu\mu$F/cm^2)	T slope (kcal/mole)	Frequency slope
Anion vacancies	Cation vacancies			
∞	0	0·120	58·1	1·5
0	∞	0·013	82·3	1·5
0	0	110	74·8	2·0
experimental		87	80	1·62

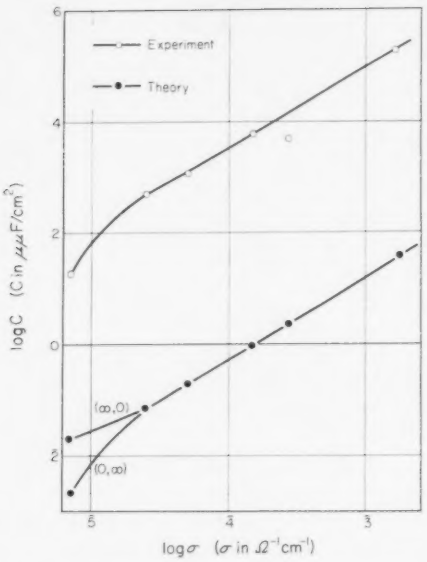

FIG. 7. Variation of polarization capacity at 300 c/s with conductivity for KCl crystals containing $SrCl_2$. Experimental results have been adjusted to $2L = 0{\cdot}4$ cm. $T = 636°C$.

The frequency dependence of capacity in the impure crystals was fairly constant from temperature to temperature. However, the mean value for the slope, which varied from 1·68 to 1·88, appears to be significantly higher than the 1·50 predicted by equation (5) for complete blocking of the cation vacancies. Values of the blocking parameter intermediate between 0 and ∞ would not however be in accord with the accurately linear log C vs. log f curves. The agreement between the shapes of observed and calculated log C vs. T^{-1} curves is reasonable with the exception of the crystal containing $2{\cdot}0 \times 10^{-4}$ mole fraction of strontium chloride.

The values of capacity at 636°C and 300 c/s were corrected to the values expected for a crystal of thickness 4 mm using the square law predicted by the theory (which was verified for pure potassium chloride).

For the impure crystals the graph of log C vs. log σ is a straight line of slope 1·43 compared with the predicted value 1·50. When the values for the pure crystal are included the general shape of the curve agrees with (0, ∞) rather than (∞, 0) (Fig. 7), in accord with the conclusion above. The experimental point lying below the upper line in Fig. 7 refers to the crystal which had an exceptionally long anneal before measurements were made.

The polarization resistance at 300 c/s (see Table 4) is of the order of magnitude predicted from the theoretical equation

$$\omega C = -\Delta(1/R)$$

although $\Delta(1/R)$ varies as approximately ω^{-1} rather than $\omega^{-1/2}$. The smallness of the effect precluded a detailed study.

Apart from the large discrepancy in magnitude between observed and calculated effects, which is discussed below, these results are in accord with FRIAUF's theory provided that we assume that in the pure crystals (intrinsic region) anion vacancies are blocked and cation vacancies free while in the doped crystals the cation vacancies are completely blocked. It is worth emphasizing that the choice between (0, ∞) and (∞, 0) is independent of the present uncertainty in the values of transport numbers in pure potassium chloride. Noting that the transport number of cations is $t_K = \sigma_K/\sigma$ so that

$$\frac{d \log t_K}{d(1/T)} = \frac{t_{Cl}(E_{Cl} - E_K)}{R}$$

where E_{Cl} and E_K are the activation energies for diffusion of chloride ion and potassium ion respectively, it is easily shown that, for the (∞, 0) case:

$$\frac{d \log C}{d(1/T)} = \frac{3}{2} \times \frac{d \log \sigma}{d(1/T)} + \frac{(E_{Cl} - E_K)(\frac{1}{2} + t_{Cl})}{R} \qquad (6)$$

The observed values are:

$$\frac{d \log C}{d(1/T)} = \frac{-80 \times 10^3}{R};$$

$$\frac{3}{2} \times \frac{d \log \sigma}{d(1/T)} = \frac{-67{\cdot}4 \times 10^3}{R}$$

Whatever the value of t_{Cl} the observed and calculated values of $d \log C/d(1/T)$ cannot agree unless $E_K > E_{Cl}$ and this is certainly not true. Our original choice of (0, ∞) based on LAURENT

and BENARD's data (see Table 5) is thus independent of possible inaccuracies in this data.

It is not clear, why in spite of agreement in general character, the observed capacities should be a factor of 10^3 to 10^4 greater than those calculated from the theory. A similar discrepancy observed in silver chloride has been attributed[4] to the blocking of cation vacancies at internal barriers in the crystal. However, this is ruled out by the dependence of C on L^{-2} in the pure crystal since for internal blocking C should vary as L^{-1}. Enhancement of polarization effects by the higher defect concentration at the surface, due to the space charge effect discussed by LEHOVEC[12] and others is unlikely to account for such a large factor. (Using the values of MOTT and LITTLETON[13] for the work done in taking an anion, and in taking a cation, from a normal lattice site to infinity, the surface concentration is found to be only a factor of five greater than in the bulk at 600°C).

A possible reason for the discrepancy is that FRIAUF's theory assumes that $eV/kT \ll 1$. For $V =$ 100 mV, $eV/kT \simeq 1{\cdot}3$ at 600°C. However, the independence of C of applied voltage, and the absence of harmonics in the bridge balance in all but the most heavily doped crystal, suggest that this is not the cause. A further approximation is that $4\pi e^2 nD/EkT$ is assumed $\ll 1$. This is approximately so for the pure crystal, but not for the more impure ones. However, the fact that the discrepancy does not vary much with impurity content argues against this as the major cause. The consistently high values of the frequency slope may be due to these approximations and it is evident that the equations of FRIAUF are not really adequate for the alkali halides at such high temperatures. D.C. measurements have also been made on these and other crystals. The results are again more complex than the JAFFÉ theory might lead one to hope and will be discussed in a forthcoming paper.

The behaviour of the crystal with evaporated platinum electrodes (Fig. 8) is similar to that observed by FRIAUF for silver bromide with painted silver electrodes; he also noted a decrease in capacity after passing direct current. The layer of platinum vanished during the experiment, presumably by diffusion into the salt. Although the capacities without additional electrodes are more reproducible than with applied electrodes, the anomalously low capacity of the doped crystal which was annealed in the presence of the electrodes before measurements (Fig. 7), and the tenacity with which the clean foil will stick to the crystal after annealing, suggest that a very slow chemical reaction of the materials may be taking place.

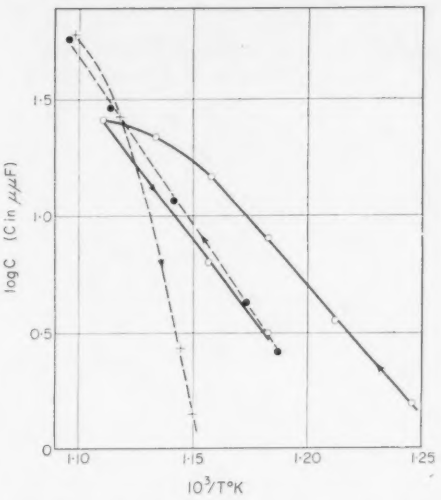

FIG 8. Dependence of polarization capacity at 300 c/s on T^{-1} for pure KCl with evaporated platinum electrodes. Arrows indicate the direction of the thermal cycling.

Acknowledgements—We are indebted to Dr. E. E. SCHEINDER for the loan of Dr. PARKER's thesis and to The Chemical Society for a grant towards the cost of apparatus used in this research.

REFERENCES

1. LIDIARD A. B., *Handbuch der Physik* **20,** 246 (1957).
2. Much of the earliest work has been reviewed by JOFFE A. F., *The Physics of Crystals.* McGraw Hill, New York (1928).
3. FRIAUF R. J., *J. Chem. Phys.* **22,** 1329 (1954).
4. NINOMIYA T. and SONOIKE S., *Photographic Sensitivity*, (Tokyo Symposium), Vol. II, p. 81. Maruzen, Tokyo (1958).
5. PARKER N. S. and SCHEINDER E. E., *Nature, Lond.* **178,** 326 (1956); PARKER N. S., Thesis, University of Durham (1954).
6. GARDNER H. J., BROWN C. T. and JANZ G. J., *J. Phys. Chem.* **60,** 1458 (1956).
7. ALLNATT A. R. and JACOBS P. W. M., to be published.

8. PHIPPS T. E. and PARTRIDGE E. G., *J. Amer. Chem. Soc.* **51,** 1331 (1929).
9. JAFFÉ G., *Ann. Phys. Lpz.* **16,** 217, 249 (1933).
10. JAFFÉ G. and LE MAY C., *J. Chem. Phys.* **21,** 920 (1953).
11. LAURENT J-F. and BENARD J., *J. Phys. Chem. Solids* **3,** 7 (1957).
12. LEHOVEC K., *J. Chem. Phys.* **21,** 1123 (1953).
13. MOTT N. F. and LITTLETON M. J., *Trans. Faraday Soc.* **34,** 485 (1938).

Vol. 1
196

J. Phys. Chem. Solids Pergamon Press 1961. Vol. 19, Nos. 3/4, pp. 291–298. Printed in Great Britain.

A STUDY OF A DILUTE CONCENTRATION OF DISORDER IN THE β-Cu–Zn SUPERLATTICE

J. S. CLARK* and N. BROWN†

Metallurgy Department, University of Pennsylvania, Philadelphia, Pennsylvania, U.S.A.

(*Received* 15 *August* 1960; *revised* 8 *December* 1960)

Abstract—A study was made of the disorder quenched in β-Cu–Zn. At low temperatures, 25–250°C, the predominant defect appears to be a wrong pair of Cu and Zn atoms whose observed value of energy of formation is 7·2–8·0 kcal/mol. The energy of motion during reordering is 14 kcal/mol. and it appears that a vacancy is trapped in the vicinity of a wrong pair of atoms.

1. INTRODUCTION

THE STRUCTURE sensitive properties of solid solutions are not completely understood because the detailed structure of solid solutions cannot be measured directly. The deviations from the completely random solution which have been recognized are clustering, short range order, and long range order; it is these details of the atomic distribution which are responsible for the complexity of their behavior. If one superposes non-equilibrium states which are produced by quenching, the situation becomes even more complex. Thus the behaviour of quenched alloys is still far from being understood as shown by the work of WECHSLER and KERNOHAN[1, 2], NOWICK and SLADEK[3] and the discussion between DIENES and WECHSLER[4, 5]. It appears that the quenched-in concentration of vacancies in alloys is greater than that in pure metals so that any investigations of alloys are still far in advance of existing theories. Even theories of long range order are no more than mathematical idealizations which do not completely describe the atomic distribution. Perhaps the many experimental observations cannot be properly explained until the actual atoms are observed with a microscope.

This paper is specifically concerned with an investigation of the effect of qnenching on the electrical resistivity of β-Cu–Zn. There has been previous work on β-Cu–Zn by SMITH[6], GREEN and BROWN[7], BROWN[8] on the effect of quenching on the yield point, and by CLAREBROUGH[9] on internal friction. Previously SMITH found no resistivity effect on quenching.

In the large, we would like this paper to be considered as an investigation of defects in a system which is almost completely in a state of long range order. Thus far, all attempts to quench-in a large amount of disorder in β-Cu–Zn have been unsuccessful. In this investigation, it is believed that the basic system is a matrix of long range order in which may be quenched a small but nearly equilibrium amount of disorder. The decay and the activation energy of formation of this small amount of disorder have been investigated.

2. EXPERIMENTAL

The β-Cu–Zn specimens were made from extruded 0·070 in. wire. The analysis was 51·5 per cent Cu with 0·01–0·001 per cent Fe as the major impurity, and the remainder Zn. The wires were milled flat to a thickness of 0·013 in. Specimens were water quenched and then immediately placed in liquid nitrogen at which temperature the resistivity was measured. The decay in resistivity was done isothermally at various elevated temperature and appropriate times after which the specimen was quenched to liquid nitrogen in order to measure the resistivity.

Some specimens were designed so that both

* Engineer, E. I. du Pont de Nemours, Inc., Wilmington, Delaware.

† Professor of Metallurgy, Metallurgy Department, University of Pennsylvania, Philadelphia, Pa.

yield point and electrical resistivity could be measured on the same specimen in order to correlate the electrical resistivity measurements with previous investigations of the yield point.

It was found that a single specimen could be used to investigate the effect of quenching temperature on electrical resistivity because all quenched-in resistance could be annealed out completely at low temperatures so that the prior thermal history of the specimen was completely erased. The investigation was conducted with several specimens all of which gave identical results except that each had a somewhat different residual resistance.

3. RESULTS

The variation of quenched-in electrical resistivity with quenching temperature was observed over the range of 50–530°C. Fig. 1 is a typical result. The degree of long range prior to quenching was obtained from X-ray data by CHIPMAN and WARREN[10]. The quenched-in resistivity for high quenching temperatures around T_c is related to a prior investigation of the yield point by BROWN[8]. The change in resistivity which is produced by quenching from below 350°C is an entirely new and surprising observation. It is to be noted that the magnitude of the quenched-in resistivity is large compared to that which can be quenched into pure metals for comparable quenching temperatures.

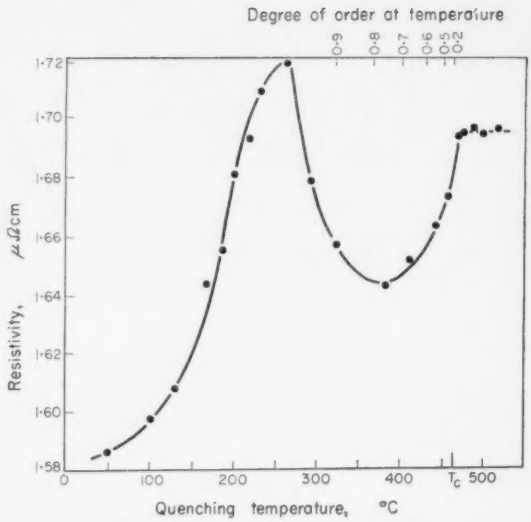

FIG. 1. Quenched-in resistivity vs. quenching temperature. Resistivity measured at −196°C.

The typical kinetics of isothermal decay of the quenched-in resistivity are shown in Fig. 2 for a high temperature quench and in Fig. 3 for a low temperature quench. Possibly the large resistivity produced at low quenching temperatures has

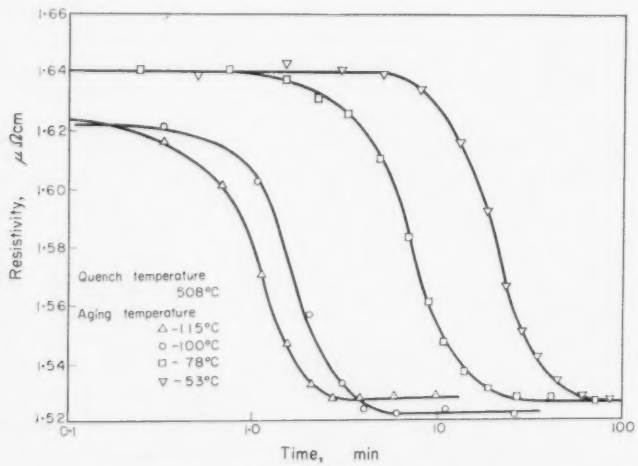

FIG. 2. Decay curve of high temperature quenched-in resistivity vs. time for various decay temperatures.

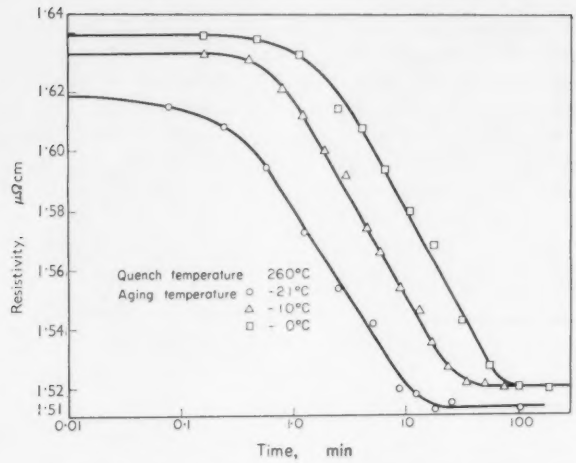

FIG. 3. Same as Fig. 2 for a low quenching temperature.

hitherto escaped detection because it decays so rapidly. Since the resistivity associated with the peak produced by quenching from a low temperature anneals out very rapidly compared to that for a high temperature quench, it was possible to separate the two effects as shown in Fig. 4 where the upper curve is the as quenched state and the lower curve is the resistivity after a short time anneal. Thus, the two defects which are produced may be separated as shown in Fig. 5. Curve B represents the newly discovered quenched-in resistivity, and curve A is associated with the defect which also produces the quenched-in strengthening as observed in a prior investigation.[8] Curve A could just as well be a plot of yield point vs. quenching temperature. In other words the strengthening associated with a high temperature quench is essentially proportional to the increase in resistivity.

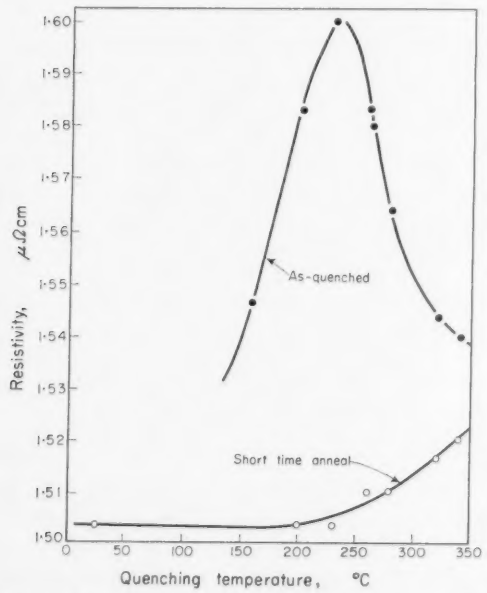

FIG. 4. Resistivity vs. quenching temperature after a short time anneal.

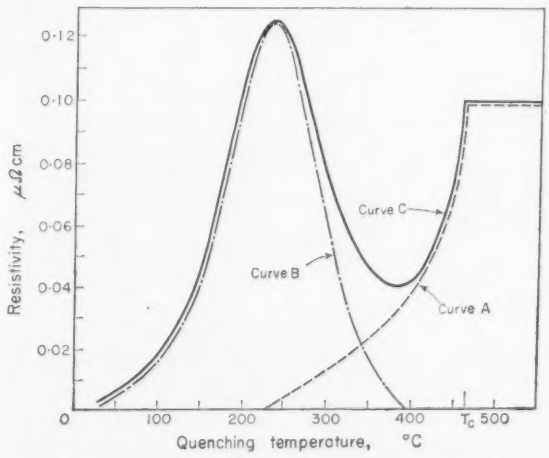

FIG. 5. Resistivity vs. quenching temperature showing separation of the two defects.

In order to determine whether the defect associated with curve B increased the strength, the specimen was quenched and the increase in resistivity was observed as shown in Fig. 1. The specimen was then pulled at −25°C very slightly in order to determine the yield point as shown in Fig. 6. The specimen was then given a short time anneal which removed the resistivity introduced by quenching between 25 to 350°C as shown in Fig. 4. The yield point was determined again at

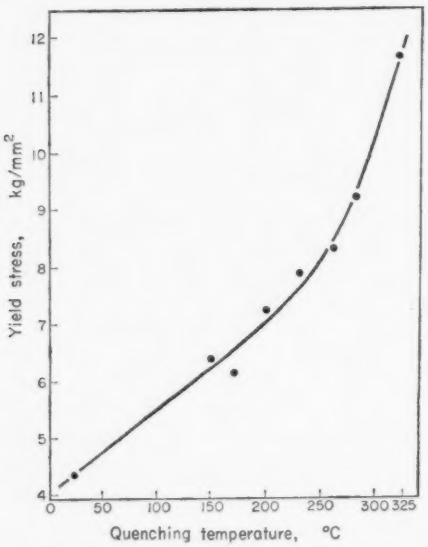

FIG. 6. Yield point at −25°C vs. quenching temperature.

−25°C; it was found that the yield point was the same as that before the short time anneal except for the very small amount of work hardening produced during the first pull. It can be concluded that the defect associated with curve B (Fig. 5) does not affect the macroscopic yield point, whereas that associated with curve A affects both resistivity and yield point in proportional amounts.

6. ANALYSIS

The nature of the defects was analyzed by conventional methods. The activation energy of motion was determined from the decay curves (Figs. 2 and 3) by plotting log time for a given fraction of decay vs. $1/T$. The results shown in Table 1 for three representative quenching temperatures were independent of the fraction that decayed.

Within the error of present measurements, it can be said that the energy of motion, Q_M, during decay is independent of quenching temperature, and we will now use the average value of 14 kcal/mol. This value is close to other observations on

Table 1

Quenching temperature, °C	Q_M, kcal/mol
508	13·4
465	14·3
260	13·8

decay in quenched β-Cu–Zn by GREEN and BROWN[7] measuring yield point, 15 kcal/mol, and CLAREBROUGH[9] measuring internal friction, also 15 kcal/mol. The difference between 14 and 15 kcal/mol is not considered significant at this time.

KUPER *et al.*[11] have measured the diffusion of Cu and Zn in β-Cu–Zn and found that at temperatures of 264–381°C, Q_D (Cu) = Q_D (Zn) = 36 kcal/mol. Thus, according to the usual analysis,

$$Q_D = Q_M + Q_F$$

the energy of formation, Q_F, of a vacancy should be about 22 kcal/mol. In order to determine the energy of formation of the low temperature defect, the portion of curve B (Fig. 5) between 25 and 250°C was analyzed. The maximum that occurs will be discussed later because it appears to be associated with a loss of defects during the quench via an interaction with the overlapping defect produced at higher quenching temperatures. Thus, assuming that a negligible amount of the defect is lost during a quench between 25°C and 210°C, the energy of formation was obtained from the usual assumption that

$$\rho_Q \sim C = A \exp(-Q_F/kT) \qquad (1)$$

where ρ_Q is the quenched-in resistivity, C is the concentration of the defect, A is an entropy factor, Q_F energy of formation of the defect, and T is the quenching temperature. The graphical analysis in Fig. 7 gives a value of Q_F = 7·2–8·0 kcal/mol. Thus, it appears that the defect is not primarily

a vacancy because this experimental value of Q_F is much smaller than Q_F for a vacancy as deduced above.

The low experimental value of Q_F should rule out vacancies as the low temperature defect. The most likely source of this resistivity is disorder in an essentially ordered matrix. The large difference between the resistivity of the ordered and disordered state is an ample reservoir from which the low quench temperature resistivity can be obtained. Fig. 8[12] shows the resistivity in β-Cu–Zn

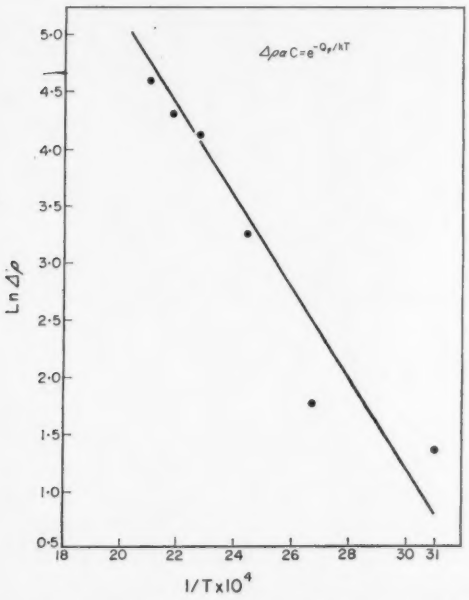

FIG. 7. Determination of Q_F of low temperature defect.

as a function of temperature. From an extrapolation of the resistivity of the disordered state to a lower temperature, it is estimated that there is 8μ ohm cm difference between the completely ordered and disordered states. Quenching from about 260°C produces a 0·14μ ohm cm of resistivity which is about 2 per cent of the resistivity difference between the completely ordered and disordered states. Now the amount of disorder, (1–S), which exists at 250°C is also about 2 per cent as determined from the X-ray data of CHIPMAN and WARREN[10]. The most likely source of this resistivity is the small amount of quenched-in disorder. Q_F, as determined above, is 8 kcal/mol and should correspond to the energy to form a wrong pair in the nearly completely ordered matrix. This represents a new discovery in β-Cu–Zn because hitherto it has always been assumed that equilibrium states of partial long range order could not be quenched into β-Cu–Zn. It appears that small equilibrium amounts of disorder can be quenched-in if the quenching temperature is sufficiently low.

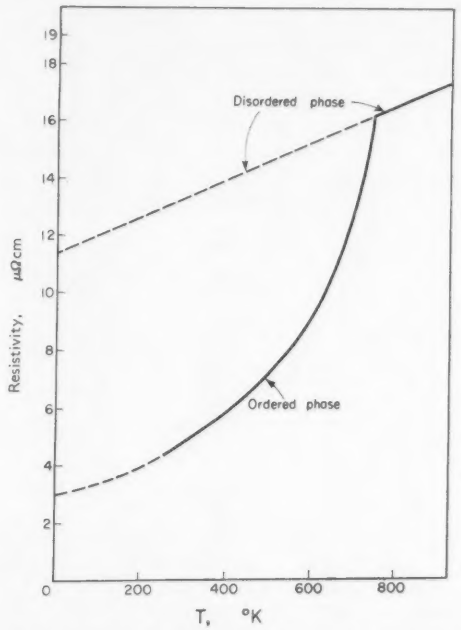

FIG. 8. Resistivity of β-Cu–Zn as a function of the temperature.

There are now more detailed questions to be answered concerning the small amount of disorder in the nearly completely ordered matrix. We will be concerned with the range of quenching temperature between 25–250°C where there is no overlap with the other defect. Since (1–S) is less than 2 per cent in this range, the disordered pairs are sufficiently dilute so that they can be treated as isolated defects. Now two extreme possibilities will be considered: (1) the defect is purely a pair of isolated wrong atoms or (2) it is purely a bound pair of wrong atoms. In general both defects should coexist. A wrong atom pair is defined by a Cu and Zn atom each being on a wrong site with

respect to the superlattice. The superlattice is b.c.c. and consists of two interpenetrating simple cubic lattices one of which is occupied by a single species of atoms when complete long range order exists. Since the present alloy is not exactly stoichiometric, this means that when $S = 1$, all of the minority species, zinc atoms, are on one sublattice.

In order to determine whether the defect is a bound wrong atom pair i.e. nearest neighbors exchange sites or pairs of isolated wrong atoms, we shall use some elementary statistical mechanics.[13] The calculation will be made for ideal stoichiometry of N Cu–Zn molecules (N Cu and N Zn atoms). n is the number of isolated wrong pairs (n wrong Zn and n wrong Cu atoms). For isolated wrong pairs, the number of arrangements is for dilute concentrations

$$W \simeq \left[\frac{N!}{(N-n)!n!}\right]^2 \tag{2}$$

The free energy is given by

$$F = nE - kT \ln W \tag{3}$$

where E is the energy to form an isolated wrong pair. It can be shown that

$$E = 16\{1/2(\epsilon_{AA}+\epsilon_{BB})-\epsilon_{AB}\} = 16\epsilon \tag{4}$$

where ϵ_{AA} etc., are the conventional nearest neighbor bond energies, and ϵ is the net interaction energy, which is positive in order to produce long range order. Thus,

$$F = 16n\epsilon - 2kT \ln \frac{N!}{(N-n)!n!} \tag{5}$$

Setting

$$\frac{\partial F}{\partial n} = 0,$$

one obtains for the dilute concentration of isolated wrong pairs

$$C_1 = \frac{n}{N} \simeq \exp(-8\epsilon/kT) \tag{6}$$

Seitz[14] has previously considered the equilibrium concentration of bound pairs of defects in alkali halides. For a dilute solution of bound wrong pairs the number of arrangements is

$$W \simeq \frac{8^n N!}{(N-n)!n!} \tag{7}$$

where n is the number of bound wrong pairs, and N is again the total number of Cu–Zn molecules. The energy to produce a bound wrong pair is 14ϵ.

$$F = 14n\epsilon - kT \ln W \tag{8}$$

Setting

$$\frac{\partial F}{\partial n} = 0$$

$$C_B = \frac{n}{N} \simeq 8 \exp(-14\epsilon/kT) \tag{9}$$

The relative concentration of the two defects is

$$\frac{C_B}{C_1} = 8 \exp(-6\epsilon/kT)$$

If we use the Bragg and Williams theory where

$$\epsilon = \frac{kT_c}{4}$$

and since $T_c = 465°\text{C}$ then

$$C_B > C_1 \qquad T > 258°\text{C}$$

$$C_B < C_1 \qquad T < 258°\text{C}$$

In the range of immediate interest, 25–250°C, isolated pairs should be more numerous according to the above calculation.

Another way to determine whether the bound wrong pairs or isolated wrong pairs are more prevalent in the range 25–250°C is to compare the value of Q_F as obtained experimentally via equation (1) with the energies of formation predicted by equations (6) and (9). Equation (6) predicts that Q_F for an isolated wrong pair is 8ϵ and equation (9) for a bound wrong pair predicts 14ϵ. Using the Bragg–Williams approximation $\epsilon = kT/4$; then Q_F for an isolated pair is 3 kcal/mol and for a bound pair 5 kcal/mol. Using the quasi chemical theory of Li[15] Q_F for an isolated pair is 3·5 kcal/mol and for a bound wrong pair 6 kcal/mol. Thus, the experimental value of 8 kcal/mol favors a predominance of bound wrong pairs. However, the most

important result is the fact that the experimental value of Q_F is close to both theoretical values. Most likely the existing theories for the energy to place an atom in a wrong site are not good enough for more accurate predictions. Probably the experimental value for Q_F is closer to actuality than that supplied by present theories.

If we use the experimental value of 8 kcal/mol for Q_F then the concentration of wrong pairs comes out to be about 0·5 per cent at 250°C. This value corresponds to about 1 per cent disorder and may be more reliable than the X-ray data which is not better than about 3 per cent in the region of almost complete long range order. A large discrepancy between X-ray measurements of long range order in AuCu and measurements of the heat of formation have recently been pointed out by ORR[16], LUCIAT-LABRY and HULTGREN.

The resistivity is about 0·14 μohm cm per 1 per cent of wrong pairs which is about 1/10 the expected value for the resistivity of 1 per cent vacancies. This is reasonable because a vacancy should perturb the periodicity of the lattice potential more than a wrong pair.

The lack of strengthening associated with quenching from 250°C is readily understandable if the defect is a pair of isolated wrong atoms because slip will only further isolate the wrong atoms and not increase the energy of the system. However, bound wrong pairs would produce a strengthening because slip would convert some bound wrong pairs to isolated wrong pairs. The energy to convert a bound wrong pair to an isolated wrong pair is ϵ. The number of bound wrong pair bonds per unit area of a (110) slip plane

$$C = 3/4 \frac{C_B}{\sqrt{(2)b^2}}$$

The strengthening associated with disordering the bound wrong pairs is calculated using the idea of FISHER[17] for short range order strengthening

$$\tau = \frac{3/4\, C_B \epsilon}{\sqrt{(2)b^3}}$$

Letting $C_B = 0{\cdot}01$, $b = 2\times10^{-8}$ cm, $\epsilon = kT_c/4$

$$\tau = 1{\cdot}5\times10^{7} \text{ dynes}$$

Now the base strength of the as quenched state is 8×10^{8} dynes/cm^2. Thus, the strengthening would be about 2 per cent of the base strength of the alloy and too small to be observed by the usual stress–strain measurement as indicated by the experimental observation.

The kinetics of decay will be crudely analyzed to determine the diffusion distance for the disappearance of the defect. The diffusion distance or more properly the square root of the number of random jumps before the wrong pair becomes a right pair is

$$X = \sqrt{Dt}$$

where ν is the diffusion coefficient and t is the time. From Fig. 3, $t = 60$ sec and $T = 294$°K for the process to decay by one-half. It will be assumed that

$$D = \frac{b^2\nu}{\alpha} \exp(-14000/RT)$$

where $\nu = 10^{13}$ sec^{-1}, $b = 1\times10^{-8}$ cm, and α is an entropy factor which in the case of an order structure like β-Cu–Zn should be about 8 (the usual value for b.c.c.). The activation energy for motion is that obtained experimentally. Thus

$$X = 50b/\sqrt{\alpha}$$

This value is reasonable if the decay process is simply a reordering of wrong atoms where initial concentration is about 1 per cent. It is not too grossly inconsistent with an interchange of atoms via a vacancy near a bound wrong pair since a direct interchange is not expected. ELCOCK[18] has shown that with a vacancy mechanism it takes a minimum of six jumps to cause diffusion without creating a net disorder. The above calculation assumes the vacancy is already near one atom of a wrong pair; this assumption represents an overestimation for X. However, if the vacancy were randomly distributed in a concentration demanded by an activation of self-diffusion of 36 kcal/mol, then X would be about $10^{-6}\,b$ which is much too small. It is suspected that the concentration of vacancies in the neighborhood of a bound wrong pair is greater than the average. This would be consistent with the kinetics. Also it is expected that it is somewhat easier to create a wrong pair in the neighborhood of a vacancy than in a perfect crystal so that upon quenching the bound wrong pair tends to trap a vacancy in its vicinity.

The behavior of β-Cu–Zn is similar to that of 50–50 Au–Cd as shown by HUNTINGTON *et al.*[19] Au–Cd is in a state of long range order up to its melting point. They found that Q_d (Au) = 29·8 kcal/mol and Q_d (Cd) = 27·9 kcal/mol. WECHSLER[1] found Q_M = 13·4 kcal/mol and Q_F = 8·7 kcal/mol for the defect produced by quenching. HUNTINGTON *et al.* also suggested that vacancy motion eradicated the defect which was probably short range disorder in the matrix of nearly complete LRO.

The maximum in quenched-in resistivity shown by curve B Fig. 5 is similar to that in Cu–Al alloy observed by WECHSLER and KERNOHAN[2] who suggested that at higher temperatures the rate of decay increases. Also the observed Q_F by WECHSLER and KERNOHAN[2] was 3 kcal/mol which is small compared to Q_F of vacancies in pure Cu.

The defect produced by the high temperature quench has been fully discussed by BROWN[8] and seems to be associated with the interaction between dislocations and the rapid formation of long range order during the quench. Preliminary work with the electron microscope indicates that there is a profound change in the dislocation distribution after a high temperature quench. The strengthening associated with the high temperature quench supports this viewpoint.

5. CONCLUSIONS

1. A small, but equilibrium amount of disorder may be quenched in β-Cu–Zn.
2. The disorder has been associated with a dilute concentration of wrong pairs whose activation energy of formation is 8 kcal/mol.
3. The energy of motion associated with reordering is 14 kcal/mol.
4. The wrong pairs produce no measurable increase in the strength of β-Cu–Zn.
5. A resistivity of 0·14 μ ohm cm is produced by a 1 per cent concentration of wrong pairs.

Acknowledgements—Dr. G. H. VINEYARD suggested the distinction between isolated and bound wrong pairs. Dr. J. N. HOBSTETTER provided many helpful discussions as did our colleagues in the School of Metallurgical Engineering. The Atomic Energy Commission gave support for this work.

REFERENCES

1. WECHSLER M. S., *Acta Met.* **5,** 150 (1957).
2. WECHSLER M. S. and KERNOHAN R. H., *Acta Met.* **7,** 599 (1959).
3. NOWICK A. S. and SLADEK R. J., *Acta Met.* **1,** 131 (1953).
4. DAMASK A. C. and DIENES G. J., *J. Phys. Chem. Solids* **12,** 105 (1959).
5. WECHSLER M. S. and KERNOHAN R. H., *J. Phys. Chem. Solids* **12,** 107 (1959).
6. SMITH C. S., *Trans. Amer. Inst. Min. (Metall.) Engrs.* **152,** 144 (1943).
7. GREEN H. and BROWN N., *Trans. Amer. Inst. Min. (Metall.) Engrs.* **197,** 1240 (1953).
8. BROWN N., *Acta Met.* **7,** 210 (1959).
9. CLAREBROUGH L. M., *Acta Met.* **5,** 413 (1957).
10. CHIPMAN D. and WARREN B. E., *J. Appl. Phys.* **21,** 696 (1950).
11. KUPER A. B., LAZARUS D. and TOMIZUKA C. T., *Phys. Rev.* **104,** 1536 (1956).
12. BORELIUS G., *Proc. Phys. Soc. Lond.* **49,** 77 (1937).
13. MOTT N. F. and GURNEY R. W., *Electronic Processes in Ionic Crystals*, p. 26. Clarendon Press, Oxford (1948).
14. SEITZ F., *Rev. Mod. Phys.* **18,** 384 (1946).
15. LI Y. Y., *J. Chem. Phys.* **17,** 447 (1949).
16. ORR R. L., LUCIAT J. and HULTGREN R., *Acta Met.* **8,** 431 (1960).
17. FISHER J. C., *Acta Met.* **2,** 9 (1954).
18. ELCOCK E. W., *Proc. Phys. Soc. Lond.* **73,** 250 (1959).
19. HUNTINGTON H. B., MILLER N. C. and NERSE V., *Bull. Amer. Phys. Soc.* March Meeting, p. 182 (1960).

Vol. 196

J. Phys. Chem. Solids Pergamon Press 1961. Vol. 19, Nos. 3/4, pp. 299–303. Printed in Great Britain.

L'INFLUENCE D'IRRADIATION AUX NEUTRONS RAPIDES SUR LE LUMINOPHORE ZnS–Mn

P. JASZCZYN

Institut de recherches nucléaires Académie Polonaise des Sciences, Swierk, Pologne

(*Received* 27 *July* 1960; *revised* 8 *December* 1960)

Résumé—On étudie l'influence de l'irradiation aux neutrons rapides sur les bandes bleue et orange de luminescence du phosphore ZnS–Mn excité par la lumière de Wood.

Summary—The ZnS–Mn phosphor is irradiated with fast neutrons. The influence on the blue and orange luminescent bands is studied.

SMITH et TURKEVICH ont montré[1] que l'irradiation préalable dans la pile atomique diminue considérablement le rendement de la photoluminescence du phosphore ZnS–Cu. Les défauts de structure créés par les neutrons rapides peuvent servir de pièges à trous,[2] qui s'y recombinent sans émission.

Il a paru intéressant d'étudier l'influence d'irradiation aux neutrons sur le spectre d'émission du phosphore ZnS–Mn (10^{-4}) excité par la lumière de Wood. Ce spectre se compose de deux bandes principales : la bande bleue provenant de la luminescence de recombinaison et la bande orange émise par les centres Mn^{++} "discrets". Ces centres peuvent être excités, soit par l'absorption directe de l'ultraviolet, soit par le transfert résonant des centres "bleux" excités, soit par le transfert d'énergie se dégageant pendant les recombinaisons des trous libres avec les électrons près de ces centres.[3] L'étude d'extinction de la bande bleue et du renforcement de la bande orange du ZnS–Mn par l'infrarouge a suggéré que ces effets (ainsi que la variation du spectre avec l'echauffement du phosphore de $-180°C$ jusqu'à $+20°C$) sont liées à la libération des trous des centres "bleux" excités, et à leur recombinaison avec l'excitation des centres "organges".[4] Ce transfert d'énergie par l'intermédiaire des trous libres doit être évidemment sensible aux défauts de structure créés par irradiation dans la pile.

La poudre ZnS–Mn (10^{-4}) 5 pour cent NaCl hex. préparée et aimablement mise à notre disposition par Dr. A. A. TCHEREPNEV a été irradiée dans la pile atomique "EWA" à Swierk, le temps d'irradiation étant de 2 à 140 min et l'intensité du flux 10^{13} neutrons par sec cm^2. Quelques jours après l'irradiation dans la pile, l'intensité de deux bandes d'émission excitée par la lumière de Wood à la température $+20°C$, $-70°C$ et $-180°C$ a été mesurée; aux basses températures on a aussi mesuré l'intensité de la luminescence sous l'action simultanée de la lumière de Wood et de l'infrarouge. Les mesures de contrôle faites au bout de 3 mois ont prouvé la reproductibilité de tous les résultats reçus.

Ces résultats montrent, que l'intensité des deux bandes s'abaisse avec la dose des neutrons (mesurée par le temps d'irradiation); cette variation étant très rapide pour les premières doses et plus lente ensuite (Fig. 1).

Puisque le degrés d'extinction de la bande bleue est différent de celui de la bande orange, le rapport des intensités de deux bandes : I_0/I_b varie avec le temps d'irradiation dans la pile (Fig. 2) A la température $-180°C$ la bande bleue est plus fortement éteinte que la bande orange et le rapport I_0/I_b croit avec la dose des neutrons. Ce caractère de la courbe I_0/I_b (dose) est encore plus prononcée à $-70°C$ quand la libération des trous de centres bleux devient plus forte, mais l'intensité de la bande orange n'a augmenté que de 63 pour cent. Le caractère de la courbe I_0/I_b change à la

température ambiante : la bande bleue est déjà fortement éteinte (13 fois plus faible qu'à $-180°C$) et la bande orange, pour laquelle le rôle du transfert par l'intermédiaire des trous a considérablement augmenté, (l'intensité de la bande orange à $+20°C$ est plus que 4 fois grande qu'à $-180°C$) se montre beaucoup plus sensible aux défauts introduits par les neutrons, que la bande bleue, et en conséquence la valeur I_0/I_b tombe rapidement.

aux ions Mn^{++} interstitiels[4e] relativement à la bande orange.

La valeur W_{IR} présentée dans les Tableaux 1 et 2 est égale au rapport de l'intensité de la luminescence avec l'action simultanée du rayonnement infra-rouge à l'intensité de cette luminescence sans les rayons infra-rouges. Les W_{IR} mesure ainsi l'extinction de la bande bleue ($W_{IR} < 1$) et le renforcement de la bande orange ($W_{IR} > 1$) par

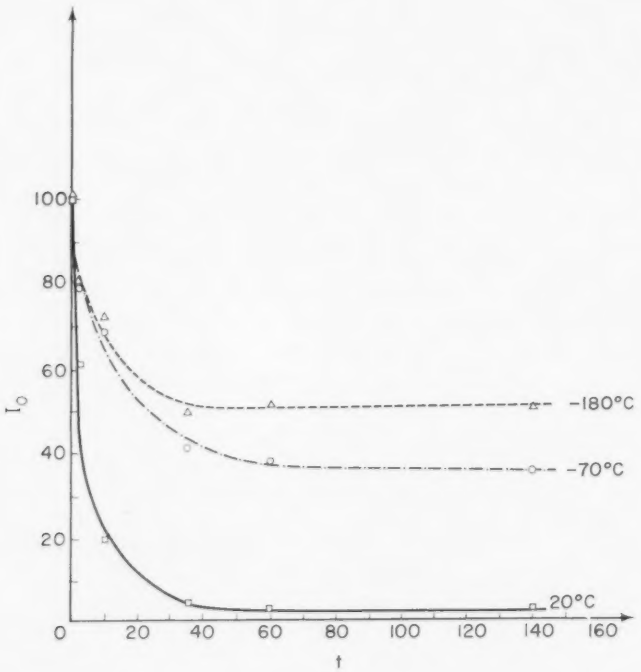

FIG. 1. La variation de l'intensité de la bande orange I_0 de luminescence de ZnS–Mn (10^{-4}) avec le temps d'irradiation dans la pile. Pour le phosphore non irradié:
à $+20°C$ $I_0 = 1000$, à $-70°C$ $I_0 = 390$, à $-180°C$ $I_0 = 240$.

Il ressort des spectres présentes sur la Fig.3(a) et 3(b), que l'irradiation aux neutrons semble produire non seulement la baisse du rendement de la luminescence et la variation du rapport des intensités des deux bandes mais aussi un déplacement du spectre vers les courtes longeurs d'ondes et—à la température ambiante—le renforcement de la bande rouge $\lambda_{max} = 615\ m\mu$ due évidement l'infra-rouge. Les Tableaux 1 et 2 montrent que W_{IR} diminue en général avec la dose des neutrons. Or, pour les poudres irradiées dans la pile l'extinction de la bande bleue devient plus prononcée et le renforcement de la bande orange plus faible et même, pour les irradiations plus longues, ce renforcement est remplacé à $-70°C$ par l'extinction ($W_{IR} < 1$).

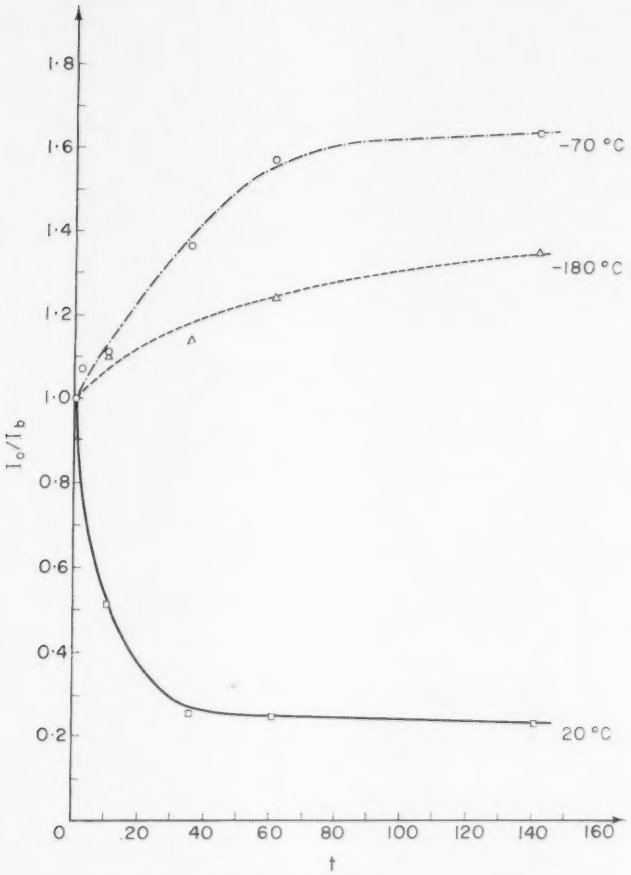

FIG. 2. La variation du rapport I_0/I_b (l'intensité de la bande orange à l'intensité de la bande bleue) dans le spectre de luminescence de ZnS–Mn (10^{-4}) avec le temps d'irradiation dans la pile. Pour le phosphore non irradié : à +20°C I_0/I_b = 1000 à −70°C $I_0/I_b = 25$ à −180°C $I_0/I_b = 18$.

Tableau 1

ZnS–Mn(10^{-4}) à −180°C	$W_{IR} = I_\infty^{UV+IR}/I_\infty^{UV}$					
Temps (min) / W_{IR}	0	2	10	35	60	140
Bande orange	2,96	2,68	2,64	1,67	1,50	1,64
Bande bleue	0,62	0,60	0,61	0,33	0,32	0,40

Vol. 19
1961

Tableau 2

ZnS–Mn(10^{-4}) à −70°C $W_{IR} = I_{\infty}^{UV+IR}/I_{\infty}^{UV}$

W_{IR} \ Temps (min)	0	2	10	35	60	140
Bande orange	2,50	2,22	1,81	0,83	0,43	0,45
Bande bleue	0,31	0,33	0,28	0,16	0,10	0,12

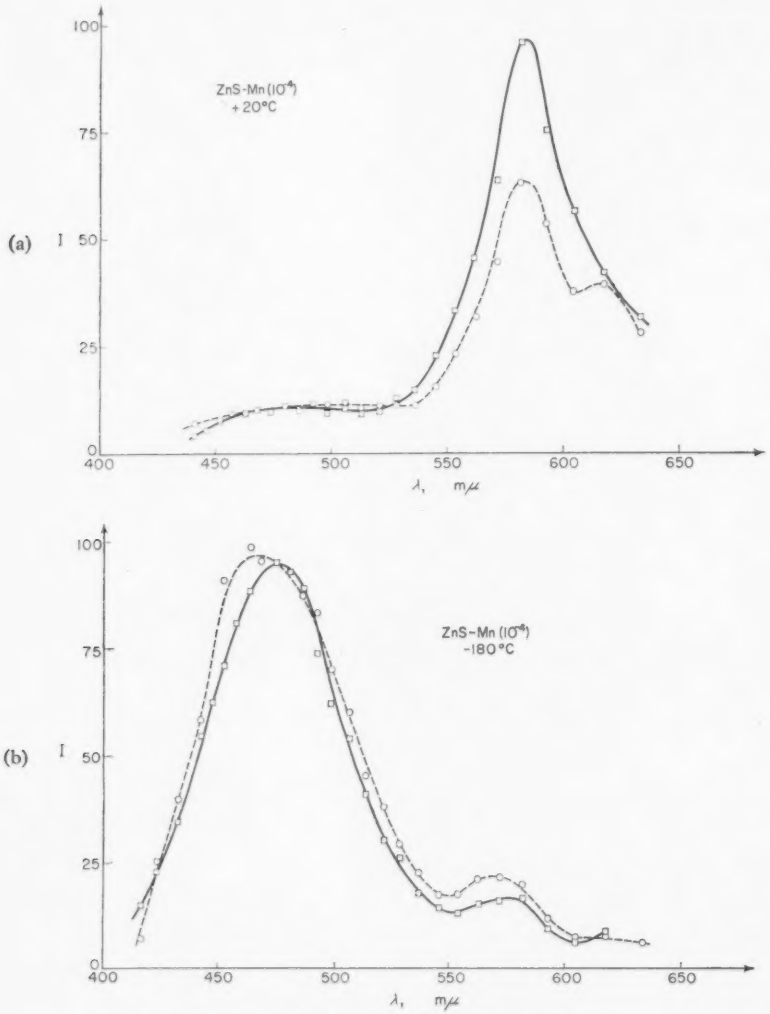

FIG. 3. Le spectre de luminescence de ZnS–Mn (10^{-4}) —— non irradié; – – – – – irradié préablement dans la pile pendant 10 mins.

Tableau 3

ZnS–Mn(10^{-4}) / L'intensitè de la luminescence	Non irradié dans la pile	Irradié 140 min dans la pile				
		Non Chauffé	Chauffé dans l'azote			
			1h à 200°C	3h à 200°C	3h à 200°C 2h à 400°C	3h à 200°C 2h à 400°C 1h à 600°C
Bande orange	100,0	2,6	4,5	4,7	6,0	52,0
Bande bleue	100,0	11,0	17,0	17,0	20,3	74,5

Tableau 4

ZnS–Mn(10^{-4}) / Le rapport des intensitès	Non irradié dans la pile	Irradié 140 min dans la pile	
		Non chauffé	Chauffé dans l'azote 3h à 200°C 2h à 400°C 1h à 600°C
I^{+20}/I^{-70}	2,56	0,19	1,83
I^{+20}/I^{-180}	4,16	0,21	2,30

I^t = l'intensité de la bande orange de luminescence à la temperature t°C.

L'analyse quantitative des effets observés exige d'une étude plus en détail, mais déjà les résultats montrent la sensibilité de "l'effet de l'infra-rouge" aux défauts de structure en accord avec le mécanisme proposé.

Par l'echauffement dans l'azote des échantillons irradiés aux neutrons on arrive à retablir partiellement l'intensité de leur luminescence (Tableau 3) et sa variation avec la temperature d'excitation (Tableau 4).

On n'a pas reussi cependant à retablir complètement les valeurs primordiales de l'intensité, l'echauffement prolongé diminuant la luminosité des echantillons irradiés ainsi que des echantillons non irradiés aux neutrons.

Remerciements—Je voudrais remercier mes collègues du Groupe d'Irradiations ainsi que de Service de l'Exploitation de la Pile de leur collaboration.

BIBLIOGRAPHIE

1. Smith A. W. and Turkevich J., *Phys. Rev.* **94**, 4, 857 (1954).
2. Smith A. W., *Phys. Rev.* **101**, 4, 1263 (1956).
3. Kröger F. A., *Luminescence in Solids containing Manganese*. Thèse, Amsterdam (1940).
4. Jaszczyn P.
   (a) *Festkörperphysik und Physik der Leuchstoffe*, p. 299. Akademieverlag, Berlin (1958);
   (b) *Opt. i Spektrosk.* **7**, 691 (1959);
   (c) *Acta Phys. Polon.* **17**, 427 (1959);
   (d) *Physik und Chemie des Kristallphosphore*, Arbeistagung in Greifswald 1959, en presse.

J. Phys. Chem. Solids Pergamon Press 1961. Vol. 19, Nos. 3/4, pp. 304–307. Printed in Great Britain.

MAGNETIC MOMENTS OF YTTRIUM–IRON GARNETS CONTAINING LIGHT RARE EARTH IONS*

A. AHARONI and M. SCHIEBER

Department of Electronics, Weizmann Institute of Science, Rehovoth—Israel.

(*Received* 19 *September*; *revised* 29 *November* 1960)

Abstract—The saturation magnetization between 100 and 700°K was measured in the compounds having a general formula of $Y_{6-x}M_xFe_{10}O_{24}$, with $x = 0$–6 for M = Sm, $x = 0$–4 for M = Nd, $x = 0$–2 for M = Pr and $x = 0$ and 1 for M = La. No compensation temperature was observed in the studied temperature interval. The low temperature magnetic moments of the Sm and La series are the same as for $Y_6Fe_{10}O_{24}$, i.e. about 10 Bohr magnetons. For the Nd and Pr series, values of 11 for $x = 2$ Pr to 13 Bohr magnetons for $x = 4$ Nd were obtained. The Curie temperatures for all these garnets are 550 ± 10°K.

THE RARE earths Sm to Lu are known to enter into iron garnets.[1,2] This has not been found possible for the larger ions of Nd, Pr and La. However, Nd can be substituted for Y up to $\frac{2}{3}$ of the yttrium in a garnet structure.[3,4] Similar substitutions of the other rare earths have evidently been made recently by DILLON and NIELSEN[5]. It is not clear from their abstract to what amount these were introduced, and if any saturation measurements were carried out besides the ferromagnetic resonance in which these authors were mainly interested. Substitution of gadolinium and samarium have recently been reported.[6,7]

We were interested to find out to what extent could the large ions of Pr^{3+}, Ce^{3+} and La^{3+} be substituted for the Y in the garnet structure, and observe the change of magnetization due to the replacing of the diamagnetic Y^{3+} by the paramagnetic Nd^{3+} and Pr^{3+} ions in the same sublattice. This seemed important because most of the works are substitution for the iron in the octahedral and tetrahedral sublattices,[8–13] rather than for the Y.

Yttrium and rare earth oxides from Lindsay Co. certified 99·9 per cent purity and ferric oxide from Fisher certified reagent purity were thoroughly mixed in an agate mortar according to the formula $Y_{6-x}M_xFe_{10}O_{24}$ where M is Sm, Nd, Pr, Ce and La and x varied from 0 to 6. The samples were then pressed to pellets and fired in an interval of 1340–1380°C, for a holding period of 8 hr.

No volatilization effects could be determined either by weighing or by comparing the emission spectrum of the unreacted with the reacted material, so that the chemical composition of the reacted ferrite can be taken as that of the unreacted components.

X-ray powder diffractions with a CuKα radiation taken on the samples, showed a shift of lines as a function of the composition, indicating an increase of the unit cell lattice parameter and showing thus the maximum amount of the rare earth ion which can be incorporated in the garnet structure. For Sm^{3+} this maximum was $x = 6$, for Nd, $x = 4$, for Pr, $x = 2$, for Ce, $x = 0$ and for La, $x = 1$. If higher proportions of these rare earths are introduced, one obtains part of them in a perovskite form, which is easily identified in the X-ray pattern.

The lattice constants of these garnets are being calculated and will be published elsewhere.[14]

The pure X-ray phase samples were also checked

* Part of a thesis by M.S. to be submitted to the Hebrew University, Jerusalem, in partial fulfilment of the requirements for a Ph.D degree. Part of this paper was presented at the October 1960 meeting of the Israel Chemical Society.

for magnetite by a method described before. No magnetite was found in the samples. This is in agreement with the experiments made by SEIDEN *et al.*[15] on the nonstoichiometric yttrium–iron garnets fired in oxidizing atmosphere.

The saturation magnetization was measured on the pure garnet phase samples by the ponderometric method[16] between 100 and 700°K by comparing the magnetic moments with that of metallic nickel. The measurements are subject to an error of ± 2 per cent.

No compensation temperatures were observed in the studied temperature interval. Our results for the samarium or yttrium–iron garnets and for the mixed samarium–yttrium series are in fair agreement with the data published by PAUTHENET[17] and by CUNNINGHAM and ANDERSON[7]. It is only at the lowest temperature that our data are slightly larger than theirs.

The results for the Sm–Y iron garnets are plotted in Fig. 1. The magnetization for the different values of x is not given since the data are close together and inseparable. Fig. 2 is a plot of the results for mixed Pr–Y iron garnets. It is seen that the low temperature saturation magnetization increases somewhat with increased contents of praesodymium. This can be explained[18] by S and L being *antiparallel* for the ions in which the f shell is less than half full, in contradistinction with the heavy rare earths ($Z > 64$) in which L, S and J are all parallel. The *spin* of the Pr interacts with that of the iron in the [24(d)] site and is thus antiparallel to the net iron magnetization. However, the net magnetic moment J of the Pr ion is antiparallel to its spin and thus the net magnetization of the garnet is increased. This effect is more pronounced in Fig. 3 which is a plot of the result for mixed Nd–Y iron garnets. The low

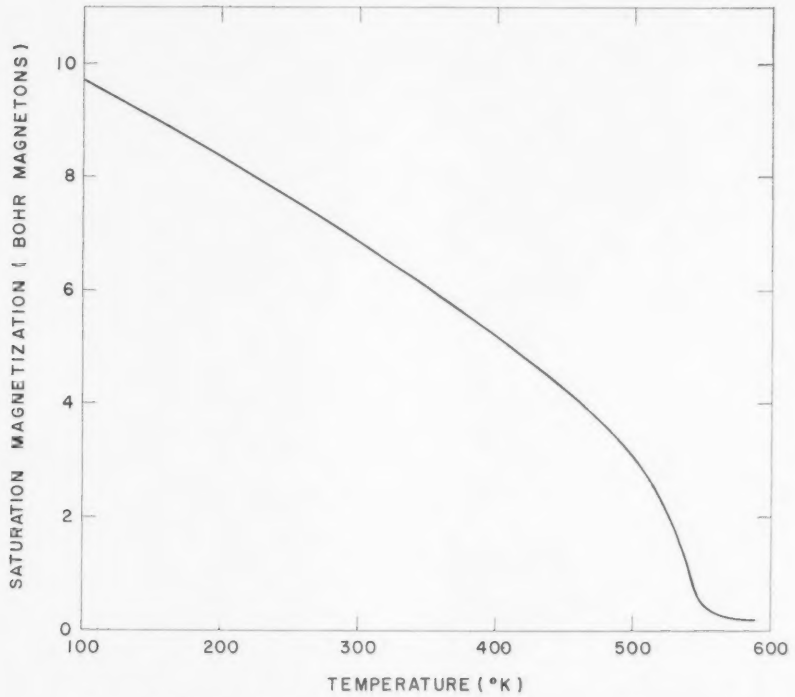

FIG. 1. Variation of the magnetic moment with temperature for samarium–yttrium–iron garnets.

Vol. 19
1961

temperature saturation magnetization *increases* with the increased Nd contents and reaches 13 Bohr magnetons per formula as compared with about 10 Bohr magnetons for the YIG. The Curie temperature is 550 ± 10°K as in all the other garnets studied in fair agreement with the value of 545°K of GELLER[19] or 560°K of PAUTHENET[17] result of a larger number of magnetic interactions.[20]

Acknowledgements—The authors wish to thank Prof. E. H. FREI under whom this work was done. Thanks are also due to J. LIPKIN who built the electronic counter used for the magnetic measurements.

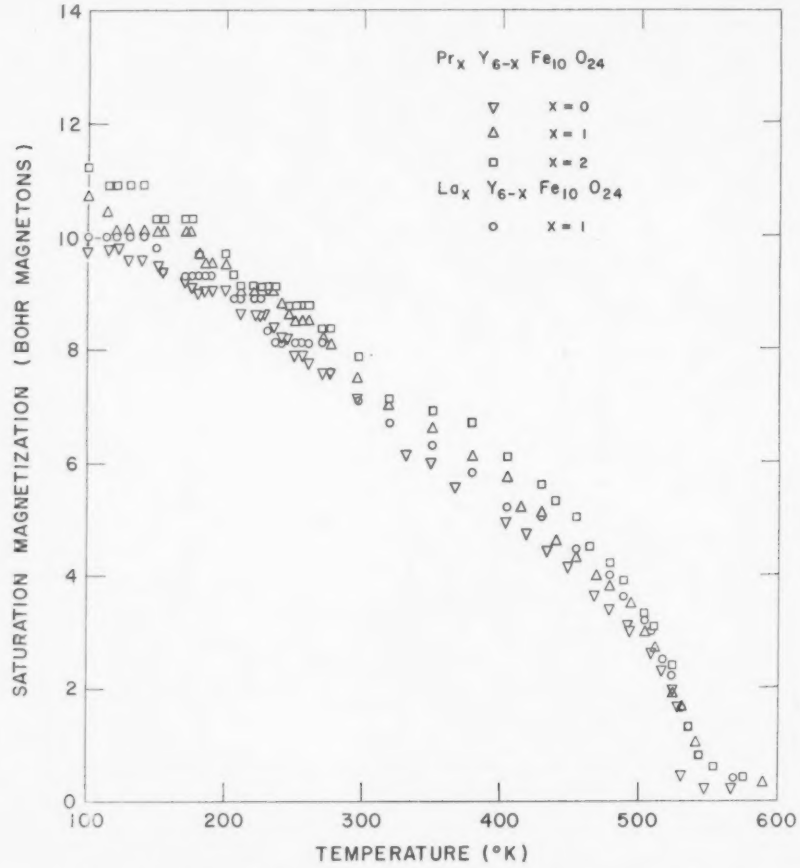

FIG. 2. Variation of the magnetic moment with the temperature for praesodymium and lanthanum–yttrium–iron garnets.

and slightly lower than 570°K of CUNNINGHAM and ANDERSON[7]. Within the accuracy of our measurements, it would be difficult to say whether the addition of a paramagnetic ion such as Sm or a little stronger paramagnetic ion such as Nd or Pr would have increased the Curie temperature as a

REFERENCES

1. BERTAUT F. et FORRAT F., *J. Phys. Radium* **18,** 305 (1957).
2. BERTAUT F. et FORRAT F., *C.R. Acad. Sci., Paris* **242,** 382 (1956).
3. GOLDRING G., SCHIEBER M. and VAGER Z., *Bull. Res. Coun. Israel* **8F,** 12 (1960).

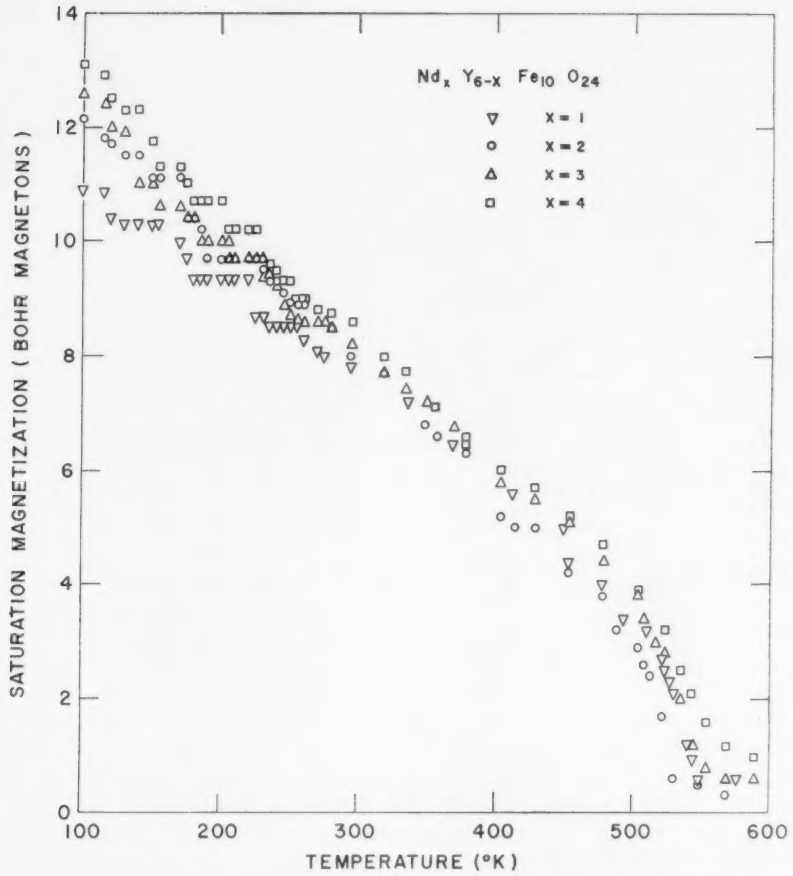

FIG. 3. Variation of the magnetic moment with temperature for neodymium–yttrium–iron garnets.

4. GOLDRING G., SCHIEBER M. and VAGER Z., *J. Appl. Phys.* **31,** 2057 (1960).
5. DILLON J. F., Jr. and NIELSEN J. W., *Phys. Rev.*, to be published.
6. ANDERSON E. E., CUNNINGHAM J. R., Jr. and MCDUFFIE G. E., *Bull. Amer. Phys. Soc.* (ser. II) **4,** 241 (1959).
7. CUNNINGHAM J. R., Jr. and ANDERSON E. E., *J. Appl. Phys.* **31,** 45S (1960).
8. GILLEO M. A. and GELLER S., *Phys. Rev.* **110,** 73 (1958).
9. GELLER S. and GILLEO M. A., *J. Appl. Phys.* **29,** 380 (1958).
10. PAUTHENET R., *J. Appl. Phys.* **29,** 25S (1958).
11. VILLIERS G. and LORIERS J., *C.R. Acad. Sci., Paris* **245,** 2033 (1957).
12. VILLIERS G., PAUTHENET R. and LORIERS J., *J. Phys. Radium* **20,** 382 (1959).
13. OSBORNE J. M., Mullard Research Laboratories, Technical note no. 353 (1959).
14. SCHIEBER M. and KALMAN Z., *Acta Cryst., Camb.*, to be published.
15. SEIDEN P. E., KOOL C. K. and KATZ J. M., *J. Appl. Phys.* **31,** 1291 (1960).
16. RATHENAU C. W. and SNOEK S. L., *Philips Res. Rep.* **1,** 239 (1946).
17. PAUTHENET R., Thesis, Grenoble 1957.
18. WHITE R. L., private communication.
19. GELLER S. and GILLEO M. A., *J. Phys. Chem. Solids* **3,** 30 (1957).
20. GILLEO M. A., *Phys. Rev.* **109,** 777 (1958).

Vol. 19
1961

J. Phys. Chem. Solids Pergamon Press 1961. Vol. 19, Nos. 3/4, pp. 308–320. Printed in Great Britain.

MAGNETOSTATIC MODES OF A FERROMAGNET SLAB*

R. W. DAMON and J. R. ESHBACH

General Electric Research Laboratory, Schenectady, New York

(*Received* 14 *July* 1960)

Abstract—The characteristic modes of a thin slab magnetized in its plane are obtained in the magnetostatic limit. It is found that the magnetostatic mode spectrum is bounded by the same frequency limits as for the spheroid. In the slab, however, the mode configuration clearly changes from a volume distribution to a surface wave as the frequency is increased above the extrapolated spin-wave region. In general, the characteristic functions are travelling waves which propagate along the slab transversely to the applied d.c. magnetic field. The mode distribution in wave-vector space is obtained for both the volume and surface modes, and the dependence of mode density on wavelength is discussed. The mode density variation shows that the volume modes connect smoothly to the spin-wave spectrum of a medium of infinite extent. The surface modes also exist even at very short wavelengths, but become statistically less important as the wavelength decreases.

I. INTRODUCTION

THE RESONANT modes of ferromagnetic samples have been previously calculated in the magnetostatic limit for spheres[1] and for spheroids with the applied d.c. magnetic field along the axis of revolution.[2] It is of interest to determine similar solutions in other geometries. Since the characteristic modes of a thin slab magnetized in its plane permit fairly straight forward solutions, we have examined this geometry in some detail. Many properties of the modes of this system are similar to those of the spheroidal solutions, and the simpler form of the results is of considerable assistance in obtaining an intuitive understanding of these modes.

In particular, it has been noted that the magnetostatic mode spectrum for a spheroid extends over a larger frequency range than the spectrum of the spin-wave approximation extrapolated to long wavelengths,[3] but transition between these two mode types has been complicated by the difference in mathematical form of the solutions.

The magnetostatic mode spectrum for a slab occupies the same band as the spectrum for a spheroid. In the case of the slab, however, the proper modes are plane waves for all wavelengths and one can readily understand the connection between the magnetostatic mode spectrum, in which boundary conditions are introduced, and the spin-wave spectrum of the infinite medium. It is found that the magnetostatic modes, whose frequencies lie outside of the spin-wave manifold are surface waves, while those within the spin-wave manifold extend throughout the volume of the sample. The mode density spectrum is utilized to discuss further the relation between these magnetostatic modes and spin-waves.

The problem of electromagnetic propagation in ferrite loaded transmission systems is of considerable interest, and the mode spectrum of waveguides containing ferrite slabs has been studied.[4] The magnetostatic modes of the ferrite slab in air are unperturbed by the introduction of conducting walls in certain locations. This leads to a connection between the magnetostatic mode spectrum and the propagation characteristics, and indicates the nature of these modes from an alternative point of view.

II. CHARACTERISTIC EQUATION

The modes of oscillation to be derived are due to purely magnetostatic forces arising from the externally applied d.c. magnetic field and the dipolar fields of the sample magnetization. The conditions under which forces due to exchange

* This paper is a more detailed version of the work reported in brief form in *J. Appl. Phys.* **31,** 104S (1960).

interaction and electromagnetic induction may be ignored have been discussed by WALKER[2]. Briefly, it is assumed that the characteristic distance for phase reversal of a magnetostatic mode is sufficiently long that exchange coupling is unimportant and yet is small compared to the wavelength for electromagnetic propagation in the medium. It is well known that this magnetostatic condition is valid over a considerable wavelength range.

We follow WALKER's approach and notation in setting up the characteristic equation for our problem. The procedure amounts to the simultaneous solution of Maxwell's equations and equation of motion of the sample magnetization, consistent with the proper boundary conditions.

In the magnetostatic limit, Maxwell's equations become

$$\nabla \times \boldsymbol{H} = 0 \tag{1.A}$$

$$\nabla \times \boldsymbol{B} = 0 \tag{1.B}$$

The boundary conditions require the continuity of the normal component of $\boldsymbol{B}$ and the tangential component of $\boldsymbol{H}$ at the sample surface, and these fields must approach zero at large distances from the sample.

Let the applied internal d.c. magnetic field, H_i, lie in the z direction. The magnetization may be written

$$\boldsymbol{M} = M_0\boldsymbol{i}_z + \boldsymbol{m}e^{i\omega t}$$

where M_0 is the saturation magnetization, $\boldsymbol{i}_z$ is a unit vector in the z direction, and $\boldsymbol{m}$ is the r.f. part of the magnetization, assumed small compared with M_0 and, therefore, lying in the x–y plane, since $|\boldsymbol{M}|$ is assumed to be constant.

The magnetic field is

$$\boldsymbol{H} = H_i\boldsymbol{i}_z + \boldsymbol{h}e^{i\omega t}$$

where h is the r.f. part of the magnetic field and may have x, y, and z components.

Equations (1.A) and (1.B) must be satisfied by the r.f. as well as the d.c. components of $\boldsymbol{H}$ and $\boldsymbol{M}$, and we therefore require

$$\nabla \times \boldsymbol{h} = 0 \tag{2.A}$$

$$\nabla \cdot (\boldsymbol{h} + 4\pi\boldsymbol{m}) = 0 \tag{2.B}$$

Equation (2.A) permits the introduction of a magnetic potential, ψ, such that $\boldsymbol{h} = \nabla\psi$, and equation (2.B) becomes

$$\nabla^2\psi + 4\pi\nabla \cdot \boldsymbol{m} = 0 \tag{3}$$

The equation of motion of the magnetization, neglecting losses, is

$$\frac{d\boldsymbol{M}}{dt} = \gamma(\boldsymbol{M} \times \boldsymbol{H}) \tag{4}$$

where γ is the gyromagnetic ratio. Substituting for $\boldsymbol{M}$ and $\boldsymbol{H}$ and retaining only the linear terms in $\boldsymbol{m}$ and $\boldsymbol{h}$, the equations of motion in component form become

$$4\pi m_x = \kappa\frac{\partial\psi}{\partial x} - i\nu\frac{\partial\psi}{\partial y}$$

$$4\pi m_y = i\nu\frac{\partial\psi}{\partial x} + \kappa\frac{\partial\psi}{\partial y} \tag{5}$$

where

$$\kappa = \frac{\Omega_H}{\Omega_H{}^2 - \Omega^2}, \qquad \nu = \frac{\Omega}{\Omega_H{}^2 - \Omega^2},$$

$$\Omega_H = \frac{H_i}{4\pi M_0}, \qquad \Omega = \frac{\omega}{4\pi\gamma M_0}$$

Substituting expressions (5) into equation (3), the potential inside the sample must satisfy

$$(1+\kappa)\left(\frac{\partial^2\psi^i}{\partial x^2} + \frac{\partial^2\psi^i}{\partial y^2}\right) + \frac{\partial^2\psi^i}{\partial z^2} = 0 \tag{6}$$

Outside the sample, where $\boldsymbol{M} = 0$ and thus $\kappa = 0$, Laplace's equation must be satisfied.

$$\nabla^2\psi^e = 0 \tag{7}$$

The equations up to this point would apply to a sample of arbitrary shape having a uniform internal d.c. field. We now choose the particular geometry of a slab of thickness s (in the x-direction), with infinite lateral extent and magnetized in its own plane (in the z-direction) (See Fig. 1).

For this geometry the demagnetizing factor for the polarizing field vanishes, $N_z = 0$. Thus the internal field is equal to the applied d.c. field, $H_i = H_0$.

The boundary condition on the normal component $\boldsymbol{B}$ requires that

$$(1+\kappa)\left[\frac{\partial\psi^i}{\partial x} - i\nu\frac{\partial\psi^i}{\partial y}\right]_{x=\pm s/2} = \left.\frac{\partial\psi^e}{\partial x}\right|_{x=\pm s/2} \tag{8}$$

and the continuity of tangential $\boldsymbol{H}$ requires

$$\psi^i\big|_{x=\pm s/2} = \psi^e\big|_{x=\pm s/2} + \text{constant} \tag{9}$$

where the constant may be taken to be zero.

It is appropriate to treat the problem in rectangular

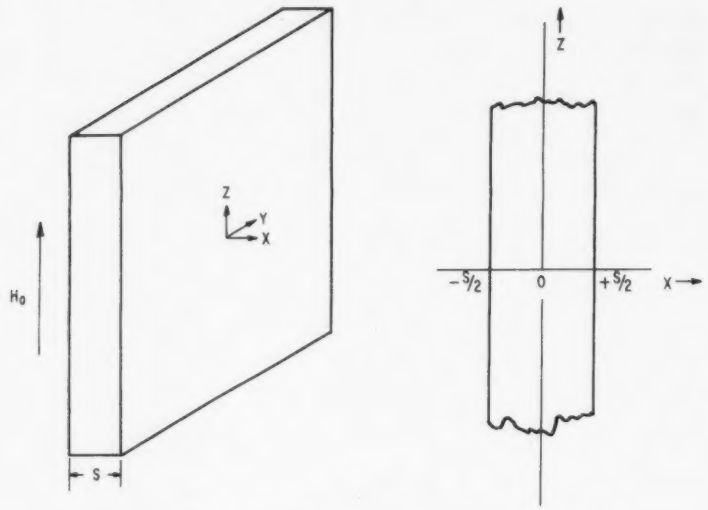

FIG. 1. Coordinate system orientation.

coordinates in which the potential is separable and may be written

$$\psi(x, y, z) = X(x)Y(y)Z(z)$$

Taking Y^i and Z^i as internal solutions and Y^e and Z^e as external solutions, the boundary equations (9) requires that $Y^i = Y^e = Y$ and $Z^i = Z^e = Z$. Thus the interior and exterior potentials may be written

$$\psi^i = X^i YZ$$

$$\psi^e = X^e YZ$$

Acceptable solutions will be simple exponential or sinusoidal functions of x, y and z. Only sinusoidal functions with real arguments are admissible for Y and Z, since these functions should remain finite as y and z tend to $\pm\infty$. Outside the sample Laplace's equation then requires that X^e be an exponential function .Thus we take

$$\begin{aligned} X^e &= c\exp(-k_x^e x), && x > s/2 \\ &= d\exp(k_x^e x), && x < -s/2 \end{aligned} \quad (10)$$

where k_x^e is a positive, real number.

Within the sample we take

$$X^i = a\sin(k_x^i x) + b\cos(k_x^i x) \quad (11)$$

where k_x^i may be either real or imaginary.

From equation (8) it is found that Y must be of the form

$$Y = \exp(ik_y y) \quad (12)$$

and thus only travelling waves are admissible in the y-direction.*

For Z, the choice of origin is arbitrary and we take

$$Z = \cos(k_z z) \quad (13)$$

Substituting these functions in equations (6) and (7) yields the relations

$$(1+\kappa)(k_x'^2 + k_y') + k_z'^2 = 0 \quad (14)$$

$$k_x^{e2} - k_y^2 - k_z'^2 = 0 \quad (15)$$

which will be used in discussing the mode spectrum.

Substituting equations (10) and (11) in the boundary condition, equation (9), yields the relations between the coefficients of X^i and X^e:

$$\begin{aligned} a &= \frac{c-d}{2}\,\frac{\exp\left(\frac{-k_x^e s}{2}\right)}{\sin\left(\frac{k_x^i s}{2}\right)} \\ b &= \frac{c+d}{2}\,\frac{\exp\left(\frac{-k_x^e s}{2}\right)}{\cos\left(\frac{k_x^i s}{2}\right)} \end{aligned} \quad (16)$$

* This situation is analogous to WALKER's observation[3] that the azimuthal variation in the spheroid case must be $e^{im\phi}$.

Vol. 1
1961

Substituting for ψ^i and ψ^e in equation (8), one finds from the boundary at $+s/2$

$$(1+\kappa)k_x^i\left[\frac{c-d}{2}\cot\left(\frac{k_x^i s}{2}\right)-\frac{c+d}{2}\tan\left(\frac{k_x^i s}{2}\right)\right]$$
$$-c\nu k_y = -ck_x^e$$

and at $-s/2$

$$(1+\kappa)k_x^i\left[\frac{c-d}{2}\cot\left(\frac{k_x^i s}{2}\right)+\frac{c+d}{2}\tan\left(\frac{k_x^i s}{2}\right)\right]$$
$$-d\nu k_y = dk_x^e \qquad (17)$$

Solving each of these expressions for c/d and equating the results gives the characteristic equation

$$(k_x^e)^2+2k_x^e k_x^i(1+\kappa)\cot(k_x^i s)$$
$$-(k_x^i)^2(1+\kappa)^2-(\nu k_y)^2 = 0 \qquad (18)$$

Equation (18) together with equations (14) and (15) determines the mode spectrum consistent with the boundary conditions. For a fixed magnetic field, these equations may be considered as a set of three relations between the five variables ω, k_x^i, k_x^e, k_y, and k_z; where ω enters through the quantities κ and ν. Two of the variables may, therefore, be eliminated and the allowed modes will be found to lie on surfaces in the three-dimensional space represented by the remaining variables. Since the slab is of infinite extent in the y- and z-directions we expect that k_y and k_z will have continuous characteristic values and may be chosen arbitrarily. Two types of representations of the allowed modes are of most interest. In one, the modes lie on surfaces in ω, k_y, k_z-space and in the other, the surfaces are in k_x^i, k_y, k_z-space. Solving for the surfaces in ω, k_y, k_z-space one finds that they are described by the solution to the equation

$$(1+\eta^2)+2|(1+\eta^2)^{1/2}|\left(-\frac{1+\eta^2+\kappa}{1+\kappa}\right)^{1/2}$$
$$\times(1+\kappa)\cot\left[|k_y|s\left(-\frac{1+\eta^2+\kappa}{1+\kappa}\right)^{1/2}\right]$$
$$+(1+\kappa)^2\left(\frac{1+\eta^2+\kappa}{1+\kappa}\right)-\nu^2 = 0 \quad (19)$$

where $\eta = k_z/k_y$.

The surfaces in k_x^i, k_y, k_z-space are given by

$$(1+\eta^2)-2\left|(1+\eta^2)^{1/2}\left|\frac{k_x^i k_z}{k_y k_t^2}\right|\cot(k_x^i s)\right.$$
$$\left.-\left[\frac{k_x^i k_x^2}{k_y k_t^2}\right]^2\right|-\left(\frac{k}{k_t}\right)^4\left(1+\frac{k_t^2}{k^2\Omega_H}\right) = 0 \qquad (20)$$

where $k_t^2 = k_x^{i2}+k_y^2$ and $k^2 = k_x^{i2}+k_y^2+k_z^2$

These equations will be discussed in the following two sections.

III. MODE SPECTRUM AND MODE CONFIGURATION

The characteristic equation, in the form of equation (19), determines the frequency spectrum as a function of k_y and k_z. Before discussing the detailed behavior of the solution, however, it is interesting to note some of the gross features that are determined by the restrictions imposed by equations (14) and (15) alone. Note that these expressions are quite general and do not depend on boundary conditions. For example, if all k's are real,* equation (14) is equivalent to the spin-wave dispersion relation extrapolated to long wavelengths obtained in an infinite medium. This is easily shown since

$$(k_x^{i2}+k_y^2)/(k_x^{i2}+k_y^2+k_z^2) = \sin^2\theta$$

where θ is the angle of propagation of the spin-wave relative to the magnetic field direction and by substituting this in equation (14) along with the expression for κ, we obtain

$$\Omega^2 = \Omega_H^2+\Omega_H\sin^2\theta \qquad (21)$$

independent of sample shape or dimensions. Also from equation (14) we see that all components of the wave vector within the sample can be real only at frequencies for which $(1+\kappa)$ is negative. The dependence of $(1+\kappa)$ and ν on frequency is shown in Fig. 2. It is seen that the region of negative $(1+\kappa)$ extends from $\Omega = \Omega_H$ to $\Omega = (\Omega_H^2+\Omega_H)^{1/2}$, which is the frequency range of the extrapolated spin-wave band. Any allowed modes in our problem which lie outside of this range must, therefore, have k_x^i imaginary, corresponding to

* We recall that k_x^i is the only wave-vector component that may be either real or imaginary in our present problem.

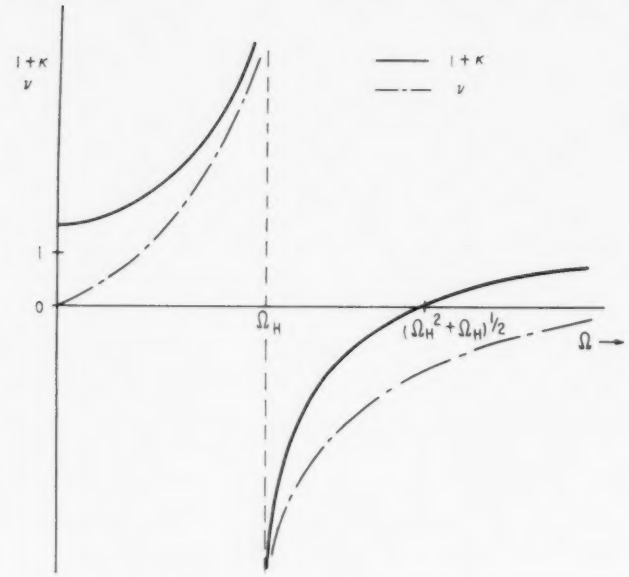

FIG. 2. Dependence of $(1+\kappa)$ and ν on frequency.

Vol. 1
1961

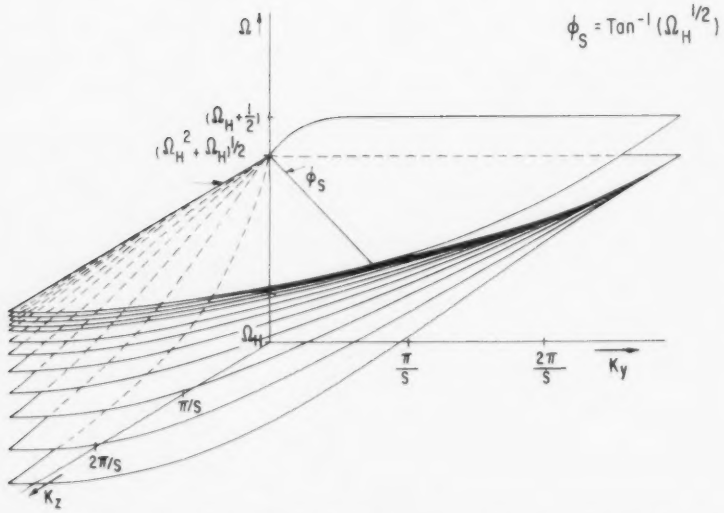

FIG. 3. Magnetostatic mode spectrum of a ferromagnetic slab magnetized in its plane.

exponential rather than sinusoidal dependence on x.

In Fig. 3 we have sketched the surfaces in Ω, k_y, k_z-space which are the solutions to equation (19). Only one quadrant of the Ω k_y, k_z variables is shown but the surfaces extend into the other quadrants by simple reflections through the Ω, k_y- and Ω, k_z-planes. There is an infinite number of these curved surfaces which lie between $\Omega = \Omega_H$ and $\Omega=(\Omega_H^2+\Omega_H)^{1/2}$, the density increasing as one approaches $\Omega = (\Omega_H^2+\Omega_H)^{1/2}$, and there is one surface which emerges above $\Omega = (\Omega_H^2+\Omega_H)^{1/2}$ reaching $\Omega = (\Omega_H+1/2)$ as its highest frequency. Any point on these surfaces corresponds to an admissible solution to the problem and carries with it a specific value of k_x^i and k_x^e which can be found by substitution of Ω, k_y and k_z into equations (14) and (15).

In this representation it is convenient to consider the intersection of this array of surfaces with a plane which includes the Ω-axis and is at an angle $\phi = \tan^{-1}\eta$ ($\eta = k_z/k_y$) to the Ω, k_y-plane. For a given value of η the multiplicity of surfaces is confined between the frequencies $\Omega = [\Omega^2+(\Omega_H/1+\eta^2)]^{1/2}$ and $\Omega = (\Omega_H^2+\Omega_H)^{1/2}$, with the exception of the one surface above $(\Omega_H^2+\Omega_H)^{1/2}$. Again, this is just the range permitted by equation (14) for a given k_z/k_y when all wave-vector components are real (volume modes) and, in fact, it may be shown that any solution within this range must have all real wave-vector components.

We will consider two regions of the mode spectrum separately; first, for $(1+\kappa) < 0$, all wave-vector components are real corresponding to volume modes and, second, for $(1+\kappa) > 0$, k_x^i is imaginary resulting in surface modes.

(a) *Volume modes*, $(1+\kappa) < 0$

The characteristic frequencies for the special case $k_y = 0$, ($\eta = \infty$), are shown in Fig. 4. In this case equation (19) reduces to

$$2\cot[\alpha|k_z|s] = \alpha - 1/\alpha \qquad (22)$$

where $\alpha = (-1/1+\kappa)^{1/2}$.

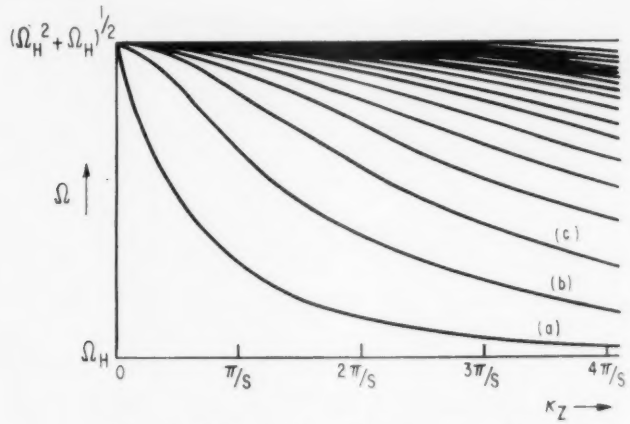

FIG. 4. Magnetostatic mode spectrum of a ferromagnetic slab magnetized in its plane for $k_y = 0$.

At a fixed frequency, Ω, the value of α is determined and the multiple roots of equation (22) are equally spaced in k_z, as is evident in Fig. 4.*

It is of interest to consider some of the mode configurations corresponding to various points on the curves of Fig. 4. From equations (14) and (15) we find that when $k_y = 0$, $k_x{}^{es} = k_z^2$ and $k_x{}^{is} = k_z^2(-1/1+\kappa)$. There is actually rather little variation of k_x^i along a given curve such as (a), (b), or (c), etc., since the frequency dependence of $1+\kappa$ almost cancels the effect of changing k_z. On any given curve k_x changes by only π/s as k_z goes from 0 to ∞. The point on curve (a) at $k_z = 0$ corresponds to the uniform mode for the slab. As k_z is

* This figure is drawn for $\Omega_H \gg 1$ because in this limit equation (22) becomes independent of Ω_H (and therefore of H_0 and M_0). Fig. 4 is approximately correct even for $\Omega_H \approx 1$ (i.e. $H_0 \approx M_0$), since as Ω_H becomes large, $(\Omega_H^2+\Omega_H)^{1/2} \to (\Omega_H+0{\cdot}5)$, while even for $\Omega_H = 1$, $(\Omega_H^2+\Omega_H)^{1/2} = \sqrt{(2)} = \Omega_H+0{\cdot}414$.

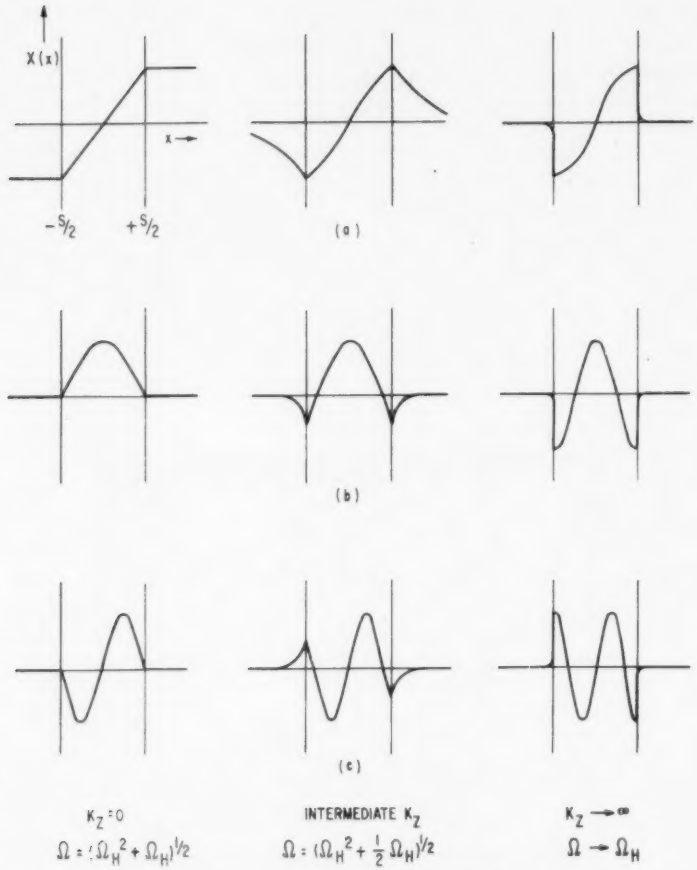

FIG. 5. (a) Magnetic potential $X(x)$ as a function of k_x along curve (a) of Fig. 4. (b) $X(x)$ vs. k_x along curve (b) of Fig. 4. (c) $X(x)$ vs. k_x along curve (c) of Fig. 4.

increased and one moves along this curve, the x-variation of the mode pattern changes as shown in Fig. 5(a).

The x-variation of the mode patterns for points along curves (b) and (c) of Fig. 4 are similarly shown in Figs. 5(b) and 5(c).

It is seen that all these modes for which $k_y = 0$, have equal amplitude at the two surfaces of the slab.

It may also be noted that the infinite set of modes at $k_y = 0$, $k_z = 0$, $\Omega = (\Omega_H^2 + \Omega_H)^{1/2}$ is a complete set of spatial harmonics so far as variation in the x-direction is concerned. Thus it is possible to have configurations for which there is no variation in the y- and z-direction but which are quite arbitrary in the x-direction within the slab. These modes have no r.f. fields outside the slab. Such modes may be understood intuitively, since it is known that for the ordinary uniform mode for a thin slab, no r.f. field extends outside of the sample and therefore other slabs having uniform modes of arbitrary phase and amplitude may be added to it without interaction to represent a mode of arbitrary x-variation. KITTEL[5], for example, has shown that the resonant frequency of a transversely magnetized conducting ferromagnetic sheet is $\omega = \gamma[BH]^{1/2}$, or $\Omega = (\Omega_H^2 + \Omega_H)^{1/2}$, just as in an insulating sheet, even though the phase varies and the amplitude falls off exponentially from the surface. This variation arises, of course, from the driving field configuration due to skin depth phenomena.

The more general case, i.e. $k_y \neq 0$, in the region of all real wave-vector components $(1 + \kappa < 0)$, has two important features. First, the mode amplitude at the two surfaces of the slab is not equal, and second, the entire pattern travels in the y-direction with phase velocity ω/k_y. In the x-direction the mode patterns are standing, sinusoidal waves as before, but the spatial phase varies with η, leading, in general, to unequal amplitudes at the two surfaces. Both signs of k_y are permitted, but at a

given frequency reversal of the sign of k_y reverses the propagation direction and also reflects the mode pattern through the plane $x = 0$ at the center of the slab. The result is the same as if the slab were rotated 180°C about the z-axis. Since these two modes are degenerate in frequency, they may be combined to form two new modes, but in each of these combination modes the configuration propagates in opposite directions on the two sides of the slab. Thus these combination modes cannot be described by separable characteristic functions.

gives rise to the surface shown in Fig. 3 which emerges from the manifold of volume mode surfaces at $\eta = (1/\Omega_H)^{1/2}$ and $\Omega = (\Omega_H^2+\Omega_H)^{1/2}$, and which has $\Omega = (\Omega_H+1/2)$ as its maximum frequency. Points on this characteristic surface give rise to surface modes; since k_x^i is imaginary for $(1+\kappa) > 0$, the mode amplitudes are maximum at the surfaces of the slab and are attenuated toward the interior. Furthermore, it may be shown that there are no other solutions of equation (19) than those already discussed.

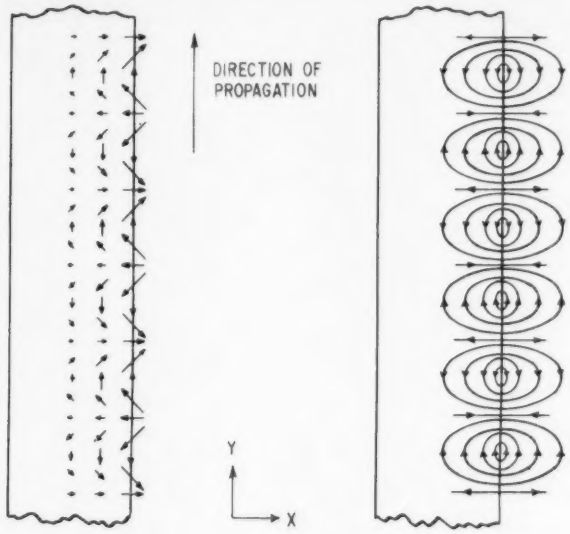

FIG. 6. Mode configuration for short wavelength surface waves with $k_z = 0$.
(a) Transverse magnetization.
(b) Transverse magnetic fields.

(b) *Surface modes*, $(1+\kappa) > 0$

On examination of equation (19) it is found that if $|\eta| < (1/\Omega_H)^{1/2}$ the equation has a root lying outside of the frequency range of the volume modes.* This root

Consider first the surface wave solutions for which $k_z = 0$. From equations (14) and (15) these solutions must have $k_x = |k_y|$ and $k_x^i = \pm ik_y$, corresponding to mode configurations which are sinusoidal waves in the y-direction travelling with phase velocity ω/k_y, and are attenuated in a characteristic length $1/|k_y|$ as one goes from the surface of the slab toward either interior or exterior. As $|k_y|$ increases these modes therefore cling more closely to the surface of the slab.

From equation (19) the dependence of the frequency of these mdoes on k_y (i.e. for $k_z = 0$) is found to be

$$\Omega^2 = \Omega_H^2+\Omega_H+[2+2\coth(|k_y|s)]^{-1} \qquad (23)$$

The long wavelength limit, $k_y = 0$, occurs at $\Omega^2 = \Omega_H^2+\Omega_H$ and the mode configuration approaches that of the uniform mode for a slab. At very short wavelengths the frequency approaches $\Omega = (\Omega_H+1/2)$ as

* For examination of this root the argument of the cot term of equation (19) is imaginary and it is convenient to rewrite equation (19) in terms of real quantities as:

$$(1+\eta^2)+2|(1+\eta^2)^{1/2}|\left(\frac{1+\eta^2+\kappa}{1+\kappa}\right)^{1/2}$$
$$\times(1+\kappa)\coth\left[|k_y|s\left(\frac{1+\eta^2+\kappa}{1+\kappa}\right)^{1/2}\right]$$
$$+(1+\kappa)^2\left(\frac{1+\eta^2+\kappa}{1+\kappa}\right)-\nu^2 = 0$$

Vol. 19
1961

might be expected since the magnetization configuration becomes similar to that of a parallel array of axially magnetized cylinders. The configuration of the transverse magnetization and magnetic fields for this case are shown in Fig. 6. With reversal of the direction of propagation, the maximum amplitude shifts to the opposite surface of the slab.

The surface modes for $k_z \neq 0$ (i.e. $\eta \neq 0$) cling to the surface of the slab even more tightly for a given k_y, and at $\eta = (1/\Omega_H)^{1/2}$, the decay constant of the surface waves becomes infinite. This is the limiting value of η for surface modes and further increase of η yields solutions with volume mode character of infinite wave-vector.*

metry which led to equivalent modes with $\pm k_y$. This removes the degeneracy of modes of opposite k_y, and propagation occurs in only one direction at a given frequency. This result corresponds to the Ferrite–Air II modes of FLETCHER and SEIDEL[4], which are obtained by considering sections of the surface wave sheet in the k_y–k_z–Ω diagram (Fig. 3) at planes of $k_z z_0 = m\pi$, and restricting k_y to values $k_y < 0$. Although we consider only the magnetostatic limit, the spectrum thus includes some of the same modes found in a complete treatment of the ferrite-loaded waveguide. We of course do not find those modes which depend explicitly on propagation effects, viz. the FA–1 and F–M modes of FLETCHER and

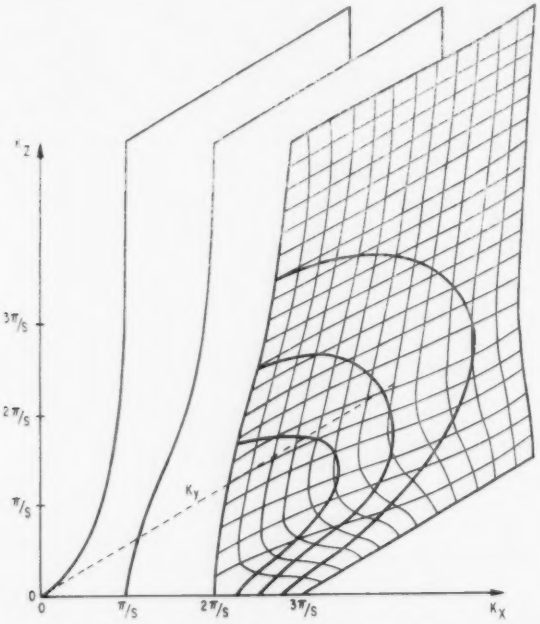

FIG. 7. Sketch of characteristic surfaces in k-space for volume modes of a slab. Only one surface is shown, but a periodic set of surfaces with similar form exists. The intercepts in the k_x–k_z and k_x–k_y planes are shown for other surfaces.

A connection of the magnetostatic mode spectrum to the modes obtained in ferrite-loaded waveguides might be noted. If two conducting walls are placed parallel to the x–y plane, spaced a distance z_0 apart, the mode spectrum will be identical to that obtained in this analysis, except that the additional condition $\cos k_z z_0 = \pm 1$, or $k_z z_0 = m\pi$, must be satisfied. A conducting wall in the y–z plane, on the other hand, destroys the symmetry which led to equivalent modes with $\pm k_y$. This removes the degeneracy of modes of opposite k_y, and propagation occurs in only one direction at a given frequency. This result corresponds to the Ferrite–Air II modes of FLETCHER and SEIDEL[4], which are obtained by considering sections of the surface wave sheet in the k_y–k_z–Ω diagram (Fig. 3) at planes of $k_z z_0 = m\pi$, and restricting k_y to values $k_y < 0$. Although we consider only the magnetostatic limit, the spectrum thus includes some of the same modes found in a complete treatment of the ferrite-loaded waveguide. We of course do not find those modes which depend explicitly on propagation effects, viz. the FA–1 and F–M modes of FLETCHER and SEIDEL. Certain waveguide modes occurring for $(1+\kappa) < 0$ have been discussed by SEIDEL[4], who found that propagation occurs with real values of k_x, but the mode configuration differs because of the conducting boundaries.

IV. MODE DISTRIBUTION IN WAVE-VECTOR SPACE

Two equivalent representations of the characteristic modes were indicated in Section II, equations (19) and (20). For some purposes, the characteristic equation (20), expressed in terms of

* Linear combinations of degenerate surface waves may also be made to form modes which are essentially propagating around the slab, i.e. in opposite directions at the two surfaces.

wave-vector components, is the most useful. This representation of the modes will later be used in discussing the mode density. In this section, we will consider the form of the solutions of equation (20). As in the preceding section, two cases must be considered since k_x^i may be either real or imaginary; k_y and k_z are always real. For real k_x^i there is a multiplicity of solutions due to the second term in equation (20), while only a single solution is obtained for imaginary values of k_x^i.

$\Omega^2 = \Omega_H^2 + \Omega_H$. As the frequency, and thus θ, is decreased, the constant-frequency-cone intercepts a multiplicity of sheets, but the spacing of the intercepts increases. As $\Omega \to \Omega_H$, the frequency-cone intercepts the characteristic surfaces only for very large values of $\eta(k_y \to 0)$ and large values of k_z. At a given angle η, intercepts with the plane η = constant are obtained for all frequency-cones with $\theta > \tan^{-1}\eta$, corresponding to the minimum frequency $\Omega_\eta^2 = \Omega_H^2 + \Omega_H(\eta^2/1+\eta^2)$ at which roots were obtained in Section 3.

The characteristic surfaces are warped, for values of $k_y^2 + k_z^2 \approx k_x^2$. As $k_y^2 + k_z^2$ becomes large, however, the

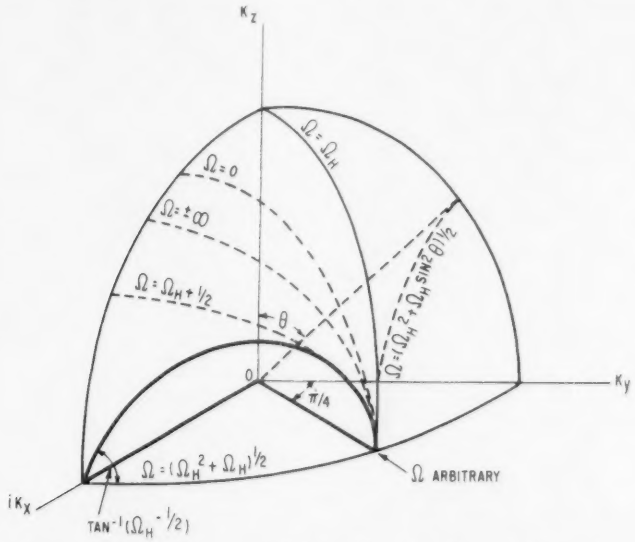

FIG. 8. Sketch of characteristic surface in k-space for surface modes of a slab. Only one octant is shown, but the remainder of the surface can be obtained by reflection in the coordinate planes. Loci of specific frequencies are shown as obtained from equation (14).

Consider first the volume modes, for which k_x^i is real. The characteristic surfaces determined by equation (20) for this case are sketched for reference in Fig. 7. Only one of the characteristic surfaces is shown in the figure, but surfaces corresponding to other solutions of equation (20) are indicated by their intercepts in the k_x^i–k_z and k_x^i–k_y planes.

The connection with the previous representation in k_y–k_z–Ω space can be made by considering the intercept of these surfaces with the surfaces of constant frequency. From equation (14), surfaces of constant frequency are cones of revolution about the k_z-axis, with semi-apex angle

$$\theta = \sin^{-1}\left[\sqrt{\left(\frac{\Omega^2-\Omega_H^2}{\Omega_H}\right)}\right].$$

Thus the k_x^i–k_y plane, $\theta = \pi/2$, corresponds to frequency surfaces approach equally spaced, parallel planes occurring at the poles of $\cot k_x^i s$, i.e. $k_x^i s = n\pi (n = 0, 1, 2, \ldots)$. Imposition of periodic boundary conditions in y and z would, of course, result in a rectangular array of mode points in these planes.

The intercepts of these surfaces with the k_x^i–k_z plane take the form

$$2\cot k_x^i s = \frac{k_x^i}{k_z} - \frac{k_z}{k_x^i}$$

This yields a series of simple curves each varying from $k_x^i s = n\pi$ to $(n+1)\pi$ as the ratio k_z/k_x^i varies from 0 to ∞. The zeroes of $\cot k_x^i s$ occur on the line $k_x^i = k_z$. All curves are of similar shape with the exception of that near the origin which differs slightly because of the limiting value of this expression as $k_x^i \to 0$. The variation

by $k_x^i = \pi$ on each curve corresponds to the increase by 180° in the x-variation of the magnetization shown in Fig. 5 as the frequency changes from $\Omega = \sqrt{(\Omega_H^2+\Omega_H)}$ to $\Omega = \Omega_H$.

To obtain the behavior near the k_x^i–k_y plane, consider the limit of equation (20) as $k_z \to 0$. With the exception of the k_y-axis on which there is no solution, this has a root at each pole of cot $k_x^i s$ for $k_z = 0$ independent of k_y. As k_z is increased slightly, the surfaces bend toward smaller k_x^i, and for $k_y \ll k_x^i$ there is a rapid shift of π in the value of $k_x^i s$. At larger values of k_y, a change in k_x^i also occurs as η increases, but the variation is less than that obtained near the k_x^i axis.

For imaginary k^i, corresponding to the frequency range $(\Omega_H^2+\Omega_H)^{1/2} < \Omega < \Omega_H+1/2$, the solution of equation (20) yields a single surface in k-space.* One octant of the surface represented by this expression is sketched in Fig. 8 where the k-space axes are ik_x^i, k_y, and k_z. In this k-space surfaces of constant frequency are cones of elliptical cross-section whose axes are either the ik_x^i- or the k_y-axis depending on the frequency. Several of these surfaces are indicated in Fig. 8 for specific frequencies.

As indicated in Fig. 8, the characteristic surface intersects the ik_x^i–k_y plane along the ik_x^i-axis and along the line $ik_x^i = k_y$. In general, the plane $k_x^i = 0$ corresponds to the frequency $\Omega = (\Omega_H^2+\Omega_H)^{1/2}$ and thus points along the ik_x^i axis correspond to the point in k_y–k_z–Ω space where $k_y = 0$, $k_x^i = 0$, $\Omega = (\Omega_H+\Omega_H)^{1/2}$. Along the line $ik_x^i = k_y$, however, the frequency is arbitrary since all constant frequency surfaces include this line. The frequency on the characteristic surface near this line may be found by determining which constant frequency surface it approximates as this line is approached. Since the line $ik_x^i = k_y$ corresponds to the intercept in k_y–k_z–Ω space of the characteristic surface with the k_y–Ω plane, we expect the frequency to vary from $(\Omega_H^2+\Omega_H)^{1/2}$ to $(\Omega_H+1/2)$ as we move out along $ik_x^i = k_y$ from the origin. Indeed, for very small ik_x^i and k_y the characteristic surface of Fig. 8, is approximated by the plane $k_z = 0$, corresponding to $\Omega = (\Omega_H^2+\Omega_H)^{1/2}$. (This region of the characteristic surface is not indicated in Fig. 8.) For large k_y the characteristic equation is approximated by $k_z/[k_y^2-(ik_x^i)^2] = -1/(1+4\Omega_H)$ which is the equation for the constant frequency surface for which $\Omega = (\Omega_H+1/2)$.

* It is convenient to express the characteristic equation in terms of real variables, which we do by replacing k_x^i by $-(ik_x^i)^2$ in equation (2) where ik_x^i is real. We obtain

$$1+\eta^2-2\frac{|k_y|(ik_x^i)}{k_y^2-(ik_x^i)^2}\eta^2\sqrt{[(1+\eta^2)]} \times \coth(ik_x^i)s+\left[\frac{(ik_x^i)k_y}{k_y^2-(ik_x^i)^2}\right]^2\eta^4 - \frac{1}{\Omega_H}\left[\Omega_H+\frac{k_y^2-(ik_x^i)^2}{k_y^2+k_z^2-(ik_x^i)^2}\right] \times \left[\frac{k_y^2+k_z^2-(ik_x^i)^2}{k_y^2-(ik_x^i)^2}\right] = 0 \quad (2)$$

V. MODE DENSITY

It has been indicated earlier that the spin-wave spectrum of an infinite medium in the exchange-free range of wavelength has an upper bound at a frequency $\Omega^2 = \Omega_H^2+\Omega_H$. The magnetostatic mode spectrum, on the other hand, extends to $\Omega = \Omega_H+1/2$ although the form of the solution changes at the spin-wave limit. It is of some importance to understand the connection between these two approximations, since the mode spectrum plays an important role in the theory of resonance line-widths and relaxation effects.[6] The density of modes as a function of frequency and wave-vector is of particular interest because this quantity enters directly into calculations of the scattering of spin excitation. The mode density also provides a convenient means for comparing the magnetostatic and spin-wave approximations.

We first obtain an expression for the density of spin-wave modes in the exchange-free region. For the usual assumption of periodic boundary conditions, the spin-wave modes are uniformly distributed with density C_v modes per unit volume of k-space. In this case the number of modes of wave-vector with magnitude k and propagating at an angle θ to the internal magnetic field is proportional to the volume in k-space,

$$dN_v = 2C_v 2\pi k^2 \sin\theta\, dk d\theta \quad (24)$$

Combining this with the spin-wave dispersion relation, equation (21), we obtain the frequency dependence,

$$dN_v = C_v 4\pi k^2\, dk \frac{\Omega\, d\Omega}{\Omega_H \cos\theta} = C_v 4\pi k^2\, dk \frac{\Omega\, d\Omega}{\Omega_H(\Omega_H^2+\Omega_H-\Omega^2)^{1/2}} \quad (25)$$

Note that the dependence on Ω and on k are separable, and we may write $dN_v = C_v 4\pi k^2\, dk \rho_v(\Omega)\, d\Omega$. The density becomes infinite at the top of the

band, and decreases monotonically with frequency to the bottom of the band, $\Omega = \Omega_H$. It is interesting that the mode density does not vanish at $\Omega = \Omega_H$, although equation (24) implies zero density at $\theta = 0$. The explanation is in the spin-wave dispersion relation, which leads to a variation of frequency with propagation angle for small θ which is sufficiently slow to overcome the zero of $\sin\theta$.

If the periodic boundary condition is removed in the y- and z-directions, the exchange-free spin-wave modes would fill planes of constant k_x with periodicity $k_x s = \pi$, just as found in the limit of large $k_y^2+k_z^2$ for the magnetostatic modes.* It is thus clear that no distinction can be made between spin-waves and the volume modes obtained in this analysis, and the principal effect of the boundary conditions is to shift the mode distribuion slightly for $k_s < k_x$. Thus the mode density function for spin-waves is approximately correct for the magnetostatic modes, and becomes exact at sufficiently short surface wavelengths.

For modes in the region $1+\kappa > 0$, the density could also be obtained from the representation in ik_x–k_y–k_z coordinates, but it is more convenient to use the representation of Section 3 in terms of k_y–k_z–Ω. Again, taking the limit of periodic boundary conditions, it is assumed that the mode distribution is uniform on the k_y–k_z plane of Fig. 3, with density of C_s modes per unit area. The number of modes per unit frequency interval in the range $(\Omega_H^2+\Omega_H)^{1/2} < \Omega < (\Omega_H+1/2)$ is then proportional to the slope $d\tan^{-1}\eta/d\Omega$ of the characteristic surface. Although this slope is a function of wavelength for small values of k_y, at sufficiently large k_y the characteristic equation (19) is independent of wavelength and the frequency is a function only of η. Thus the surface mode density can be written,

$$dN_s = 4C_s k_s \frac{d\tan^{-1}\eta}{d\Omega}\, dk_s d\Omega \qquad (26)$$

In this limit equation (19) becomes

$$[(1+\eta^2)^{1/2}+(1+\kappa)^{1/2}(1+\eta^2+\kappa)^{1/2}]\pm\nu = 0 \qquad (27)$$

* Since the combination $k_y^2+k_z^2$ will be used considerably in this section, it is convenient to define a "surface wave-vector" $k_s^2 = k_y^2+k_z^2$.

The choice of sign in equation (27) corresponds to the two directions of propagation on opposite sides of the slab. Substituting for κ and ν in terms of Ω and Ω_H and differentiating the resultant expression for Ω, we obtain

$$d\Omega/d\tan^{-1}\eta = (1+\eta^2)\, d\Omega/d\eta$$
$$= \frac{\Omega H\eta}{2}\left[(1+\eta^2)^{1/2} - \frac{(1+1/\Omega_H)}{(1+\eta^2)^{1/2}}\right] \qquad (28)$$

From equation (27) the terms in η and $(1+\eta^2)^{1/2}$ can be expressed as a function of frequency and the mode density of equation (26) becomes

$$dN_s = 4C_s k_s \Omega_H\{2(\Omega^2-\Omega_H^2)-\Omega_H$$
$$-2\Omega[\Omega^2-\Omega_H(\Omega_H+1)]^{1/2}\}^{-1/2}$$
$$\times[\Omega^2-\Omega_H(\Omega_H+1)]^{-1/2}\, dk_s d\Omega \qquad (29)$$

or

$$dN_s = 4C_s k_s\, dk_s \rho_s(\Omega)\, d\Omega.$$

Obviously, this function has a pole at $\Omega^2 = \Omega_H^2+\Omega_H$ from the second term in the denominator. The first term also yields a pole at $\Omega = \Omega_H+1/2$. This latter result differs from previous estimates of mode density in this region, in which the mode density was expected to vanish at the upper frequency limit.

The frequency dependence of the density functions $\rho_v(\Omega)$ and $\rho_s(\Omega)$ are sketched in Fig. 9. Note that these functions exhibit a different dependence on the wave-vector components. Both the surface and volume mode density tend to increase with wave-vector, however, but the volume modes increase as k^2 while the surface modes increase only linearly with k_s. Thus the modes lying above the frequency $\Omega = (\Omega_H^2+\Omega_H)^{1/2}$ become statistically unimportant at sufficiently short wavelengths, while the modes below $\Omega = (\Omega_H^2+\Omega_H)^{1/2}$ connect smoothly to the mode spectrum of spin-waves in an infinite medium.

VI. DISCUSSION

The geometry treated here is one to which previous analyses of magnetostatic modes are not applicable, and this investigation thus extends the analytical results to a new, yet common, sample

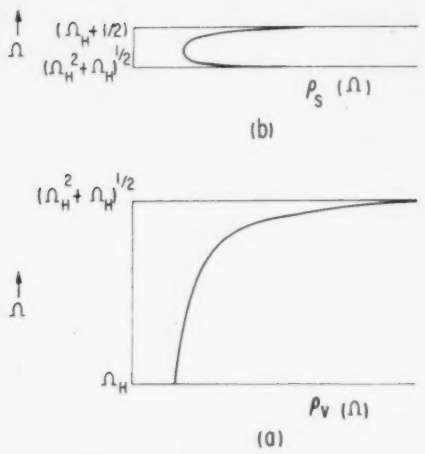

FIG. 9. Frequency dependence of the mode density functions.
(a) Volume modes.
(b) Surface modes.

configuration. The results obtained here are related to the problem of propagation in ferrite-loaded waveguide, but experiments designed to measure propagation effects usually do not satisfy the assumptions of this analysis, and more direct experiments are required.

DILLON has observed magnetostatic modes in discs cut from single crystals of manganese ferrite and yttrium iron garnet,[7] with the applied d.c. field both in the plane of the disc and also normal to it. Recently, RODRIGUE has observed magnetostatic modes in rectangular polycrystalline slabs.[8] In all these cases the observed mode spacings and intensities appeared to follow regular series. The general features of these modes, such as the region of d.c. field in which they were observed and their dependence on sample magnetization, are in agreement with magnetostatic mode theory. It appears most likely that the observed modes are series which have the least permissible variation through the slab thickness but have different numbers of loops and nodes over the transverse slab dimensions. Thus to correlate these results with the theory presented here would require introduction of definite boundaries in the y–z plane. Approximate solutions should be relatively easy to obtain from our results for the case of the thin rectangular slab, but this has not yet been carried out.

In the slab geometry, a clear distinction is found between volume and surface modes, and the mode density spectrum in the surface mode region differs from previous results in spheres. The dependence of the density spectrum on sample shape is not known in detail, but our result arises basically from the symmetry of the characteristic surfaces in k_z and other geometries should have similar symmetry properties; thus it appears likely that a pole of mode density should exist at $\Omega = \Omega_H + 1/2$ for other sample shapes, although the detailed density spectrum might be quite different. Since resonance line-width and other resonance parameters depend on the details of the mode density spectrum and its wavelength dependence, experiments on samples of this configuration may lead to better understanding of the role of these modes in resonance phenomena.

REFERENCES

1. MERCEREAU J. and FEYNMAN R. P., *Phys. Rev.* **104,** 63 (1956).
2. WALKER L. R., *Phys. Rev.* **105,** 390 (1957).
3. WALKER L. R., *J. Appl. Phys.* **29,** 318S (1958); WHITE R. L., *J. Appl. Phys.* **30,** 182S (1959).
4. See for example: SEIDEL H., *Proc. Inst. Radio Engrs, N.Y.* **44,** 1410 (1956); FLETCHER R. C. and SEIDEL H., *J. Appl. Phys.* **30,** 1475S (1959). MIKAELYAN A. L. and STOLYAROV A. K., *Radiotekh. elektron.* **4,** 1079 (1959).
5. KITTEL C., *Phys. Rev.* **73,** 155 (1948).
6. See for example: CLOGSTON A. M., SUHL H., WALKER L. R. and ANDERSON P. W., *J. Phys. Chem. Solids* **1,** 129 (1956); WHITE R. L., *J. Appl. Phys.* **30,** 1825S (1959); KASUYA T., *Prog. Theor. Phys. Osaka* **12,** 802 (1954); SUHL H., *J. Phys. Chem. Solids* **1,** 209 (1957).
7. DILLON J. F., Jr., *Bull. Amer. Phys. Soc.* (ser. 2) **1,** 125 (1956); to be published.
8. RODRIGUE G. P., Jr., Paper presented at I.R.E.–P.G.M.T.T. National Symposium, Coronado, California; May 9–11 (1960).

Vol. 196

J. Phys. Chem. Solids Pergamon Press 1961. Vol. 19, Nos. 3/4, pp. 321–330. Printed in Great Britain.

CYCLOTRON RESONANCE IN BISMUTH—II

J. E. AUBREY*

Royal Society Mond Laboratory, Cambridge, England

(*Received* 31 *October* 1960)

Abstract—Preliminary work on cyclotron resonance in bismuth reported earlier[2] has been extended in order to check the detailed form proposed for the electron energy band, and to look for evidence of resonances from the holes. At high fields ($H \geqslant 2000$ G), the surface resistance, R, is found to pass through a minimum, and then to increase with H. This departure from the monotonically decreasing form expected from the theory of AZBEL' and KANER can be explained by the circumstance that at high fields, the radii of the electron orbits become comparable with, and eventually smaller than the skin depth, and this brings about a change from the anomalous, to the classical skin effect regime. Values of the zero field surface resistance support the view that the Fermi surface consists of three electron ellipsoids and a single hole spheroid.

1. INTRODUCTION

AZBEL' and KANER[1] first predicted that the surface impedance of a metal under anomalous skin effect conditions should vary periodically with the reciprocal of the magnetic field strength when the field is applied parallel to the specimen surface. This prediction was confirmed by AUBREY and CHAMBERS[2] (hereinafter referred to as I) working on bismuth and the present paper describes an extension of the work reported in I, using the same frequency (about 9 kMc/sec), and the same experimental technique (measurement of the Q of a resonator consisting of a single-crystal rod of bismuth, about one half-wavelength long, in a coaxial shield). The aim of the present work was to check some of the details of the electron energy band structure (Sections 2 and 3), to look for evidence of resonances from the holes (Section 4), to account for the behaviour of the surface resistance at high fields (Section 6) and to estimate the total area of the Fermi surface in bismuth (Section 7).

For the case of a single quadratic electron energy band, AZBEL' and KANER found the following approximate expression for the surface impedance, $Z = R+iX$,

$$Z \simeq Z(0)[1-\exp(-2\pi ix)\exp(-2\pi x/\omega\tau)]^{1/3} \quad (1)$$

where $Z(0)$ is the zero-field impedance and $x = \omega/\omega_c = \omega m^*/eH$. Fig. 1 illustrates the kind of dependance of surface resistance, R, upon x which equation (1) implies, where $\omega\tau$ has been given the particular value 2π. Thus by plotting an experimental curve of R against H^{-1}, and measuring the period, $\Delta(H^{-1})$, of the oscillations, the effective mass m^* of the electrons can in principle be found. In the work to be described,

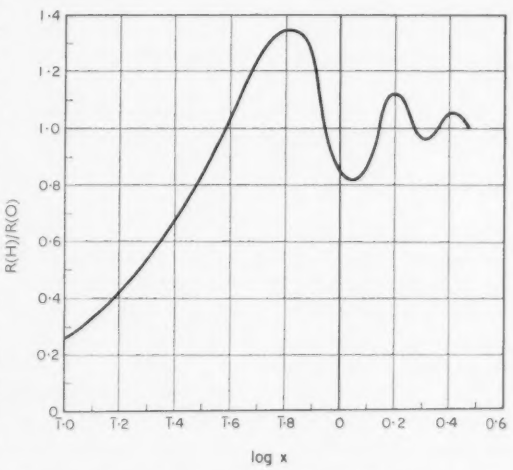

FIG. 1. Plot of the real part R, of Z [equation (1)] against $\log_{10}x$, for $\omega\tau = 2\pi$, assuming $Z(0) = R(0)(1+\sqrt{3}\,i)$.

* Present address: The Welsh College of Advanced Technology, Cathays Park, Cardiff.

it was frequently difficult to measure the period, $\Delta(H^{-1})$, either because the value of $\omega\tau$ was too low, or because several sets of oscillations from groups of carriers with different effective mass values were superimposed. In such cases, the most prominent feature of the curves of resistance against field, namely, the first resistance maximum, was used to calculate the effective mass of the carriers using the relation (Fig. 1),

$$m^* = 0{\cdot}7\, eH/\omega. \tag{2}$$

Although the field H at which the first maximum occurs depends only slightly on the precise value of $\omega\tau$, this equation nevertheless gives only a rough estimate of the effective mass since the phase of the oscillations is often different from that predicted by the theory of AZBEL' and KANER[3]. Moreover the position of the first maximum is more liable to perturbation by other groups of carriers than is the following minimum which is the first true "resonance"[3]; despite this we preferred to use the position of the maximum since the position of the minimum was often somewhat ill-defined. No details of the band structure are determined however from the effective mass values found in this way, which may in fact be in error by up to 30 per cent.

The ϵ–$\boldsymbol{k}$ relation for one of the groups of conduction electrons in bismuth has the form[4]

$$2m_0\epsilon/\hbar^2 = \alpha_1 k_1^2+\alpha_2 k_2^2+\alpha_3 k_3^2+2\alpha_4 k_2 k_3 \tag{3}$$

where the energy is measured from the minimum in the conduction band and the components of $\boldsymbol{k}$ are measured from the point in $\boldsymbol{k}$-space where the energy minimum occurs, k_1, k_2, and k_3 being parallel to diad, bisectrix and triad axes respectively. The symmetry elements of the reciprocal lattice demand that there be three† equivalent ellipsoids of the form (3) arranged at intervals of $2\pi/3$ about the triad axis, and if we call (3) ellipsoid I, the equations of the other two, which we shall label II and III, may be obtained from (3) by rotating the co-ordinate system by $\pm 2\pi/3$, respectively, about the k_3 axis.

The general expression for the effective mass‡ of the electrons belonging to ellipsoid I for a direction of magnetic field specified by the direction cosines λ_1, λ_2, λ_3 has the form

$$(m_0/m_{\mathrm{I}}^*)^2 = \lambda_1^2(\alpha_2\alpha_3-\alpha_4^2) -2\lambda_2\lambda_3\alpha_1\alpha_4+\lambda_2^2\alpha_1\alpha_3+\lambda_3^2\alpha_1\alpha_2 \tag{4}$$

and similar expressions can easily be found which give m_{II}^* and m_{III}^* as functions of orientation. It will be convenient to list the expressions for the effective mass values of the electrons belonging to all three ellipsoids when the magnetic field is directed along the simple crystallographic directions, ($\lambda_1 = 1$, $\lambda_2 = \lambda_3 = 0$), ($\lambda_2 = 1$, $\lambda_3 = \lambda_1 = 0$), ($\lambda_3 = 1$, $\lambda_1 = \lambda_2 = 0$) which will be referred to respectively as the $2_\parallel$, $2_\perp$, and $3_\parallel$ orientations. These are as follows,

$2_\parallel$ orientation:

$$m_{\mathrm{I}}^* = \frac{m_0}{(\alpha_2\alpha_3-\alpha_4^2)^{1/2}} \tag{5}$$

$$m_{\mathrm{II}}^* = m_{\mathrm{III}}^* = \frac{2m_0}{[(\alpha_2\alpha_3-\alpha_4^2)+3\alpha_1\alpha_3]^{1/2}} \tag{6}$$

$2_\perp$ orientation:

$$m_{\mathrm{I}}^* = \frac{m_0}{(\alpha_1\alpha_3)^{1/2}} \tag{7}$$

$$m_{\mathrm{II}}^* = m_{\mathrm{III}}^* = \frac{2m_0}{[3(\alpha_2\alpha_3-\alpha_4^2)+\alpha_1\alpha_3]^{1/2}} \tag{8}$$

$3_\parallel$ orientation:

$$m_{\mathrm{I}}^* = m_{\mathrm{II}}^* = m_{\mathrm{III}}^* = \frac{m_0}{(\alpha_1\alpha_2)^{1/2}} \tag{9}$$

We now review briefly the central result arrived at in the work reported in I. Fig. 2 shows a curve of surface resistance against magnetic field for a $2_\parallel$ specimen, taken from I, but plotted in a somewhat different way. The two groups of oscillations correspond to the two effective mass values (5)

† It will be seen in Section 7 that the minima in the conduction band occur at the Brillouin zone boundary. If this were not the case, each of the three ellipsoids would be duplicated by the inversion symmetry of the reciprocal lattice.

‡ The effective mass which is meant here is the "cyclotron mass" applicable in equation (1), and is given by $\hbar^2/2\pi\, d\mathscr{A}/d\epsilon$ where $\mathscr{A}$ is an area of cross section of the Fermi surface cut by a plane normal to the direction of the magnetic field.

Vol. 196

and (6), and from the value $m_{\mathrm{I}}^{*} = 0{\cdot}11\ m_0$ deduced from the period of set I, the quantity $\alpha_2\alpha_3 - \alpha_4^2$ was found to be of the order 100. When this was taken in conjunction with SHOENBERG's values of the products $\alpha_1\alpha_i$ $(i = 2, 3, 4)$, the following set of α's was found which differs somewhat from the set deduced originally by SHOENBERG[4]:

$$\alpha_1 = 168,\quad \alpha_2 = 2{\cdot}0,\quad \alpha_3 = 100,\quad \alpha_4 = 10\dagger \qquad (10)$$

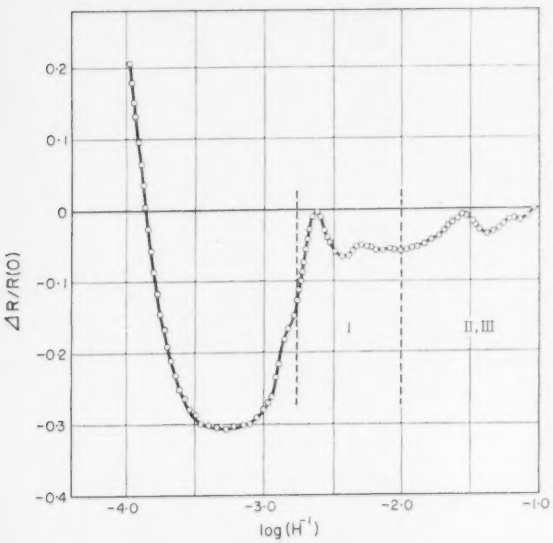

FIG. 2. Surface resistance of a $2_{\parallel}$ specimen plotted against $\log_{10}(H^{-1})$, showing two sets of oscillations marked I and II, III.

The following sections describe some additional work which has necessitated a slight revision of the set of values (10).

2. INVESTIGATION OF THE PRINCIPAL ORIENTATIONS IN BISMUTH

(i) *The $2_{\parallel}$ orientation*

Since m^* falls very rapidly from the peak value (5) as one departs from this orientation, and since the value found in I was less than half the value $0{\cdot}25\ m_0$ predicted by Shoenberg's set of α's, it was thought necessary to investigate orientations in the neighbourhood of $2_{\parallel}$ carefully to see whether the value observed was indeed the peak value. A single specimen was used whose axis was within a few degrees of $2_{\parallel}$, and provision was made for tilting the magnetic field away from the (vertical) specimen axis. This was achieved by providing a pair of coils, one on either side of the main solenoid, so as to form a rough Helmholtz pair which contributed a variable horizontal component to the magnetic field at the specimen, the whole coil assembly being mounted on a turntable so that the resultant field could be made to lie along any direction within a cone of angle about 8°.‡

These experiments indicated that the value found in I needed little correction, the final estimate being

$$m_{\mathrm{I}}^{*} = 0{\cdot}119 \pm 0{\cdot}003\, m_0$$

From equation (5) we therefore have that

$$\alpha_2\alpha_3 - \alpha_4^2 = 70{\cdot}5 \pm 4{\cdot}4 \qquad (11)$$

Since the two sets of resistance oscillations in Fig. 2 are well resolved, the period of the low-field oscillations and the corresponding m^* can also be determined fairly accurately, and since the quantity $\alpha_2\alpha_3 - \alpha_4^2$ is already known, $\alpha_1\alpha_3$ can be determined using equation (6); from the effective mass,

$$m_{\mathrm{II}}^{*} = 0{\cdot}0090 \pm 0{\cdot}0002\, m_0$$

we find

$$\alpha_1\alpha_3 = 16400 \pm 820 \qquad (12)$$

As was mentioned in I, both sets of oscillations at this orientation have a phase shift of approximately $\pi/2$ towards lower fields.

(ii) *The $2_{\perp}$ orientation*

Figure 3 shows a surface resistance curve for a specimen of this orientation, and maxima can be seen to occur at the fields

676, 135, 68 and 26 G

According to the three ellipsoid scheme for the conduction band, the effective mass of the electrons

† SMITH[5] has shown that α_4 is positive.

‡ According to AZBEL' and KANER[1], the angle between H and the surface of the specimen must be less than δ/l, where δ is an effective skin depth given by $R/2\pi\omega$, and l is the mean free path. For bismuth, this angle is typically of the order of several degrees, considerably larger than for a good metallic conductor.

Vol. 19
1961

belonging to ellipsoid I has the value (7) and the electrons belonging to the other two ellipsoids have the degenerate mass value (8) at this orientation. If the values (11) and (12) are substituted into these expressions, the effective mass values are found to be 0·0156 m_0 and 0·0078 m_0, and if equation (2) is now assumed to be valid, the first resistance maxima corresponding to these masses should occur at the fields 72 and 36 G. It seems plausible therefore to identify the two low-field resistance

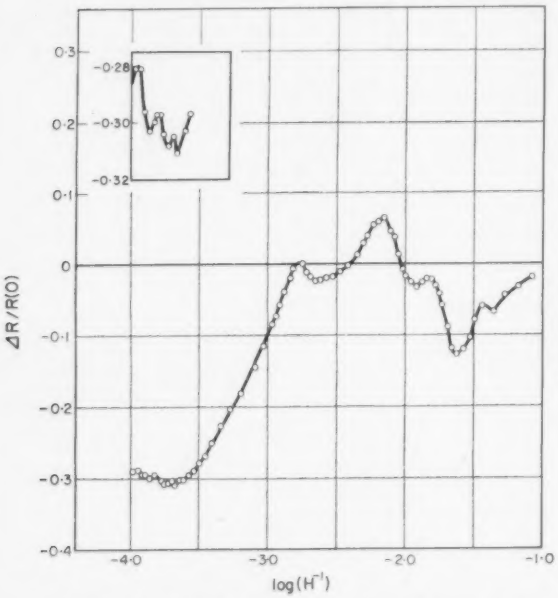

FIG. 3. Surface resistance of a $2_\perp$ specimen plotted against $\log_{10}(H^{-1})$. The inset is a plot of the high field region on an enlarged ordinate scale with unchanged abscissa.

peaks as the first maxima of the two electron resonance patterns, the agreement between the observed and expected values of the fields being as good as can be expected since the possibility of a phase shift has not been taken into account, and also the overlapping of two resonance patterns leads to a further displacement of the maxima [see Fig. 7 of Ref. (3)].

The maxima found at higher fields (676 and 135 G) cannot readily be explained by the three ellipsoid model of the electron band. Interpreted as the first maxima of two separate sets of oscillations, they correspond to effective masses of the order 0·15 and 0·03 m_0 respectively, and it is conjectured that they are hole resonances (see Section 4).

(iii) *The* $3_\parallel$ *orientation*

The effective mass of the electrons is triply degenerate at this orientation but because each of the three ellipsoids is tilted out of the trigonal plane, the individual m^*'s do not pass through turning values at this orientation. A small tilt of the field

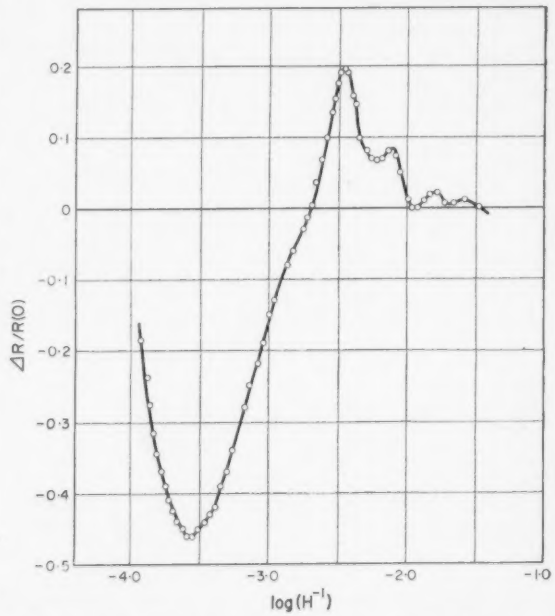

FIG. 4. Surface resistance of a $3_\parallel$ specimen plotted against $\log_{10}(H^{-1})$.

away from the triad axis can therefore lead to an increase or a decrease of the individual m^*'s, and because of the great elongation of the ellipsoids, the change of m^* with angle of tilt is very rapid.

In order to align the field accurately along the triad axis, the field-tilting technique used in the study of the $2_\parallel$ orientation was used. A specimen was chosen whose triad axis was within 2° of the specimen axis and the direction of the field was adjusted until the curve of resistance against field showed the best coincidence of the individual resonance patterns. Such a curve is shown in Fig. 4, the resonance behaviour taking place

between 500 and 50 G; when H is misaligned, the main peak in the figure rapidly splits into separate peaks. Since the oscillations in R are not periodic in H^{-1}, we can make only a rough estimate of the electron effective mass from the position of this main peak, and using equation (2) we find,

$$m^* = 0{\cdot}06\, m_0.$$

This is quite close to the value $0{\cdot}055\, m_0$ expected from the set of conduction band parameters finally arrived at in Section 5 [equations (9) and (14)]. The departure of the oscillations in Fig. 4 from periodicity in H^{-1} is believed to be due to the occurrence of a resonance from a group of holes with effective mass comparable to that of the electrons at this orientation (see Section 4).

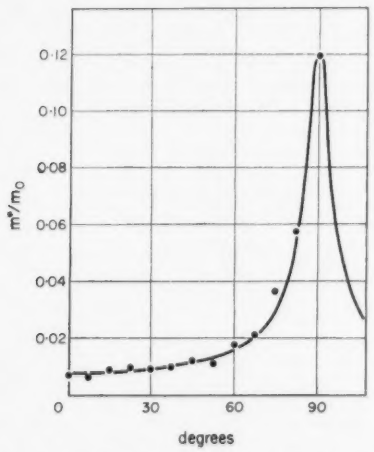

FIG. 5. Variation of the electron effective mass with orientation in the trigonal plane. The curve is a plot of equation (13), using the values (11) and (12), the abscissa being $\cos^{-1}\lambda_2$. Nine of the experimental points were obtained from three specimens of intermediate orientations and the remaining four from $2_\parallel$ and $2_\perp$ specimens.

3. INTERMEDIATE ORIENTATIONS IN THE TRIGONAL PLANE

The relation

$$(m_0/m^*)^2 = \lambda_1^2(\alpha_2\alpha_3 - \alpha_4^2) + \lambda_2^2\alpha_1\alpha_3 \qquad (13)$$

gives the dependence of m^* upon orientation in the trigonal plane ($\lambda_3 = 0$) for ellipsoid I, and similar expressions hold for ellipsoids II and III. Equation (13) was tested by investigating three specimens whose orientations lay at intermediate orientations between $2_\parallel$ and $2_\perp$ in the trigonal plane, three distinct effective mass values being observable at each orientation. The specimens had a rather low value of $\omega\tau$ so that only the first resistance maxima could in general be distinguished. Because of this limitation, the effective mass values have been calculated from the positions of the resistance maxima assuming somewhat arbitrarily that the phase shift of $\pi/2$ observed at the $2_\parallel$ orientation was present in each case, and the values obtained in this way have been plotted in Fig. 5; the curve in the figure is a plot of equation (13) using the values of the quantities given in equations (11) and (12). The experimental points clearly follow the trend of the curve quite well and an individual point may lie off the curve either because the assumed phase is not appropriate or because the position of the resistance peak is displaced owing to the proximity of a resonance from one or more of the other groups of carriers.

4. EVIDENCE FOR HOLES IN BISMUTH

The two resistance peaks which occurred at the higher fields in Fig. 3 ($2_\perp$ orientation) cannot be accounted for by the three ellipsoid scheme for the conduction band alone, and it is therefore believed that they are hole resonances. Peaks corresponding to these also appeared in the resistance curves obtained for specimens of intermediate orientations, and the fields at which they occurred are shown in Fig. 6. The lower field peak was found to diminish in height on moving away from the $2_\perp$ orientation, and had almost vanished at an angle of 15° from $2_\perp$. On approaching the $2_\parallel$ orientation, the higher field resonance changed from being a peak as in Fig. 3 (at 680 G) to being an inflection in the curve as in Fig. 2 (at 710 G). The reason for this is that as the $2_\parallel$ orientation is approached, m_I^* increases and the corresponding resonance moves to higher fields and eventually approaches the hole resonance. At the same time the electron resonance becomes dominant and at $2_\parallel$ almost obscures the hole resonance. From Fig. 6 it can be seen that the position of the higher field resonance varied by only about 10 per cent for orientations in the trigonal plane, and since the position of the resonance was found to differ by as much as 6 per cent for two specimens of the same

orientation, it seems likely that the effective mass associated with this peak is isotropic in the trigonal plane. The mass value itself can be estimated from the position of the peak, and by using equation (2) the ordinate scale in Fig. 6 has been converted from H to m^*.

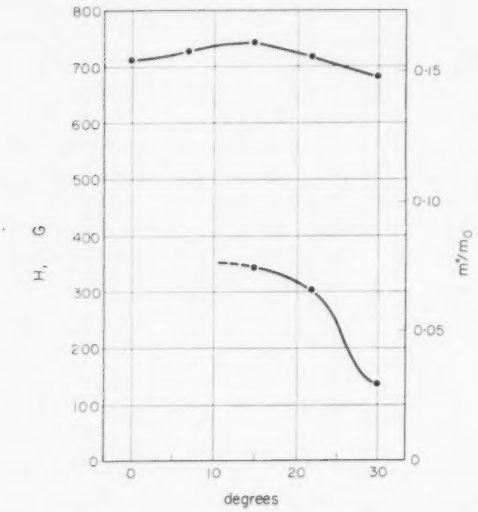

FIG. 6. Left-hand ordinate scale: positions of the resistance peaks interpreted as hole resonances. Right-hand ordinate scale: the corresponding effective mass values calculated from equation (2). Abscissa: angle between specimen axis and a diad axis of the crystal. (The specimen axes lie in the trigonal plane.)

No clear-cut evidence for a hole resonance was found for specimens of the $3_{\parallel}$ orientation (see Fig. 4). However the departure of the resistance oscillations from periodicity in H^{-1} and the distortion of the curve from the simple expected form of Fig. 1 (the three electron masses are degenerate at this orientation) suggest that the holes resonate in the same magnetic field range as the electrons. Since the resistance at the first minimum does not in fact fall below the zero-field value, it seems probable that the first maximum of the hole resonance would occur in this neighbourhood, and equation (2) then provides the rough estimate $m^* = 0{\cdot}04\, m_0$. This is in satisfactory agreement with the value $0{\cdot}047\, m_0$ found by BRANDT[6] at this orientation from his de Haas–van Alphen measurements.

5. DISCUSSION OF THE BAND STRUCTURE OF BISMUTH

(i) *The electron band*

SHOENBERG's work on the de Haas–van Alphen effect in bismuth[4] provides the following values with 5 per cent accuracy,

$$\alpha_1\alpha_2 = 336, \quad \alpha_1\alpha_3 = 16{,}800, \quad \alpha_1\alpha_4 = 1680,$$
$$\epsilon_0 = 2{\cdot}83 \times 10^{-14} \text{ erg}.$$

The present work provides values of $\alpha_2\alpha_3 - \alpha_4^2$ and $\alpha_1\alpha_3$, our estimate of the latter (12) being in good agreement with SHOENBERG's value. If the values of the two quantities (11) and (12) found here are adopted in conjunction with SHOENBERG's values of $\alpha_1\alpha_2$ and $\alpha_1\alpha_4$ we finally arrive at the following set of α's,

$$\alpha_1 = 196, \quad \alpha_2 = 1{\cdot}71, \quad \alpha_3 = 84, \quad \alpha_4 = 8{\cdot}6 \tag{14}$$

Each of these values is believed to be accurate to 10 per cent.†

(ii) *The hole band*

BRANDT[6] and BRANDT *et al.*[7] have recently found a new set of de Haas–van Alphen oscillations in bismuth which they associate with the holes. They deduce that the Fermi surface in the hole band is a spheroid of the form

$$2m_0(\epsilon_1 - \epsilon_0)/\hbar^2 = \beta_1(k_1^2 + k_2^2) + \beta_3 k_3^2 \tag{15}$$

where ϵ_1 is the band overlap and the components of $\boldsymbol{k}$ are measured from the point in $\boldsymbol{k}$-space where the energy maximum in the hole band occurs, k_3 being parallel to the triad axis. The spheroid parameters have the values

$$\beta_1 = 21{\cdot}2, \quad \beta_3 = 1{\cdot}46, \quad \epsilon_1 - \epsilon_0 = 2{\cdot}5 \times 10^{-14} \text{ erg}. \tag{16}$$

It has already been seen that BRANDT's hole mass for the $3_{\parallel}$ orientation (given by $\beta_1^{-1} m_0$) supports the explanation given for the form of the $3_{\parallel}$ curve (Fig. 4) in the resonance region. The result

† A crucial test of any given set of α's is whether or not the products $\alpha_1\alpha_i$ ($i = 2, 3, 4$) agree with SHOENBERG's values. Some sets of α's which have appeared in the literature recently [see Table IV of Ref. (5)] can be shown to be somewhat inaccurate by subjecting them to this test.

Vol. 196

(upper branch in Fig 6.) that one group of carriers, believed to be holes, has an effective mass which is isotropic in the trigonal plane and has the approximate value $0{\cdot}15\ m_0$ is also in agreement with BRANDT's work, his value of m^* in the trigonal plane being $(\beta_1\beta_3)^{-1/2}m_0 = 0{\cdot}18\ m_0$.

The single-spheroid model of the hole band does not account for the intermediate-field resistance peak observed at some orientations in the trigonal plane (lower branch in Fig. 6). This may be indicative of a departure of the constant energy surfaces from a simple spheroidal shape or of the existence of a further group of carriers. Also, the possibility that the peak is a spin resonance cannot be dismissed.[9]

There is no indication in the present work that there are heavy holes with $m^* \simeq m_0$ in bismuth (c.f. GALT *et al.*[8] and CHANDRASEKHAR[10]). The suggestion that such a band might exist was first made by HEINE[11] to account for the rather large linear term found by some workers in the specific heat of bismuth.[12] The most recent specific heat measurements[13] indicate that the linear term is not as large as was supposed, but it is still too large to be accounted for by the total density of states at the Fermi level calculated on the basis of the present model of the band structure. However, as the existence of heavy holes now seems doubtful, this discrepancy remains unexplained at present.

Finally, the period of the de Haas–van Alphen oscillations which BRANDT finds at the $3_{\parallel}$ orientation $[\Delta(H^{-1}) = 1{\cdot}57 \times 10^{-5}\ \mathrm{G}^{-1}]$ is in remarkably good agreement with periods previously found at this orientation in galvanomagnetic experiments (see Table I of the review article by KAHN and FREDERIKSE[14] for a recent compilation of the values). This period has previously been ascribed to the electrons, but differs markedly from SHOENBERG's de Haas–van Alphen period $[\Delta(H^{-1}) = 1{\cdot}18 \times 10^{-5}\ \mathrm{G}^{-1}$, quoted wrongly as $1{\cdot}4 \times 10^{-5}$ in Ref. (14)], as remarked by BABISKIN[15]; in view of BRANDT's work it seems reasonable to believe that the galvanomagnetic oscillations were in fact not due to the electrons but to the holes.

6. THE HIGH FIELD BEHAVIOUR OF THE SURFACE RESISTANCE

In contrast to the theoretical prediction of equation (1), that the surface resistance should go to zero as H increases beyond the range where the oscillations occur, it was found experimentally that $R(H)$ passes through a minimum value and then begins to increase (Figs. 2, 3 and 4). The reason for the breakdown of equation (1) is the following. It is assumed in the theory that $\delta \ll r$, where δ is the skin depth and r is the radius of the electron orbits in the metal. The orbit radius is given roughly by p_0/eH, where p_0 is the Fermi momentum, and since this is unusually small in bismuth, the orbit radii are considerably smaller for a given value of the magnetic field than in a good metallic conductor. At the same time, δ is unusually large owing to the small number of carriers present, thus the inequality $\delta \ll r$ begins to break down at quite moderate field strengths. Thus if the typical values $\delta = 10^{-4}$ cm and $p_0 = 2 \times 10^{-21}$ gm cm sec^{-1} are assumed, we find that $\delta = r$ at $H = 1250$ G.

When *all* the electrons are able to spiral completely within the skin depth and therefore move in an approximately uniform r.f. field between collisions, the classical relation

$$R(H) = \left(\frac{2\pi\omega}{\sigma(H)}\right)^{1/2} \qquad (17)$$

should hold, where $\sigma(H)$ is the d.c. conductivity in the field H. The increase in R with H at the high field limit is then due to the familiar decrease in the d.c. conductivity as the magnetic field increases (see e.g. KAPITZA[16]). The values of $R(H)$ found experimentally in this region are indeed given quite closely by equation (17), though a precise test of the relation cannot easily be carried out owing to the difficulty of setting up a specimen reproducibly in the magnetic field for both r.f. and d.c. experiments; a difference in setting of as little as 1° can give spurious results because of the very large transverse magnetoresistance of bismuth.

A factor which has not been taken into account yet in this discussion is the quantization of the orbits in the magnetic field. This should be unimportant so long as $\hbar\omega_c \ll kT$, which for bismuth at 4°K requires that H be less than about 2000 G; when H increases beyond this value the effect of the quantization of the electron orbits should become apparent. The inset in Fig. 3 illustrates a set of oscillations in the surface resistance which are due to quantization and are periodic in H^{-1}

with period

$$\Delta(H^{-1}) = 4{\cdot}3 \pm 0{\cdot}2 \times 10^{-5}\ \mathrm{G}^{-1}.$$

The d.c. resistance of the same specimen also showed pronounced oscillations with the period

$$\Delta(H^{-1}) = 4{\cdot}0 \pm 0{\cdot}1 \times 10^{-5}\ \mathrm{G}^{-1},$$

and these are both in good agreement with one of the de Haas–van Alphen periods for the electrons at this orientation, namely $4{\cdot}25 \times 10^{-5}\ \mathrm{G}^{-1}$.[4]

The phases of the r.f. and d.c. oscillations were in agreement to $\pm 0{\cdot}2\pi$, and the relative amplitudes were also consistent with equation (17), the amplitude of the r.f. oscillations being about half that of the d.c. oscillations.

Table 1

Orientation	Σ (ohm^{-1})	$\sigma \times 10^{-5}$ (ohm cm)$^{-1}$	$\Sigma_c = \left(\frac{\sigma}{2\pi\omega}\right)^{1/2}$ (ohm^{-1})	Σ_c/Σ
$2_\parallel$	$25{\cdot}5 \pm 1{\cdot}1$	7·3	45·3	1·8
$2_\perp$	$19{\cdot}2 \pm 0{\cdot}7$	9·6	52·0	2·7
$3_\parallel$	$18{\cdot}3 \pm 0{\cdot}8$	7·2	45·0	2·5
polycrystal	$15{\cdot}1 \pm 0{\cdot}6$	1·1	17·6	1·2

7. SURFACE CONDUCTANCES IN ZERO FIELD

Absolute values of the zero-field surface conductances ($\Sigma = R^{-1}$) of single crystal specimens of the three principal orientations and of a polycrystalline specimen, deduced according to the procedure outlined by PIPPARD[17] are given in Table 1, together with the d.c. conductivities of the specimens at 4°K. Values of the total Fermi surface area, S, and of the related parameter σ/l, where σ is the d.c. conductivity and l is an average mean free path, can in principle be found from the value of the surface conductance of a polycrystalline specimen in the anomalous skin effect limit using the relations

$$S = \left(\frac{8}{9}\right)^3 \frac{2\pi^3 3^{3/2} \hbar\omega^2 \Sigma^3}{e^2} \qquad (18)$$

(CHAMBERS[18]), and

$$\sigma/l = \left(\frac{8}{9}\right)^3 3^{1/2}\pi\omega^2\,\Sigma^3 \qquad (19)$$

(REUTER and SONDHEIMER[19]).* (More precisely, the mean value of Σ^3 for single crystal plane surfaces averaged over all orientations should be used in these expressions, PIPPARD[22].) The ratio Σ_c/Σ in Table 1 is a measure of how far the metal departs from the conditions of the classical skin effect, ($\delta \gg l$), the ratio being unity under classical conditions and increasing in value as the metal becomes more anomalous; when the ratio exceeds 2·2, the measured value of Σ is within 10 per cent of the limiting value. Clearly the polycrystalline specimen is still far from the anomalous limit, and this may be attributed to the short mean free path in the sample. (Its resistance ratio, $\rho(290°\mathrm{K})/\rho(4°\mathrm{K})$ was only 13·5, which is a typical value for a polycrystalline specimen of the material used and which is less by a factor of ten than for a good

* These relations hold for specular reflection of the carriers at the surface of the metal. The suggestion that the scattering is specular in bismuth was first made by SMITH[5] and this view appears to have received confirmation from the thin-conductor work of FRIEDMAN and KOENIG[20], who base the interpretation of their results on the theory of PRICE[21]. However, since the apparent resistivities measured by FRIEDMAN and KOENIG remained unchanged on etching the electropolished specimen surfaces, there still appears to be some doubt as to whether the scattering at a polished surface is specular. For the case of diffuse scattering, the relations differ from the above by the absence of the numerical factor $(8/9)^3$ from the right-hand side of the equations.

single crystal specimen. The most probable cause of the low resistance ratios of polycrystalline specimens is the considerable amount of physical imperfection in the individual crystallites caused on cooling a sample down to liquid helium temperatures by the anisotropic expansion coefficient and the ease with which the crystals cleave in the trigonal plane.)

Since the surface conductance of the polycrystalline specimen cannot be used in equations (18) and (19), a mean conductance must be estimated from the single crystal values. These themselves are averages since the specimens were cylindrical, and it will be assumed that the arithmetic mean of the three single crystal values, $\overline{\Sigma} = 21{\cdot}0$ ohm^{-1} is a sufficiently close estimate of $(\overline{\Sigma^3})^{1/3}$. We then find,

$$S = 17{\cdot}6 \pm 5{\cdot}1 \times 10^{13}\ \text{cm}^{-2} \qquad (20)$$

$$\sigma/l = 1{\cdot}14 \pm 0{\cdot}33 \times 10^{8}(\text{ohm cm}^2)^{-1} \qquad (21)$$

So far we have neglected the fact that the measured values of Σ are about 10 per cent less than the limiting values, and we have also neglected the effect of relaxation. DINGLE[23] has introduced a parameter $\boldsymbol{\nu}$ from which the importance of relaxation effects can be estimated, and CHAMBERS[24] has given a series of curves essentially of Σ against $\sigma^{1/2}$ for a series of values of $\boldsymbol{\nu}$, which he expressed in the form

$$\boldsymbol{\nu} = 7{\cdot}88\nu(m^*/m_0)^{3/2}(\sigma/l)^{-5/4}.$$

If the estimate (21) of σ/l and the mean electron mass $m^* = 0{\cdot}03\ m_0$ are used, then for $\nu = 9$ kMc/sec we find $\boldsymbol{\nu} = 0{\cdot}025$. At this value of ν, the effect of relaxation is to *increase* the observed Σ by about 9 per cent above the value which would otherwise be found. In other words, the effect of relaxation almost exactly compensates for the fact that the specimens were not at the anomalous limit, and we have therefore used the mean value $\overline{\Sigma}$ without correction to calculate S and σ/l. The errors quoted in (20) and (21) allow for the compensation being inexact, as well as for the probable difference between $\overline{\Sigma}$ and the true value of $(\overline{\Sigma^3})^{1/3}$.

The value of σ/l found here differs from the value $2{\cdot}74 \times 10^7$ found by PIPPARD and CHAMBERS[25] and the value $1{\cdot}53 \times 10^7$ found by CHAMBERS[24] from a re-evaluation of the PIPPARD and CHAMBERS data. These figures were deduced from measurements of $\Sigma(\sigma)$ at three different temperatures and in the analysis it was implicitly assumed that σ/l was independent of temperature. In fact, however, the number of carriers, and therefore σ/l, increases rapidly with temperature,[2] and this invalidates such an analysis.

It is of interest to compare the value of S found above with the total surface area of the electron ellipsoids and the hole spheroid. Each ellipsoid has an approximate surface area of $4{\cdot}2 \times 10^{13}$ cm^{-2} and the spheroid has an area $5{\cdot}6 \times 10^{13}$ cm^{-2}, making a total of $18{\cdot}2 \times 10^{13}$ cm^{-2} which is in good agreement with the value (20). This confirms the theoretical work of MASE[26] and HARRISON[27] who find that the energy extrema occur at the boundaries of the Brillouin zone so that the number of separate portions of the Fermi surface is not doubled by inversion symmetry. (See also LAX *et al.*[28].) This conclusion differs from that arrived at by SMITH[5] from his anomalous skin effect measurements at 25·5 kMc/sec. The systematically high surface conductance values found by SMITH made it necessary for him to assume that the reflection of the carriers at the metal surface is specular, as mentioned before, and also that the Fermi surface consists of six electron ellipsoids and two hole spheroids whose total surface area is of the order 40×10^{13} cm^{-2}. A more likely explanation of SMITH's high values is to be found in the greater effect of relaxation at the higher frequency which he used, and a rough calculation indicates that most of the discrepancy can be removed by making a relaxation correction to SMITH's conductance values.

Two further points need mentioning. First, the assumption of diffuse scattering of the carriers at the metal surface increases our estimate of S to $25{\cdot}0 \pm 7{\cdot}3 \times 10^{13}$ cm^{-2}, but this is still not large enough to accommodate six ellipsoids and two spheroids. The theoretical estimate $S = 18{\cdot}2 \times 10^{13}$ cm^{-2} falls within the error of this value as well as of the value (20) so that we are not able to make a decisive choice between specular and diffuse reflection from the present results. Secondly, poor surface finish may reduce the measured surface conductance below the true value,[29] but the present results are unlikely to be significantly in error from this cause since the specimen surfaces were electropolished and were highly specular optically.

Vol. 19
1961

Acknowledgements—I wish to thank Dr. D. SHOENBERG, F.R.S., and Dr. R. G. CHAMBERS for supervising this work at different stages, and Dr. CHAMBERS for his helpful advice during the preparation of the manuscript. I also wish to express my gratitude to the Department of Scientific and Industrial Research for the award of a maintenance grant, and to Professor E. BURSTEIN for the hospitality of his group at the University of Pennsylvania where much of the writing was done.

REFERENCES

1. AZBEL' M. Ya. and KANER E. A., *Soviet Phys. JETP* **3,** 772 (1956); AZBEL' M. Ya. and KANER E. A., *J. Phys. Chem. Solids* **6,** 113 (1958).
2. AUBREY J. E. and CHAMBERS R. G., *J. Phys. Chem. Solids* **3,** 128 (1957).
3. AUBREY J. E., *Phil. Mag.* **5,** 1001 (1960).
4. SHOENBERG D., *Proc. Roy. Soc.* **A170,** 341 (1939); SHOENBERG D., *Phil. Trans.* **A245,** 1 (1952).
5. SMITH G. E., *Phys. Rev.* **115,** 1561 (1959).
6. BRANDT N. B., *Soviet Phys. JETP* **11,** 975 (1960).
7. BRANDT N. B., DUBROVSKAYA A. E. and KYTIN G. A., *Soviet Phys. JETP* **10,** 405 (1960).
8. GALT J. K., YAGER W. A., MERRITT F. R., CETLIN B. B. and BRAILSFORD A. D., *Phys. Rev.* **114,** 1396 (1959).
9. SMITH G. E., GALT J. K. and MERRITT F. R., *Phys. Rev. Letters* **4,** 276 (1960).
10. CHANDRASEKHAR B. S., *J. Phys. Chem. Solids* **11,** 268 (1959).
11. HEINE V., *Proc. Phys. Soc. Lond.* **A69,** 513 (1956).
12. KEESOM P. H. and PEARLMAN N., *Phys. Rev.* **96,** 897 (1954); RAMANATHAN K. G. and SRINIVASAN T. M., *Phys. Rev.* **99,** 442 (1955); KALINKINA I. N. and STRELKOV P. G., *Soviet Phys. JETP* **7,** 426 (1958).
13. PHILLIPS N. E., *Phys. Rev.* **118,** 644 (1960).
14. KAHN A. H. and FREDERIKSE H. P. R., *Solid State Physics*, Vol. IX, p. 257. (edited by SEITZ F. and TURNBULL D.) Academic Press, New York (1959).
15. BABISKIN J., *Phys. Rev.* **107,** 981 (1957).
16. KAPITZA P., *Proc. Roy. Soc.* **A119,** 358 (1928).
17. PIPPARD A. B., *Proc. Roy. Soc.* **A191,** 370 (1947).
18. CHAMBERS R. G., *Proc. Roy. Soc.* **A215,** 481 (1952).
19. REUTER G. E. H. and SONDHEIMER E. H., *Proc. Roy. Soc.* **A195,** 336 (1948).
20. FRIEDMAN A. N. and KOENIG S. H., *IBM Journal* **4,** 158 (1960).
21. PRICE P. J., *IBM Journal* **4,** 152 (1960).
22. PIPPARD A. B., *Proc. Roy. Soc.* **A224,** 273 (1954).
23. DINGLE R. B., *Physica* **19,** 311 (1953).
24. CHAMBERS R. G., *Physica* **19,** 365 (1953).
25. PIPPARD A. B. and CHAMBERS R. G., *Proc. Phys. Soc. Lond.* **A65,** 955 (1952).
26. MASE S., *J. Phys. Soc. Japan* **13,** 434 (1958); MASE S., *J. Phys. Soc. Japan* **14,** 584 (1959).
27. HARRISON W. A., to be published.
28. LAX B., MAVROIDES J. G., ZEIGER H. J. and KEYES R. J., *Phys. Rev. Letters* **5,** 241 (1960).
29. CHAMBERS R. G., Ph.D. thesis, University of Cambridge (1951).

Vol. 196

J. Phys. Chem. Solids Pergamon Press 1961. Vol. 19, Nos. 3/4, pp. 331–337. Printed in Great Britain.

DIFFUSION OF THALLOUS IONS IN POTASSIUM BROMIDE, MEASURED BY THE SPECTROPHOTOMETRIC METHOD

A. GLASNER, A. REJOAN and R. REISFELD

Department of Inorganic and Analytical Chemistry, The Hebrew University, Jerusalem, Israel

(*Received* 17 *November* 1960)

Abstract—The diffusion of thallous ions in potassium bromide, in the *impurity* range of temperatures, was measured by the spectrophotometric method.[1] The energy of activation Q was found to be 23,500 cal/mole. The pre-exponential factor D_0 varied with the experimental conditions, the effect being attributed to variations in the "face boundary", as indicated by experiments carried out under a reduced atmospheric pressure.

From experiments with pressed pellets it was deduced that the original equation (containing the factor 6^2 to account for the "face boundary") used in calculating the diffusion constants D needed correcting as follows: $D = (E_t/E_\infty)^2 l^2/(10\cdot3)^2 t$. This gives for the diffusion of thallous ions in potassium bromide: $D_{Tl^+} = 0\cdot23 \exp(-23{,}500/RT)$ cm²/sec.

Previous values of D and D_0 reported for the diffusion of thallous and lead ions in potassium chloride should similarly be divided by a factor of three.

Vol. 19
1961

1. INTRODUCTION

A PREVIOUS article[1] reported the first diffusion constants for foreign ions in alkali halides, which had been measured spectrophotometrically. The present article gives information on the following features of general interest, arising partly from the specific nature of the method:

1. The diffusion constant of thallous ion in potassium bromide at various temperatures in the impurity range, and comparison of the results with those obtained in potassium chloride.
2. The effects caused by varying the anion of the impurity salt.
3. The effect of reduced atmospheric pressure on the parameters of the diffusion.
4. The effect of hydrostatic pressure applied to the mixture before the process of diffusion.

2. EXPERIMENTAL

Materials

Potassium bromide, thallous chloride, and certain other salts employed, were "Baker Analyzed" reagents.

Thallous bromide was prepared[2] from the sulphate by the addition of hydrobromic acid to its solution. The precipitate was washed, dried at 120°C, and then further heated to 200°C. All manipulations were carried out under protection from light.

Technical

The potassium bromide and thallous salt were mixed in the form of finely ground dry powders, and heated at constant temperatures to effect diffusion. At predetermined intervals, samples weighing about 200 mg were taken, from which clear and transparent disks were prepared by the application of a total pressure of 25,000 lb. After measurement of the spectra and optical density at the maximum absorption wavelength, the disks were weighed and the optical density corrected, by simple proportion, to that of a standard 200 mg disk. All these manipulations, and the apparatus used, were as described in the previous article.[1]

Maximum optical density

The spectra of the doped disks exhibited two maxima, irrespective of the thallous salt used

(bromide or chloride), at wavelengths 215 and 260 mμ. The short wavelength band is superimposed on the "leg" of an unidentified and variable absorption band present in the "pure" potassium bromide disks; only the long wavelength absorption was therefore used in these measurements.

The optical densities, obtained after prolonged heating of the powdered mixtures E_∞, are indicated in Fig. 1. The E_∞ values were also measured by

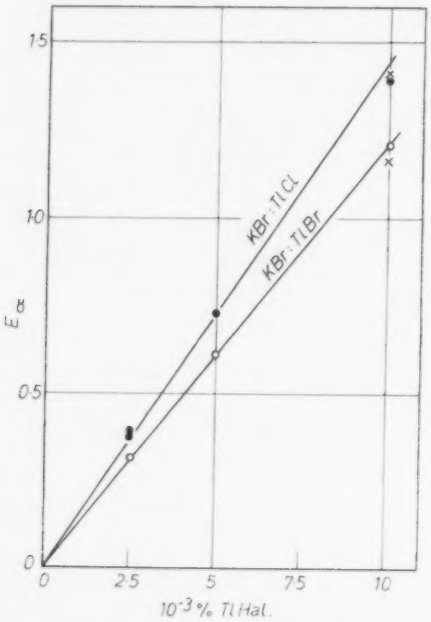

FIG. 1. E_∞, at $\lambda = 260$ mμ, of KBr:TlBr and KBr:TlCl disks of various concentrations, × indicates points obtained with dry powders.

a "wet" procedure; 700 mg portions of the dry potassium bromide powder were wetted by one ml of an aqueous solution of thallous bromide or thallous chloride of such concentration as to give 0·0025, 0·005 and 0·01 per cent solid mixtures by weight. After drying the powders with infrared light, they were reground, and the measured absorptions of the disks prepared from them were plotted in Fig. 1. It may be seen that the points lie on a straight line (the divergence at high absorptions being probably due to the characteristics of the spectrophotometer). The E_∞ values thus obtained for the 0·01 per cent KBr:TlBr and KBr:TlCl mixtures were 1·215 and 1·445 respectively, these values being inversely proportional to the formula weights of the thallous halogenides, as they should be.

Measurements following hydrostatic pressure

Diffusion constants in mixtures, previously subjected to various hydrostatic pressures, were measured at a single temperature, namely 197°C. A few series of pellets were pressed (from the same batch of mixed powder) at nominal pressures ranging from 1000 to 25,000 lb. These pressures correspond, with the die employed, to 350 and 8750 kg/cm². A series was placed in the oven all at the same time, each pellet having been separately wrapped in aluminium foil, in order to prevent any sublimation and diffusion from one pellet to another. The pellets were removed from the oven at intervals of 30 min to 10 hr, and again pressed at 25,000 lb, in order to obtain clear transparent disks ready for the spectral measurement.

3. RESULTS

(a) KBr:TlBr *powders*

Two independent series of measurements were made with 0·01 per cent KBr:TlBr powders in the temperature range 141–207°C. A few E_t^2 (optical density at time t) vs. t plots are shown in Fig. 2. They demonstrate the reproducibility of the spectrophotometrically measured diffusion and the extent of linearity of the curves at various temperatures, i.e. their conformity with the basic equation[1]:

$$D = \frac{(E_t/E_\infty)^2 l^2}{36t} \qquad (1)$$

where l is the mean length of an edge of the cubical grains in the mixture (= 20 μ in this work).

The diffusion constants at each temperature were calculated from the slopes of the initial linear part of the curves exemplified in Fig. 2, using equation (1). Also, the logarithms of these slopes (log s) were plotted against the inverse of absolute temperature (see Fig. 3) in order to evaluate the activation energy Q. The results of the two parallel series of measurements may be summed up by the equation:

$$D_{Tl^+}(\text{in KBr}) = 0{\cdot}69 \exp(-23{,}500/RT)\ \text{cm}^2/\text{sec}$$

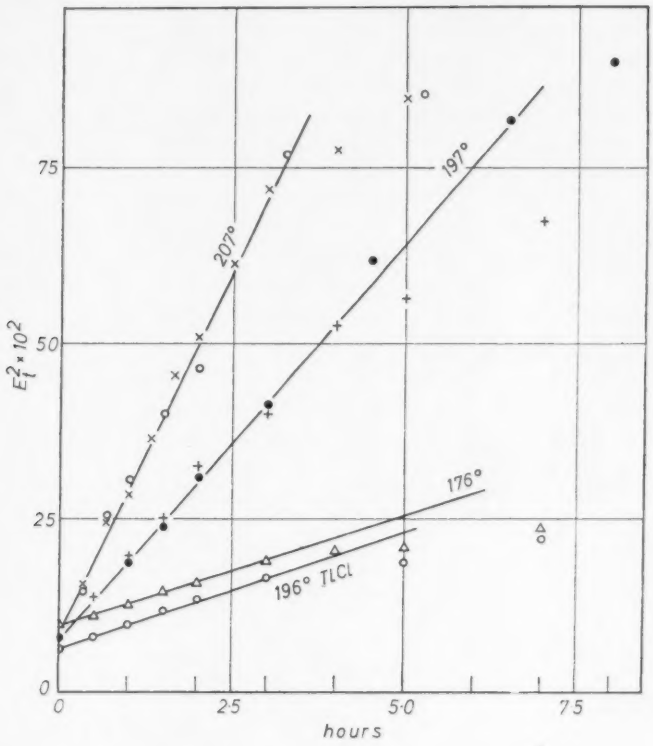

FIG. 2. Some E_t^2 vs. time plots of the diffusion of thallous ions in potassium bromide. The curve for KBr:TlCl powders is so marked. The different points on the same curve are of parallel experiments.

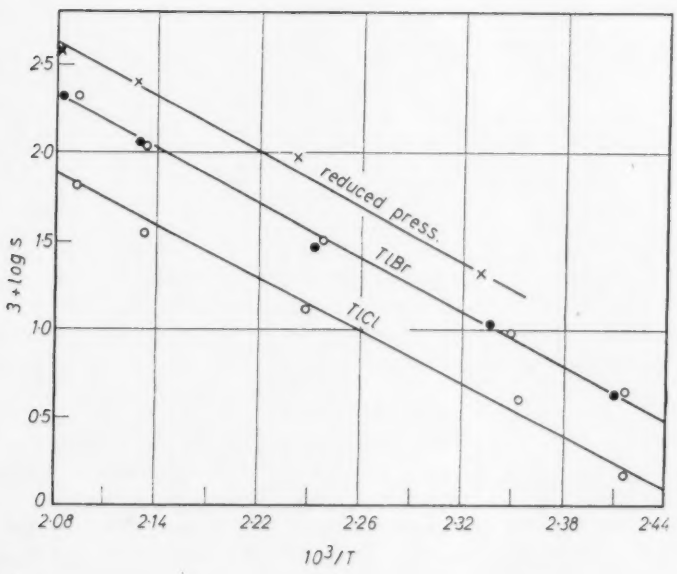

FIG. 3. Arrhenius plots for the diffusion of thallous ions in potassium bromide. Experimental conditions are indicated on the curves.

Vol. 19
1961

(b) KBr:TlCl *powders*

Measurements were made at five constant temperatures in the range 141–205°C, with powders containing 0·01 per cent thallous chloride by weight. The absorption bands, as already stated, were situated at the 215 and 260 mμ wavelengths characteristic for the bromide medium. The "E_t^2 vs. time" curves deviated from linearity at a rather low percentage of diffusion; i.e. equation (1) applies at the highest temperature (205°C) only to less than 30 per cent of the total thallous chloride in the mixture, as against 60 per cent in the case of thallous bromide.

Results are illustrated in the respective Figs. 2 and 3, and may be summed up by the equation:

$$D_{\mathrm{TlCl}}(\text{in KBr}) = 9{\cdot}1 \times 10^{-2} \times \exp(-22{,}850/RT)\ \mathrm{cm^2/sec}$$

(c) KBr:TlBr *powders under reduced pressure*

A series of diffusion measurements were made in partly evacuated vessels under a constant pressure of 2 mm Hg, in the temperature range 142–207°C. In this series also the powders contained 0·01 per cent thallous bromide by weight. The E_t^2 vs. t curves at various temperatures are given in Fig. 4, and the Arrhenius plot of their slopes s in Fig. 3. The calculated diffusion equation is:

$$D_{\mathrm{Tl}^+}(\text{in KBr, 2 mm Hg}) = 1{\cdot}45 \times \exp(-23{,}600/RT)\ \mathrm{cm^2/sec}.$$

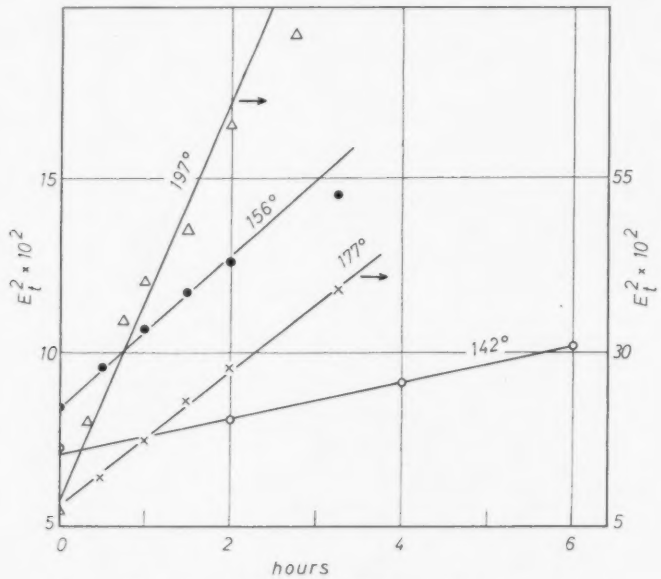

FIG. 4. E_t^2 vs. time plots for KBr:TlBr powders under reduced pressure: 2 mm Hg. For curves at 177 and 197°C use right hand scale on ordinate.

The activation energy Q agrees well with that obtained in the parallel experiments under atmospheric pressure (~695 mm Hg), the pre-exponential factor D_0, on the other hand, is higher by a factor of two.

(d) KBr:TlBr *pellets*

These experiments were made at a single temperature (197°C), by the techniques explained under Experimental. Some of the E_t^2 vs. t curves are shown in Fig. 5; they deviate very early from linearity. The logarithms of the slopes s against

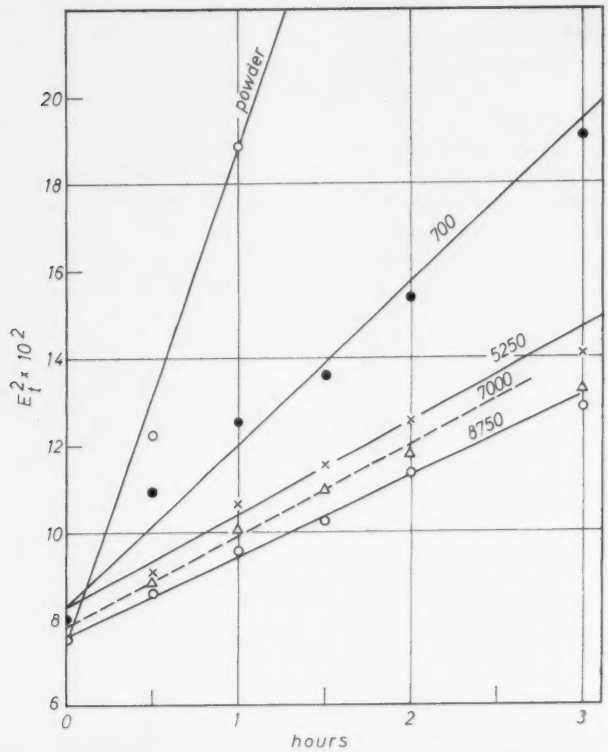

FIG. 5. E_t^2 vs. time plots for KBr:TlBr pellets at 197°C. The pressures (in kg/cm²) applied on preparing the pellets are indicated on the curves.

hydrostatic pressure in kg/cm² were plotted in Fig. 6, and in Table 1 the diffusion constants calculated by equation (1) were recorded. For comparison some other D values obtained in this work at 197°C are also given.

From both Fig. 6 and Table 1 it may be seen that (a) on applying a pressure of 350 kg/cm², the diffusion constant is reduced to about one-third of its value in powders, (b) a further increase of pressure up to 3500 kg/cm² does not produce any

Table 1. *Diffusion constants* D *at* 197°C, *obtained with pellets prepared under various hydrostatic pressures, and with powders*

Pressure kg/cm²	350	700	1750	3500	5250	7000	8750
$D \times 10^{12}$ cm²/sec	2·35	2·44	2·23	2·10	1·52	1·30	1·08
Powders	TlBr				TlCl		
	a	b	2 mm Hg				
$D \times 10^{12}$ cm²/sec	7·16	7·55	15·6		1·64		

appreciable change in the diffusion constants, (c) from 5250 kg/cm^2 and upwards there is another progressive reduction in the diffusion constants.

4. DISCUSSION

In order to confirm the reliability of the spectrophotometric method used in this work, it was considered advisable to make two parallel measurements of the diffusion of thallous bromide in potassium bromide through the whole range of temperatures. The reproducibility of the results was found to be satisfactory; the calculated diffusion constants at each temperature differed by only a few per cent, and there is a good agreement in the activation energies (Fig. 3) and pre-exponential factors D_0 of the two series when evaluated separately.

With respect to the activation energy, the same value was also obtained when the diffusion took place at a reduced pressure of 2 mm Hg, as well as when thallous *chloride* was mixed with potassium bromide. The activation energy for the diffusion of thallous ions in potassium *bromide* is therefore 23·5 (± 0·25) kcal/mole, which is 1·7 kcal lower than the activation energy for the diffusion of the thallous ions in potassium *chloride*, reported in the previous article, This should be compared to $\Delta Q = 0{\cdot}4$ kcal for the difference in the activation energies of the self diffusion of the potassium ion in the two alkali halides.[3] Considering that the width of the "strait" between two chloride ions, in the potassium chloride lattice at equilibrium, is $(3{\cdot}14\sqrt{(2)} - 3{\cdot}62 = 0{\cdot}82$ Å), larger than that between two bromide ions in potassium bromide $(3{\cdot}29\sqrt{(2)} - 3{\cdot}92 = 0{\cdot}73$ Å), the somewhat lower activation energies observed with potassium bromide should be attributed to the greater polarizability of the bromide ion.

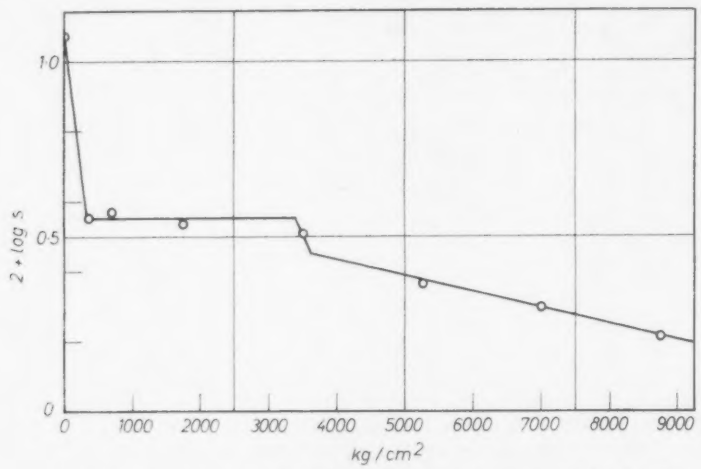

FIG. 6. Logarithms of relative diffusion rates (as expressed by the slope s) in pressed pellets against pressures applied.

The pre-exponential factor D_0 with KBr:TlCl powders was found to be only about $\frac{1}{7}$th of that of the KBr:TlBr powders. This discrepancy seems to be connected with the restricted applicability of equation (1), as demonstrated in Fig. 2; i.e. the early deviation of the slopes of the E_t^2 vs. t curves from linearity is also responsible for the comparatively low D_0 values obtained in this case. The phenomenon is probably caused by the formation of an intervening KCl layer between the potassium bromide lattice and the diffusing foreign salt. The obvious conclusion is, that for most reliable results diffusion measurements should be made with mixtures containing the same anion.

In passing, it should, however, be mentioned,

without further comment, that D_0 with KCl:TlCl powders was found to be about ten times as large as with the KBr:TlBr powders.

The reduction of atmospheric pressure to 2 mm Hg, during the process of diffusion, evoked a twofold increase of D_0. This increase is nearly the same as that observed with KCl:TlCl powders[1] and with KCl:$PbCl_2$ powders (not reported), and it is clearly due to an increase of the "face boundary" by a factor of $\sqrt{(2)}$.

The interpretation of the results with pressed pellets (Fig. 6 and Table 1) seems to be as follows. The application of a pressure of 350–700 kg/cm^2 on the potassium bromide powders is sufficient to eliminate practically all free space and air pockets between the grains, as indicated by LAURENT and BÉNARD's measurements of the relative densities of the compressed powders and of the mono-crystal.[4] Hence it may be inferred that in the compact pellet the "face boundary" for diffusion is only 1/1·72 of that in the powders, the ratio of $D_{\text{pellet}}/D_{\text{powder}}$ being the square of this value, namely $\frac{1}{3}$. On increasing the hydrostatic pressure up to 3500 kg/cm^2, no further reduction in D was observed (maximum density is attained, according to LAURENT and BÉNARD, at a pressure of 2700 kg/cm^2). However, on increasing the pressure to 5250 kg/cm^2 there is a further decrease in D owing to the deformation of the lattice and the inactivation of the vacancies, as proposed in the previous article.

If the above interpretation of the results with pressed pellets is correct, these experiments reveal the exact area of the "face boundary" around each single grain of thallous bromide in the powdered mixture, this being $1{\cdot}72 \times 6l^2$, instead of $6l^2$ previously assumed. Hence, equation (1) should be written:

$$D = \frac{(E_t/E_\infty)^2 l^2}{(10{\cdot}3)^2 t} \qquad (2)$$

and all D and D_0 values with powders so far recorded should be divided by a factor of *three*.

The above conclusion may be subjected to further tests. For example, some of the measurements contemplated are: (a) the influence of reduced atmospheric pressure on the diffusion constant in pellets prepared under a pressure of 350–700 kg/cm^2 (no effect, or only a small one, is expected), and (b) the activation energy of diffusion Q in the same pellets (Q should be equal to the value obtained with powders, but not to that obtained with disks subjected to high pressures).

Finally, a few comparative remarks on LAURENT and BÉNARD's work[5] on self diffusion in polycrystalline alkali halide pellets, in the *intrinsic* range, seem to be called for. These authors found that, although the activation energy Q remained constant, the D_0 values of several halogen ions (and of caesium) increased inversely with the mean diameter of the crystal grains in the pellets. They interpreted their results by diffusion along the surface of the grains, ahead of the bulk diffusion, and proved its existence by autoradiographic exposures. This is in harmony with our results, which show that pressures greater than about 5000 kg/cm^2 applied to the pellets restrict the bulk diffusion, whereby the otherwise slower surface diffusion becomes evident. LAURENT and BÉNARD's experiments also indicate that, at least with respect to the anion vacancies, the strain produced in the polycrystalline pellets by pressure is not relieved by heat treatment even at the higher temperatures of the intrinsic range.

REFERENCES

1. GLASNER A. and REISFELD R., *J. Phys. Chem. Solids* **18,** 345 (1961).
2. KENDALL J., CRITTENDEN E. D. and MILLER H. K., *J. Amer. Chem. Soc.* **45,** 972 (1923).
3. PHIPPS T. E. and PARTRIDGE E. G., *J. Amer. Chem. Soc.* **51,** 1331 (1929).
4. LAURENT J. F. and BÉNARD J., *J. Phys. Chem. Solids* **3,** 7 (1957), Fig. 5.
5. LAURENT J. F. and BÉNARD J., *J. Phys. Chem. Solids* **7,** 218 (1958).

Vol. 19
1961

J. Phys. Chem. Solids Pergamon Press 1961. Vol. 19, Nos. 3/4, pp. 338–348. Printed in Great Britain.

ACTIVITY MEASUREMENTS IN OXIDE SOLID SOLUTIONS: THE SYSTEMS NiO–MgO AND NiO–MnO IN THE TEMPERATURE INTERVAL 1100–1300°C*

W. C. HAHN, JR. and A. MUAN

The Pennsylvania State University, University Park, Pennsylvania

(*Received* 31 *October* 1960; *revised* 20 *January* 1961)

Abstract—Activities of NiO in NiO–MgO and NiO–MnO solid solutions have been measured by equilibrating oxide samples with pure metallic Ni in atmospheres of known oxygen partial pressures. The system NiO–MgO is ideal, within limits of experimental error, whereas the system NiO–MnO shows considerable positive deviation from ideality in the temperature interval studied in the present investigation, 1100–1300°C.

I. INTRODUCTION

MANY activity measurements of components in liquid oxides have been reported, as demonstrated by the voluminous literature in the field of slag chemistry. In constrast, very little is known about the thermodynamic behavior of components in oxide solid solutions.

The present paper deals with activity measurements in two such solutions, NiO–MgO and NiO–MnO, both with sodium chloride structure. Complete solubility has been shown to exist between NiO and MgO at 900°C,[1] whereas the system NiO–MnO exhibits only partial solid solubility at 350°C.[2] It will be shown in the present investigation that the latter system exhibits complete solid solubility above 1100°C.

Consider the reaction

$$2NiO_{\text{solid solution}} = 2Ni_{\text{metal}} + O_{2\text{gas}}$$

in which NiO dissolved in another oxide dissociates to metal and gas. The activity of NiO in the solid solution, relative to pure NiO as a standard state, is then expressed as

$$a_{NiO} = \left(\frac{P_{O_2}}{P_{O_2}^*}\right)^{1/2}$$

Here P_{O_2} and $P_{O_2}^*$ are the partial pressures of oxygen of the gas phase in equilibrium with metallic iron and the oxide solid solution or the pure NiO, respectively. The equation holds only if the metal phase is essentially pure Ni. The oxide combinations used in the present investigation were chosen with this consideration in mind. Both MgO and MnO are so much more stable than NiO that for all practical purposes $a_{Ni} = 1$ in the metal phase present in all mixtures used in this investigation.

II. EXPERIMENTAL METHOD

1. *General procedure*

The experimental method used was analogous to that developed by FOSTER and WELCH[3]. It consisted of four steps:

(*a*) Determination of K_T for the reduction of NiO to Ni.

(*b*) Determination of *d*-spacing change with composition in oxide solid solutions.

(*c*) Equilibration of various members of the solid solution series with a metal phase and gas phase of known O_2 partial pressure.

(*d*) Determination of compositions of solid solutions resulting from step (*c*) by means of data obtained in step (*b*).

2. *Starting materials*

"Baker Analyzed" reagent grade NiO was the

* Contribution No. 59-110 from the Department of Metallurgy, College of Mineral Industries, The Pennsylvanian State University, University Park, Pennsylvania.

source of nickelous oxide used in the present investigation. Its reported analysis was as follows: NiO, 99·5 per cent; nitrogen compounds (as N), 0·003 per cent; chloride, 0·003 per cent; sulfate, 0·005 per cent; lead, 0·001 per cent; copper, 0·005 per cent; cobalt, 0·005 per cent; iron, 0·004 per cent; zinc, 0·005 per cent, alkalies and earths (as SO_4), 0·13 per cent. The reagent was heated in a drying oven at approximately 100°C prior to its use as a constituent in mixtures for the samples.

The source of magnesium oxide was "Baker Analyzed" reagent grade MgO of reported analysis as follows: insoluble in HCl, 0·020 per cent; soluble in water, 0·020 per cent; loss on ignition, 0·62 per cent; silica, 0·010 per cent; ammonium hydroxide precipitate, 0·020 per cent; chloride, 0·005 per cent; nitrate, 0·005 per cent; sulfate and sulfite (as SO_4), 0·005 per cent; barium, 0·002 per cent; calcium, 0·030 per cent; heavy metals as lead, 0·002 per cent; iron, 0·003 per cent. The MgO was prepared for use by igniting it at 1200°C for 24 hr, cooling over P_2O_5 and immediate weighing.

Manganous oxide was prepared from "Baker Analyzed" reagent grade MnO_2 of reported analysis as follows: MnO_2, 100·0 per cent; insoluble in HCl, 0·015 per cent; chloride, 0·002 per cent; nitrate, 0·025 per cent; sulfate, 0·025 per cent; iron, 0·03 per cent; earths and alkalies (as SO_4), 0·10 per cent. The MnO_2 was first heated at 1100°C in air for 24 hr to produce Mn_3O_4. The resulting Mn_3O_4 was then heated in commercial tank H_2 for two hours at 1100°C to produce manganous oxide of composition $MnO_{1.005}$, as determined by the method described below. (It is to be noted that the partial pressure of oxygen in the H_2 used in this investigation was high enough to prevent reduction of manganese oxide to metallic manganese.) Reduction of MnO_2 in two steps was employed in order to avoid the "spattering" produced by the violent decomposition of MnO_2 directly to manganous oxide at high temperatures.

The manganous oxide was analyzed by methods developed during the course of a previous investigation in this laboratory.[4] The sample, weighing approximately 0·1 g, was placed along with approximately 0·75 g of $Fe(NH_4)_2(SO_4)_2 . 6H_2O$ in 25 ml of distilled water and 10 ml of 1:4 H_2SO_4; 3 ml of 49 per cent HF was added. The solution was boiled for 10 min to dissolve all the sample. Upon cooling to room temperature, 25 ml of distilled water and 15 ml of 2 per cent H_3BO_3 were added and the solution was titrated with 0·05 N $KMnO_4$.

The nickel used was premium grade powder of representative analysis as follows: nickel, 99·9 per cent min.; carbon, 0·20 per cent max.; sulfur, 0·001 per cent max.; iron, 0·03 per cent max.; others, 0·01 per cent max.

3. *Control of atmosphere*

The method used for controlling oxygen pressures was similar to that used by DARKEN and GURRY[5] and later by MUAN[6]. The atmospheres were obtained by mixing CO_2 and H_2 at room temperature; the partial pressures of oxygen at the temperatures of the experiments were then calculated from the data compiled by COUGHLIN[7]. The gases used were of reported compositions 99·98 per cent CO_2 and 99·5 per cent H_2. The rate of flow of each of the two gases was measured separately by means of two capillary flow meters with bleeder tubes inserted on both ends of the capillaries to maintain a constant pressure drop. A series of mutually interchangeable capillaries of different openings was at hand so that a wide range of mixing ratios could be obtained with manometer readings of convenient magnitude. A third manometer was inserted in the line to measure the rate of flow of gas through the furnace tube. The flow meters were calibrated individually with the various capillaries, using a standard wet test meter.

4. *Furnaces and temperature control*

A vertical tube furnace with an 80 per cent Pt–20 per cent Rh resistance winding was used in this investigation. The furnace was equipped with ground glass joints fused to the top and bottom of the mullite furnace tube. The upper ground glass attachment was drawn out to a long, relatively narrow tube to prevent air from diffusing into the furnace tube. The gas from the mixer passed through the furnace tube from bottom to top.

Furnace temperatures were regulated by means of a Celectray controller. The thermal gradient at the hot spot did not exceed 2°C over one inch at 1400°C.

5. *Method of equilibration*

Equilibrium was approached from both sides

Vol. 19
1961

in all runs carried out in the present investigation. In the case of the Ni–O system, one sample of metallic Ni and one sample of NiO were kept side by side in the furnace at chosen temperature and chosen oxygen partial pressure for 3–5 hr. After quenching the samples rapidly to room temperature, the phases present were determined by visual examination, supplemented in preliminary experiments by X-ray examination.

Contamination of samples by crucible materials was avoided by pressing powders into discs which were then drilled to permit their suspension in the furnace from wires of pure nickel. The discs weighed approximately 0·2 gm; they were 1·0 cm in diameter and approximately 1 mm thick. The oxide samples were pressed at 25,000 p.s.i. and the pure metal samples at 6000 p.s.i.

That the method described above did in fact

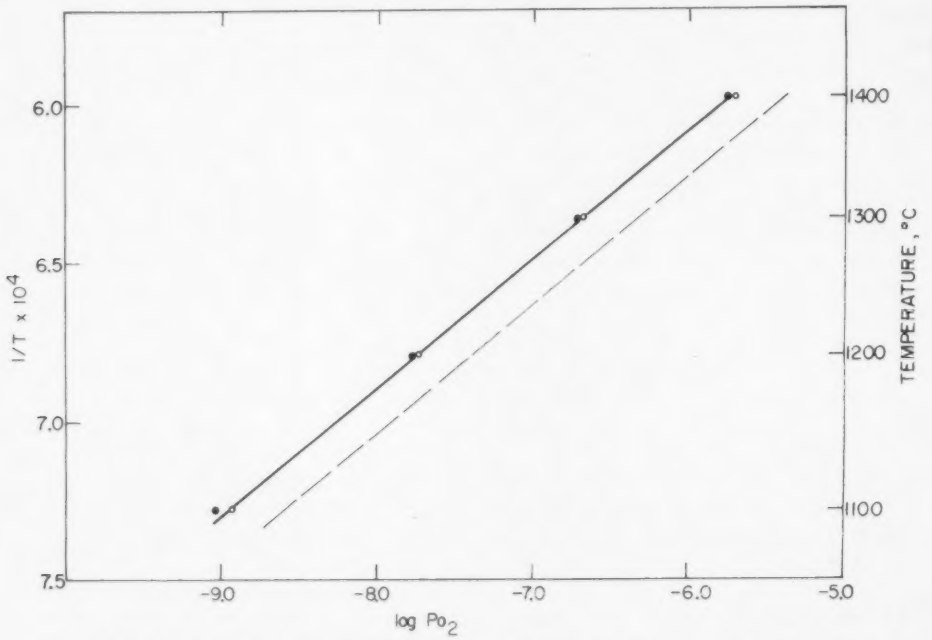

FIG. 1. Stabilities of the phases Ni and NiO as a function of oxygen partial pressure (log scale in atmospheres) and temperature (inverse °K scale). Solid and open circles represent observed stable occurrences of Ni and NiO, respectively. The solid line is drawn to fit the experimental data by the method of least squares. The dashed line is drawn to represent the same equilibrium based on data tabulated by COUGHLIN[7].

In the case of oxide solid solutions, one sample with NiO content above the equilibrium value and one sample with metallic nickel and oxide of NiO content below the equilibrium value were equilibrated side by side at chosen temperature and oxygen partial pressure for approximately 22 hr. It was found important to use starting oxide materials whose NiO contents were reasonably close to those at equilibrium, in order to avoid the presence of large quantities of metal phase which had a tendency to impair attainment of equilibrium.

eliminate contamination was shown by the following observations. Samples of mixtures containing NiO, when run under conditions such that no metal phase was produced, exhibited the same *d*-spacing whether suspended from a nickel or a platinum wire and in atmospheres which were very reducing or slightly oxidizing with respect to the Ni–NiO equilibrium.

The samples used to establish variations of *d*-spacing with compositions in the oxide solutions were run in the furnace in much the same manner

as described above. However, in these cases it was necessary to prevent the formation of a metal phase in order that the final composition would be the same as initially. In view of the above observation of negligible variation of *d*-spacing within a range of oxygen partial pressure, it was possible to prepare all of these samples in atmospheres which were slightly oxidizing with respect to the Ni–NiO equilibrium.

General Electric XRD-3 diffractometer unit with scanning speed of 0·2° per minute and unfiltered iron radiation was used in these experiments. Metallic Ni served as an internal standard, based on the unit cell dimensions reported by SWANSON and co-workers.[8]

The (200)-reflections of the oxide solid solutions

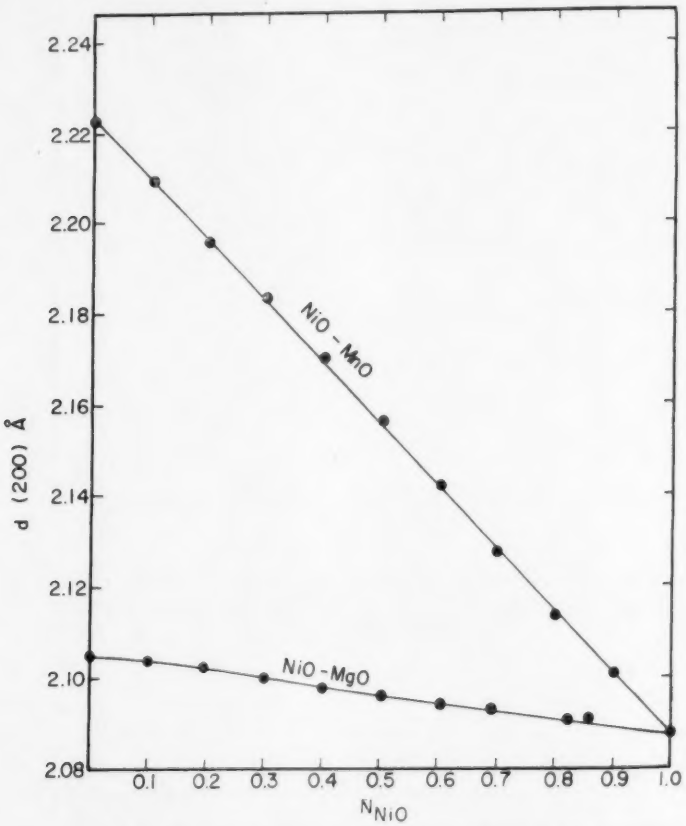

FIG. 2. Changes in *d*-spacing with composition in the systems NiO–MgO and NiO–MnO. Dots represent experimentally determined values, and straight lines connect points for *d*-spacings of the pure end numbers.

6. *X-ray analysis*

Compositions of oxide solid solutions were determined by accurate *d*-spacing (200) measurements and comparison with known standards. A of interest in the present study occur at a value of 2θ in the neighborhood of 50° when iron radiation is used. This reflection was chosen rather than a higher angle reflection because the lower intensities and broadness of the latter reflections introduced difficulties in the determination of their position which more than vitiated the attendant advantages.

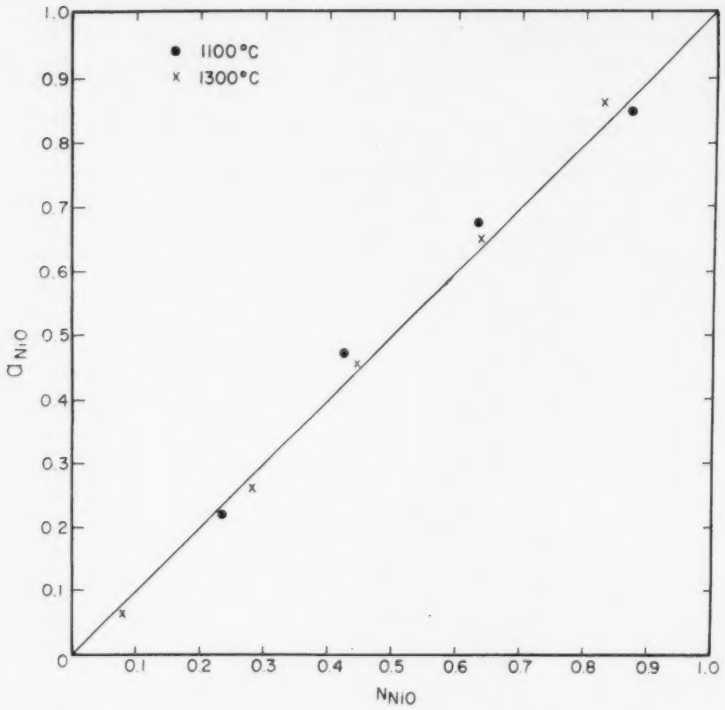

FIG. 3. Activity of NiO as a function of composition in the system NiO–MgO at 1100 and 1300°C. Symbols used are explained in upper left corner of diagram.

Table 1. *Critical runs for determination of the equilibrium* $2NiO = 2Ni + O_2$

Temperature, °C	$1/T \times 10^4$, °K^{-1}	$-\log P_{O_2}$	Duration of run, hr	Observed stable phase
1100	7·28	8·920	5	NiO
1100	7·28	9·034	5	Ni
1200	6·79	7·721	3	NiO
1200	6·79	7·763	3	Ni
1300	6·36	6·671	4	NiO
1300	6·36	6·705	5	Ni
1400	5·98	5·718	4	NiO
1400	5·98	5·758	4	Ni

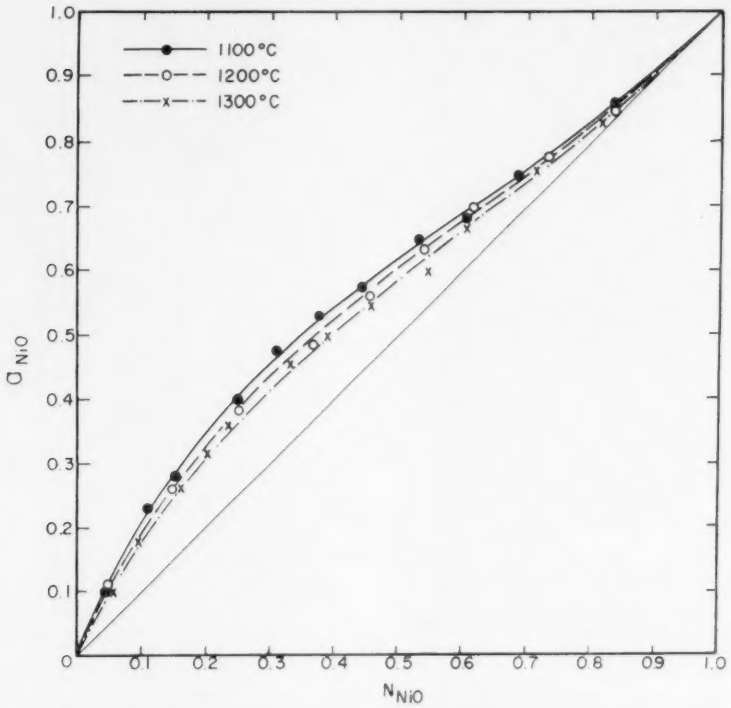

FIG. 4. Activity of NiO as a function of composition in the system NiO–MnO at 1100, 1200 and 1300°C. The symbols used are explained in upper left corner of diagram.

Table 2. d(200) *as a function of composition in the systems* NiO–MgO *and* NiO–MnO *as measured on samples heated at* 1300°C *for* 22 *hr in an atmosphere with* $P_{O_2} = 10^{-6.650}$ *atm. and quenched to room temperature*

The system NiO–MgO			The system NiO–MnO		
N_{NiO}	2θ	d(200), Å	N_{NiO}	2θ	d(200), Å
0·000	54·77	2·1045	0·000	51·65	2·2221
0·099	54·79	2·1038	0·100	51·97	2·2094
0·195	54·82	2·1027	0·200	52·31	2·1960
0·301	54·90	2·0999	0·301	52·64	2·1832
0·399	54·96	2·0977	0·400	52·98	2·1702
0·499	55·01	2·0960	0·504	53·35	2·1562
0·604	55·06	2·0942	0·600	53·73	2·1421
0·691	55·09	2·0932	0·700	54·13	2·1275
0·824	55·16	2·0907	0·800	54·51	2·1138
0·868	55·16	2·0907	0·900	54·87	2·1010
1·000	55·22	2·0886	1·000	55·22	2·0886

Table 3. *Activity measurements in the system* NiO–MgO

$-\log P_{O_2}$	N_{NiO} in starting mixture	End of run		N_{NiO} of solution, end of run	Calculated activity of NiO
		2θ	d(200), Å		
		1100°C			
10·297	0·195*	54·84	2·1020	0·22	0·22
	0·301	54·86	2·1013	0·25	
9·625	0·399*	54·96	2·0977	0·41	0·47
	0·499	54·97	2·0970	0·44	
9·317	0·604*	55·06	2·0942	0·61	0·68
	0·691	55·08	2·0935	0·65	
9·118	0·824*	55·16	2·0907	0·85	0·85
	0·868	55·18	2·0900	0·90	
		1300°C			
9·081	0·000*	54·78	2·1041	0·06	0·06
	0·099	54·79	2·1038	0·10	
7·857	0·195*	54·88	2·1006	0·28	0·26
	0·301	54·88	2·1006	0·28	
7·366	0·399*	54·98	2·0970	0·44	0·46
	0·499	54·99	2·0967	0·45	
7·058	0·604*	55·07	2·0939	0·63	0·65
	0·691	55·08	2·0935	0·65	
6·825	0·824*	55·15	2·0911	0·82	0·85
	0·868	55·16	2·0907	0·85	

* Metallic nickel added to starting mixture.

The 2θ values were measured with an accuracy of approximately $\pm$ 0·01°, corresponding to an accuracy in d-spacing of $\pm$ 0·0004 Å.

III. RESULTS AND DISCUSSION

The equilibrium

$$2NiO = 2Ni + O_2$$

was investigated in the temperature interval 1100 to 1400°C and at oxygen partial pressures ranging from $10^{-8.920}$ to $10^{-5.758}$ atm. Data obtained in critical runs appear in Table 1 and are shown graphically in Fig. 1. Conditions for coexistence of Ni and NiO are expressed by the equation

$$\log P_{O_2} = 9{\cdot}043 - 24{,}730[1/T]$$

and the standard heat of reaction, ΔH^0, as determined (by method of least squares) from the slope of the curve in Fig. 1, is 113,140 $\pm$ 2300 cal. This agrees adequately with the value of 112,520 $\pm$ 650 cal as tabulated by COUGHLIN[7] for the same temperature interval.

Changes in d-spacing with composition for the (200)-reflection in the systems NiO–MgO and NiO–MnO are shown in Table 2 and Fig. 2.

Vol. 1
196

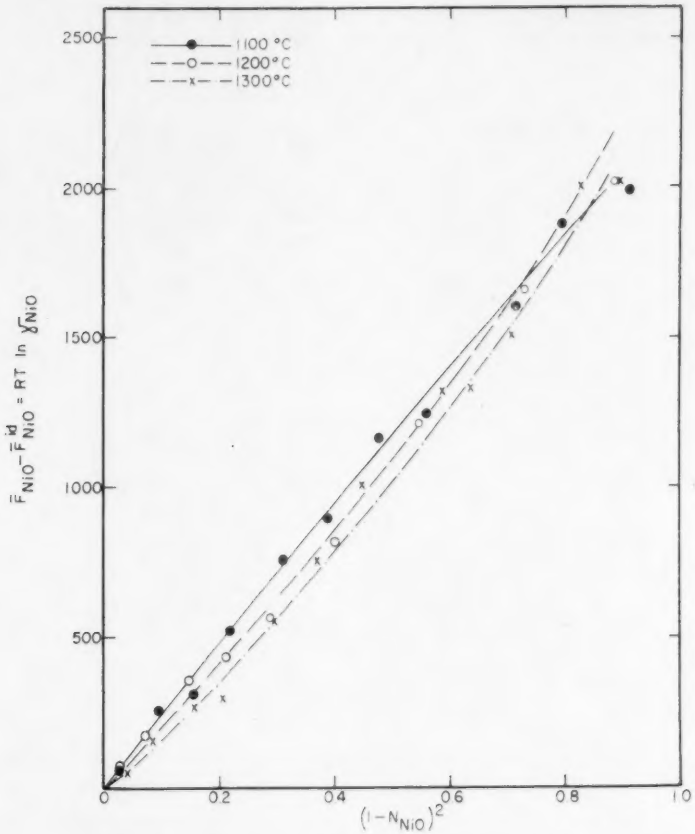

FIG. 5. Excess partial molal free energy of NiO dissolved in MnO at 1100, 1200 and 1300°C. Symbols used are explained in upper left corner of diagram.

Results of activity measurements are summarized in Tables 3 and 4 and shown graphically in Figs. 3 and 4 .

The activity values listed in these tables have estimated accuracies increasing from approximately ± 0·02 at the highest NiO contents to approximately ± 0·01 at the lowest NiO contents of the oxide solid solutions.

Compositions (N_{NiO}) of solid solution crystals in the NiO–MgO series are accurate to approximately ± 0·03. This relatively wide limit is imposed by the flatness of the *d*-spacing vs. composition curve (Fig. 2). In the NiO–MnO system the *d*-spacing vs. composition curve is much steeper, and compositions (N_{NiO}) can be determined to approximately ± 0·003. The limiting factor in this solid solution series in most instances is the degree of attainment of equilibrium. This is shown (Table 4) by the spread in N_{NiO} values obtained by approaching the equilibrium from different directions. It is seen that the over-all accuracy of N_{NiO} in the system NiO–MnO varies in the range from approximately ± 0·003 to ± 0·035.

Excess partial molal free energy of NiO dissolved in MnO at 1100, 1200 and 1300°C is shown as a function of $(1-N_{NiO})^2$ in Fig. 5 (for a discussion of the significance of this function, the reader is referred to the book by DARKEN and GURRY[9]).

It is concluded from the data presented in the

Table 4. Activity measurements in the system NiO–MnO

$-\log P_{O_2}$	N_{NiO} in starting mixture	End of run		N_{NiO} of solution, end of run	Calculated activity of NiO
		2θ	$d(200)$ Å		
1100°C					
10·996	0·000*	51·78	2·2169	0·045	0·10
	0·100	51·79	2·2166	0·047	
10·297	0·100*	52·00	2·2081	0·112	0·22
	0·200	52·01	2·2078	0·114	
10·088	0·100*	52·12	2·2034	0·145	0·28
	0·200	52·16	2·2018	0·159	
9·781	0·200*	52·48	2·1893	0·250	0·40
	0·301	52·48	2·1893	0·250	
9·625	0·301*	52·63	2·1836	0·294	0·47
	0·400	52·73	2·1798	0·321	
9·533	0·301*	52·90	2·1732	0·370	0·53
	0·400	52·96	2·1709	0·387	
9·462	0·400*	53·15	2·1638	0·440	0·57
	0·504	53·18	2·1626	0·447	
9·358	0·504*	53·41	2·1540	0·512	0·64
	0·600	53·56	2·1484	0·550	
9·317	0·600*	53·74	2·1417	0·601	0·68
	0·700	63·77	2·1407	0·608	
9·233	0·700*	54·00	2·1322	0·668	0·74
	0·800	54·04	2·1307	0·680	
9·118	0·800*	54·53	2·1131	0·808	0·85
	0·900	54·69	2·1074	0·853	
1200°C					
9·677	0·000*	51·81	2·2158	0·052	0·11
	0·100	51·82	2·2153	0·056	
8·904	0·100*	52·13	2·2031	0·148	0·26
	0·200	52·13	2·2031	0·148	
8·581	0·200*	52·48	2·1893	0·250	0·38
	0·301	52·49	2·1890	0·252	
8·370	0·301*	52·88	2·1740	0·364	0·49
	0·400	52·92	2·1724	0·375	
8·242	0·400*	53·22	2·1611	0·458	0·56
	0·504	53·25	2·1600	0·466	

* Metallic nickel added to starting mixture.

Vol. 196

Table 4 (Contd.)

$-\log P_{O_2}$	N_{NiO} in starting mixture	End of run		N_{NiO} of solution, end of run	Calculated activity of NiO
		2θ	$d(200)$, Å		
		1200°C			
8·143	0·504*	53·52	2·1499	0·540	0·63
	0·600	53·53	2·1497	0·542	
8·055	0·600*	53·77	2·1407	0·608	0·70
	0·700	53·82	2·1388	0·620	
7·961	0·700*	54·15	2·1268	0·710	0·78
	0·800	54·31	2·1210	0·753	
7·885	0·800*	54·52	2·1134	0·807	0·85
	0·900	54·74	2·1056	0·868	
		1300°C			
8·661	0·000*	51·81	2·2158	0·050	0·10
	0·100	51·83	2·2149	0·057	
8·207	0·000*	51·93	2·2110	0·088	0·17
	0·100	51·95	2·2102	0·094	
7·860	0·200*	52·16	2·2018	0·159	0·26
	0·301	52·19	2·2008	0·167	
7·701	0·200*	52·31	2·1961	0·200	0·31
	0·301	52·33	2·1953	0·205	
7·582	0·200*	52·43	2·1914	0·236	0·36
	0·301	52·44	2·1909	0·240	
7·369	0·301*	52·75	2·1790	0·327	0·46
	0·400	52·82	2·1763	0·347	
7·296	0·400*	52·96	2·1709	0·388	0·50
	0·504	52·97	2·1706	0·390	
7·218	0·400*	53·19	2·1623	0·449	0·54
	0·504	53·22	2·1611	0·457	
7·139	0·504*	53·53	2·1496	0·542	0·59
	0·600	53·53	2·1496	0·542	
7·046	0·600*	53·73	2·1421	0·600	0·66
	0·700	53·80	2·1395	0·616	
6·936	0·700*	54·11	2·1282	0·700	0·75
	0·800	54·20	2·1249	0·724	
6·848	0·800*	54·54	2·1126	0·815	0·83
	0·900	54·55	2·1123	0·817	

* Metallic nickel added to starting mixture.

Vol. 19
1961

tables and diagrams that the system NiO–MgO behaves ideally, whereas the system NiO–MnO shows considerable positive deviation from linear relationship. The latter system approaches the behavior of a regular solution, as the excess partial molal free energy is approximately proportional to $(1-N_{NiO})^2$ and is very little dependent on temperature.

Acknowledgements—This work was sponsored by the American Iron and Steel Institute.

REFERENCES

1. Holgersson S. and Karlsson A., *Z. anorg. Chem.* **182,** 255–271 (1929).
2. Passerini L., *Gazz. Chim. Ital.* **59,** 144–154 (1929).
3. Foster P. K. and Welch A. J. E., *Trans. Faraday Soc.* **52,** 1636–1642 (1956).
4. Hahn W. C., Jr. and Muan A., *Amer. J. Sci.* **258,** 66–78 (1960).
5. Darken L. S. and Gurry R. W., *J. Amer. Chem. Soc.* **67,** 1398–1412 (1945).
6. Muan A., *Trans. A.I.M.E.* **203,** 965–976 (1955).
7. Coughlin J. P., Bureau of Mines Bulletin 542. U.S. Government Printing Office, Washington, D.C. (1954).
8. (a) Swanson H. E. and Tatge E., National Bureau of Standards Circular 539. U.S. Government Printing Office, Washington, D.C. (1953).
   (b) Swanson H. E., Fuyat R. K. and Ugrinic G. M., National Bureau of Standards Circular 539. U.S. Government Printing Office, Washington 25, D.C. (1953).
9. Darken L. S. and Gurry R. W., *Physical Chemistry of Metals.* McGraw-Hill, New York (1953).

Vol.
196

BOOK REVIEWS

D. CURIE: **Luminescence Cristalline.** Dunod, Paris, 1960. 209 pp.

A DECADE ago the textbooks on luminescence by Kroger, Garlick, Adirowitsch, Pringsheim and Leverenz were all published within the span of a few years. Since then there have been and continue to be advances in the fundamental understanding of solid-state luminescence in both ionic and semiconducting phosphors. Although this work has been summarized in review articles and in reports of symposia, this pocket sized French monograph by Professor CURIE is the first textbook to take advantage of the increased understanding of luminescence in crystals achieved during the past decade.

This book is based on a series of lectures on the luminescence of crystals given by the author at the Faculté des Sciences de Paris. Although the author and his colleagues at the Laboratoire de Luminescence are best known for their research on electroluminescence, this text is almost exclusively confined to photoluminescence. The approach is largely theoretical.

After carefully defining the terms used in the field of luminescence, the author reviews radiation theory deriving the transition probabilities for the absorption and emission of electromagnetic radiation by atomic systems. He then treats in considerable detail "quasi atomic" impurity systems, such as Tl^+ in KCl:Tl, with the aid of the configuration coordinate model. The experimental determination and use of this model for more complex phosphors such as tungstates, willemite and the halophosphates are also considered. Photoconducting phosphors are introduced by a brief theoretical treatment of band to band transitions and by a brief discussion of the band structure of Ge and InSb. Recombination radiation in Si, edge emission in ZnS and CdS, and exciton spectra are then considered. The phosphorescent sulfides, for example, ZnS activated with Cu, are discussed in considerable detail. Their preparation, intrinsic optical properties, and the relative ionic and covalent character of the bonding are reviewed. The various types of luminescent centers and the equally varied theories of the energy levels involved in the excitation and emission of this class of phosphors are discussed with reasonable impartiality. Finally, the possible nature of trapping states and the role of traps in phosphorescent, thermoluminescent and optical stimulation phenomena is reviewed experimentally and analyzed theoretically. Among the theoretical aspects which are not included are the thermodynamic limitations of solid-state luminescence and the application of crystal field theory to transition and rare earth metal luminescent centers.

The text is not without speculations and errors. For example, the author attributes the depths of traps in ZnS to hydrogen molecule-like states whereas the depths probably arise from the large central cell correction for the coactivators or donors in this material. The errors are, however, surprisingly few considering the complexity of the field of luminescence.

This book is recommended to those interested in the luminescence of inorganic crystals. Because of the prevalence of equations and figures and because of the simplicity of presentation, only a limited knowledge of French is needed in order for solid state chemists and physicists to profitably study this compact monograph.

F. E. WILLIAMS

G. S. CHRISTIANSEN and PAUL H. GARRETT: **Structure and Change, an Introduction to the Science of Matter.** W. H. Freeman, San Francisco and London, 1960. xv + 608 pp., 63*s*.

"NEITHER Physics nor Chemistry has meaning independent of the other . . . the great theories of one are the great theories of the other, . . . and even the practitioners of the two sciences are mostly interchangeable." While one may take issue with the last part of this statement from *Structure and Change*, it is by and large true, and CHRISTIANSEN and GARRETT have clearly shown the great interdependence of the two sciences in their introductory text. They have combined most of the information usually presented in freshman courses of physics and inorganic chemistry together with a seasoning of astronomy, physical geography and history to make a most

readable book. It is complete enough to be used as a text for students planning to major either in physics or chemistry, although its broad approach will probably lead more often to its being used for a physical science survey course.

The first of the three major sections starts with a description of the apparent movements of the planets and of the difficulties encountered by Ptolemy in devising a model that would permit the positions and movements to be satisfactorily calculated. The Copernican heliocentric system enabled the positions to be calculated with greater ease, but with no greater accuracy because circular orbits were used. The observation of the phases of Venus by Galileo, however, provided the convincing evidence that the Copernican model was correct. This introduction is used to lead the student into a discussion of force, motion, and mechanics.

The general approach is strongly reminiscent of that recommended in 1946 by J. B. CONANT in his small book *On Understanding Science*. It differs from the *Harvard Case Histories of Science*, however, in that it is a complete course in chemistry and physics, and there is little quotation of original papers. This historical approach is used throughout, so that some feeling for CONANT's *Tactics and Strategy* of science is developed.

The first section continues with a more or less standard attack on atomic theory, the periodic table, the gas laws, etc., but concludes with an extensive description of the earth, the atmosphere, and weather. The second major section includes fundamentals of electricity and magnetism, valence, electrochemistry, and some most elementary chemical thermodynamics. The final section is concerned with light, the concepts of modern physics, and the usual discussions of atomic structure and nuclear energy.

In spite of the novelty of the presentation, the scope of the chemistry and physics is rather standard for a freshman text. For a book whose central theme is "the science of matter" it is disappointing to find that the properties of solids are almost completely neglected. No reference is made to problems of mechanical strength, semiconduction or any aspect of solid state reactions. Only about three pages are devoted to crystal structure. Magnetism is discussed at some length, but purely phenomenologically. Metallurgy is represented as being concerned only with the reduction of metals from their ores.

Except for this major oversight, the book is refreshing and scholarly. It is attractively printed, profusely illustrated with excellent drawings and well bound.

J. E. BURKE

M. J. BUERGER: **Crystal-Structure Analysis.** John Wiley, New York, 1960. 668 pp. $18.50.

IT IS a novel experience for me to review a single-volume textbook that sells for $18.50, and I approach the task with some trepidation.

Technically, *Crystal-Structure Analysis* is superb. The type is large and, in my reading, I found no typographical error. The illustrations are numerous and clear; in a photograph on p. 109, for example, we can see—reduced by a factor of about 2—not only a crystal of diameter I estimate at 0·8 mm., but also the glass capillary on which it is mounted and which is probably not thicker than 0·2 mm. (Only on pp. 486–7, where are presented photographs of Patterson–Tunnell Fourier summation strips, is the quality of the illustrations poor—and here it is very poor.) The tables are well planned and clearly presented; the binding is attractive and seems to be sturdy. The publishers are certainly to be congratulated on the construction.

Although I have some complaints, in general I applaud Professor BUERGER's latest effort and feel that it is a welcome addition to the pitifully small library of crystallographic texts. In the Preface he says that he hopes the book "will serve as an introduction to the subject of crystal-structure analysis"; and with this in mind he has obviously made an effort to present the simple aspects of the subject and to develop these aspects from the simplest of concepts. I thoroughly approve of such a philosophy; however, there are a number of instances where it is over-done. I shall come to them later.

The first 240 pages of *Crystal-Structure Analysis* deal with the fundamentals of diffraction and the collection of X-ray diffraction data; the discussion is simple but thorough, and should be of great value to a beginning crystallographer. The next 100 pages cover methods of determining simple

Vol. 1
196

structures—and many of my complaints are centered in this portion of the book, which I find too detailed and somewhat trivial. Fourier series and reciprocal space are discussed for the next 150 pages, again in rather exhausting detail. Eighty pages are devoted to special methods of phase determination, such as heavy-atom techniques and direct methods. Refinement procedures are allocated only 40 pages, and the final five pages are devoted to the calculation of interatomic distances and angles from the derived coordinates. Thus, the sequence is roughly that normally encountered in a crystal-structure determination.

Most of the aspects of X-ray crystallography are discussed in great detail, but a few receive only passing notice. The determination of unit-cell parameters is not discussed at all, and although this topic received full coverage in the author's earlier work, *X-ray Crystallography*, many advances have been made in the intervening eighteen years. Disordered structures are not discussed, and anisotropic temperature factors are only briefly mentioned. For a discussion of Patterson methods, the reader is referred to another earlier work, *Vector Space*. It is this reviewer's opinion that it would have been better to have included these topics while condensing much of the remaining presentation.

My major objection to *Crystal-Structure Analysis*, though, is that much of the discussion is so detailed as to be almost painful. As one example, on p. 243 a method for computing the number of molecules in the unit cell, given the lattice constants, the density, and the molecular weight, is presented. Along the way the constant $1{\cdot}660 \times 10^{-24}$ is introduced in order to convert from atomic weight units to grams. The derivation of this constant is given in a footnote. It consists of multiplying the atomic weight of oxygen, 16, by 2 to obtain the molecular weight of an oxygen molecule, dividing by Avogadro's number, and multiplying by 1/2 to obtain the mass of an oxygen atom, $2{\cdot}6565 \times 10^{-23}$ grams; this, in turn, is divided by 16 to yield the desired constant—which, of course, is nothing but the reciprocal of Avogadro's number.

Although this example is a flagrant one, it is not atypical. Also on p. 243 we find the equation $G = NM/V$, followed on p. 244 by $N = GV/M$ and $NM = GV$. On pp. 235–236, $y = Ax$ is followed immediately by $A = y/x$. Almost all of p. 254 is spent in a tabulation of the twenty-four ways (many of which, as the author points out, are duplicates) in which two iron atoms and four sulfur atoms can be distributed among two four-fold positions (called "equipoints") and four two-fold positions. On p. 205, it takes two intermediate equations to go from "$-\log I_0 + \log I = -\mu t$" to "$I = I_0 \exp(-\mu t)$". Further examples are numerous.

But I do not wish to be too harsh, as I believe that much of the presentation is particularly valuable because of its thoroughness. The bibliography is extensive, and I would rate *Crystal-Structure Analysis* as an excellent reference book. I would hesitate to recommend it as a textbook, however, not only because of its high cost but because I feel that, by presenting so much detail of a trivial nature, it talks down to the reader. I do not believe today's student wishes to be talked down to, or should be.

RICHARD E. MARSH

ERRATA

J. B. MULLIN and K. F. HULME, Orientation-dependent distribution coefficients in melt-grown InSb crystals, *J. Phys. Chem. Solids* **17,** 1 (1960).

The first line of the following figure captions should read as follows:

FIG. 2. Photograph of crystal end $\times 3\frac{1}{7}$.

FIG. 3. Photograph of crystal end $\times 3\frac{1}{7}$.

FIG. 4. Photograph of crystal end of R15 $\times 3\frac{1}{7}$.

G. B. GUTHRIE and J. P. MCCULLOUGH, Some observations on phase transformations in molecular crystals, *J. Phys. Chem. Solids* **18,** 53 (1961).

The address of the above authors is as follows:

Thermodynamics Laboratory,
Petroleum Research Center,
Bureau of Mines,
U.S. Department of the Interior,
Bartlesville,
Oklahoma, U.S.A.

Vol. 19
1961